JOINT EUROPEAN TORUS JET

JET–P(95)31

Many Authors

JET Posters Presented at the 22nd EPS Conference on Controlled Fusion and Plasma Physics

(3rd-7th July 1995, Bournemouth, UK)

Volume 1

Volume 2

MONDAY

ITER Relevant ρ_* Scaling Experiments for ELMy H-modes in JET

B Balet, D Campbell. J P Christiansen, J G Cordey, C Gormezano, C Gowers, C Lowry, E Righi, D Muir, G R Saibene, M Stamp, P M Stubberfield.
JET Joint Undertaking, Abingdon, Oxfordshire, OX14 3EA, UK.

BACKGROUND

Previous Larmor radius scaling experiments completed on TFTR, JET and DIII-D were done in an L-mode plasma and the scaling of the global confinement was found to be Bohm-like and in agreement with the ITER89P L-mode scaling expression. The operational regime, proposed for ITER is the ELMy H-mode regime and the scaling in this regime derived by the ITER data base[1] group was the ITER93H scaling expression. This scaling expression has a close to gyro-Bohm scaling ($\chi \sim \chi_{Bohm}\, \rho_*^{0.8}$). The ITER expert group on confinement and transport has asked that ρ_* scaling experiments in which the remainder of the dimensionless parameters q_ψ, κ, β, ν_* are close to their ITER values be performed on all of the experiments with similar geometry to ITER so that the ITER93H scaling can be confirmed. ELMy H-mode ρ_* scaling experiments[2] have already been completed by the DIII-D team and a gyro-Bohm scaling was found.

Two series of ρ_* scaling experiments have been completed on JET and the first results are reported below.

1. PULSES AT 1MA/1T AND 2MA/2T WITH $\kappa = 1.7$, $q_\psi(0.95) = 3.4$, $\beta_l = 0.6$, $\nu_* = 0.008$.

(note powers required to achieve these conditions are well above the H-mode threshold).

Flux surface geometry

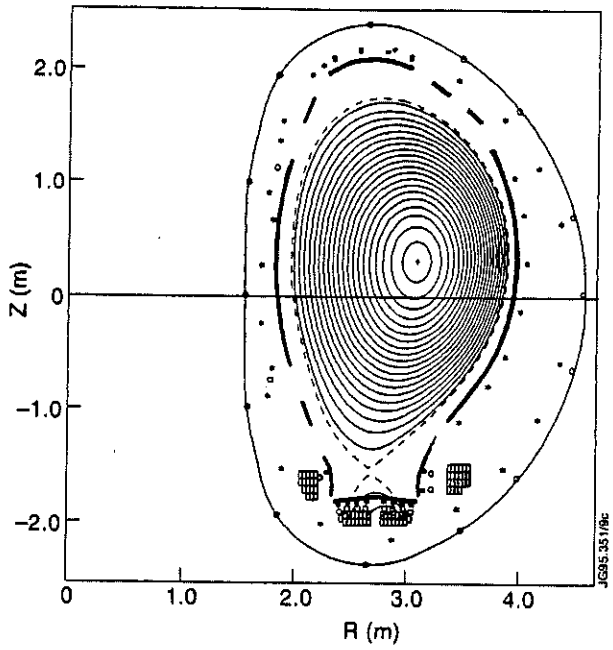

Fig.1: Geometry for 1MA/1T and 2MA/2T pulses, $q_\psi(0.95)$ = 3.4, κ = 1.7, triangularity δ ~ 0.2, β_n= 1.6, β_l = 0.6.

Pulse Characteristics

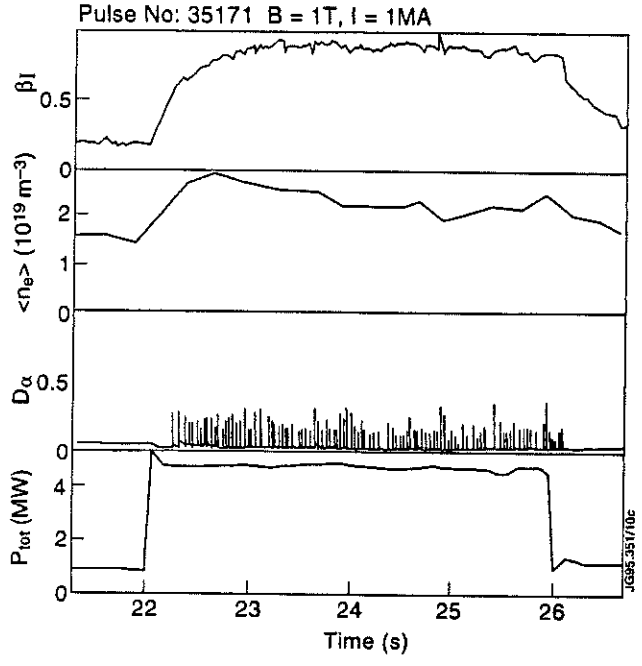

Fig.2(a) $\beta_{poloidal}$, volume average density, D_α, and total input power versus time for the 1MA/1T pulse #35171.

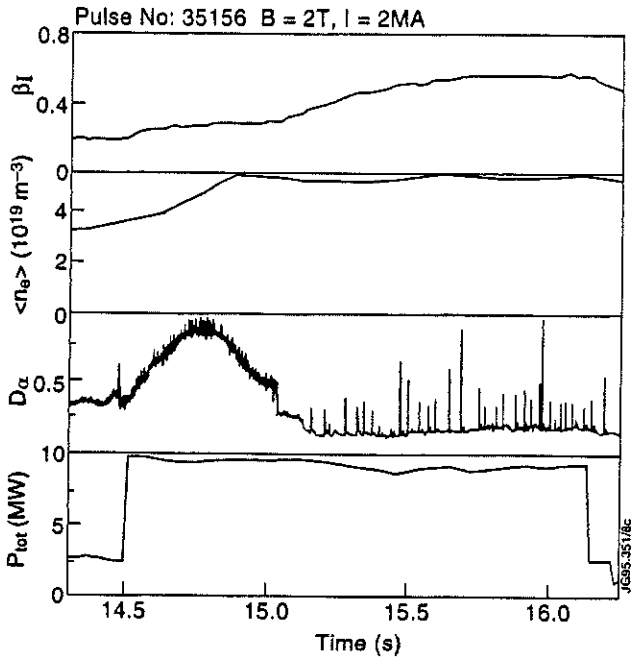

Fig.2(b) $\beta_{poloidal}$, volume average density, D_α, and total imput power versus time for the 2MA/2T pulse 35156.

Summary of the global confinement characteristics

Pulse no.	B(T)	I (MA)	$<n_e>/10^{19}$ m^{-3}	P(MW)	W_{tot}(MJ)
35171(25s)	1	1	2.2	4.85	1.05
35156(16.1s)	2	2	5.5	9.18	3.35

Pulse no.	W_{th}(MJ)	τ_{th}	H_{93}	H_{89}
35171	0.84	0.17	0.86	1.44
35156	3.2	0.35	0.9	1.8

The approximate linear scaling of τ_{th} with B indicates a gyro-Bohm dependence.

(gyro-Bohm $\tau_{th} \propto B$, Bohm $\tau_{th} \propto B^{1/3}$, Goldston $\tau_{th} \propto B^{o}$, Stochastic $\tau_{th} \propto B^{-1/3}$).

Local Analysis

The local transport analysis of the pulses 35171, 35156 has been completed using the TRANSP code, full data consistency was achieved for both pulses.

Scaled electron temperature profiles (raw data)

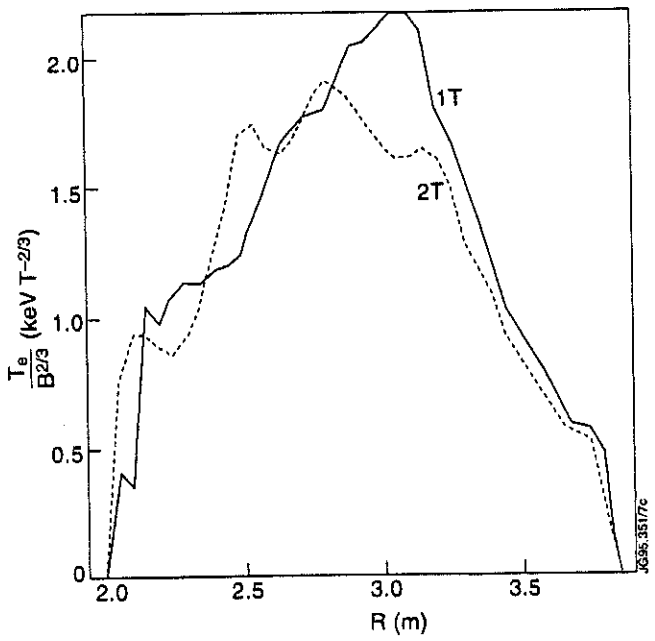

Fig.3(a) Temperature profiles from Lidar normalised by $B^{2/3}$ for pulses 35171, 35156.

Scaled density profiles (raw data).

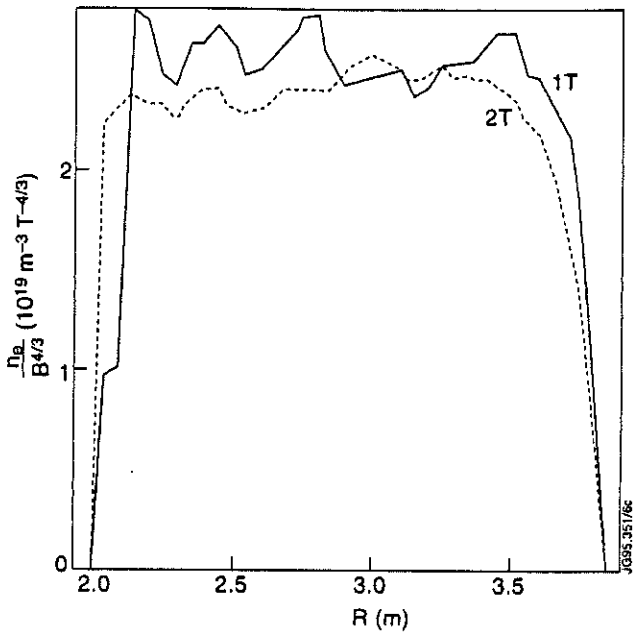

Fig.3(b) Density profiles from Lidar normalised by $B^{4/3}$ for pulses 35171, 35156.

χ_{eff} profiles and their ratio

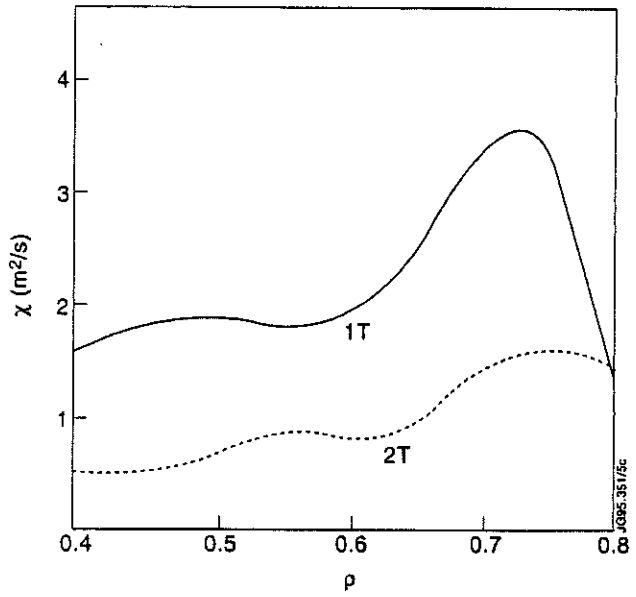

Fig.4(a) Effective thermal diffusivity versus normalised radial co-ordinate ρ for pulses 35171, 35156.

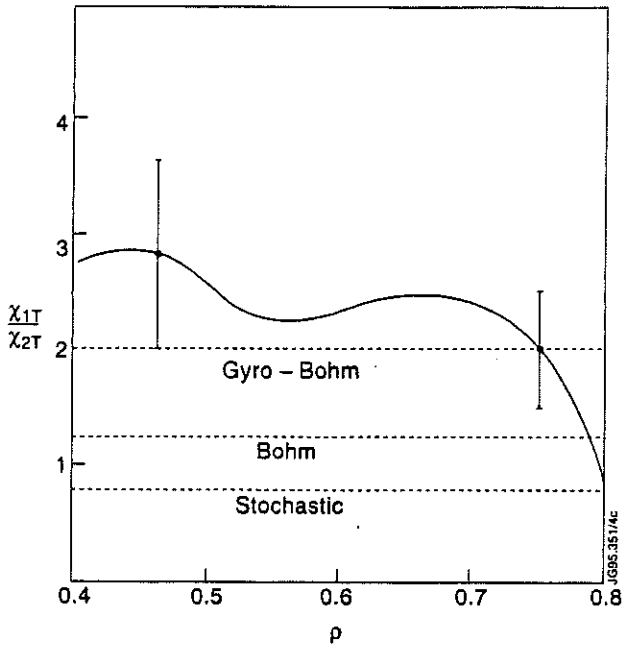

Fig.4(b)Ratio of the effective thermal diffusivities versus the normalised radial co-ordinate ρ for the 1T and 2T pulses. The dashed lines are the expected ratio for gyro-Bohm, Bohm and Stochastic scaling.

gyro-Bohm behaviour $\chi \propto \frac{1}{B}$

2. PULSES AT 1.6MA/1.7T AND 2.8MA/3T, q_ψ (0.95) = 3.7, κ = 1.8 β_l = 0.7, ν_* = 0.007.

(The power level in the 3T case was only just above the threshold power for H-modes).

Geometry

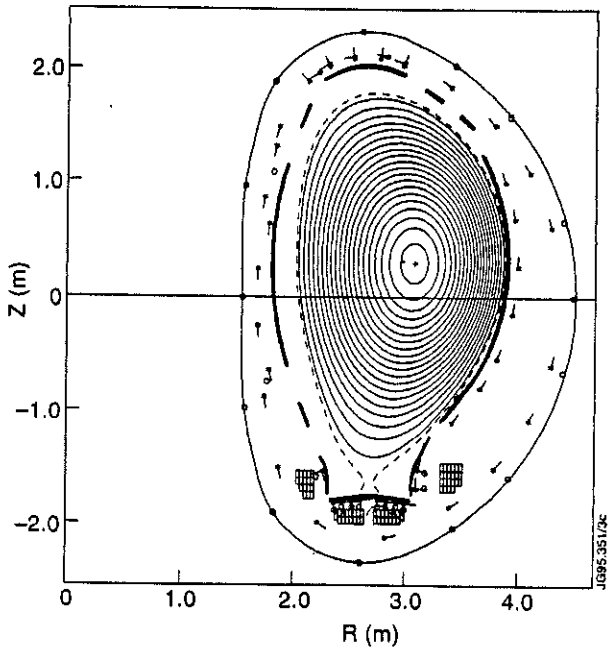

Fig.5: Geometry for the 1.6MA/1.7T and 2.8MA/3T pulses, $q_\psi(0.95)$ = 3.7, κ = 1.8, triangularity δ ~ 0.25, βn = 1.6, β_{tt}= 0.7.

Pulse Characteristics

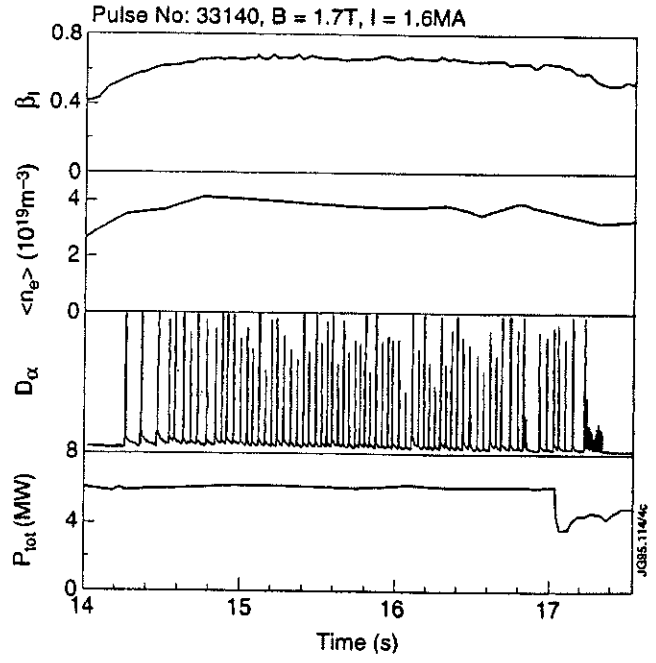

Fig.6(a) $\beta_{poloidal}$, volume average density, D_α, and the total input power for pulse 33140 (1.6MA/1.7T).

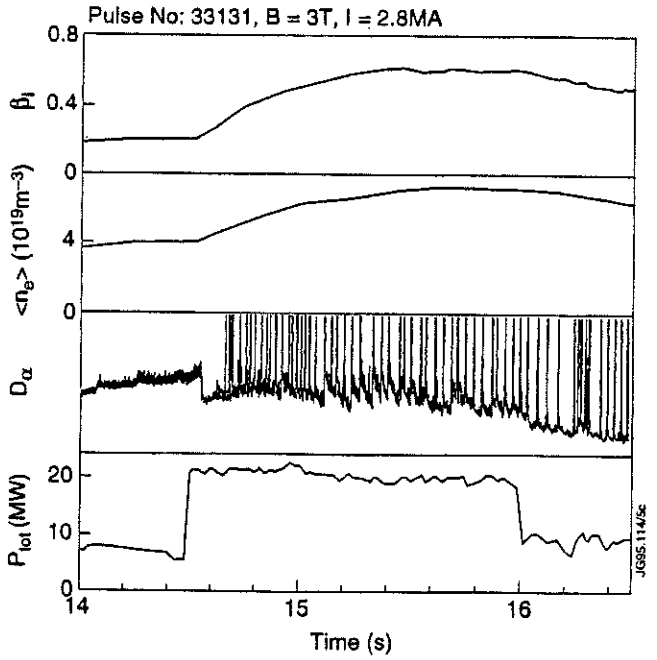

Fig.6(b) $\beta_{poloidal}$, volume average density, D_α, and the total input power for pulse 33131 (2.8 MA/3T).

Summary of global confinement characteristics

Pulse no.	B(T)	I(MA)	$\langle n_e \rangle 10^{19}\ m^{-3}$	P (MW)	W_{tot}
33140(16.6s)	1.7	1.6	3.6	6.3	2.5
33131(15.6s)	3	2.8	7.6	19.6	7.6

Pulse no.	W_{th}	τ_{th}	H_{93}	H_{89}
33140	2.3	0.36	0.95	2.05
33131	7.3	0.37	0.85	1.8

The scaling of $\tau_{th} \propto B^{0.05}$ gives a Bohm or Goldston like dependence.

DISCUSSION

The difference in the global energy confinement scaling between the two sets of pulses can be mainly attributed to a difference in the ELMing behaviour. In the 3T pulse the ELMS are of the compound type with the plasma returning to the L-mode state following each ELM.

By examining the scaling of the non-dimensional power versus ρ_*^{-3} for the four pulses one can see that the gyro-Bohm scaling cannot be maintained for dimensionally similar pulses as ρ_* is decreased since eventually the H→L threshold would be crossed, this is illustrated in Fig. 7.

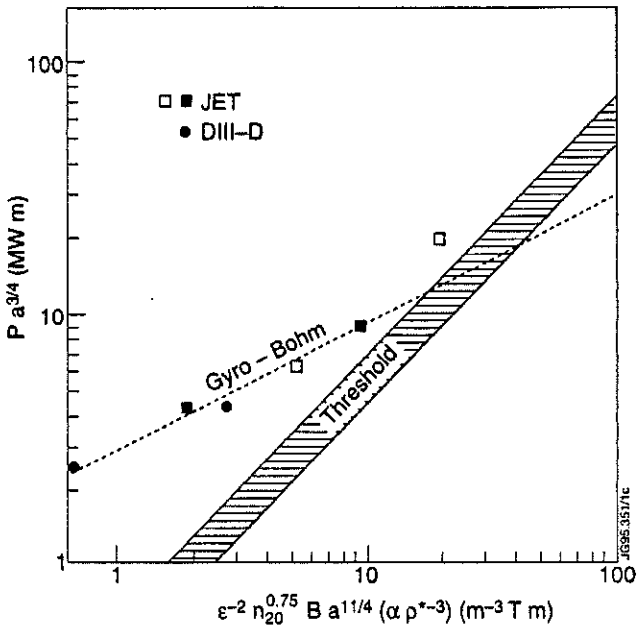

Fig.7:Normalised power $Pa^{3/4}$ versus $n^{0.75}$ $Ba^{11/4}$ ($\propto \rho^{*-3}$). The dashed line is the H-mode threshold expression from S.M. Kaye [3], the DIII-D points are from C. Petty et al.[2].

Comparing the global confinement data with the recommended ITER scaling expression 0.85* ITER93H we see that all the data from the ρ_* scaling series of experiments is very close to the recommended scaling Fig. 8. The 93H scaling is close to gyro-Bohm scaling as $\chi \propto \chi_{Bohm}\ \rho_*^{0.8}$ and so this is not surprising

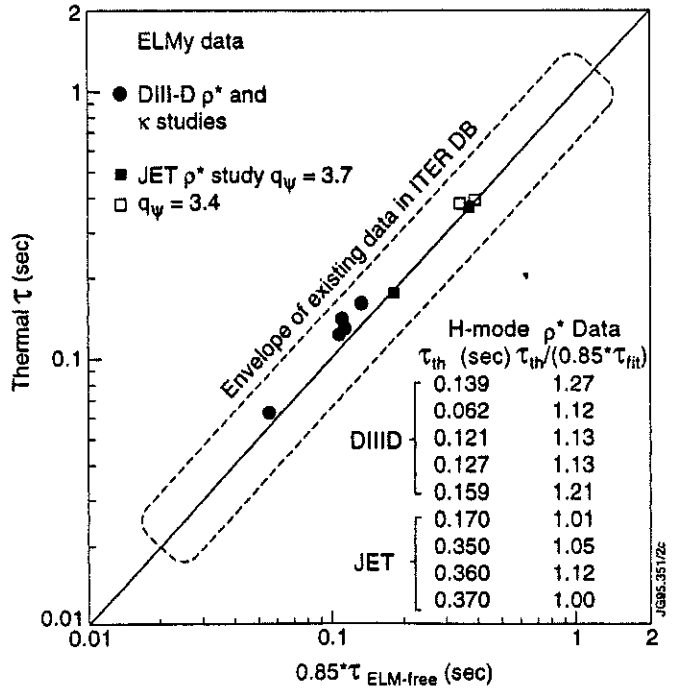

Fig.8: τ_{eth} versus 0.85 × $\tau_{\varepsilon 93H}$ for the JET and DIII-D data from C. Petty et al. [2].

However the results clearly show that one cannot expect this scaling to be valid for powers close to the threshold and this has implications for ITER which operates close to the H-mode threshold at full field.

SUMMARY

- **At power levels well above the H-mode power threshold both the global and local transport of these dimensionally similar pulses exhibits a clear gyro-Bohm like dependence.**

- **This confirms the validity of the close to gyro-Bohm like scaling of the ITER93H scaling expression.**

- **For pulses close to the threshold the transport follows a more Bohm/Goldston scaling, following the scaling essentially of the H-mode power threshold.**

ACKNOWLEGEMENT

It is a pleasure to acknowledge many useful discussions with Drs. C. Petty and T. Luce from G.A.

REFERENCES

1) K. Thomsen et al., Nucl. Fusion 34 (1994) 131.
2) C.C. Petty, T.C. Luce, K.H. Burrell et al., "Non-dimensional Transport Scaling in DIII-D: Bohm versus Gyro-Bohm Resolved. GA-A21904 (1995).
3) S.M. Kaye et al., IAEA-CN-60/E-P-3. Seville (1994).

Transport Analysis of the Giant ELMs in JET

V V Parail[1], P Bak, B Balet, J G Cordey, A Cherubini, M Erba, N Deliyanakis, M F F Nave[2], L Porte, E Springmann, A Taroni, G Vayakis.

JET Joint Undertaking, Abingdon, Oxfordshire, OX14 3EA, UK.

[1] Permanent address: RRC "Kurchatov Institute", Moscow, Russia.

[2] Associação EURATOM/IST, Lisbon, Portugal.

SUMMARY

Analysis of experimental data shows that typical giant (type I in accordance with DIII-D definition [1]) ELM in JET has a global character. It is initiated by a very short MHD event with an overall duration less than 1msec. Electron temperature decreases during this short time not only near plasma edge but far inside the plasma volume. The MHD event is usually followed by a much longer phase of enhanced transport (with $t \geq (10 \div 30)$) msec. Numerical analysis confirms that this second part of the giant ELM can be reproduced with an assumption that plasma transport properties correspond to L-mode confinement during this interval. Comparative analysis shows that this second part of the ELMs actually determines the global energy confinement in ELMy H-mode despite of the fact that an effective electron thermal diffusivity is much larger during the MHD event. Numerical simulation performed with the different transport models has indicated that the duration of L-mode phase is probably controlled by the impurity radiation - the longer is the time when the edge temperature is controlled by the impurities the longer is the duration of an L-mode phase.

INTRODUCTION

Giant ELMs give another interesting example of the fast global modification of plasma transport properties in JET. Following the DIII-D definition [1] we will discuss here only type I ELMs which repetition frequency increases with the heating power and which lead to a significant reduction in the energy content ($\Delta W/W \geq 0.1$).

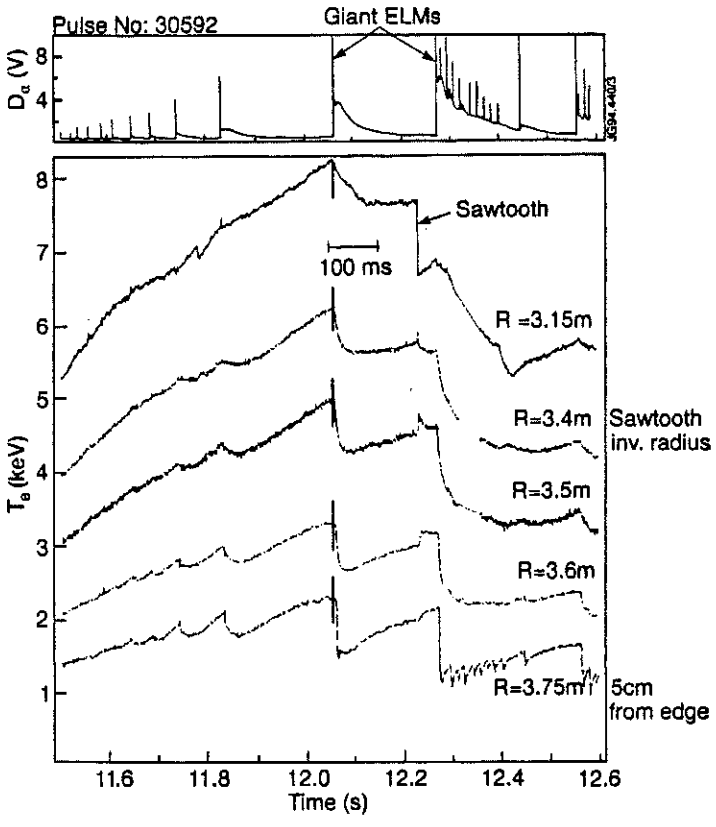

Figure 1. Time evolution of the D signal and of the electron temperature at different radii during giant ELMs in shot #30592.

The characteristic evolution of electron temperature during successive giant ELMs measured by the new 48 channels heterodyne radiometer system is shown in Figure 1, together with the D signal.

These measurements indicate that JET giant ELMs have a global character-the electron temperature is changed during the MHD event not only near plasma edge but far inside plasma volume. The characteristic radial extent of T_e drop at the onset of the ELM increases with ELM amplitude and reaches value of R comparable with plasma minor radius. The ELM appears to be triggered by a very short MHD event (with ≤ 1 msec), which is accompanied by the excitation of a broad band range of magnetic fluctuations (see Figure 2). This short MHD burst is usually followed by a relatively long (with $\Delta\tau_L \propto (10 \div 30)$ msec) phase of enhanced transport, after which the plasma returns to a quiescent H-mode phase. This second part of giant ELM is accompanied by a broad band of density fluctuations with a spectrum which is similar to those in L-mode plasma.

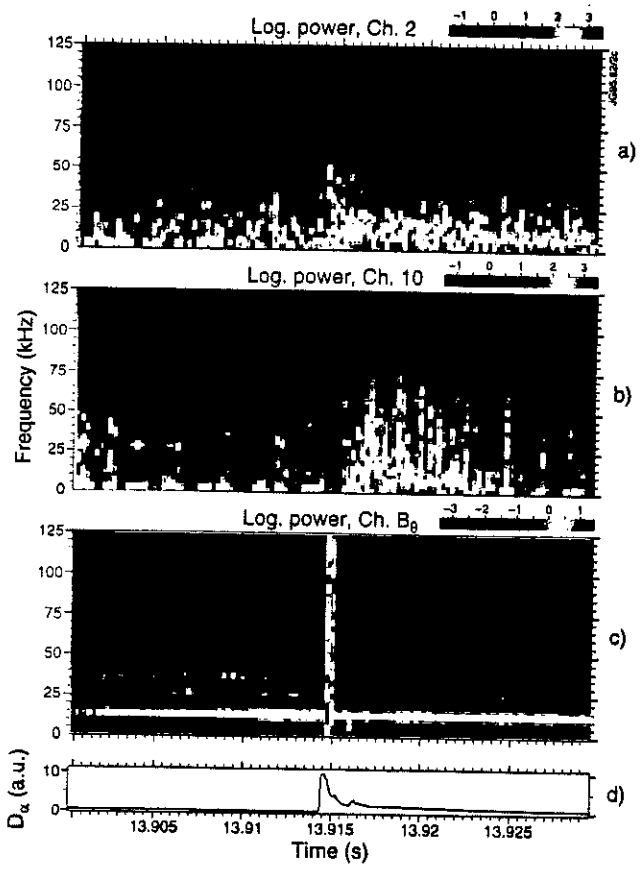

Figure 2. Time windowed power spectral analysis of a)channel 2 ($n=0.73e19m^{-3}$, $R=3.87m$), b) channel 10 ($n=6e19m^{-3}$, $R=3.77m$) and c) magnetic field fluctuations for shot #33032.

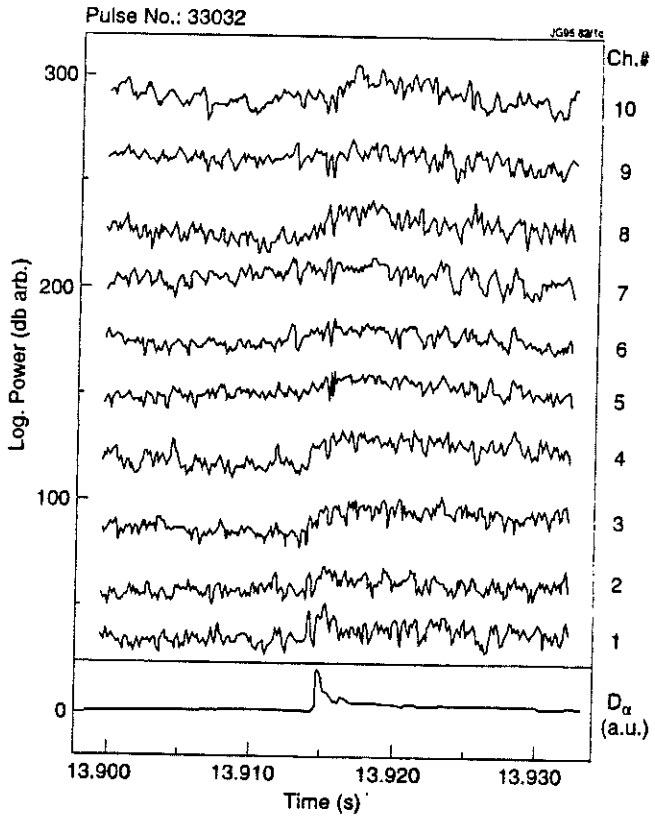

Figure 3. Broad-band activity, 10-125 kHz, on reflectometer channels 1 to 10, shot #33032.

Figure 3 shows the data from the recently installed multichannel O-mode reflectometry, spanning the frequency range 18-70 GHz, corresponding to critical densities in the range $(0.43\text{-}6)\times10^{19}m^{-3}$. The data indicate the relative increase in the fluctuation level for each channel, spanning the outer 10 cm of the edge plasma. In the outermost channels this increase is coincident with the rise of the D signal. In the innermost channels there is a delay of the order of

1 msec. Each giant is also accompanied by the burst of the impurity radiation which duration is comparable to the duration of the period with enhanced fluctuations.

Such a behaviour is similar to that found in DIII-D in the intermediate range of heating power and called compound ELMs [1]. Compound ELMs are quite regular in JET when the heating power is well above the threshold of L-H transition.

The main goal of our work was to perform the predictive numerical modelling of the typical giant ELMs in JET trying to find the answers to the following questions:

1. Is it possible to describe the evolution of the electron temperature during the short MHD event with a diffusive transport model, and if it's possible, which model could be used;
2. Could be the second, long phase of ELM with enhanced transport, described as a temporary transition back to L-mode;
3. Which part of the giant (compound) ELM - MHD or L-mode phase plays the dominant role in determination of the global, time average energy confinement in JET;
4. Does the impurity's radiation play a significant role in the determination of the ELM duration or it is a side effect;
5. And finally we tested different kind of transport models and boundary conditions trying to find the best agreement between experimental results and those of the numerical simulation.

DESCRIPTION OF THE MODELS

We will use different kinds of transport modes to describe three characteristic phase of the giant ELM: MHD event, L-mode-like phase and the phase of a quiescent H-mode. First of all we will use the "original" Bohm-type model proposed in [2] and used for the description of both L and ELM-free H mode JET plasmas:

$$\chi_e = \alpha_e \frac{c|\nabla(nT_e)|}{eBn} aq^2 \quad \text{and} \quad \chi_i = \chi_i^{neo} + \alpha_i \frac{c|\nabla(nT_e)|}{eBn} aq^2 \tag{1}$$

where $\alpha_i^L \approx 3\alpha_e^L \approx 6\cdot 10^{-4}$ for L-mode and $\alpha_i^H \approx 3\alpha_e^H \approx 6\cdot 10^{-5}$ for H-mode [3]. This model was also used to simulate short MHD event. In order to model this phase we adopt the following expression for the electron thermal diffusivity:

$$\chi_e^{MHD} = \chi_e^L \left(1 + \alpha \cdot \exp\left(\frac{1-\rho}{\Delta\rho}\right)\right) \tag{2}$$

where χ_e^L is the electron thermal diffusivity in L-mode, α is a numerical factor (varying from ELM to ELM, generally 10), is the normalised radial co-ordinate (ρ =1 at the separatrix) and $\Delta\rho$-normalised radial width of the region with enhanced transport (usually $\Delta\rho \leq 0.2$-0.3). We point out

that we are not proposing equation (2) as a model for the MHD event: from the use of equations (1-2) we will deduce the radial width of the MHD event and we will be able to evaluate the impact of the MHD event on the global confinement time. The second model under consideration is a modified version of equation (1) which explicitly assumes that the source of the plasma turbulence is localised near the separatrix, but due to either non-linear, or toroidal effects this turbulence produces anomalous transport everywhere and not only near the plasma edge:

$$\chi_e = \alpha_e \frac{c|\nabla(nT_e)|}{eBn} aq^2 \cdot \left|\frac{\nabla T_e}{T_e}\right|_{edge} \quad \text{and} \quad \chi_i = \chi_i^{neo} + \alpha_i \frac{c|\nabla(nT_e)|}{eBn} aq^2 \cdot \left|\frac{\nabla T_e}{T_e}\right|_{edge} \tag{3}$$

This model does not require any change of the coefficients α_e and α_i during L-H transition - the modification of the transport coefficients (3) is the direct result of the variation of the electron temperature near the separatrix.

We used two different approaches to describe the evolution of T_e near the separatrix. The simplest way is to take the edge temperature from the experiment. The second possibility is to calculate the edge temperature by using an appropriate boundary condition. We utilised different boundary condition for L and H-mode plasma. In both cases we simplified the problem by integrating the transport equations across the SOL. In L-mode plasma it leads to the following boundary condition:

$$\chi n \nabla T + \frac{3}{2} T D \nabla n \approx -\alpha \frac{\Delta}{L_{II}} V_{SOL} T n \tag{4}$$

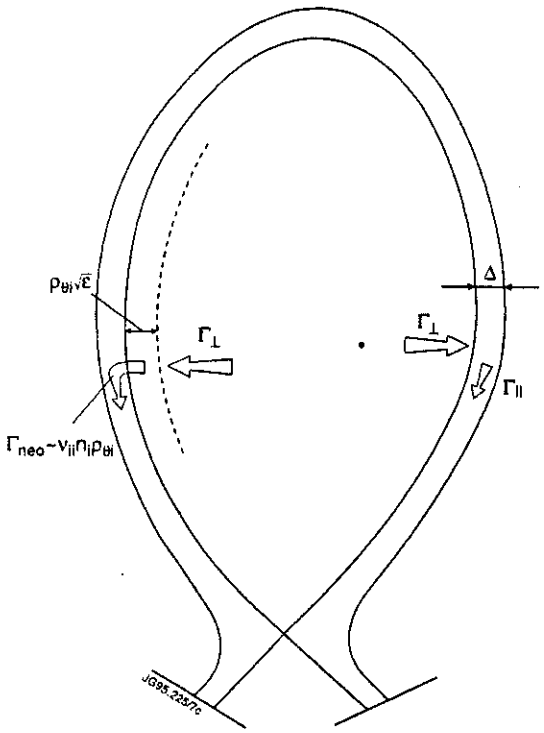

Figure 4. Schematic cartoon of the boundary condition.

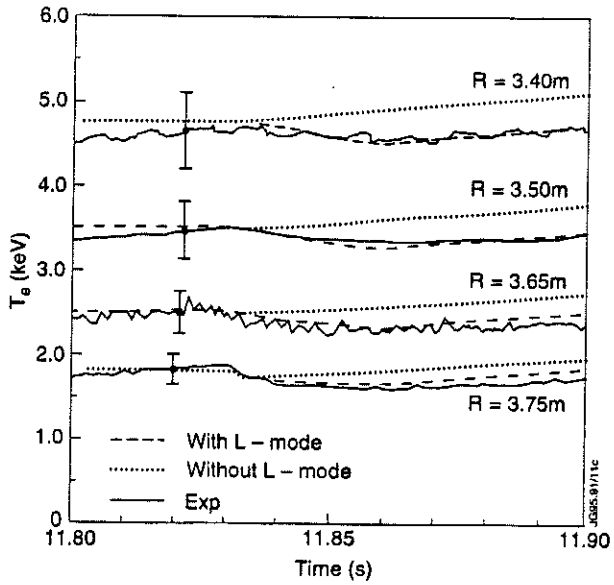

Figure 5. Time evolution of the experimental and simulated electron temperature at different radii; shot #30592

where T and n are plasma parameters near the separatrix and $\Delta \propto \sqrt{DL_{II}/V_{SOL}}$.

In H-mode plasmas we assume that the only mechanism of plasma losses through the separatrix is the direct losses of the banana ions [4], which leads to the following boundary condition for ion's heat flow (we assume that the electron heat flux is similar to the ion's one, Figure 4):

$$\chi n \nabla T + \frac{3}{2} T D \nabla n \approx -\frac{\chi_i^{neo}}{\rho_{pol}^i} T n \tag{5}$$

NUMERICAL SIMULATIONS

We simulated a series of typical giant ELMs in JET trying to find which part of the ELM is the most important for the determination of the experimentally observed energy confinement in the ELMy H-mode. In the first series of simulations we used the "original" Bohm-type model for all three phases - MHD event, L-mode phase and H-mode phase. The characteristic example of such simulations is shown in Figure 5 for one of the ELM of shot #30592. As it can be seen, the L-mode phase is necessary in order to obtain reasonable agreement with the data.

From our simulations we can also deduce an information on the relative importance of the various phases in determining the global energy confinement time of ELMy H-mode JET plasmas. In order to proceed in this way, we have to define a proper time average of the energy confinement time for ELMy H-mode plasmas $\left\langle \tau_E^{th} \right\rangle$:

$$\frac{1}{\left\langle \tau_E^{th} \right\rangle} = \frac{1}{\Delta t_\Sigma} \left(\frac{\Delta t_{MHD}}{\tau_E^{MHD}} + \frac{\Delta t_L}{\tau_E^L} + \frac{\Delta t_H}{\tau_E^H} \right) \tag{6}$$

where τ_E^{MHD}, τ_E^L, and τ_E^H are the computed energy confinement time during MHD , L-mode and H-mode phases of the compound ELM respectively and Δt_{MHD}, Δt_L and Δt_H - the characteristic duration of these phases. For further discussion it is convenient to introduce the enhancement factor $H_\chi \equiv \left\langle \tau_E^{th} \right\rangle / \tau_E^{ITER89-L}$ which shows how much an effective energy confinement time in ELMy H- mode exceeds the level of L-mode confinement. The main characteristic of plasma confinement of the three successive ELMs of shot #30592, discussed earlier, of the compound ELMs of shot #33032 and of shot #33648 are listed in the Table. From this table the relative importance of the various phases of ELMs in determining of the time average electron thermal conductivity of ELMy H-mode JET plasma can be deduced. For example, the parameter $\Delta t_{MHD} \cdot \tau_E^L / \Delta t_L \cdot \tau_E^{MHD}$ in the Table shows the relative importance of the MHD phase. It follows from our analysis that in the case of giant ELMs the L-mode phase is the most important one in

determining the global confinement in JET, while the MHD event is less important due to its short duration.

shot	Δt_{mhd} (ms)	τ_E^{MHD}(s)	Δt_L (ms)	τ_E^L(s)	Δt_H(ms)	τ_E^H(s)	$\langle\tau_E\rangle$(s)	$\frac{\Delta t_{MHD}\cdot\tau_E^L}{\Delta t_L\cdot\tau_E^{MHD}}$	H
#33648	1	0.05	40	0.25	120	1	0.53	0.125	2.13
#33032	2	0.04	40	0.41	80	2.3	0.67	0.5	1.8
#30592 large	3	0.04	30	0.18	130	1.1	0.45	0.45	2.1
#30592 medium	3	0.06	30	0.2	180	1.15	0.6	0.33	2.8
#30592 small	2	0.06	20	0.2	70	1.3	0.49	0.33	2.3

Our next step was to use the new boundary conditions which allow to simulate the evolution of the edge temperature self-consistently. The result of the numerical simulation of the giant ELM from the shot #33648 with new and old boundary conditions is shown in Figure 6. The main conclusion of the simulation is that depending on the longitudinal velocity V_{SOL} in the SOL the electron temperature near the separatrix either returns to its high level (which corresponds to H-mode confinement) or stay on a very low level. We did not manage to reproduce the experimentally observed slow recovery of the edge temperature. The qualitative explanation of this fact can be understood from Figure 7.

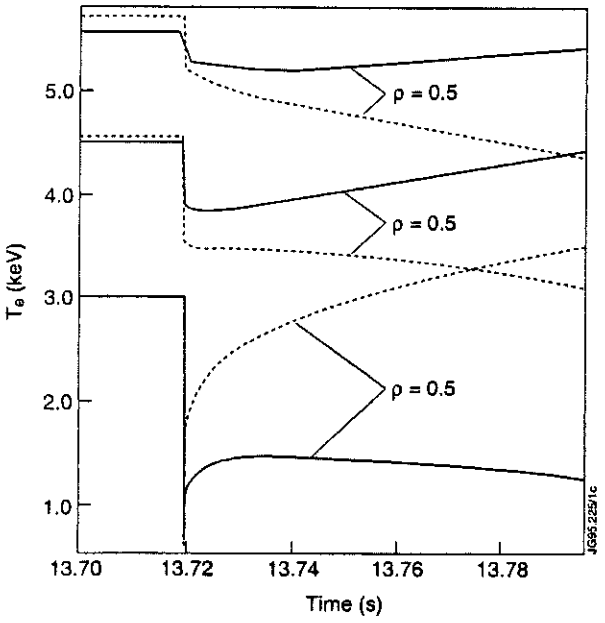

Figure 6. Evolution of the simulated T_e with the new boundary condition for shot #33648.

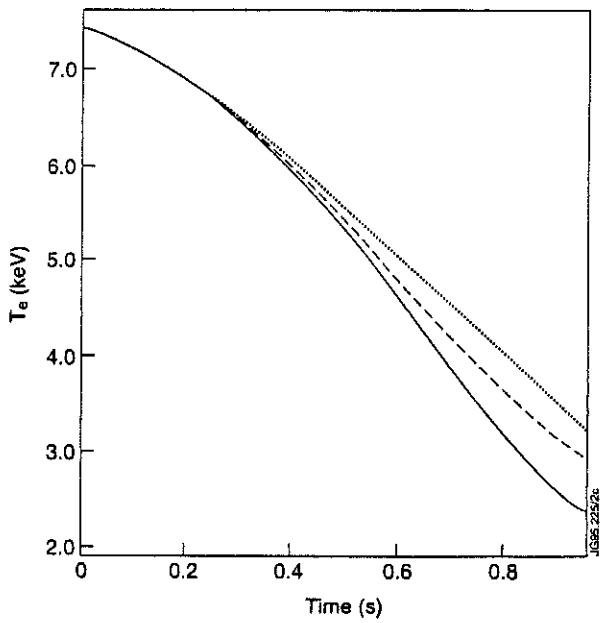

Figure 7. Cartoon of the T_e profile evolution during ELM.

In our simple model plasma has no such a characteristic time as it is observed in experiment - the filling of the temperature drop near the edge, produced by the short MHD event, turns out to be much shorter. It follows also from Figure 5 and 6 that both new and old boundary conditions

when used with the "original" Bohm-type model have certain difficulty in the modelling of the temperature in the mid radius region - experimentally observed transition from the phase with enhanced transport (L-mode-like) to the quiescent H-mode is smooth.

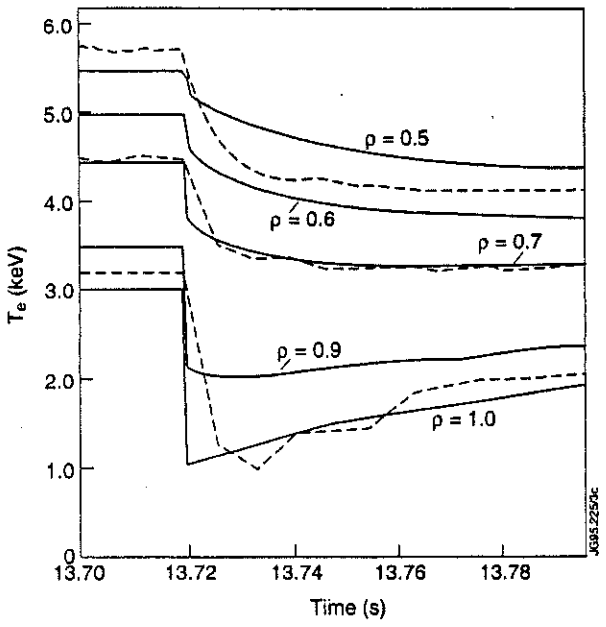

Figure 8. Time evolution of the experimental and simulated T_e evolution with modified Bohm model; shot #33648.

Therefore our next step was to try the modified Bohm-type expression for the energy transport in order to reach better agreement with experiment. As it was mentioned earlier, the selected "modified" Bohm-type model depends explicitly on the relative temperature gradient near the separatrix. Therefore it automatically changes transport in the confined region depending on the boundary conditions (the heat flux through the separatrix) and the level of the radiation near the edge. The results of the numerical simulation of the giant ELM from shot # 33648 with either prescribed edge temperature or with new boundary conditions without any radiative losses and "modified" Bohm-type model are shown on Figure 8 and allow us to conclude that the new model gives qualitatively good agreement in the mid-radius temperature evolution, but still cannot reproduce slow recovery of the edge temperature when used together with the new boundary conditions.

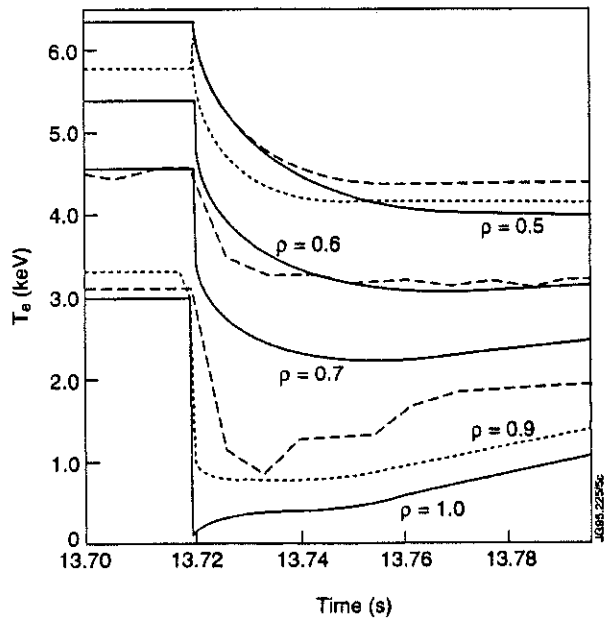

Figure 9. Time evolution of the experimental and simulated T_e evolution with modified Bohm model and imposed radiation; shot #33648.

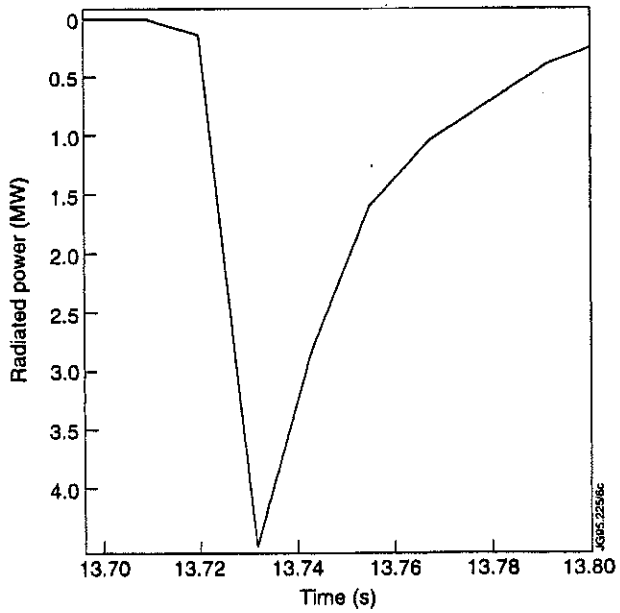

Figure 10. Time evolution of the radiated power.

Finally we studied the role of the impurity radiation on the evolution of the edge temperature. Figure 9 shows the result of the modelling of the ELM from shot #33648 with new model, self-consistent boundary conditions and imposed evolution of the impurity radiation profile (shown in the Figure 10). The result allows us to conclude that the evolution of the impurities during the giant ELM can control the evolution of plasma energy content not only because it imposes new energy sink but also because it can be responsible for the modification of the anomalous transport coefficients.

CONCLUSIONS

Experimental study and transport analysis of giant ELMs in JET revealed that such ELMs have a composite structure - each of them is triggered by a short MHD event which modifies the electron temperature not only near plasma edge but also far inside the plasma volume. This short MHD event turns into a much longer phase of enhanced transport that could be modelled as an L-mode. A quiescent H-mode phase then follows. Therefore the ELMy H-mode plasma in JET (in cases when type I ELMs are dominant) is a composition of three different phases: short (with $\tau_{MHD} \approx 1ms$) MHD with transport coefficients much larger that in L-mode plasma, longer (with $\tau_L \approx 10-30ms$) phase of enhanced transport during which transport corresponds to L-mode confinement and finally ELM-free H-mode phase. The relative importance of each phase depends on the amplitude of the ELM with the general trend that relative importance of the L-mode phase grows with ELM amplitude. Numerical analysis shows the general trend that relative importance of L-mode phase grows with ELM amplitude. Numerical analysis shows the importance of the impurity radiation for the explanation of the duration of the L-mode phase of Giant ELMs.

REFERENCES

[1] Schissel, D.P., et al., Proc. 19th European Conference on Controlled Fusion and Plasma Physics, Innsbruck, Austria, 1992, Vol.1, p. 235.

[2] Taroni A., et al., Plasma Physics and Contr. Fusion, **36**, (1994), 1629.

[3] Parail V., et al., 15th IAEA Conference on Plasma Physics and Contr. Nuclear Fusion Research, Seville, Spain 1994, CN-60/A-2-II-3.

[4] Weisen H., et al., Nuclear Fusion **31**, (1991), 2247.

Influence of Edge Instabilities on JET High Performance

T C Hender[1], B Alper, N Deliyanakis, G T A Huysmans, T T C Jones, R W T König, K D Lawson[1], P J Lomas, F B Marcus, M F F Nave[2], D P O'Brien, L Porte, B Schunke, P Smeulders, P R Thomas.

JET Joint Undertaking, Abingdon, Oxfordshire, OX14 3EA, UK.

[1] UKAEA Government Division, Fusion, Culham, Abingdon, Oxon, OX14 3EA, UK. (UKAEA/EURATOM Fusion Association)

[2] Associação EURATOM/IST, Inst Superior Tecnico, Lisbon, Portugal.

ABSTRACT

Giant ELMs, or coupled giant ELMs and sawteeth, are a fairly common cause of performance limitation in high neutron yield discharges. These ELMs lead to a rapid decline in the D-D neutron production rate (dR_{dd}/dt~$-10^{17}s^{-2}$). This decline is related to an impurity influx causing dilution of the fuel ions and a decrease of T_i. Detailed scans show a strong correlation between ELM free period and edge magnetic shear. This suggests ideal ballooning modes may be responsible for the giant ELMs, it remains unclear however if the ballooning modes establish an edge dP/dr limit or actually cause the ELMs.

INTRODUCTION

- High D-D neutron yield plasmas (I_p=3-4MA) established in new JET divertor configuration.
- Hot ion mode discharges ($T_i(0)$~20keV, $T_e(0)$~10keV) established by high power neutral injection (P_{NBI}~15-20MW) into low target density plasmas

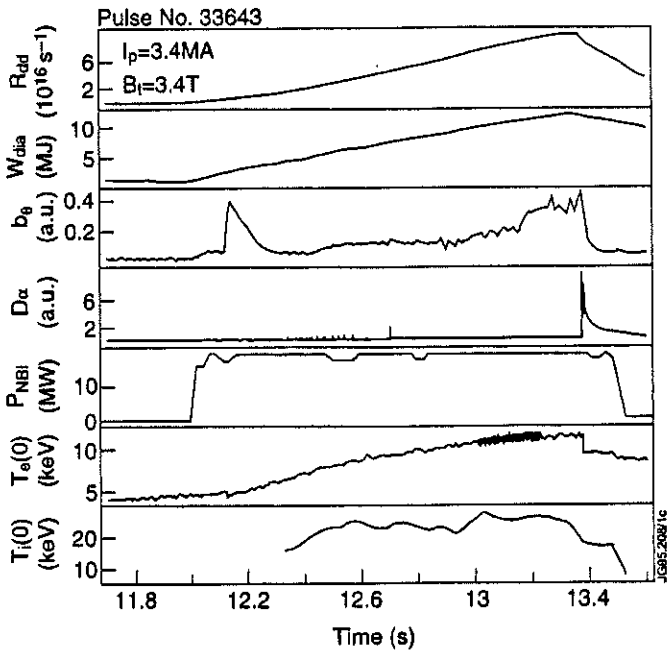

Record neutron yield Pulse 34643. Note termination of high neutron yield phase due to MHD. (The 'activity' on T_e at t~13.1s is due to an increased sampling frequency)

- With very few exceptions the high performance phase in these discharges is terminated by MHD activity.
- The main processes involved are:-.
  - Giant ELMs
  - Internal MHD (Sawteeth and Mirnov Oscillations, discussed in Smeulders et al poster/paper)
- In ~30% of discharges an MHD event occurs before R_{dd}(max) which lowers its rate of increase
- In nearly all discharges an event at R_{dd}(max) causes a rapid decline ($dR_{dd}/dt \sim -10^{17} s^{-2}$)

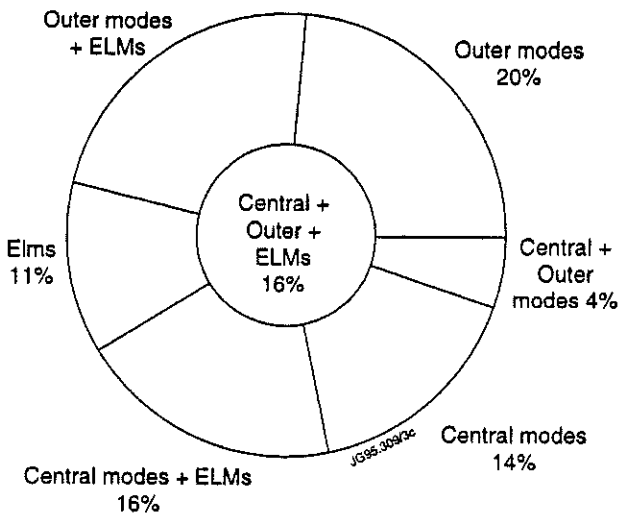

EXPERIMENTAL RESULTS

- Typical pulse (I_p=3MA, B_t=3.4T) in which an ELM limits neutron yield

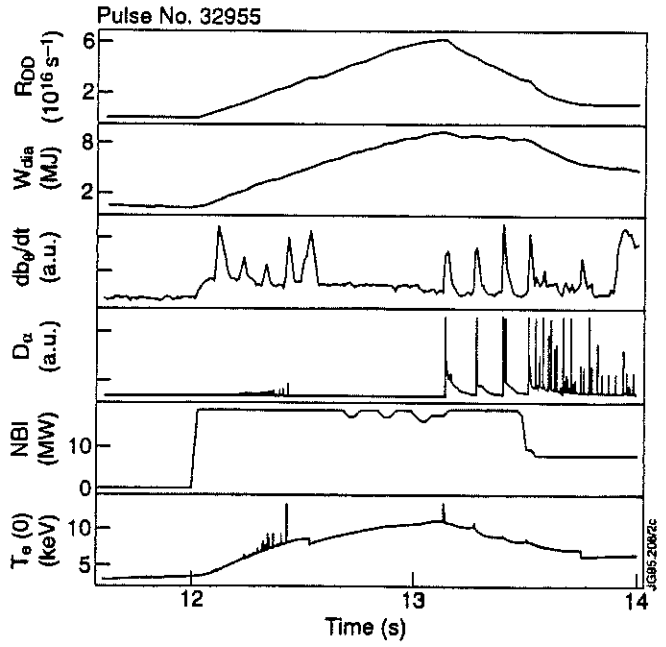

- Although these are termed ELMs due to their D_α character they affect a substantial part of major radius, with inversion ~15cm within separatrix

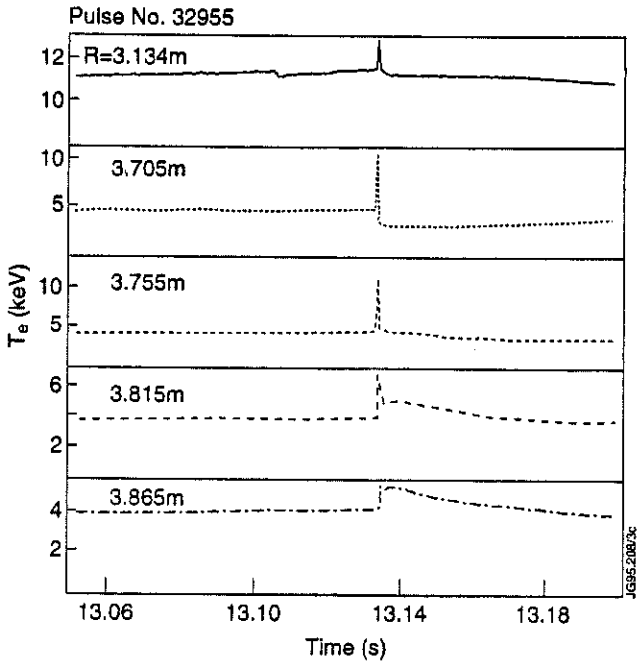

Temperature from ECE. Spikes are due to non-thermal emission.

- ELMs may also occur simultaneously with sawteeth

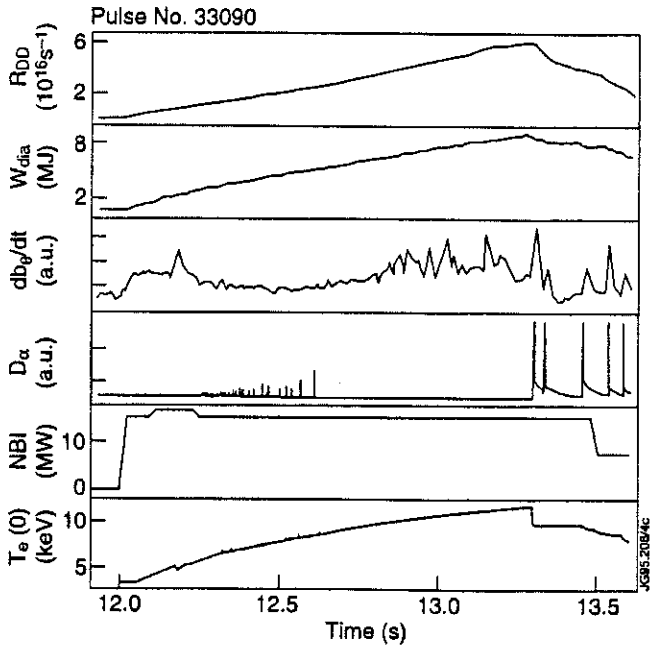

- In which case entire minor radius is affected

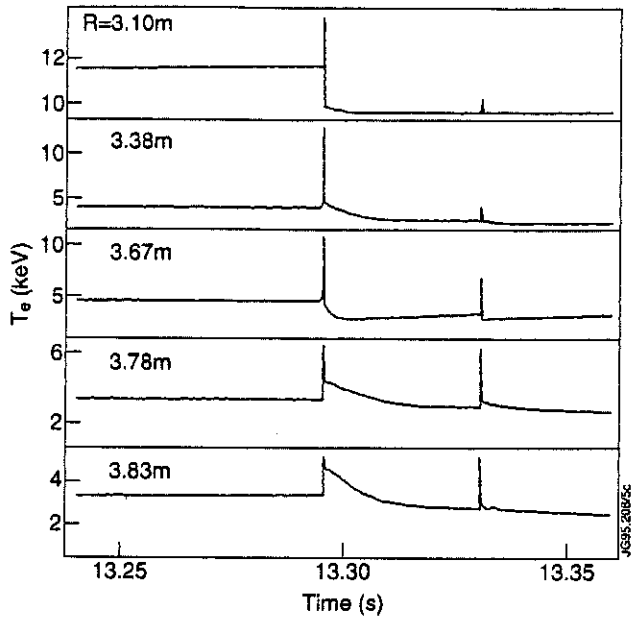

CONSEQUENCES OF ELMS

- Giant ELMs lead to enhanced radiative power loss which is transiently comparable to input power and typically represents a 1MJ energy loss per ELM

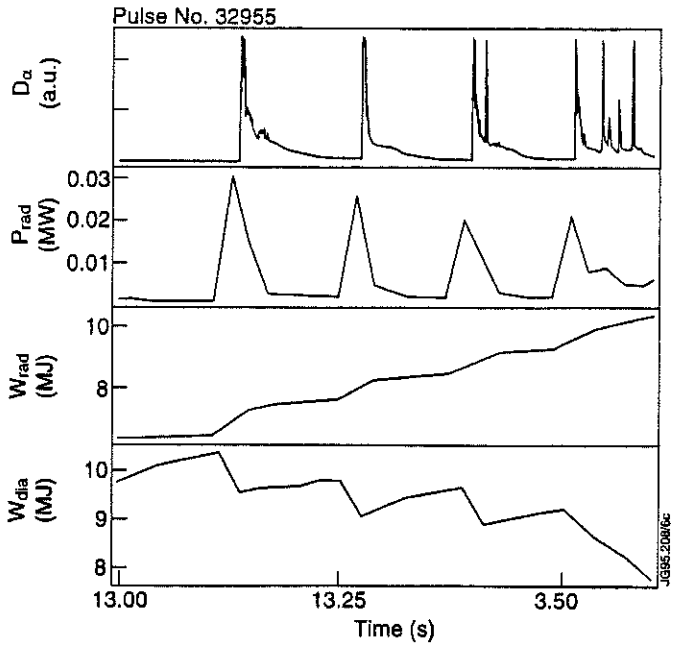

- Energy loss however does not directly account for the decline of neutron yield; typically neutron yield declines substantially faster than W^2
- Analysis shows that there are two effects which contribute to the reduction in neutron yield:-
  - Increase in impurity concentration due to the ELM which dilutes the deuterium fuel ion
  - Marked reduction in ion temperature after the ELM.

- Carbon concentration is the major contributor to Z_{eff} and accounts for approximately a 10 to 15% reduction in neutron yield due to dilution

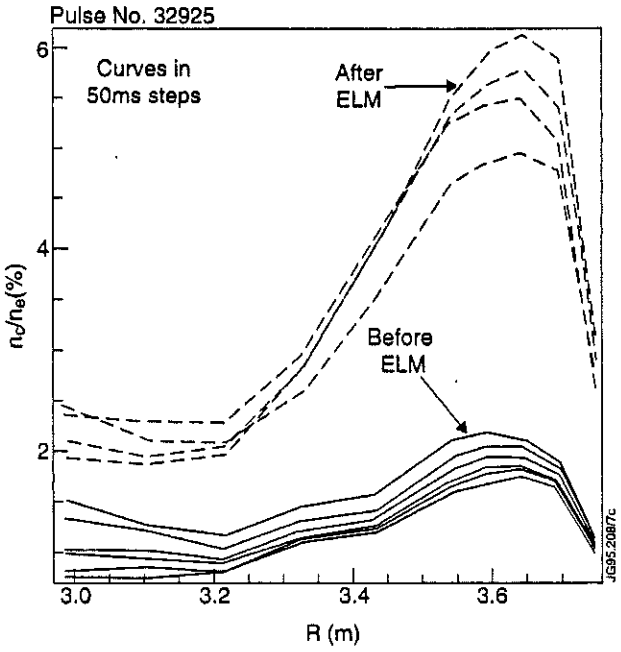

- Remainder of reduction in R_{dd} occurs because of a decline in ion temperature.

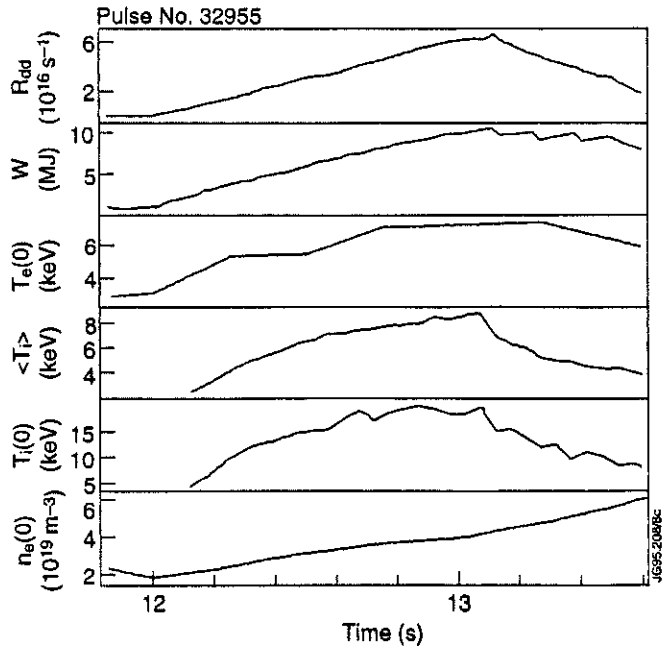

- It should be noted that giant ELMs do not always lead to an irreversible decline of R_{dd}
- Majority of giant ELMs lead to irreversible declines exceptions being those which terminate a burst of internal MHD activity or those which follow a sawtooth initiated decline

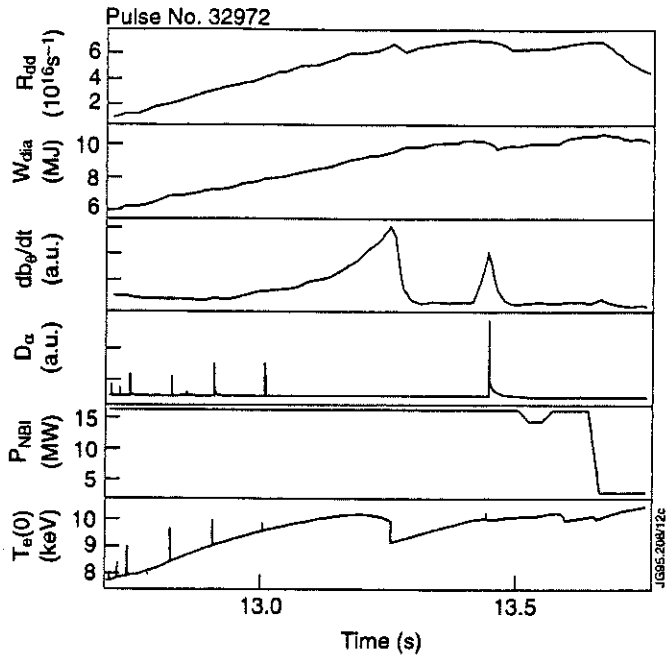

- Soft X-ray views (250μm Be filters) show rapid bursts of emission at top and bottom of the vessel.

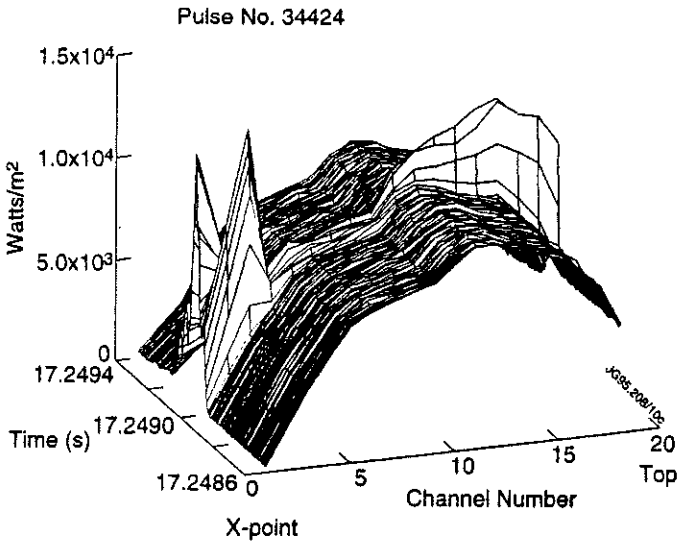

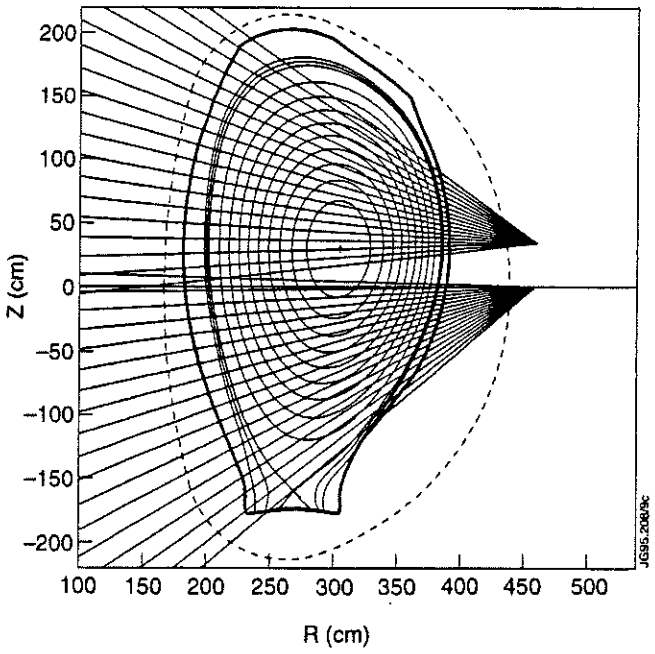

INTERPRETATION OF RESULTS

- Giant ELMs and other internal instabilities limit the highest performance plasmas (with I_p=3-4MA) to a relatively modest normalised β_n (=β/[I(MA)/a(m)B(T)]) of about 2

- However hot ion modes at more modest current (Ip=1.7MA), with the same q_ψ as their higher current and performance relatives, reach a very high β_n=3.5 to 4

- These discharges are marginally stable to ideal ballooning over much of minor radius and marginal to n=1 kink mode with an ideal wall at the JET vacuum vessel location

- Despite this some instabilities limit β in both high and low current discharges

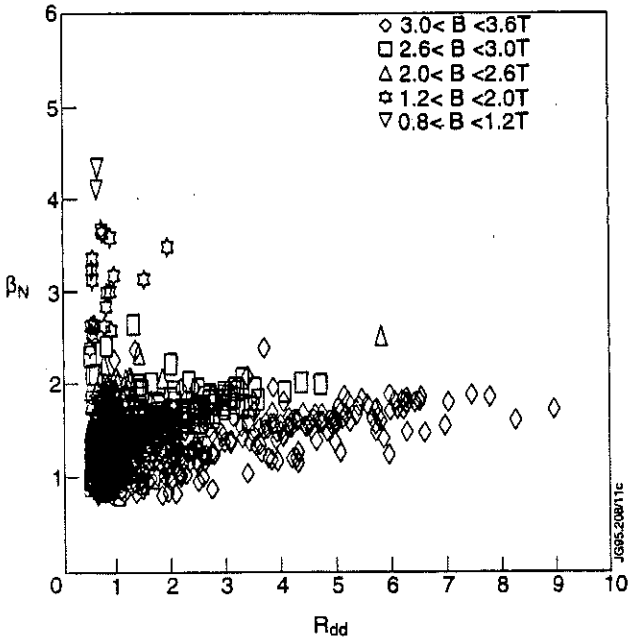

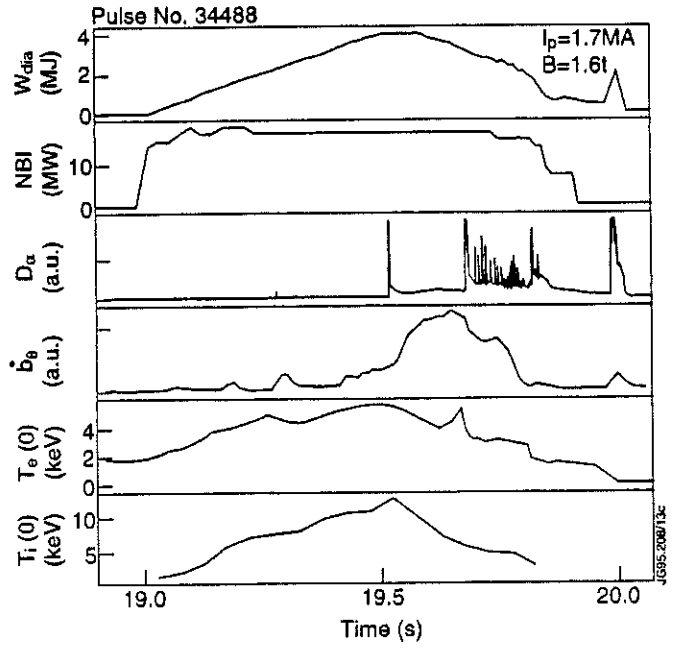

- Suggests observed instabilities are a local edge related limit
  - This is consistent with lower observed ion temperature gradient scale lengths in the lower current discharges.
  - Lower current discharges have a more optimal core pressure profile

- Early operation in the new JET divertor configuration was limited by repetitive ELMs with no clear ELM-free period
- Scans over plasma shape indicated increasingly long ELM free periods were established as the plasma triangularity (and thus implicitly the edge magnetic shear) was raised.
- Subsequent detailed scans show the edge magnetic shear is the key parameter governing ELM free period and thus performance.
- Note that, in the highest shear pulse the ELM-free period exceeds the beam heating duration
- This relationship to edge shear is qualitatively consistent with ballooning modes limiting the maximum edge pressure gradients
- Comparisons between edge ballooning limits and experimental edge pressure gradients at the time of the performance limiting ELM show good agreement
- However edge pressure gradients in discharges where internal MHD limits performance also approach the ideal ballooning limit

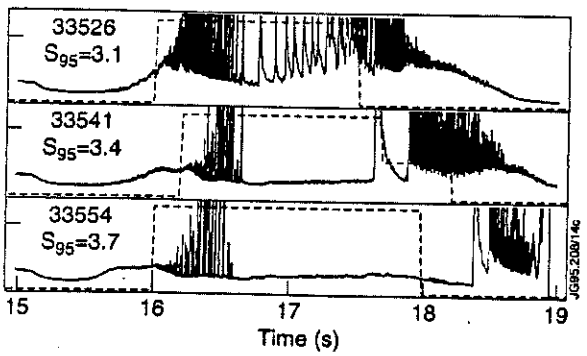

D_α signals showing increase in ELM free period as the edge shear (S_{95}) increases.

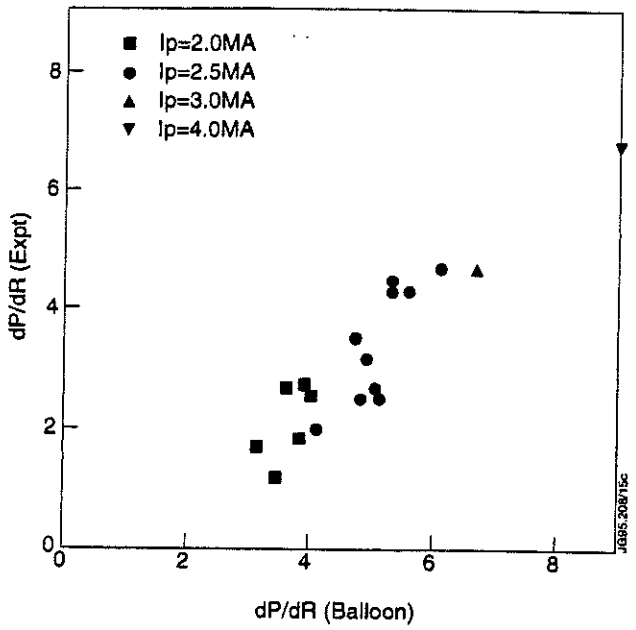

Fig 5 Edge pressure gradients on the outboard midplane (in units of $10^5 Pam^{-1}$) in experiment just before performance limiting MHD event versus calculated ballooning limit at 95% flux surface.

- The fact that the edge pressure gradient approaches the ballooning limit irrespective of the MHD event occurs because the plasma shape has been optimised to the point where this is so
- Suggests that the ideal ballooning modes establish an edge pressure gradient limit but are not necessarily the cause of the ELM. Particularly since the ELM originates some way within the plasma

SUMMARY

- Giant ELMs, or coupled giant ELMs and sawteeth, are a common cause of performance limitation in high neutron yield discharges
- These ELMs lead to a rapid decline in the D-D neutron production rate ($dR_{dd}/dt \sim -10^{17} s^{-2}$).
- This decline is related to an impurity influx causing dilution of the fuel ions and a decrease of T_i
- Detailed scans show a strong correlation between ELM free period and edge magnetic shear
- It remains unclear however if the ballooning modes establish an edge dP/dr limit or actually cause the ELMs.

ACKNOWLEDGEMENT

The UKAEA authors were jointly funded by the UK Department of Trade and Industry and EURATOM.

Analysis of Cold Pulses produced by Impurity Injection in JET

R De Angelis[1], N Deliyanakis, F De Luca[2], R Giannella, G Gorini[2], A Jaccia[3], H Jäckel, P Mantica[3], L Porte, V Parail, E Springmann, A Taroni.
JET Joint Undertaking, Abingdon, Oxfordshire, OX14 3EA, UK.
[1] Associazione Euratom-ENEA sulla Fusione CRE Frascati, Italy.
[2] Dipartimento di Fisica, Universita degli studi di Milano, Milano, Italy.
[3] Istituto di Fisica del Plasma, Associazione Euratom-ENEA-CNR, Milano, Italy.

SUMMARY

Laser ablation of impurities has been used to generate cold pulses in JET.

Fourier analysis of the temperature profiles evolution and heat transport simulation evidence that non local effects have to be invoked to represent radial heat propagation both in Ohmic and H-modes.

INTRODUCTION

The analysis of the propagation of perturbations of the electron temperature provides a useful mean to understand the mechanisms of radial heat transport in a tokamak. The outward propagation of sawteeth, originated spontaneously in the centre of most tokamak discharges, has been extensively used to determine the incremental electron thermal diffusivity $\chi_e^{inc} = \partial q/\partial(n\,\nabla T)$.

Perturbative phenomena of different origin can be usefully analysed [1,2] to extend the availability of the method to non sawtoothing discharges and to compare the diffusivities obtained from waves of different physical origin, frequency, direction of propagation etc.

The present work concentrates on the analysis of cold pulses originated by fast cooling of the plasma edge induced by laser- blow off impurity injection in JET.

The inward propagation of these "cold pulses" and the rapidity of the perturbation allowed to observe marked non-local features of the radial heat propagation which are closely similar to results obtained in the analysis of ELMs in JET[3].

METHOD

Injection of non-recycling impurities (Ni, Mo, Al...) in the JET plasma is obtained by laser ablation of metallic depositions on glass substrates.

Although the Q-switched laser pulse is very short (10 ns), the temporal width of the impurity pulse is of the order of a few milliseconds at the plasma edge (Fig.1), due to the intrinsic velocity spread of the particle beam. This pulse width is still much shorter than typical particle and heat diffusive times so that the impurity source can be considered comparatively fast.

Correspondingly Abel inverted bolometric signals (Fig. 2) show that the injected impurities may induce strong radiation cooling which is concentrated initially (i.e. on time scales shorter than the particle diffusive time) outside the surface r/a = 0.9.

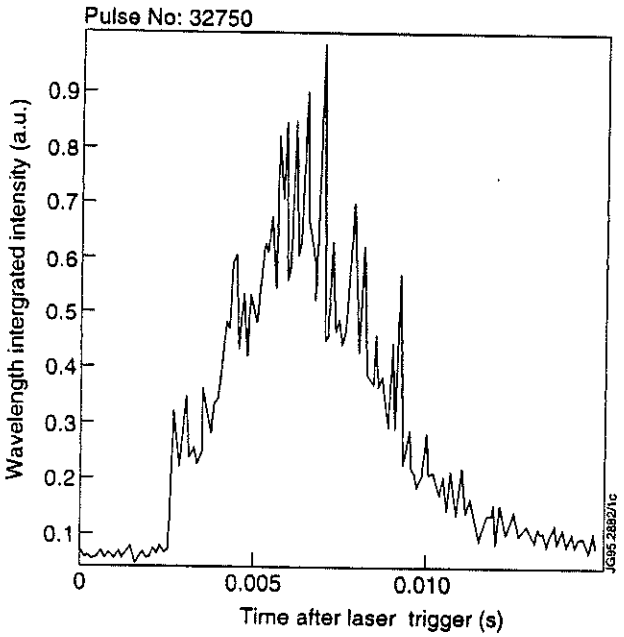

Fig.1: Visible light emission during laser blow-off injection of Ni. The emission is monitored along a line of sight coincident with the injected particle flight path.

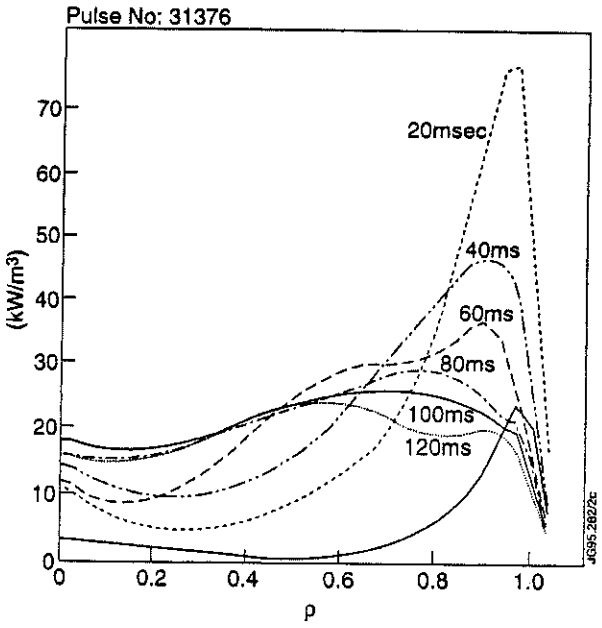

Fig.2: Abel inverted profiles of bolometer traces.

It is generally observed in JET that when these enhanced radiation losses $\Delta P_{rad} \geq 2MW$, the perturbations of the edge temperature become appreciable (Fig.3). A cold pulse is subsequently generated which propagates toward the plasma centre .

Accurate description of the propagation of the temperature profile perturbation, is obtained by the analysis of the experimental data from the high resolution (6kHz sampling rate), 48 channel ECE radiometer.

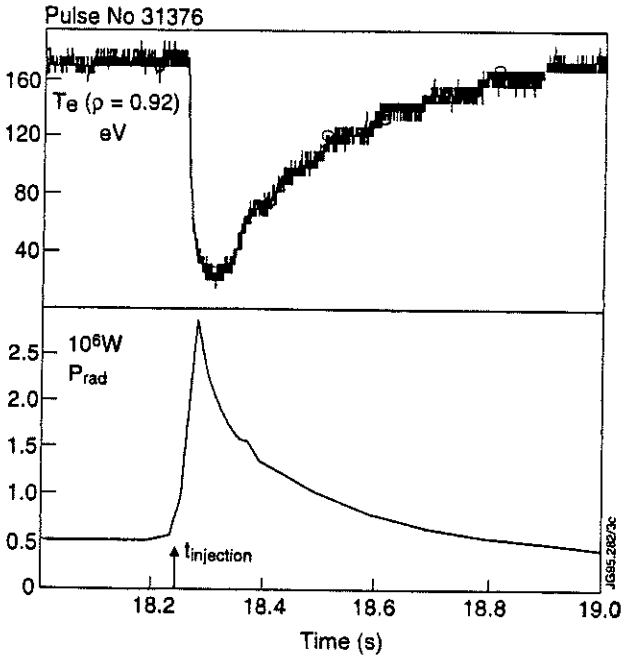

Fig.3: Time traces of the ECE temperature and integrated bolometric emission.

RESULTS

The time evolution of the electron temperature following the impurity injection in a Ohmic discharge, is shown in Fig. 4 at various normalised radii ρ = r/a.

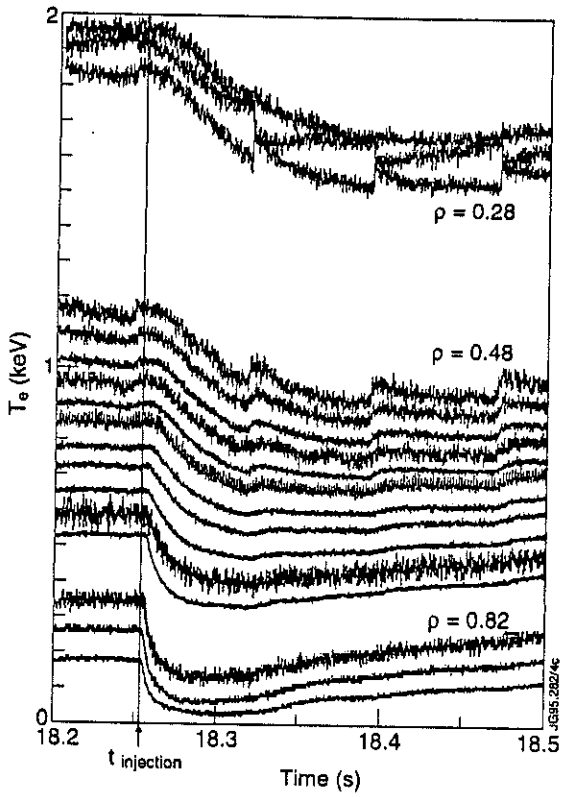

Fig.4: Time traces of T_e at various r/a positions.

It can be seen that a prompt change of the T_e time derivative, occurs over a wide radial extension. At intermediate radii (near field region: ρ ≈ 0.6 to ρ ≈ 0.8) the rapidity of the response to the edge perturbation is seen to decrease moving inwards, while further in (far field region: ρ<0.6) dT_e/dt does not vary appreciably with the radius.

The Fourier analysis of $T_e(\rho,t)$ [4] is reported in (Figs. 5, 6) in terms of the amplitude and phase of three different frequencies against the radial position. One can distinguish three different regions: the outer one (ρ > 0.8) is affected by the presence of the radiative losses as demonstrated by the amplitudes decreasing with r.

The intermediate region there features a normal diffusive behaviour ($\phi' = |A'/A|$) and a value of thermal diffusivity χ_e^{inc} in accordance with evaluations from the analysis of the simultaneous sawtooth. Finally, the inner region (r<0.6), characterised by a non diffusive phase-amplitude relation, reflects the very fast non-local behaviour indicated by the short propagation time (Δt≤4ms) between the plasma periphery and the centre.

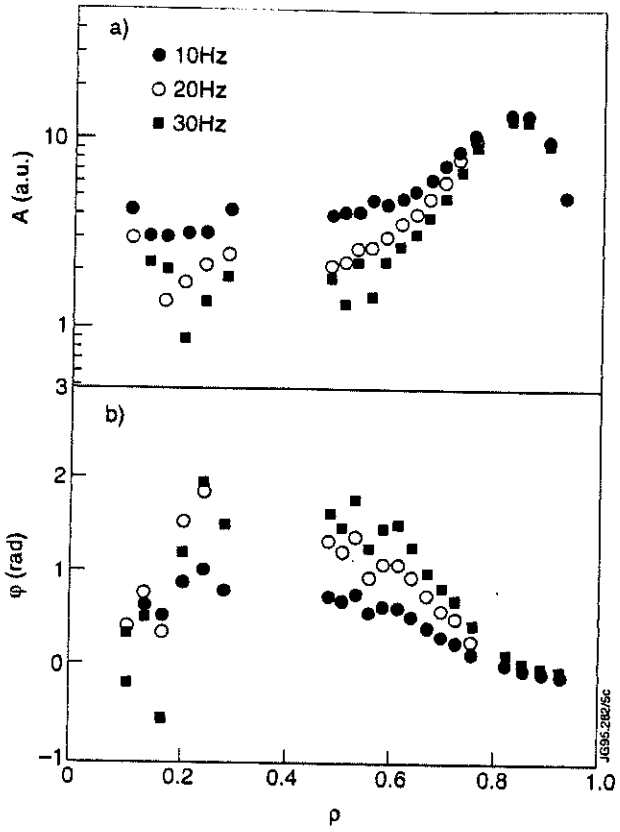

Fig.5: Fourier analysis of T_e (ρ,T) amplitude.

Fig.6: Fourier analysis of T_e (ρ,T) phase.

TRANSPORT ANALYSIS

Simulation of $T_e(\rho,t)$ has been obtained by solving the energy transport equations with the JETTO transport code assuming the experimental P_{rad}, n_e, T_e profiles and prescribing adequate expressions for χ_e. Impurity deposition and transport are not considered explicitly but through the variation of the Z_{eff} value deduced from spectroscopic data.

Fig. 7 shows a comparison of the experimental electron temperature time evolution at different radii with simulations assuming a Bohm-like expression for $\chi_{e,i}$[5], which is typically satisfactory for JET Ohmic and L discharges:

$$\chi_{e,i} = \alpha^L_{e,i} c|n \ \nabla T_e|a \ q^2/(eBn)$$

where

$$\alpha^L_i \approx 2\alpha^L_e \approx 5\ 10^{-4}$$

With this choice for $\chi_{e,i}$ the stationary temperatures before the cold pulse are reproduced within errors but there is a poor agreement after the perturbation.

Similar results have been obtained with a Rebut-Lallia expression for $\chi_{e,i}$.

These simulations suggest that following the initial edge perturbation there is a rapid increase of the thermal diffusivity also at radial positions where no appreciable modifications of the local

plasma parameters have yet taken place [6].

The simulation of Fig. 8 assumes that the thermal diffusivity is a function of the edge temperature:

$$\chi_{e,i}(\rho,t) = \chi_{e,i}\left(\rho, t_{injection}\right)\left[\frac{T_{e,edge}(t)}{T_{e,edge}\left(t_{injection}\right)}\right]^{-0.6}$$

It appears that for Ohmic pulses the large modification of χ_e at the plasma centre is essential for a consistent interpretation of the experiment. Such a strong modification of the diffusion coefficient is not strictly necessary at intermediate values of the normalized radius to reproduce the experimental data.

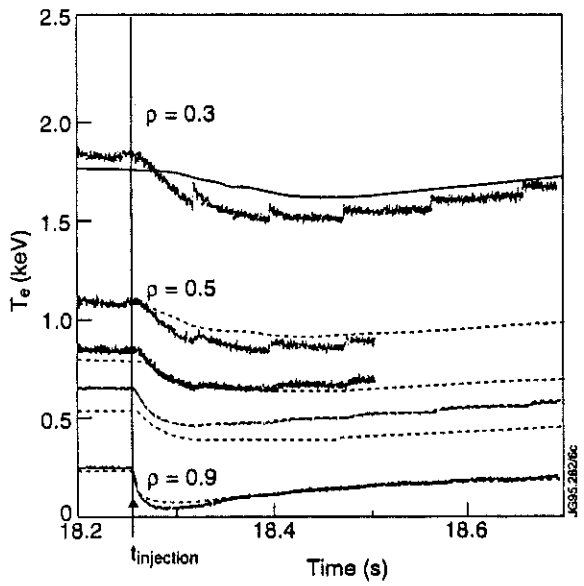

Fig.7: Simulation of $T_e(r,t)$ using a Bohm-like thermal diffusivity.

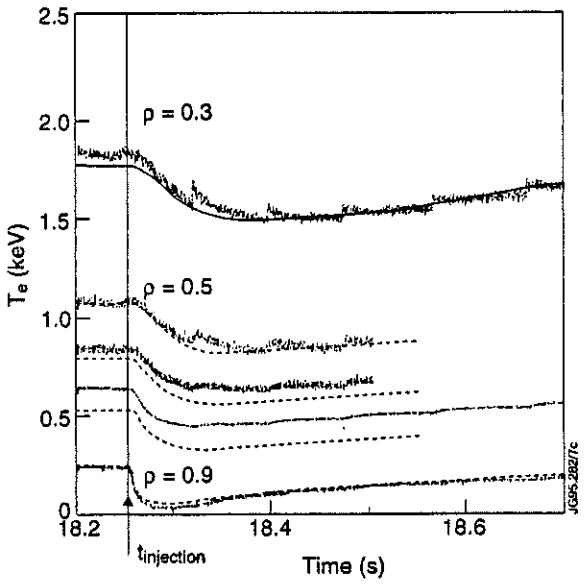

Fig.8: Simulation of $T_e(r,t)$ using a non-local thermal diffusivity, dependent on the edge temperature.

This is confirmed by analysis performed by means of a linearised transport code, where only the perturbation $T_e(\rho,t)$ to the electron temperature profile is modelled in terms of a time dependent incremental electron heat diffusivity $\chi_{inc}(\rho,T)$. Such analysis confirms the evidence that a prompt increase in χ_{inc} is taking place at large distance from the source of the perturbation.

H-MODE

Laser induced cold pulses in H modes are more difficult to study due to non stationarity of the discharges and the similarity with Elms. The example in Fig.9 also shows that, consistently with

the lower H mode transport coefficients, the effect in the plasma centre is typically very small.

The simulation in Fig. 10 was obtained by assuming that for a short time (5 msec) after the cold pulse, the thermal diffusivity increased by a factor ~8 over its stationary value (which would correspond to the transition from a typical χH-mode to a typical χL-mode.

A dependence of cinc on T_{edge} as in the Ohmic discharge, was not acceptable in this case.

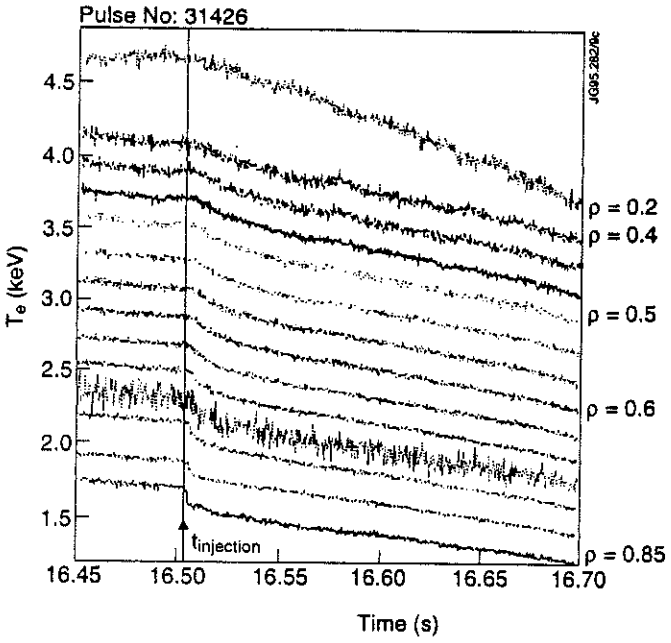

Fig.9: Time traces of $T_e(r,t)$ H-mode.

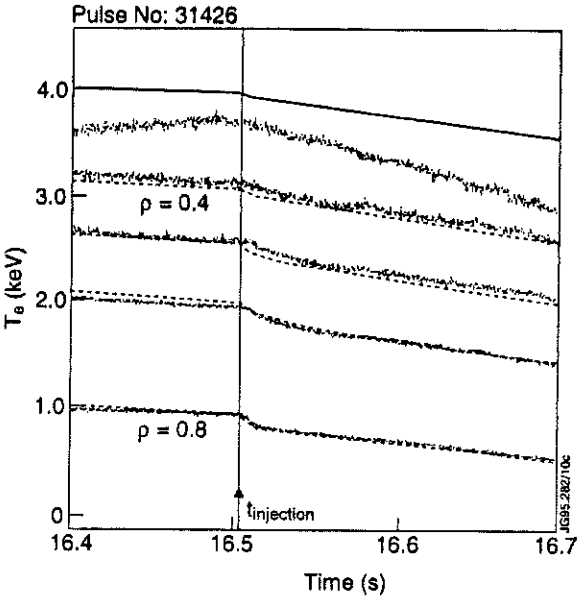

Fig.10: H-mode, simulation of $T_e(r,t)$, obtained using a variation of the thermal conductivity from χ(H-mode) to χ(L-mode) a short time (5ms).

COMPARISON WITH AN ELM

Fig. 11 shows some experimental traces comparing the effects of an Elm to a cold pulse occurring in the same H-mode discharge.

It appears that both perturbations give rise to very fast propagation to inner radii even though the perturbations are clearly different in the bolometer traces (as the impurities injected remain confined in the discharge for A long time) and H -Alfa intensities. Fig 12 shows that also the Abel inverted bolometer profiles are more concentrated in the external periphery in the Elm case.

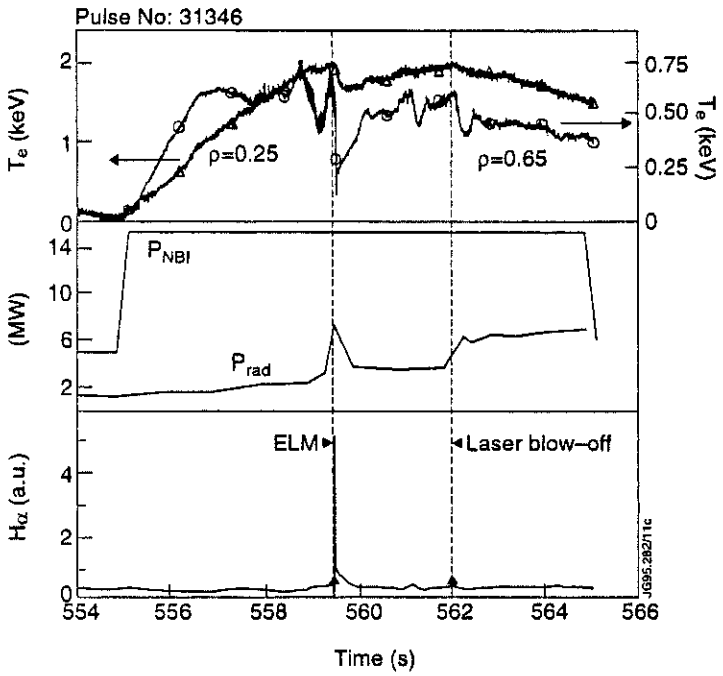

Fig.11: H-mode, comparison of an ELM and a cold pulse.

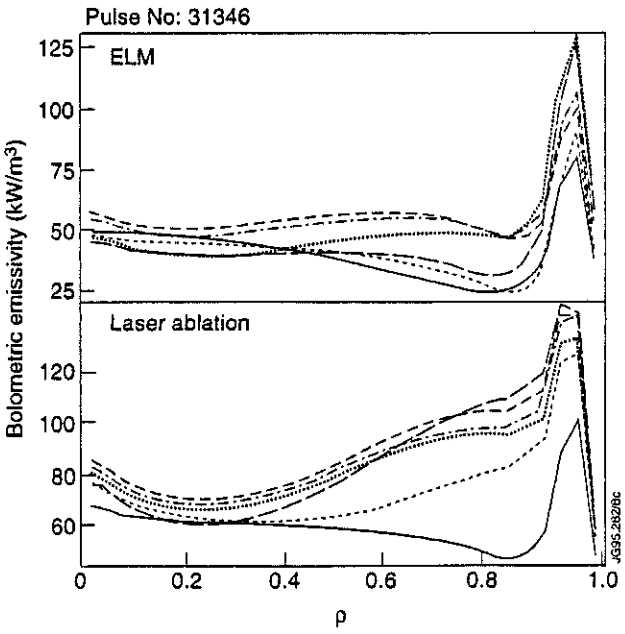

Fig.12: Bolometric profiles, ELM and cold pulse.

CONCLUSIONS

Generation of cold pulses by laser ablation of impurities has proven as a useful tool for studying heat transport in JET plasmas.

Although more precise assessment of the behaviour of the electron heat conductivity requires further experimentation, it emerges clearly that the propagation of the pulse is accompanied by a simultaneous fast increase of χ_{inc} over a large radial extension.

Similar features in the propagation have been also observed in perturbations produced by Elms which are produced spontaneously in the plasma edge of H mode discharges and propagate inward. Conversely, laser cold pulses have been observed on any confinement regime.

REFERENCES

1 M. W. Kissick et al. Nucl. Fus. vol 34, n.3, 349 (1994)

2 J. O' Rourke, R. Giannella, 35th A.P.S (1993), JET-P(93) 99, 41

3 V. Parail et al. 15th Int. Conf. On Plasma Phys. and contr. Nucl. Fus. Seville, Spain, 1994 Paper CN-60/A-2-II-3

4 P. Mantica et. Nucl. Fus. 32 (1992) 2203

5 A. Taroni et al. Plasma Phys. Contr. Fus. 36 (1994) 1629-1646

6 The JET team Proc. 15th Int. Conf. On Plasma Phys. and contr. Nucl. Fus. Seville, Spain, 1994 Paper CN-60/A-2-III-1

Bulk Plasma Impurity Behaviour with the New JET Configuration

R Barnsley[1], H Chen[2], P McGinnity[3], K D Lawson[4], I H Coffey[3], R Giannella, M von Hellermann, L Lauro-Taroni, N J Peacock[4], M Singleton[5].

JET Joint Undertaking, Abingdon, Oxfordshire, OX14 3EA, UK.

[1] Leicester University, LE1 7RH.

[2] Southwestern Institute of Physics, Chengdu, China.

[3] Queens University Belfast, BT7 1NN.

[4] AEA Culham Laboratory, OX14 3DB.

[5] Cork University, Republic of Ireland.

INTRODUCTION

Bulk plasma impurities were monitored by VUV, XUV and soft x-ray spectroscopy, with an emphasis on obtaining quantitative data. Absolutely-calibrated line intensities have been modelled, with the aim of deriving impurity concentrations by passive spectroscopy. Impurity radiated power components, derived by fitting line intensities to the total radiated power, have been used to monitor impurities both during discharges and over long sequences of discharges.

EXPERIMENTAL DETAILS

From the beginning of operations in 1994, impurities were monitored by a broad-band soft x-ray spectrometer /1/, developed from the instruments widely used for x-ray astronomy /2/. This was a valuable complement to the existing VUV and XUV grating instruments, particularly for quantitative measurements, because it can be more easily absolutely calibrated, and can measure the continuum. The monitor section of the instrument is a four-channel scanning monochromator, and uses a combination of crystals and synthetic multilayers to cover almost completely the spectrum between 0.3nm and 10nm (fig.1). It monitors the main impurities under all discharge conditions, including D-T discharges /3/. An advantage of the soft x-ray band is that most transitions of interest are strong, well isolated, and have relatively simple atomic physics. The full accessible spectrum can be surveyed in about 500ms, although normally a narrow band is scanned, giving a time resolution down to 50ms for repesentative lines of the main impuritues.

The sensitivity function C_λ is synthesised from the instrument sensitivity equation by a computer code. This contains details of the instrument geometry, mass absorption coefficients for the window materials and detector gas mixture, and measured or theorectical diffractor data as available. The sensitivity function of the first two orders of the TAP channel (thallium acid

phthalate, 2d=2.577nm) is shown in figure 2, its form being dominated by window transmissions and by the diffractor reflection integral. The accuracy of this calibration is estimated to be about 30%, limited mainly by uncertainties in the crystal data, and details of the input beam vignetting function. Extensive work on the essential characterisation of Bragg diffractors /4/ is being continued /5/, particularly for synthetic multilayers, and to assess radiation damage.

The consistency of the calibrated soft x-ray spectra with other measurements has been tested by two independent methods, also shown in figure 2. The cross is based on an analysis of the bremsstrahlung and recombination continuum, averaged over a range of discharge conditions. The analysis included the T_e and n_e profiles and Z_{eff}, and was averaged over a large number of discharges. The points are based on modelling results from charge-exchange recombination spectroscopy (CXRS). The continuum method shows the best agreement, and is also a more direct test of the calibration, being free of the code-modelling uncertainties.

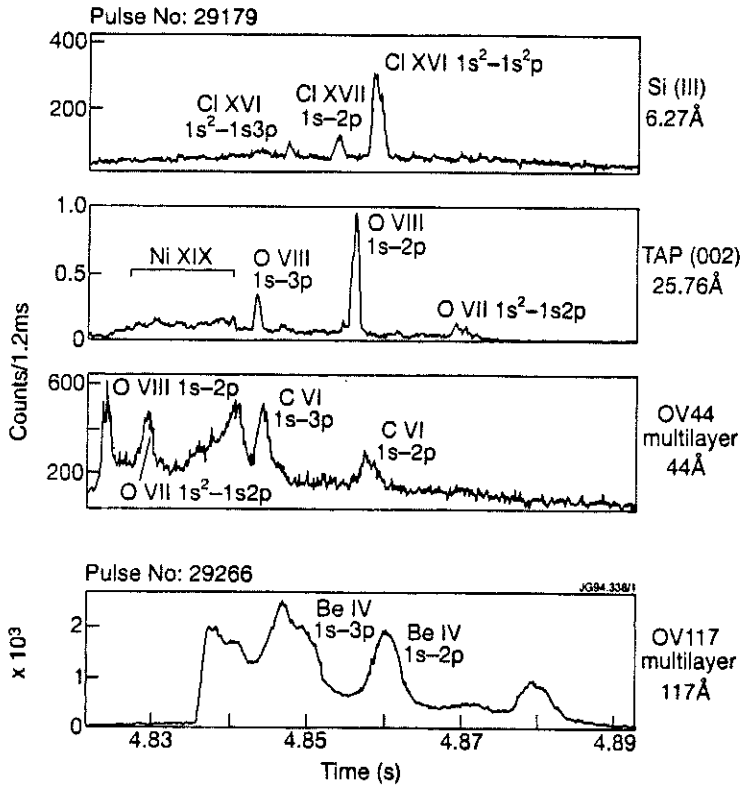

Figure 1. Soft x-ray spectra of the main intrinsic impurities, recorded using a four-channel scanning Bragg monochromator.

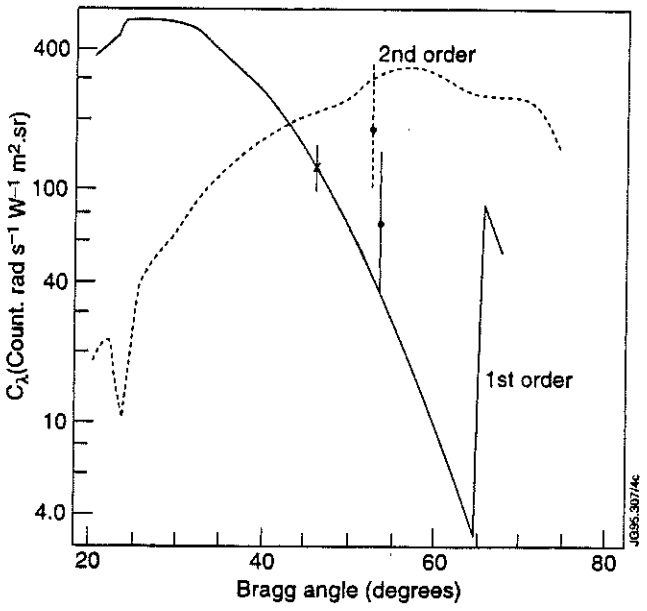

Figure 2. Absolute calibration of the first two reflection orders of the TAP channel (Thallium Acid Phthalate 2d=2.577nm). Included are equivalent values derived from the continuum (cross) and line intensities (points).

SIMULATION OF CALIBRATED LINE INTENSITIES

The determination of impurity concentrations from central-chord passive spectroscopy is a severe problem, particularly for the light impurities that usually dominate the fuel dilution in devices with low-Z limiters. Some progress has been made here by modelling soft x-ray line intensities with the SANCO impurity transport code. Using data from divertor gas-puffing experiments, transport parameters were derived by modelling the impurity profiles measured by CXRS.

Either neon or nitrogen were puffed into ELMy H-modes with typically 10MW of neutral-beam heating. The light impurity abundance profiles measured by CXRS were hollow, with the peak at about r/a=0.75, and were modelled with profiles of the transport coefficients D and V shown in figure 3. These transport profiles are characterised in the centre by low diffusion and a small outward convection, and near the edge by moderate diffusion and strong inward convection.

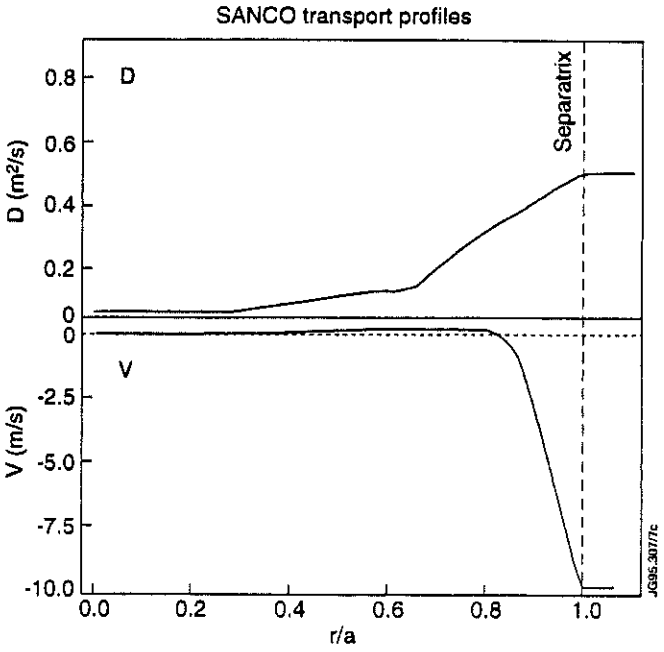

Figure 3. Radial profiles of transport coefficients D and V, determined by modelling the CXRS Carbon and Neon profiles.

Figure 4 shows the simulated line emission profiles for Nitrogen, where the observed N VII lines radiate predominantly from within the separatrix. Figure 5 shows simulated and measured N VII Lyβ intensity, where the simulation has been normalised to the N Ly β measurement. Based on the measurement, the simulation predicts a peak Nitrogen concentration of 10% of n_e at r/a=0.4: approximately twice the CXRS value at the same radius.

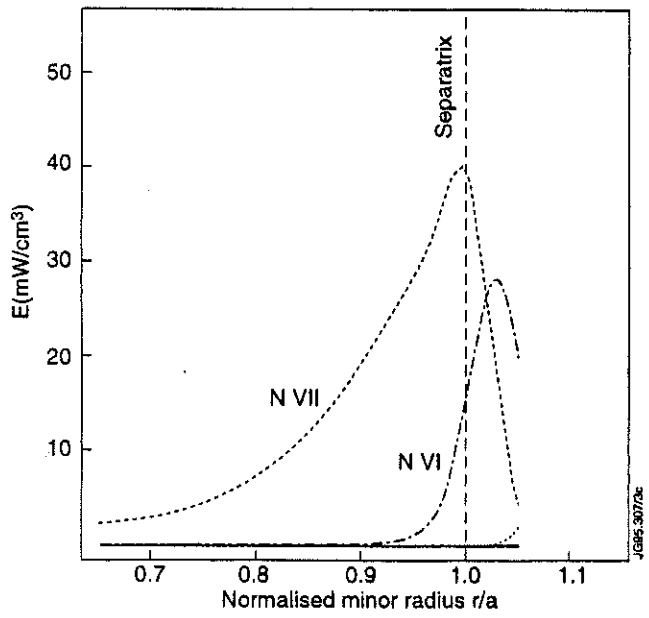

Figure 4. SANCO modelled emissivity profiles of Nitrogen ions.

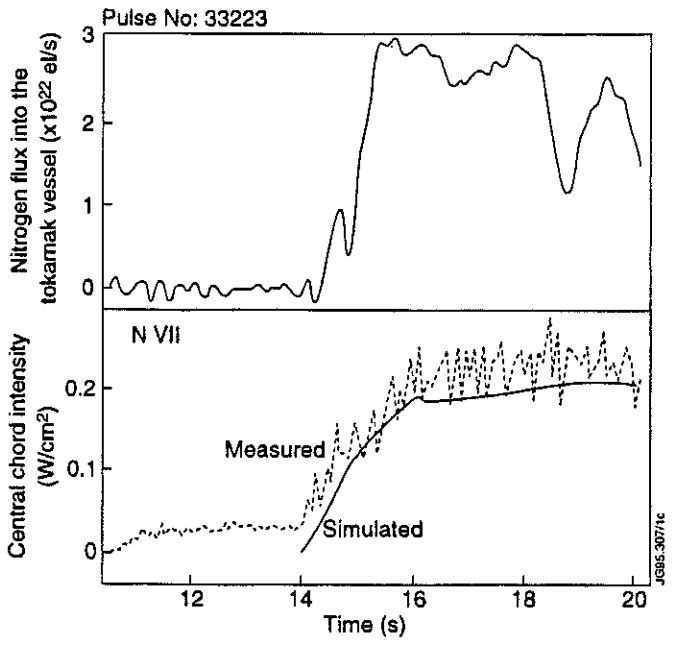

Figure 5. Measured and simulated N VII Lyβ central chord intensity during a Nitrogen puff.

The Neon X Ly β measurement and simulation shown in figure 6, are independent of each other in that the simulation is based solely on CXRS measurements, while the measurement is the absolutely calibrated soft x-ray line intensity. The peak Neon concentration was about 0.4% of n_e at r/a=0.75. The measurement is about 40% lower than the simulation, a discrepancy which is similar to the uncertainty in the instrument calibration. However, the simulation is subject to uncertainties in the atomic physics, the transport, and the measured T_e and n_e profiles, as well as those in the CXRS measurement, that are estimated to total at least a factor two.

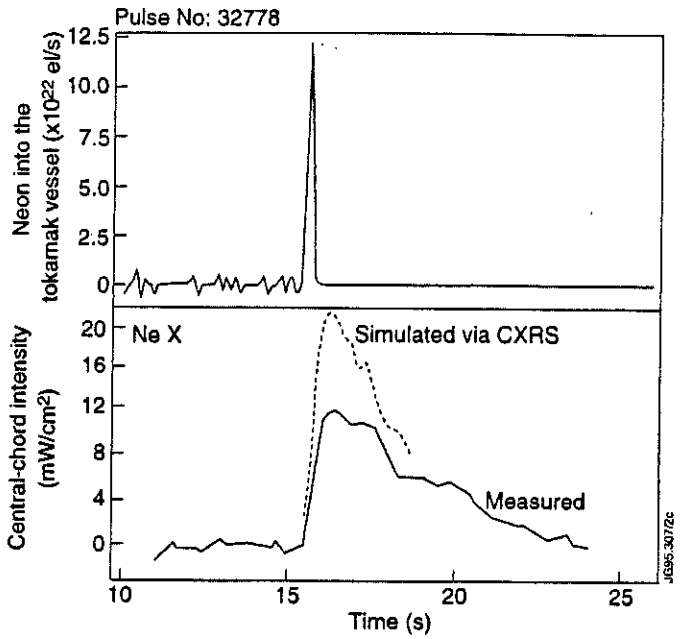

Figure 6. Simulated Ne X Lyβ derived from CXRS, compared with the independently calibrated soft x-ray spectroscopic measurement.

This analysis gives a point of reference between passive and active spectroscopy, from which the passive measurements might be extended to other impurities, and to non-beam-heated phases of discharges. Given the cumulative uncertainties inherent in this comparison, the resultant factor-two agreement is considered to be successful.

IMPURITY BEHAVIOUR

The technique of deriving impurity radiated power components by fitting VUV and XUX line intensities to the total radiated power /6/, has now been extended to the soft x-ray spectroscopic data. It relies on observing ions whose line radiation has been found empirically to represent the radiated power from the relevant impurity, and on analysing a large number of discharges to ensure consistency of the fitting coefficients. In the VUV and soft x-ray regions, the most suitable ionisation stages have been found to be H-like for Be, C, and O, Li-like for Cl, and Be-like for Cr, Fe and Ni.

During the first half of 1994 operations, the condition of the machine was monitored using regular reference discharges. Figure 7 shows the elemental radiated power components together with their sum and total radiated power for such a discharge. The plasma was formed on the outboard limiter, was then moved to an X-point magnetic configuration, followed by phases on the outboard and inboard limiters, thereby allowing the condition of each surface to be assessed /7/.

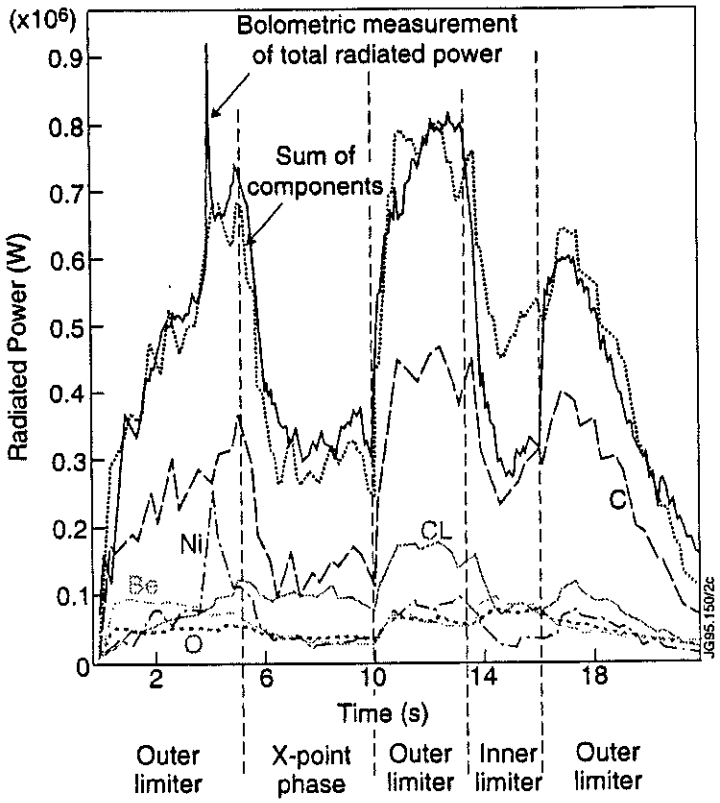

Figure 7. A fit of the soft x-ray spectroscopic line intensities to the total radiated power, for a reference discharge.

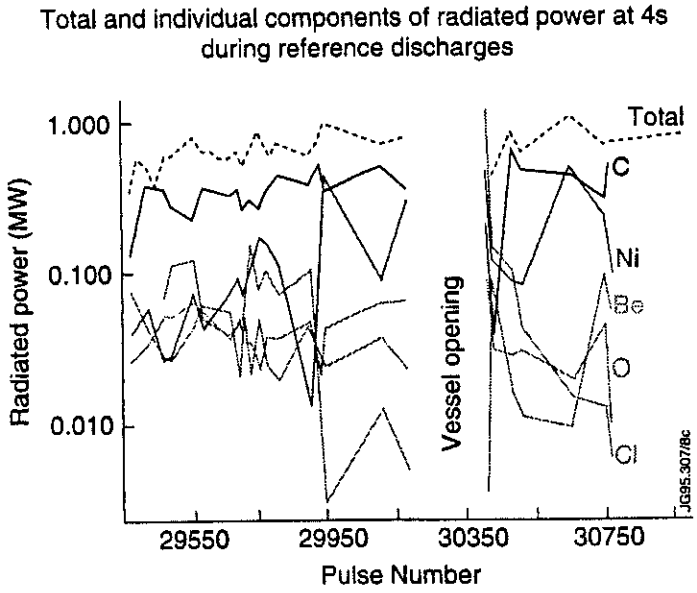

Figure 8. Total radiated power and main impurity components, measured during the outer limiter phase of a series of reference discharges.

The evolution of the main impurities during a series of reference discharges (fig.8) shows that the most significant change occurs to Cl. At the start of operations in 1994, Cl was a major radiator, but after about 1000 discharges it had declined to negligible levels, while briefly returning after each vessel opening. This is probably due to gettering by the metals, which have been shown to be anticorrelated with Cl /8/.

A useful guide to the general impurity radiation is to normalise the average Ohmic P_{rad} to the current I_p (table 1). The level of $< P_{rad} /I_p>$ for the first half of 1994 (0.23MW/MA) was very similar to that for equivalent discharges in 1989 (0.22MW/MA). As in the 1989 C-limiter/Be-evaporation phase, C is the major low-Z radiator, and Be is at very low levels except for a few shots following a Be evaporation. Ni, Fe and Cr are higher with the new configuration, mainly due to the larger area of exposed vacuum vessel, than in 1990/92, when the walls had a larger covering of carbon tiles.

Table 1. Comparison of $<P_{rad} /I_p>$, first-wall material, and major radiating impurities, for recent years' operations.

Start of operations	$<P_{rad}/I_p>$ (MW/MA)	First-wall material	Main radiating impurities
1987	0.41	C, Ni antenna screens.	C, O, Ni.
1989	0.30	C.	C, Cl, Ni, O.
1989	0.22	C, Be evaporation.	C, Cl, Ni, Be.
1990	0.18	C/Be.	Be, C, Cl.
1991	0.20	C/Be.	Be, C, Cl, Ni.
1994	0.23	C, Be evaporation.	C, Cl, Ni, Fe, Cr.

An all-shot survey of the P_{rad} components of Be, and O (figure 9) shows the Be trend after Be evaporations. There is a general downward trend in O, as well as short-lived decreases after each evaporation.

The bulk-impurity line-intensities from Ohmic X-point plasmas are significantly lower than from limiter plasmas particularly for the light impurities, for a combination of possible reasons, including global density changes, T_e and n_e profile changes, and divertor screening. For example, the reduction during the X-point phase of the reference discharge (fig.7) is believed to be mainly due to the reduction in density caused by increased pumping by the carbon divertor target. Impurity time histories (fig.10) for a high performance H-mode discharge with 19MW of NBI show marked decreases in the CIV and OV signals during the transition to X-point. In this case the reduction may be mainly a profile effect, where the light ions move into regions of lower n_e. The decrease

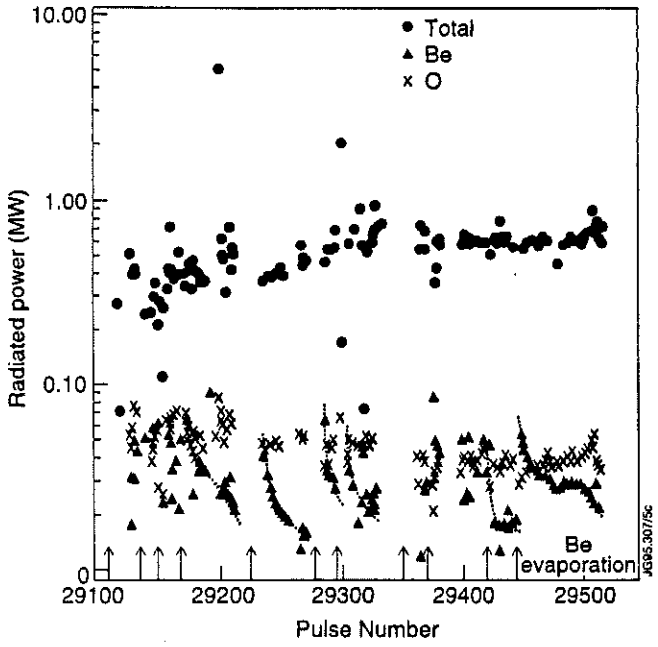

Figure 9. Total, Beryllium and Oxygen radiated power at 4s for a series of discharges. Dotted lines indicate the trend after beryllium evaporations

is less pronounced for the more central NiXXVI ion, whose intensity then rises during the ELM-free period, with sharper increases at the occurence of giant ELMs. Further analysis is required to isolate the above effects in this data.

A comparison between carbon and beryllium divertor target materials (figure 11), shows lower intensities of both BeIV and CVI with the Be target. Influxes of the respective target materials occur during neutral-beam heating at low density, while at higher densities the influxes are much reduced, or are absent.

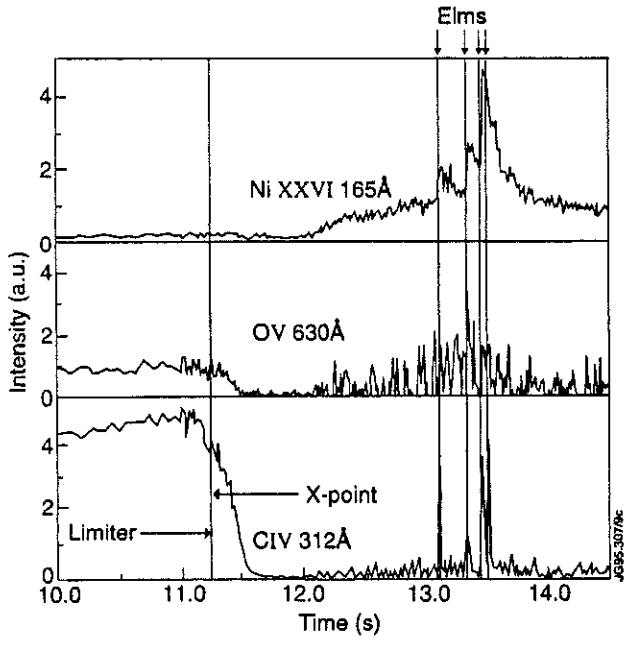

Figure 10 Time histories of three representative VUV lines for a high performance discharge.

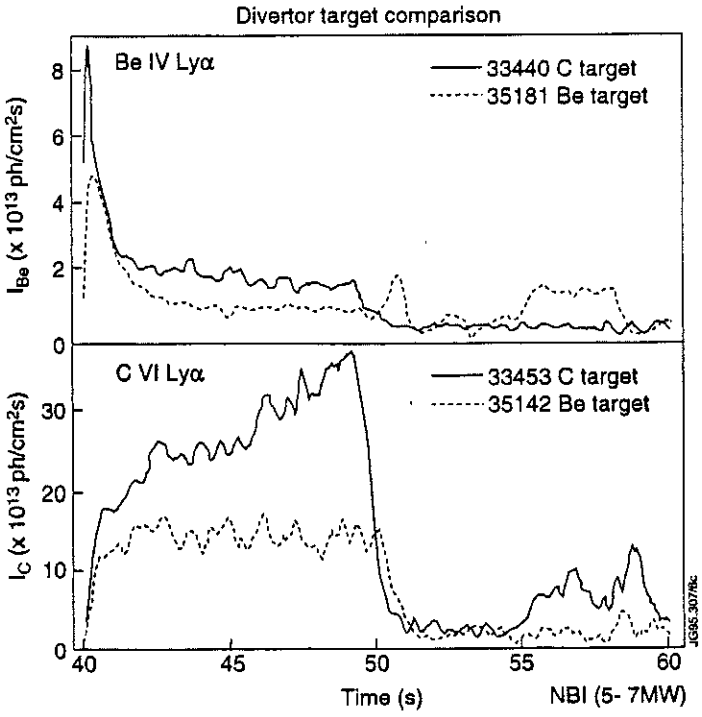

Figure 11. Comparison of Be VI and C VI line radiation for low density discharges (line av. n_e ~ 6.5 . $10^{19}/m^2$) on beryllium or carbon divertor target materials.

CONCLUSION

The use of absolutely-calibrated soft x-ray spectra, combined with code modelling, has provided a comparison between passive and CXRS measurements.

The technique of deriving impurity radiated power components has been valuable for the analysis of long sequences of discharges.

The total radiated power is similar to previous years, particularly when comparable first-wall materials were used. After a long series of discharges, while there are often exceptions, C is the major low-Z radiator, Be and O are low, Cl is negligible, while radiation from Ni, Fe and Cr is higher.

REFERENCES

1. R Barnsley et al, Rev. Sci. Instrum. 57(8) (1986) 2159.
2. K D Evans et al, Space Sci. Instrum. 2(1976) 105-123 and 339-348.
3. R Barnsley et al, Rev. Sci. Instrum. 63(10) (1992) 5023.
4. M Lewis, P A Maksym, K D Evans, Astron. Astrophys. 87(1980) 213-223.
5. N J Peacock et al, Rev. Sci. Instrum. 66(2) (1995) 1175.
6. K D Lawson et al, 17th EPS Amsterdam (1990).
7. G Saibene, A Rossi et al. J. Nucl. Mat. 220-222 (1995) 617-622.
8. K D Lawson, N J Peacock. AEA Culham Report. TAN-92-1-5, (1992).

HC was supported by IAEA fellowship (CPR/94004P) through AEA.

A Scaling Law for the Confinement Time of Non Recycling Injected Impurities in JET and Tore Supra

R Giannella, M Mattioli[1], C Demichelis[1], B Denne-Hinnov,
T Dudok de Wit[1,3], G Magyar, R Myrnäs[2].
JET Joint Undertaking, Abingdon, Oxfordshire, OX14 3EA, UK.
[1] Association Euratom-CEA sur la Fusion, CEN Cadarache, F-13108 St Paul -lez-Durance, France.
[2] Department of Physics, University of Lund, Sweden.
[3] Present address: Laboratoire de Physique et Chimie de l'Environnement, F-45071, Orléans, France.

1. INTRODUCTION

Data bases have been set up for the particle confinement times τ_p of non recycling impurities injected in laser ablation experiments in the JET and Tore Supra tokamaks [1]

No dependence of τ_p on the charge of the injected element or on the background gas (D or ^{4}He) was found in these discharges.

2. DESCRIPTION OF EXPERIMENTS AND OF DATA SETS

The data analysed here are from L-mode plasmas produced in the limiter, single null X-point or double null X-point configuration. In all but two pulses (Tore Supra) sawtooth activity was present.

The background gas was D_2 or ^{4}He. The total number of pulses in the data set used for statistical analysis is 133 (63 from Tore Supra and 70 from JET).

Operational ranges explored with our data sets

- **Tore Supra**
  - R ~ 2.3 m; a_L ~ 0.75 m; κ ~1
  - V_P ~ 28 m^3 (plasma volume)
  - I_P = 0.8 - 1.7 MA
  - B_T = 2.6 - 4.0 T
  - $\langle n_e \rangle$ = 1. - 4. 10^{19} m^{-3}
  - P_{in} up to ~ 7 MW
- **JET**
  - R ~ 3 m; a_L ~ 1.1 m; κ ~1.6
  - V_P ~ 125 m^3 (plasma volume)
  - I_P = 2 - 7 MA
  - B_T = 1.45 - 3.45 T
  - $\langle n_e \rangle$ = 1. - 4.3 10^{19} m^{-3}
  - P_{in} up to ~ 15 MW

Correlation table for the joint data set

	$\log(\langle n_e \rangle)$	$\log(B_t)$	$\log(V_p)$	$\log(I_p)$	$\log(P/n_e V_P)$
$\log(\langle n_e \rangle)$	1				
$\log(B_T)$	0.127	1			
$\log(V_p)$	-0.225	-0.632	1		
$\log(I_p)$	-0.155	-0.489	0.931	1	
$\log(P_{in}/\langle n_e \rangle V_P)$	0.139	0.487	-0.579	-0.511	1

($\langle n_e \rangle$ = vol. averaged el. density, B_T = tor. magnetic field
V_P = plasma volume. I_p = plasma current, P_{in} = total heating power)

Strong correlation between current and plasma volume.

However the influence of I_P on τ_p can be independently analysed in the separate data sets from the two machines where the volume is not varying significantly.

Information on the dependence of τ_p on the plasma volume can also be checked against experimental values of τ_p, as found in the published literature (see fig.1) the experimental ranges of τ_p in OH discharges from various tokamaks are shown as function of $a_L R^{0.5} \kappa^{0.5}$ $\left(\propto \sqrt{V_p}\right)$.

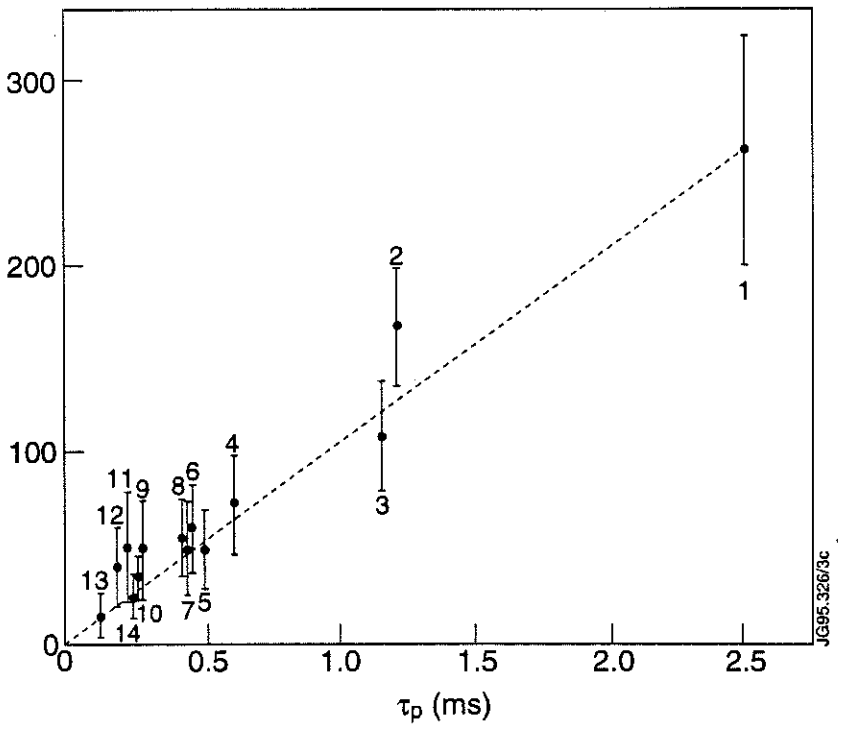

Fig.1 Experimental τ_p values versus $a_L R^{0.5}$ $\kappa^{0.5}$ for several tokamaks: 1 JET, 2 TFTR[2] 3 Tore Supra, 4 Textor[3], 5 ASDEX[4] , 6 PLT[5], 7 T10[6], 8 PDX[7], 9 DITE[8], 10 TEXT[9], 11 TFR[10], 12 FT[11], 13 Alcator C[12], 14 Alcator C MOD[13]. The vertical bars show the range of the reported experimental values. All data refer to ohmic plasmas with deuterium as background gas.

Elements injected	
• **Tore Supra** Manganese [Mn] (Z = 25, M = 55) Nickel [Ni] (Z = 28, M = 59) Copper [Cu] (Z = 29, M = 64) Germanium [Ge] (Z = 32, M = 73)	• **JET** Aluminium [Al] (Z = 13, M = 27) Titanium [Ti] (Z = 22, M = 48) Iron [Fe] (Z = 26, M = 56) Cobalt [Co] (Z = 27, M = 59) Nickel [Ni] (Z = 28, M = 59) Germanium [Ge] (Z = 32, M = 73) Zirconium [Zr] (Z = 40, M = 91) Molibdenum [Mo] (Z = 42, M = 96) Silver [Ag] (Z = 47, M = 108)

Analysis technique to deduce τ_p	
• **Tore Supra** Eigenmode analysis of soft X-ray signals ⇒ *select slowest eigenmode*	• **JET** Fit exponential decay to intensities of Li-, Be-, Na- or Mg-like $\Delta n = 0$ transitions

3. PREVIOUS SCALING LAWS

- **Marmar et al. for Alcator C (1982)** [12]

$$\tau_A[ms] = 0.075\ a_L[cm]\ M_{bg}\ R[cm]^{0.75}\ Z_{eff} / (Z_{bg}\ q_{cyl})$$

  - does not fit our data (fig. 2)
  - indicates dependence on background plasma

    cannot be verified from our database because practically all our data are obtained in D_2 or ^4He discharges and M_{bg}/Z_{bg} is constant.

- **Hawkes et al. for JET (1989)** [14]

$$\tau_H[ms] = 90\ \ n_e[10^{19}\ m^{-3}]^{0.4}\ q_y^{0.5}$$

Mostly from 3 MA ohmically heated discharges or very low additional power

⇒ dependence on power or plasma current could not be studied

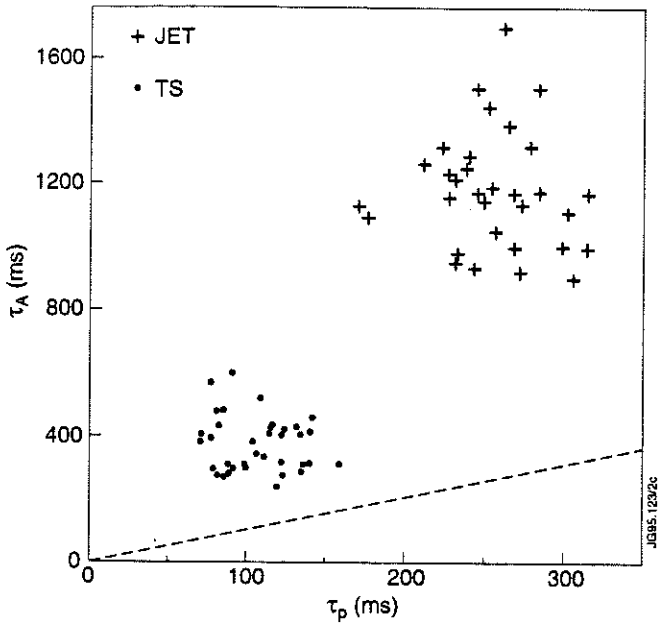

Fig 2 Impurity confinement time τ_A as predicted by the scaling law proposed by Marmar et al. (1982) versus experimental τ_p-values for ohmic plasmas. Dots: Tore Supra; crosses: JET. The dashed line shows $\tau_A=\tau_p$.

4 . TREND OF τ_p WITH THE INPUT POWER PER PARTICLE (P_{in}/n_e)

A strong negative dependence of τ_p- on the total heating power P_{in} appears from the data (fig.3)

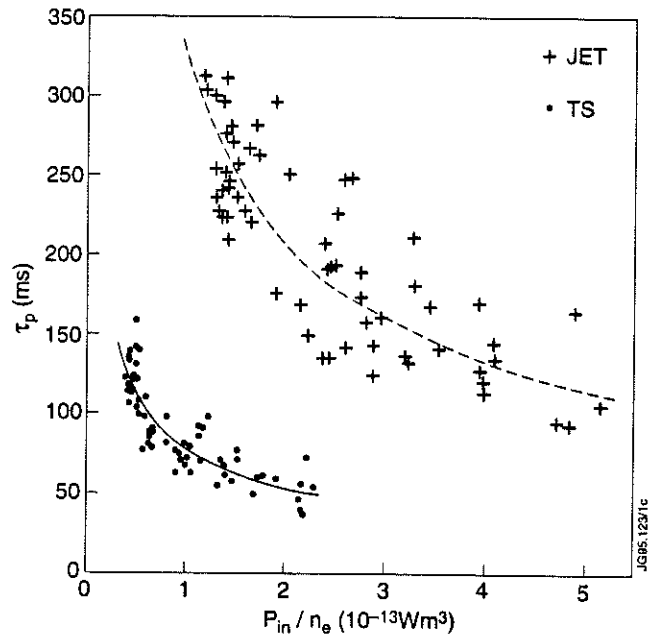

Fig.3 Independent best fits of τ_p versus the dominant parameter $P_{in}/<n_e>$ for Tore Supra and JET. Along with the experimental τ_p-values the best fits of τ_p are presented: the fitted lines correspond to the following equations: $\tau_p = 9.8\ 10^{-6}\ (P_{in}/<n_e>)^{-0.53}$ (Tore Supra), $\tau_p = 1.18\ 10^{-6}\ (P_{in}/<n_e>)^{-0.65}$ (JET). The units are ms, W and m^{-3} for τ_p, P_{in} and n_e, respectively. The logarithmic standard deviations of the best fits (defined below) are σ_{bf} =0.068 and σ_{bf}=0.073, respectively.

5. SEARCH OF APPROPRIATE SCALING LAW FROM THE NEW DATA SETS

We looked for a monomial scaling law of the form

$$\tau_{sl} = 10^{a} \prod_{i=1}^{m} \rho_i^{k_i}$$

where p_i indicates the generic parameter. A linear regression was performed minimising the logarithmic standard deviation for the best fit

$$\sigma_{bf} = \sqrt{\frac{1}{N-(m+1)} \sum_N (\log(\tau_p) - a - \sum_i (k_i \log(p_i))^2}$$

An analysis of sensitivity of τ_p to the different parameter has been performed.

We started from the assumption that the main ordering parameter of the impurity confinement time is $P_{in}/(<n_e>V_p)$. Therefore we analysed the meaningfulness of possible dependencies on other parameters by comparing the standard deviations of different linear regressions. The best fitting exponents a and k_i are shown in the different columns of the table below. In the last two rows σ_{bf} as well as the linear standard deviation ssl of the scaling law $\sigma_{sl} = \sqrt{\frac{1}{N} \sum_N (\tau_{sl} - \tau_p)^2}$ are also given.

Result of linear regressions for the combined Tore Supra - JET data set						
	dominant parameter	analysis of sensitivity to other parameters				three parameters
	1	2	3	4	5	6
a	0.85	0.98	0.99	1.19	0.67	0.87
10^a	7.2	9.7	9.8	15.8	4.7	7.4
$k(P_{in}/(<n_e>V_p))$	-0.79	-0.78	-0.595	-0.715	-0.56	-0.57
$k(<n_e>)$		-0.14				
$k(I_p)$			0.50			0.31
$k(B_T)$				-0.52		
$k(V_p)$					0.29	0.13
σ_{bf}	0.110	0.108	0.070	0.105	0.071	0.068
σ_{sl} (ms)	37.65	36.15	25.0	38.4	25.5	24.35

Our best choice for a scaling law for τ_p is therefore

$$\tau_{sl}\,[ms] = 7.4\; V_p^{0.70\pm0.08}\; I_p^{0.31\pm0.09}\; \left(P_{in}/\langle n_e\rangle\right)^{-0.57\pm0.03}$$

where P_{in} is measured in MW, I_p in MA, n_e in $10^{19}m^{-3}$ and V_p in m^3.

Similar dependencies on I_P are found when one analyses the two data sets separately and uses I_P as a second parameter together with $P_{in}/\langle n_e\rangle$ in the linear regression.

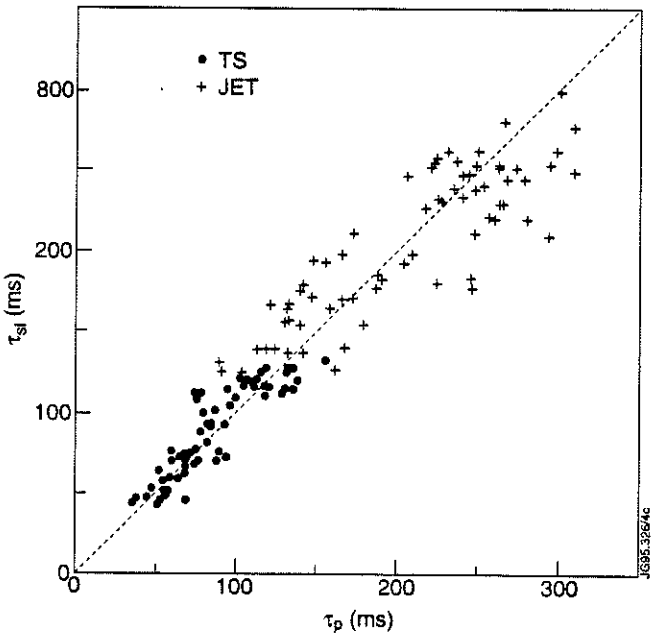

Fig.4 Impurity confinement time τ_{sl} as predicted by the scaling proposed in this paper versus experimental τ_p-values (dots: TS, crosses: JET). The dashed line shows $\tau_{sl}=\tau_p$.

6. CONSISTENCY WITH OTHER EXPERIMENTAL RESULTS AND WITH DIMENSIONAL CONSTRAINTS

The parametric dependence of the proposed scaling law is very close to that found independently for the two machines and appears to be broadly consistent with the experimental results obtained in ohmic discharges on other tokamaks (see fig. 5).

The proposed scaling law also satisfies the Connor-Taylor constraint[4]. applicable to finite β collisional models:

$$5\,\kappa_B + \kappa_I + 8\,\kappa_n + 3\,\kappa_P - 4\,\kappa_R - 4\,\kappa_a + 5 = 0$$

where the κ's are the exponents in the scaling expression for B_T, I_p, n_e, P_{in}, R and a_L, respectively.

The sums of the positive and negative terms are 9.87 (±0.26) and -10.11 (±0.96). Therefore the left hand side of equation above is equal to -0.24 (±1.10).

Constraints deriving from less general plasma models are not satisfied by this scaling law.

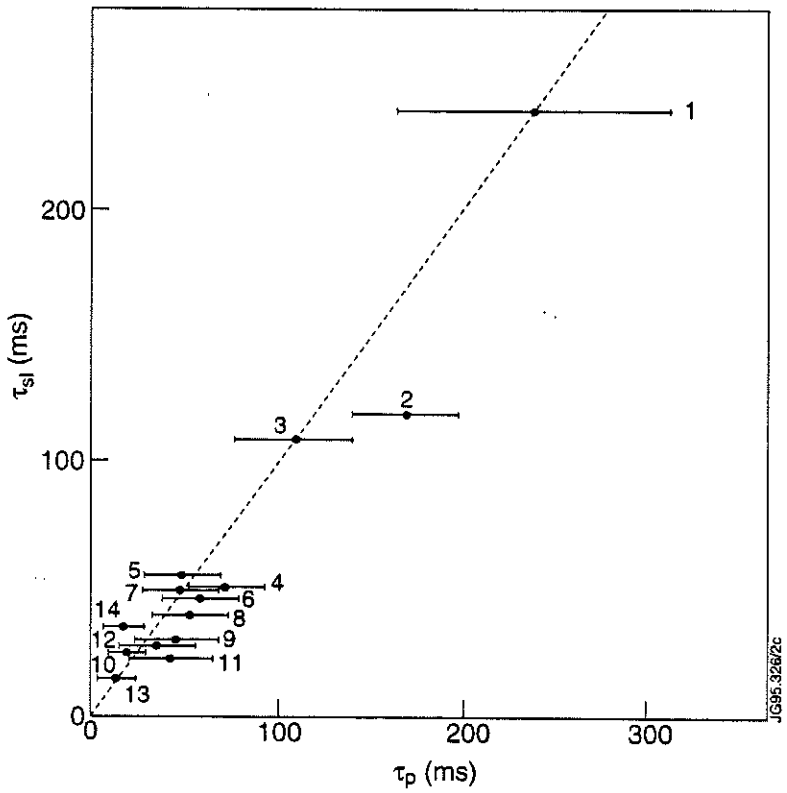

Fig. 5 Experimental τp values versus the impurity confinement times predicted by the scaling law proposed in this paper for several tokamaks: 1 JET, 2 TFTR, 3 Tore Supra, 4 Textor, 5 ASDEX, 6 PLT, 7 T10, 8 PDX, 9 DITE, 10 TEXT, 11 TFR, 12 FT, 13 Alcator C, 14 Alcator C MOD. The horizontal bars show the range of the reported experimental values. All data refer to ohmic plasmas with deuterium as background gas

7. COMPARISON OF THE IMPURITY CONFINEMENT TIMES WITH THE GLOBAL ENERGY CONFINEMENT TIMES

The global energy confinement times τ_E for the same discharges is also available in our databases. τ_E is defined as the ratio of the diamagnetic energy to the total input power P_{in}. τ_E and τ_p are of the same order but different, their average ratio τ_E/τ_p being ~2.5.

The logarithmic linear regression of τ_E gives

$$\tau_{E\text{-}sl}\ [\text{ms}] = 54\ I_p^{0.73\pm.12}\ V_p^{0.34\pm.11}\ n_e^{0.32\pm.08}\ B_T^{0.01\pm.14}\ P_{in}^{-0.41\pm.04} \qquad (\text{MA, m, m, } 10^{19}\ \text{m}^{-3}\text{, T. MW})$$

and standard deviations σ_{sl} = 82 ms σ_{bf} = 0.089.

This scaling is not far from the ITER89-P [16] scaling law

$$\tau_{E\text{-}ITER89}\ [\text{ms}] = 38\ M_{bg}^{0.5}\ I_p^{0.85}\ R^{1.2}\ a_L^{0.3}\ \kappa^{0.5}\ n_e^{0.1}\ B_T^{0.2}\ P_{in}^{-0.5}$$

(σ_{sl} =130 ms)

or from the scaling proposed by Taroni et al. [17]

$$\tau_{E\text{-}T}[ms] = 73\ I_p\ R^{1.5}\ n_e^{0.5}\ B_T^{-0.5}\ P_{in}^{-0.5}$$

(σ_{sl} =100 ms)

Comparison of the above scalings for τ_E with the scaling for τ_p indicates that

- the ratio of τ_E/τ_p should increase with I_p and decrease with increasing plasma size and density.
- A more moderate trend to increase with increasing total input power is also expected.
- The dependence of τ_E/τ_p on B_T remains uncertain, as the trends of the two confinement times independently are.

The logarithmic linear regression of this ratio leads to

$$\tau_E/\tau_p\ [ms]=6.4\ I_p^{0.40\pm.16}\ V_p^{-0.32\pm0.15}\ n_e^{-0.17\pm.12}\ B_T^{0.02\pm.20}\ P_{in}^{0.16\pm.05}$$

and to a logarithmic standard deviation σ_{bf} = 0.123. The high value of σ_{bf} found is due to the large relative uncertainty on τ_E/τ_p that is obtained as the ratio of two independently measured quantities. Because of this uncertainty the width of the interval spanned by the experimental value of τ_E/τ_p (1.2 to 4.7) appears to be to a larger extent due to the experimental error than to the different parametric dependence of the two confinement times on plasma parameters. Indeed the predictor given by the equation above only varies between 1.9 and 3.4 in our database.

REFERENCES

[1] M. Mattioli, R. Giannella, R. Myrnäs et al. to be published in Nucl. Fus. (1995).

[2] B.C. Stratton, R.J. Fonck, R. Hulse et al. Nucl. Fusion 29 (1989) 437.

[3] J. Castracane, L. Könen, A. Pospieszczyk et al. Nucl. Fusion 31 (1991) 947.

[4] J. Roth and G. Janeschitz Nucl. Fusion 29 (1989) 915.

[5] S. Cohen, J. Cecchi, C. Daughney et al. J. Vac. Sci. Technol. 20 (1982) 1226.

[6] A.A. Bagdasarov, V.I. Bugarya, N.L. Vasin et al. Proc. 12th EPS Conf. on Contr.Fus. and Pl. Phys. Part I (1985) 207.

[7] S. Suckewer, J. Cecchi, S. Cohen et al. Phys. Lett. 80A (1980) 259.

[8] N. Hawkes, N.J. Peacock, R. Barnsley et al. Proc. 14th EPS Conf. on Contr.Fus. and Pl. Phys. Part I (1987) 101.

[9] W.K. Leung, W.L. Rowan, J.C. Wiley et al. Plasma Phys. Controll. Fusion 28 (1986) 1753.

[10] TFR GROUP, Phys. Lett. 87A (1982) 169.

[11] R. De Angelis, R. Bartiromo, G. Mazzitelli and A.A. Tuccillo Proc. 15th EPS. Conf. on Contr.Fus. and Pl. Phys. Part I (1988) 179.

[12] E.S. Marmar, J.E. Rice, J.L. Terry and F.H. Seguin, Nucl. Fus. 22 (1982) 1567.

[13] M.A.Graf, J.E. Rice et al. Rev. Sci. Instr. 66 (1995) 636.

[14] N. Hawkes,.Z. Wang, R. Barnsley et al. Proc. 16th EPS Conference on Contr. Fus. and Pl. Phys. Part I (1989) 79.

[15] J.W. Connor and J.B. Taylor Nucl. Fusion 17 (1977) 1047.

[16] P.N. Yushmanov, T. Takizuka, K.S. Riedel et al. Nucl. Fusion 30 (1990) 1999.

[17] A. Taroni, M. Erba, E. Springmann and F. Tibone Plasma Phys. Controll. Fusion 36 (1994) 1629.

A Semi-empirical Drift-wave Model for the Simulation of Impurity Transport and Comparison with JET Experiments

L Lauro Taroni, J W Connor[1], R Giannella, F Romanelli[2], H R Wilson[1].
JET Joint Undertaking, Abingdon, Oxfordshire, OX14 3EA, UK.
[1] UKAEA Government Division, Fusion, Culham, Abingdon, Oxfordshire, UK.
[2] Associazione Euratom-ENEA sulla Fusione, Frascati, Italy.

INTRODUCTION

Results from systematic studies on trace impurities (Ni, Fe, Mo) injected into **L-mode** plasmas in JET have characterised the radial and parametric dependences of the impurity diffusivity D and convective velocity v, where the impurity flux Γ_Z is written $\Gamma_Z=-Dn_Z+vn_Z$ [1,2]

- **in L-mode diffusion is the dominant transport mechanism** over most of the **bulk** plasma
- **in the plasma core, inside a critical radius r_c, the transport is slow** (but still 2-10 times neoclassical),
- **in the outer region the transport is highly anomalous,** and scales in a similar manner to heat transport with average outer values of $\mathbf{D \propto \nabla T_e}$.
- **the radial position r_c can be put in relation with the position where the magnetic shear**

$$s \equiv \frac{d(\ln q)}{d(\ln r)} \cong 0.5$$

(where q is the safety factor and r the radial coordinate along the minor radius, a)

In the following the theoretical transport coefficients (in particular their radial dependence) derived from various classes of electro-static microinstabilities that are predicted to exist in tokamaks will be assessed against their experimental measurements.

COMPARISON OF JET IMPURITY TRANSPORT DATA WITH EXISTING THEORETICAL MODELS

The comparison of the experimental transport coefficients with the ones predicted from various theories has been carried out with particular attention to the performance of the models in saw-toothing and sawtooth-free plasmas with various currents and q-profiles.
The L-mode discharges analysed for this comparison are:

#	inj.imp.	I (MA)	$n_e(0)10^{19}m^{-3}$	$T_e(0)$ keV	$x_c=r_c/a$
27414	**Ni**	**2**	**3.8**	**4**	**0.35**
27410	**Ni**	**3**	**4.7**	**4.5**	**0.38**
27416	**Ni**	**5**	**3.3**	**4.8**	**0.56**
18112	**Mo**	**3**	**2.9**	**9**	**0.38**
27342	**Fe**	**3.5**	**4.7**	**4.2**	**0.43**

- In all these cases the electron density profiles are fairly flat in the central region.
- The discharge 18112 is a monster sawtooth (note the high central T_e).
- All other discharges show flattened Te profiles in the central region, due to the sawtooth activity.
- $T_i = T_e$ has been assumed

In these experiments only trace levels of impurity were injected, which are therefore not expected themselves to excite impurity driven modes.

For low impurity concentrations ($Zn_z/n_e<0.1$), the transport of impurities is determined by **pure plasma modes.**

SLAB MODELS:

1. Ion temperature gradient (ITG) [3]

A slab analysis of this mode is relevant in slab geometry only when $L_s < \frac{R}{2}$, where $L_s = Rq/s$ is the shear length and R the major radius.

As can be seen from fig.1, this inequality is **never** satisfied for the above shots.

This was observed also in the shots used to analyse the ion thermal transport [4] and appears to be a general characteristic of JET discharges.

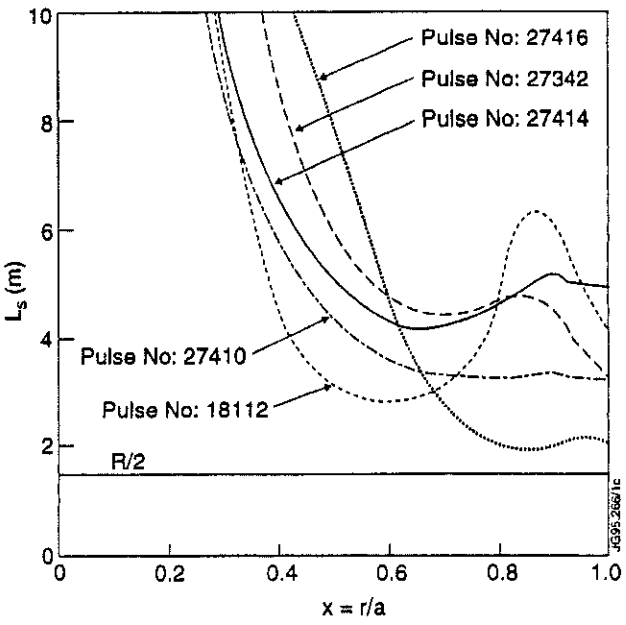

Fig.1. Shear length L_s as a function of the normalised radius for the 5 discharges

the slab ITG mode
cannot
be invoked to interpret transport in JET

2. Trapped electron driven mode [5]

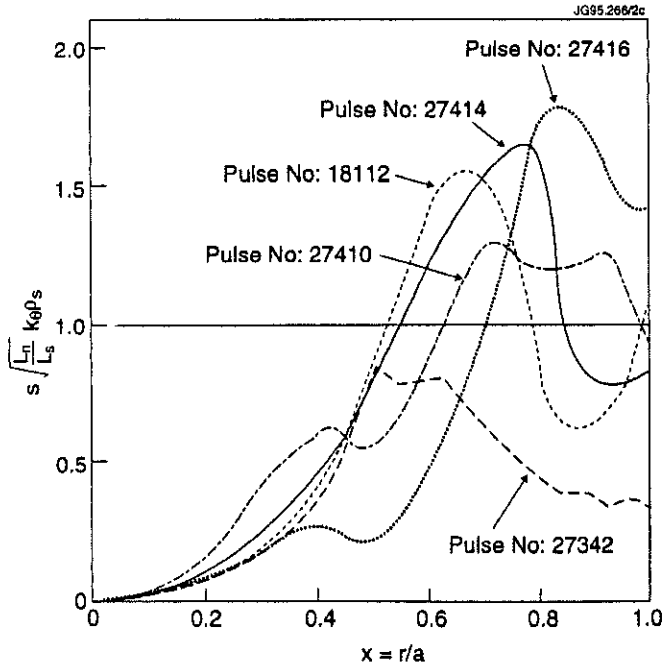

Fig.2. Radial profiles of $s(L_n/L_s)^{0.5}$ for each discharge

The analysis of this mode shows that in order to have transport

$$s\sqrt{\frac{L_s}{L_n}}\cdot k_\vartheta \rho_s \rangle 1 .$$

Here k_ϑ is the poloidal mode number, ρ_s the ion Larmor radius evaluated with the electron temperature and $L_n = \frac{n}{\nabla n}$ the electron density profile scale length.

As can be seen in fig.2 (where this inequality is shown for $k_\vartheta\rho_s=1$), regions of **marginal** validity for this model may exist towards the plasma edge, for **x≡r/a>0.5.**

But, the full expression of the diffusivity contains a $T_e^{3/2}$ term (pure gyro-Bohm scaling) which leads to a **radial decrease of the transport in this outer region.**

TOROIDAL MODES

1. Toroidal ITG mode [6]

The form of D for this instability is predicted to be:

$$D_z \approx \frac{\varepsilon_n}{\sqrt{\tau}} \left(\frac{\eta_i^{0.5}}{s\, q\, \varepsilon_n^{0.5}} \right)^{0.5} \frac{\rho_i\ v_{th,i}}{L_n}$$

where $\eta_i = \frac{L_n}{L_T}$ with $L_T = \frac{T}{\nabla T}$ the temperature scale length, $\varepsilon_n = \frac{L_n}{R}$, $\tau = \frac{T_e}{T_i}$, ρ_i the ion Larmor radius and $v_{th,i}$ the ion thermal speed.

This result is valid when η_i exceeds a critical value η_c, given in [6]

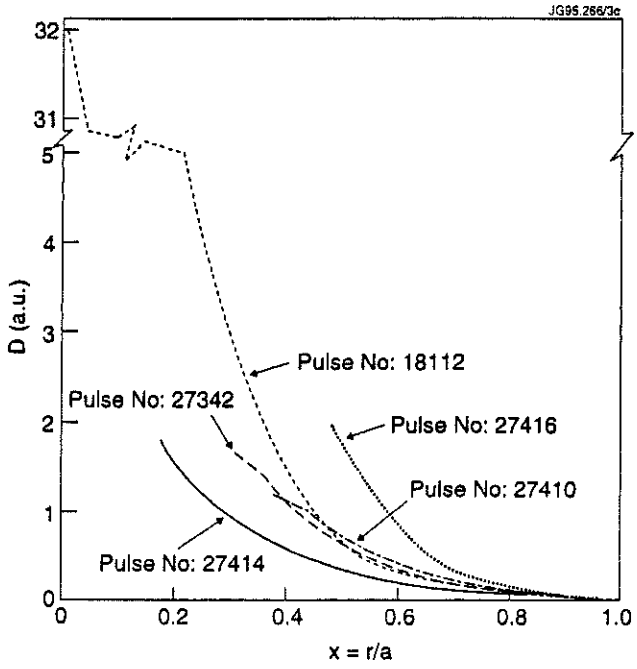

Fig.3.Predictions of the quasi-linear estimate of D based on the toroidal ITG mode.

Fig.3 shows the predictions from this model, as far as the radial shape is concerned, for the chosen discharges.

In the case of the monster sawtooth $\eta_i \rangle \eta_c$ everywhere.

> Also this model implies a **pure gyro-Bohm scaling** $\left(\rho_i^2 v_{th,i} / L_n\right)$ and leads to **lower transport towards the outer region, in contrast with the experimental observations**

Note also that the dependence on q and s is in the opposite direction to the experimental observations.

2. Trapped Ion Instability (ITG driven) [7]

The quasi-linear estimate of the diffusion coefficient is

$$D \approx \frac{k_\vartheta \rho_i}{4}\left[\frac{\varepsilon_n\sqrt{2\varepsilon}}{1+\tau}\right]^{0.5}(1+\eta_i)^{1.5}\,\frac{\rho_i^2 v_{th,i}}{L_n}$$

and is shown in fig.4.

The central depression in the diffusivity predicted by this theory in sawtoothing discharges is a consequence of the flattening of the temperature profile, as is clearly demonstrated by the **poor prediction in the case of a peaked temperature profile** (pulse 18112).

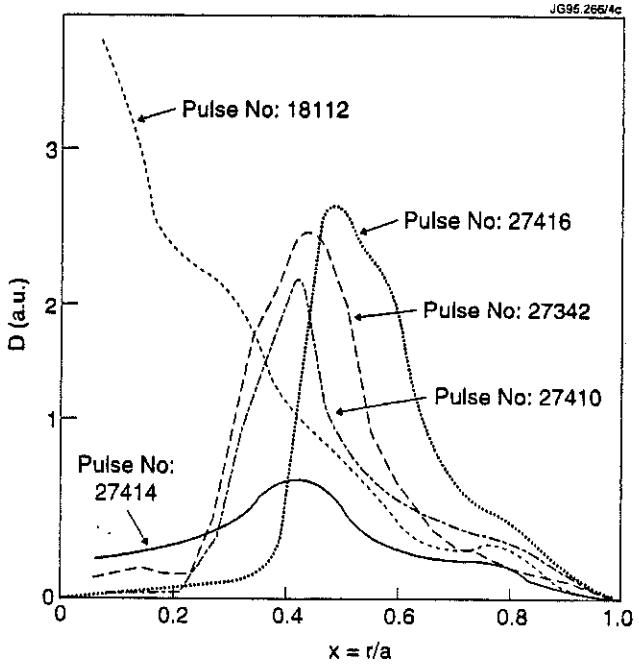

Fig.4.Predictions for the quasi-linear estimate of D based on the trapped ion mode.

The trapped-ion model does **not** give a good description of the anomalous transport

---

SUMMARY of the theoretical models analysed so far.

Conventional models based on **drift-wave** mechanisms are **unsatisfactory** for the main reason that the **diffusivity** associated with these waves assumes the radial correlation length $L_r=O(\rho_i)$. Therefore, due to the resulting dominant $T^{3/2}$ (pure gyro-Bohm) dependence (which it is difficult to offset by other geometrical factors) the diffusivity **decreases towards the outer region.**

TOROIDAL COUPLING of MODES

- **Global mode structures due to toroidal coupling** [8,9] of neighbouring modes

  → **enhanced estimate of the correlation length:** $L_r \approx (a\rho_i/s)^{1/2}\exp(-c/s)$

  → **semi-empirical model of anomalous transport**

Explicit expressions for the transport coefficients are:

$$D = \alpha D_B \left|\frac{a}{L_T}\right| \frac{\exp\left(\frac{-2c}{s}\right)}{s} \quad \text{and} \quad v = -\frac{D}{R}$$

where $D_B = \frac{cT}{eB}$ is the usual Bohm diffusion term (B being the magnetic field).

This form

- fits the required decrease in the low-shear region, irrespective of the sawtooth activity
- fits the dependence on the temperature gradient
- is independent of the impurity charge Z
- is close to the Bohm-like coefficient for energy transport proposed in ref.[10]

The shape function $\frac{\exp\left(\frac{-2c}{s}\right)}{s}$ vanishes towards the plasma centre where $s \rightarrow 0$.

In this region, however, L_r should not fall below ρ_i.

Therefore a gyro-Bohm-like term needs to be added in order to have a residual transport in the region of low shear. The resulting diffusivity is:

$$D = \alpha D_B \left\{ \left|\frac{a}{L_T}\right| \frac{\exp\left(\frac{-2c}{s}\right)}{s} + \beta \frac{\rho_i}{a} \right\}$$

The search for a set of values for the numerical factors α, β and c in this semi-empirical model that give a reasonable prediction for both the **radial extent of the low transport region** and the **average magnitude of the diffusivity in the region of fast transport** for all the discharges has lead to:

$$\alpha = 0.008 - 0.01$$
$$\beta = 3.5 - 4$$
$$c = 1.2 - 1.4$$

The resulting semi-empirical diffusivities are shown in fig.5 and they are compared with the experimental ones [1].

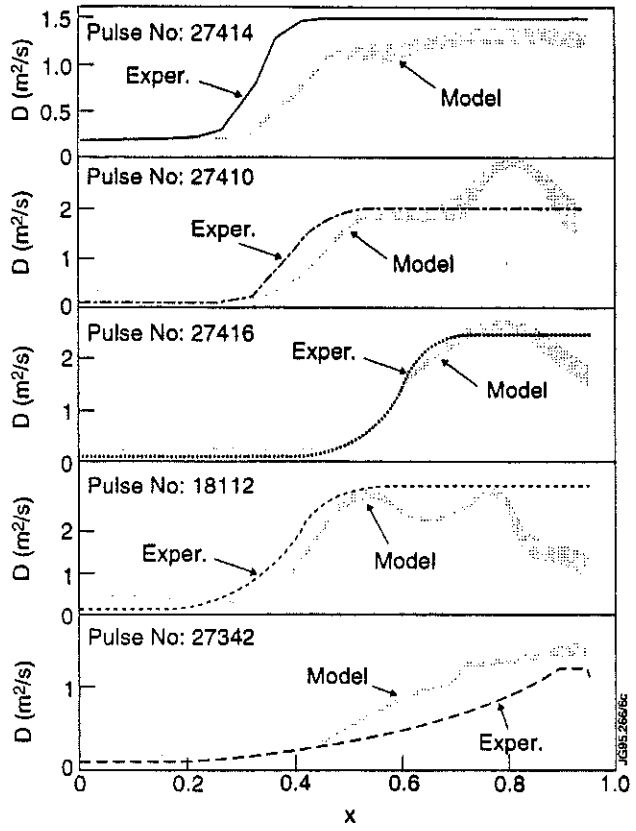

Fig.5. Comparison of the experimental D with the one predicted from the semi-empirical model for each discharge.

The performance of this semi-empirical model (with the ad hoc treatment of the periphery) has been assessed by means of predictive simulations for the listed discharges.

As an example, the comparison of some experimental data with their corresponding simulated results is shown for the case of the discharge #27410 in the next figures.

Fig.6 shows the time histories of the normalised brightness for various ionised states of the injected Ni together with their simulation.

Setting up a Predictive Model

This model is not expected to describe the last few cm close to the separatrix. Ad hoc treatment of this region is needed[11] for the predictive simulation, i.e. a **peripheral transport barrier** (decrease of D and strong increase of the inward convection v) preventing too fast an outward diffusion of the lower-intermediate ionised ions.

Observations

Even if diffusion is the dominant transport mechanism, a small convection is necessary for a good simulation of the time evolution of the brightness lines [1]. The **v** predicted by this model **is probably too small, and does not vanish in the centre,** as it would be desirable.

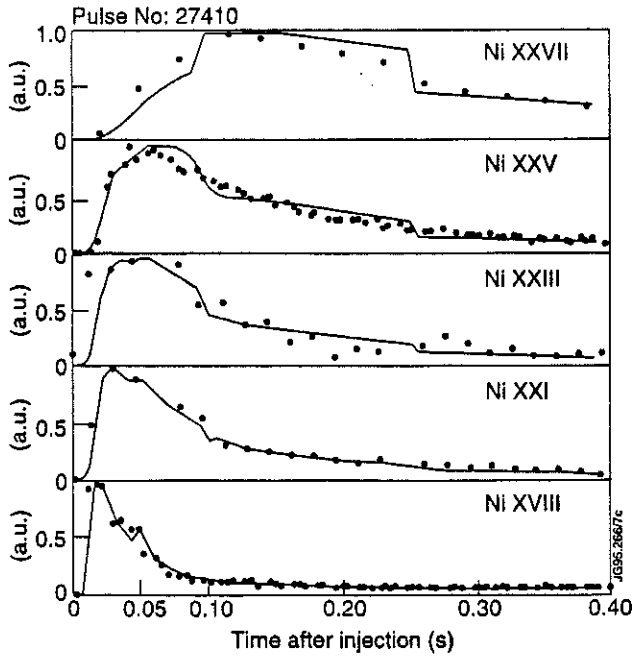

Fig.6. Time history of some experimental (dots) spectroscopic lines and their simulation (solid lines) for discharge #27410.

Fig.7 shows the experimental profiles of the perturbation to the soft X-ray emissivity and the corresponding simulated ones.

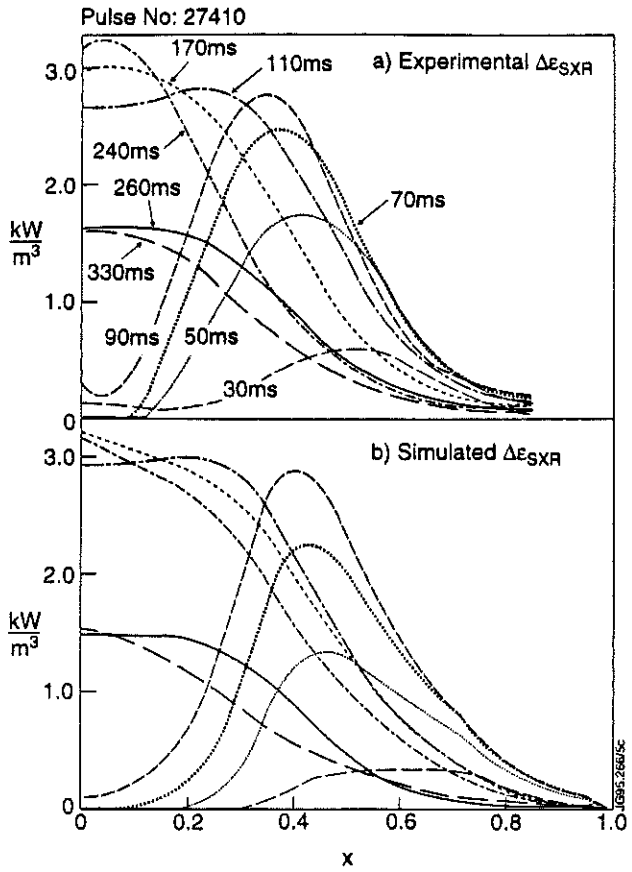

Fig.7. Experimental and simulated emissivity profiles for discharge #27410

CONCLUSIONS

- The conventional drift-wave models fail as they imply a pure gyro-Bohm scaling
- The enhancement of the correlation length due to the toroidal coupling of neighbouring modes has led to a promising expression for the anomalous transport coefficients

REFERENCES

[1] R Giannella et al, Nucl. Fus. 34 (1994) 1185
[2] D.Pasini, M Mattioli et al, Nucl Fus. 30 (1990) 2049
[3] W.Horton et al, Phys.Fluids 24 (1981) 1077
[4] J.W. Connor et al, Plasma Phys. Contr. Fusion, 35 (1993) 585
[5] F.Gang et al,Phys.Fluids B 3 (1991) 68
[6] F.Romanelli, Phys.Fluids B 1 (1989) 1018
[7] H.Biglari et al, Phys.Fluids B 1 (1989) 109
[8] F.Romanelli and F.Zonca, Phys.Fluids B 5 (1993) 4081
[9] J.B.Taylor and H.R.Wilson, Culham Lab.Report, UKAEA FUS 279 (1995)
[10] A.Taroni et al., Plasma Phys. Contr. Fus. 36 (1994) 1629
[11] B.Denne-Hinnov et al., Proc.20th EPS Conf. Lisbon (1993), Vol17C,I-55

Disruption Control by an m/n=9/5 Static Helical Magnetic Field

Q Yu[1].
JET Joint Undertaking, Abingdon, Oxfordshire, OX14 3EA, UK.
[1] Permanent address: Institute of Plasma Physics, Hefei, 230031, P.R. China.

ABSTRACT:

The growth of the m/n=2/1 tearing mode in the presence of a small m/n=9/5 static helical field is studied numerically. The amplitude of the m/n=2/1 mode is found to be reduced as the magnitude of the m/n=9/5 field increases. The m/n=2/1 mode becomes stable when the m/n=9/5 magnetic island essentially overlaps the q=2 flux surface. Two nonlinearly saturated states of the m/n=2/1 mode are found in the presence of a small m/n=9/5 field. With a sufficiently large magnitude of the m/n=9/5 helical field oscillations of the amplitude of the m/n=2/1 mode are excited.

1. INTRODUCTION

Disruption control is an important issue in tokamaks. The tearing mode with mode number m/n=2/1 is generally considered to be the most dangerous instability[1-2], and in recent years the control of this mode has attracted much research interest. Several methods have been suggested, including magnetic feedback and modification of the current profile using localised current drive or heating[3-4].

In the present work the nonlinear growth of resistive tearing mode is studied for a new kind of equilibrium configuration in which a zeroth-order axisymmetric equilibrium field is superposed with a small m/n=9/5 helical field. This equilibrium configuration is shown to be more stable for the tearing mode than the conventional axisymmetric configuration.

2. THEORETICAL MODEL

Cylindrical geometry is employed corresponding to the large aspect-ratio tokamak approximation. The basic equations are the Ohm's law and the equation of motion.

$$\partial_t \psi + (\mathbf{v}\cdot\nabla\psi) = -\eta j_z \tag{1}$$

$$\rho\, d_t \nabla^2 \phi = \mathbf{z}\cdot(\nabla\psi \times \nabla j_z) + \mathbf{z}\cdot\nabla\times[\nu(\nabla^2\mathbf{v})] \tag{2}$$

where ψ is the flux function, $\mathbf{B}= B_{0z}\mathbf{e_z} - (nr/mR)B_{0z}\mathbf{e}_\theta + \nabla\psi\times\mathbf{z}$, ϕ is the stream

function, $\mathbf{v}= \nabla\phi\times\mathbf{z}$, **B, v** and j_z denote the magnetic field, plasma velocity and the current density along **z** direction (toroidal direction), and the subscript 0 denotes an equilibrium quantity. η and ν are the plasma resistivity and viscosity, ∂_t denotes $\partial/\partial t$ and $d_t = \partial_t + \mathbf{v}\cdot\nabla$.

ψ and ϕ are expanded in Fourier series,

$$\psi = \psi_{0(r)} + \Sigma\, \psi_{m/n(r,t)}\exp[i(m\theta - n\varphi)] \tag{3}$$

$$\phi = i\Sigma\, \phi_{m/n(r,t)}\exp[i(m\theta - n\varphi)] \tag{4}$$

where θ and φ are the poloidal and the toroidal angles.

Equations (1)-(4) has been solved numerically. The effect of the m/n=9/5 helical field is taken into account by choosing the boundary value

$$\psi_{9/5(r=a)} = A_{9/5} a B_{z0} \tag{5}$$

where $A_{9/5}$ is a prescribed value for the calculation, representing the amplitude of the m/n=9/5 field, and a is the minor radius. The equilibrium has a safety factor $q(r)=1.078[1+(r/0.56a)^4]^{1/2}$, $S_{R(r=0)} = \tau_R/\tau_A = 10^5$ and $S_{\upsilon(r=0)} = \tau_\upsilon/\tau_A = 10^7$, where the Alfven time $\tau_A = a\rho^{1/2}/B_{z0}$, the resistive time $\tau_R = a^2/\eta$ and the viscous time $\tau_\upsilon = \rho a^2/\upsilon$, ρ being the plasma density. The q=2 surface is located at $r_s = 0.7a$.

3. RESULTS

Figure 1 shows the nonlinear evolution of $w_{2/1}$ for different values of $A_{9/5}$, where the dimensionless parameter

$$w_{m/n}= 4|(\psi_{m/n}/ \psi_0'')_{r=rs}|^{1/2}/a \qquad (6)$$

represents the magnetic island width of the m/n mode normalised to the minor radius.

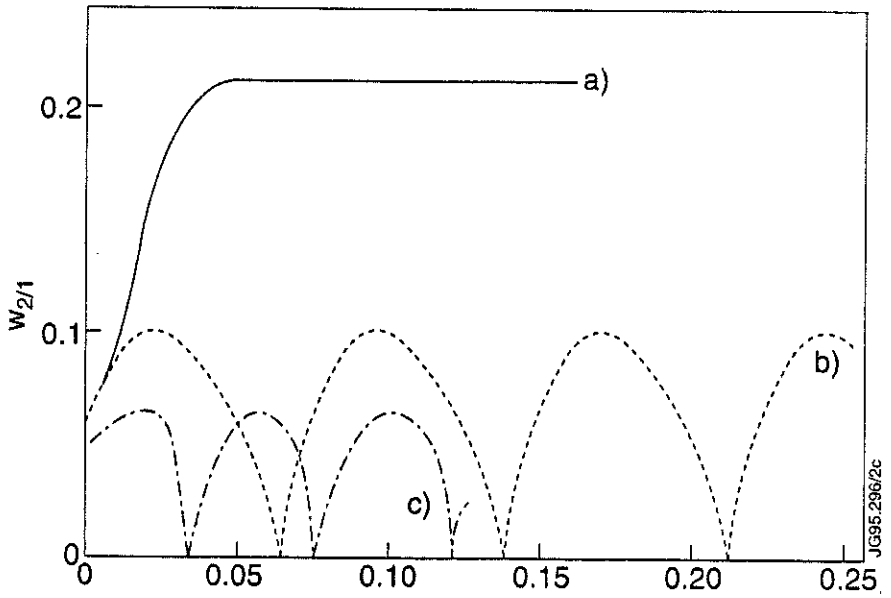

Fig.1 Nonlinear evolution of $w_{2/1}$ with different magnitudes of the m/n=9/5 helical field: $A_{9/5}$=0 for (a), $A_{9/5}=3.8\times10^{-3}$ for (b), and $A_{9/5}=7.0\times10^{-3}$ for (c)

Curve(a) is the reference case, with $A_{9/5}$=0. Since the equilibrium q(r) profile is unstable to the m/n=2/1 mode, the m/n=2/1 mode grows from a small initial value to nonlinear saturation. The width of the magnetic island at saturation is $w_{2/1}$=0.21

When an m/n=9/5 helical field is applied from t=0, $w_{2/1}$ at saturation decreases as $A_{9/5}$ increases. In Fig.1 the strength of the helical field is $A_{9/5}=3.8\times10^{-3}$ for curve(b), $A_{9/5}=7.0\times10^{-3}$ for curve(c). When $A_{9/5}$ is large enough($A_{9/5}=8.0\times10^{-3}$), the m/n=2/1 mode becomes stable and $w_{2/1}$ decays from its initial value.

For small $A_{9/5}$, the growth leads to a stationary saturated amplitude. For $A_{9/5}>3.8\times10^{-3}$, the nonlinear amplitude of the perturbations begins to oscillate. The oscillating period is of a small fraction of the resistive time, and its amplitude decreases as $A_{9/5}$ increases.

Two nonlinearly saturated states of the m/n=2/1 mode are found in the presence of a small m/n=9/5 field. When the simulation is carried out with $A_{9/5}$ initially zero, and a small m/n=9/5 field is then turned on ($A_{9/5}=3.8\times10^{-3}$) after $w_{2/1}$ reaches saturation, the saturated value, $w_{2/1}$ =0.21, is unaffected. However, when $A_{9/5}=3.8\times10^{-3}$ is applied from t=0, $w_{2/1}$=0.11 at saturation. When $A_{9/5}$ is large enough(for example, $A_{9/5}=8.0\times10^{-3}$), only one saturated state is found, and the saturated amplitude of $w_{2/1}$ does not depend on the time at which the m/n=9/5 field is turned on.

Figure 2 shows the nonlinear saturated amplitude of $w_{2/1}$, $w_{9/5}$ and the overall island width w as functions of $A_{9/5}$, where w is the total radial width occupied by the m/n=2/1 and m/n=9/5 magnetic islands normalised to minor radius. The m/n=9/5 field is applied from t=0. We note the following results: (1) for small $A_{9/5}$, $A_{9/5}<3.5\times10^{-3}$, $w_{2/1}$ is essentially not changed, (2) when $A_{9/5}$ $>8\times10^{-3}$, the m/n=2/1 mode is stable, and (3) $w_{9/5}$ is different from the vacuum case because of the plasma response.

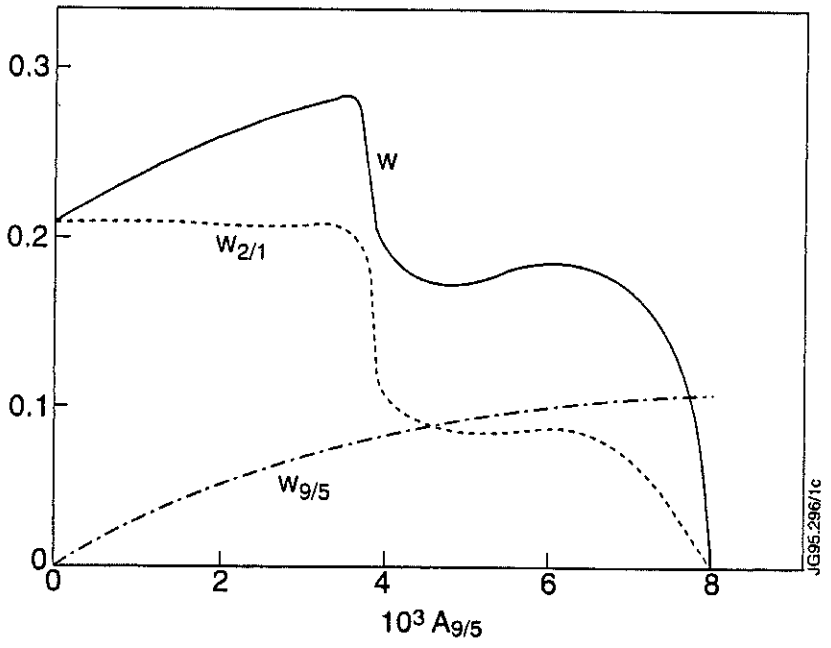

Fig.2 Nonlinear saturated amplitude of $w_{2/1}$ $w_{9/5}$ and w versus $10^3 A_{9/5}$.

4. SUMMARY

The growth of m/n=2/1 tearing mode has been studied numerically in the presence of a small m/n=9/5 helical field. In the case studied it is found that:

(1) $w_{2/1}$ decreases as $A_{9/5}$ increases. $w_{2/1}$ is reduced from 0.21 to zero when $A_{9/5}$ changes from zero to 8×10^{-3}, the corresponding $w_{9/5}$=0 - 0.11.

(2) Two nonlinearly saturated states of the m/n=2/1 mode are found in the presence of a small m/n=9/5 field.

(3) Oscillations of the amplitude of the m/n=2/1 mode are excited with sufficiently large magnitude of the m/n=9/5 helical field.

ACKNOWLEDGEMENT:

I am grateful to Dr. J. A. Wesson for his help in preparing this paper.

REFERENCE

[1] H. P. Furth, J. Killeen, and M. N. Rosenbluth, Phys. Fluids **6**, 459 (1963).
[2] H. P. Furth, P. H. Rutherford, and H. Selberg, Phys. Fluids **16**, 1054(1973).
[3] E. Lazzaro and M. F. F. Nave, Phys. Fluids **31**, 1623 (1988).
[4] A. W. Morris, Plasma Phys. and Controll. Fusion, **34**, 1871(1992).

The Influence of Edge Currents and Pressure Gradients on the MHD Stability of Low-n External Kink Modes

G T A Huysmans, C D Challis, M Erba, W Kerner, V V Parail.
JET Joint Undertaking, Abingdon, Oxfordshire, OX14 3EA, UK.

INTRODUCTION

- Low-n external kink modes are a possible cause for the giant Edge Localized Modes (ELMs) (and slow roll-overs) that often terminate the good performance phase of hot-ion H-modes (see posters T. Hender and P. Smeulders). Fast ECE T_e measurements show that the giant ELM affects a large volume of the plasma on a very short time scale (<<1 ms). In addition, low-n mode activity has been observed during large ELMs.
- For typical JET plasma shapes a finite edge current is required for access to the second stable regime for ballooning modes. If the edge current required is too large, a kink mode will become unstable before the second stable regime is reached and no stable route to second stability exists.

In this poster the stability of the low-n external kink mode is studied as a function of the edge current density and the edge pressure gradient. First the general behaviour of the external kink mode in a circular plasma is discussed. Then, the kink and ballooning stability and access to the second stable regime is discussed for two types of JET discharges, a hot ion H-mode and a high β_{pol} discharge.

The MHD stability calculations performed with the CASTOR code in toroidal geometry. The HELENA, code linked to the TRANSP and JETTO transport codes, is used to calculate the equilibrium and the metric as input for the CASTOR code.

CIRCULAR PLASMAS

The growth rate of the low-n external kink mode mainly depends on the value of the edge current (see **Fig.1**). However, the edge pressure gradient in the region of the localisation of the mode has a strong influence (see **Fig.2**). For small pressure gradients well below the ballooning limit, a finite pressure gradient is stabilising the external kink mode. This effect is most

pronounced for the lowest toroidal mode numbers. For edge pressure gradients close to the ballooning limit, the pressure gradient becomes destabilising for the n>1 modes. This is because the higher-n modes can be more localised on the outside in the bad curvature region.

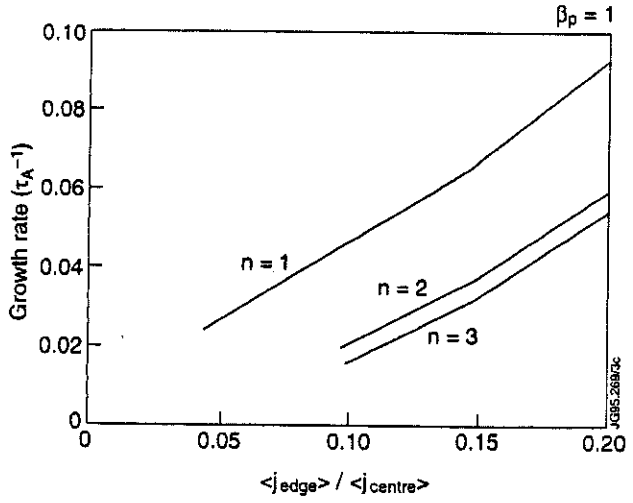

Fig.1 The growth rate of the n=1,2 and 3 external kink mode in a circular plasma as a function of the edge current density. (a/R=0.3,β_{pol}=1)

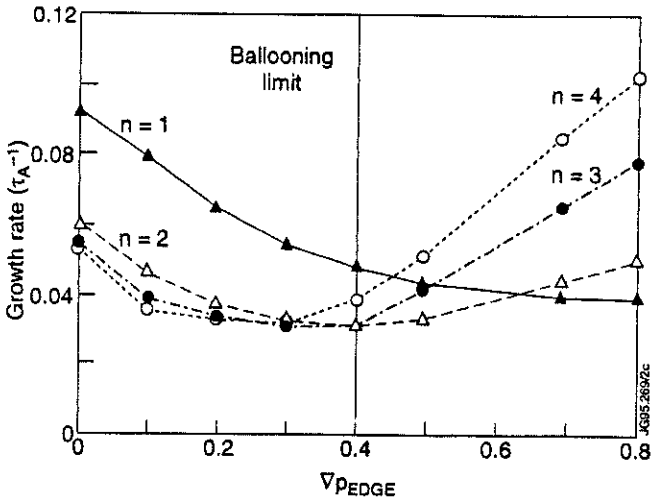

Fig. 2 The growth rate of the external kink for toroidal mode numbers n=1, 2, 3 and 4 as a function of the edge pressure gradient. The ballooning limit is also indicated.

(MORE ON) CIRCULAR PLASMAS

Fig.3 shows the stability diagram for ballooning modes (at ψ=0.95) and the n=3 external kink mode in the plane of the edge pressure gradient and the edge current.

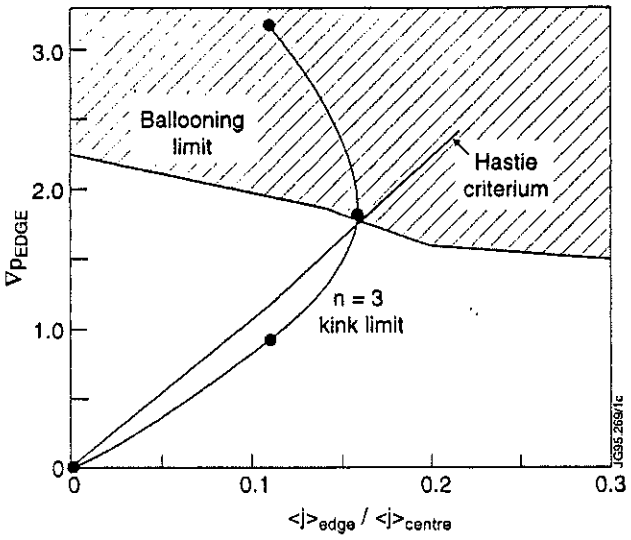

Fig.3 Stability diagram for ballooning and external kink modes for a circular plasma. (a/R=0.3, β_{pol}=1.)

Included in the **Fig.3** is the local stability criterion by J. Hastie for kink modes, which also predicts the stabilising effect of the edge pressure gradient. This criterion does however not contain the destabilising effect of the pressure gradient. The agreement with the full calculation is reasonably good for low values of the pressure gradient.

Hastie's local kink stability criterion :

$$p'\left\{\frac{d}{d\psi}\oint Jd\chi - p'\oint\frac{Jd\chi}{B_p^2}\right\} + F'\left\{q' - 2p'\oint\frac{FJd\chi}{R^2B_p^2} - F'\oint\frac{JB^2d\chi}{R^2B_p^2}\right\} > 0$$

JET HOT ION H-MODE DISCHARGES (low triangularity)

The JET hot-ion H-mode discharge #30591(see **Fig. 4**) is analysed with respect to kink and ballooning modes. The good performance phase is terminated by a giant ELM at t=12.2s. (I=2.5MA, β_N=2.5). The evolution of the discharge is modelled with the JETTO transport code. The resulting profile of the total toroidal current density is shown in **Fig.5** included is the bootstrap current profile. The total bootstrap current is increasing linearly in time up to the point of the giant ELM.

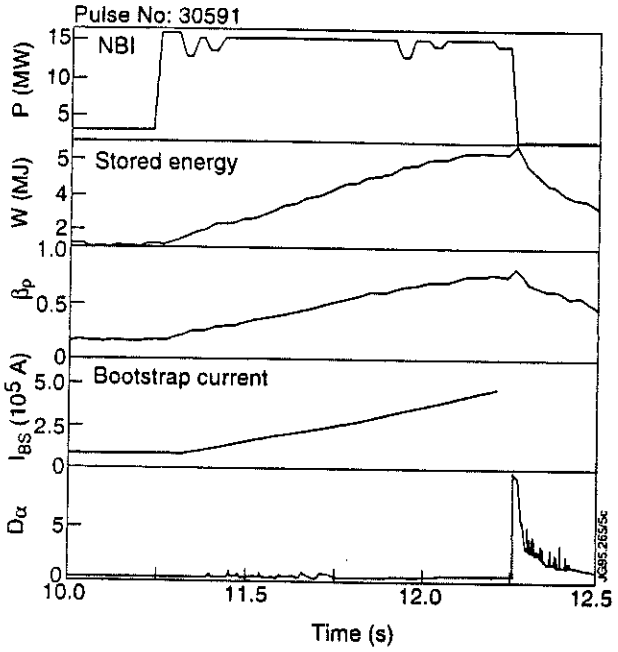

Fig 4a Traces of the NBI heating power, stored energy, poloidal beta, the total bootstrap current and D_α. for discharge #30591.

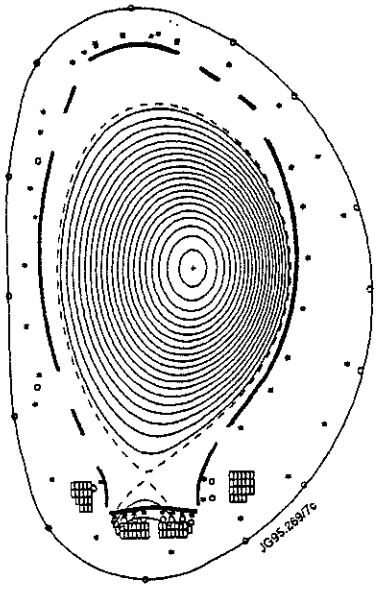

Fig. 4b The plasma shape of discharge #30591, δ= 0.2.

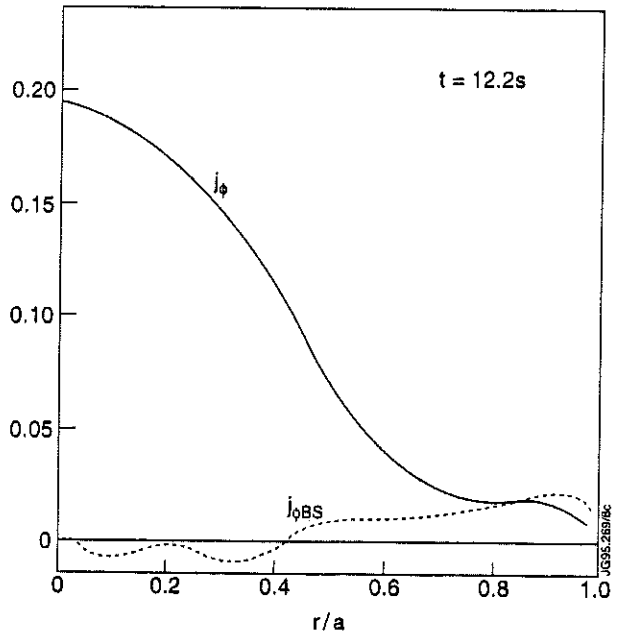

Fig. 5 The toroidal current density profile and the profile of the bootstrap current as a function of the minor radius.

MHD STABILITY OF A JET HOT ION H-MODE DISCHARGE (low triangularity)

The stability diagram for this low triangularity discharge is shown below (**Fig. 6**). The figure is calculated by changing the pressure gradient and the current density in the region ψ=0.95-1.0, keeping the total poloidal β fixed.

The value of the pressure gradient and the edge bootstrap current as obtained from the JETTO simulation is indicated in **Fig. 6**, showing that the values of the bootstrap current are potentially large enough to drive an external kink unstable.

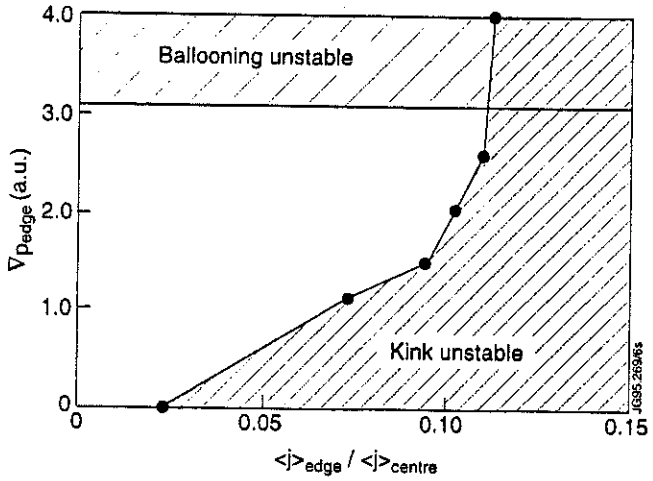

Fig.6 Stability diagram for discharge #30591, t=52.2s. The ballooning mode stability is evaluated at ψ=0.95. The external kink has a toroidal mode number n=3.

It is clear from **Fig.6** that for this discharge with a low triangularity there is no access to the second stable region for ballooning modes. A low-n kink mode would become unstable well before the plasma edge becomes reaches the second stability region.

JET HIGH BETA POLOIDAL DISCHARGE

Transiently improved confinement has been observed in some JET high β_{pol} discharges (see poster G. Sips). This has been correlated with oscillations in the total current. Discharge #32344 is an example of this (see **Fig. 7**). Repeating the discharge with pre-programmed current ramps yielded a similar phase of improved confinement. The edge pressure gradient show a marked increase during this phase.

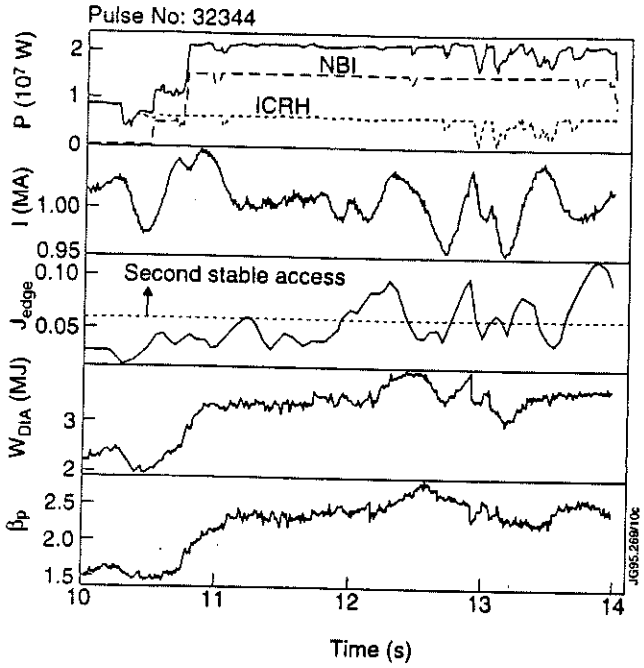

Fig 7a Traces of the total heating power, total current, edge current density (from TRANSP), the stored energy and poloidal β for discharge #32344.

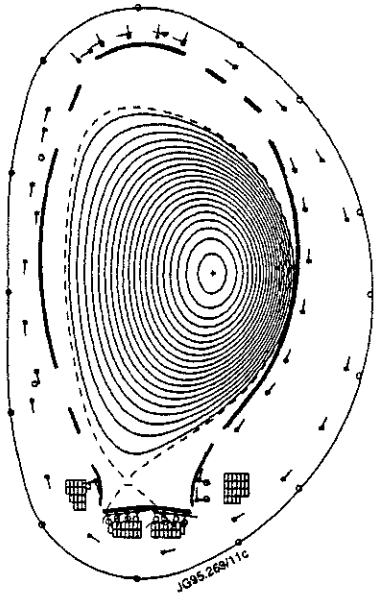

Fig. 7b The plasma shape of discharge #32344.

The current profile evolution of this discharge was analysed with the TRANSP code. The evolution of the current profile is plotted in **Fig.8**. Due to the high value of β_{pol} (>2.5) and the inherent high value of the triangularity only a small edge current is required to bring the plasma edge from ψ = 0.95 to 1.0 into the second stable region with respect to ballooning modes. The value of the current density at which ψ =0.95 becomes stable is indicated in **Fig.7a**. The time at which the experimental edge current exceeds this value correlates well with the observed improved confinement and increasing edge gradients.

HIGH β_{pol}; ACCESS TO SECOND STABLE REGIME

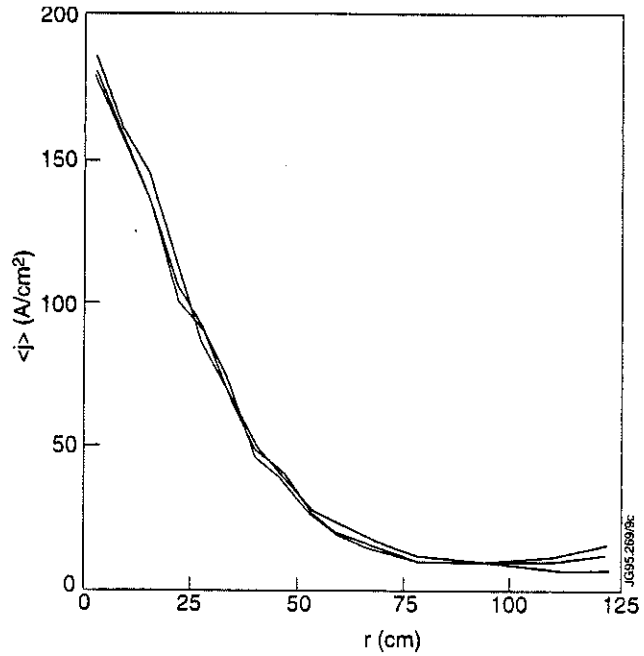

Fig 8 The development of the toroidal current density profile during the oscillation in the total current from at t=51.75s, t=52.0s and t=52.25s, showing the increase in the edge current density.

Results of the n=1 external kink stability calculation are shown in Fig.9 together with the ballooning stability curve. The n=1 and n=2 kinks are very stable in this configuration. An open gap does exist between the ballooning and the kink stability curves giving acces to a region where large pressure gradients and the associated edge currents are stable.

The experimental path the discharge follows in the grad(P)- J_{edge} plane is indicated in **Fig.9**. Before the ramp of the current the pressure gradients at the edge are calculated to be marginally stable to ballooning modes.

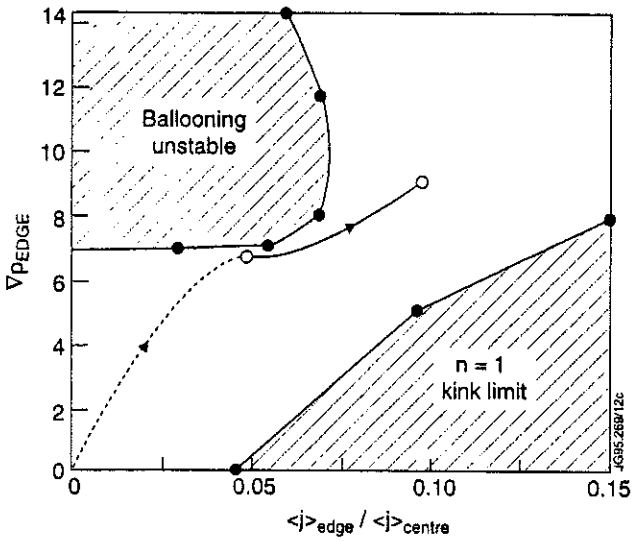

Fig. 9 Stability diagram for high β_{pol} discharge #32344 at t = 52.25 s.

CONCLUSIONS

- Localised external kink modes (also called peeling modes) are destabilised by a finite value of the *edge current.*
- *Low values of the edge pressure gradient* (well below the ballooning limit) have a stabilising effect on the external kink mode especially on the n=1 mode. With increasing *pressure gradient (of the order of the ballooning limit)* the external kink mode is destabilised by the pressure, at first for the higher-n kink modes.
- The value of the edge bootstrap current obtained from transport simulations of hot-ion H-modes can be large enough to drive an external kink unstable. The external kink, which is very localised at the edge, is a possible cause for the giant ELMs that can limit the performance in the hot-ion H-mode discharges.
- At the low values of β_{pol} and triangularity there is no access to the second stability region, external kink modes become unstable well before the edge becomes second stable to ballooning modes.
- The observed improved confinement phases in the JET high poloidal beta discharges due to current ramps agree well with the stability calculations of ballooning and kink modes and the predicted access to the second stable regime.

Bifurcations and Magnetic Reconnection

C Tebaldi[1], M Ottaviani, F Porcelli[2].
JET Joint Undertaking, Abingdon, Oxfordshire, OX14 3EA, UK.
[1] Permanent address: Dept of Mathematics, University of Lecce, Lecce, Italy.
[2] Permanent address: Dept. of Energetics, Politecnico di Torino, Turin, Italy.

ABSTRACT

The sequence of equilibria of two-dimensional reduced magnetohydrodynamics (RMHD) has been studied as a function of the tearing mode stability parameter Δ'. After a first bifurcation from the symmetric state occurring at $\Delta' \approx 0$, which gives origin to a state of slightly broken symmetry with a small magnetic island, the system undergoes a second bifurcation, of tangent type, at $\Delta' \approx 1$. Once this value is crossed, no stationary solution with a small island exists. The system rapidly evolves to a state of macroscopic size islands. This general property of RMHD is proposed as a basic ingredient of the observed intermittent magnetic events in tokamaks.

INTRODUCTION.

Intermittent enhancement of magnetohydrodynamic (MHD) activity is a common experimental observation in laboratory plasmas.

In Tokamak plasmas, examples are the sawtooth relaxation, the so called edge-localised modes (ELMs) occurring in high confinement regimes and disruption events that lead to a sudden termination of the current discharge.

Often these events are preceded by a well identified precursor, namely the occurrence of an observable slowly growing magnetic island inside the plasma.

The trigger problem[1].

The excitations that break the symmetry of the initial state are of the "soft" type. For values of some control parameter slightly above the stability threshold of the axisymmetric state, the system settles in a neighbouring state of slightly broken symmetry, for example an equilibrium with a small saturated magnetic island.

Natural conceptual framework to deal with this problem: the theory of bifurcations in dynamical systems [2].

Strategy:

a) Investigate the nature of the second bifurcation from the nonsymmetric saturated state.

b) Look for a tangent (saddle-node) bifurcation or a subcritical (hard) Hopf-type. Upon a slow variation of the control parameter, both types of bifurcations lead to abrupt ("catastrophic") changes in some observable quantity.

This work: we analyse the sequence of bifurcations occurring in a slab model of reduced resistive MHD (RRMHD), when the tearing mode stability parameter Δ' is varied.

Main result: after a first bifurcation (occurring at $\Delta' \approx 0$) leading to a saturated tearing mode with a small amplitude magnetic island, the system undergoes a tangent bifurcation at $L\Delta' \approx 0$, where L is a macroscopic scale length (size). Above this value of Δ' no equilibria with small islands exist. The system jumps to a state where the island width is of order L.

Side result: the existence of the precursor is naturally predicted, as it corresponds to the state of slightly broken symmetry occurring between the first and the second bifurcations.

The model.

We consider a two-dimensional incompressible plasma obeying the usual RRMHD equations.

$$\partial_t U + [\varphi, U] = [J, \psi] + \mu \nabla^2 U \tag{1}$$

$$\partial_t \psi + [\varphi, \psi] = -\eta (J - J_o) \tag{2}$$

where:

φ is the *stream function*,

U the *vorticity*,

ψ the *magnetic flux function*,

$J = -\nabla^2 \psi$ the *current density*,

J_o the *equilibrium current density*.

$[A,B] = \partial_x A \partial_y B - \partial_y A \partial_x B$ is the usual advection operator.

Lengths are normalised to L and times to the Alfven time $\tau_A = L / v_A$

$\mu = 1/R$ is the *viscosity* (the inverse of the Reynolds number)

$\eta = 1/S$ is the *resistivity* (the inverse of the Lundquist number)

Domain: a square box $L_x \times L_y$ with *periodic boundary conditions.*

Drive: the current J_o (the resistivity is taken constant).

We take $L_x = 2\pi$, $L_y = 2\pi/\varepsilon$ which defines the *slab aspect ratio* ε

The control parameters are ε, S and $P = R/S$ (the magnetic Prandtl). In this work we study Eqs.(1-2) by varying ε and S at constant $P = 0.2$.

We choose $J_o = \cos x$. The symmetric equilibrium is then $J = J_o$ and $\varphi = 0$.

Stability analysis. In the limit of large Lundquist number the system is tearing unstable[3] when $k_y = m/\varepsilon < 1$. m is a poloidal mode number. The stability condition is customarily expressed in term of the parameter Δ', which is, in this case

$$\Delta' = 2\kappa \tan(\kappa\pi/2) > 0 \qquad (3)$$

where $\kappa^2 = 1 - k_y^2$.

In the following discussion we will use the more familiar Δ' as a control parameter instead of ε.

Numerical Investigation of the bifurcation sequence

The sequence of equilibria of the system (1-2) is studied by solving the steady state equations obtained with a truncated spectral decomposition in Fourier amplitudes.

A suitable tool to find the solutions of the truncated system is Newton's method, used in connection with the theorems of bifurcation theory[4].

Here we report results obtained for $0 \le \Delta' \le 1.15$ and $S \le 10^3$ which where found unaffected by the truncation procedure.

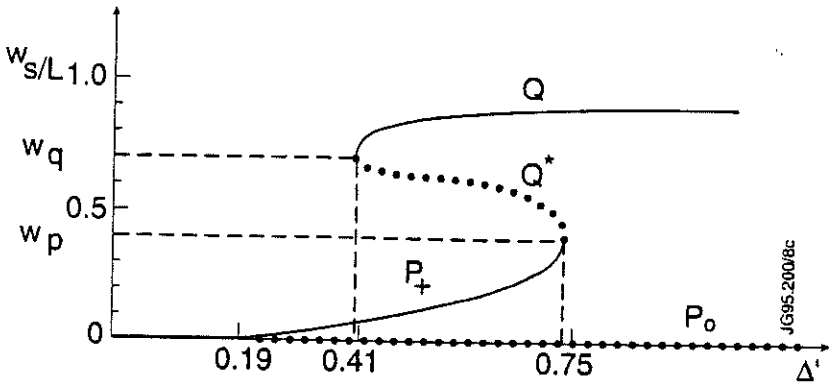

Fig.1: Normalised island width for the stable (solid lines) and unstable (dotted lines) equilibria versus Δ', forS=10³.

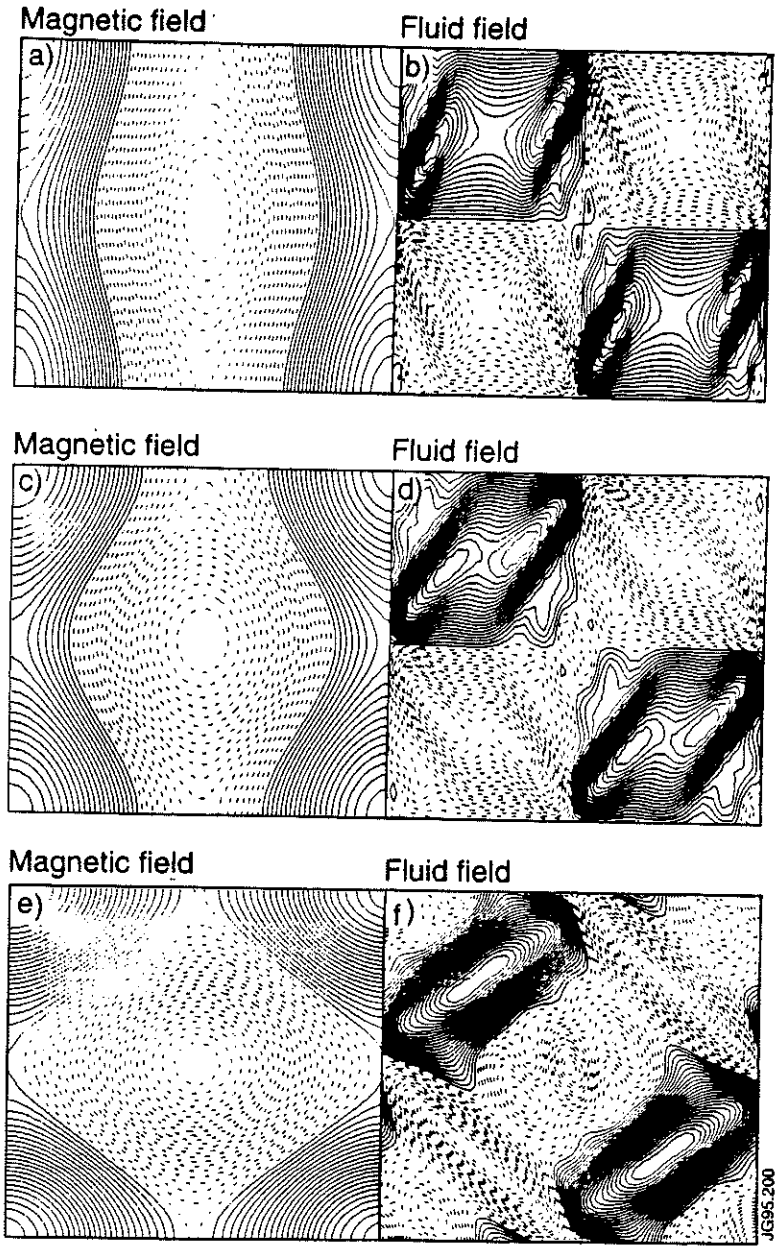

Fig.2: Contour plots of φ and Ψ. a) and b) small stable island solution, c) and d) unstable island solution and e) and f) large unstable island solution.

Normal form equation around the tangent bifurcation point.

$$d\xi / dt = \xi^2 + \delta p \tag{4}$$

where ξ is a normalized coordinate in the direction tangent to the center manifold at the bifurcation point and δp the deviation of the normalized control parameter from the bifurcation point.

All the other degrees of freedom are "slaved".

Just above the critical value no local equilibrium exists. As ξ grows δp becomes quickly irrelevant in Eq.(4) and the evolution is explosive.

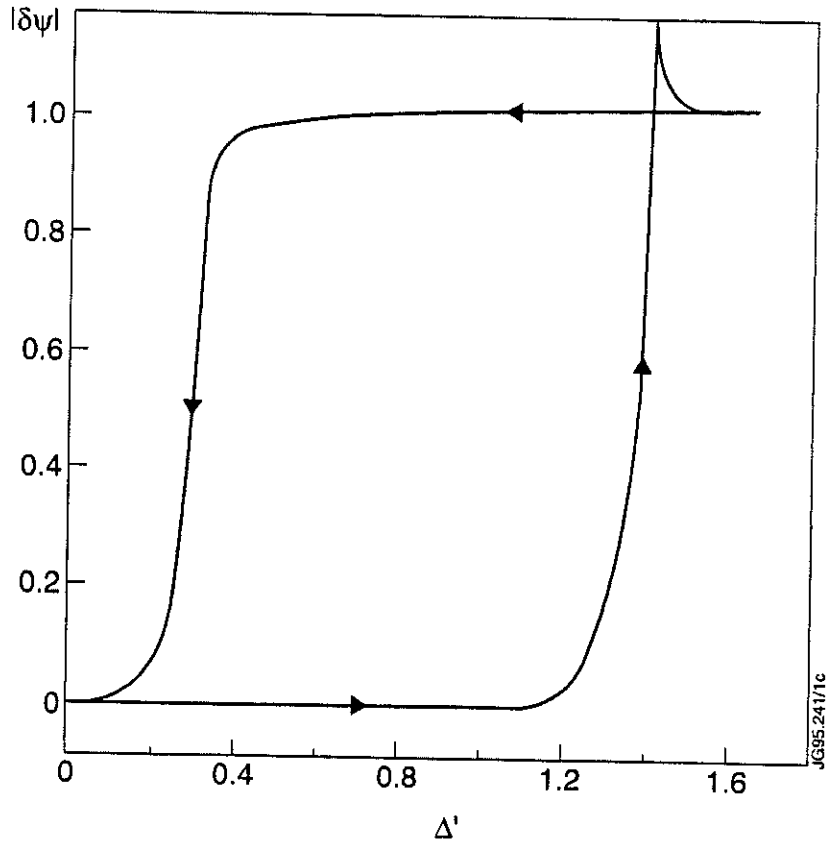

Fig.3 A typical hysteresis cycle, observed by solving Eqs.(1-2) with an initial value code, by varying Δ' slowly in time.

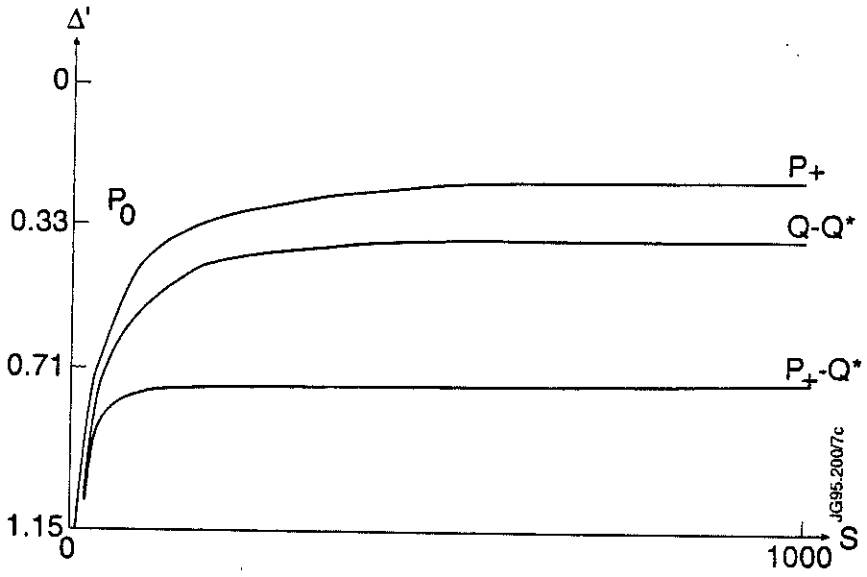

Fig.4 Stability boundaries in the (S, Δ') plane.

Discussion and conclusions.

Relation of our results to previous work.

a) *Bifurcation studies.*

- Thyagaraja[5]: analytic calculation of the saturated island width using an expansion in Δ' at zero magnetic Prandtl number. Formally the expansion breaks down when Δ' *is near unity.* In that limit, however the author finds two coalescent solutions.
- Wesson *et al.* [6]: tearing instabilities in cylindrical geometry. Quasilinear-type, heuristic modification of the linear eigenvalue problem.
  Two solutions which coalesce when a critical value of the current is reached. Above this value no solution exists. (Proposed as a possible mechanism for low-β disruptions.

Both findings can be explained by the $P_- - Q^*$ confluence of Fig.1.

- Maschke and Saramito[7] studied the sequence of bifurcations at constant slab aspect ratio and using S as bifurcation parameter.
- Parker, Dewar and Johnson[8] studied the bifurcation sequence with an initial value code with variable slab aspect ratio at a constant Lundquist number.

No tangent bifurcation was detected in either work.

We attribute this to the choice of boundary conditions in [7-8] (rigid boundary conditions with zero radial flows at the walls). This choice strongly limits the island growth. The proper condition would seem to be $\partial_x v \rightarrow 0$ at the boundary.

b) *Initial value problem from an initial state close to the unstable symmetric state.*

Three regimes:

1) For small $\Delta'<1/LS$ the island grows as in Rutherford[9] $w \approx \eta\Delta' t$ and saturates at modest amplitude on the resistive time scale[10-11].

2) For very large $\Delta'>(1/L)S^{1/3}$ the island is expected to reach the macroscopic size on the much faster Sweet-Parker time scale $\tau_{SP} \approx (\tau_R \tau_A)^{1/2}$
3) In the intermediate regime $1/L<\Delta'<(1/L)S^{1/3}$ Waelbroek[12] has shown that a transition between Rutherford and Sweet-Parker regimes occurs when the island has reached a width $w \approx 1/\Delta'$. Therefore no saturation is expected in this regime.

Our findings support Waelbroeck picture. Indeed one can see from Fig.1 that saturation of the initial value problem with small island width is possible only when $\Delta' < 1/L$.

Conclusions.

- To the extent that the island width is somewhat less than the system size we expect that our findings are largely independent of geometry or specific boundary conditions. Therefore they suggest a qualitative explanation of sudden reconnection events observed in laboratory plasmas. On the basis of our analysis we propose that these events occur from a state of already broken symmetry when the second bifurcation (a catastrophe) takes place. This state of slightly broken symmetry can be identified as the precursor state in which a small island can in principle be observed.

- A characteristic signature of the tangent bifurcation is the hysteresis cycle. This should be kept in mind when investigating this phenomenon experimentally.

- An open question is what happens in reality when the hard event takes place. Strictly speaking, on the basis of our analysis, one would be tempted to conclude that a true disruption takes place, as in Ref. 6,, since the final state has an island of macroscopic size. (The exception would be the sawtooth which occurs "internally").

- However one should also consider that RRMHD gives only a partial description of the plasma. In particular the fast transport processes occurring during the crash are not described by RRMHD. These processes could alter the resistivity or other relevant parameters in a way that effectively introduces a feedback in the system that limits the growth of the magnetic island. If this were the case, repetitive relaxation events like ELMs would occur. Naturally, the

proper analysis of such phenomena requires more refined models.

The authors acknowledge useful discussions with A. Thyagaraja, F. Waelbroeck and J. Wesson who brought previous literature to their attention.

References

[1] J. A. Wesson, A. W. Edwards and R. S. Granetz, Nucl. Fusion **31**, 111 (1991).

[2] J. Guckenheimer and P. Holmes, "Nonlinear Oscillations, Dynamical Systems and Bifurcations of Vector Fields", Springer (Applied Math. Series n. 42), New York (1986).

[3] H. P. Furth, J. Killeen and M. N. Rosenbluth, Phys. Fluids **6**, 459 (1963).

[4] C. Tebaldi, in "Nonlinear Dynamics" (World Scientific, Singapore,1989).

[5] A. Thyagaraja, Phys. Fluids **24**, 1716 (1981).

[6] J.A. Wesson, A. Sykes and M.F. Turner, Proceeding of the Tenth International Conference on Plasma Physics and Controlled Nuclear Fusion Research, vol. 2, p. 23, IAEA (1985).

[7] B. Saramito and E. K. Maschke, in "Magnetic Turbulence and Transport", Edited by P. Hennequin and M. A. Dubois (Editions de Physique, Orsay, 1993), p. 33.

[8] R.D. Parker, R.L. Dewar and J.L. Johnson, Phys. Fluids **B2**, 508 (1990).

[9] P. H. Rutherford, Phys. Fluids **16**, 1903 (1973).

[10] R. B. White, D. A. Monticello, M. N. Rosenbluth and B. V. Waddell, Phys. Fluids **20**, 800 (1977).

[11] R. Y. Dagazian and R. B. Paris, Phys. Fluids **29**, 762 (1986).

[12] F.L. Waelbroeck, Phys. Fluids **B2**, 2372 (1989).

Neutral Gas Pressure Measurements in the JET MK I Pumped Divertor

J K Ehrenberg, D J Campbell, S Clement-Lorenzo, E B Deksnis, H Y Guo, P J Harbour, G Haas[1], L D Horton, J Lingertat, A Loarte, C G Lowry, G F Matthews, G K McCormick, R D Monk[2], D P J O'Brien, R Reichle, G R Saibene, R Simonini, M F Stamp, D Stork, A Taroni.

JET Joint Undertaking, Abingdon, Oxfordshire, OX14 3EA, UK.

[1] Max-Planck-Institut für Plasmaphysik, Boltzmannstr. 2, D-85748 Garching, Germany.

[2] Royal Holloway College, University of London, Surrey, TW20 0EX, UK.

I. INTRODUCTION

Particle recycling on divertor target plates gives rise to the formation of a neutral particle flux or neutral pressure in the divertor. This neutral particle pressure provides the basis for plasma refuelling, affecting plasma core and plasma edge parameters (temperature, density, profiles) with consequences for power and particle deposition in the divertor and for core plasma confinement.

In JET we have measured the neutral pressure in the MK I pumped divertor by means of an array of special ASDEX-type ionisation gauges [1], and correlated it with:

- the magnetic geometry of the divertor plasma,
- the transition from attached to detached divertor plasma phases,
- the main plasma density and input power,
- the occurence of Elms in H-mode discharges,
- code-calculations to simulate plasma edge conditions.

II. EXPERIMENTAL DETAILS

- The gauges measure a local neutral particle flux in the sub-divertor volume. The flux can be converted to pressure or density provided a gas temperature and isotropic conditions are assumed. A local sub-divertor gas temperature of 323K was estimated, owing to the many water cooled structures in the vicinty of the gauges (JET vessel wall temperature is 573K).

- The locally measured flux (or pressure) at the gauge position is determined
  - by the plasma strike zone position at the target plates,
  - by the transmission probabilities of neutrals through the divertor gaps,
  - by the radial conductance of the divertor gaps (over a radial distance of about 0.2m the radial and the vertical conductances are of similar order),

- by the integrating effect of the sub-divertor volume,
- by the divertor cryo-pump.

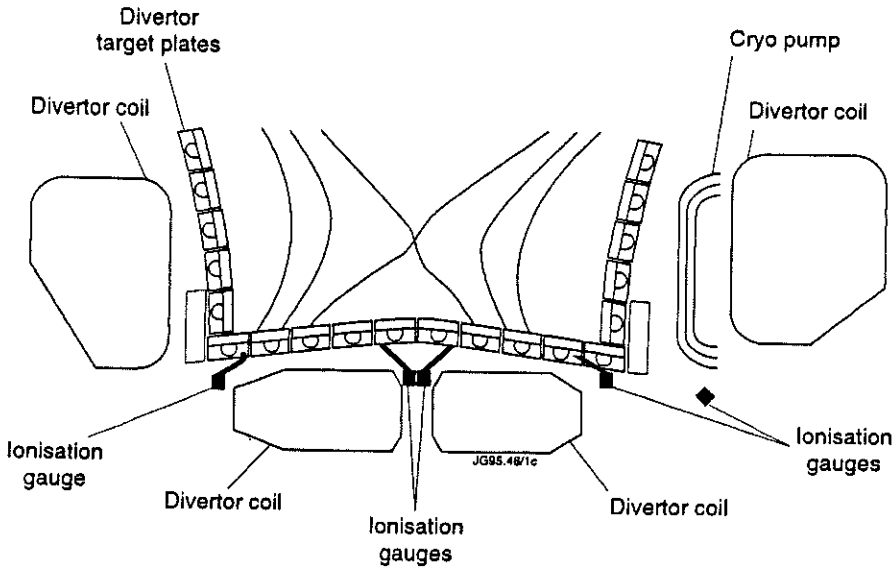

Figure.1: Distribution of pressure gauges in the sub-divertor volume.

III. EXPERIMENTAL RESULTS AND DISCUSSION

1. Pressure distribution as a function of magnetic divertor plasma configuration

Ohmic plasma, current 2MA., toroidal field 2.8T, average plasma density 3.5 10^{19} $1/m^3$.

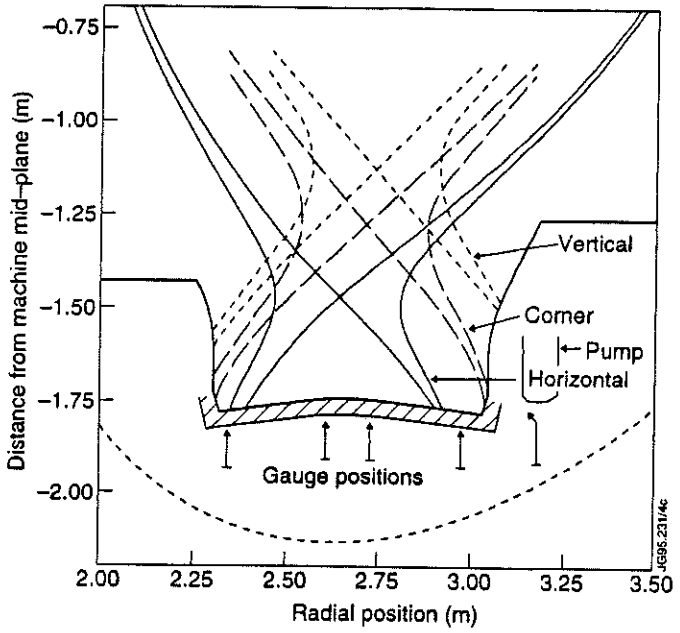

Figure.2: Three divertor plasma configurations.

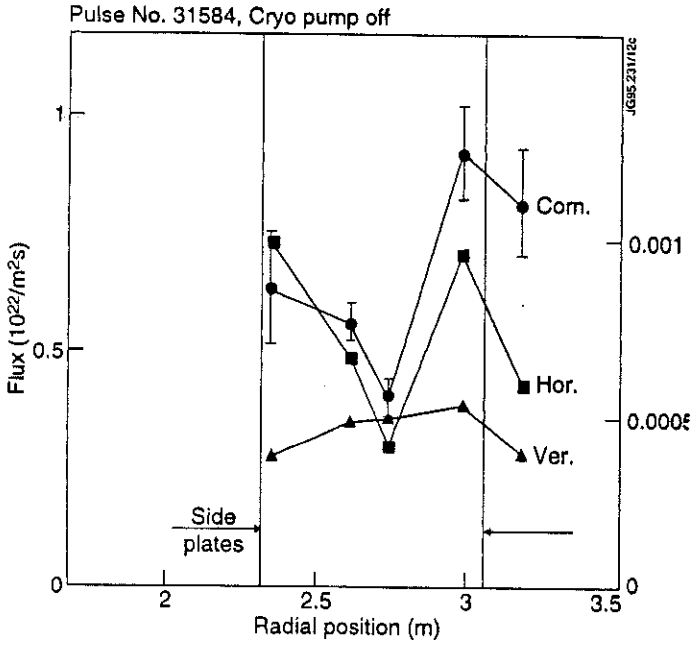

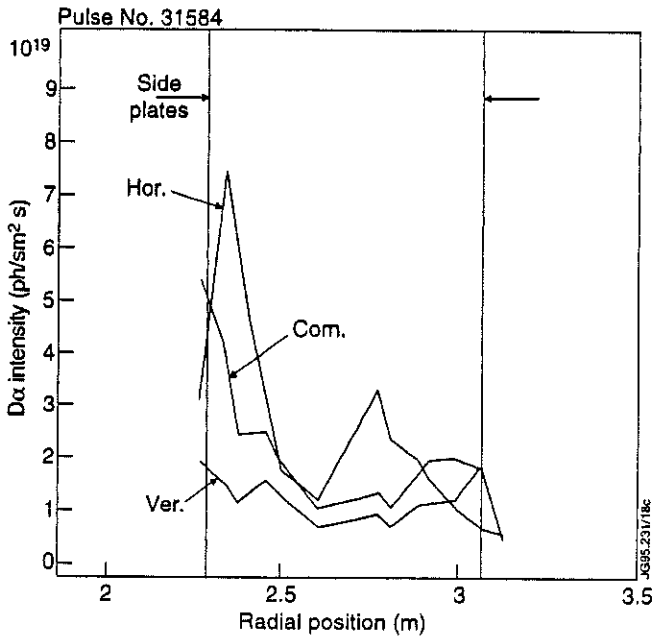

*Figure.3: a) Measured neutral particle flux (pressure) distribution and b) D-alpha intensity distribution in the divertor with the **cryo-pump 'off'** for three configurations as indicated in fig.2.*

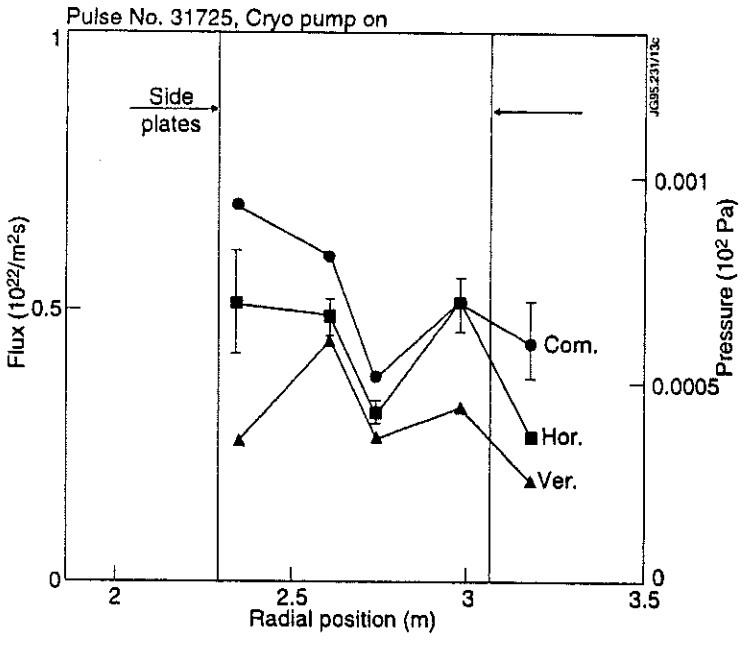

*Figure.4: Measured neutral particle flux (pressure) distribution with the **pump 'on'** for three configurations as indicated in fig.2.*

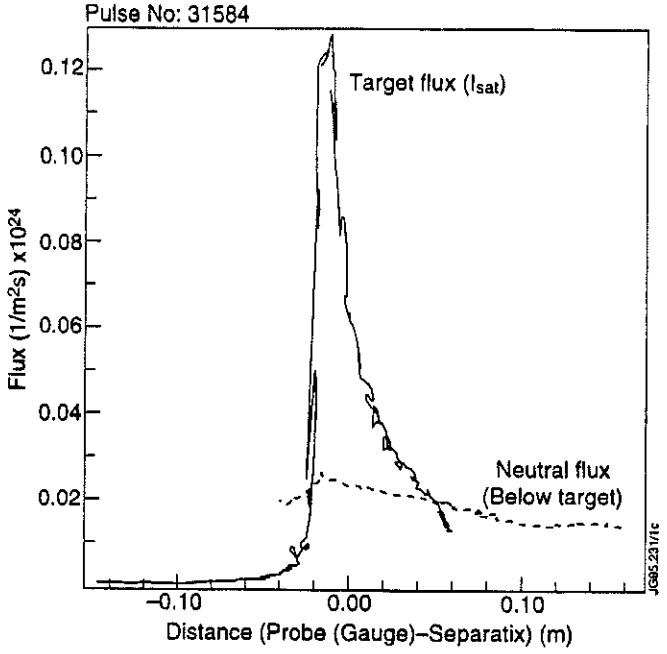

Figure.5: Sweeping the outer plasma strike zone over a pressure gauge produces a profile of the neutral particle fluxes in the sub-divertor volume. The measured ion-saturation flux on the target at the position of the pressure gauge is also shown.

- For horizontal configuration the pressure distribution is double peaked with maxima at the plasma strike zones. Fewer neutral particles escape to the private region compared to the outer SOL.
- The corner position reaches the highest pressure at the cryo-pump, probably due to

additional neutrals entering the cryo-pump area through toroidal gaps in the corner of the divertor structure.

- For the vertical configuration most of the sub-divertor volume is within the private region of the divertor plasma, hence the uniformity of the distribution at lower average pressure.
- Active pumping lowers the pressure at the pump by about 40%.
- Assessments of particle fluxes for the **vertical** configuration indicated (#31584) (see figure 6):

a) The external fuelling flux is about 3 10^{21} atoms/s.

b) The total particle flux pumped by the cryo-pump (independently calibrated) is about 2.9 10^{21} atom/s (good agreement with the external flux ,constant density).

c) The total target ionic flux is estimated at 10^{23} atoms/s. Hence, a flux of the order of percent of the ionic target flux gets pumped.

d) The total back-flux of atoms (1/2 molecule) from the sub-divertor volume into the private region of the divertor is about 5 10^{21} atoms/s (exp. transmission probability, ≈4%).
This flux and the pumped flux must be balanced by the neutral flux entering the sub-divertor volume, which in turn must be on average about 4% of

e) a neutral flux (CX, FC atoms) that hits the divertor surface. This flux would then be about 1 10^{23} atoms/s, (which is similar to the total ionic divertor flux).

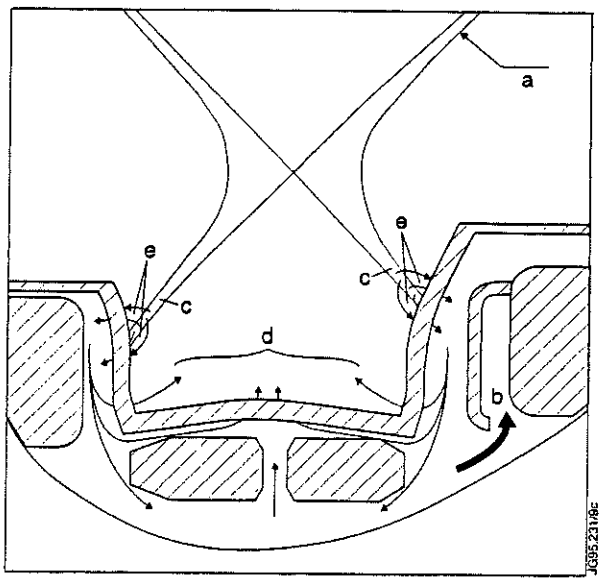

Figure.6: Conjectured particle flux distribution in the JET divertor for a vertical configuration. a)-e) denotes fluxes quantified at the left

2. Neutral pressure during transition from attached to detached divertor plasmas

- Despite a reduction of the charged particle flux (ion saturation signal in fig.7) when approaching a detached plasma phase, the neutral pressure in the divertor still increases. This could indicate the presence of volume recombination

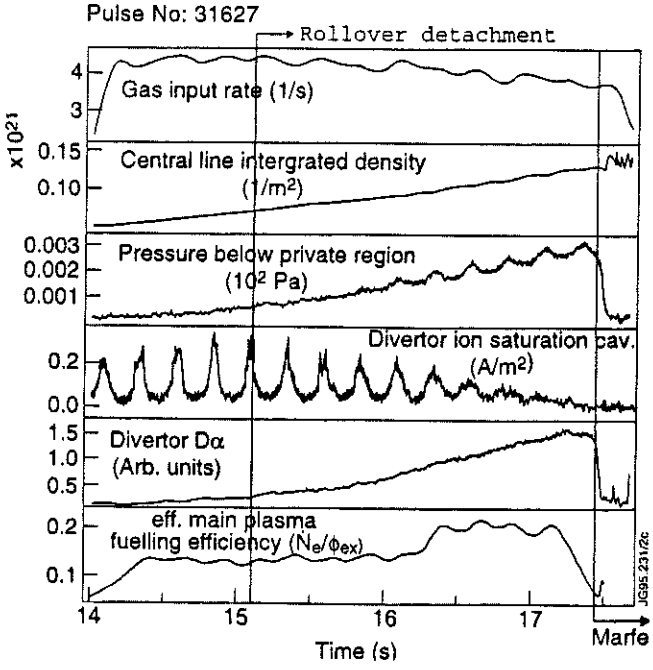

Figure.7: A survey of the change of some parameters during a 2 MA, 2.8T ohmic plasma with density rise leading to plasma detachment.The plasma strike zones where swept with a frequency of 4Hz.

processes at low electron temperatures (<2eV) (see K Borrass) with increased neutral particle leakage from the divertor plasma.

- During detachment the neutral particle pressure distribution peaks in the private region consistent with the observation by Langmuir probes that detachment starts at the separatrix.

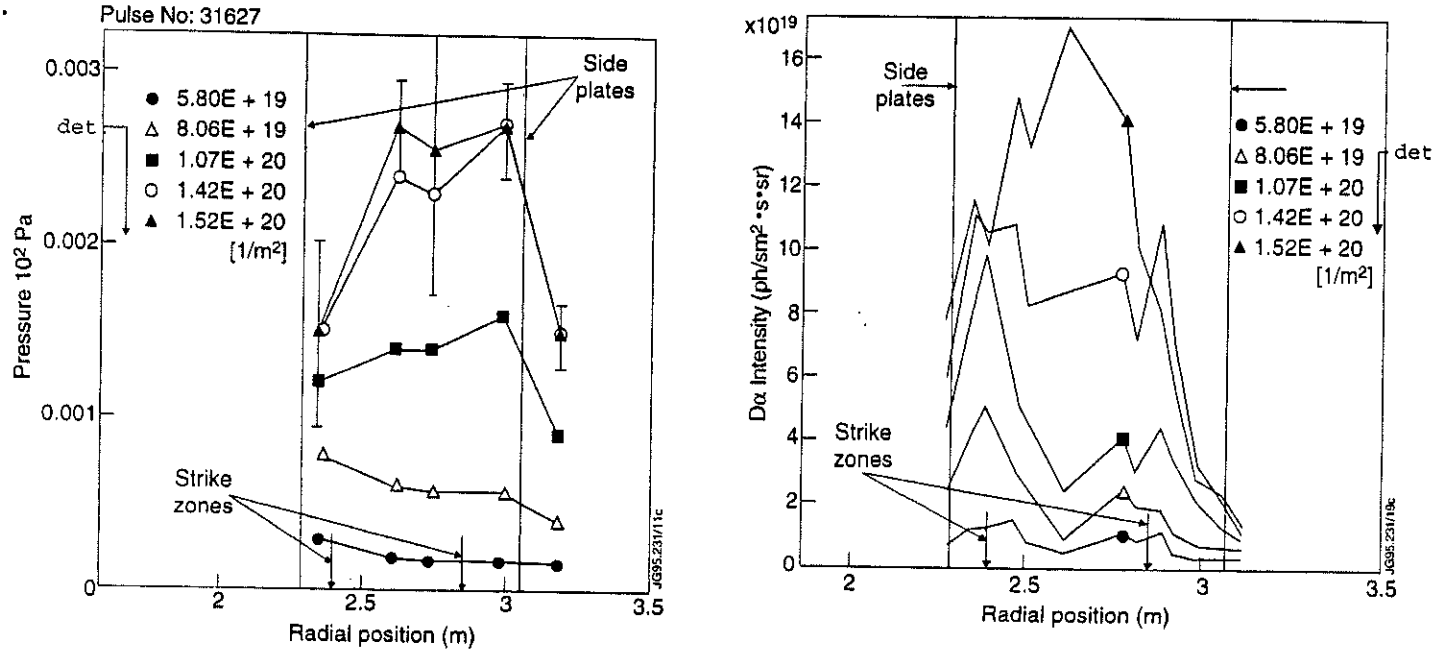

Figure.8: a) Neutral pressure profile and b) D-alpha profile across the divertor during transition from attached to detached divertor plasma with central line integrated density as the parameter.

- During detachment neutrals are still concentrated between the divertor plasma strike zones as can be deduced from observation of a pressure modulation during strike zone sweeping.
- During detachment the effective plasma fueling efficiency (def.: (plasma particle inventory change) / (gas input rate)) increases, suggesting increased fuelling through the X-point

3. Realtionship between neutral pressure and plasma density in various confinement regimes

- In attached L-mode (and ohmic) plasmas neutral pressure change can be approximated by density squared dependence

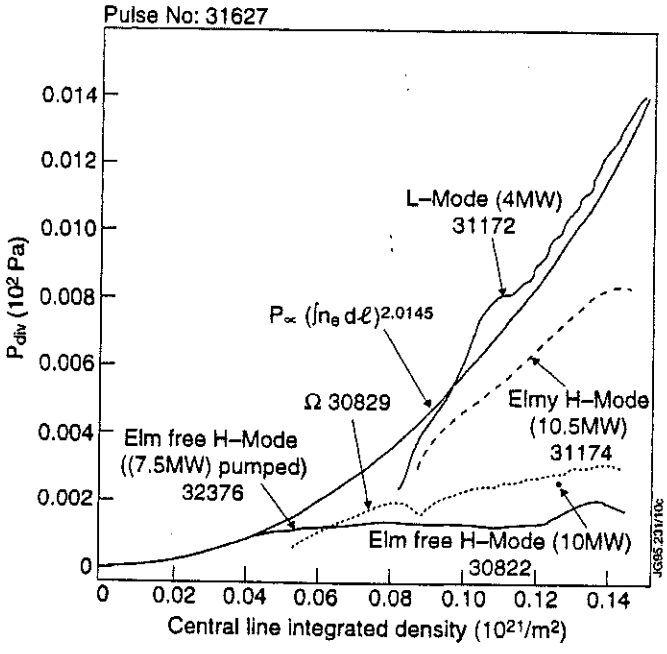

Figure.9: Density dependence of neutral pressure below private region of divertor plasma for discharges with 2MA, 2.8T at different input powers, except #32376 which had 2.4 MA/2.4T. The line is a fit to #31172.

(consistent with two point model for SOL transport).

- L-mode, and ELMy H-mode produce the highest pressure (largest particle outflux) in the sub-divertor volume, consistent with confinement degradation compared to ohmic conditions.
- During ELM-free H-mode (t ≅ 0.4 s) neutral pressure and density are 'decoupled'. Particle outflow does not increase with density indicating the presence of a plasma transport barrier.

4. Density control in H-mode discharges with cryo-pump 'on'

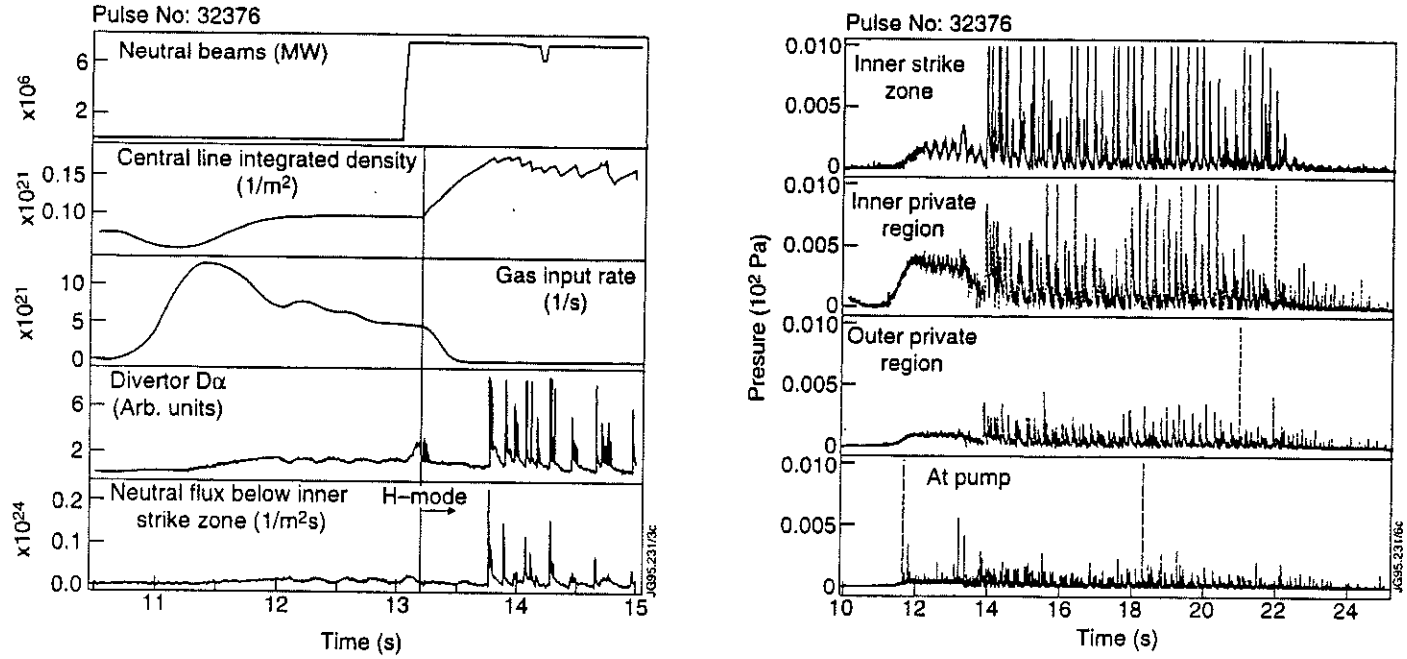

Figure.10: a) Some parameters of a discharge (2.4 MA, 2.4 T) with transition of plasma confinement from ohmic to L-mode to ELM-free H-mode and to ELMy H-mode. b) Pressure modulation at different positions below the divertor target area.

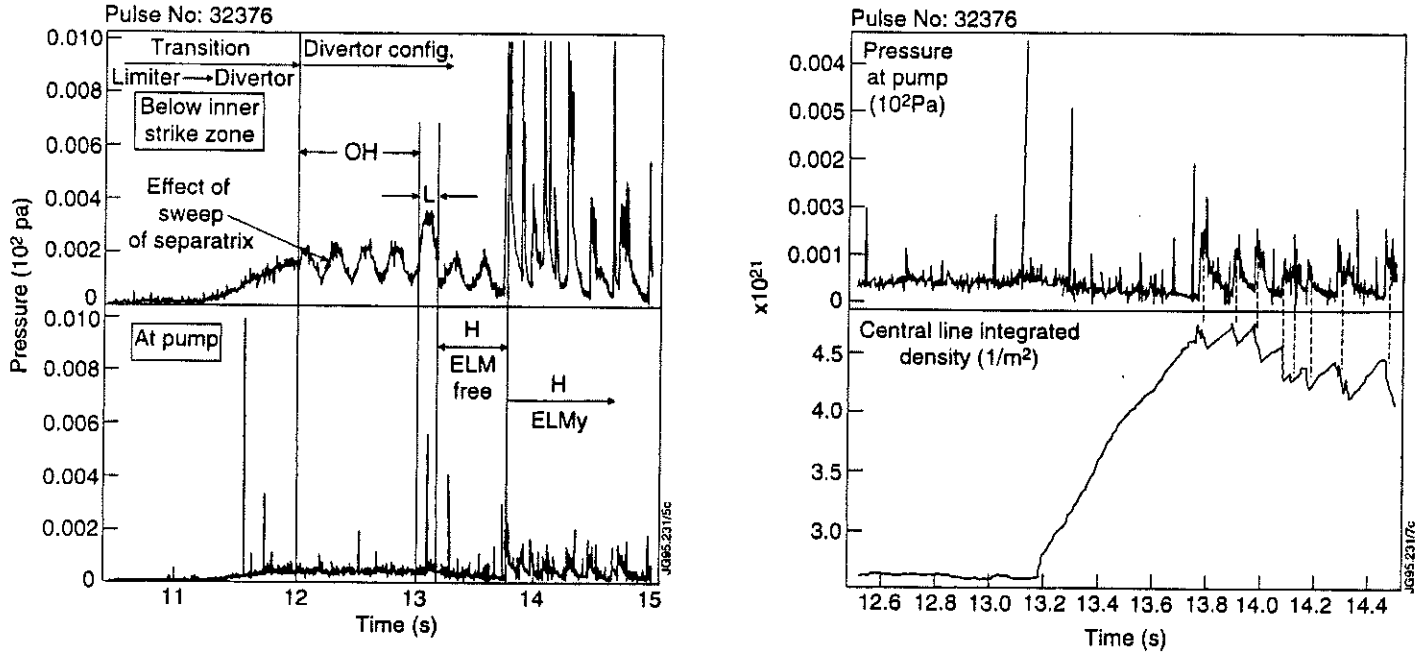

Figure.11: a) Expanded view of the period where confinement changes; b) correlation between pressure rises at the cryo pump and density decreases.

- ELM triggered pressure modulation at strike zones is similar to the modulation of D-alpha signal. ELMs are stronger at inner strike zone compared to outer strike zone (ion grad B-drift towards target).
- Integrating effect of the sub-divertor volume leads to weaker pressure rise at the cryo-pump.
- ELM-free H-mode results in relatively low pressure (≅3-5 10^{-4} hPa) at the pump. In this pressure range the particle removal rate by the cryo-pump is 3-5 10^{21} atoms/s.
- ELMs can raise temporarily pressure at the pump by a factor of 10 or more.
- In contrast to un-pumped ELMy discharges there is no neutral pressure accumulation in the divertor when the cryo pump operates (see J Lingertat et al.).

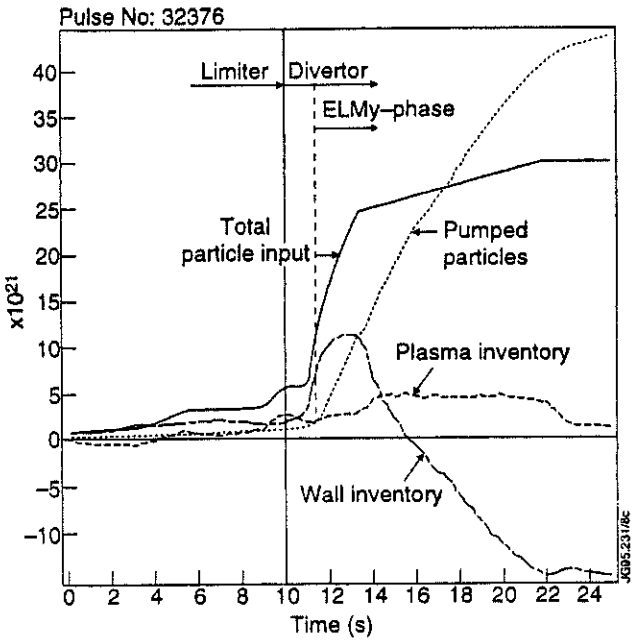

Figure.12: Particle balance calculation for the ELMy divertor discharge of figure 8. At the time of the onset of ELMs the pumping of particles from divertor/walls becomes significant.

- The core plasma density decrease during ELMs is less than the pressure increase in the divertor would suggest. There is particle release from the divertor/walls during the ELMy period (see figure 12). In some cases during very giant ELMs this can even lead to a net density increase rather than decrease (see J Lingertat et al.)

5. Comparison of experimental neutral flux data with results from simulation calculations

- First attempts to simulate divertor plasma conditions using the EDG2D/NIMBUS-code including a 2-dimensional model of the MK I divertor (see figure 13):
- Discharge #30830: I_p=2MA, B_t=2.8T, P_{NBI}=6.5 MW,$\langle n_e \rangle$=3 10^{19} m^{-3}, L-mode

Results:

- Calculated average neutral particle (atoms) flux in sub-divertor volume: 1.2 10^{23} atoms/m^2s

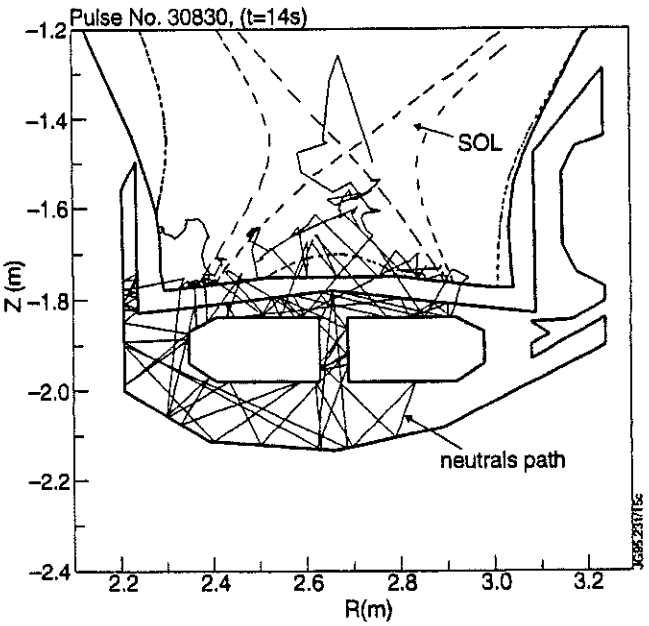

Figure.13: #30830, simulated neutral particle paths in the MK I divertor during a L-mode divertor discharge.

- Measured flux (average of three pressure gauges): ≥0.4 10^{23} atoms/m^2s

IV. SUMMARY AND CONCLUSIONS

- In attached plasmas the peak neutral pressure in the sub-divertor volume is closely related to the plasma strike zone position, ie. the source for first generation neutrals. Peak pressure is about a factor of two above average pressure.
- The structure of the MK I divertor allows radial neutral particle flows below the target area into the divertor plasma/ private plasma region at a rate comparable to the external fuelling rate.
- In detached plasmas the neutral pressure gets peaked in the private plasma region, consistent with increased neutral particle leaking from the separatrix region of the plasma strike zone.

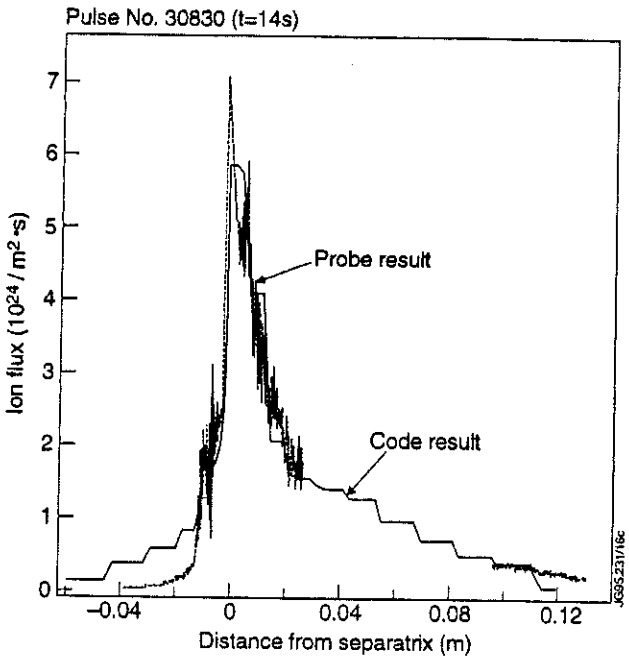

Figure.14: #30830, simulated and measured ion-saturation flux at outer strike zone during L-mode.

- For the same central plasma density, particle pressure in the divertor is highest for L-mode confinement and ELMy H-modes compared to ohmic conditions and quiescent H-mode consistent with observed confinement degradation. In L-mode and in ohmic conditions the pressure follows about a central density squared dependence consistent with predictions of a two point model for particle and energy transport in the SOL and profile consistency.
- In ELM-free H-mode the neutral divertor pressure is independent of the central density, suggesting the presence of a plasma transport barrier.
- ELMs cause strong, asymmetric pressure modulations below the targets (stronger at the inner strike zone, ion gradB-drift towards target).
- In ELMy discharges the pressure increase is larger than expected from the plasma density decrease, indicating wall/target plate depletion of hydrogen due to power deposition in ELMs.
- First EDGE2D/NIMBUS code calculations to simulate sub-divertor neutral flux data using a 2-dim. MK I divertor model do not yet match well experimental data but first results are of the right order.

V. References

[1] G. Haas et al., J. Nucl. Mater. 121, 151 (1984)

Recycling, Divertor Parameters and SOL Transport for High Performance Discharges in the New JET

K McCormick[1], J Ehrenberg, A Loarte, R Monk[2], R Simonini, J Spence, M Stamp, A Taroni, G Vlases.

JET Joint Undertaking, Abingdon, Oxfordshire, OX14 3EA, UK.

[1] Max-Planck-Institut für Plasmaphysik, EURATOM Association, 85748 Garching, Germany.

[2] Royal Holloway College, University of London, Surrey, TW20 0EX, UK.

1. INTRODUCTION:

Major changes from 1991 to the new JET of 1994/95:

☆ Installation of the Mk I CFC divertor with cryopump vs. previous upper graphite dump plates.

☆ Largely inconel walls vs. graphite in 1991

⇒ H-modes were initially characterized by type I ELMs vs. the ELM-free behavior of 1991.

⇒ The neutron production rate was initially poorer during the hot-ion H-mode.

Since neutral particle recycling was initially perceived to be higher than for 1991, and it is known from other machine experience [1-4] that high recycling can be deleterious to the quality of H-modes, this paper examines the relationship between recycling signals and the D-D reaction rate (R_{DD}) for 1991 vs. 1994/95. The horizontal DAH and vertical DAV D_α chords of fig.1 are used. One 1991 and three 1994/95 divertor equilibria are considered.

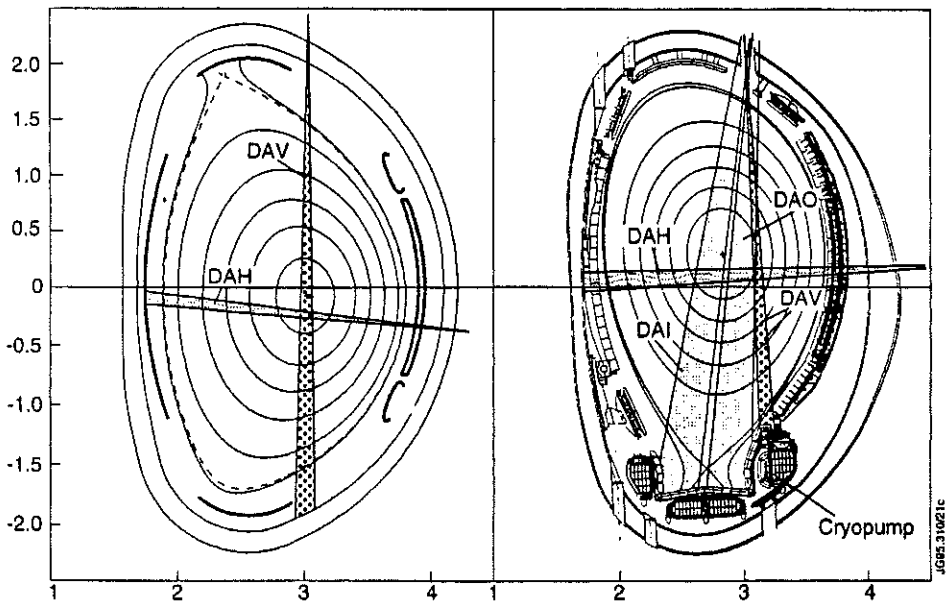

Fig. 1: Horizontal (DAH) and vertical (DAV) D_α viewing chords for the 1991 SNU configuration (left) and MkI (HFE). The MkI inner (DAI) and outer (DAO) target views are shown.

- Specifically, the questions are addressed:
  - Is there a difference in recycling 1991 vs.1994?
  - Are benefits realized from the different divertor equilibria with respect to recycling neutrals?

- Outline:
  – Document the temporal behavior (fig.2) and statistical (fig.4) dependence of R_{DD} on DAV.

- Model the measured target plate parameters for the hot ion mode with the transport code EDGE2D/NIMBUS, establishing SOL transport parameters ⇒ from which subsequent predictive calculations permit an inter-equilibria comparison of recycling fluxes to the main SOL as well as calibrating DAV among the configurations.

2. GENERIC TIME BEHAVIOR OF DIVERTOR PARAMETERS FOR THE HOT ION MODE

The hot-ion H-mode used to achieve high performance in terms of stored energy W_{dia} and D-D reaction rate is of transient nature. Referring to fig.2, after NBI initiation at 12.0 sec:

- Both W_{dia} and R_{DD} increase linearly with time until t ~ 12.95 s, where a "rollover" occurs.
- P_{NI}~17 MW, dW_{dia}/dt ~9 MW, P_{RAD}~1 MW ⇒ P_{target}~7 MW. At the "rollover", P_{tar} increases.
- During the phase up to the rollover, $\bar{n}_e$ increases by a factor of about three (1.2 - >3.4x10^{19}/m^3).
- The fast DAV signal registers an initial period of benign mini-ELMs followed by an ELM-free phase and then an abrupt increase at the "rollover", implying the flux to the divertor has intensified.

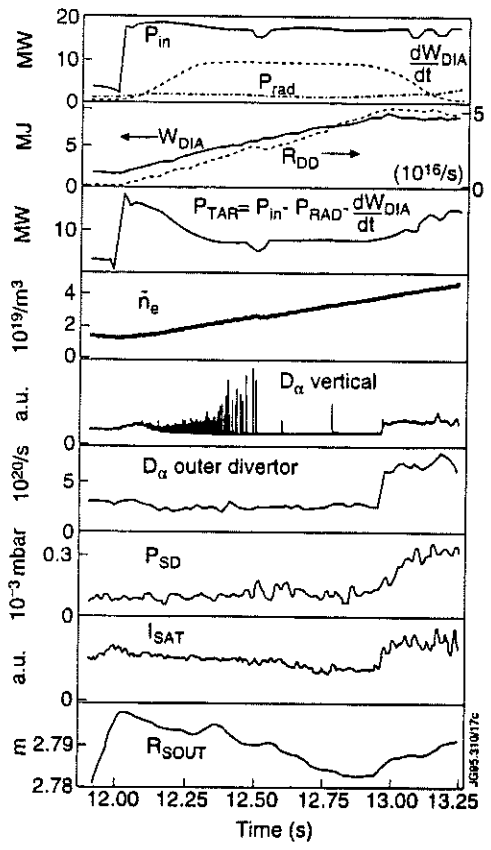

Fig.2: Time traces for global (top four boxes) and divertor parameters, including the "slow rollover" phase in RDD and W_{dia} beginning at t=52.95 sec. Shot #33641.

- At the rollover, the (slow) outer target plate D_α signal DAO and the neutral pressure measured in the subdivertor volume P_{SD} also both increase around a factor of three. The saturation current I_{sat} to a target plate triple Langmuir probe changes a factor of two.
- Of particular note is that, up to the rollover, all divertor signals remain relatively constant at the levels prevailing immediately after transition into the H-mode - although $\bar{n}_e$ increases dramatically!
- Time-resolved Langmuir probe measurements indicate the target plate profiles of n_{ed} and T_{ed} remain ~ invariant over this period. The jump in I_{sat} at the rollover is composed mostly of an n_{ed} increase, with a moderate augmentation in T_{ed}.

=> On JET, during the ELM-free period of the hot-ion H-mode, n_{es}, T_{es}, and λ remain roughly fixed near values attained after the L-H transition, independent of what is happening in the core plasma.

- **This has been observed for the SOL n_e profile on ASDEX as well /5/.**

3. PLASMA AND MAGNETIC GEOMETERY DATA FOR THE FOUR CONFIGURATIONS

- The Single Null Up (SNU) configuration of 1991 had a small x-point height, a high flux expansion at the target plate, and was a geometrically open "divertor". (See fig.1) The SF, HFE and DNHF1 cases, chronologically implemented in this order, evince an evolution from a high to low x-point, and from a very low flux expansion upwards to values still below those of SNU. (Table I)
- Both edge shear and upper triangularity of the main plasma increase in going from SF to HFE and DNHF1. However, SNU attains significantly larger values of these quantities. (Table I).

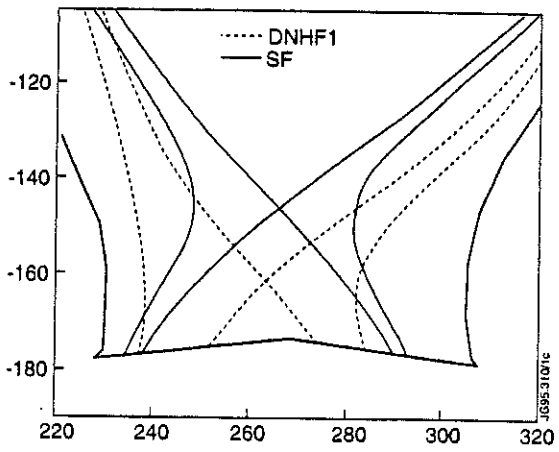

Fig.3: SF (Standard Fat) and DNHF1 ("Double Null " High Flux Expansion) equilibria for the MkI divertor. The 1cm midplane flux lines are used to illustrate the flux expansion.

Configuration	SNU	SF	HFE	DNHF1
x-pt height [m]	0.084	0.284	0.132	0.126
flux exp. inside	17.6	3.4	12.6	13.6
flux exp.outside	15	2.5	8	10
shear at q_{95}	4.4	3.25	3.6	3.75
upper tri.	0.51	0.19	0.21	0.28

Best Example	#26087	#32823	#32919	#33643
I_p / B_t / q_{95}	3.2/2.8/3.7	4.1/3.4/2.8	3.1/3.4/4.1	3.9/3.4/3.1
Volume [m^3]	101	81	83	79
P_{NI} [MW]	14.9	18.5	18.2	18.5
W_{DIA} [MJ]	11.6	10	10.8	12.3
R_{DD} [s^{-1}]	8.4×10^{16}	5.6×10^{16}	7.6×10^{16}	9.3×10^{16}
limited by:	rollover	ELM	rollover	rollover
δt to limit [s]	1.35	1.08	1.09	1.30

δN_{etotal} (main plasma) and $\int$of Φ_{pump}, Φ_{gas}, Φ_{beam} over 1st sec of NBI				
$\int\Phi_{epump}dt$	0	-1.08	-1.38	-0.72
$\int\Phi_{egas}dt$	2.65×10^{21}	0	0	0.37
$\int\Phi_{ebeam}dt$	1.16	1.6	1.55	1.54
δN_{etotal}	1.44	1.68	1.84	2.0
$\delta N_e / \int$beam	1.24	1.05	1.19	1.31

Table I: Magnetic geometry, plasma properties and global particle balances for the best high performance shots of each configuration.

- SNU has a 25% larger core volume than the 1994-95 cases, and with less P_{NI} achieves an R_{DD} comparable with the best of the 1994/95 campaign (#26087 vs. #33643). (Table I)
- A particle balance **over the first second of neutral beam injection** for the best shots of each configuration indicates an increase in core electron content somewhat above (5-30%) the beam input.
- Although there is little apparent difference between 1991 and 1994/95 in the ratio of the increase in core electron content after one sec. (δN_e) to the beam input in that time ($\int\phi_{beam}dt$), remember
  - in 1991 moderate gas puffing was employed,
  - in 1994/95 gas puffing was generally avoided and the cryopump was operative
- The particle balances indicate the walls are being depleted by the cryopump for these discharges, a typical result. (See J. Ehrenberg, G. Saibene, this conference)

4. RELATIONSHIP OF RECYCLING TO HIGH PERFORMANCE FOR ALL CONFIGURATIONS

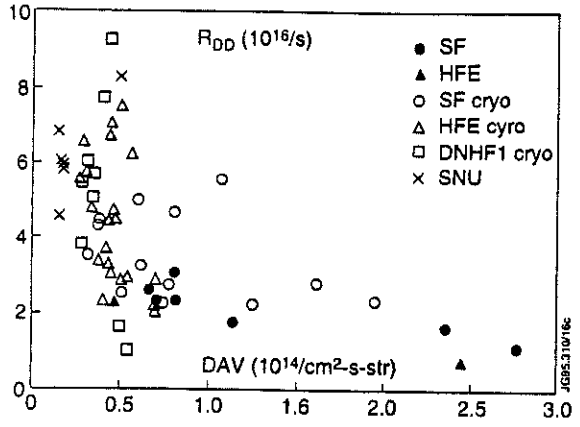

Fig. 4a: D-D reaction rate RDD vs. the vertical D_α signal DAV (taken after the L-H transition) for theconfigurations with and without the cryopump.

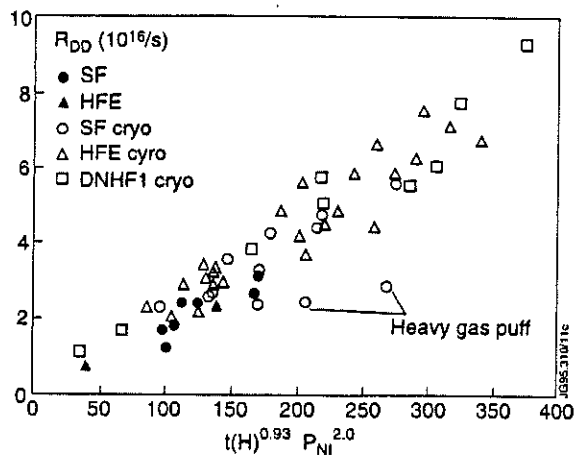

Fig. 4b: A fit to the points of fig. 4a using t(H) and P_{NI}.

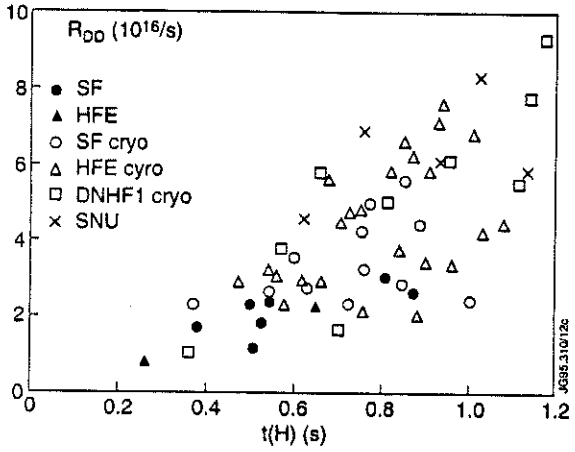

Fig. 4c: RDD vs. the ELM-free period from the data of fig.4a.

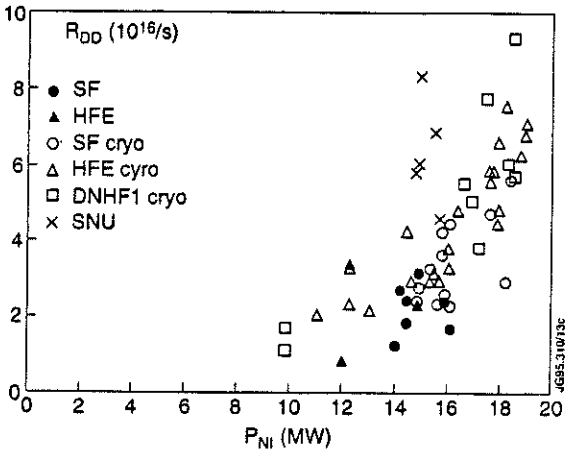

Fig. 4d: RDD vs. P_{NI} for the points of fig. 4a.

- The DAV is that after the L-H transition.
- Lower DAV is associated with higher R_{DD}. BUT, at lower levels DAV is not evidently of over-riding importance.
- The highest R_{DD} values are not attained at the lowest DAV levels - for all configurations!
- A regression (fig.4b) on the data set of fig. 4a yields

$$R_{DD} \sim t(H)^{0.93\pm0.09}\ PNI^{2.0\pm0.17}\ .$$

t(H) is measured beginning at the L-H transition, ignoring the mini-ELMs, up to the event ending high performance (either a rollover or giant ELM).

- The points with heavy gas puffing before NBI clearly deviate from the general trend of the other shots where emphasis was placed on establishing low recycling conditions before injection.
- The upper envelope of points in fig. 4c exhibits R_{DD} is proportional to the ELM-free time period t(H) as the regression of fig.4b has indicated and as expected from the time traces of fig.2.
- The 1991 points conform to the trend of 1994/95.
- At their power level the 1991 SNU shots clearly outperform those of 1994/95. This can be largely attributed to the larger plasma volume and associated higher τ_E of 1991. (see T.Jones et al., this conference)

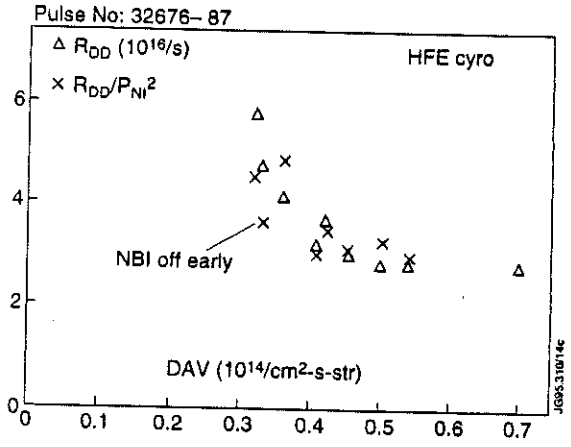

Fig. 4e: RDD and RDD/P_{NI}^2 vs. DAV for a consecutive series of shots, from a subset of fig. 4a.

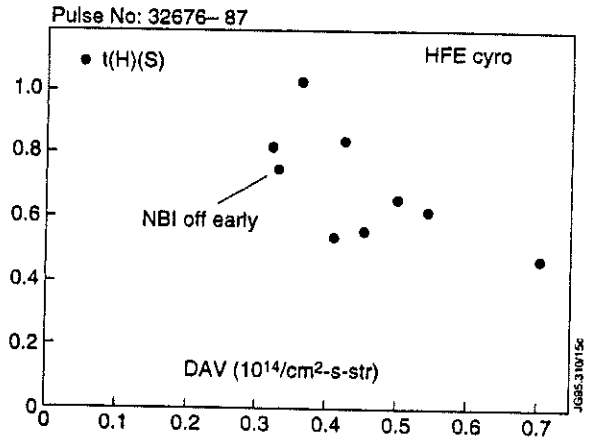

Fig. 4f: The ELM-free period t(H) vs. DAV for the points of fig. 4e.

- The systematic effect of DAV on R_{DD} for low recycling is best examined in a well-defined subset of fig.4a [6]:

=> Fig. 4e considers nine practically consecutive shots under the same global conditions on the same day with small variation in P_{NI} for a cryo-pumped HFE configuration. The R_{DD} dataset and R_{DD} normalized to P_{NI}^2 (in conformity with the regression of fig.4b) illustrates that R_{DD} increases with decreasing DAV even at these levels.

- Plotting t(H) vs. DAV reveals a tendency towards longer ELM-free intervals for lower DAV, although the trend is not entirely unique. This weak colinearity of DAV with t(H) disallows a regression for R_{DD} based on DAV as well as t(H) and P_{NI}.
- An operational hypothesis for the role of recycling in high performance discharges is that low edge densities (with the connection: low recycling = low DAV <=> low n_{es})
  - allow more peaked beam deposition profiles
  - delay the development of pressure-gradient-driven instabilities conjectured to terminate the high performance phase (T.Hender, P.Smeulders, K.Lawson, this EPS) thereby enhancing t(H) and R_{DD}.
- The second component of this scenario is that edge shear and triangularity will increase stability limits, thereby allowing the ELM-free phase to proceed longer before encountering termination.
- Thus, the ELM-fee period t(H) in the regression $R_{DD} \sim t(H)^{0.93} P_{NI}^{2.0}$ implicitly represents the positive combined effects of reduced pressure gradients and higher stability limits while sorting out the power dependence of the points, enabling intershot comparisons on a common basis.
- In what now follows, the efficacies of the various divertor configurations in regulating the neutral flux from the divertor to the main chamber and on into the SOL-, core-plasma will be estimated via code calculations. This permits study of configurational recycling aspects divorced from the effects of shape parameters (edge shear and triangularity) otherwise always present in experiments.

5. HOT-ION H-MODE DIVERTOR PLASMA PARAMETERS FOR THE JET MkI DIVERTOR:

Configuration Shot Number	SF #30917	HFE #32919	DNHF1 #33643
J_{sat}: peak [A/cm^2] λ [cm]	30 0.8 (0.32)	7.9 3.5 (0.44)	7 3.5 (0.35)
n_e: peak [10^{13}/cm^3] λ [cm]	3.6 0.9 (0.36)	0.7 4.2 (0.53)	0.6 4.0 (0.40)
T_e: peak [eV] λ [cm]	30 1.9 (0.76)	52 12 (1.50)	56 9.3 (0.93)
$q_{\|\|}$: peak [MW/m^2] λ [cm]	70 0.6 (0.24)	33 2.6 (0.33)	31 2.5 (0.25)
$D_{\alpha\ out}$ [10^{15}/cm^2-s-str]	2.0	0.34	0.29

Table II: Outer target plate Langmuir probe data and D_α for MkI. T_i=T_e is assumed here. The SF case had poor RDD performance. (λ) gives λ projected to the outer midplane.

- In the hot-ion H-mode, T_{ed} ~30-60eV. For low recycling conditions (low D_α) n_{ed} <1x10^{19}/m^3. #30917 (SF) exhibits high recycling => high n_{ed}, and is the only SF shot with good profile data.
- Typically, $\lambda_{T_e} > \lambda_{n_e}, \lambda_{J_{sat}}$
- The λ_{n_e}, $\lambda_{J_{sat}}$ falloff lengths, projected to the outer midplane to account for flux expansion differences at the target, are 0.2 - 0.5 cm.
- The divertor plasma at the target plates is well characterized for the 1994/95 campaign, in contrast to that of 1991, furnishing an excellent database for modelling.

6. EDGE2D/NIMBUS MODELLING OF THE FOUR CONFIGURATIONS:

- IR camera measurements detect most of the power calculated to reach the target plate P_{tar} (S.Clement, this EPS), in contrast to the less satisfactory diagnostic situation in 1991. But, the Langmuir probes typically account for < 20% of P_{tar} (assuming T_e=T_i and an energy transmission factor γ=8). Since probe J_{sat} values are quite compatible with measured D_α levels, the underestimate of power flow likely lies in assumptions for T_i and γ. Thus, the code calculations employ upstream power inputs of P_e=1MW and P_i=5MW. Such a power splitting is not inconsistent with core transport analysis (M. Erba, et al. this conference), and has been used in this sense in the past [7].
- Attempts were made to model the divertor plasma using pure diffusive perpendicular transport, or with a pinch. Diffusive transport alone does not prove acceptable for the higher flux expansion cases, where the computed density profiles are unrealistically broad. The necessity of a pinch to model experiment is also found for other operational regimes on JET (see A. Taroni et al., this conference).
- Other model inputs:

- **n_{es} = 7 x 10^{18}/m^3** (Very low recycling cases demand a somewhat lower n_{es}.) **No impurities.**
- **$D_\perp$ = 0.3 m^2/s, $\chi_{\perp e}$ = 0.8 m^2/s, $\chi_{\perp i}$ = 1.5 m^2/s,** all constant in flux space, **v_{pinch} = -9 m/s**
- 100% recycling at the walls and target. The cryopump is activated. Pumped neutrals are refuelled in the plasma core. A 4% target plate transmission for neutrals is assumed, representing the effect of slots in the MkI divertor. Higher transmissions can lead to enhanced fuelling of the private flux region, effecting more peaked profiles (see A.Loarte et al., this conference); this option is not explored here.

7. PREDICTIVE CODE RESULTS - COMPARISON TO EXPERIMENTS

- The code produces divertor parameters similar to experiment for 1994/95. However, n_{ed} for SNU is predicted to be a factor of two higher than for the other configurations, which does not appear to be compatible with the (sparse) data available at the SNU target plate . Further work is required to match the experimental class of hot-ion H-mode plasmas in detail. Nonetheless, experience from many input parameter scans shows the following results are relatively robust.
- For these runs, $T_i \sim 5T_e$.

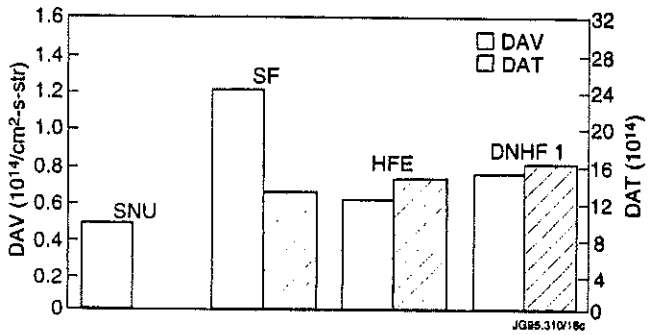

Fig. 5a: Code comparison of DAV and total target plate D_α (DAT) among the cases. The DAT scale is 20x that of DAV.

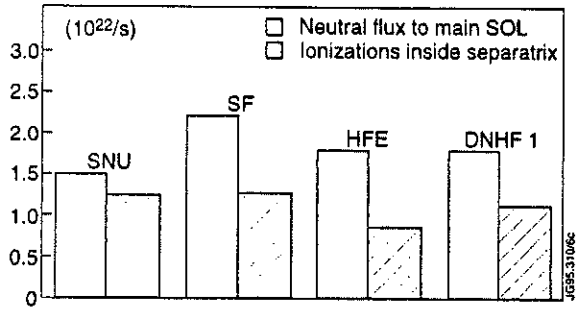

Fig. 5b: Code-predicted neutral fluxes to the SOL above the x-point, and ionization rate inside the separatrix.

Configuration		SNU	SF	HFE	DNHF1
DAH	expt.	0.6	1.4	1.1	1.1
[10^{13}]	code	0.3	0.8	0.5	0.5
DAV	expt.	4.4	7.5	5	6.6
[10^{13}]	code	5	12.3	6.2	7.7
DAT	expt.		118	100	96
[10^{13}]	code		134	148	165

Table III Comparison of experimental - (best RDD cases of Table I) and code- predicted D_α signals.

- In principle the ratios of predicted DAV can be used to normalize DAV in the plots of fig.4, thereby removing differences related to viewing geometry. Thus, with respect to SNU the points will move to lower values (closer to SNU) by factors of 0.8 - 0.4 depending on the configuration.
- The code-predicted neutral flux to the main SOL (left bars of fig. 5b) varies little (1.5 - 2.2 x 10^{22}/s), showing no strong configurational dependence .
- The ionization rate inside the separatrix also varies weakly (0.9 -1.3 x 10^{22}/s). In principle, HFE will experience 30% fewer core ionizations than SNU or SF for the given boundary conditions.
- Table III shows the code underestimates the experimental horizontal D_α by only a factor of two for the "best R_{DD} cases" of table I. Hence, within the code framework there is not much opportunity for wall sources to contribute significantly to the neutral balance.
- The predictions for DAV and DAT come closer to experiment in absolute magnitude than does DAH. The ratio DAT/DAV (1994/95) varies between 11 - 24 in the code and 15 - 20 for the experimental points of table IV. For DAV<1x10^{14} in fig. 4a, DAT/DAV varies over the range 14-25.

8. SUMMARY AND CONCLUSIONS

- **For hot-ion H-mode conditions,** based on predictive EDGE2D/NIMBUS calculations, there is no indication that any of the divertor equilbria of the new JET offer significant advantages over the SNU situation of 1991 with respect to neutral fluxes to the main SOL, or ionizations within the core.

- To model the hot-ion H-mode divertor parameters, at least approximately, for recycling studies of the new JET it has been necessary to assume an inwards pinch along with:

  $n_{es} \approx 7 \times 10^{18}\ m^{-3}$
  $v_{pinch} = -9$ m/s, $D_{\perp} = 0.3\ m^2/s$, $\chi_{\perp e} = 0.8\ m^2/s$, $\chi_{\perp i} = 1.5\ m^2/s$
  $P_e = 1$MW, $P_i = 5$MW

  Langmuir probe measurements dictate that little of the power to the target plate $P_{tar} = P_{in}$ - dW/dt - P_{RAD} can be in the electrons, considering $n_{ed} \leq 1 \times 10^{19}\ m^{-3}$ and $T_{ed} \approx$ 30-60eV and an estimated power flow of less than $20\% P_{tar}$ (assuming $T_e = T_i$ and γ=8). However, power balance is indicated by the IR camera, leading to the conclusion that most of the main core power loss is in the ions. This result seems basically consistent with neoclassical loss processes (M.Erba et al., this conference).

- Evidence exists there is a minimum level of recycling below which high performance is no longer improved, and even affected deleteriously. Assisted by the cryopump, the new JET MkI divertor certainly accesses this region. (Fig.4a) Moreover, MkI experience with Be-target-plates is that a modest gas puff during the NBI-phase is necessary to suppress ELMs.

- A commonly observed feature of the ELM-free H-mode is that recycling signals as well as other divertor plasma properties remain approximately constant at the level prevailing after the L-H transition => implying upstream edge conditions are not changing. This state comes to an end at termination of the high performance phase either through enhanced ion flux to the divertor associated with the "slow rollover" in W_{dia} or via a giant ELM.

9. REFERENCES

[1] S.M. Kaye et al., J. Nucl.. Mater. **121** (1984) 115
[2] ASDEX Team, Nuclear Fusion 29 (1989) 1959
[3] G.L. Jackson et al., J. Nucl. Mater. 162-164 (1989) 489
[4] K. McCormick, M. Bessenrodt-Weberpals, J. Nucl. Mater. 176-177 (1990) 89
[5] G.K. McCormick, Z.A. Pietrzyk et al., J. Nucl. Mater.162-164 (1988) 264
[6] G. Saibene, 2nd European Fusion Physics Workshop (Brussels, Dec. 1994)
[7] A. Loarte, A. Chankin, S. Clement et al., J. Nucl. Mater. 220-222 (1995) 606

Investigation of Momentum Detachment in a Static Gas Target

K Borrass, G T A Huysmans.
JET Joint Undertaking, Abingdon, Oxfordshire, OX14 3EA, UK.

INTRODUCTION

A gas target, providing a pressure drop along field lines (momentum detachment), has been found to be a prerequisite for achieving acceptable divertor conditions in ITER [1]. Momentum transfer from ions to neutrals by elastic and cx-collisions (friction) has been identified as the basic mechanism to achieve this [2]. In steady state, the friction force excerted onto the neutrals has to be balanced either by:

- transverse losses of neutral momentum
  - ion-neutral induced transport or prompt losses
  - neutral-ion mean free path $\lambda_{n\text{-}i}$ SOL width

  Dynamic gas target

or

- the neutral pressure gradient
  - neutral-ion mean free path $\lambda_{n\text{-}i}$ << SOL width
  - transverse momentum losses small, plasma pressure balanced by neutral pressure

  Static gas target

In this paper the potential of a static gas target (SGT) to provide a drop of the plasma pressure along B and to reproduce the other characteristic phenomena of detachment is investigated with a view to JET discharges.

MODEL DESCRIPTION

Geometry

A simplified geometry (see **Fig. 1**) is used, i.e. a slab geometry with constant pitch magnetic field.

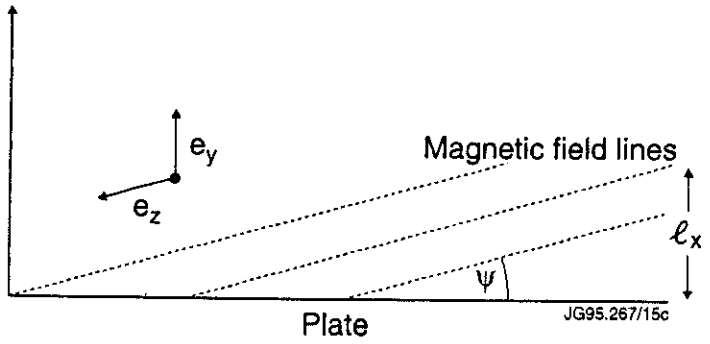

Fig.1: Slab geometry with inclined field lines used in the model.

Equations

Fluid description of SOL plasma and neutrals (high collisionality regime) [4]:

- The plasma is described by the continuity, parallel momentum, and energy equation for ions and electrons.
- The neutrals move independently of magnetic field, i.e. two components of the neutral momentum, parallel to **B** and perpendicular to the plate, are taken into account. The neutral temperature is assumed to be equal to the ion temperature. Both neutrals and ions are then described by one energy equation.

The equations are averaged in the perpendicular direction assuming an exponential decay of the variables. Transverse neutral losses are assumed to be negligible.

Sol-One Code

The resulting seven 1-D equations for the ion and neutral densities, ion and neutral parallel velocities, the neutral perpendicular velocity and the ion/neutral and the electron temperature are solved numerically with the **SOL-ONE code** [3]. The variables are discretized using Petrov-Galerkin linear finite elements. The full time dependence of the variables is solved using an implicit scheme for the time stepping. Steady state solution are obtained in typically 50-100 iterations.

DESCRIPTION OF STUDY POINT

Experimentally, detachment is usually approached by ramping up the density at otherwise fixed plasma parameters. In most devices detachment is a gradual process, which exhibits a roll-over of I_{sat}^{+} , followed by a gradual decrease. Simultaneously the D_α signal increases and the divertor pressure drops by an order of magnitude at basically unchanged upstream conditions. **Fig. 2** shows this behaviour for a JET high density Ohmic discharge.

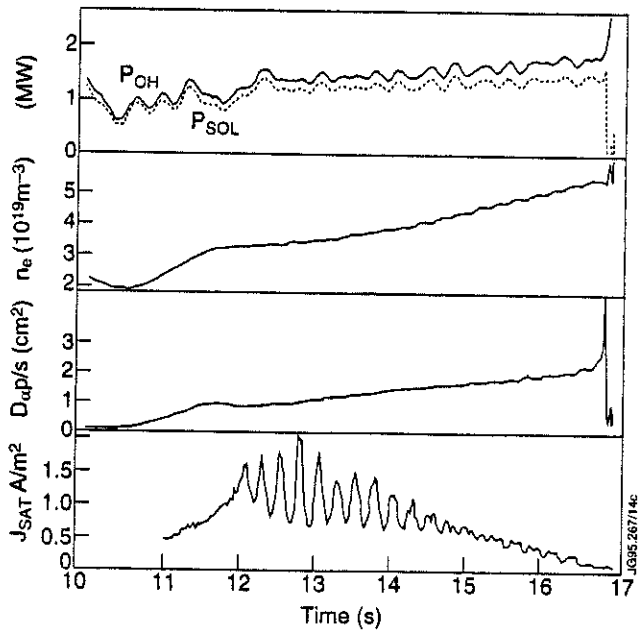

Fig. 2 Traces of the heating power, average density, the D_α signal and the ion saturation current for JET discharge #30829.

A discharge similar to 30829 (see **Fig. 2**) which shows a drop of I_{sat}^{+} at nearly constant net input power is taken as our study point. The adopted input parameters are:

P_{in} = 0.6 MW (per leg)
sin(ψ) = 0.1
L = 2640 cm, L_x (plate to X-point) = 240 cm
profile decay lengths = 2 cm

The density ramp up scenario is simulated by a sequence of runs to steady state with successively increasing particle content, N_{tot}, at otherwise constant input powers.

RESULTS

The results of the N_{tot} scan are shown in the **Fig. 3a** to **d**. At a total particle content of around $N_{tot}=6x10^{16}$ the solution changes dramatically from a normal low recycling solution to a high recycling solution (See **Figs. 4a** and **b**).

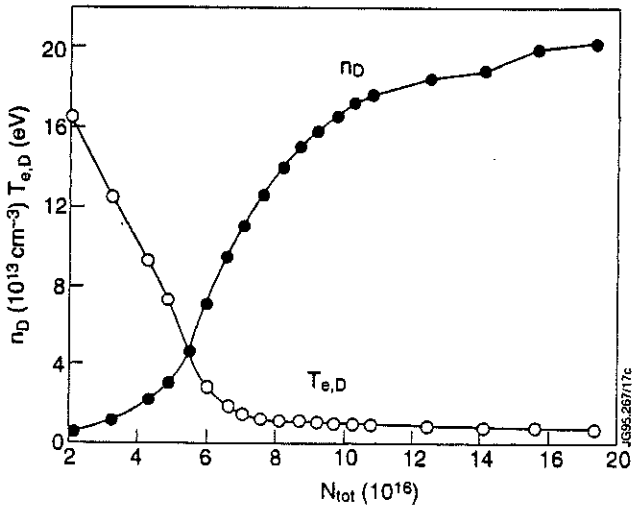

Fig. 3a The density and electron temperature in the divertor versus the total number of particles in the system.

For T_e > 5 eV, P(divertor)/P(upstream) =1/2 holds as expected for a system where i-n neutral collisions do not play a role. With decreasing divertor temperature $T_{e,D}$, the ratio of the divertor to upstream pressure indeed drops, indicating an additional pressure drop along the magnetic field (detachment). However this is mainly due to an increase in upstream pressure at constant divertor pressure.

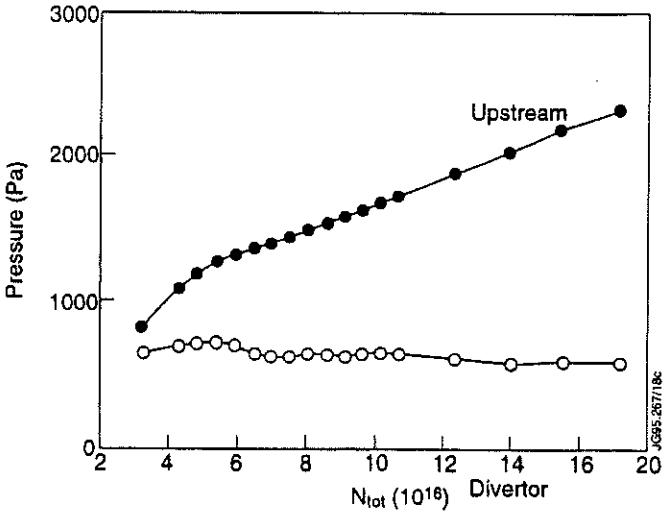

Fig. 3b The upstream and divertor pressure versus the total number of particles.

RESULTS

Different from what is seen in experiment, I_{sat}^{+} (proportional to the particle flux, **Fig. 3c**) is increasing up to the point of detachment and then stays constant. Volume recombination is negligible, so that the total number of ionizations equals the number of particles hitting the plate. Hence, one would not expect a continuously increasing D_α signal as observed in experiment.

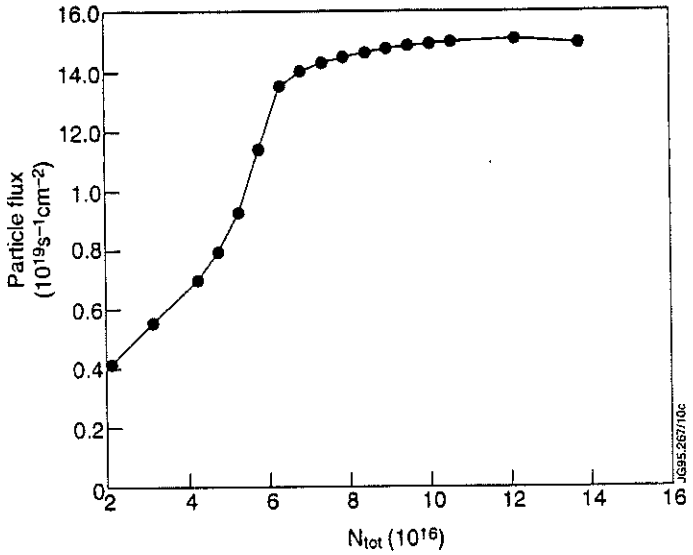

Fig. 3c The particle flux onto the target versus the total number of particles.

Generally, all divertor quantities (n_D, $T_{e,D}$ and I_{sat}^{+}) tend to saturate with increasing number of particles, while the upstream quantities (n_s and P_s) increase linearly. This indicates that the additional particles mainly accumulate in the upstream region (see **Fig.3d**).

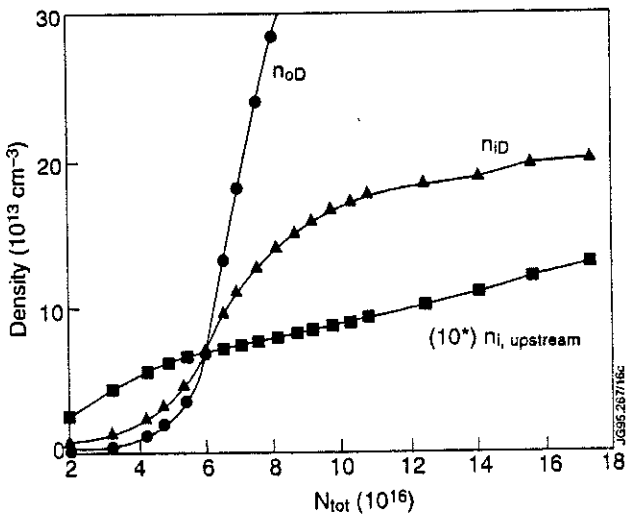

Fig. 3d The neutral and ion density at the divertor and the upstream density (x10) versus the particle content

High Recycling Solution (N_{tot} = 4.2 x 10^{16})

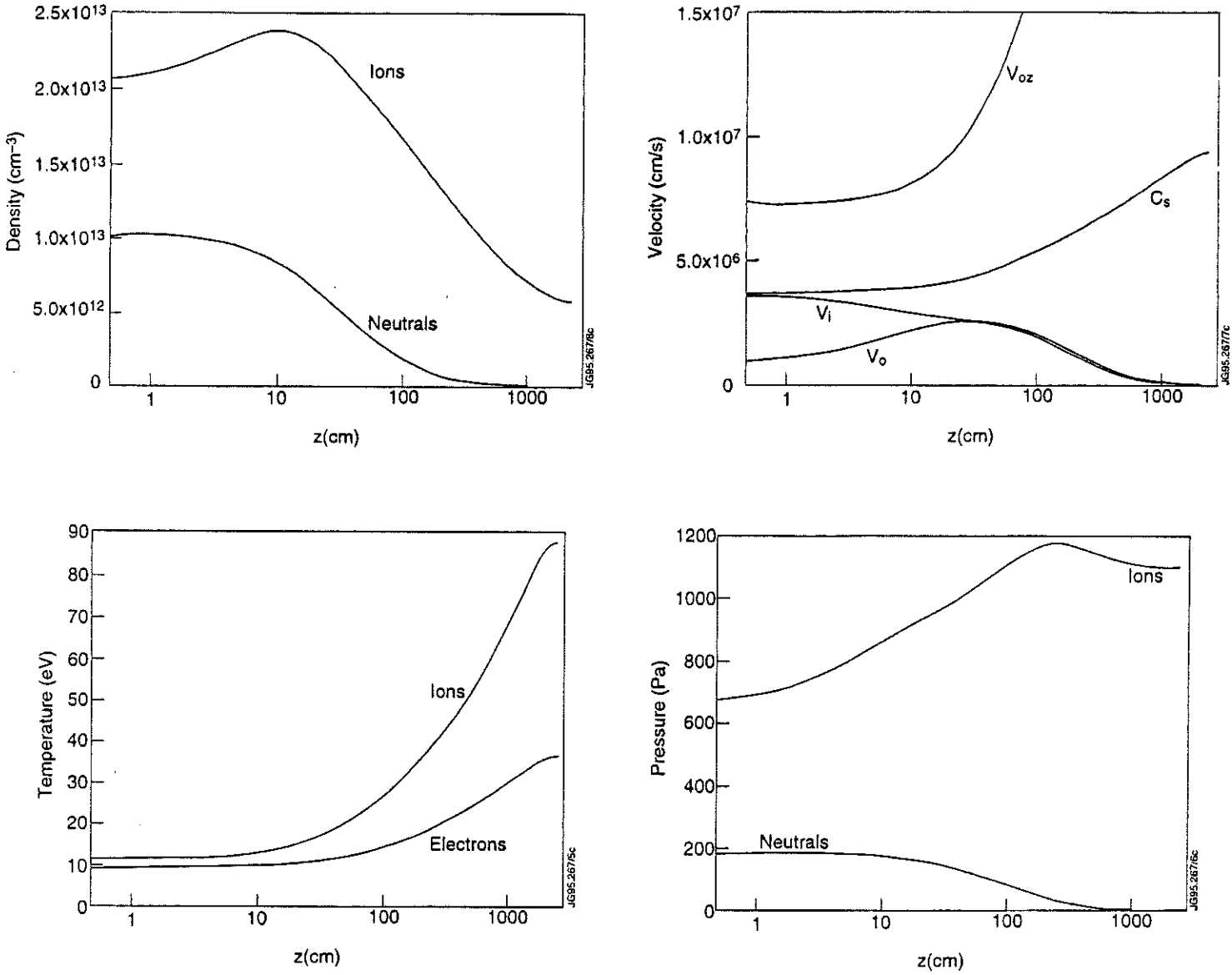

Fig. 4a Details of a solution before detachment with a high divertor temperature and a low neutral density and pressure. Shown are the basic variables that are solved for in the SOL-ONE code, the ion and neutral densities, the ion/neutral temperature and the electron temperature, and the ion (v_i) and neutral velocities, v_0 (perpendicular to the plate) and v_{0z} (parallel to B).

ADDITIONAL DETAILS

'Detached' Solution (N_{tot} = 17 x 10^{16})

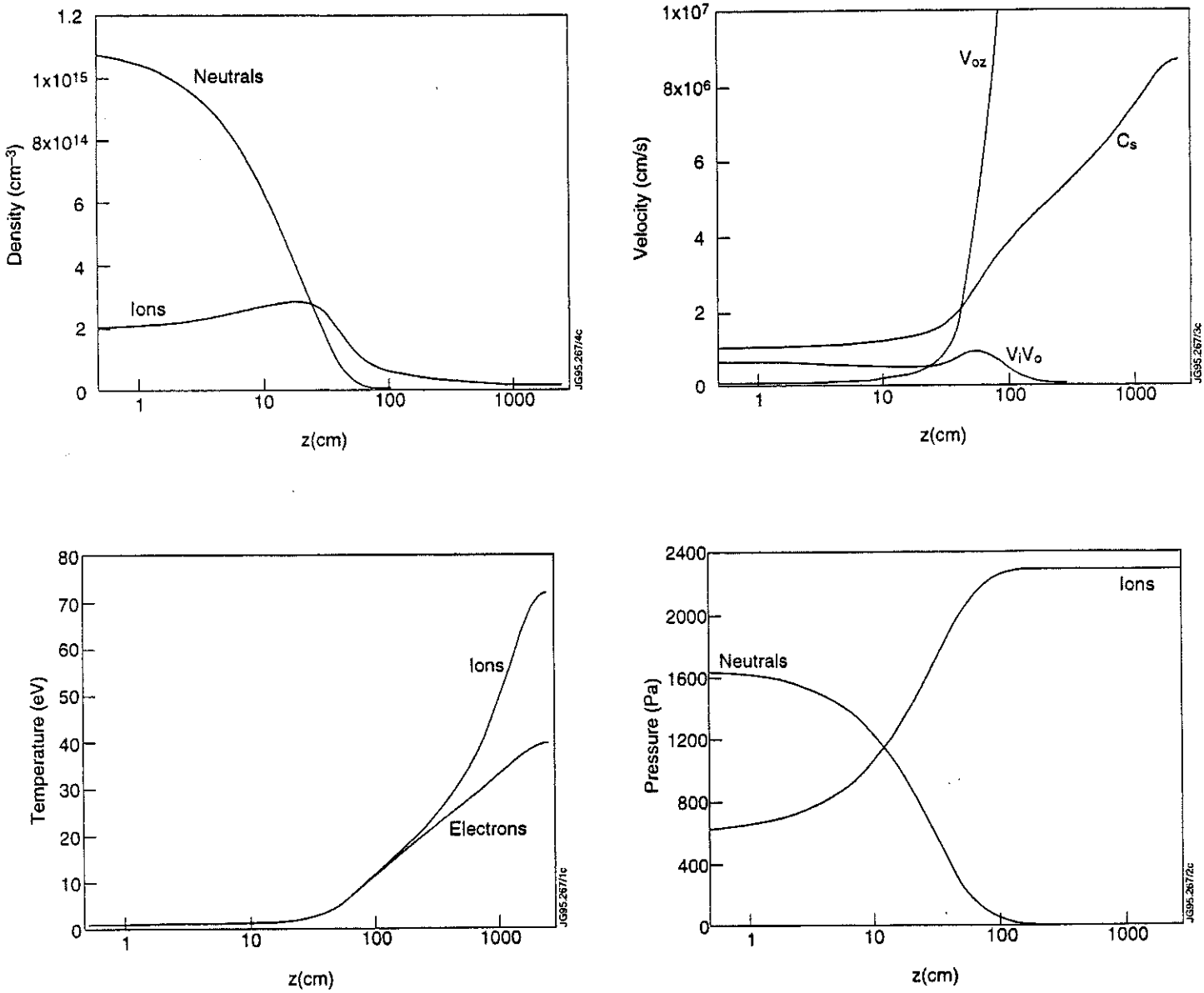

Fig. 4b Details of a solution after detachment with a low divertor temperature and a high neutral density and pressure.

DISCUSSION and CONCLUSION

A typical JET density ramp-up discharge has been modelled with the SOL-ONE 1-D SOL transport code in the fluid limit. With increasing particle content a transition to a detached regime with a strong pressure drop along B is observed. However, the experimentally observed drop of

I^+_{sat} and the increase of the D_α signal are not reproduced. With increasing particle content, plasma parameters in the divertor tend to saturate while upstream quantities continuously increase, i.e, the additional particles tend to accumulate in the upstream region.

There are two potential causes for the failure of the model to reproduce the JET experimental findings:

- *Invalidity of the fluid limit:* The SGT regime, in order to prevail, requires two conditions to be fulfilled:
  - $\lambda_{n\text{-}i} / \Delta << 1$, i.e. the neutrals are collisional with respect to i-n collisions,
  - $\Delta / (l^* \sin(\psi)) << 1$, in order to make transverse neutral induced transport negligible,

  The first condition is marginally satisfied ($\lambda_{n\text{-}i} \sim 1$ cm, $\Delta \sim 3$ cm). However, the second condition with $l^* \sim 50$ cm and $\sin(\psi) \sim 50$ cm is rather difficult to fulfil in JET and generally in configurations with moderate flux expansion.
- *Additional physics effects:* It has been generally found difficult to describe the drop in I^+_{sat} (and the increase in D_α) by i-n collisions alone. Recent studies of the dynamic gas target region have revealed that, with (radiative and three body) recombination included, both the drop of I^+_{sat} and an increase of D_α follow naturally. In the present study the same recombination model is included, but recombination is insignificant since the ion density stays at comparatively low values in the gas target region. It is, however, believed that recombination, possibly with H_2 catalysed recombination included, is an essential element in the full picture.

A similar problem has been considered in Ref. [5], where it was shown that I^+_{sat} / P_s and P_D / P_s should drop with decreasing T_D. This is not in contradiction with our findings. However, we disagree with its conclusion that this provides an explanation of the typical experimental observations. In fact, we find that in a scenario that models the experiment, i.e., when N_{tot} is ramped up at constant input power, the reduction of I^+_{sat} / P_s and P_D / P_s is mainly due to an increase of P_s instead of a reduction of I^+_{sat} and P_D. Also, the divertor temperature is clamped and temperatures below a certain value cannot be obtained (except by a drop of the input power).

REFERENCES

[1] Borras, K., Janeschitz, G., Nucl. Fusion **34** (1994) 1203.

[2] Stangeby, P.C., Nucl. Fusion **33** (1993) 1695.

[3] Huysmans, G., Borras, K., SOL-ONE, A 1-D Scrape-off Layer Transport Code, in preparation.

[4] Post, D.E., Lackner, K., in Physics of Plasma-Wall Interactions in Controlled Fusion, (Post, D.E., Behrisch, R., Eds), Plenum Press, New York and London (1986).

[5] Krasheninnikow, S.I., Catto, P.J., Helander, P., Sigmar, D.J., Soboleva, T.K., Thermal Bifurcation of Scrape-off Layer Plasma and Divertor Detachment, Report PFC/JA-94-28, Massachusetts Institute of Technology (1995).

A New Approach to the Evaluation of I-V-Characteristics and Application to Highly Collisional Divertor Plasmas

K Günther
JET Joint Undertaking, Abingdon, Oxfordshire, OX14 3EA, UK.

1. INTRODUCTION

Langmuir probes are a simple and indispensable tool for the investigation of the edge plasma in magnetic fusion devices. In the form of single probes mounted in the divertor plates, they are widely used in tokamak fusion experiments to monitor the electron density and temperature of the divertor plasma. However, there is growing doubt about the correct evaluation of measured current-voltage-characteristics. In fact, there is little reason to expect that traditional probe theory, predicting simple exponential *I-V*-characteristics up to high values of the electron current in relation to the ion saturation current, is still applicable when the probe is operated in a strong magnetic field.

Recent divertor-probe results at JET underline the problem. In the case of a dense and cold divertor plasma close to or in the state of detachment, rather low values of the electron-to-ion ratio of saturation currents, I_p^-/I_p^+, are found, in a number of cases even smaller than unity. Moreover, the electron temperatures derived essentially from the slopes of the characteristics at the floating point according to $T_e = eI_p^+(\mathrm{d}V_p/\mathrm{d}I_p)$ appear to be substantially overestimated in comparison with predictions from SOL code calculations for this type of discharges [1] (e.g., 12 eV contrasted with 2 eV).

The present paper is an attempt to make a first step towards resolving the problem on the basis of non-ambipolar fluid theory applied to the plasma between the probe-tip Debye-sheath and the adjacent and opposite return sheaths. The very simple model used for the "environment " of the probe has already been treated earlier [2], assuming a non-resistive plasma, and this approach is useful in providing a general understanding of, among other things, low I_p^-/I_p^+ ratios in a magnetized plasma. However, with regard to T_e, the downward correction it predicts cannot exceed a factor of two. Clearly, in the particular case of highly collisional cold divertor plasmas the plasma resistivity (finite Spitzer conductivity) must be taken into account. The present paper upgrades the theory in this respect, describes a corresponding routine procedure of data evaluation in order to derive corrected, i.e. lower, values of T_e, and reports first results.

2. FUNDAMENTALS

2.1. General Aspects of Langmuir Probe Measurements in Strong Magnetic Fields

- Operating a Langmuir probe means applying a voltage to, and measuring the current through, a network of "resistors" of different type: probe-tip and return sheaths (R_{PS} and R_{RS}, respectively), cross-field ($R_\perp$) and longitudinal ($R_{||}$) resistances of the plasma. $R_{||}$ is the only linear one.
- Classical single probe theory deals only with the probe-tip sheath, i.e. R_{PS}, assuming $R_\perp = R_{||} = 0$. As part of the voltage drops at $R_\perp$, $R_{||}$, and R_{RS}, T_e will always be overestimated in this way.
- Saturation of the electron current at a low level cannot be caused by R_{RS} alone as long as a *finite* $R_\perp$ allows the current to flow more and more away from the probe's flux tube across the field when the voltage is increased. Only a current-limiting $R_\perp$, becoming asymptotically infinite, can be responsible.

2.2. Perpendicular Electric Current in a Magnetized Plasma According to Fluid Theory

The total momentum balance in a magnetized plasma

$$\boxed{\vec{j}\times\vec{B} = \vec{\nabla}p + (k_i + k_{cx})Nm_i n\vec{v} + m_i\vec{\Gamma}\cdot\vec{\nabla}\vec{v} + \vec{\nabla}\cdot\vec{\pi}}$$

shows that the cross-field current is a matter of forces that balance the associated *Lorentz force* $\vec{j}\times\vec{B}$. In the presence of anomalous processes, this relation holds true provided that fluctuations of the magnetic field are unimportant. Exactly this approach underlies non-ambipolar scrape-off layer models [3,4].

In a Cartesian coordinate system defined by

x along $\vec{B}$ *y* $\perp$ to both $\vec{B}$ and the surfaces *p* = *const.* *z* along *p* = *const.* and $\perp$ to $\vec{B}$

it is the *z*-components of the momentum balance equations (for ions and electrons separately) that determine the *y*-fluxes in question (j_y = en ($v_{iy} - v_{ey}$) is the corresponding electric current density):

$$eBnv_{iy} = -\left\langle en\frac{\partial U}{\partial z}\right\rangle - R_z - \underbrace{(k_i + k_{cx})Nm_i n v_{iz}}_{\text{sources due to neutrals}} - \underbrace{m_i n\left(v_{iy}\frac{\partial v_{iz}}{\partial y} + v_{ix}\frac{\partial v_{iz}}{\partial x}\right)}_{\text{inertia (conv. momemtum flux)}} + \underbrace{\frac{\partial}{\partial y}\eta_\perp\frac{\partial v_{iz}}{\partial y} + \cdots}_{\text{viscosity}}$$

$$eBnv_{ey} = -\left\langle en\frac{\partial U}{\partial z}\right\rangle - R_z$$

turbulence friction

anomalous diffusion classical diffusion

$$-eBD_\perp\frac{\partial n}{\partial y} \qquad -R_z = -\frac{en}{\sigma_\perp}j_z \approx -\frac{en}{\sigma_\perp B}\frac{\partial p}{\partial y}$$

Conclusions

- Density-gradient driven transport is ambipolar ($D_{\perp i} = D_{\perp e}$).
- A perpendicular electric field E_y affects the ions *alone* and *indirectly* via v_{iz}, the drift velocity due to ExB-drift. This cannot generally be put together by writing $v_{iy} = e\mu_{\perp i}E_y$. However, $\mu_{\perp e} = 0$ is obvious.

3. THE SIMPLEST MODEL: FLUSH MOUNTED PROBE IN A 100% RECYCLING SOL PLASMA

- Scrape-off plasma sustained by ionization of neutrals only, i.e. $\vec{\nabla}_\perp \cdot \vec{\Gamma}_i = 0$.

- Consequence for particle balance:

  Condition imposed on integral density of neutrals $\int_{-L}^{+L} dx N(x)$

- $\vec{B}$ = const.

- Approximations: $T_e = const.$,
  $T_i = const.$,
  neglect of viscosity.

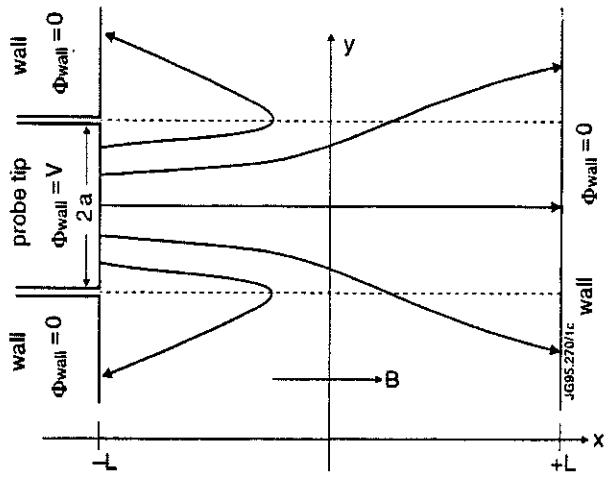

Fig.1: Schematic of a flush mounted probe in a scrape-off layer. Φ designates electric potentials. Arrowed lines indicate the electric current flow if V > 0.

3.1. Basic Physical Parameters

$$C = \frac{a}{\rho}\frac{1}{\sqrt{Z+\mu}} \quad \text{where} \quad \rho = \frac{\sqrt{m_i T_e}}{ZeB} \quad \mu = \frac{\langle \sigma_{cx} v \rangle}{\langle \sigma_i v \rangle}$$

a=projected probe tip half width

$$\vartheta = \frac{a}{\lambda} \quad \text{where} \quad \lambda = \sqrt{\frac{D_\perp L}{f c_s}}$$

$f = f(\mu/Z) < 1$ density profile factor

$$\gamma^2 = \frac{e^2 n_0^* c_s L}{T_e \sigma_{\parallel}} = \frac{L}{1.96\,\lambda_{ei}}\sqrt{\frac{m_e}{m_i}\left(Z + \frac{T_i}{T_e}\right)}$$

n_0^* = sheath edge density, probe unbiased

λ_{ei} = mean free path of electrons

L has to be treated as a *reduced* (effective) connection length which excludes that part of the scrape-off layer where the density of neutrals is low and the electron temperature is high.

3.2. Non-Resistive Case ($\sigma_{\parallel} = \infty$) in Slab Geometry

The longitudinal constancy of Φ, the normalized extra plasma potential induced by biasing the probe, allows the equations to be integrated along field lines. This results in an ordinary differential equation for $\Phi(y)$, the "probe equation" (see [2]), which incorporates the boundary conditions at the sheath edges:

$$a^2\frac{d^2\Phi}{dy^2} - \frac{\varepsilon^*}{2}\left(a\frac{d\Phi}{dy}\right)^2 = C^{*2}F(V,\Phi,y/a) = C^{*2}\begin{cases}1-\frac{1}{2}\left(1+e^{V}\right)e^{-\Phi} & \text{for } |y/a|<1\\ 1-e^{-\Phi} & \text{for } |y/a|\geq 1\end{cases}$$

V = normalized probe voltage $\qquad C^{*2} = C^2 + \vartheta^2\frac{T_i}{ZT_e} \qquad \varepsilon^* = 2\left(\frac{\vartheta}{C^*}\right)^2$

Probe current density: $\qquad \bar{j}_p(V) = en_0^* c_s \frac{1}{a}\int_0^a dy\, e^{-\varepsilon^*\Phi(y)/2}\left[e^{V-\Phi(y)}-1\right]$

Analytical results

Linearized equation yields floating-point slope

$$\left.\frac{d\bar{j}_p}{dV_p}\right|_{\bar{j}_p=0} = \frac{en_0^* c_s}{T_e/e}\,s_0 \qquad s_0\left(C^*\right) = \frac{1}{2} + \frac{\sinh C^*}{2C^*\exp C^*}$$

Normalized saturation currents:

$$\bar{j}_p^{\pm} = en_0^* c_s S_0^{\pm}$$

$$S_0^- = \frac{2}{\vartheta\sqrt{1+\varepsilon^*}} \qquad S_0^+ \approx \exp\left[\frac{\varepsilon^*}{2}\left(\frac{1}{s_0}-1\right)\right]$$

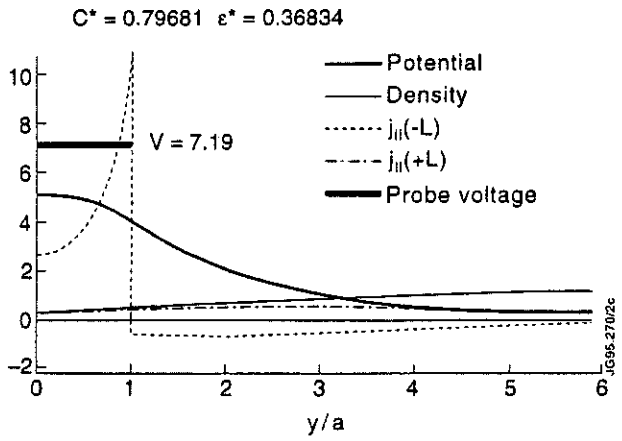

Fig.2: Potential $\Phi(y)$ and related profiles at the sheath edges for a positive probe voltage. Parameters according to 91.2% of electron-current saturation at $S_0^- = 5$.

The role of the density

- The saturation of the electron current is due to the density reacting to biasing the probe, which leads to a depletion of density in the flux tube connected to the probe tip if $V >> 0$ according to the relation $n^*(y)/n_0^* = \exp\left(-\varepsilon^*\Phi(y)/2\right)$ that follows from the model.
- This density effect is caused by the limiting influence of diffusion on the cross-field current: There would be no saturation of the electron current if $D_{\perp} = \infty$ corresponding to $\varepsilon^* = \vartheta = 0$.
- It is a typical non-linear effect which does not affect the vicinity of the floating point: That is why s_0 depends on C^* only.
- Pin-plate probe experiments [5] give evidence for this behaviour of both Φ and n.

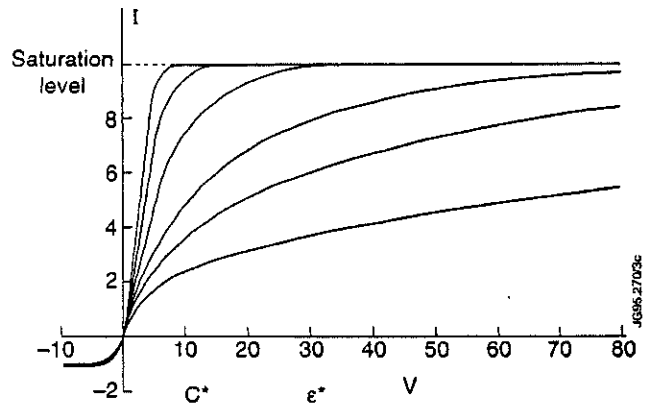

C*	ε*
0.10728	2.18351
0.38072	0.39551
0.79681	0.11319
1.59853	0.03038
2.48256	0.01282
4.99977	0.00319

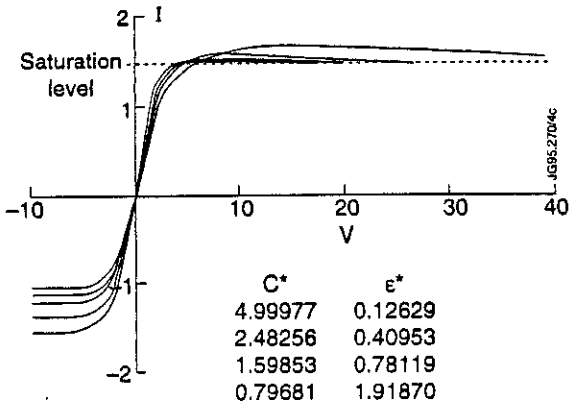

C*	ε*
4.99977	0.12629
2.48256	0.40953
1.59853	0.78119
0.79681	1.91870
0.38072	4.47798

Fig. 3. Examples of calculated I-V-characteristics (normalized). Two families of curves (left and right) corresponding to two electron-current saturation levels.

3.3. Resistive Case (Linearized Treatment) in Slab Geometry

For reasons of feasibility, the equations have been linearized (V,Φ, and $\ln(n/n_0)$ treated as small quantities), which yields the floating-point slope of the *I-V*-characteristic only. 2-D probe equation:

$$\boxed{C^{*2}L^2\frac{\partial^2\Phi}{\partial x^2} + \gamma^{*2}a^2\frac{\partial^2\Phi}{\partial y^2} = 0} \qquad \gamma^{*2} = \gamma^2\frac{C^{*2}}{C^{*2}+\vartheta^2}$$

Boundary conditions at the sheath edges:

$$\boldsymbol{x = +L}\text{:}\quad -L\frac{\partial\Phi}{\partial x} = \gamma^{*2}\Phi$$

$$\boldsymbol{x = -L}\text{:}\quad -L\frac{\partial\Phi}{\partial x} = -\gamma^{*2}\Phi + \gamma^{*2}V\theta(a-|y|) = -\gamma^{*2}\Phi + \gamma^{*2}V\int_0^\infty dk\,\frac{2\sin k}{\pi k}\cos\left(\frac{y}{a}k\right)$$

Solution by Fourier transformation:

$$\Phi(x,y) = \frac{V}{\pi}\int_0^\infty dk\left[\frac{\mathrm{ch}\left(\frac{\gamma^*}{C^*}\frac{x}{L}k\right)}{\frac{k}{C^*\gamma^*}\mathrm{sh}\left(\frac{\gamma^*}{C^*}k\right) + \mathrm{ch}\left(\frac{\gamma^*}{C^*}k\right)} - \frac{\mathrm{sh}\left(\frac{\gamma^*}{C^*}\frac{x}{L}k\right)}{\mathrm{sh}\left(\frac{\gamma^*}{C^*}k\right) + \frac{k}{C^*\gamma^*}\mathrm{ch}\left(\frac{\gamma^*}{C^*}k\right)}\right]\frac{\sin k}{k}\cos\left(\frac{y}{a}k\right)$$

The result is the floating-point slope according to the first-order relation $\bar{j}_p(V) = en_0^* c_s \frac{1}{a}\int_0^a dy\,[V-\Phi(y)]$:

$$\left.\frac{d\bar{j}_p}{dV_p}\right|_{\bar{j}_p=0} = \frac{en_0^* c_s}{T_e/e}\,s \qquad s(C^*,\gamma^*) = 1 - \frac{2}{\pi}\int_0^\infty dk\, \frac{sh\left(\frac{2\gamma^*}{C^*}k\right) + \frac{k}{C^*\gamma^*}ch\left(\frac{2\gamma^*}{C^*}k\right)}{\left[1+\left(\frac{k}{C^*\gamma^*}\right)^2\right]sh\left(\frac{2\gamma^*}{C^*}k\right) + 2\frac{k}{C^*\gamma^*}ch\left(\frac{2\gamma^*}{C^*}k\right)}\,\frac{\sin^2 k}{k^2}$$

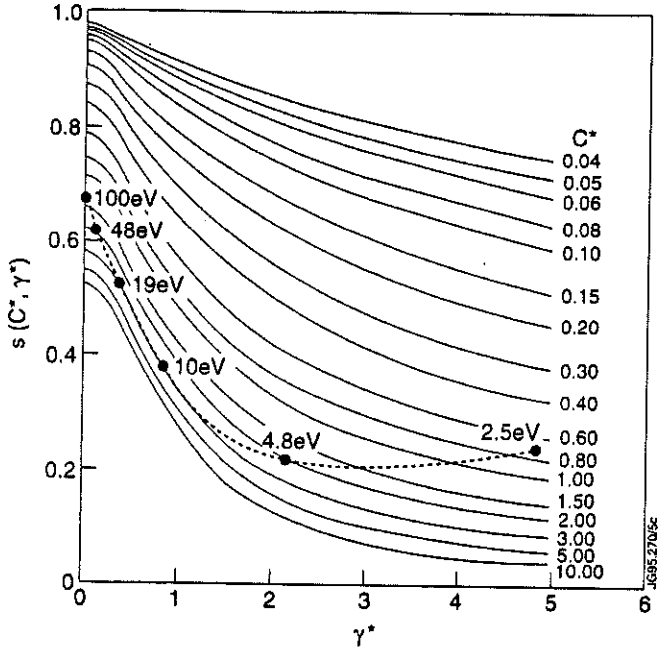

Fig. 4. Normalized floating-point slope of the I-V-characteristic as a function of the parameters C^* and γ^*. The dependence of the latter on T_e is exemplified by the broken line which corresponds to a realistic case (JET pulse No 31627 at 15.855 s - see Fig. 5).

4. EVALUATION OF EXPERIMENTAL DATA

Objective: Find a realistic value of T_e by using

Experimental Data	Theoretical Relations	Calculations of Parameters
$T_e^{orthodox} = e I_p^+ \left.\frac{dV_p}{dI_p}\right\|_{I_p=0}$	$s(C^*,\gamma^*)$	$C^2 = \frac{Z^2 e^2 B^2 a^2}{m_i T_e \left(Z + \langle\sigma_{cx} v\rangle/\langle\sigma_i v\rangle\right)}$
ion saturation current density $\bar{j}_p^+$	$S_0^-(\vartheta, C^*)$ $S_0^+(\vartheta, C^*)$	$\hat{\gamma}^2 = 5.262\,\frac{Z(L/m)\,(\bar{j}_p^+/Acm^{-2})}{(T_e/eV)^{5/2}}$
saturation current ratio I_p^-/I_p^+	$S^+(\vartheta, C^*, \gamma^*)$ approximation	ϑ by marginal estimation (see below)

and solving $$T_e = \frac{s\left(C^*(T_e),\gamma^*(T_e)\right)}{S^+\left(\vartheta,C^*(T_e),\gamma^*(T_e)\right)}\, T_e^{\text{orthodox}}$$ for T_e.

Note that the *measured* j_p^+ has to be looked upon as $en_0^* c_s S^+$ (effect of density rise).

4.1. Upper Limit for T_e

Set $\vartheta = 0$ and obtain

$$S^+ = 1 \qquad C^* = C \qquad \gamma^* = \gamma = \hat{\gamma}\ .$$

4.2. Lower Limit for T_e

Derive two *overestimated* values of ϑ from

(i) measured saturation-current ratio I_p^-/I_p^+ by setting

$$\frac{I_p^-}{I_p^+} = \frac{S_0^-}{S_0^+} = \begin{cases} \dfrac{2}{\vartheta\sqrt{1+2\left(\vartheta/C^*\right)^2}} & \leftarrow \text{overestimated} \\ \exp\left[\left(\vartheta/C^*\right)^2\left(\dfrac{1}{s_0(C^*)}-1\right)\right] & \leftarrow \text{underestimated} \end{cases}$$ } with respect to the (unknown) resistive version

(ii) classical diffusion coefficient $D_\perp = n\left(T_e + T_i/Z\right)/\left(B^2\sigma_\perp\right)$ (take $n = n_0^*$ to be save) by using

$$\vartheta = \frac{a/\rho}{\gamma}\sqrt{\frac{f}{1.96Z}}\ ,$$

take *the smaller one* and obtain

$$C^* = \sqrt{C^2 + \vartheta^2 T_i/(ZT_e)} \qquad \gamma^* = \gamma C^*/\sqrt{C^{*2}+\vartheta^2} \qquad \gamma = \hat{\gamma}/\sqrt{S^+\left(\vartheta,C^*,\gamma^*\right)}\ .$$

As can be seen, this procedure requires some self-consistency loops.

5. RESULTS

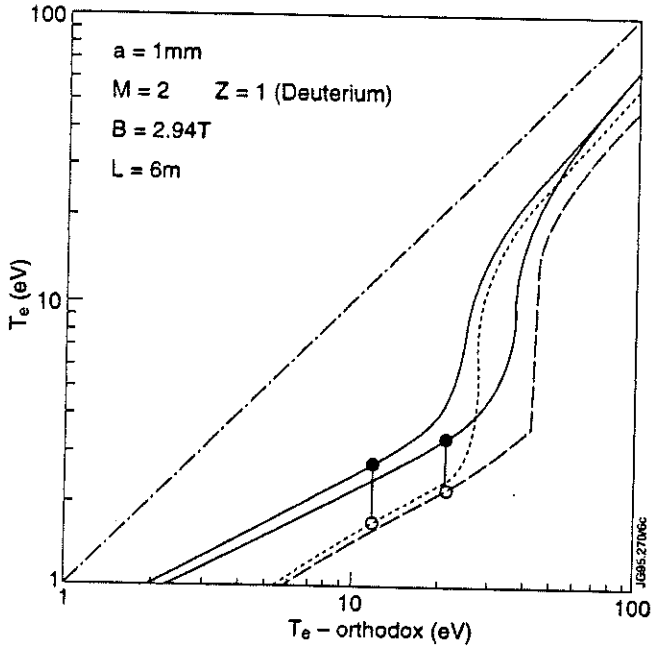

Fig. 5. Upper (solid) and lower (dashed) limits for T_e in dependence on $T_e^{orthodox}$. Parameters of probe No 21 in JET pulse No 31627 at 15.855 s ($j_p^+ = 7.3$ A/cm^2, upper curves) and 15.885 s ($j_p^+ = 18$ A/cm^2, lower curves).

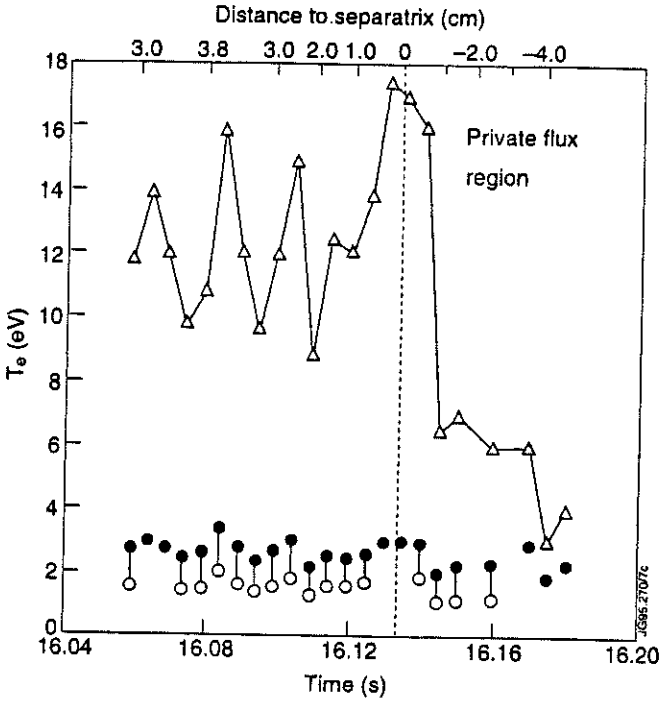

Fig. 6. $T_e^{orthodox}$ (solid line) contrasted with upper and lower limits of T_e (full and open circles) for probe No 21 in JET pulse No 31627 during separatrix sweeping in a dense divertor plasma prior to detachment.

6. CONCLUSIONS

1. Ordinary non-ambipolar fluid theory [3,4] can provide a basic understanding of *I-V*-characteristics from probes in a magnetic field, including very small values of the ratio of saturation currents I_p^-/I_p^+ .
2. The resistivity of the plasma becomes crucial in dense and cold divertor plasmas which, if ignored, causes too-high electron temperatures to be derived from measured *I-V*-characteristics.
3. The resistive version of the simple 100%-recycling model with $\vec{B} = \text{const.}$ can deliver drastically reduced electron temperatures which seem to be not unreasonable in the light of code predictions [1].
4. The quantitative results presented have to be regarded as preliminary only for a number of reasons:
   - Retaining the model itself, improvements are necessary with respect to (i) using cylindrical geometry, (ii) finding empirical rules of choosing suitable values of L (effective connection length), (iii) solving the nonlinear version of the model to provide the theoretical saturation current levels.
   - Beyond the 100%-recycling model, which is far from reflecting the actual situation in a divertor SOL, it is most crucial to take account of (i) magnetic shear, (ii) pre-existing plasma currents and cross-field drift motions of the plasma, (iii) profiles of T_e, n, and neutral density along $\vec{B}$.

     Ultimately, a biased Langmuir probe ought to be treated as an integral part of the scrape-off layer as a whole, described in terms of non-ambipolar fluid theory.

TUESDAY

'Helium and Neon Transport Experiments at JET'

M von Hellermann, K Barth, A J Bickley, D Campbell, U Gerstel, J de Haas, D Hillis[1], L Horton, A Howman, R König, L Lauro-Taroni, C Mayeux, P Nielsen, W Obert, G Saibene, M F Stamp, D Stork, M Wade[1], K-D Zastrow.

JET Joint Undertaking, Abingdon, Oxfordshire, OX14 3EA, UK.
[1] ORNL, Oak Ridge, Tenessee, USA.

I. Introduction

The confinement and transport behaviour of fully stripped helium representing the fusion 'ash' is of central interest for the operation and design of future fusion devices. In the pumped divertor phase of JET, dedicated helium transport experiments were carried out based on edge and central (beam) fuelling. Exhaust studies involve the use of argon frost on the divertor cryo-pump in order to achieve active pumping of helium. Charge exchange spectroscopy measurements are used to monitor the evolution of helium density profiles. Transport and exhaust of neon and nitrogen was investigated in radiative divertor experiments.

II. Helium Confinement and Exhaust Studies

The helium content $N_{tot} = \int_0^1 dV \cdot n_{He^{2+}}(\rho)$ added by the short (0.1s) gas-puffs is of the order 2 to $3 \cdot 10^{20}$ (or 5% of the total plasma particle content). Particle replacement times are experimentally determined by the measurement of the volume integrated impurity density profiles (He, Ne, N) and the temporal evolution of inward and outward radial particle flows: $\tau_p^* = \frac{\int dV \cdot n_Z(\rho)}{A \cdot (\Gamma_{out} - \Gamma_{in})}$

pulse	comment	P_{NBI} MW	I_p MA	$n_e(0)$ $10^{19}m^{-3}$	$n_\alpha(0)$ $10^{18}m^{-3}$	$T_e(0)$ keV	puff at t(s)	Ar-frost	τ_p^* (sec)	τ_E (sec)
33333	ELMy H-mode scan of x-point	10.5	2.0	5.0	2.1	5.0	14.0	yes	5-10	0.25
33476	L-mode	5.0	2.0	3.5	1.8	3.5	14.5	no	>11	0.24
33994	L-mode	13.0	2.0	3.5	4.2	4.0	15.0	yes	4-7	0.25
33995	ELMy H-mode	4.0	2.0	4.0	3.4	3.0	15.0	yes	>12	0.45
34324	ELMy H-mode	4.0	2.0	4.0	1.5	3.0	15.0	no	>22	0.64

Table I Overview of plasma data in representative helium edge puff experiments with active argon frost pumping (divertor target tiles are graphite).

Typical τ_p^* values for helium are of the order 8 to 15s (H-mode) in the case of active argon-frost pumping, compared to 20 to 30s in the case of no argon-frost (Fig.1). Corresponding values for L-mode confinement are approximately half the values of the H-mode case. The observed alpha particle replacement times exceed energy confinement times τ_E, which are of the order 0.3 to 0.5sec, by more than a factor of 20 (H-mode, argon-frost) and 10 (L-mode, argon-frost). The L-mode evolution of the helium content (no active helium pumping) (Fig.1a) is decribed by a sharp decrease after the gas puff settling to a level which is determined by the recycling level. Time dependent variations of the particle replacement time following the initial pump phase indicate saturation effects in argon frost pumping. Sweeping of the x-point and the location of the strike zone with respect to the pump duct leads to significant changes in deduced particle decay rates (Fig.2). Wall pumping does not appear to play a significant role and no obvious difference is found between exhaust rates in pulses following extensive helium glow-discharges.

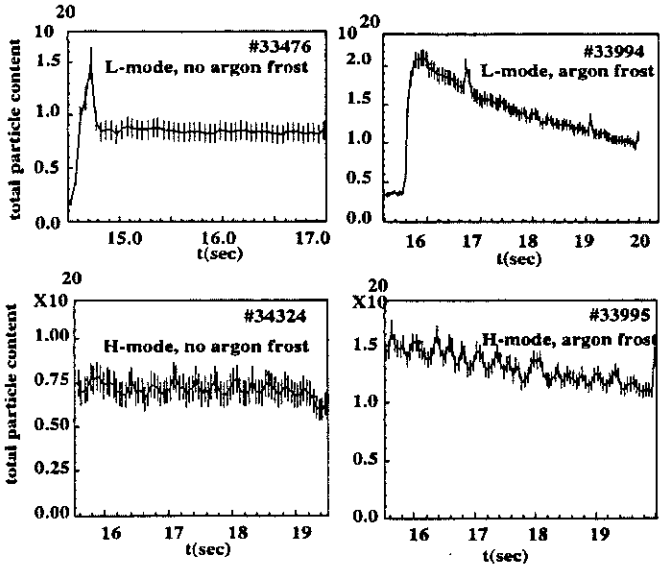

Fig.1 Decay of total alpha particle content in the case of no Ar-frost for a) H-mode, b) L-mode and active Ar frost pumping, c) H-mode d) L-mode.

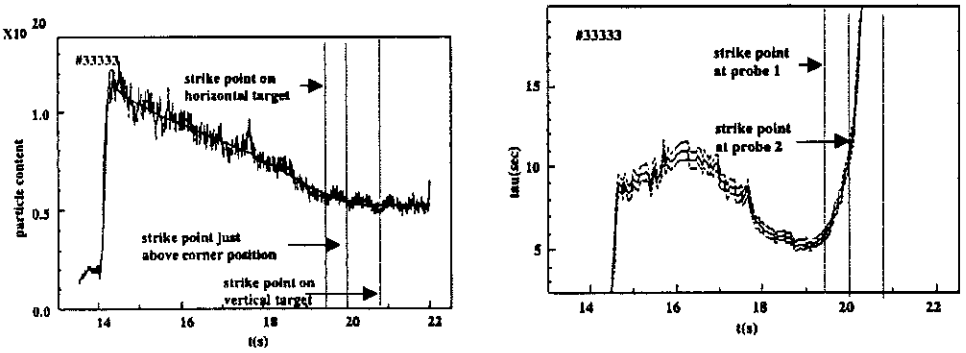

Fig.2 a) Particle content and b) variation of replacement time in the case of sweeping of x-point and strike zone position. The decay rate reaches a maximum (or τ_p^* a minimum) at a position close to the corner points of the divertor. Next to no pumping is observed when the strike zone is on the vertical target plates.

III Neon exhaust in radiative divertor plasmas

Distinctively lower particle replacement times are observed in the case of neon gas-puff experiments (see table II), which were carried out as part of divertor radiative cooling studies. Similar to helium the H-mode particle confinement time τ_p^* is about 2 to 3 times the L-mode case. Fig.3 shows the rapid decay of the Ne^{10+} content following a puff of 200ms. Neon particle repalcement times are about 5 to 10 times the energy replacement time.

pulse	comment	P_{NBI} MW	I_p MA	$n_e(0)$ $10^{19}m^{-3}$	$n_{Ne}(0)$ $10^{17}m^{-3}$	$T_e(0)$ keV	puff at t(s)	τ_p^* (sec)	τ_E (sec)
32778	ELMy-H-mode	18.0	3.0	5.0	1.1	5.0	16.5	5.5	0.38
33958	L-mode	10.0	2.0	3.0	2.0	4.5	15.5	1.6	0.20
34372	L-mode	14.0	2.0	2.5	1.6	5.0	15.0	1.5	0.26

Table II Overview of plasma data in neon edge fuelling and exhaust studies in L- and H-modes

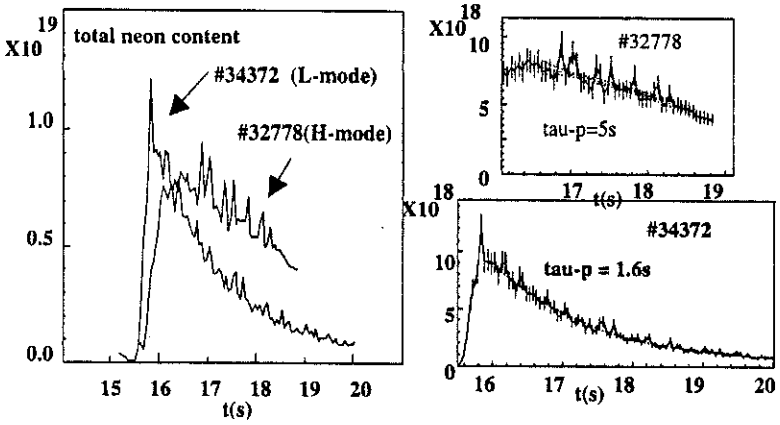

Fig.3Total confined neon content and its replacement time in L-mode and H-mode

III. Helium exhaust studies at radiative divertor

pulse	comment	P_{NBI} MW	I_p MA	$n_e(0)$ $10^{19}m^{-3}$	$n_{He}(0)$ $10^{18}m^{-3}$	$T_e(0)$ keV	puff at t(s)	τ_p^* (sec)	τ_E (sec)
35452	ELMy-H-mode	5.5	2.0	3.0	1.6	4.0	15.0	10	0.26
35458	ELMy-H-mode	7.0	2.0	3.5	2.0	4.5	15.0	15	0.27
35460	L-mode	2.5	2.0	2.5	3.0	4.5	15.0	>4	0.55

Table III Overview of plasma data in He edge fuelling and exhaust studies in L- and H-modes (Be-tile)

IV. Experimental transport data derived from gas-puffing experiments

Diffusion coefficients and convective velocities may be derived from particle flows and gradients ∇n_z measured during the period of density perturbation following a brief plasma edge gas puff. Neglecting

source and sink terms, which is justified in particular during high replacement with a much reduced particle transport across the magnetic separatrix, for core radii ($\rho<0.9$) and ion temperatures well above 1 keV, values for diffusion D and convection velocity v may be derived from a plot of normalised particle flow versus normalised gradients ($\frac{\Gamma_z}{n_z} = -D\frac{\nabla n_z}{n_z} + v_z$).

The key issue for particle transport experiments is the deduction of *local particle densities* from spectroscopic measurements, this involves the unambiguous extraction of a *local ion velocity distribution function*. Substantial progress has been achieved in the last experimental campaign at JET by the simultaneous measured of carbon and helium CX spectra. By imposing the ion temperature deduced from CX CVI the uncertainties in the analysis of the HeII spectrum ('plume' effect etc.) can be much reduced. Additional proof is provided by results from high resolution X-ray spectroscopy measurements of $T_i(\rho=0.4)$. Systematic errors in deduced helium densities profile gradients are introduced by error propagation in neutral beam density calculations which depend on the electron density, magnetic field configuration, geometry and the actual impurity composition. The main instrumental errors affecting directly transport data are errors in the relative calibration of each radial channels (the JET CX diagnostic uses up to 11 channels for the reconstruction of a radial density profile). To overcome the instrumental graininess of the profile smooth functions (*polynomial, spline, analytical*) are fitted to experimental data. Similar smoothing procedures are applied for the deduction of time derivatives. The error bars on the experimental data include both statistical and systematic errors. The error propagation for gradients and particle flows as deduced from the spline fits are shown in Fig.4 with values for D and v as derived from the slope and interception of flow versus gradient.

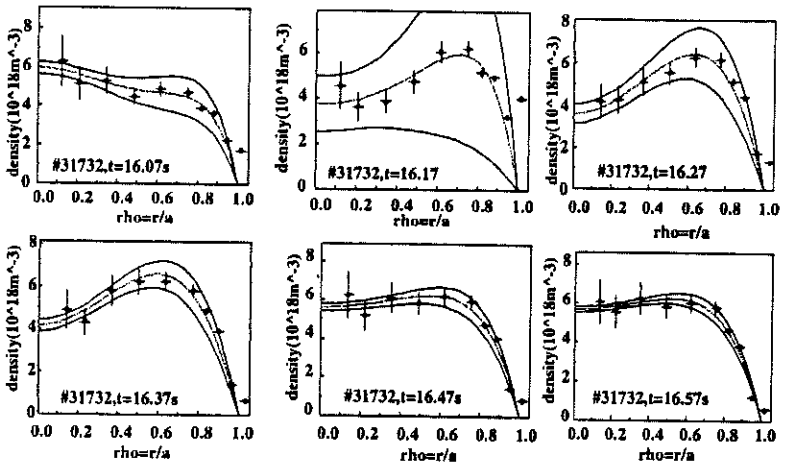

Fig.4 The characteristic behaviour following a short (0.1s) He puff into the plasma into an H-mode is an instantaneous increase and subsequent fast decay at the outermost channels, and a slow increase at the plasma centre reaching steady state after 300 to 500 msec. The radial profile changes from a flat to parabolic profile before the puff to a distinctively hollow profile immediately after the puff and finally to steady state profiles which are similar to the electron density profile.

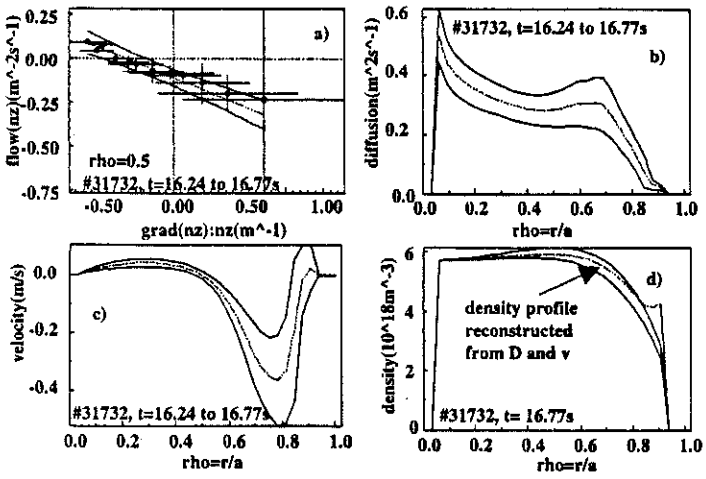

Fig.5 Deduction of transport data from $\Gamma(n_z)/n_z$ vs. $\nabla(n_z)/n_z$, b) and c) D and v profiles, d) steady state reconstruction of density profiles from v(r), D(r) and comparison with experimental upper and lower error bars.

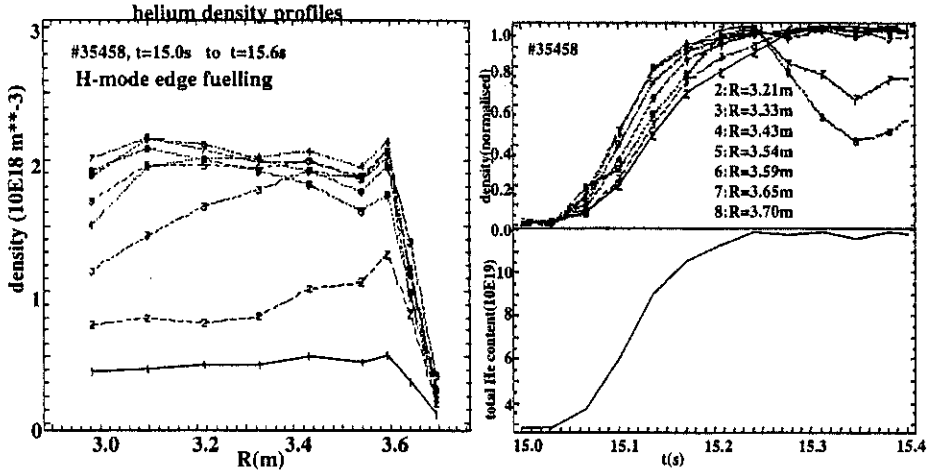

Fig.6 Helium gas puff experiment in radiative divertor conditions. Beryllium target tiles. a) profile evolution shown every 100ms b) Normalised traces for 7 different radial positions with 35ms time resolution c) total helium content.

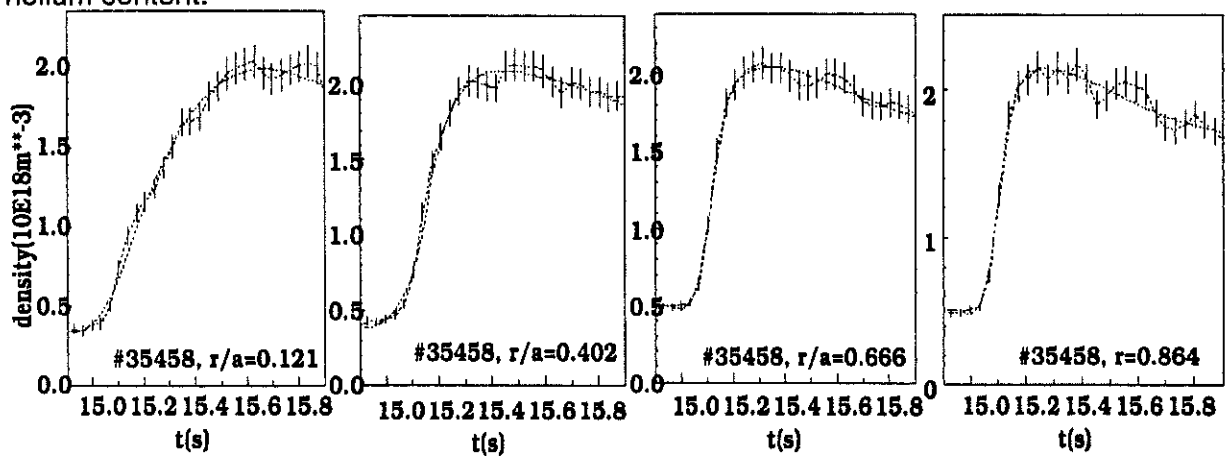

Fig.7 Experimental data and spline fit shown for 4 minor radii. Vertical bars indicate statistical errors.

B) Neon transport studies

Neon density profiles (similar to the intrinsic impurity carbon) are generally hollow (both in L- and H-mode) and convection velocities are directed outwards for the major part of the profiles.

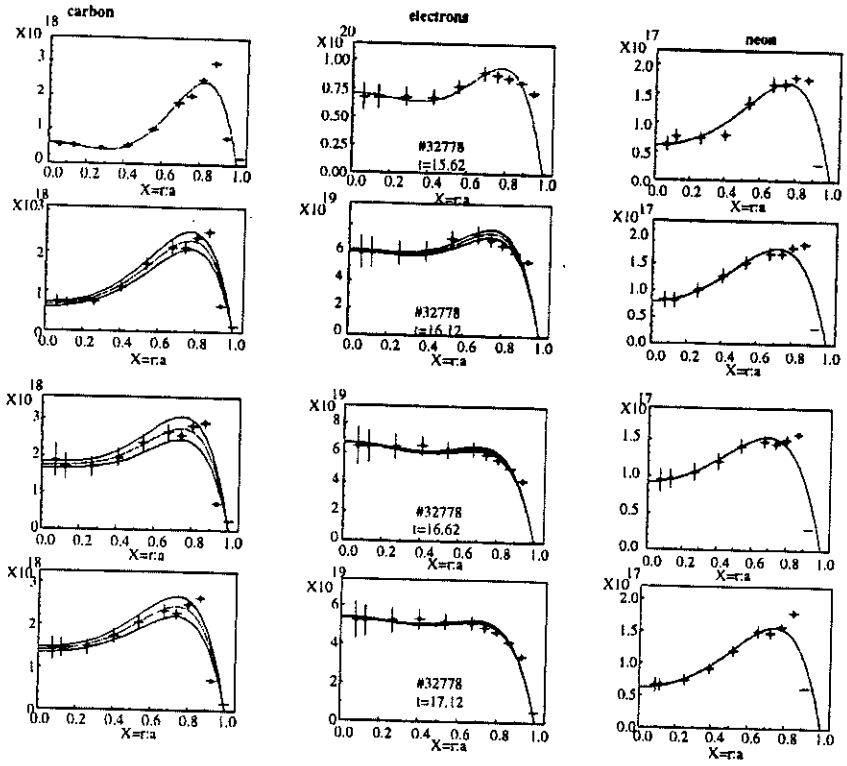

Fig. 8 Neon, carbon and electron density profiles measured by CXRS and LIDAR respectively in a H-mode Ne gas puff experiment.

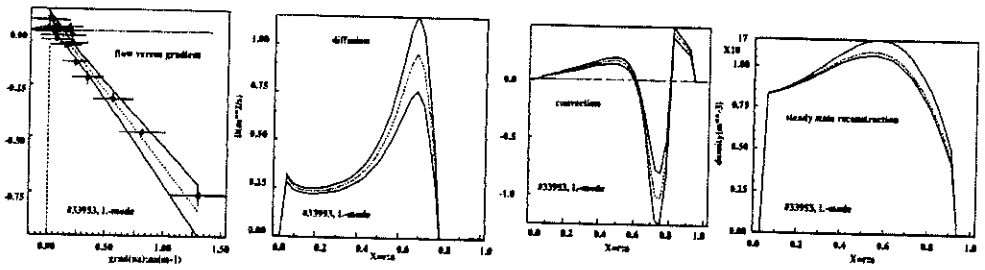

Fig.9 Deduction of neon transport data in L-mode confinement phase.

V. Beam fuelling experiments

A few experiments were performed comparing edge and core fuelling of helium making use of the two neutral beam boxes at JET one acting as a source of high energy neutral helium and the second as diagnostic beam. The wave form of the two beam banks was selected to provide approximately constant input power to the plasma. Similar as in the edge fuelling case one CX instrument was dedicated to the measurement of CVI ion temperature profiles and the second to the simultaneous measurement of the fuelled impurity (helium) and intrinsic impurity (beryllium). Two examples, representing H-mode and L-

mode, show characteristic profile forms and temporal evolution (5). In contrast to gas fuelling at the plasma edge, the particle sources for beam fuelling are well defined and established by numerous consistency checks. For example the total injected particle content can be verified by beam current data, and source rate profiles determine sensitively beam-thermal neutron rates which is independently measured.

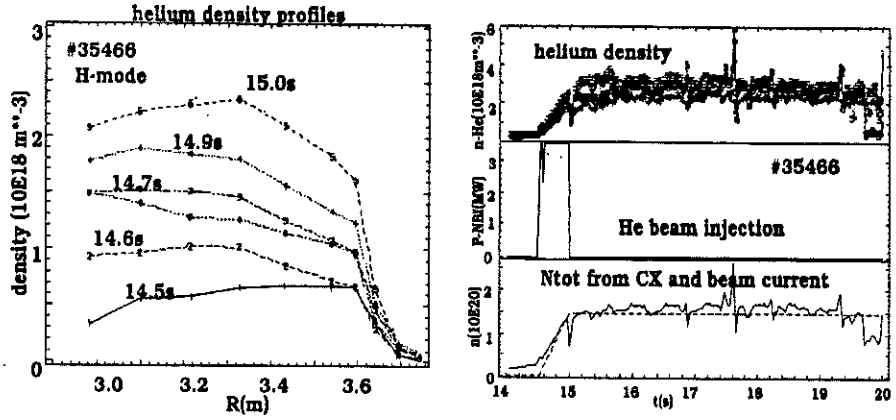

Fig.10 a) H-mode case, #35466, He-beam central fuelling (14.5s to 15.0s), profiles (1 to 7) shown every 0.1s. b) time traces of helium density, NBI power and particle content.

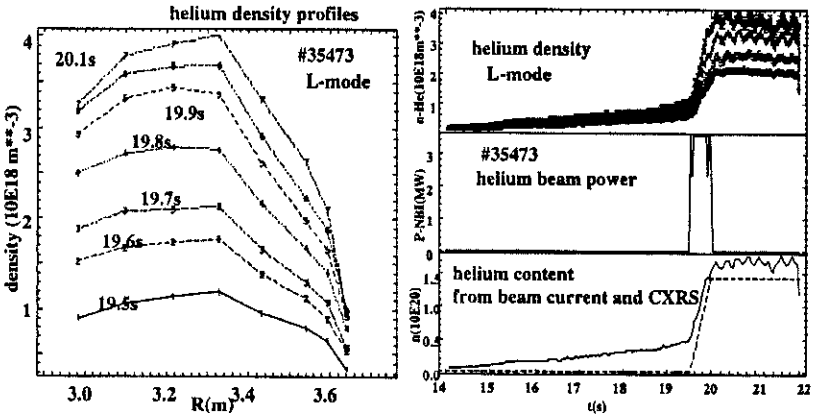

Fig.11 a) L-mode case, #35473 He-beam central fuelling (19.5s to 20.0s), profiles (1 to 7) shown every 0.1s. b) time traces of helium density, NBI power and particle content.

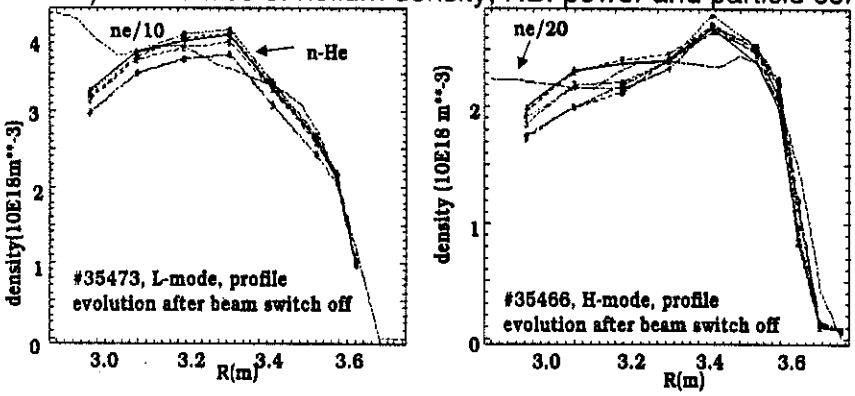

Fig. 12 Redistribution of profiles after switch-off of He-beams a) L-mode, time slices every 35ms starting at 20.1s, electron density profile (ne) divided by 10 for comparison b) H-mode, time slices every 35ms starting at 15.1s, electron density (ne) divided by 20.

A preliminary analysis of helium beam fuelling results shows that the re-distribution of helium is very fast and profiles similar to those of the electron-density are reached in H- and L-mode in less than 100msec, that is on a time scale which is comparable to the time corresponding fast particle reach steady state conditions.

Conclusion

Edge and central fuelling experiments were performed in the JET divertor phase. Active pumping was achieved by deposition of an argon frost layer on the divertor cryo-pumps. The present assessment of observed helium exhaust rates indicates that substantial work needs to be carried out to achieve acceptable values of τ_p^* which are tolerable for a burning fusion reactor. The observed replacement time of helium is of the same order or in excess of the NB pulse length and the results presented here need to be taken with a grain of caution.

Transport data deduced from experimental profiles of helium, neon and nitrogen seeded divertor plasma are currently evaluated.

Modelling the Neutralisation and Energy Distribution Function of MeV Ions during combined ICRF and NBI Heating in JET

A J Stuart, S C Dalla, L-G Eriksson, A Gondhalekar.
JET Joint Undertaking, Abingdon, Oxfordshire, OX14 3EA, UK.

1. INTRODUCTION:

Impurity Induced Neutralisation (IIN) of hydrogenic ions [1], introduced to model the flux of MeV energy atoms emitted by JET plasmas during hydrogen minority ion cyclotron resonance frequency heating of deuterium plasmas (D(H) ICRF heating), is applied to analyse combined D(H) ICRF and deuterium neutral beam injection (NBI) heating in JET. During high power D(H) ICRF heating, when 80-140 keV NBI was applied, simultaneously (i) the ICRF driven proton tail temperature T_p was observed to decrease slowly, (ii) a reduction in the proton density n_p in the tail took place, and (iii) a deuteron distribution was created with energy $0.25 \leq E(MeV) \leq 1.1$ during NBI heating. These measurements suggest the inference that during NBI the RF power available for fundamental frequency heating of proton minority decreases, that a share of the ICRF power goes to second harmonic heating of the high energy deuteron species, and that the share of the power to beam deuterons is enhanced by depletion of protons relative to deuterons in the plasma centre.

We test this hypothesis by applying IIN modelling and modelling of hydrogen minority ICRF heating to the measurements. To this end we present (i) measurements of hydrogen and deuterium fluxes, using a high energy neutral particle analyser (NPA), showing the behaviour mentioned above, (ii) an outline of the IIN model and a tabulation showing its application to the above data in order to deduce the energy distribution function f(E) of the ICRF driven protons and deuterons, (iii) modelling of the Stix energy distribution function $f_s(E)$ for the experimental conditions with the aim to test the conjecture that n_H / n_D decreases during NBI.

2. EXPERIMENTAL SETUP AND MEASUREMENT OF EVOLUTION OF HYDROGEN FLUX :

Measurements were made with the NPA located at the top of the torus with its vertical line-of-sight intersecting the ICRF resonance and the oct.4 NB at the plasma centre. The measured

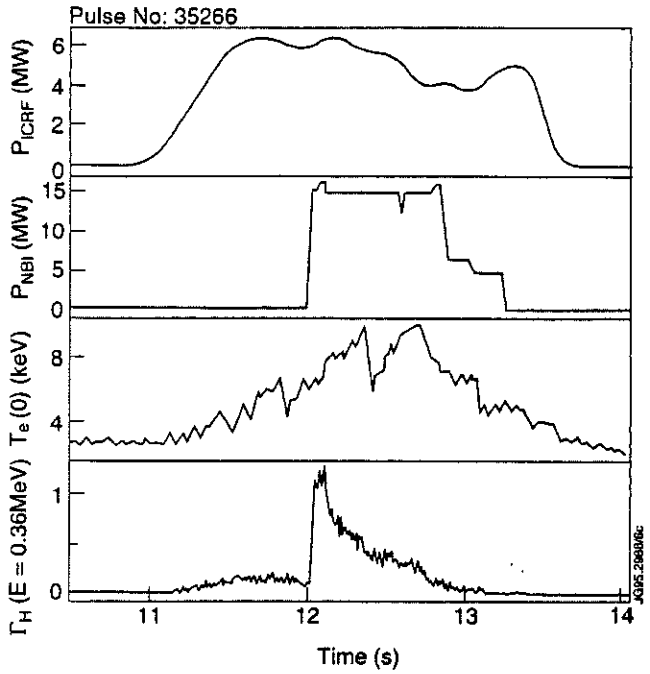

Fig.1: Deuterium plasma with B_ϕ =3.2T, I_ϕ =4.7MA, n_e (0)=3-6x10^{19} m^{-3} , and Z_{eff}≈2. RF power at f=51.4 MHz, in dipole antenna configuration, was applied for D(H) ICRF heating at the plasma centre. NBI deuterium was applied at 80keV in oct.4 and at 140keV in oct.8. The last trace shows evolution of 0.36 MeV hydrogen flux received by the NPA from the plasma.

hydrogen flux Γ_H(E) is due to neutralisation of ICRF driven protons with v_z / $v_\phi \geq 2x10^2$, their banana tips lying on the line-of-sight and within the ICRF power deposition region. Thus Γ_H(E) and inferred f_p(E) are representative of the plasma core region. Fig.1 shows evolution of ICRF and NBI powers, T_e(0) and Γ_H(E) in one NPA channel. As expected, Γ_H(E) arises with application of ICRF and is amplified due to increased electron donor density when NBI is applied at t=12s. However Γ_H(E) decays to zero at t=13s whilst ICRF and NBI are still applied. Fig.2 shows that such evolution of Γ_H(E) occurs at all energies. We show in the following that this is due to a combination of reduced plasma transparency for the exiting high energy hydrogen atoms and reduced n_H/n_D due to NBI induced dilution and/or transport. Fig.3 shows deuterium flux, Γ_D(E), demonstrating that when NBI is applied, ICRF power is channelled to second harmonic heating of high energy beam deuterons.

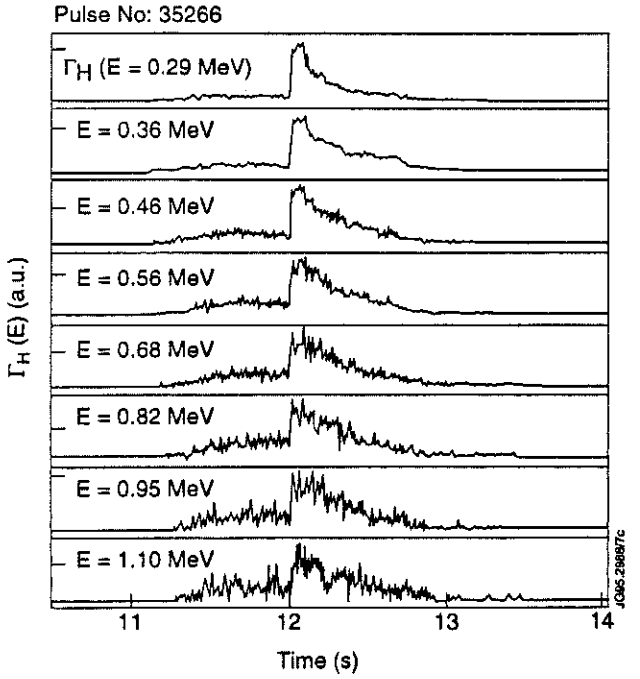

Fig.2: Hydrogen flux Γ_H(E) received in the eight channels of the NPA spanning 0.29≤E(MeV)≤1.1. The increase at t=12 s is due to NBI raising the number density of electron donors which are either [H] ions or the beam atoms themselves.

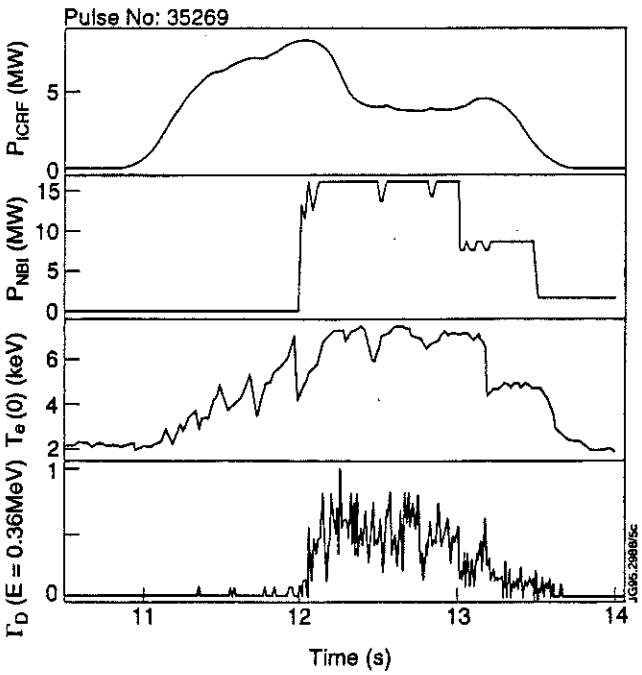

Fig.3: Evolution of deuterium flux Γ_D(E) at E=0.36 MeV during combined ICRF and NBI heating. Notice that Γ_D(E) arises only when NBI is applied. Low energy thermal deuterons are unaffected by the ICRF; only beam deuterons are heated.

3.DEDUCTION OF $f_p(E)$ FROM MEASURED FLUX, $\Gamma_H(E)$, USING IIN MODELLING:

Agents for neutralisation of MeV energy protons are hydrogen-like [H] ions of the main impurities in JET plasmas, carbon and beryllium[1]. Populations of such [H] ions are sustained by charge exchange with deuterium atoms present in the plasma due to recycling, NBI, and NB halo. When the NPA line-of-sight intersects a NB contributions due to direct CX with beam and halo atoms also arise. Then,

$$f_p(E) = \Gamma_H(E) / \{ P_v(E) \times \varepsilon(E) \} \quad \text{where}$$

$$P_v(E) = \langle \sigma v \rangle^d_{cx} n_d + \langle \sigma v \rangle^b_{cx} n_b + \langle \sigma v \rangle^h_{cx} n_h + \Sigma \langle \sigma v \rangle^q_{cx} n_q + \langle \sigma v \rangle_r n_e$$

$\varepsilon(E)$ is plasma transparency for the exiting high energy hydrogen atoms and $P_v(E)$ is the total proton neutralisation rate. $P_v(E)$ is the sum of rates due to: charge exchange with thermal deuterium atoms, beam atoms, halo atoms, different species of [H] impurity ions q; and recombination respectively. Densities n_q for C^{5+} and Be^{3+} are computed in a steady state, infinite, homogeneous plasma with characteristic parameters of the plasma centre using measured densities of C^{6+} and Be^{4+} and using a statistical balance formalism for ionisation equilibrium between impurity nuclei and [H] ions. Only collisions with electrons and neutral deuterium are considered; minority species are assumed to have no effect on the ionisation balance. Hydrogenic impurity ions created in octant 8, 9m away around the torus, may migrate to octant 4 and, in a similar way, those created in octant 4 by cx from NBI may leave the region viewed by the NPA: we denote the corresponding coupling coefficients by γ_8 γ_4.

An investigation has been performed using a collisional-radiative model [2] modified to include the effects of electron transfer from ground state deuterium atoms ($D^0(1s)$) to carbon nuclei in order to determine the relative density of excited states of C^{5+} with respect to their ground state. The 2s metastable state has a relative density of $2\text{-}7 \times 10^{-5}$, the remainder having much lower densities. An estimated ratio of the cross-section for electron transfer from 2s compared with 1s of 16 implies that the contribution to the flux from excited states is at most 0.2%.

The background thermal deuterium atom density n_d is the only free parameter in this model. It is deduced by matching $f_p(E)$ at two close time points either side of a controlled increase of neutral density by NBI, and assuming that $f_p(E)$ does not change during this time. In #35266 the best fit between the two deduced distribution functions is given by $n_d = 10^{12}$ m^{-3}.

Table I shows details of calculation of $P_v(E)$ and $\varepsilon(E)$ at E=0.36 MeV at four different time points in the pulse shown in fig.1. From such calculations the energy distribution functions for protons shown in fig.4 and for deuterons shown in fig.5 are constructed.

Table I:

Central plasma parameters:	t=11.9s	t=12.15s	t=12.5s	t=12.8s
electron density, $n_e(0)$ [10^{19} m^{-3}]	2.8	3.0	3.9	6.3
electron temperature, $T_e(0)$[keV]	5.5	7.8	8.7	7.8
average plasma ion charge, Z_{eff}	1.8	1.7	2.2	2.0
best fitted thermal deuterium density n_d (0) (m^{-3})	10^{12}	10^{12}	10^{12}	10^{12}
neutral density from octant 4 NBI at 80 kV:				
full energy component, n_b (10^{13} m^{-3})	0	18	9.5	1.4
half energy component, n_b (10^{13} m^{-3})	0	3.8	1.8	0.17
one third energy component, n_b (10^{12} m^{-3})	0	8.8	2.6	0.04
neutral density from octant 8 NBI at 140 kV:				
full energy component, n_b (10^{13} m^{-3})	0	6.5	3.9	0.95
half energy component, n_b (10^{13} m^{-3})	0	3.1	0.94	0.28
one third energy component, n_b (10^{12} m^{-3})	0	6.1	3.6	1.4
density of beryllium nuclei n_{Be} (10^{17} m^{-3})	5.4	5.2	12.	14.
coupling coefficient from octant 4 NBI: γ_4	n/a	0.037	0.038	0.045
coupling coefficient from octant 8 NBI: γ_8	n/a	0.026	0.026	0.025
density of hydrogen-like beryllium n_{Be} (10^{13} m^{-3})	3.1	16.	21.	5.7
density of carbon nuclei n_C (10^{17} m^{-3})	5.4	5.2	12.	14.
coupling coefficient from octant 4 NBI: γ_4	n/a	0.030	0.031	0.033
coupling coefficient from octant 8 NBI: γ_8	n/a	0.026	0.026	0.026
density of hydrogen-like carbon n_C (10^{14} m^{-3})	2.0	8.8	12.	3.7
P_v - neutralisation rate per 0.36 MeV proton (s^{-1})				
due to recombination with free electrons (10^{-4} s^{-1})	6.0	4.1	5.0	7.6
due to cx with [H] beryllium ions (10^{-3} s^{-1})	4.0	20.	27.	7.4
due to cx with [H] carbon ions (10^{-3} s^{-1})	2.5	11.	15.	4.6
due to cx with deuterium atoms (10^{-4} s^{-1})	0.41	94.	48.	1.7
Total P_v (10^{-3} s^{-1})	7.1	41.	48.	13.
ε - escape probability for 0.36 MeV hydrogen atoms	0.47	0.43	0.26	0.18
measured Γ_H(E=0.36 MeV) (10^{11} $m^{-2}keV^{-1}st^{-1}s^{-1}$)	1.1	5.5	2.5	0.61
deduced f_p(E=0.36MeV) (10^{13} $m^{-2}keV^{-1}st^{-1}$)	3.3	3.1	2.0	2.6

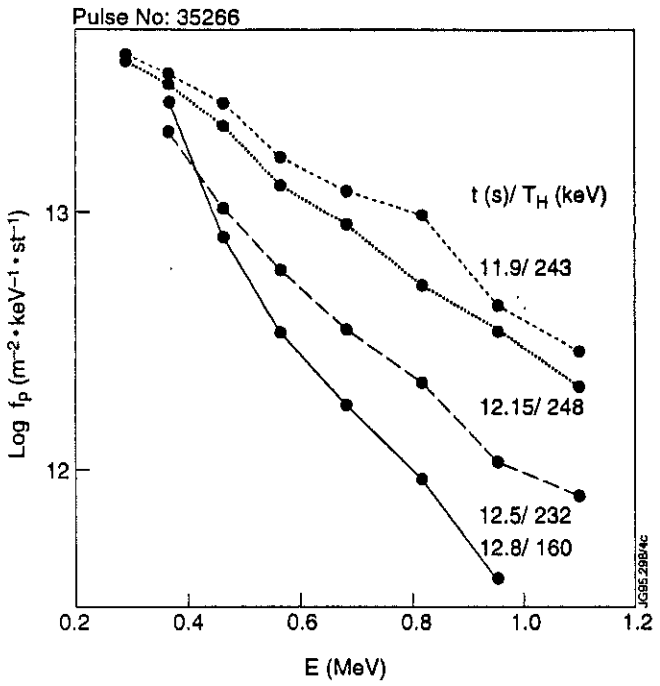

Fig.4: Deduced experimental ICRF driven proton energy distribution function $f_p(E)$, integrated along the NPA line-of-sight, at four time points t= 11.9s, 12.15s, 12.5s, and 12.85s. $f_p(E)$ at t=12.15s has been matched to that at 11.9s by adjusting the thermal deuterium density in the plasma: n_d = 10^{12} m^{-3} was determined this way. It is assumed that between 11.9s and 12.15s the proton distribution in the plasma does not change. Notice that until 12.5s the tail temperature of the distribution function remains nearly constant and thereafter reduces slowly. The hydrogen minority density in the tail above 0.3 MeV continuously decreases.

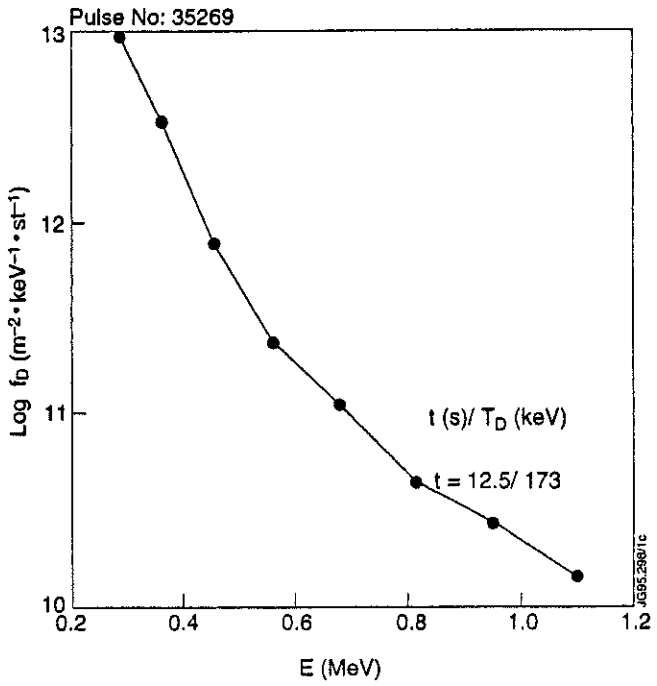

Fig.5: Experimental energy distribution function of second harmonic ICRF driven deuterons, $f_D(E)$. This is deduced by the method shown in section 3. $f_D(E)$ is averaged over the period 12.0≤t(s)≤12.5.

4. MODELLING OF ENERGY DISTRIBUTION FUNCTION OF THE ICRF DRIVEN PROTONS USING STIX'S APPROXIMATE ANALYTICAL THEORY:

The energy distribution function was modelled for the experimental conditions using the Stix theory [3] which calculates a flux surface and pitch angle averaged distribution $f_s(E)$ in the zero-banana-width approximation. $f_s(E)$ was calculated on several flux surfaces and an integral along the NPA line-of-sight constructed, corresponding to the measurements. This procedure was carried out at several time points close to those of the measurements shown in fig.4. The ICRF power deposition profile $P_H(r)$ required as input for the Stix calculation was computed using the PION-T code [4] in which the effect of NBI was simulated by rapidly increasing the deuteron majority temperature from measured $T_i \approx 4$ keV before NBI to 30keV during NB heating. This caused reduction of ICRF power available for hydrogen minority heating due to increased absorption at second harmonic of deuteron ion cyclotron frequency. Using $P_H(r)$ computed with constant $n_H / n_D = 0.1$ during the heating the modelled $f_s(E)$ gave tail temperatures strongly

decreasing with time. This behaviour, shown in fig.6, is contrary to the measurement which shows nearly constant T_p until 12.5s and then a slow decline. A better correspondence of modelled $f_s(E)$ with measurements was obtained when n_H/n_D was allowed to linearly decline from 0.1 to 0.03 during $12 \leq t(s) \leq 13$. This result in corroboration of the notion of declining n_H/n_D is only of qualitative value because: (i) while the NPA measures $f_p(E)$ for ions in a narrow pitch-angle range around $\pi/2$, $f_s(E)$ is pitch-angle averaged, (ii) the Stix model is valid in steady-state while the experimental conditions are transient with $P_H(r)$ varying on a time-scale shorter than the slowing-down time of the measured ions. These weaknesses may be overcome by using the time-dependent PION-T code in which the Fokker-Planck equation is solved without using the approximations of Stix.

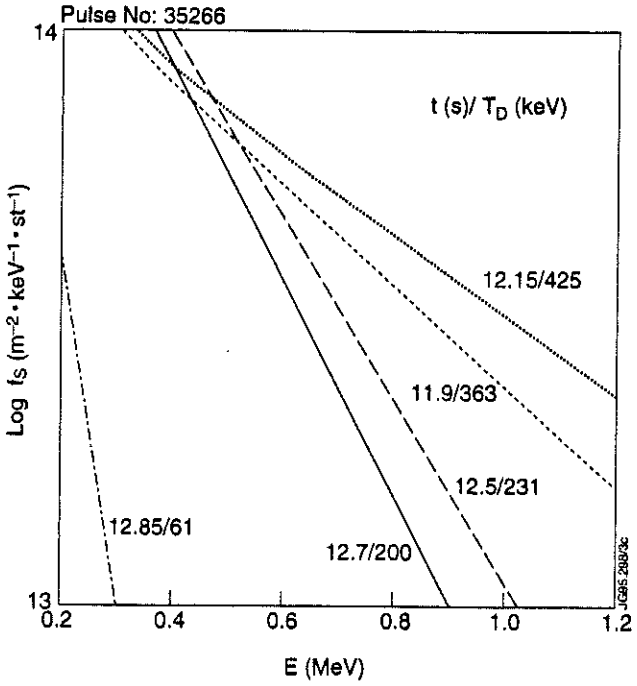

Fig.6: Result of simulation using Stix's model. The required input of radial profile of ICRF heating power density available to hydrogen minority, $P_H(r)$, was computed using the PION-T code with n_H/n_D = 0.1. The resulting Stix distribution $f_s(E)$ shows rapidly declining tail temperature, in disagreement with the measurement shown in figure 4.

5. SUMMARY:

1. The Impurity Induced Neutralisation model has been used to deduce the energy distribution function of ICRF driven protons and deuterons during combined ICRF and NBI heating.
2. Thermal deuterium density in the plasma centre of 10^{12} m^{-3} is determined with estimated uncertainty a factor of three.
3. Sharing of applied ICRF power between proton minority and NB injected high energy deuterons is observed.
4. In order to model the measured evolution of proton tail temperature during NBI it is necessary to invoke steady reduction in n_H / n_D due to beam induced dilution and/or transport.

ACKNOWLEDGEMENTS:

We would like to thank J. de Haas and D. Muir for providing electron density data.

REFERENCES:

[1] A.Korotkov and A.Gondhalekar, Europhysics Conference Abstracts 18B(1994)pt. I - 266

[2] N. N. Ljepojevic, *et al.*, J.Phys B., 17(1984)3057

[3] T. H. Stix, Nuclear Fusion 15(1975)737.

[4] L.-G. Eriksson, *et al.*, Nuclear Fusion 33(1993)1037

Runaway Electron Diffusion Measurements in the JET Tokamak

B Esposito[1], R Martin-Solis[2], P van Belle, O N Jarvis, F B Marcus, G Sadler, B Fischer, P Froissard, J M Adams[3], E Cecil[4], N Watkins[3].

JET Joint Undertaking, Abingdon, Oxfordshire, OX14 3EA, UK.

[1] Associazione Euratom-ENEA CRE, 00044-Frascati, Italy.

[2] Universidad Carlos III de Madrid, C/Butarque 15, Leganes, 28911-Madrid, Spain.

[3] AEA Technology, Harwell, Oxfordshire, Ox11 0RA, UK.

[4] Colorado School of Mines, Golden CO 80401, USA.

ABSTRACT

Runaway electrons up to few MeV energy have been detected in the plasma current ramp-up of JET low density ohmic discharges, by measuring the emitted perpendicular hard X-ray bremsstrahlung radiation.

A diffusion model, simulating the temporal evolution of the line integrated hard X-ray signals, has been used to obtain the runaway radial transport coefficient in the central region of the plasma ($r/a<0.5$): $D_r \sim 0.2$ m^2/s.

The data allow a lower limit to be set on the level of radial magnetic field fluctuations in the plasma core.

INTRODUCTION

The diffusion of runaway electrons in tokamak plasmas provides useful information for understanding the mechanisms involved in anomalous particle transport.

Both electrostatic and magnetic turbulence theories have been considered in order to explain the anomalous transport; runaway electrons are particularly suited to testing magnetic turbulence as they closely follow the magnetic field lines.

So far, the runaway diffusion coefficient has been measured in several tokamaks by using different methods and typical values are in the range $D_r = 0.05\text{-}1$ m^2/s (see [1] for a review).

The runaway electron measurements described in this paper have been performed during the start up phase of JET ohmic discharges in the 1994 campaign.
The discharge parameters were: n_e ~ 0.5-1.5 x 10^{19} m^{-3}, I_p=1-1.6 MA and B_t~2.75 T.
Three sets of instruments have simultaneously detected the X-ray bremsstrahlung emission (perpendicular to the magnetic field) of runaway electrons:

- the collimated fast electron bremsstrahlung (FEB) monitor, with 10 horizontal and 9 vertical channels [2], sensitive to X-rays in four energy windows from 133 keV to 400 keV (such cameras replace the neutron detection cameras in the neutron profile monitor when LHCD studies are in progress);
- the X-ray spectrometer, having a vertical central line of sight;
- the hard X-ray monitor scintillators, viewing at the plasma on the equatorial plane.

Both the spectrometer and the scintillators are sensitive to photons above 200 keV.

EXPERIMENTAL DATA

A typical time trace of the line integrated X-ray emission ("photon brightness") from the FEB central vertical detector (channel 15, energy window = 133-200 keV), is shown in Fig.1 for shot 29586, together with the LIDAR electron density, the plasma current, the loop voltage, the hard X-ray and neutron emission.

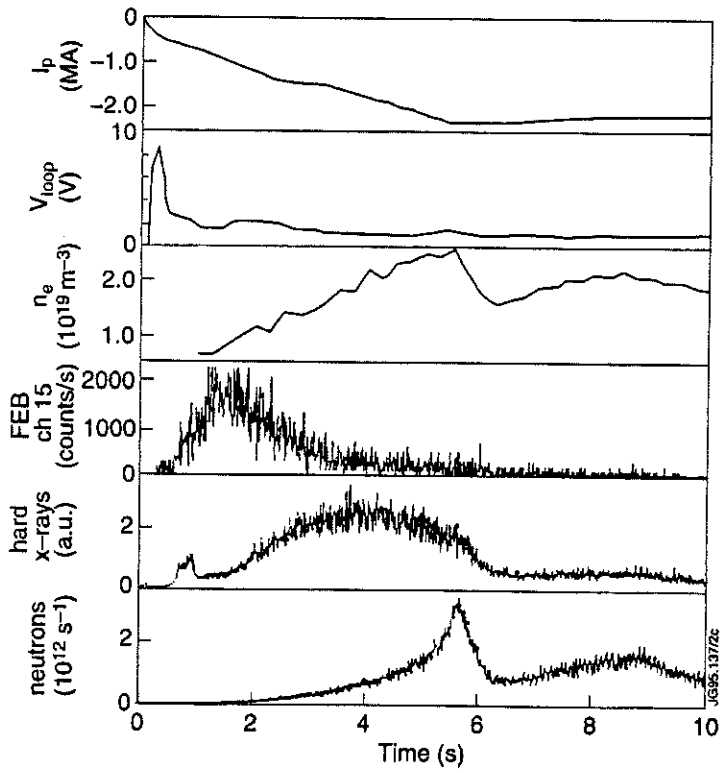

Fig.1: Time traces of plasma current, loop voltage, LIDAR electron density, FEB channel 15, hard X-rays and neutrons (discharge 29586).

The signal starts at t ~ 0.2 s after the beginning of the discharge, it increases up to a maximum at t_{peak}~1 s (t_{peak}=time of maximum signal in the central chord) and then it decays to almost zero level at t~4 s.

The same behaviour is shown by the X-ray spectrometer, whose spectra also indicate an average electron energy of roughly 2 MeV (Fig. 2).

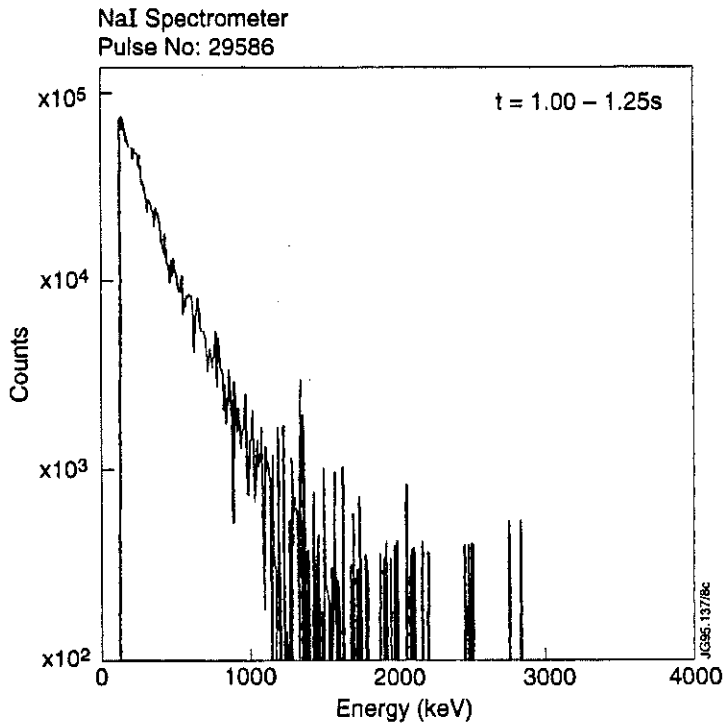

Fig.2: Bremsstrahlung spectrum measured by X-ray spectrometer at t_{peak}.

The most interesting feature of the FEB data is the different time evolution of the line integrated signals in different chords (see Fig.5).

The maximum in the measured X-ray emission is reached progressively at later times in the edge chords than in the central ones.

The effect is present on both cameras and is symmetric with respect to the plasma magnetic axis (vertical camera) and the z=0 cm plane (horizontal camera).

The brightness data are converted to the local X-ray emissivity through a 1-D inversion algorithm.

The code (ORION) uses a minimisation procedure which fits a trial FEB emissivity radial profile.

It is found that the emissivity radial profiles, initially peaked, tend to flatten with time (Fig. 3).

The local X-ray emissivity dI/dVdtdh (in W/m^3keV) can be expressed by the approximate relation:

$$\frac{dI}{dVdtdh\nu} = Cn_e n_r Z_{eff} \exp(-\frac{h\nu}{T_{ph}}) \quad (1)$$

where h is the photon energy, n_r the runaway electron density, Z_{eff} the effective ion charge and C a constant.

T_{ph} is the "photon temperature", a parameter related to the energy distribution function of the electrons and also depending on the photon energy interval in which is evaluated [3].

T_{ph}, as obtained both from FEB and X-ray spectrometer data, shows an initial increase, but after t_{peak} it remains constant at ~160 keV (Fig.4).

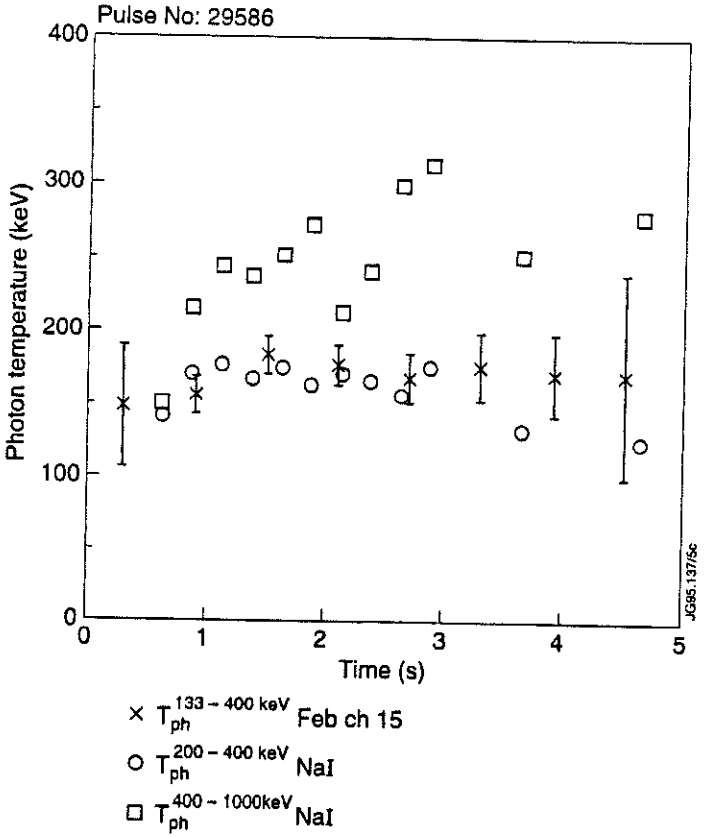

Fig.3: Photon temperature vs time.

The values of the toroidal electric field, responsible for the electron acceleration, obtained from the experimental V_{loop} are in accordance with those calculated by means of the transport code JETTO: from initial values at the edge of the plasma of ~0.25 V/m, E_t decreases to 0.04 V/m at t_{peak} (the Dreicer field at this time is: E_D~1V/m); E_t at the centre is a factor of 2 lower. The main production and acceleration of runaways takes place in the interval 0.2-1.0 s, as is also indicated by the rise of T_{ph}.

These results suggest the following picture: a beam of fast electrons may be produced in the plasma central region during the initial low density (~10^{19} m^{-3}) phase of a JET ohmic discharge.

The electrons are accelerated by the electric field above the critical energy and enter the runaway regime.

As the runaway production stops (at t_{peak} when V_{loop} < 1.5 V), the radial X-ray emission profile broadens, indicating an outward diffusion of the electrons which finally hit the vessel walls (note the peaking in the signal of the X-ray monitors at t ~ 5 s in Fig.1).

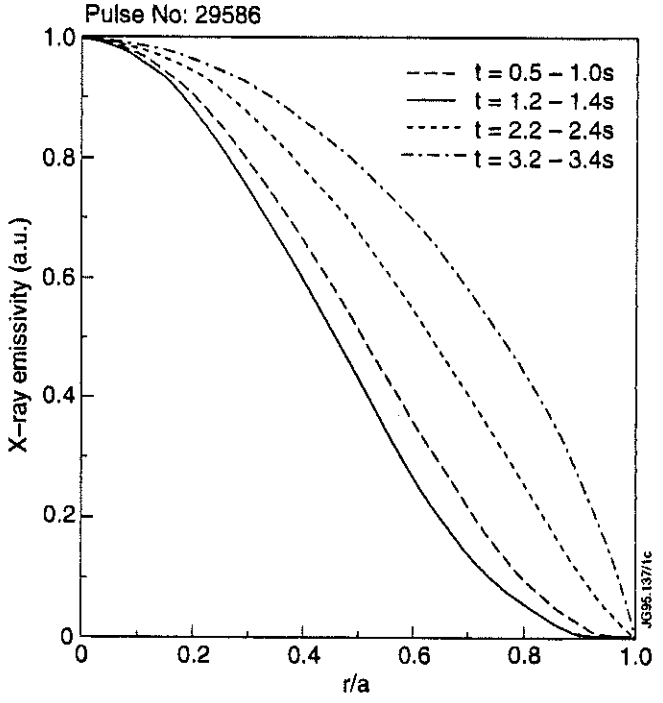

Fig.4: Time sequence of normalized inverted FEB emissivity profiles.

DIFFUSION MODEL

A diffusion model in cylindrical geometry has been used to simulate the time evolution of the X-ray bremsstrahlung brightness.

The equation governing the process is the following:

$$\frac{\partial n_r(r,t)}{\partial t} = \frac{1}{r}\frac{\partial}{\partial r}(rD_r(r)\frac{\partial n_r(r,t)}{\partial r}) + S_r \qquad (2)$$

The simulation starts at t_{peak} and the subsequent electron dynamics has been assumed to be only determined by diffusion.

Moreover, as the runaway production strongly decreases after t_{peak}, the source term S_r has been set equal to zero.

The critical energy is increasing after t_{peak}, therefore a low energy fraction of the fast electron distribution is progressively slowed down and no longer contributes to the X-ray emission. As this collisional slowing down effect is neglected in the model (i.e. the observed decay of the FEB signal is assumed to be due to diffusion only), the determination of the diffusion coefficient using eq. (2) is an upper limit .

The code uses the time traces of Z_{eff} and n_e to calculate, for each FEB line of sight, the photon brightness to be compared with the experimental one.

The initial n_r used in eq. (2) has been determined by means of eq. (1). The Z_{eff} (whose radial profile is assumed constant with radius) has been taken from the visual bremsstrahlung diagnostics and the n_e from LIDAR.

The analysis has been restricted to $r/a < 0.5$, where T_{ph} is almost flat and constant in time (the exponential factor in eq. (1) can be set equal to a constant).

At the edge, where E_t is higher, we should have an increased electron acceleration which, in turn, should produce higher X-ray emission and T_{ph}; however, this effect on T_{ph} is not apparent due to the large error bars.

The diffusion equation has been solved using a flat D_r.

The best agreement between the predicted and experimental photon brightness is found with D_r ~ 0.2 m^2/s (fig.5), for discharge 29586.

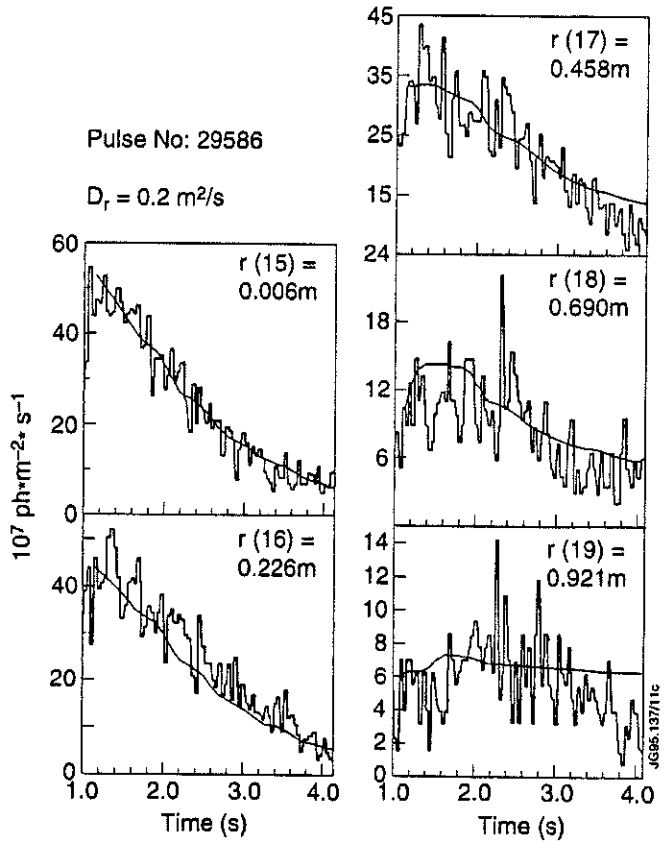

Fig. 5: Comparison between measured and simulated (smooth curves) time traces of photon brightness for FEB channels no. 15, 16, 17, 18, 19 in discharge 29586: D_r=0.2 m^2/s is used.

Depending on the discharge, D_r can vary in the range 0.14-0.21 m^2/s.

This diffusion coefficient refers to electrons having energies in the range 0.2-2 MeV and is consistent with results from other tokamaks [1].

DISCUSSION

The determined radial transport coefficient D_r can be used to set a limit on the level of fluctuating radial magnetic field (b_r) in the plasma core.

Using the relation [4] $D_r \sim qRu(b_r/B_t)^2$, in which q is the safety factor, R the major radius and u the electron velocity, it is found that $(b_r/B_t) \sim 6*10^{-6}$ (discharge 29586).

This is only true if the runaway electron diffusion is due to magnetic turbulence.

Under such an assumption, it also follows that magnetic turbulence cannot be the main cause of thermal electron transport in the plasma centre, as (with χ_e evaluated for discharge 29586 by means of power balance calculations) we get $D_r/\chi_e = 0.07\text{-}1$, while the theory predicts a much lower χ_e (according to [5] we should have $D_r/\chi_e \sim u/v_{\|th} \sim 13$).

On the other hand, electrostatic turbulence might reconcile both thermal and runaway experimental diffusion coefficients: the predicted ratio of D_r to χ_e (given in this case by $D_r/\chi_e \sim v_{\|th}/u$) is marginally consistent with the measured value, but at the same time a high value of the electric field fluctuation is needed: ~5 kV/m.

REFERENCES

[1] A.J. Wootton, FRCR #437, University of Texas (1993)
[2] P. Froissard, PhD Thesis, Universite de Provence Aix-Marseille I (1992)
[3] S.von Goeler et al., *Rev. Sci. Instrum.*, **57** (8), 2130 (1986)
[4] J.R. Myra et al., *Phys. Fluids* B **4**(7), 2092 (1992)
[5] H.E.Mynick and J.D.Strachan, *Phys. Fluids* **24(**4), 695 (1981)

Evolution and Optimisation of Neutron Emissivity Profiles in JET

F B Marcus, J M Adams[1], D S Bond[1], M A Hone, O N Jarvis, T T C Jones, R König, M J Loughlin, M F F Nave[2], G Sadler, B Schunke, P Smeulders, N Watkins[1].

JET Joint Undertaking, Abingdon, Oxfordshire, OX14 3EA, UK.

[1] AEA Technology, Harwell, Oxfordshire, UK.

[2] Associação Euratom/IST, Lisbon, Portugal.

OVERVIEW SUMMARY

The main goals of the JET program include maximising d-d (and d-t) neutron production and fusion Q. Several operational parameters are involved in this optimisation (subject to technical constraints).

- neutral beam trajectory, beam energy and power, beam particle current (16 PINIs);
- plasma axis height and MHD equilibrium (imposed by limiter and divertor shapes);
- plasma particle density & profile (subject to beam deposition, gas puffing, recycling);
- beam power step down (related to energy confinement).

The JET neutron profile monitor (Fig.1) is used to interpret the effects of these parameters, by measuring the spatial distribution of the neutron emission.

Extreme conditions are considered to highlight effects on neutron production. Topics considered are: beam deposition; plasma axis shift; the effect of density profiles.

Neutron production is examined in high performance plasmas, including those with power step down, to determine the sources and methods of optimisation.

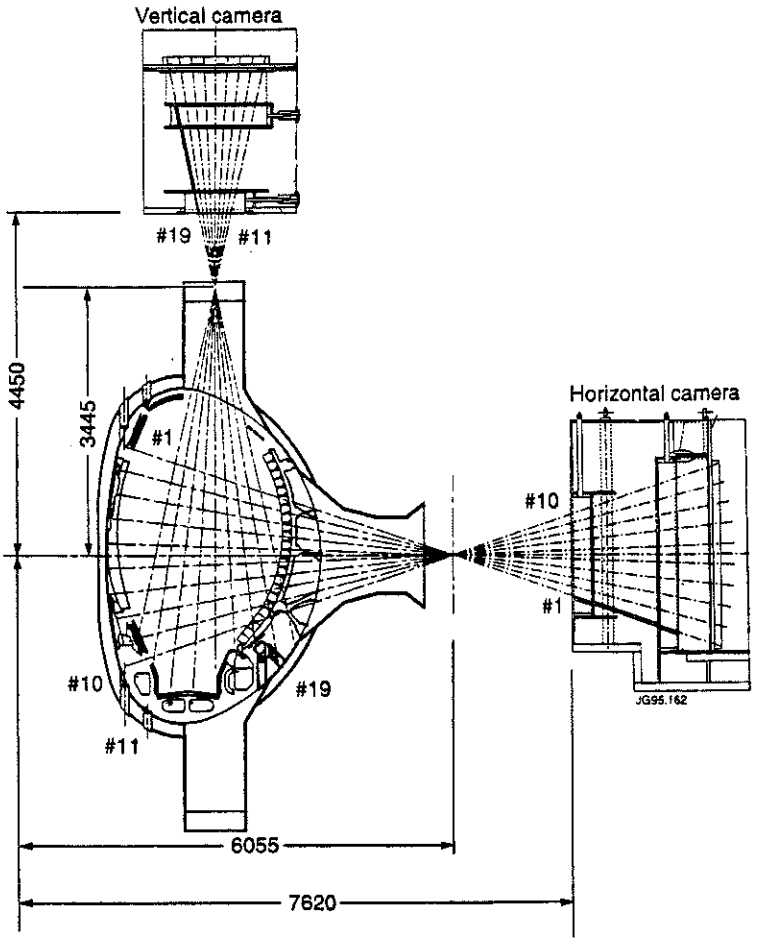

Fig.1: The viewing channels are shown of the JET Neutron Emission Profile Monitor - Upgrade Version, with channels 1-10 in the Horizontal Camera and 11-19 in the Vertical Camera. Channel separation is approximately 0.2 m in the plasma centre.

BEAM DEPOSITION

To investigate the extremes of beam trajectory, two plasma discharges were compared, both with the same MHD equilibrium, with the magnetic axis at 0.3 m above the machine mid-plane. Fig.2 shows the equilibrium at time 12.6 s, with the beam trajectories. The PINI identification numbers are shown at the beam path exits.

In #33398, PINIs #5, 6, 7 and 8 are used from both the 80 keV (plus #1 and #4) and 140 keV (plus #1) injector box, chosen preferentially **near** to the plasma axis.

In #33420, PINIs #2, 3, 4 and 5 are used from both the 80 keV (plus #1 and #8) and 140 keV (plus #7) injector box, chosen preferentially **far** from the plasma axis.

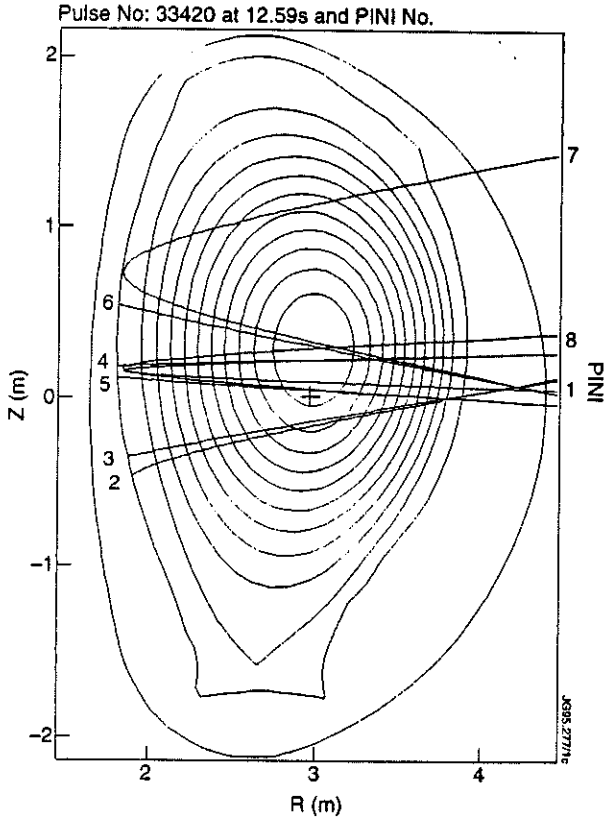

Fig.2.:MHD Equilibrium of #33420 at 12.59 sec in the JET Pumped Divertor Upgrade configuration. The Neutral Injector beam trajectory paths and PINI (Positive Ion Neutral Injector) numbers are shown.

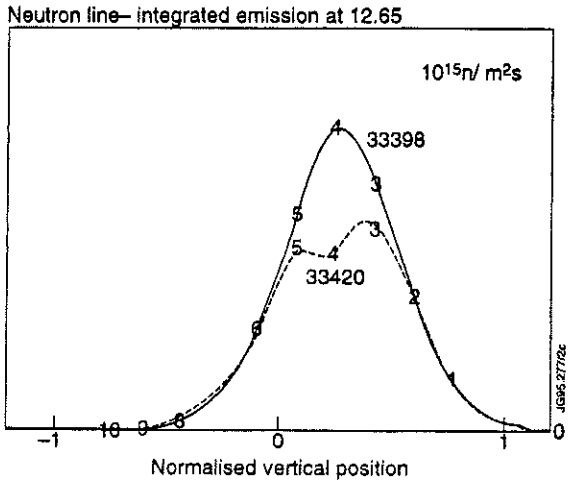

Fig.3: The line-integral neutron rates in channels 1-10, measured by the horizontal camera are shown at 12.6 s for #33398 and #33420, resulting from optimum on-axis and off-axis neutral beam trajectory. The vertical camera channels show a similar pattern of an intensity reduction and flattening in the central three channels in #33420.

The line-integral neutron rates measured by the horizontal camera at 12.6 s are shown for both discharges in Fig.3. The channels measuring off-axis neutron emission show similar rates, but the profile is slightly broader for #33420, and the chord passing through the axis measures 50% lower. The vertical camera channels show a similar pattern of an intensity reduction and flattening in the central three channels in #33420. Tomographic inversion of the data from both cameras shows that the axial neutron emissivity is a factor of two lower in #33420 with off axis injection.

However, the global properties of the two discharges, shown in Fig.4, are nearly identical in stored energy, slow roll-over behaviour, ELM-free period, and global neutron yield, with peak global rates of 1.92 compared to 1.71×10^{16} neutrons/sec in #33398 versus #33420. The conclusion is that performance is relatively insensitive to beam trajectory.

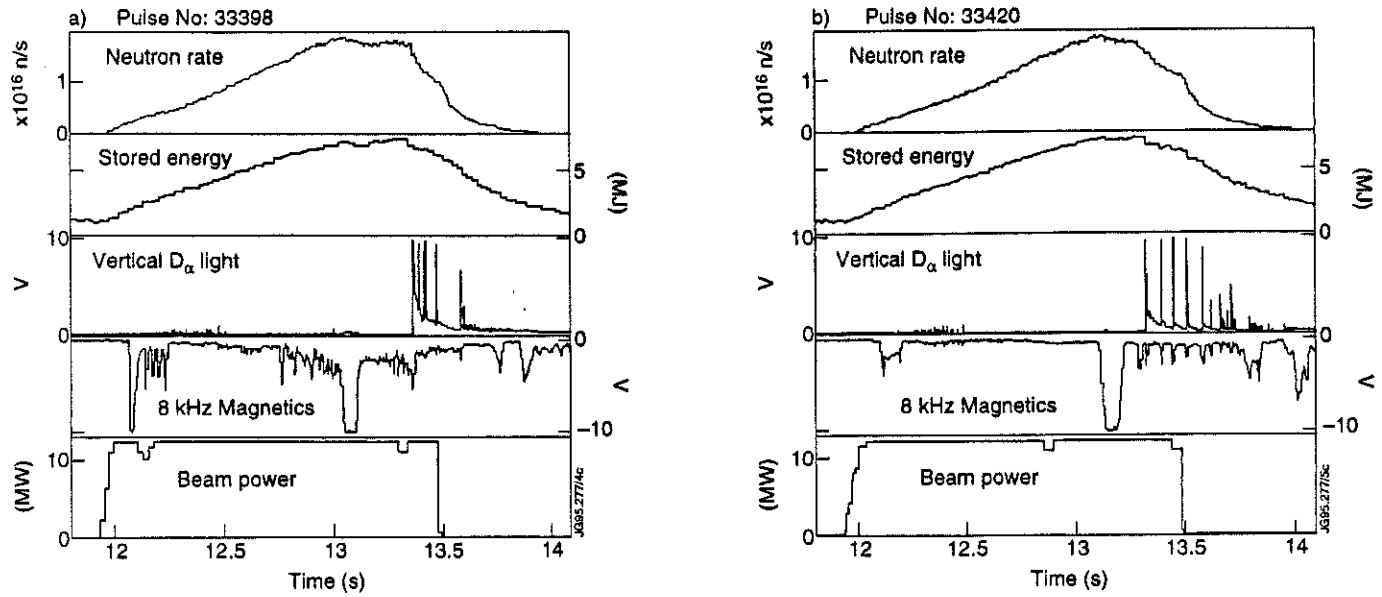

Fig.4: The neutron emission rate from fission chambers, stored energy from diamagnetic loop measurements, the D-alpha light measured along a vertical chord just outside the divertor, magnetic fields fluctuations measured by a coil at the boundary with an 8 kHz filter, and neutral beam injected power are displayed for (a) #33398 and (b) 33420. The global parameters are very similar.

PLASMA AXIS SHIFT

The magnetic axes of divertor plasmas are typically 0.3 m above the machine mid-plane, but were shifted vertically during an "axis-scan experiment" to investigate the effects on neutral beam deposition and neutron emissivity profiles.

The selection and trajectory of the 16 individual Positive ion Neutral Injector (PINI) beams was also altered.

For a fixed trajectory of the beams, the altered confinement and stability properties (particularly with regard to giant ELMs) of shifted plasmas (downwards from the typical position by 0.0-0.2 m) dominated over beam deposition changes. There was a 50% decrease in global neutron emission as the plasma axis was lowered, despite improved deposition, due to a shortened ELM-free period in the altered plasma configuration.

DENSITY PROFILES

Two 4 MA plasmas with similar MHD configuration and stored energy (~ 9 MJ), but with different electron density profiles were compared, #31893 and #32798.

In Fig.5, the electron density profiles for the two discharges are shown at times corresponding to 1 sec after the start of high power beam heating at 18.2 MW. Due to higher recycling level in #31893, the density is higher and hollow, compared to the peaked profile in #32798.

In Fig.6, the line integral neutron emissivities from the vertical camera are shown at 1 sec after beam heating begins. In #31893 with the hollow density profile, the emissivity profile FWHM of 1.1 m is much broader than in #32798, with 0.8 m, indicating that the beam is being preferentially trapped away from the plasma axis. Beam deposition calculations indicate that the high power 80 keV beams are being preferentially trapped at the plasma edge. The total emission rate in #31893 is lower (as is the peak line integral) at 1.4×10^{16}n/s compared to 2.3×10^{16}n/s.

In Fig.7, the contributions to the neutron rate calculated from CXRS measurements, their total, and the fission chamber measurements

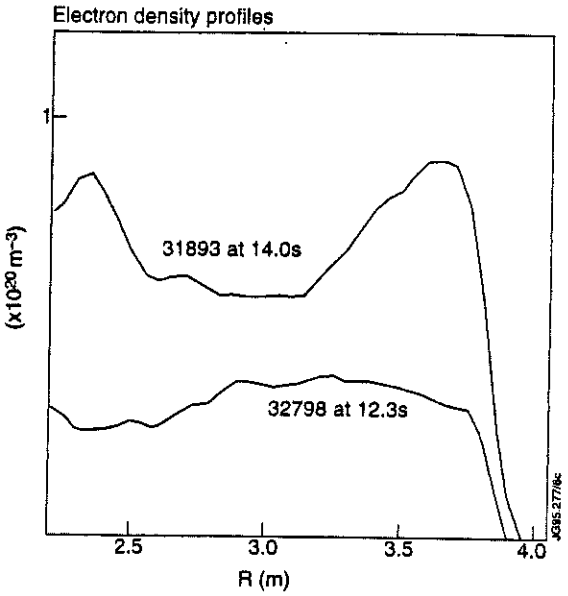

Fig.5: The electron density profiles for #31893 and #32798 are shown at 1 sec after the start of high power beam heating at 18.2 MW. Due to higher recycling level in #31893, the density is higher and hollow, compared to the peaked profile in #32798.

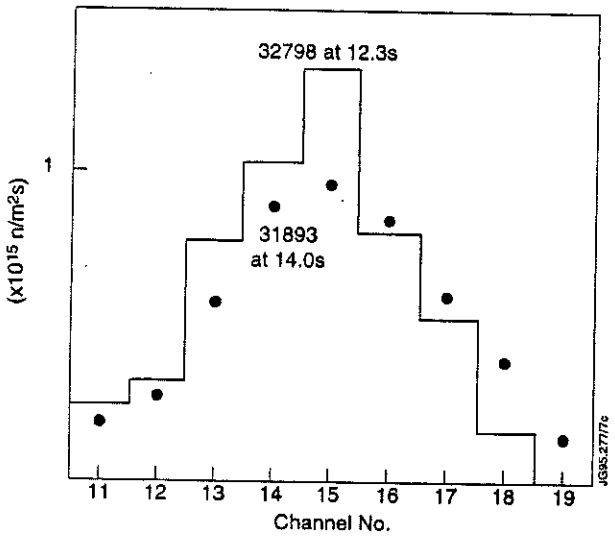

Fig.6: The line integral neutron emissivities from the vertical camera channels 11-19 are shown at 1 sec after beam heating begins. In #31893, with a hollow electron density profile, the emissivity profile FWHM (1.1 m) is much broader than in #32798 (0.8 m).

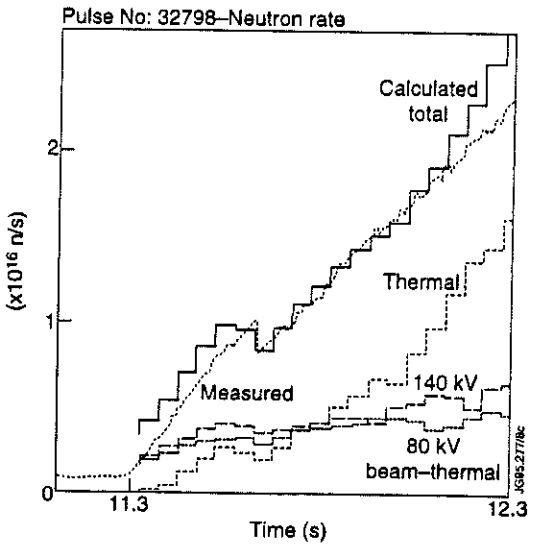

Fig.7: The contributions of 80 keV and 140 keV beam-thermal and thermal fusion to the neutron rate calculated from CXRS measurements, their total, and the fission chamber measurements are shown for #32798.

are shown for #32798. After 1.0 sec of beam heating, the beam-thermal (adding both beam contributions) neutron rate is comparable to the thermal rate. Similar proportions are found in #31893, but the CXRS measurements are less accurate near the plasma axis, since the beam penetration is reduced.

An important contribution to the reduction of neutron rate in #31893 is the strong beam trapping at the edge. Since the thermal emission is a feature of the plasma core, the beam ions deposited near the edge do not contribute, raising the axial ion temperature. Additionally, beam ions trapped near the edge in a region where the electron temperature is 1-2 keV

contribute a much lower beam-thermal neutron emission per ion than those trapped near the axis.

Furthermore, the initial rate of rise in #31893 of the neutron emission rate is about half that in #32798. Modelling of the initial rate of rise of the neutron yield in #31893 indicates an initial deuterium fraction n_d/n_e of 0.5, contributing to a reduced rate of neutron production despite beam fuelling with pure deuterium. Contamination is more deleterious at high plasma target density, since the fraction of contamination compared to beam deposited deuterium is higher than with low initial density.

HIGH PERFORMANCE PLASMAS

Recently, discharges in JET have produced global neutron rates exceeding those of previous years, for example 4.8×10^{16}n/s in #33643, a High Flux Expansion 4 MA plasma with 18.5 MW of beam heating. The neutron rate, stored energy, and plasma density all increase continuously for about 1.3 sec with full power beam heating.

The neutron emissivity profile at this time is shown in Fig.8, as determined by tomography from the neutron profile monitor. The axial emissivity of 3×10^{15}n/m^{3}s seems to be comparable to the ion thermal fusion rate calculated from ion temperature measurements. The global yield seems also due predominantly to thermal fusion. (The axial neutron emissivity exceeded by about 25% that of #26087 from 1991, which had 15 MW of heating into a larger volume.)

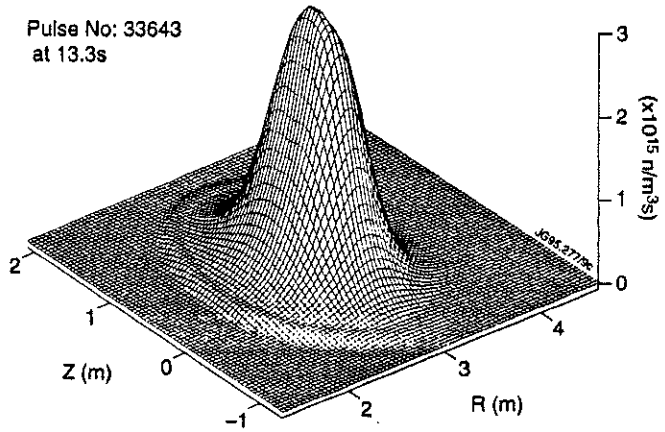

Fig.8: The 2-D neutron emissivity profile (determined by tomography from the neutron profile monitor) is shown in #33643 after 1.3 sec of full power beam heating.

The implication of these results so far are that optimisation of the fusion output is strongly related to optimisation of the thermal fusion yield, in the presence of not too high density profiles.

This hot ion ELM-free H-mode discharge was terminated by a sawtooth crash, and a giant ELM at the plasma edge.

BEAM POWER STEP DOWN

In order to maintain a discharge at a high performance level in a quasi-steady state condition, the plasma density and stored energy need to approach steady state conditions while maintaining a high rate of neutron production.

One method of achieving this is to reduce the beam power and its associated fuelling rate. The best results were obtained using a power step down by eliminating 80 keV beams and

predominantly retaining 140 keV beams, which have a low particle fuelling rate per MW delivered (and a high beam-thermal fusion rate per ion).

Under the lowest wall recycling conditions and with the in-vessel cryopump operating, the plasma volumetric density increase is equal to the beam fuelling rate, both before and after power step-down.

In #34236, high-performance, quasi-steady state operation was achieved, with an equivalent d-t fusion Q maintained above 0.5 for 1 sec, approximately the energy confinement time, as shown in Fig.9, using a simple approximation of the equivalent fusion Q in a d-t plasma, $Q \sim 2.5 \times 10^{-10}$ (NeutRate/BeamPower).

The rate of density rise is slower after step down, and the neutron rate and stored energy are nearly constant. Nevertheless, the slow increase of energy and density finally lead to a discharge terminating ELM. The ion temperature is also approaching the electron temperature. The discharge remains ELM-free during this time.

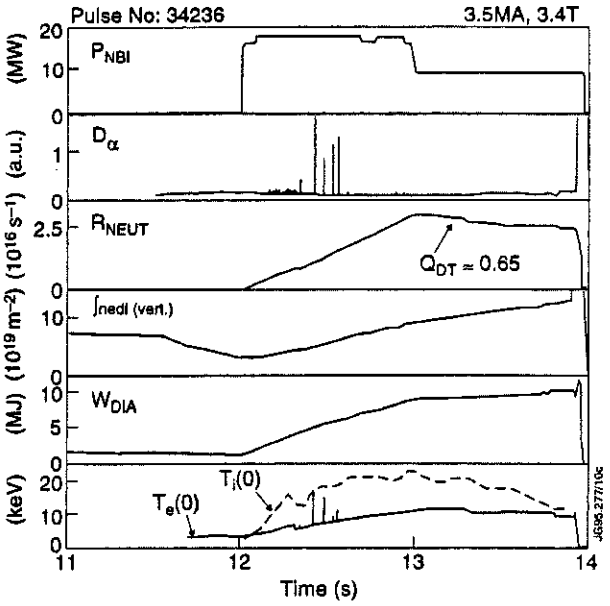

Fig.9: The neutral beam power, D-alpha light, global neutron rate, line-average electron density, stored energy from diamagnetic look measurements, and the central ion and electron temperatures are shown versus time for #34236, a beam power step down experiment.

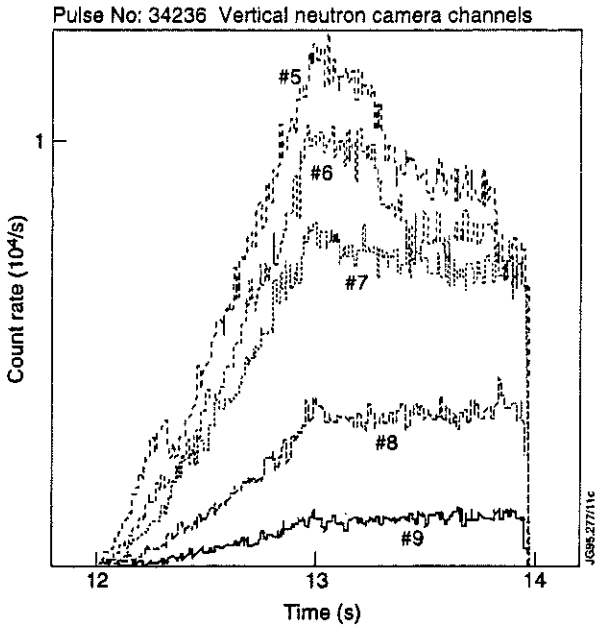

Fig.10: The count rates from the horizontal neutron camera channels 5-9 are shown for #34236. At power step down, the outer channels are unchanged, but the central channels show a drop before reaching a new steady state.

CONTRIBUTIONS TO STEP DOWN NEUTRON PRODUCTION

In Fig.10, the count rates from horizontal neutron camera channels 5-9 are shown for #34236. At power step down, the outer channels are unchanged, but the central channels show a drop before reaching a new steady state.

In Fig.11, the time dependent measured global neutron yield is shown, together with calculated global yields based on Charge Exchange Recombination Spectroscopy measurements of ion temperature and density. Shown are the 80 and 140 keV beam contributions separately, the thermal d-d contribution, and the total. The total agrees with the measured neutron rate evolution. Most of the neutrons are produced by thermal fusion. At step down, since the high current 80 keV PINIs are preferentially turned off, their beam-thermal contribution becomes negligible. It should be noted that the fusion Q thus calculated during this period is more representative of the steady state Q values for reactor extrapolation, since the energy and confinement times are nearly in steady state.

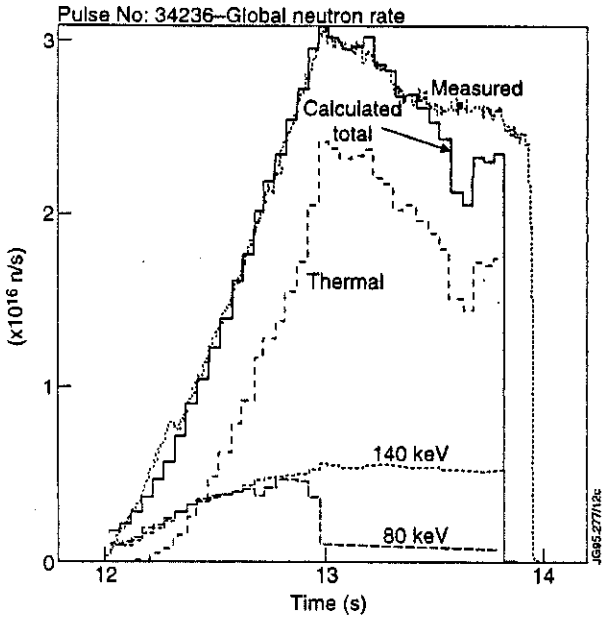

Fig.11: The contributions of 80 keV and 140 keV beam-thermal and thermal fusion to the neutron rate calculated from CXRS measurements, their total, and the fission chamber measurements are shown for #34236. Most of the neutrons are produced by thermal fusion.

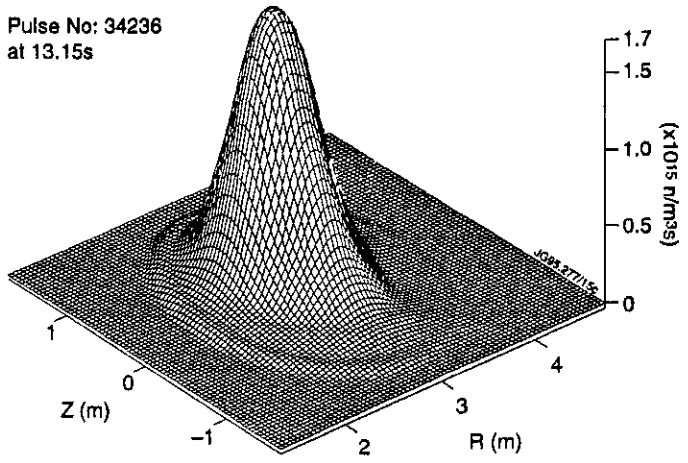

Fig.12: The 2-D neutron emissivity profile (determined by tomography from the neutron profile monitor) is shown in # 34236 at 13.15 sec.

At 13.15 s, the time of maximum fusion Q, tomographic inversion of the neutron camera data has been used to calculate the local 2-D neutron emissivity profile shown in Fig.12. The maximum emissivity is $1.7 \times 10^{13} n/m^3 s$. In Fig.13, the calculated CXRS 1-D neutron emissivity profile is shown at the same time.

The axial values are the same as shown by the tomography, and the integral totals are the same. The emissivity is dominated everywhere by thermal fusion.

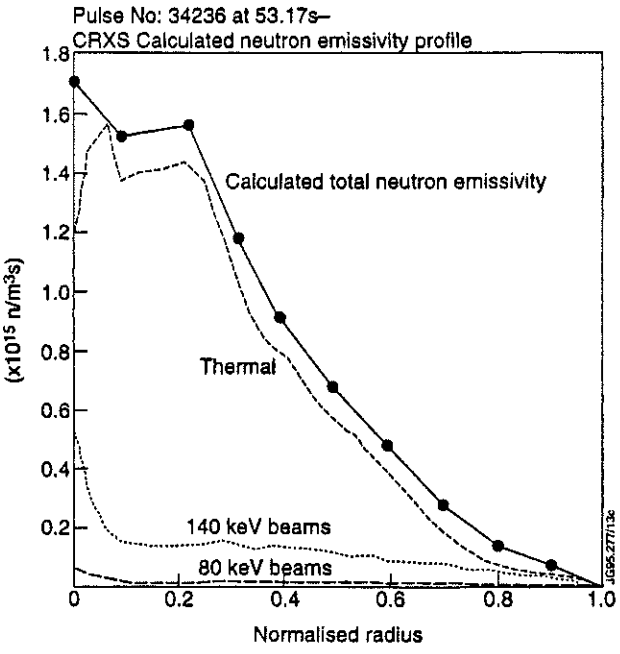

Fig.13: The 1-D neutron emissivity profile calculated from CXRS is shown at 13.15 sec for #34236. The axial emissivity is the same as in the neutron tomography profile.

STEP DOWN TO LOW BEAM POWER

In Fig.14, the results of step down from 16.4 MW to 4.5 MW are shown for the 4 MA plasma #33106.

The stored energy stayed nearly constant for 0.5 s, and the plasma was ELM-free. The energy confinement time increased from about 1 s before step down to 1.5 s after the step down, with 10 - 11 MJ of stored energy. The plasma loss power is only 6 MW, compared to the beampower of 4.5 MW (and negligible ohmic heating). The fusion Q increased briefly above 1, and

slowly decayed to 0.7. The rate of density increase was slowed. It is encouraging that ELM free H-modes can be maintained with a low loss power.

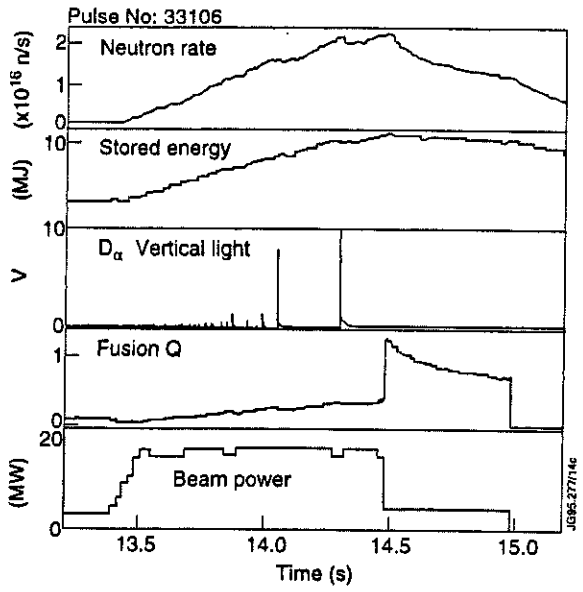

Fig.14: The neutron emission rate from fission chambers, stored energy from diamagnetic loop measurements, the D-alpha light measured along a vertical chord just outside the divertor, fusion Q factor, and neutral beam injected power are displayed for #33106.

CONCLUSIONS AND DISCUSSION

Beam Trajectory:

Neutron production is relatively insensitive to variations of beam trajectory (the plasmas studied remained in the hot-ion H-mode). The altered neutron emissivity profiles within the plasma cause only a 10% reduction in the integrated total emission.

Density Profile:

Hollow and high density profiles reduce the plasma ion temperature and broaden the neutron emissivity profile. The global emission is reduced by 40% in the specific example chosen, due to the reduced temperatures, strong beam trapping at the edge, and an initially low deuterium fraction.

High Performance:

In hot-ion ELM-free H-modes in the present JET configuration with the highest neutron production, and especially with beam power step down experiments, the d-d neutron production by thermal fusion significantly exceeds the beam thermal contribution.

Beam Step Down:

The plasma stored energy and neutron rate in the Hot-Ion ELM-free H-mode in JET are limited by various MHD instabilities (see Hender et al; Smeulders et al, this EPS conference) and not by maximum power.

Once the plasma enters the ELM-free Hot-ion H-mode via high power beam heating (to rapidly increase the density and ion temperature), the H-mode can be maintained with a step down to low input beam power at the plasma loss power level, near the L-H transition threshold of about 5-10 MW at a medium plasma density of $4\text{-}6\times10^{19}m^{-3}$. Enhanced fusion Q can be obtained at low beam power in quasi-steady state.

In present experiments, ELM-free plasmas with beam power step down are only quasi-steady state, not maintained because of the (slow) residual density increase, approximately equal to the (strongly reduced) beam fuelling rate. The problems associated with this density increase are: beam trapping near the plasma edge; ion temperature reduction; instability or H to L transition.

Quasi Steady State Advanced Tokamak Scenarios in JET

C D Challis, B Balet, V Bhatnagar, J C M de Haas, L-G I Eriksson, M Gadeberg, C Gormezano, C W Gowers, J A How, G T A Huysmans, S Ishida[1], W O K Kerner, M J Loughlin, F G Rimini, G J Sadler, A C C Sips, A Tanga, B J D Tubbing, D J Ward.

JET Joint Undertaking, Abingdon, Oxfordshire, OX14 3EA, UK.

[1] JAERI, Naka Fusion Research Establishment, Ibaraki-ken, Japan 311-01.

INTRODUCTION

It is thought that a steady state tokamak reactor will need a substantial fraction of the plasma current to be provided by the neoclassical bootstrap effect. To achieve this requires that the poloidal β be significantly greater than unity which, in turn, requires good energy confinement without the use of very high plasma currents. It is likely that such a plasma would also have to achieve $\beta_N \geq 3$ ($\beta_N = \beta_T a B_T / I_p$ in %mT/MA) if very high toroidal fields are to be avoided. Experiments have been performed in JET with the demanding aim of simultaneously achieving these conditions, high β_p, high confinement and high β_N, in steady state. The investigation of the characteristics of plasmas in this domain, the so-called 'Advanced Tokamak Scenario', is necessary to assess the prospects for steady state reactor concepts.

RANGE OF EXPERIMENTAL CONDITIONS IN 1994/1995

parameter	range
I_p	1.0 - 2.0MA
B_T	1.0 - 3.4T
q_{95}	3.0 - 11
triangularity	up to 0.45
$P_{heating}$	up to 28MW
$t_{heating}$	up to 7secs

ACHIEVEMENT OF QUASI STEADY STATE CONDITIONS

High β_p plasmas before the JET pumped divertor [1] (eg: #25264 in Fig 1)

- ELM free H mode plasmas
- very high confinement – $H_{ITER89L-P} \approx 3.7$ (ITER89L-P scaling ref [2])
- modest fast ion content in ELM free phase (≈ 10% of plasma stored energy)
- large bootstrap current (≈ 70% of plasma current)
- uncontrolled density rise in ELM free phase
- β collapse with density fall associated with large ELM

High β_p plasmas in the JET pumped divertor configuration (eg: #32847 in Fig 1)

- ELMy H mode plasmas
- high confinement – $H_{ITER89L-P} \approx 2.0$
- large fast ion content in ELMy phase (≈ 30% of plasma stored energy)
- moderate bootstrap current (≈ 50% of plasma current)
- density steady in ELMy phase
- no β collapse

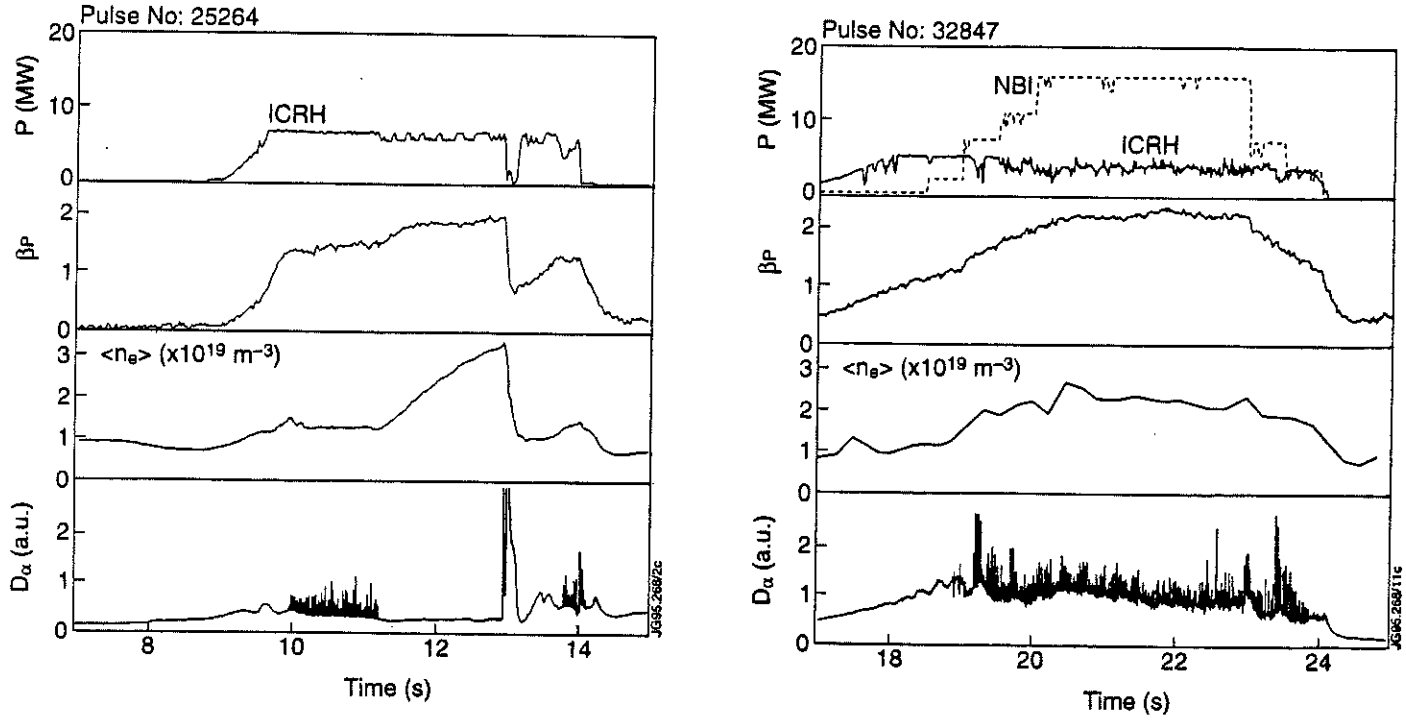

Fig.1: Comparison of two 1MA/2.8T pulses #25264 (1991) and #32847 (1994).

APPROACH TO THE ADVANCED TOKAMAK DOMAIN

A notional advanced tokamak domain, representative of steady state reactor concepts such as SSTR [3], is illustrated in Fig 2. The operating regime is constrained by:

- the need for significant bootstrap current – lower bound on β_p
- toroidal field coil technology – upper bound on q (at current required for ignition)
- plasma stability – upper bound on β_N

High values of β_p have been achieved in JET (see Fig 2)

- up to 2.8 at high q
- up to 2.0 at $q_{95} \approx 5$

However, the bootstrap current (estimated for the thermal pressure alone) is below that required for a steady state tokamak (≥ 70% of the plasma current).

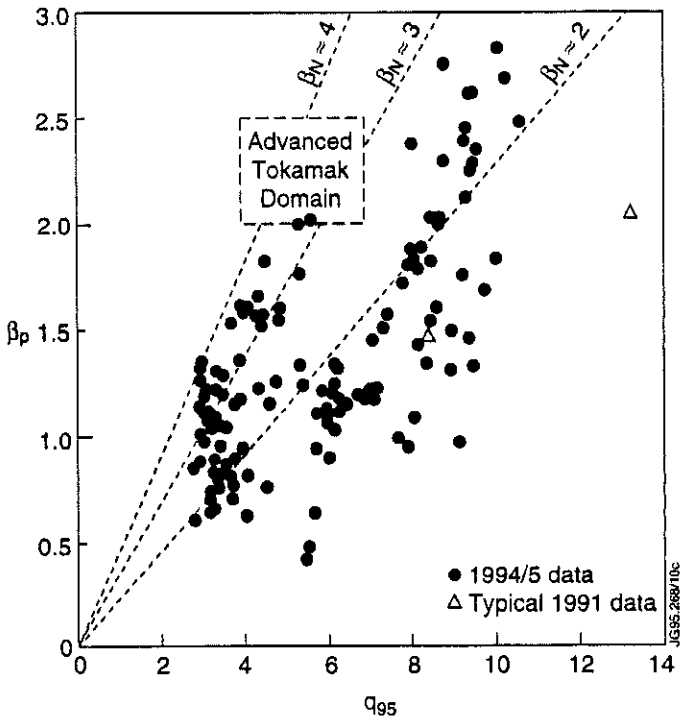

Fig 2. β_p (measured using a diamagnetic loop) plotted against q_{95}.

ACHIEVED VALUES OF β_N

An upper bound on the achievable values of β_N is shown in Fig 3. This limit is calculated for plasmas with:

- plasma current $\geq$ 1MA
- $H_{ITER89L-P} \leq 2$ (representative of the stationary plasmas in this dataset)

where the maximum additional heating power used was either full NBI heating at low q or combined RF and NBI heating at high q.

At high values of q, the plasma performance and hence the value of β_N, has been limited by the plasma confinement and available additional heating power. At $q_{95} < 4$ confinement degradation has been observed in some cases which is suggestive of a global β limit.

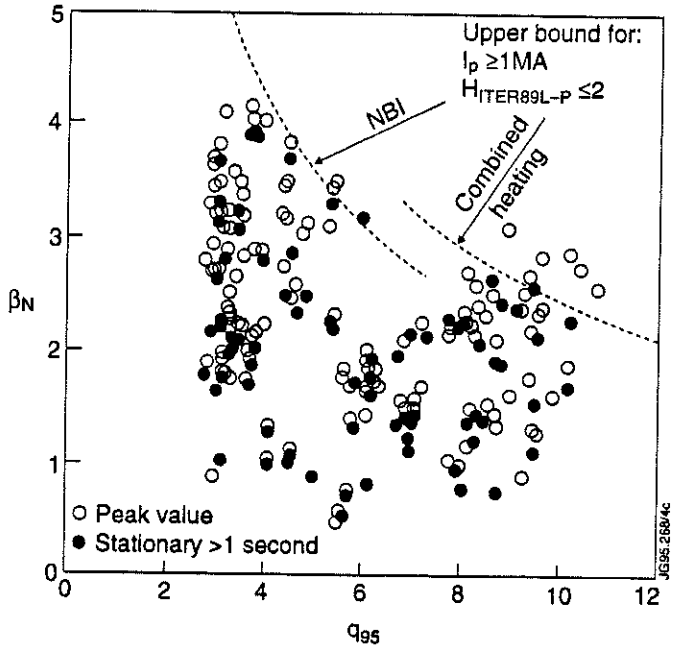

Fig 3: β_N (measured using a diamagnetic loop) plotted against q_{95}.

ACHIEVEMENT OF HIGH β_N AT $q_{95} \approx 3$

Figure 4 shows an example of a plasma with I_p = 1MA and B_T = 1T which apparently reaches a global β limit. The neutral beam heating power is increased in three steps. The total plasma stored energy increases at the first two steps, but at the third step no significant further increase is observed. $H_{ITER89L\text{-}P}$ decreases at the highest power step coincidentally with an increase in the frequency of the ELMs.

The equilibrium flux contours for this pulse are also shown in Fig 4. The plasma is characterised by

- 'ITER-like' configuration – $q_{95} \approx 3.1$
  – elongation ≈ 1.65
  – triangularity ≈ 0.2
- high β_N (≈ 3.8)
- large fast ion stored energy ($\approx$ 40% of the total plasma stored energy)

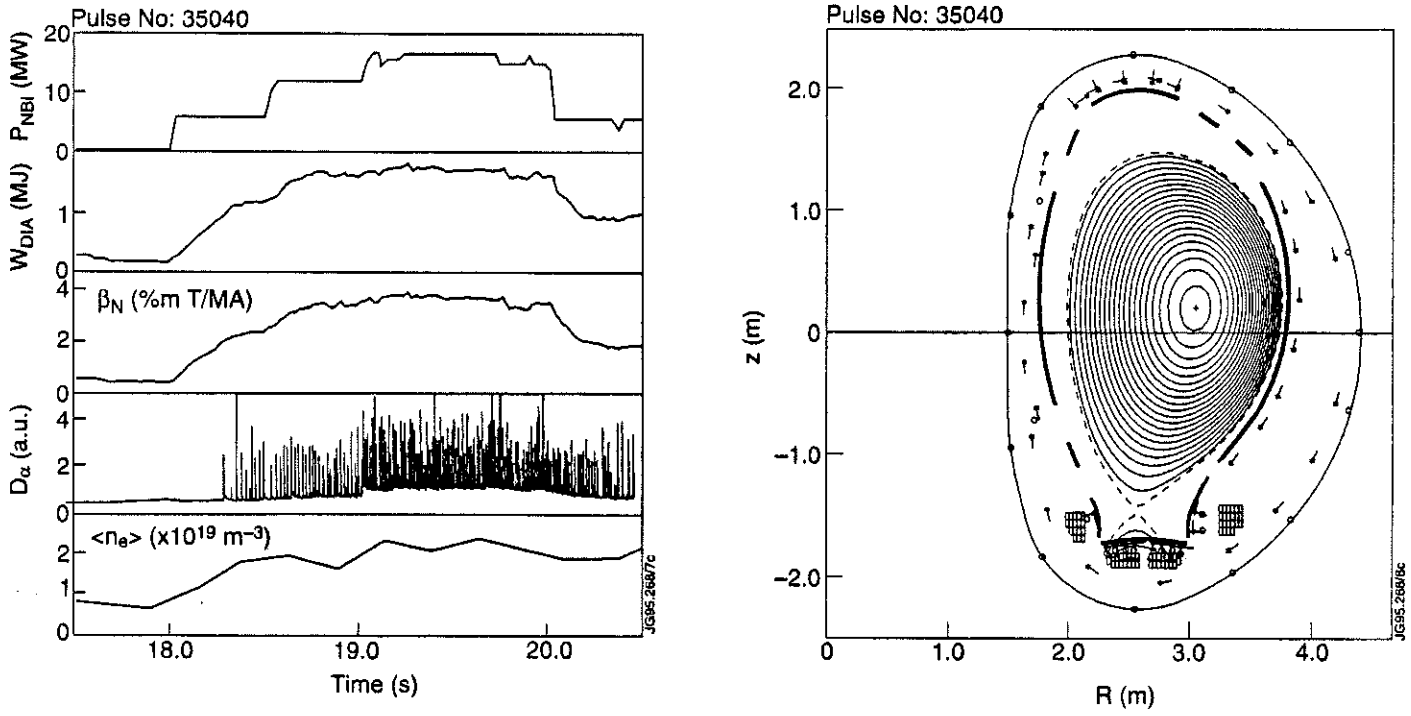

Fig 4: Time evolution of a plasma at 1MA/1T ($q_{95} \approx 3.1$) together with a plot of the equilibrium flux contours.

ACHIEVEMENT OF HIGH β_N AT $q_{95} \approx 5$

Figure 5 shows an example of a plasma with I_p = 1MA and B_T = 1.4T which shows no indication of a global β limit. This plasma achieves the same value of β_N as that in Fig 4 despite the higher toroidal field. This is due to the degraded confinement in the lower field case.

The equilibrium flux contours for this pulse are also shown in Fig 5. The plasma is characterised by

- 'steady state tokamak' configuration
  - $q_{95} \approx 4.7$
  - elongation $\approx$ 1.7
  - triangularity $\approx$ 0.4
- high β_N ($\approx$ 3.8)
- high β_p ($\approx$ 1.8)
- high confinement ($H_{ITER89L-P} \approx 2.2$)
- moderate fast ion stored energy ($\approx$ 30% of the total plasma stored energy)

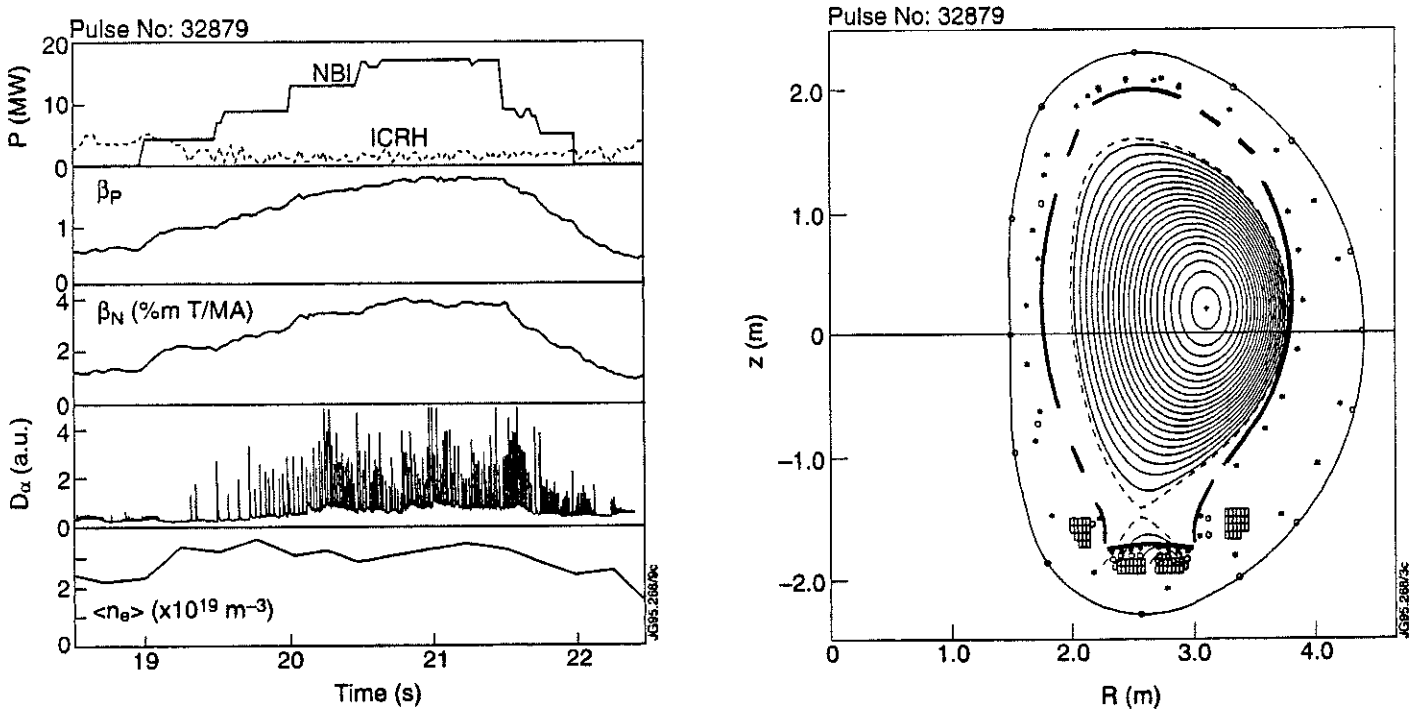

Fig 5: Time evolution of a plasma at 1MA/1.4T ($q_{95} \approx 4.7$) together with a plot of the equilibrium flux contours.

LONG PULSE EXPERIMENTS

Long pulse heating has been applied to plasmas at high β_p to assess any long timescale effects on confinement and stability due to the redistribution of the toroidal current.

Figure 6 shows an example of a plasma at I_p = 1MA and 1.4T with:

- $\beta_p \approx 1.5$
- $\beta_N \approx 3.0$
- an additional heating pulse length of 7 seconds

which reaches stationary conditions for the duration of the heating pulse.

The timescale for the redistribution of the current profile in these discharges is illustrated in Fig 7 by a TRANSP [4] simulation with typical plasma parameters and assuming that the heating power were maintained until the plasma current reached a stationary state. The simulation indicates that:

- the core current density becomes stationary after 10-15 seconds
- the peripheral current density essentially becomes stationary after 2-3 seconds

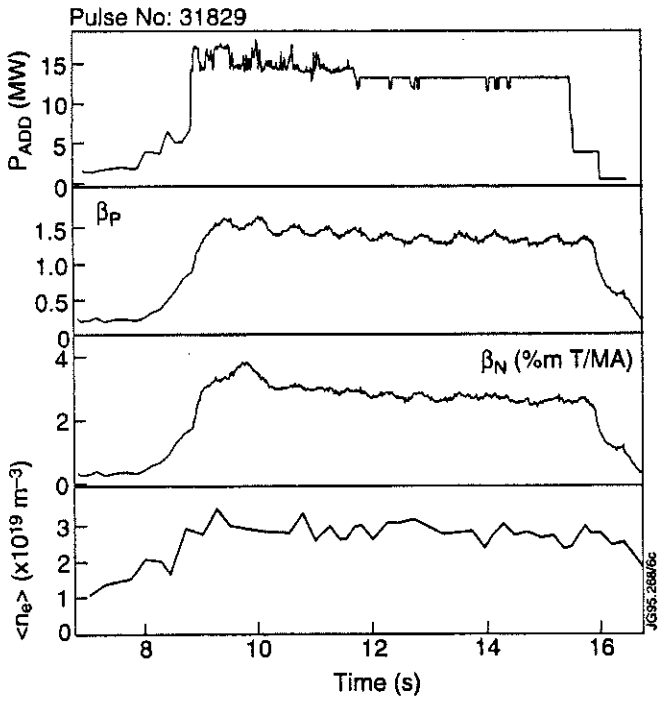

Fig.6: Time evolution of a long pulse experiment at 1MA/1.4T.

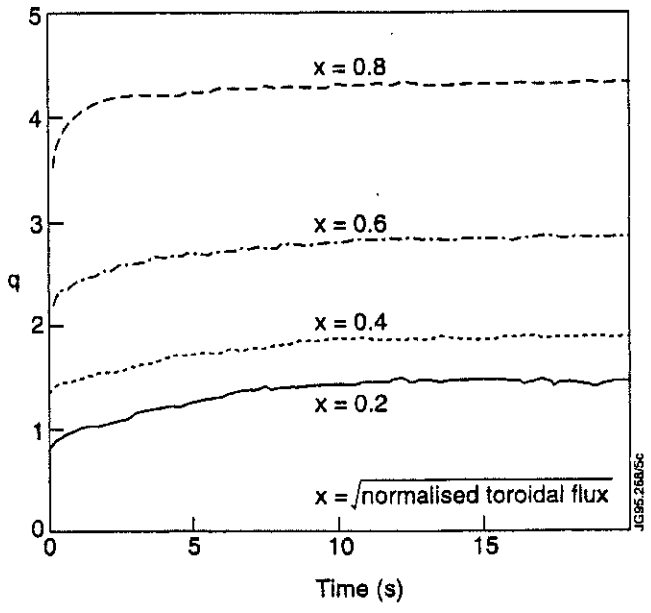

Fig.7: Time evolution of q at different radii extrapolated to steady state for a typical plasma.

CONCLUSIONS

- Quasi steady state conditions approaching those required for a steady state reactor have been achieved in ELMy H mode plasmas for pulse lengths up to 7 seconds. The following plasma parameters have been achieved simultaneously:

pulse	31829	33580	32879
β_p	1.5	1.9	1.8
β_N	3.0	3.3	3.8
$H_{ITER89L-P}$	2.0	2.2	2.2
q_{95}	4.5	6.0	4.7
$P_{heating}$ (MW)	13	18	18
$t_{heating}$ (s)	7.0	3.5	1.0

- An apparent global β limit has been observed at $\beta_N \approx 3.8$ with $q_{95} \approx 3.1$. Similar values of β_N were obtained at $q_{95} \approx 5$ but it is not possible to establish whether a β limit has yet been reached with the available heating power.

- The fast ion stored energy in these plasmas is up to 30% of the total plasma energy due to the high additional heating power and the density control by ELMs.

- The plasma current density in the plasma periphery has essentially reached its equilibrium value. Therefore, any effects on stability arising from the presence of finite edge bootstrap current density in these plasmas might reasonably be expected to be manifest on the timescale of the experiments.

- The timescale for redistribution of the plasma current profile in the plasma core is still longer than the heating pulse length of these discharges.

REFERENCES

[1] C D Challis, et al., Nucl Fusion **33**(1993) 1097.
[2] P N Yushmanov, et al., Nucl Fusion **30**(1990) 1999.
[3] M Kikuchi, Nucl Fusion **30**(1990) 265.
[4] R J Goldston, et al., J Comput Phys **43**(1981) 61.

Density Scaling of the H-mode Power Threshold in JET

E Righi, D J Campbell, J G Cordey, J Ehrenberg, R Giannella, J de Haas, P Harbour, N Hawkes, P Nielsen, L Porte, G Saibene, D F H Start, K Thomsen, M von Hellermann.
JET Joint Undertaking, Abingdon, Oxfordshire, OX14 3EA, UK.

INTRODUCTION

One of the crucial issues for the design of ITER is to establish field, size and density scaling of the power threshold. This is why the ITER Confinement Database and Transport Expert Groups have asked JET, DIII-D, ASDEX-U, JT60-U, COMPASS, C-MOD, JFT-2M and PBX-M to carry out a series of experiments in a given ITER-like configuration with $q_{95} \cong 3$. This paper presents the results obtained on the JET tokamak using both NBI and RF heating.

EXPERIMENTAL PARAMETERS

- edge safety factor $q_{95} = 3$ corresponding in JET to: 1MA/1T, 2MA/2T, 3MA/3T
- triangularity $\delta \approx 0.15$
- aspect ratio $R/a=3 \pm 0.3$
- ion ∇B drift towards the target plates (positive)
- heating scheme: D^0 into D NBI and H minority ICRF
- single null X-point standard JET fat configuration with X-point height ≈25cm
- plasma equidistant from inner and outer walls, distance ≅8 cm
- density: increased by gas puffing and by controlled NBI fuelling
- target plates material: Carbon and Beryllium
- cryopump: on

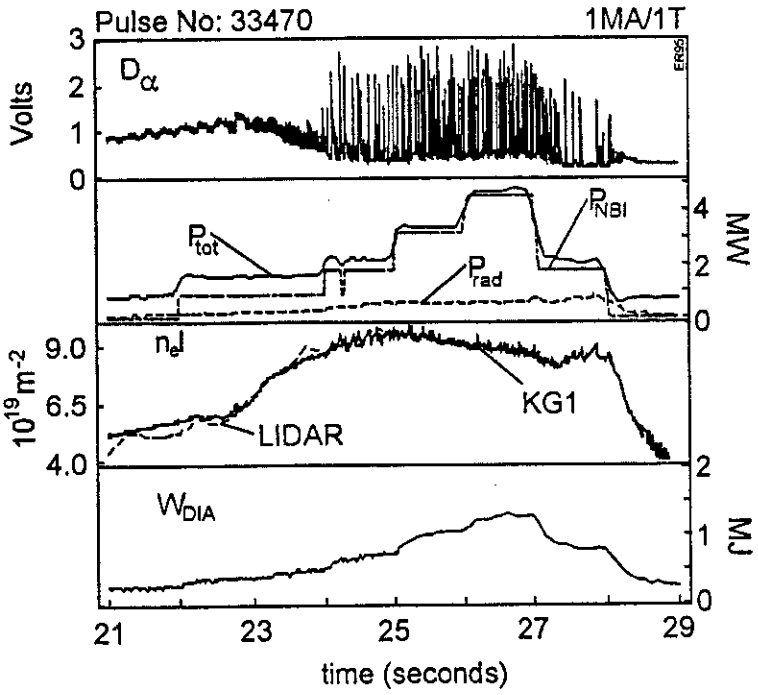

Fig.1 Transition into H-mode for a discharge in the database.

In addition some RF-only H-modes were obtained at 3MA/3.1T and 4.8MA/3.4T with Beryllium divertor target material. They indicate a reduced power threshold with ICRF heating alone.

RESULTS

This presentation shows threshold curves as groups of L-H transition data-points for different I_p/B_t values. In all the pictures the dimensions of the markers give an estimate of the uncertainty in the measurements.

Density dependence

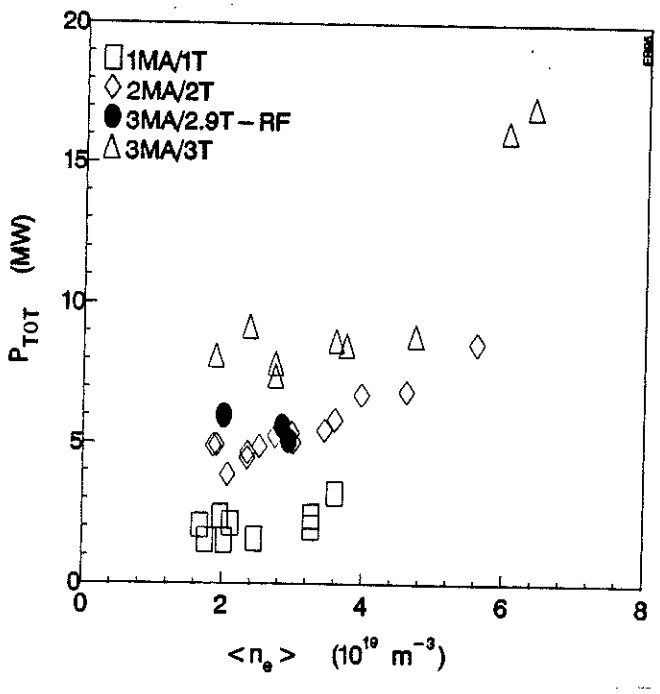

Fig.2 Dependence of the H-mode power threshold P_{TOT} on the volume averaged density

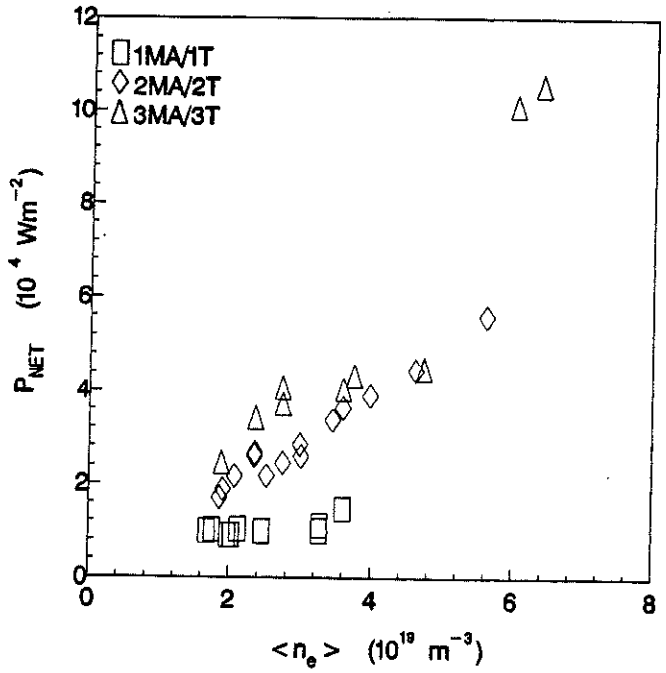

Fig.3 Dependence of H-mode power threshold, expressed as net power flux flowing through the separatrix P_{NET} on the volume averaged density

The power threshold can be expressed in two ways:

- as total power coupled to the plasma $P_{TOT} = P_{NBI} + P_{OHM}$
- as net power flux flowing through the separatrix $P_{NET} = (P_{TOT} - dW_{DIA}/dt - P_{RAD}^{bulk})/S$

where $S \equiv 140 m^2$ is the plasma surface area.

- The threshold has an approximately linear dependence on $<n_e>$, especially when expressed in terms of P_{NET}.
- Significant departure from linearity for the 3MA/3T data at low density, especially in Fig.2
- Analysis is in progress to estimate the amount of shine through of NBI (up to 20% of P_{NBI}).
- In the high density range an instability localised in the divertor region appears, the analysis of which is reported at this Conference [1].

Comparison with the ITER scaling and regression analysis

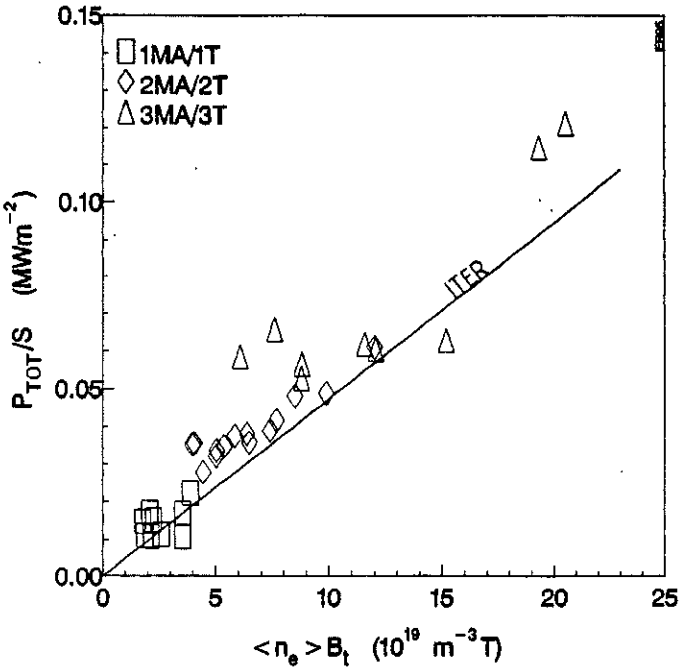

Fig.4 The ITER scaling for the H-mode power threshold is within 50% of the JET 1995 threshold database.

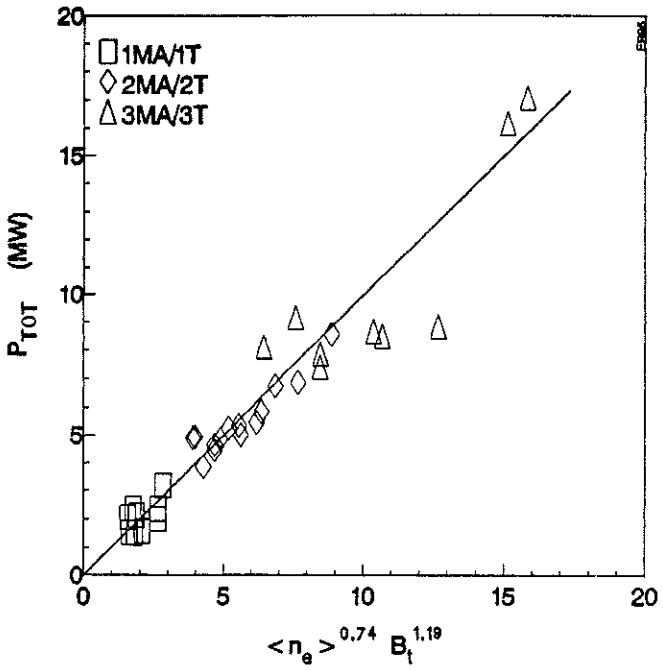

Fig.5 Non-linear regression analysis showing the dependence of the power threshold on density and magnetic field $<n_e>$ is in units of 10^{19} m^{-3}, while B_t is in Tesla

- The ITER scaling

  $$P_{TOT}/S=0.044 <n_e> B_t$$

  is well within 50% of the JET data.

- 3MA/3T series shows a clear (outside error bars) deviation from the linear scaling both at very low and at very high densities.

- Non-linear regression analysis indicates that the dataset follows a scaling law of the type:

  $$P_{TOT} \propto B_t^{1.19} < n_e >^{0.74}$$

  consistent with results from other tokamaks [2]. Although regression analysis reduces the spread of the data, the 3MA/3T data at low density still deviate from the fitting.

Edge density measurements

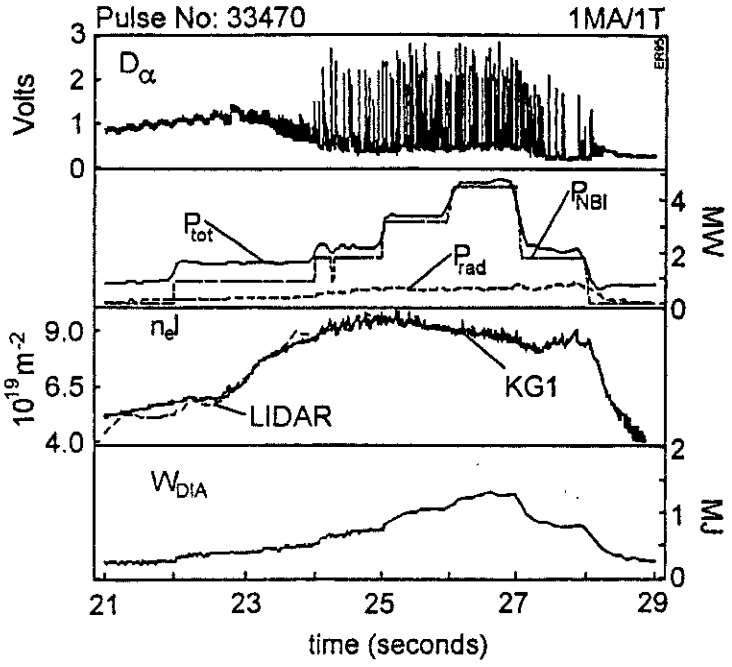

Fig.6 The transition into H-mode as seen from the plasma edge by the FIR interferometer at R=3.75m

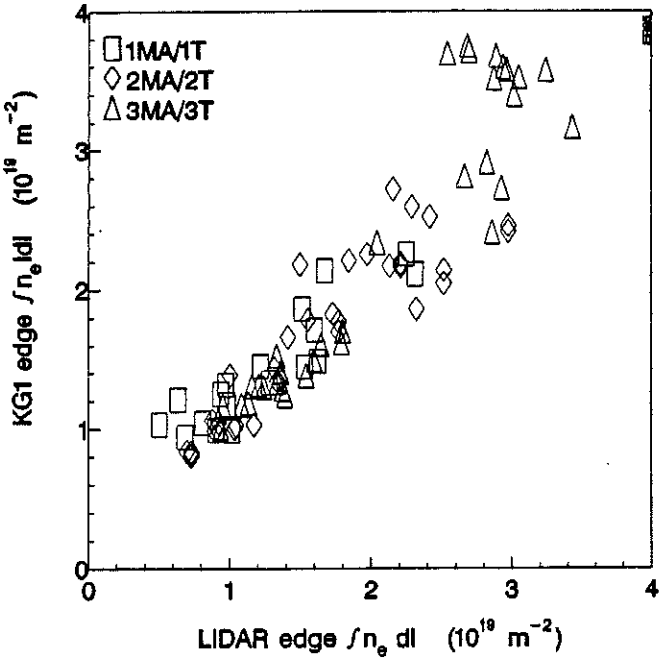

Fig.7 The edge line integrated density has been accurately measured at R=3.75m with both the KG1 and LIDAR diagnostics.

The line integrated edge density $\int n_e dl$ along a vertical line-of-sight at R=3.75m can now be measured in JET using both the KG1 interferometer and the LIDAR Thomson scattering diagnostic. The high resolution of the FIR interferometer diagnostic allows to study the L-H transition at the plasma edge (Fig.6). The accuracy of the measurements is illustrated in Fig.7.

P_{NET} at the plasma edge

- P_{NET} depends on the edge $\int n_e dl$ roughly linearly for the 2MA/2T and 3MA/3T series,
- 1MA/1T series seems to show a much weaker dependence
- not so evident B_t scaling.

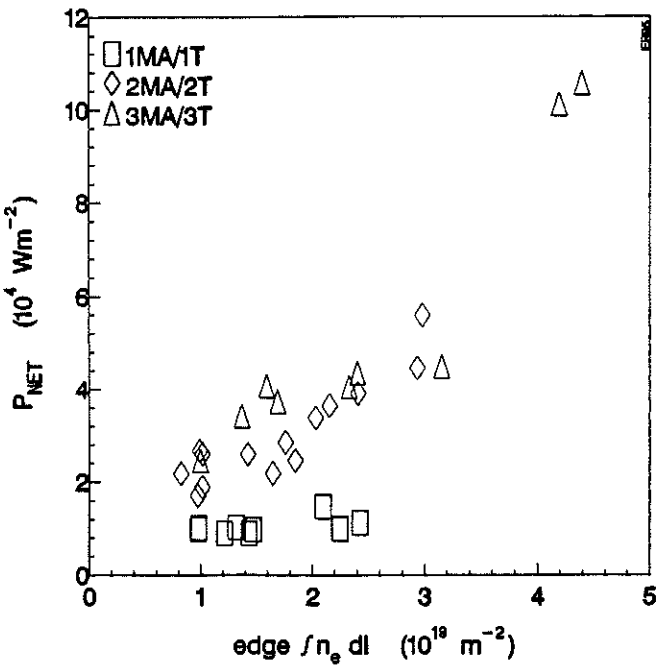

Fig.8 Dependence of the power flux through the separatrix on the edge line integrated density

Dependence of the edge electron temperature T_{ea} on the edge density

- Electron temperature at the plasma edge, T_{ea}, is measured with both the high resolution heterodyne radiometer and with the LIDAR Thomson scattering diagnostic.
- Edge T_e is roughly proportional to B_t^2 (suggesting the importance of Larmor radius)
- Not very clear edge density dependence.

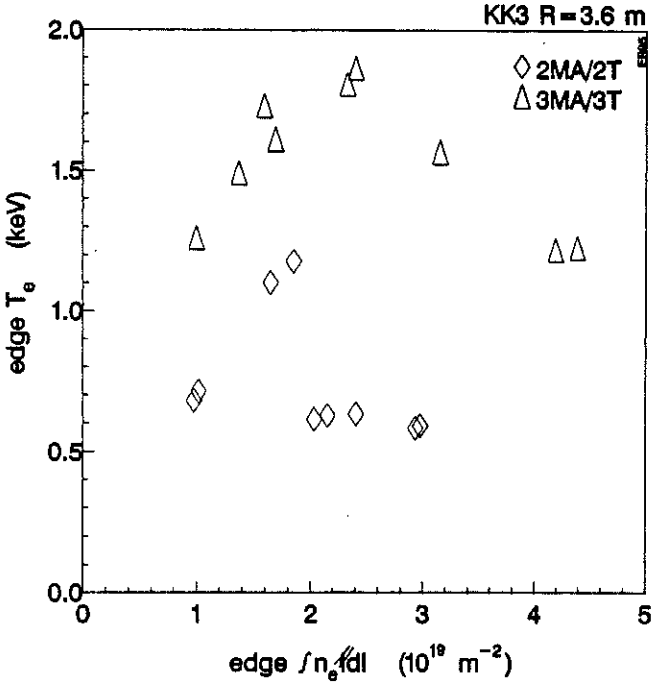

Fig.9 Edge T_e measurements taken with the KK3 heterodyne radiometer for B_t=2,3T at R=3.6m

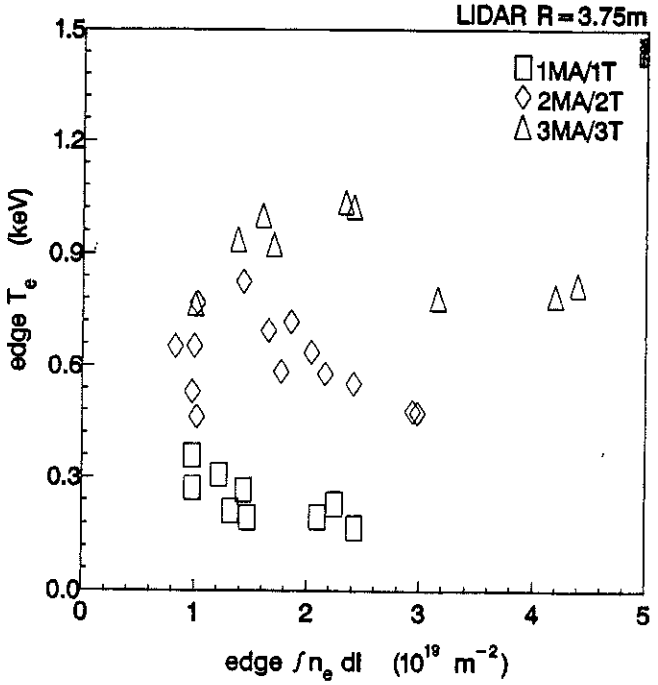

Fig.10 Same as Fig.9, but the measurements were taken with the LIDAR Thomson scattering diagnostic for B_t=1,2,3T at R=3.75m

Neutrals flux at the divertor

- Pressure gauges positioned in the divertor [2,3] allow measurements of the neutrals flux to be taken.
- Data shown have been obtained with the gauge at the opening of the cryopump.
- Cryopump affects the measurements in the sense that the absolute values of the fluxes are lower than those measured with the other gauges. However the gauges signals are proportional (see Fig.11), and results are consistent if the same gauge is used.

Preliminary results:

- A lower limit exists, around 10^{21} particles m^{-2} s^{-1}, below which no data exist: this is determined by minimum fuelling requirements for plasma formation.
- The dependence of P_{NET} on the particle flux is somewhat weaker than that with the edge $\int n_e dl$, and at high flux all three data series seem to asymptotically tend to the same enveloping curve.

- The particle flux itself depends on the edge $\int n_e dl$ (see Fig.13): future analysis will aim at linking the flux to recycling conditions in the scrape off layer independently of the edge density.
- The B_t scaling is here much clearer than in Fig.8.

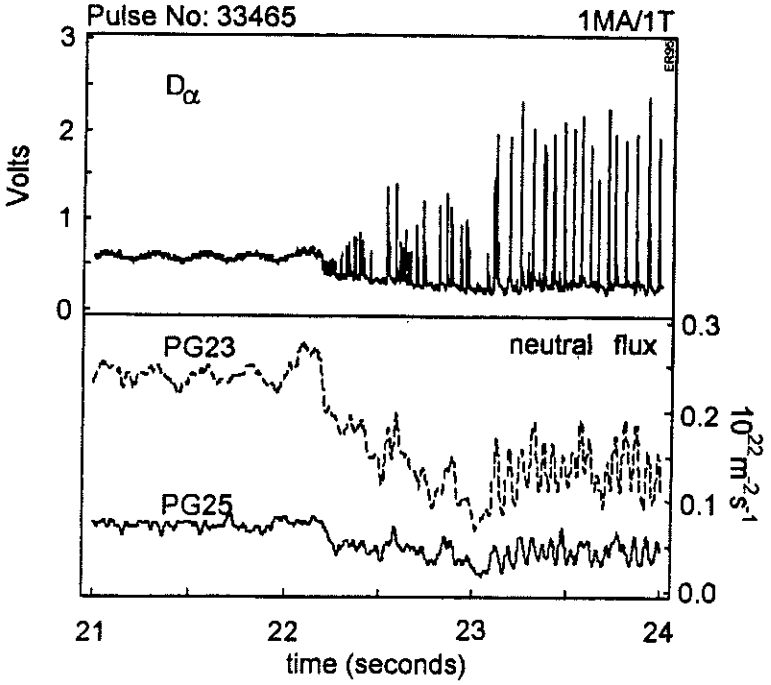

Fig.11 The L-H transition as seen from the divertor pressure gauges. In the figure PG25 indicates the gauge at the cryopump (the one used in the present analysis), while PG23 is located below the X-point private region [2,3].

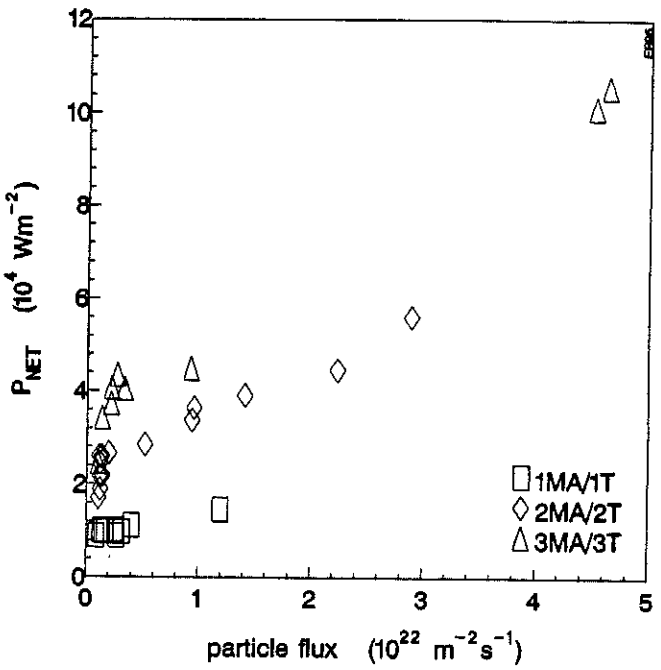

Fig.12 P_{NET} plotted against the neutrals flux measured with gauge PG25 (at the cryopump).

Results: comparison between Carbon and Beryllium divertor target tiles

The experiment has been repeated for selected discharges after the change of the divertor target tiles from Carbon to Beryllium.

- As far as the data obtained so far are concerned, no significant difference was found in the power threshold.
- At 3MA/3T and high densities no Beryllium data are presently available for comparison.

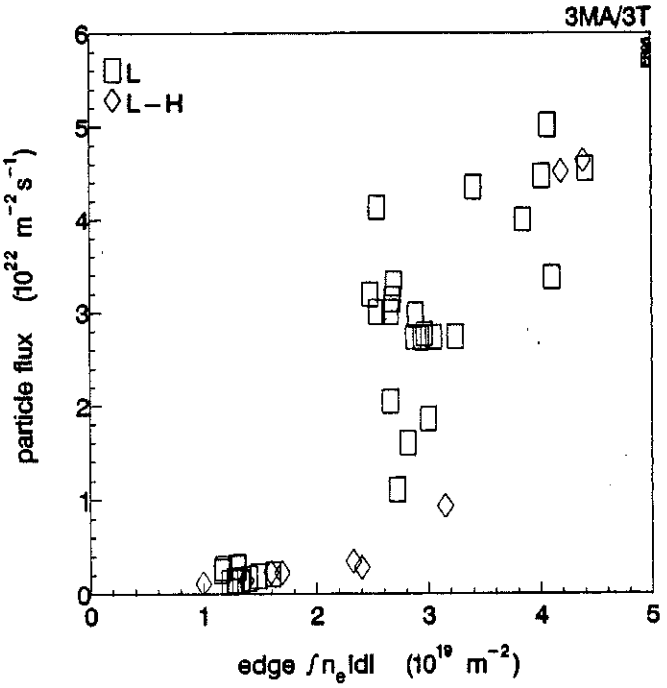

Fig.13 Example of dependence of the neutrals flux on the edge density for the 3MA/3T data series. L-H transition data-points and steady-state L-mode points are used to identify the threshold.

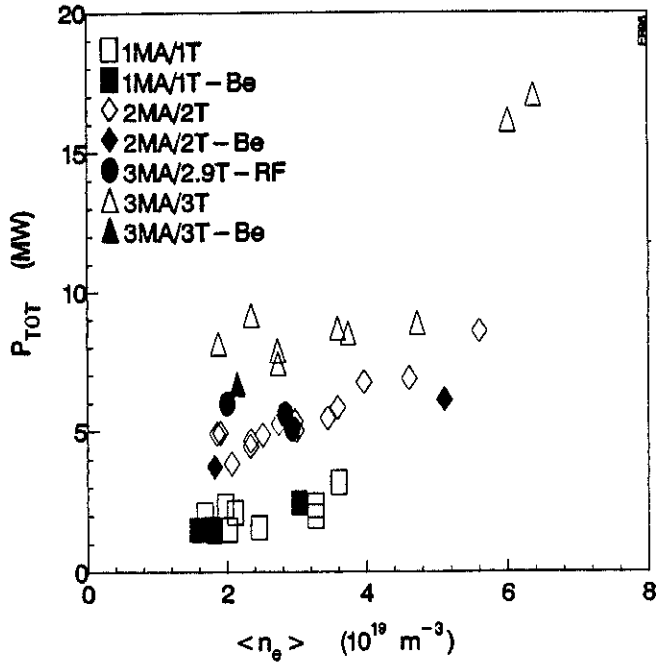

Fig.14 Comparison of the density dependence of the H-mode power threshold for Carbon and Beryllium target tiles and for RF-only H-modes (on Be tiles).

CONCLUSIONS

- P_{TOT} and P_{NET} vs $\langle n_e \rangle$:
  the dependence is roughly linear, although at low densities the 3MA/3T data deviate from linearity. RF threshold seems lower.
- Database well within 50% of ITER scaling, but deviations exist for low and high densities.
- Regression analysis:

$$P_{TOT} \propto B_t^{1.19} \langle n_e \rangle^{0.74}$$

- P_{NET} vs edge $\int n_e \, dl$:
  approximately linear dependence. Not clear scaling with the magnetic field.
- Edge T_e:
  roughly proportional to B_t^2, indicating the importance of Larmor radius scale length.
- P_{NET} vs particle flux:
  mildly non-linear dependence, tending asymptotically to an enveloping curve at high flux. Dependence on B_t is roughly linear.
- C vs Be target materials: no significant difference as far as the data obtained so far are concerned.

FURTHER REMAINING ANALYSIS

- Investigate further relationship between P_{NET} and edge parameters like T_i, not included in the present analysis.
- Establish link between L-H transition and recycling conditions at the edge, to which the measurements of particle flux are linked.
- If possible, study the relationship between L-H transition and plasma rotation.
- Compare H-mode formation using different additional heating systems (ICRF and NBI) and clarify the conditions for low power threshold with RF.
- Continue statistical analysis of database.
- Compare experimental results with current leading theories on H-mode formation.
- Release the database for public use and its inclusion in the ITER threshold database.

ACKNOWLEDGEMENTS

The authors would like to acknowledge the collaboration of Task Force D, who gave the experimental time and expertise to carry out the experiments and of Task Force T, who obtained the H-modes with ICRF heating only.

REFERENCES

1. R Monk et al., This Conference.
2. Many Authors, Proc. of the 2nd Workshop of the ITER Confinement Database and Modelling Expert Groups, San Diego, USA, 13-15 March 1995.
3. J Ehrenberg et al., This Conference.
4. G Saibene et al., This Conference.

Toroidal Momentum Slowing Down and Replacement Times in JET Divertor Discharges

K-D Zastrow, J C M de Haas, M G von Hellermann,
A C Howman, R W T König.
JET Joint Undertaking, Abingdon, Oxfordshire, OX14 3EA, UK.

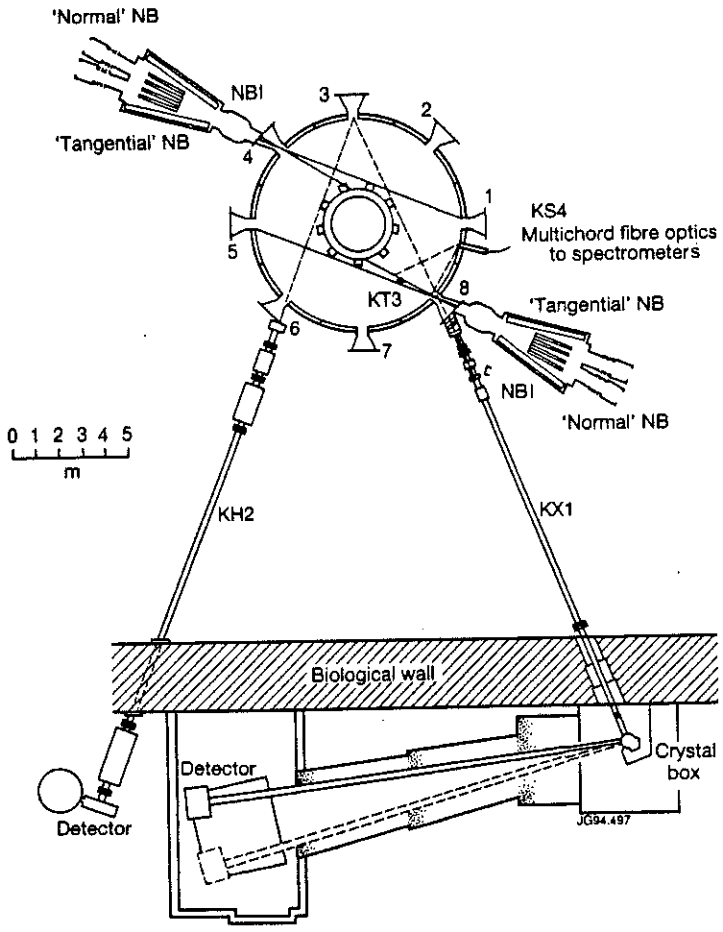

Fig.1: Lines of sight of the high resolution X-ray crystal spectrometer (KX1) (located in the geometric midplane of the torus) and the multichord visible charge exchange spectrometers (KS4) viewing the upsteered tangential beams in Octant 8.

INTRODUCTION AND SUMMARY

Several observations of correlated ion energy and toroidal angular momentum confinement during neutral beam injection (NBI) have been reported. For example, it was found on ASDEX that toroidal momentum and energy replacement times were similar [1] with τ_L approaching τ_E for values above 60 msec. On TFTR it was found that ion and momentum diffusivities are equal in L-Mode discharges [2]. At JET, correlation between central rotation frequency and ion temperature has been observed [3]. It was also found that combined neutral beam and radio frequency (RF) heating resulted in a reduced central angular frequency [3,4], whilst slightly improving the energy confinement [5]. In this paper we study the decay of the toroidal angular momentum after NBI in JET and compare the results with the behaviour of the replacement time during NBI. During NBI, when the global energy content is dominated by the ions we find that the energy replacement time is equal to that of the angular momentum. The angular momentum decay time after NBI, when the global energy content is dominated by

electrons, is up to 30% larger than the energy replacement time. In contrast to combined heating we find no evidence for stronger deterioration of momentum than energy confinement in discharges with RF heating only.

MEASUREMENTS

Toroidal angular velocity and toroidal angular momentum density

The toroidal angular velocity, ω, is derived from Doppler shift measurements using a high resolution X-ray crystal spectrometer and active visible charge exchange spectroscopy (see Fig.1).

The charge exchange recombination spectrum of $C^{+6}+D \rightarrow C^{+5}$ (8→7) is observed at 10 positions along the upsteered bottom neutral beams in Octant 8. Radial profiles, expressed in terms of the normalised minor radius, $\rho=r/a$, are constructed assuming the angular frequency to be constant on a flux surface by projecting the intersection points of the lines of sight with the neutral beams along the corresponding flux surfaces into the outer half of the magnetic midplane (see Fig. 2).

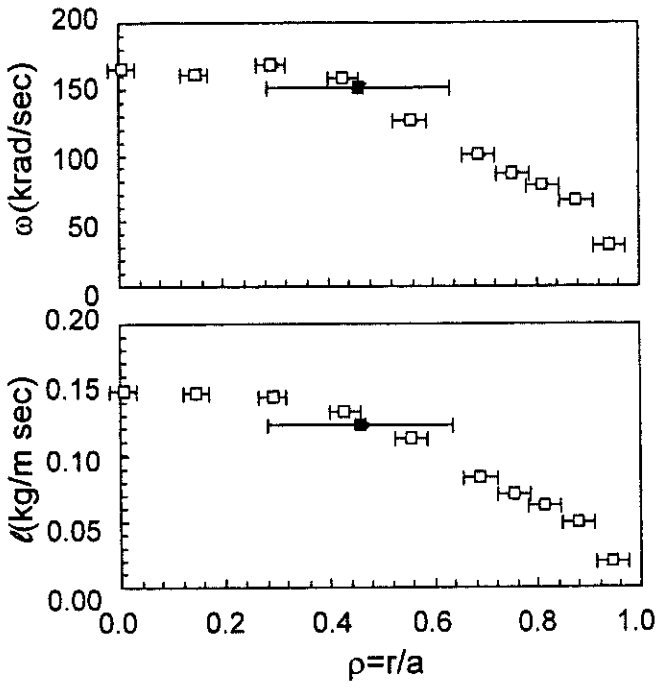

Fig.2: Radial profiles of toroidal angular velocity ω (top) and angular momentum density (bottom) of C^{+6}(□) and Ni^{+26}(■) (JET-#32969, 52.5 sec)

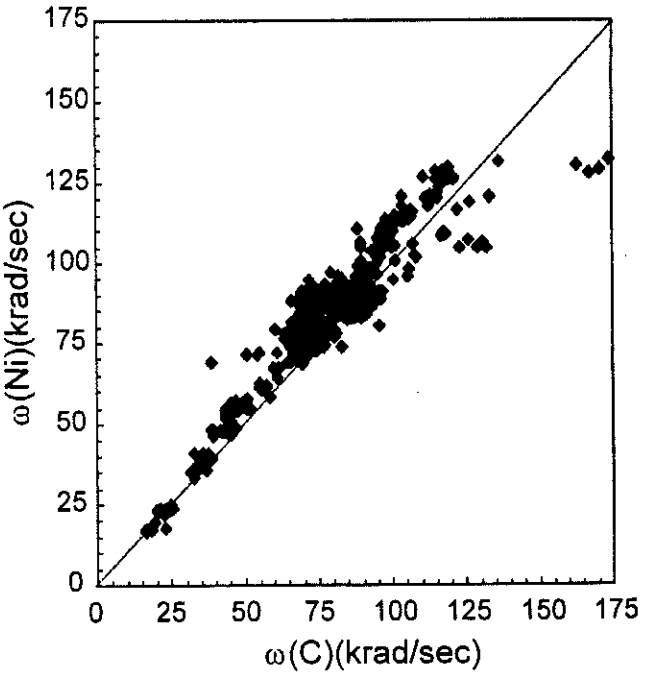

Fig.3: Comparison under steady state conditions of toroidal angular velocity measurements of C^{+6} and Ni^{+26} at the same value of $\langle\rho\rangle$ (see Fig. 2).

The resonance line *w* of helium-like nickel (Ni^{+26}) is observed along a line of sight in the geometric midplane of the torus, i.e. 20-30 cm below the magnetic axis. The impact parameter of this line of sight with respect to the torus axis is R_0=1.82 m. The corresponding effective normalised minor radius of the helium-like nickel emission shell, $\langle\rho\rangle$, and its width, $\sigma(\rho)$, (see Fig. 2) are calculated from the projected radial profiles of electron temperature and density using a coronal equilibrium model for the fraction of helium-like nickel, $f(Ni^{+26})$, and for the emissivity of the resonance line, ε_w, as

$$\rho_N = \frac{2}{4\pi}\int_{R_0}^{R_{Wall}} \rho^N \frac{f\left(Ni^{+26}\right)\cdot n_e^2\cdot\varepsilon_w\cdot R}{\sqrt{R^2-R_0^2}}\,dR \qquad (1)$$

$$\langle\rho\rangle = \frac{\rho_1}{\rho_0};\ \sigma(\rho) = \sqrt{\frac{\rho_2}{\rho_0}-\langle\rho\rangle^2}$$

The relative accuracy, due to photon statistics, of the derived angular velocity, is $\Delta\omega$=1-2 krad/sec for both diagnostics. The reference wavelength for the Doppler shift of the visible spectrum is provided by a diode pumped Nd-YAG Laser (λ= 532 nm). The achieved accuracy of the absolute level is about 5 krad/sec. The time resolution of the visible spectra is typically 50 msec.

The reference wavelength of the X-ray spectrometer was determined from a comparison of the derived angular velocities from both diagnostics under steady-state conditions (see Fig.3). The uncertainty of the absolute level is about 10 krad/sec. The time resolution of the X-ray spectra varies in the range 30-120 msec.

The toroidal angular momentum density (see Fig.2), ℓ, is calculated using the local electron density as

$$\ell = m_D\cdot n_e\cdot\omega\cdot\left(R^2+\frac{1}{2}r^2\right) \qquad (2)$$

where *R* is the major and *r* is the minor radius of the flux surface on which ω is measured. The mass contributed to the plasma by each electron is the mass of deuterium, m_D, independent of Z_{eff}, since the major plasma constituents, i.e. ^{2}H, ^{4}He and ^{12}C, have nuclei with equal number of neutrons and protons.

Angular momentum slowing down time

Directly after the neutral beam power is turned off, the toroidal angular momentum density measured with the X-ray crystal spectrometer is first observed to decay in an irregular manner (typically for about 0.2-0.5 sec). For most discharges, this is followed by a phase of exponential decay (see Fig.4). The first phase reflects the change of the radial profile from driven steady state to source free profile.

We assume that after this phase the profile decays exponentially as a whole, and that the decay time constant measured at $\rho=\langle\rho\rangle$ is representative of the global toroidal slowing down time. We analyse this decay by performing a least squares fit of the data to

$$\ell(t) = \ell_\infty + \ell_0 \exp\left(\frac{t - t_0}{\tau_\ell}\right) \tag{3}$$

The start of the time interval, t_0, is determined by maximising the significance of the fit. Furthermore we require that data of good time resolution (i.e. better than $\tau_\ell/3$) and statistical accuracy are observed for at least three decay times, and that the plasma conditions during the whole time, like plasma current, heating method, X-point phase etc., are constant. Discharges where the decay appears not to be exponential are not included in the data base.

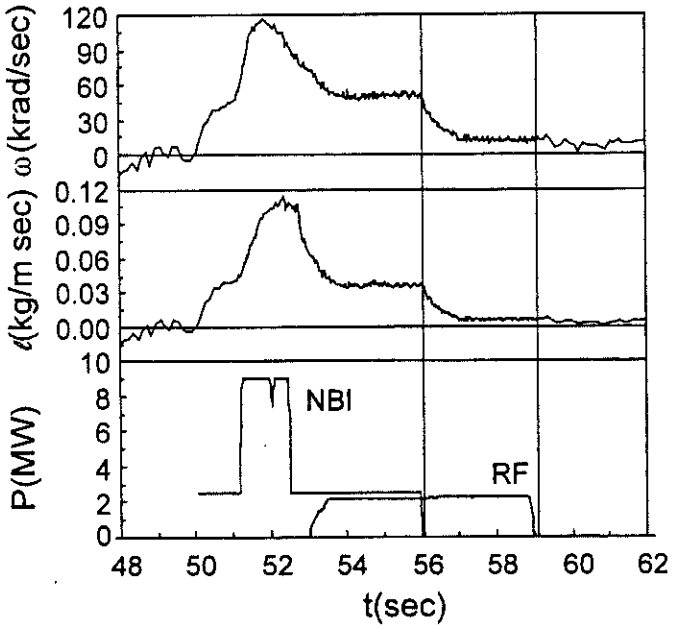

Fig.4: Top: Toroidal angular velocity, ω, measured with X-ray crystal spectroscopy. Centre: Derived toroidal angular momentum density, ℓ. Bottom: Neutral beam and radio frequency heating power. (From JET-#31898)

The best fit to the angular momentum density between t=56.03 to 59.07 is given by τ_ℓ =0.36 0.01 sec, see Eq. (3). During the same time interval one would get τ_ω=0.43 ±0.01 sec.

The energy replacement time for the same time interval is τ_E=0.24 0.05 sec.

Angular momentum and energy replacement time

During NBI we integrate the angular momentum density profile to obtain the total angular momentum, *L*, of the plasma. The torque, *M*, exerted by the neutral beams on the plasma, is calculated from an analytical beam deposition code, that takes the measured local impurity densities into account. Thus we obtain the global angular momentum replacement time as

$$\tau_L = \frac{L}{M - \frac{dL}{dt}} \tag{4}$$

During NBI we integrate measured electron and ion energy densities to obtain the total thermal energy, W_e+W_i. From the beam deposition code, we also calculate the fast energy content, W_{fast}. Thus we obtain the global energy replacement time as

$$\tau_E = \frac{W_e + W_i + W_{fast}}{P - \frac{d(W_e+W_i+W_{fast})}{dt}} \tag{5}$$

In this paper we restrict ourselves to quasi steady state conditions, $dL/dt < 0.1M$ and $dW_{tot}/dt<0.1P$. This is typically achieved after 0.5-1.0 secs of neutral beam injection at constant beam power. By this time the shine through of the neutral beams is only a few percent.

Outside the NBI phase only the electron energy density profile is available. The diamagnetic loop measurements are not accurate enough as a measure of the stored energy just after the NBI phase to derive the energy replacement time from them. We therefore approximate W_i as W_e $Ti(Ni^{+26})/T_e(<\rho>)$.

Fig. 5 shows a comparison of W_{tot} with both methods. The good agreement during the NBI phase between the simple approximation and the integration of the profiles is mainly due to the off-axis measurement of the ion temperature of Ni^{+26}. There is no volume at ρ=0, and $dV/d\rho$ increases faster than linear with . Thus the main contribution to the thermal energy is in fact from volume elements around ρ=0.3-0.5, where the measurement is performed.

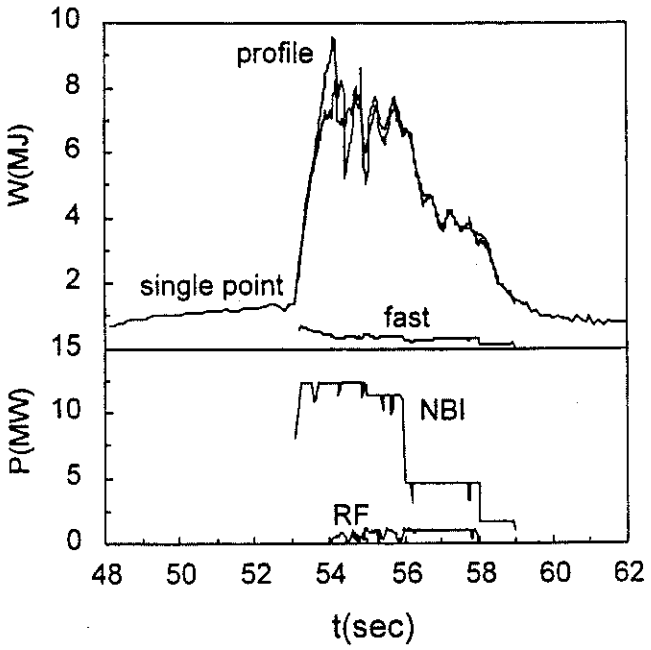

Fig.5: Top: Comparison of estimated stored energy using the single point ion temperature (Ni^{+26}), with the result from integration of the measured radial profiles of ion temperature (C^{+6}) and density. In both cases the electron energy is calculated from the radial profiles of electron temperature and density. Also shown is the calculated fast ion energy. Bottom: Neutral beam and radio frequency heating power. (From JET-#31894)

RESULTS AND DISCUSSION

A comparison of τ_ℓ with $_E$ is shown in Fig. 6 for discharges with and without radio frequency heating. Fig. 7 shows the corresponding comparison of τ_L with τ_E. It can be seen that $\tau_\ell > \tau_E$, i.e. without neutral beam heating. There are no data with τ_E significantly larger than τ_ℓ.

During NBI we find $\tau_L = \tau_E$ within the errors of the measurement. The dominant driving terms, i.e. neutral beam heating and toroidal torque, have similar radial profiles. Energy and toroidal momentum are however subject to different internal and edge losses, i.e. energy transfer between ions and electrons, radiation, ripple damping, and momentum transfer by charge exchange. Nevertheless both replacement times come out the same, in agreement with the result obtained on ASDEX [1].

In Fig. 8 we present the scaling of τ_E/τ_L and τ_E/τ_ℓ with $(W_i+W_{fast}-W_e)/W_{tot}$. This quantity is negative if the plasma energy is mostly in electrons, and positive if it is mostly in ions. The latter is the normal situation with NBI. From this figure we conclude that τ_E can at best approach τ_L (and τ_ℓ) when the plasma energy (and thus the energy confinement) is dominated by ions, and that it is smaller if the plasma energy is dominated by electrons.

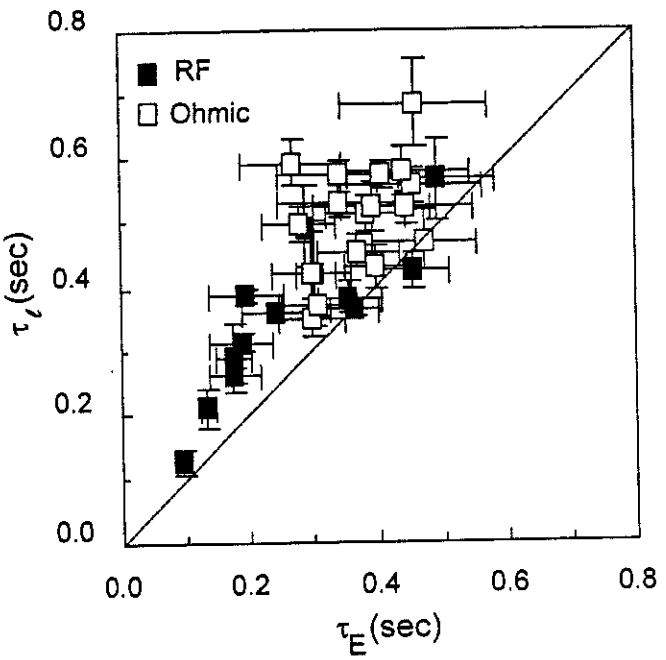

Fig.6: Time constant for exponential decay of the angular momentum density after neutral beam injection vs. simultaneously measured energy replacement time.

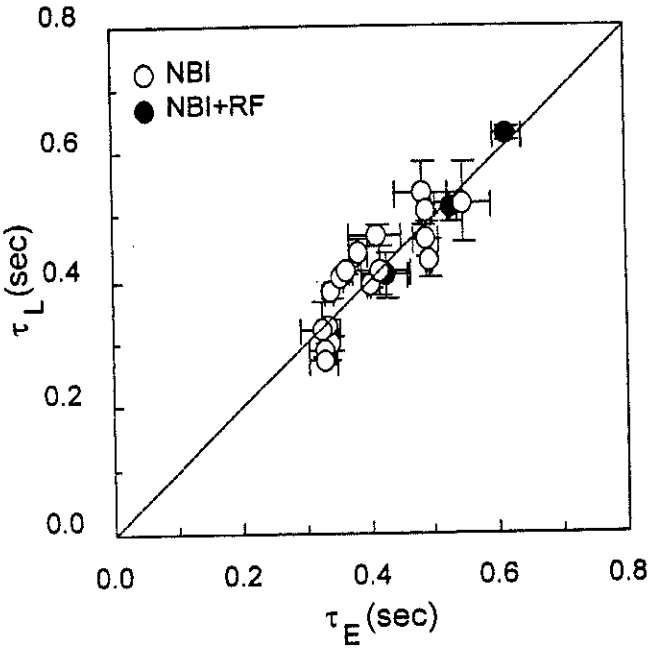

Fig.7: Angular momentum replacement time during neutral beam injection vs. simultaneously measured energy replacement time.

There is no evidence of stronger deterioration of the confinement of angular momentum compared to energy with combined neutral beam and RF heating within our data base, probably since the RF heating power during NBI accounts for less than 10% of the total heating power (see Fig. 9). Note, however, that the example shown in [5] was obtained at 1.8 MW of RF power, compared to 15 MW of NBI power. When RF heating is the dominant heating power, it can be seen that the energy replacement time without neutral beam injection degrades faster than the angular momentum decay time. This is consistent with the relative increase of the electron energy content of the plasma as shown in Fig. 8. An alternative explanation would be that there is a torque associated with RF power [6]. This should affect the steady state value, ℓ_∞, compared to discharges without RF heating, which is not seen within our data.

It has been suggested [4] that the reduction of central angular velocity in combined heating discharges is due to a coupling of RF power to the fast particles, scattering them into trapped orbits where they would not contribute to the torque but instead to heating. This explanation is consistent with our observations after neutral beam injection, i.e. that RF heating alone does not reduce momentum confinement whilst simultaneously improving energy confinement.

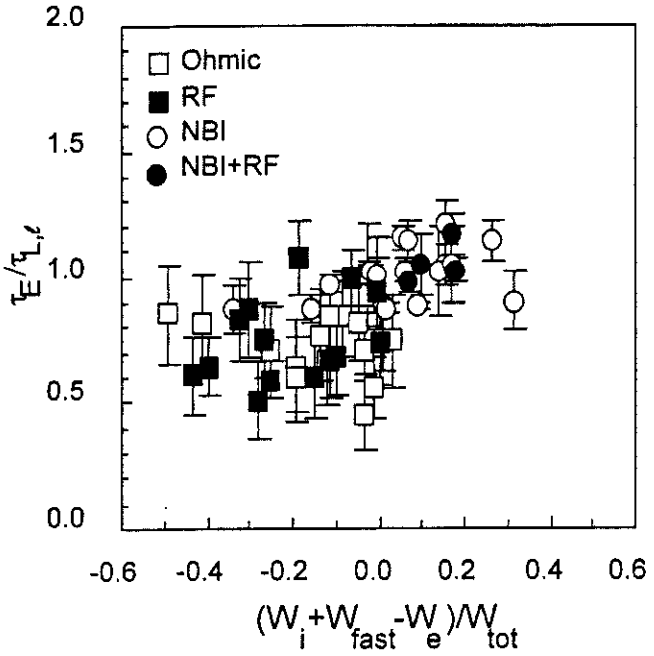

Fig.8: Scaling of the ratio of energy replacement time to angular momentum replacement time and slowing down time, respectively, with relative contribution of ions or electrons to the energy content

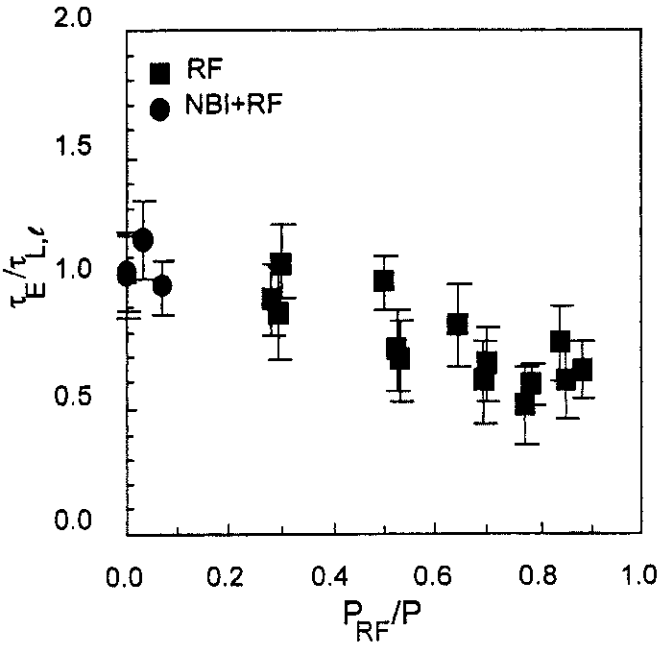

Fig.9: Dependence on the fraction of RF heating power to total heating power.

REFERENCES

[1] A Kallenbach et al, Plasma Phys. Contr. Fusion **33**, 595(1991)

[2] S D Scott et al, Phys. Fluids **B2**, 1300 (1990)

[3] H P L deEsch et al, 17th EPS Conf. Contr. Fusion and Plasma Heating, Amsterdam 1990, Part I, 89

[4] D Stork et al, 14th EPS Conf. Contr. Fusion and Plasma Physics, Madrid 1987, Part I, 306

[5] D O'Brien et al, 21st EPS Conf. Contr. Fusion and Plasma Physics, Montepellier 1994, Part I, 125

[6] L-G Eriksson et al, Plasma Phys. Contr. Fusion **34**, 863(1992)

The Optimization of Recycling in High Performance Hot-Ion H-Mode JET Discharges

K D Lawson[1], R W T König, R Sartori, N Deliyanakis, M G von Hellermann, T T C Jones, P J Lomas, A C Maas, F B Marcus, B Schunke, P Smeulders, M F Stamp, P R Thomas.

JET Joint Undertaking, Abingdon, Oxfordshire, OX14 3EA, UK.

[1] UKAEA Government Division, Fusion, Culham, Abingdon, Oxfordshire, OX14 3DB, UK.

(UKAEA/Euratom Fusion Association)

INTRODUCTION

The JET machine was upgraded for the 1994/95 operational campaign by the installation of 4 internal divertor coils, protected by arrays of Carbon Fibre Composite (CFC) tiles and a cryopump (Bertolini 1994), these all being toroidally continuous. The plasma volume in this new design is 20 % smaller.

In hot-ion H-mode high performance discharges an immediate difference was observed in the frequent ELM behaviour compared with earlier operations in which the ELMs had to be actively induced through strong gas-puffing, the use of hydrogen fuel or operation in high β regimes.

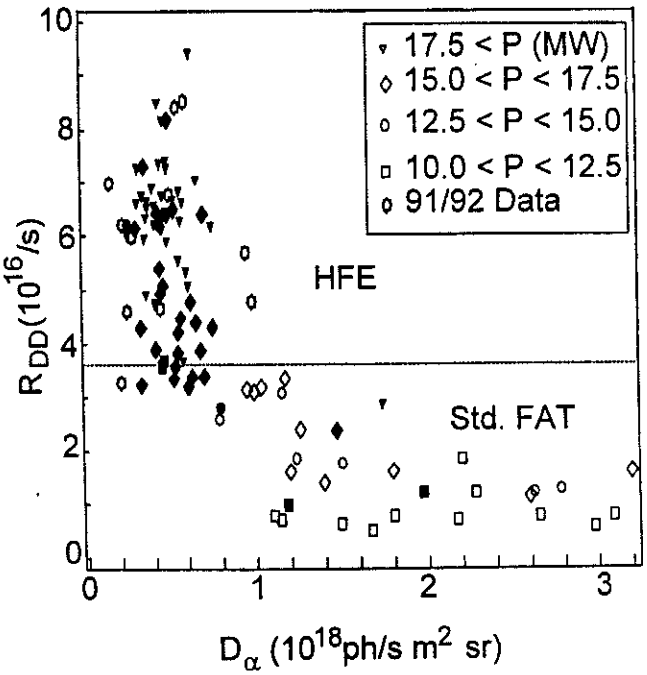

Figure 1: DD reaction rate vs vertical Dα intensity sorted by neutral beam input power P (MW) for High Flux Expansion (HFE) and standard FAT configurations. Filled symbols refer to pulses with cryopump.

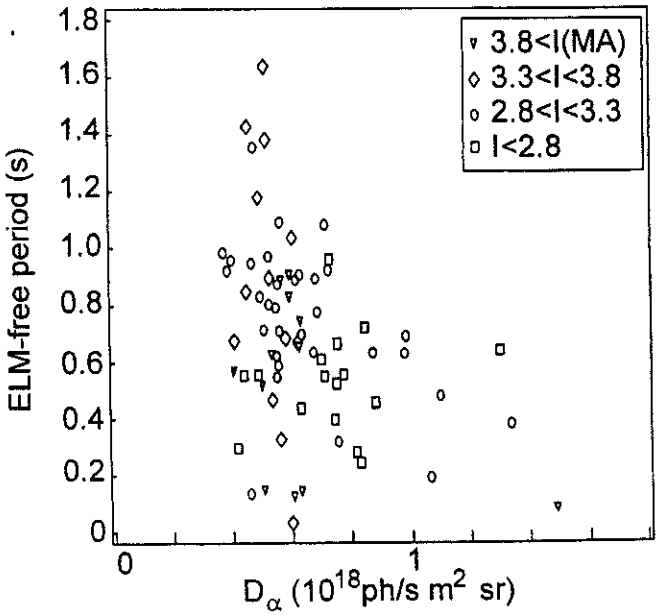

Figure 2: ELM free period vs vertical Dα intensity sorted by plasma currrent I (MA)

Correlations have been found between the peak reaction rate achieved during a pulse (figure 1) and the ELM free period (figure 2) with the particle influx as measured by the D_α line intensity, this providing the impetus for a study of the recycling behaviour in these discharges. Detailed modelling of the recycling is being dealt with by McCormick et al. (1995).

VESSEL CONDITIONING

- For the present campaign, the area of the vessel walls covered with CFC tiles has been reduced. The metallic (Inconel) inner and outer walls are protected by a number of poloidal belt limiters.
- During operations, conditioning has been achieved by D and He GDC and the use of 2 or 4 Be evaporators.
- Both the baking (300 °C) and operating temperatures (250 °C) have been reduced from those used in previous campaigns (350 and 300 °C, respectively), these being limited by the risk of possible damage to the divertor coil epoxy. While an increase in the operating temperature to 320 °C improved conditioning, little difference was observed with regard to the performance.
- The divertor tiles are mounted on water cooled supports kept at 40 °C between pulses.
- The divertor cryopump became available in August 1994 and the improvement in pumping is evident from figure 1 which includes pulses with and without cryopump. A clear reduction in the particle influx is normally observed when the cryopump is used (see also Saibene et al.).
- Figure 1 also has data from some of the best high performance discharges run during the 1991/92 operations. The D_α line intensity is comparable with measurements for the best pulses in the 1994/95 campaign.

CONFIGURATION

- In the 1994/95 campaign, even when low recycling was achieved, only a change of the magnetic configuration from the 'Standard FAT' to a 'High Flux Expansion' (HFE) configuration allowed access to a high performance regime with reaction rates > 3.5×10^{16} s^{-1}. This change was due to improved stability against ELMs as evidenced by an increase in the ELM-free period, this hardly exceeding 0.5 s in the 'standard FAT' configuration.
- Figure 3 shows the limited flux expansion that is possible in the 'standard FAT' configuration.
- Higher triangularities (figure 4) and elongations (figure 5) were achieved in the HFE configuration which have a stabilizing effect on edge pressure gradient driven modes due to the higher edge shear

(figure 6). Figures 4 to 6 show that although the optimization of these parameters was found necessary for the achievement of long ELM-free periods, other parameters must be considered to explain the wide range of performance subsequently achieved.

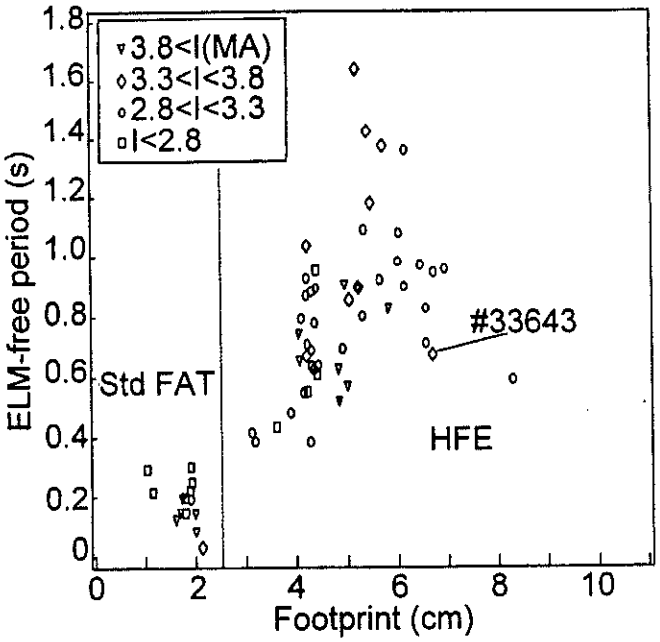

Figure 3: ELM free period vs footprint on the divertor floor of SOL flux surface 1 cm width at the plasma midplane sorted by plasma current I (MA) (footprint for pulse 26087 ~18 cm)

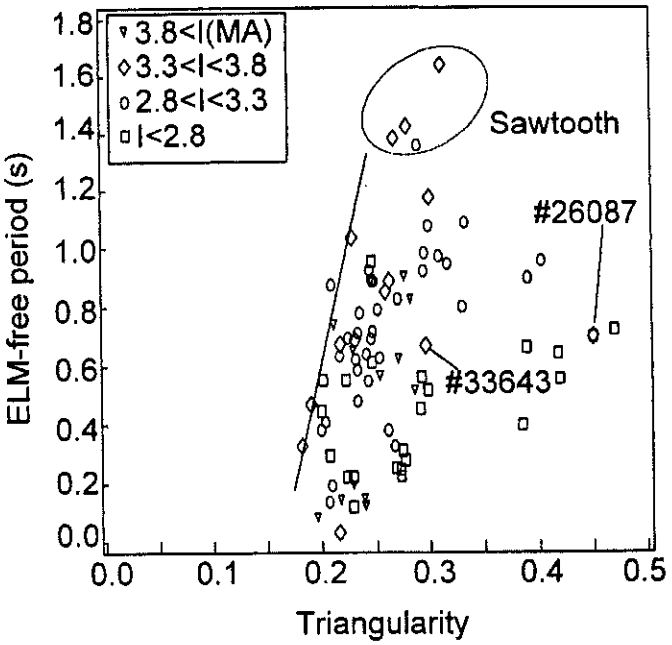

Figure 4: ELM free period vs triangularity sorted by plasma current I (MA)

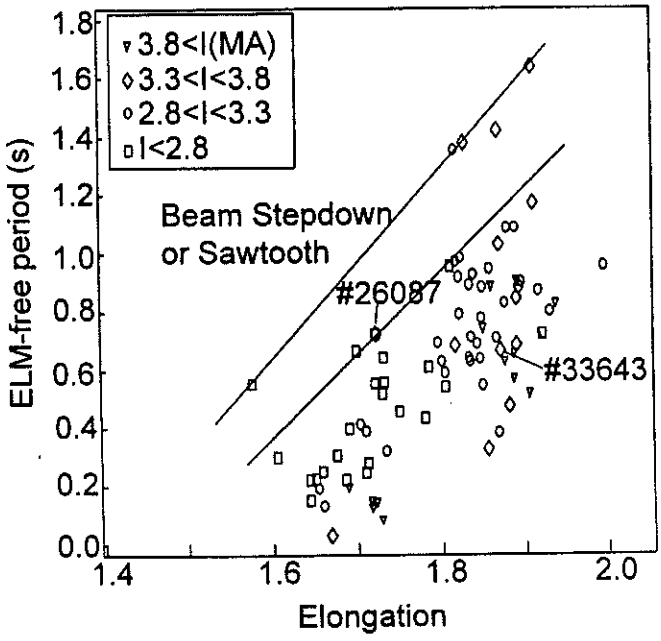

Figure 5: ELM free period vs elongation sorted by plasma current I (MA)

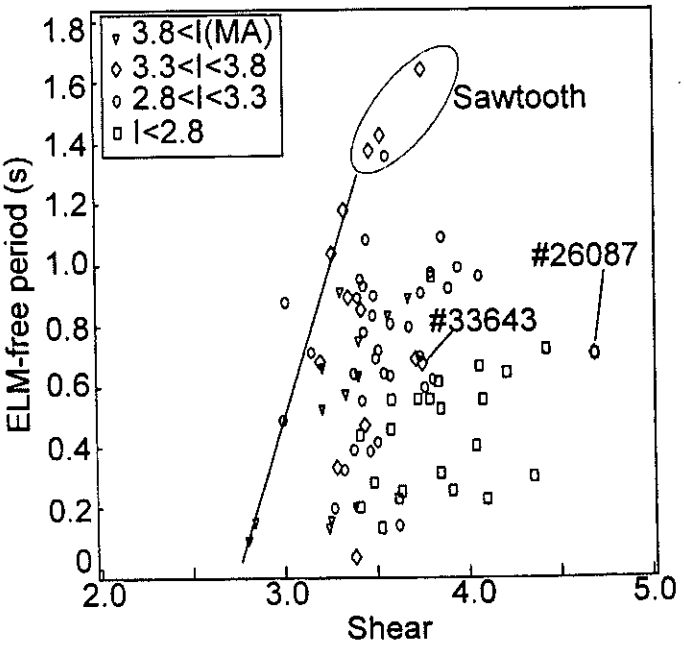

Figure 6: ELM free period vs shear at 95% flux surface sorted by plasma current I (MA)

BEAM DEPOSITION

- Of crucial importance in achieving high performance in the hot-ion regime is a low target density, which in the present campaign, is limited by the maximum permitted beam shine-through. This is illustrated in figure 7, this diagram including all of the best 30 pulses of the current operations.
- A low target density requires a sufficiently low level of recycling. In pulses having the best conditioning, the increase in the total D count corresponded to or could even fall below the beam fuelling rate. Figure 8 illustrates two such low target density pulses, 33643 and 33680. In the latter the gradient of the total deuterium content of the plasma approximately matches the beam fuelling particle flux. In the highest performance pulse 33643, the pumping is so strong that the beam fuelling is insufficient and D gas fuelling is required to maintain the plasma density. More usually in these hot-ion H-mode discharges the density rise exceeded the beam fuelling rate by ~3-4×10^{20} particles/s.

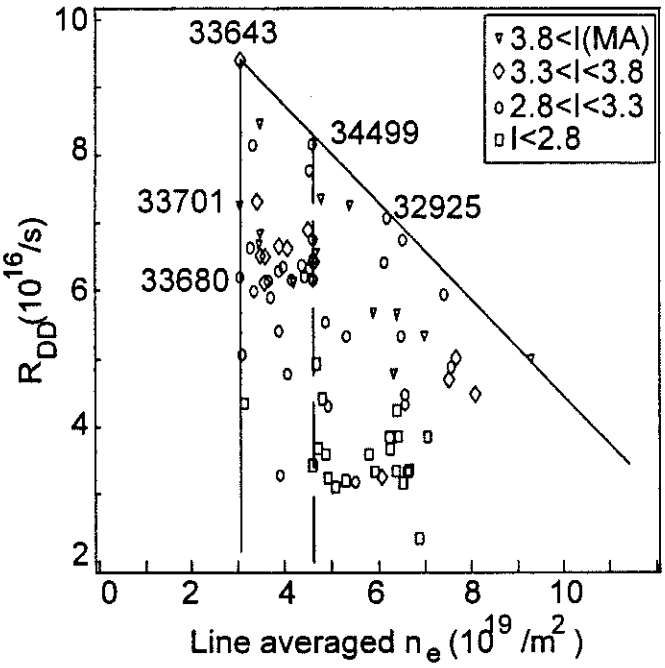

Figure 7: DD reaction rate vs line averaged target electron density sorted by plasma current I (MA). The solid lines mark the boundary of the operational space

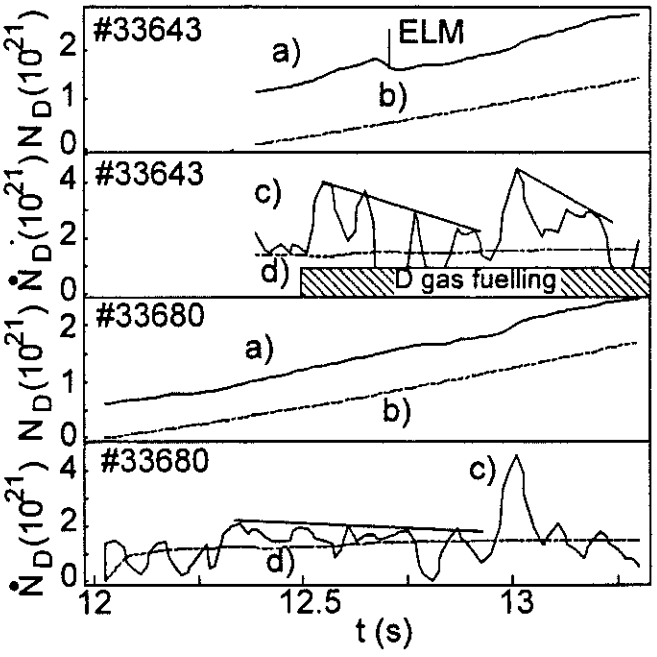

Figure 8: a) total number of deuterons in the plasma and its derivative c), b) total number of deuterons injected by NBI and its derivative d) for two low target density pulses. Pulse 33643 has gas fuelling.

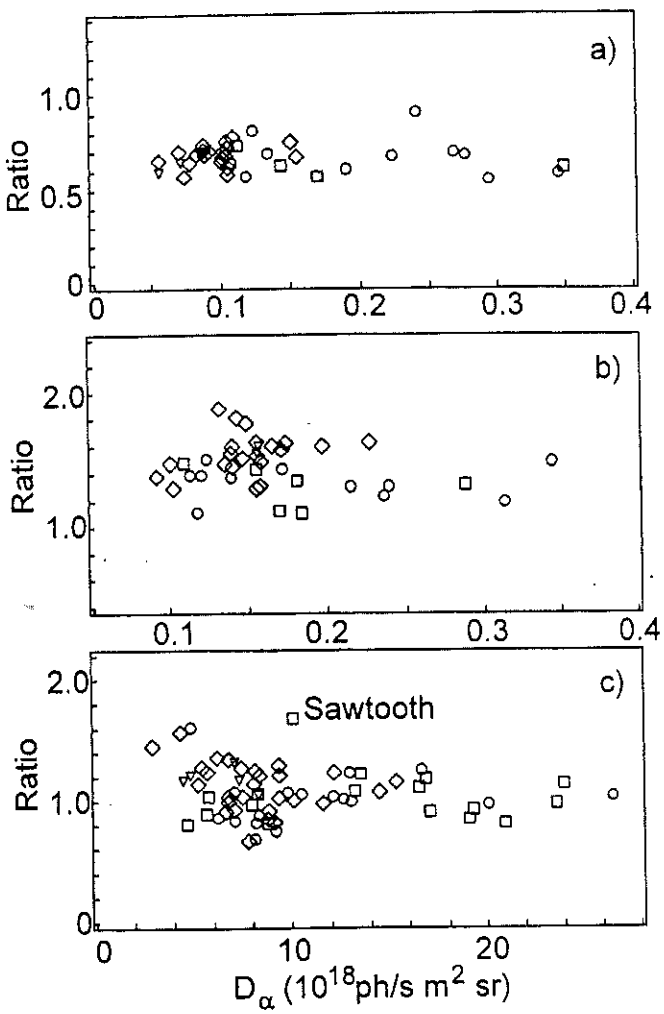

Figure 9:

a) Inverse peaking factor of beam particle deposition at start of NBI vs horizontal D_α. The peaking factor is defined as the ratio of the number of particles deposited between a normalized minor radius of 0.0 and 0.55 to those deposited between 0.55 and 0.85.

b) Ratio of initial to final peaking factors of beam deposition vs horizontal D_α. The initial value is taken at the start of NBI; the final value is taken at the roll-over of R_{DD}.

c) Ratio of initial to final n_e peaking factors vs divertor D_α. The peaking factor of n_e is defined as the ratio of electron density integrated between a major radius of 3.35 m and 3.25 m to the electron density integrated between a major radius of 3.8 m and 3.65 m.

Figures sorted by peak R_{DD} , ▽ $8\times10^{16}\leq R_{DD}$, ◇ $6\times10^{16}\leq R_{DD}<8\times10^{16}$, ○ $4\times10^{16}\leq R_{DD}<6\times10^{16}$, □ $R_{DD}<4\times10^{16}$.

- An extensive investigation of the effect of the particle influx on the beam deposition and n_e profiles showed no marked dependence, figure 9. The effect of beam deposition on the neutron emission profiles is discussed by Marcus et al. (1995). A clear effect is seen on the neutron emission profile but not on the total neutron yield.
- The evolution of the n_e and beam deposition profiles are illustrated for the highest performance pulse 33643. This is a 3.7 MA discharge, with D fuel and 18.5 MW of D NBI. An overview of the plasma parameters is shown in figure 10. In figure 11, it can be seen that, as n_e rises, the beam particles are deposited increasingly towards the plasma edge. The same behaviour is found for the power deposition profiles.

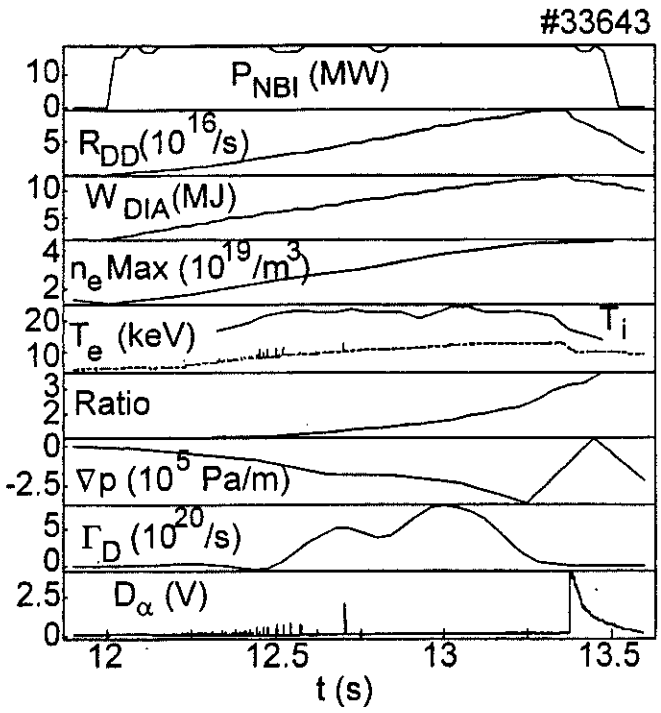

Figure 10: Overview of plasma parameters for pulse #33643, neutral beam power, DD reaction rate, total stored energy from the diamagnetic loop, maximum electron density from LIDAR, electron and ion temperature, ratio of particles deposited between normalized minor radius ρ=0.7 and ρ=1 to those deposited inside a ρ=0.3, electron + ion pressure gradient at R=3.77 m, deuterium gas influx rate, vertical Dα intensity

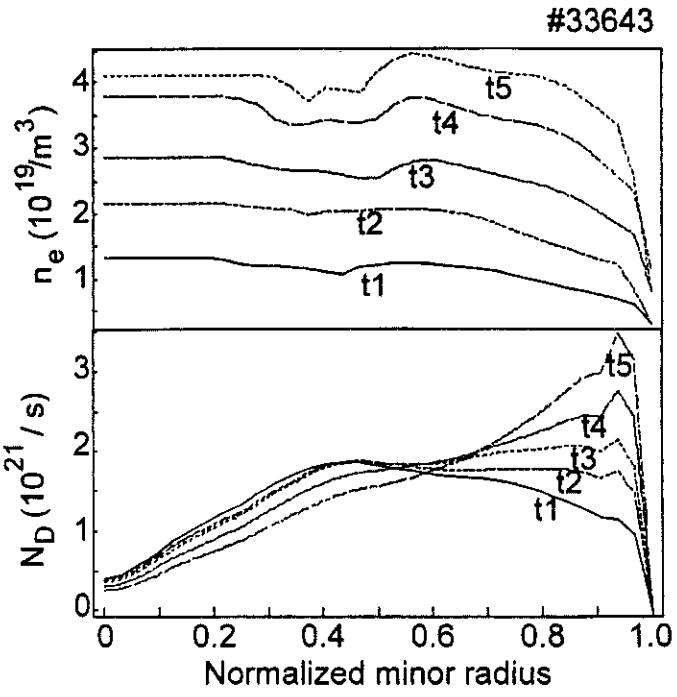

Figure 11: Electron density and calculated neutral beam particle deposition (integrated over flux surface) profile evolution vs normalized minor radius at t1=12.0 s, t2=12.4 s, t3=12.8 s, t4=13.1 s, t5=13.3 s.

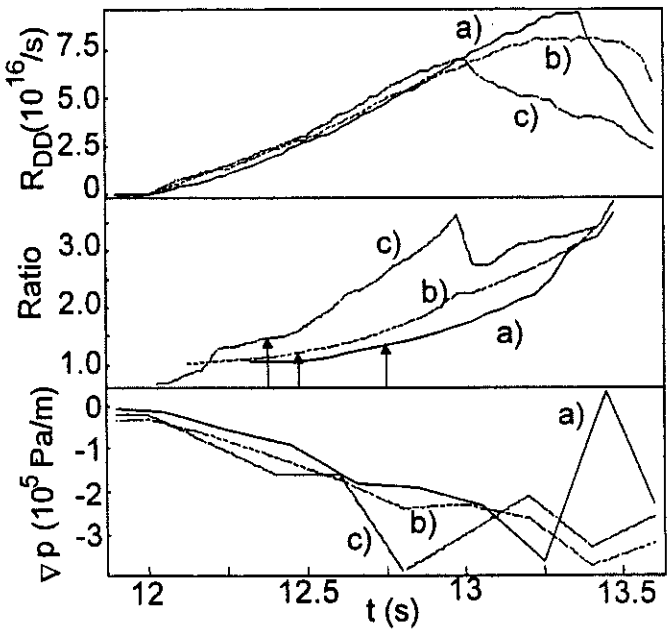

Figure 12: DD reaction rate, ratio of particles deposited as defined in fig.10 and electron + ion pressure gradient at R=3.77 m vs time for a) pulse 33643, b) pulse 34499, c) pulse 32925, which have different target densities. The ↑ indicates the end of the threshold ELM period.

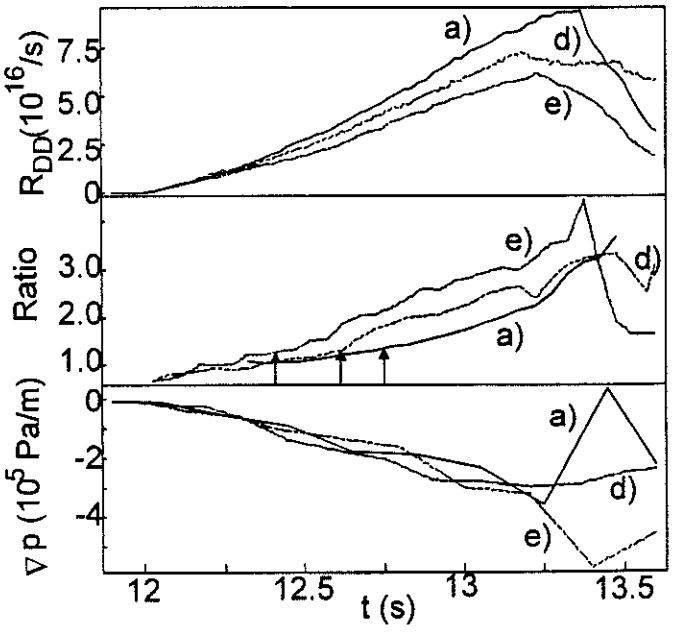

Figure 13: DD reaction rate, ratio of particles deposited as defined in fig.10 and electron + ion pressure gradient at R=3.77 m vs time for a) pulse 33643, d) pulse 33701, e) pulse 33680, which have the same target density. The ↑ indicates the end of the threshold ELM period.

- This effect is summarized in the deposition profile ratios shown in figure 12 and 13 for the pulses along the boundaries marked in figure 7. It is observed that the turnover in R_{DD} occurs at a ratio of ~2-3.
- The edge pressure gradients are determined from LIDAR n_e and T_e measurements and charge exchange spectroscopy n_i and T_i data which come from a new high resolution edge diagnostic. When data from reflectometry and hetrodyne ECE radiometry are available these are included in the calculation of the pressure profile. The best available edge pressure gradients are shown for the same pulses in figures 12 and 13.
- A correlation is observed between the duration of the threshold ELMs and the delay in the rise of the beam deposition ratios. The longer this delay the more the terminating instabilities are postponed and the higher the neutron yield. Among such instabilities, of particular concern in the present discharges are the giant ELMs (Hender et al., 1995) and the slow rollovers (Smeulders et al., 1995).
- Choosing pulses at a constant target density, the threshold ELM duration shows a relation to the particle influx as measured by D_α, figure 14, this being a possible additional explanation for the benefit of low recycling in achieving high performance.

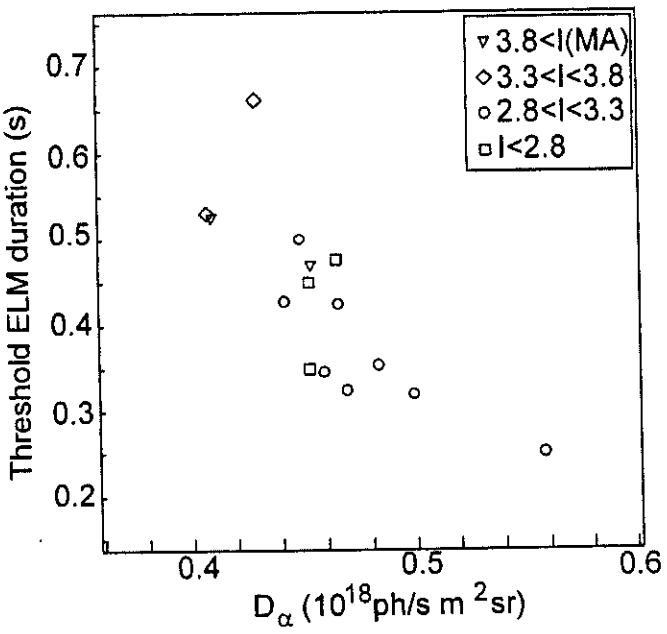

Figure 14: Duration of threshold ELMs vs vertical Dα sorted by plasma current I (MA), at constant target density for pulses along dashed line of figure 7.

In figures 15 and 16 a comparison is made for two 'standard FAT' discharges, pulse 32285 being run with the cryopump and pulse 32270 without. The poorer resilience of this configuration to edge instabilities can be seen in the shorter ELM-free period and more frequent ELMs than was observed for pulse 33643 (figure 10). The cryopump leads to the lower levels of D_α intensities in pulse 32285 and this pulse also has a longer threshold ELM duration and a delayed build-up in the beam deposition profile ratio. As for the HFE configuration, the ratio reaches values of ~2-3 at the onset of the terminating ELMs.

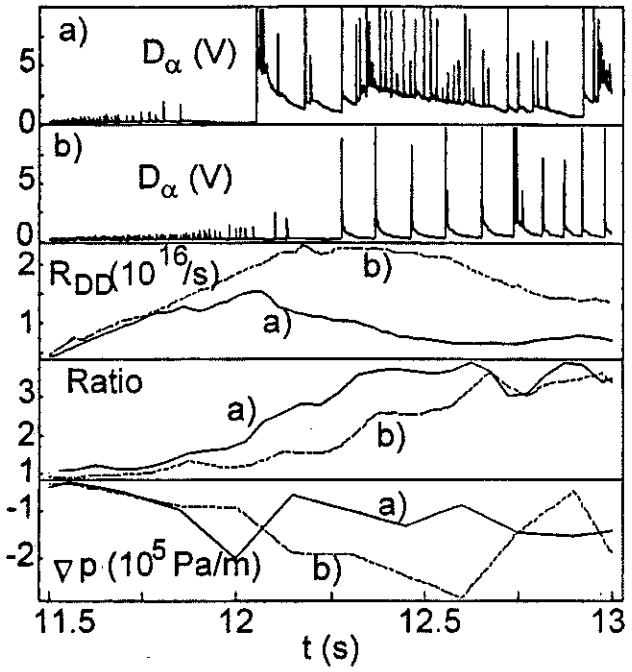

Figure 15: Comparison for standard FAT configuration pulses a) #32270 (without cryopump) and b) #32285 (with cryopump) of vertical Dα intensity, DD reaction rate, ratio of particles deposited between normalized minor radius ρ=0.7 and ρ=1 to those deposited inside ρ=0.3 and electron + ion pressure gradient at R=3.77 m.

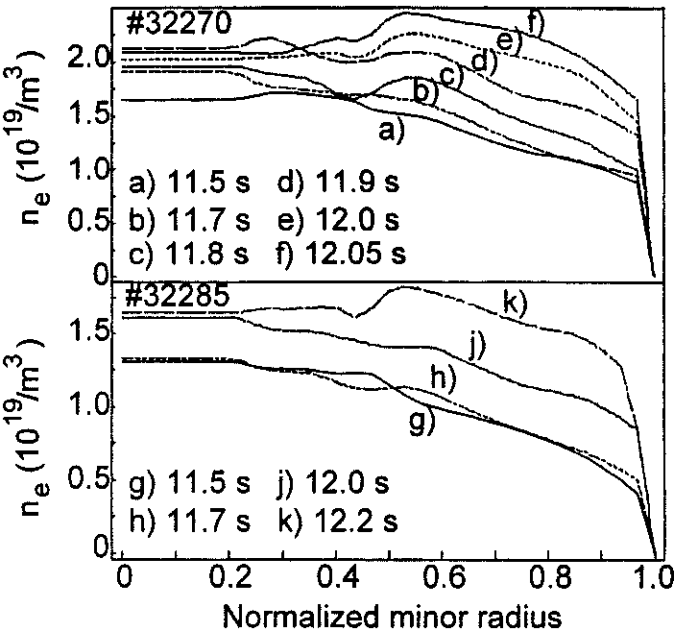

Figure 16: Electron density profile evolution for standard FAT configuration pulses #32270 (without cryopump) and #32285 (with cryopump).

CONCLUSIONS

The performance of hot-ion H-mode discharges depends crucially on the lowest target densities being achieved, this requiring low recycling. Although no correlation has been found between the deposition of neutral beams and recycling, a tentative relation is suggested between recycling and the duration of the threshold ELMs. These delay the unfavourable build-up of beam deposition in the plasma edge, which leads to the onset of the terminating instabilities.

E Bertolini and the JET Team, Proc. 18th Symposium on Fusion Technology, Karlsruhe 1994, submitted for publication in Fusion Engineering and Design

T Hender et al., 1995, this conference

F Marcus et al., 1995, this conference

K McCormick et al., 1995, this conference

G Saibene et al., 1995, this conference

P Smeulders et al., 1995, this conference

Effects of Active Pumping and Fuelling on Divertor Plasma Discharges in JET

G Saibene, M L Apicella[1], K Bart, D J Campbell, J K Ehrenberg, P J Harbour, L D Horton, C G Lowry, A Loarte, R D Monk[2], W Obert, A Rossi, R Sartori, D Stork, E Thompson.

JET Joint Undertaking, Abingdon, Oxfordshire, OX14 3EA, UK.

[1] Associazione Euratom-ENEA sulla Fusione, CRE Frascati, 00044 Frascati (Rome), Italy

[2] Dept of Physics, Royal Holloway College, University of London, Surrey, TW20 0EX, UK.

1. INTRODUCTION

Active particle control is required for steady-state operation in a reactor. The study of the effects of fuelling and active pumping on plasma properties has been one of the main topics of the JET Mk I 1994-95 experimental campaign. The new in vessel divertor cryopump has been routinely used to provide active pumping during plasma pulses. This paper presents an overview of the experiments carried out to study and characterise the influence of active pumping on the main plasma and divertor parameters. Results are presented for pure Deuterium plasmas. The effect of SOL flows on impurity penetration in the plasma is presented by HARBOUR (this Conference).

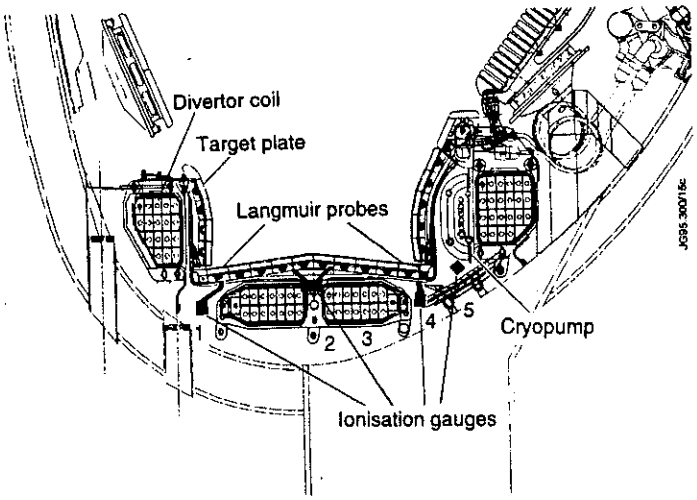

Figure 1 : poloidal cut of the divertor region, showing the location of the divertor cryopump and of the fast ionisation gauges in the sub-divertor region. The rows of tiles in the Mark I divertor are separated by gaps, accounting for approximately 10% of the total area.

1. THE FUELLING SYSTEM

Gas can be introduced into the machine from 10 modules, individually controllable. Each gas module feeds internal manifolds that provides a distributed source for the plasma.

- Two gas modules in the outer midplane
- Four modules at the top of the machine to provide poloidally uniform fuelling in the main SOL.
- Finally, four modules are in the divertor, which fuel gas into the private flux region with toroidally uniform gas inlets.
- The capability for D fuelling is of the order of 5×10^{22} D° s^{-1} steady state.

2. THE PUMPING SYSTEM

- Active particle removal during plasma discharges is provided by a toroidally continuous cryopump, located below the divertor plates (figure 1). The cryopump is operated at around 4.6 K (supercritical He), therefore all gases but H_2 and He are efficiently pumped by cryosorption.
- The pump is equipped with internal nozzles to spray and condense Ar on the He panels, to allow pumping of He and H_2 by cryotrapping.
- The effective Deuterium pumping speed of the cryopump on the vacuum vessel, including the obstruction represented by the divertor modules, is about 160 m^3s^{-1}. The speed of the pump, measured near the LN shields, is higher, about 240 m^3s^{-1}, or $\approx 1x10^{25}$ atoms $mbar^{-1}s^{-1}$.

3. DEUTERIUM PUMPING DURING PLASMA DISCHARGES

3a. Particle removal in Ω, L and H mode regimes.

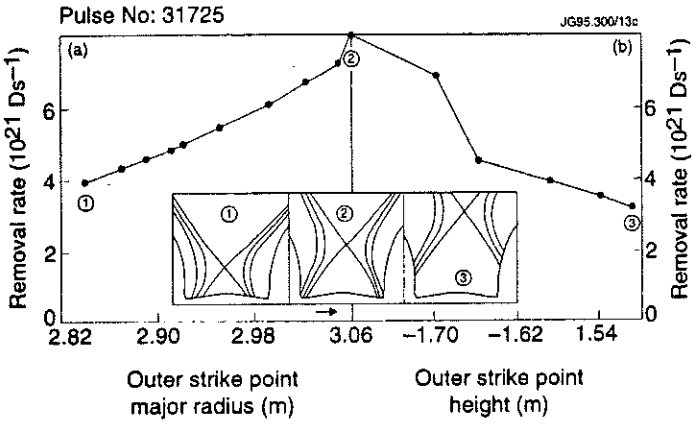

Figure 2: particle removal rate in atoms per second as function of the separatrix position, on the horizontal (a) and vertical plates (b). Pulse # 31725, 2MA, 2T. The sweep of the separatrix is carried out over 10s.

- Due to the gaps between tiles in the Mk I divertor target, particles are pumped for all separatrix positions on both the horizontal and vertical plates. The particle removal rate varies only by a factor of two, for any separatrix position (figure 2).
- Maximum pumping is obtained with the divertor strike point located in the outer corner of the target (the closest point to the cryopump).

The removal rate is directly proportional to the neutral pressure in the front of the cryopump. For a given separatrix position, this pressure depends on the plasma density and confinement regime :

- In Ohmic and L mode the pressure in the divertor increases with the plasma density
- In Elm-free H modes, both the D_α and the pressure in front of the pump are lower, due to the improved particle confinement. Typical pressures in these cases are around $5x10^{-4}$ mbar.
- However, higher particle pumping is observed during ELMy H modes. In the ELMy phase, pressure bursts in the divertor are measured 10ms after the D_α spikes. The integral particle removal associated with giant ELMs can be of the order of $1\text{-}2x10^{21}D^\circ$, that is of about 30% of the typical plasma particle content. For type 1 ELMs, the integral particle removal varies, up to approximately twice the net plasma inventory loss. The discrepancy between the plasma density loss and the particle removal associated with ELMs indicates that some of the particles removed by the pump are originated by plasma induced desorption from material surfaces.

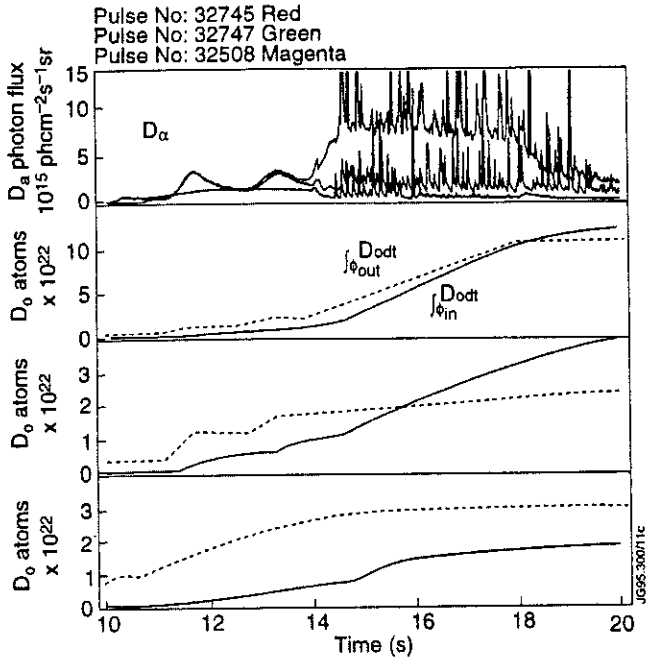

Figure 3: Divertor D_α, integrated fuelling and integrated D^0 removal for 3 ELMy H-modes: # 32747 (3 MA/2.8T, 15 MW, gas fuelled); 32745 (3MA/2.8T, 15 MW NBI, no gas) and 34508 (5MA/3.4T, 18 MW NBI, no gas)

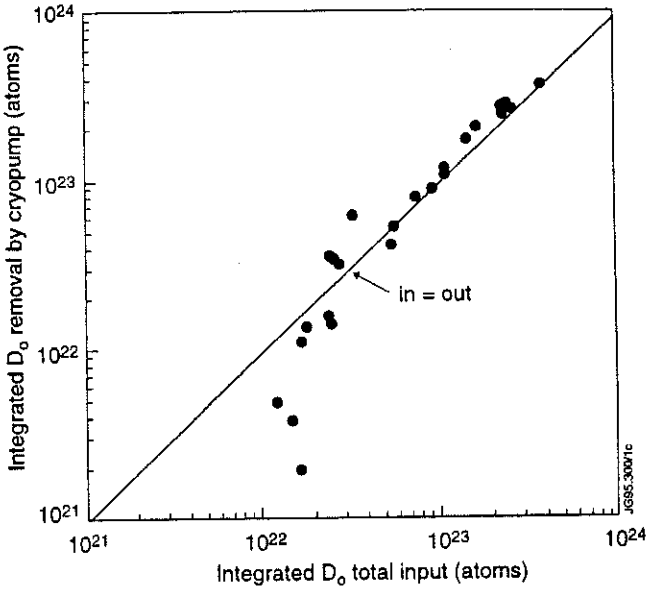

Figure 4: Total D^0 removal as function of total fuelling, for H mode discharges. The total removal can exceed the gas input for long pulses at medium-high density. Low removal fraction is measured in ELM free H modes.

In ELMy H-modes, the particle removal rate also depends on the type of ELM, on the "baseline" recycling level (i.e. on the discharge configuration, density and fuelling) and on the duration of the ELMy phase, figure 3a. For a detailed study of ELMs, refer to LINGERTAT, this conference.

1. Strong gas fuelling during the H mode phase (# 32747), causes an increase of the plasma density and of the ion flux and D_α to the divertor (figure 3b). However, the related increase of the pressure at the pump (and of the particle removal) just compensates for the increased fuelling, and the removal rate is equal to the fuelling. This is a true steady state H mode.
2. During steady state ELMy discharges with no gas fuelling in the H mode phase (# 32745, figure 3), the high removal rate associated to the ELMs exceeds the fuelling provided by the NBI. Net depletion of the Deuterium wall inventory is achieved (figure 3c)
3. For high power, low recycling discharges, (# 34508, see also McCORMICK, this conference), the integrated particle removal is far less than the total input. This is due to the low removal rate and to the short duration of the ELMy phase (figure3d).

3b. Neutral pressure in the divertor and fuelling effects. (also EHRENBERG, this conference).
To assess the influence of the separatrix position on the particle removal efficiency, a plasma discharge was designed in which the separatrix was slowly swept in 10s across both horizontal and vertical divertor plates (see figure 2). This particular configuration was used also to carry out detailed comparisons between pump on and off, and to assess the role of the gas inlet location on divertor parameters and on the fuelling efficiency. Three pulses are compared in detail

(the plasma average density was kept at $3x10^{19}m^{-3}$ for these three pulses) :

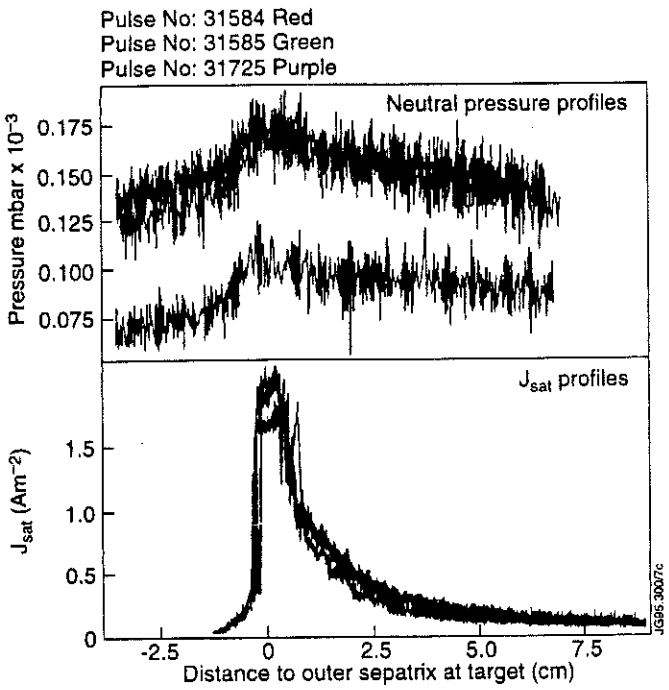

Figure 5: neutral pressure profiles and ion flux profiles for pulses 31584, 31585 and 31725, 2MA 2.8T. The profiles are mapped to the sweeping of the outer separatrix.

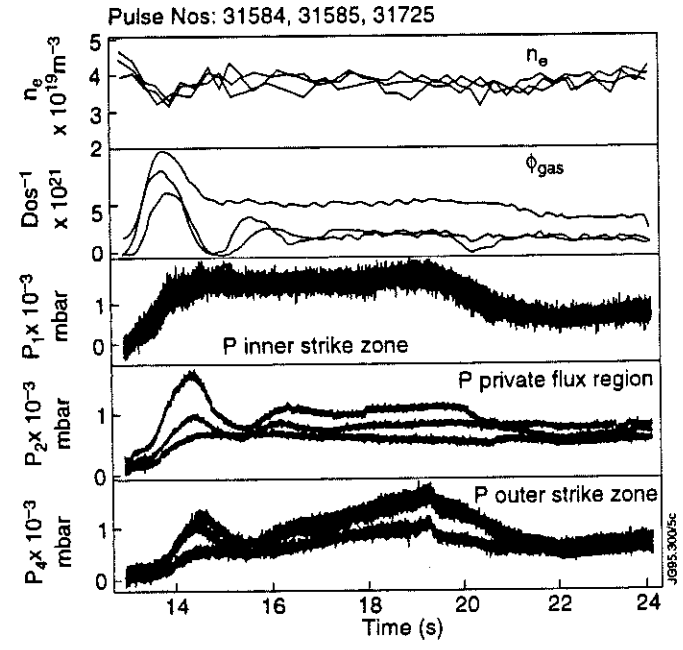

Figure 6: volume average density, gas fuelling rate and pressure in the inner target, private flux region and outer target, for the same pulses as figure 5. The separatrix is on the side plates from 19s .

Pulse number	Cryopump ?	D_2 Fuelling
31584	OFF	TOP
31585	OFF	X-point (PFR)
31725	ON	TOP

- The peak of the neutral pressure profiles (gauge 4) coincides with that of J_{sat}, measured with a triple Langmuir probe sitting at the same poloidal location in the Outer Strike Zone (OSZ).
- When the pump is on, the peak value of J_{sat} decreases by approx. 20%, but the peak pressure goes down by a factor of two.
- The characteristic decay length of the ion flux J_{sat} is 2.5cm, while λ_n for the sub-divertor neutral flux is approximately 15cm, for both the pump on and off cases. This indicates that neutral recirculation plays an important role in determining the neutral distribution. The broad pressure profiles explain the good pumping obtained in every magnetic configuration.
- With the pump off, the plasma detaches at the Inner Strike Zone on the horizontal plate, and reattaches as it goes on the vertical plates (see LOARTE and MONK, this conference). With the pump on, at the same plasma density, the detachment does not occur.
- For #31584, we compared the integrated ion and D_α fluxes to the OSZ (plasma attached) to the neutral flux as measured by the ionisation gauges below the divertor target: these are about $4.6x10^{22}s^{-1}$, and they agree within 25%. When the plasma detaches, the equivalence between ion flux and neutrals in the divertor (as seen both in the pressure and the D_α) no longer holds. This result implies that active particle exhaust can be maintained also for detached plasmas.

- The location of the gas inlets (top or divertor) does not affect the J_{sat} at the target, both with the pump on and off (figure 5). The same is observed for the neutral pressure, with the exception of the PFR. The variation of the global fuelling efficiency with the fuelling location is small, in particular when the pump is off (see HARBOUR, this conference). The global fuelling efficiency decresed with the pump on from 10% to 2%.

3c. Effects of active pumping on plasma parameters

- The changes in H-mode discharges when the cryopump is on are:

1. reduction of the D_α intensity both in the main chamber and in the divertor with a corresponding decrease of the ion flux J_{sat} to the target
2. increase in the plasma stored energy, central ion temperature T_i and neutron rate R_{DD}.

- These changes are more pronounced in plasma configurations with a medium-high "intrinsic" level of recycling (for the analysis of the influence of recycling on high performance plasmas, see LAWSON and McCORMICK, and STORK for steady state H-modes).
- The improved performance can be correlated with the changes in the density profiles for pumped plasmas. For pumped discharges, the edge density (inside the separatrix) is generally reduced, and more peaked temperature profiles are measured. This is consistent with reduced recycling from the wall, and an improved neutral beam penetration.

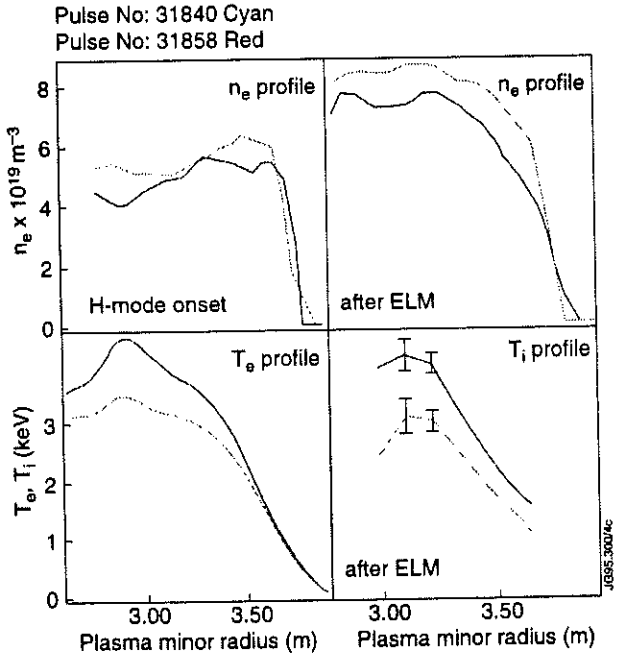

Figure 7: Density and temperature profiles inside the LCFS, for pulses #31840 (pump off) and 31858 (pump on), both at 2.5MA/2.4T. Clockwise from top-left: n_e profiles at the onset of H-mode, n_e profiles between ELMs, T_i and T_e profiles between ELMs.

- For steady state ELMy H modes at medium-high density (fig. 7), the changes of the profiles and peak values with active pumping are particularly pronounced, both in between and during ELMs.

- The time traces for the 2 pulses of figure 7 are shown in figure 8. Note that although the "pump on" pulse (#31858) has only 8MW of additional heating instead of 10MW (#31840, pump off), #31858 has the same stored energy and higher D-D reaction rate than 31840.

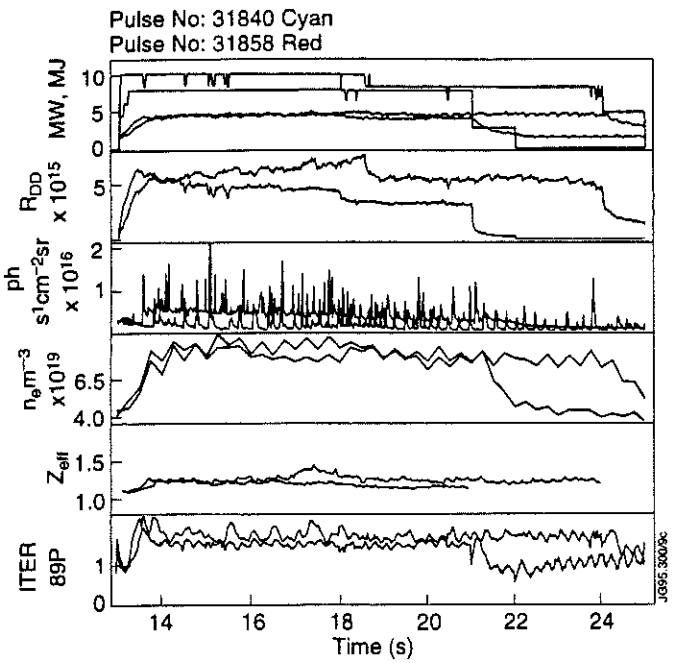

Figure 8: NBI power, stored energy, D-D reaction rate, divertor D, central average density, Z_{eff} and H factor (ITER89-Lmode), for #31840 (pump off) and 31858 (pump on). No gas feed during the H-mode.

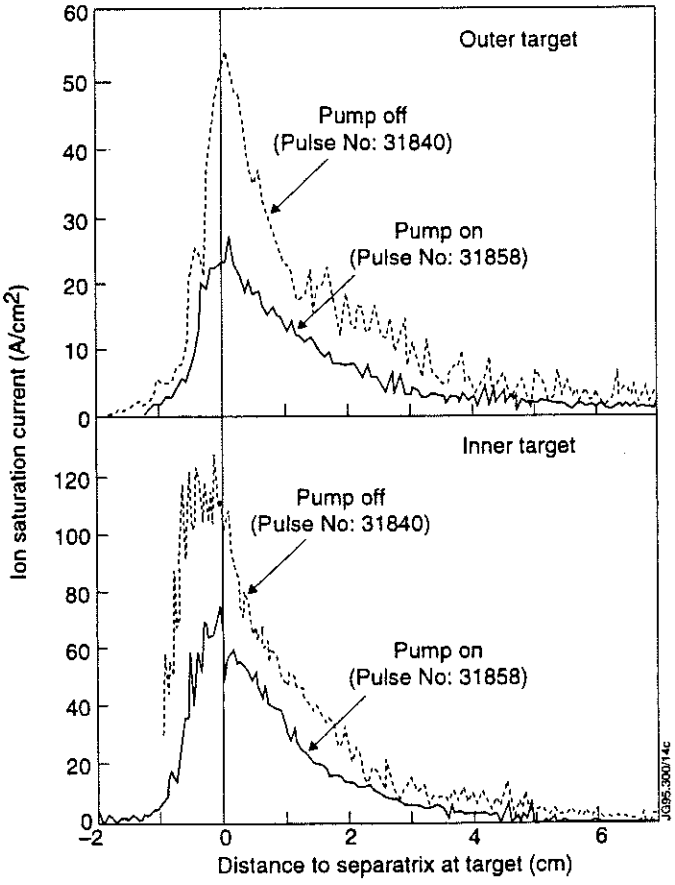

Figure 9: comparison of the ion flux profiles at the target for pulses #31840 and #31858. These profiles are taken during an ELM free period of the H mode.

The cryopump also affects the plasma parameters in the divertor.With the pump on:

- the integrated ion flux to the target decreases approximately by a factor 2, both in the ELM free and ELMy periods.
- the peak electron temperature T_e in both ISZ and OSZ increases by approximately a factor of two.
- the peak density n_e at the inner target is down by a factor of 2
- at the outer target, the reduction in n_e is a factor of 3 to 4.

The cryopump also affects the J_{sat}, n_e and T_e target profiles (figure 9):

- Between ELMs, all profiles become steeper by approximately 20% (this is also the case during longer ELM free phases).
- During ELMs, the characteristic decay lengths for n_e and T_e change. n_e profiles become generally steeper, while T_e profiles are broader with the pump on, compared to the pump off case. (Note that in ELMy discharges, the profiles are "envelopes" of peaks, and generally not exponential).

During ELMs there is some evidence that active pumping affects the balance of fluxes between inner and outer strike zone.

- The ion flux to the outer strike zone (nearer to the pump) decreases more than the flux to the inner, and the ratio between $\int J_{sat}$(in) and $\int J_{sat}$(out) changes from 1.2 to 1.7. These imbalance in the divertor fluxes does not have any detrimental effect on the core plasma.

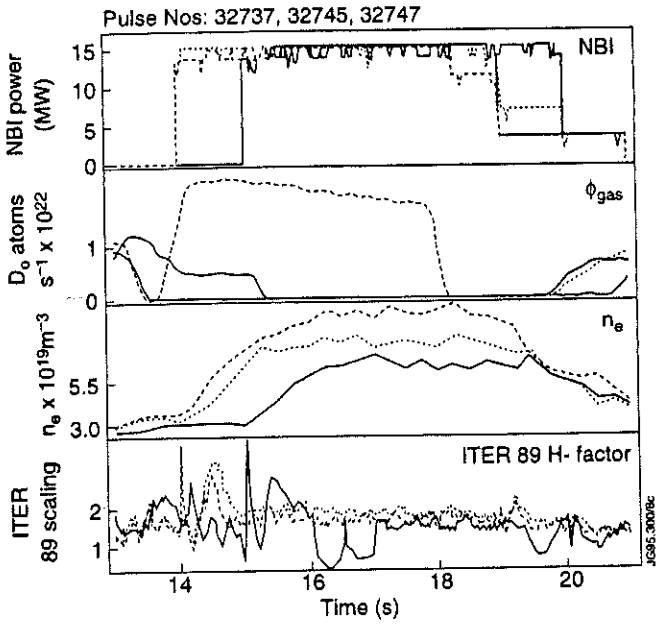

Figure10: neutral beam power, Deuterium fuelling rate, plasma density and H factor (ITER89 L mode) for pulses #32737, #32745 and #32747, all at 3MA/2.8T.

3d . Density control during H modes

- With the pump on, density control in steady state is achieved during ELMy H modes, both for neutral beam only and neutral beam+gas fuelled discharges.
- In contrast to pump off cases, where the steady state plasma density is determined by the beam fuelling and the ELM characteristics, the combination of fuelling and pumping allows a variation of the steady state density of H-mode discharges to be varied by a factor of two.

This is shown in figure 11 for the pulses:

- #32737: strike points in the corners (max. pumping position) - no gas during NBI.
- #32745: strike points well centred on the horizontal divertor plate - no gas during NBI
- #32747: strike point well centred on the horizontal divertor plate - gas flow $2x10^{22}D^{o}s^{-1}$

While it is intuitive that the pump could help to decrease the density in steady state, and it is found in the experiment, the interesting feature is that active pumping also permits higher steady state density during H-modes than obtained without cryopump. This effect is possibly related to the changes in the density profiles at the edge and in the divertor SOL, induced by the pumping.

4. He PUMPING

- A well known method to pump He with a cryopump is by cryotrapping onto condensed layers of Ar gas - Argon frosting. The JET cryopump is equipped with internal gas nozzles to spray Ar directly onto the LHe panels, that have a total surface of around 3 m^2. The typical amount of Ar used on each "spray" is between 5 and $10x10^{23}$ atoms.
- Experiments to measure He transport and exhaust have been carried out, but the Ar frost technique has proven to be difficult, and this has limited the amount of useful data we have been able to obtain.
- In contrast to the experience of DIII-D [D L Hillis et al, IAEA Conf.,1994], we find that the introduction of Ar in the vessel contaminates the plasma facing surfaces. In fact, the Ar contamination of the discharges after an Ar frost is excessive and the associated increase in the radiated power inevitably causes the plasma to disrupt. Between 2 to 3 pulses are required to recover normal divertor plasma operation.

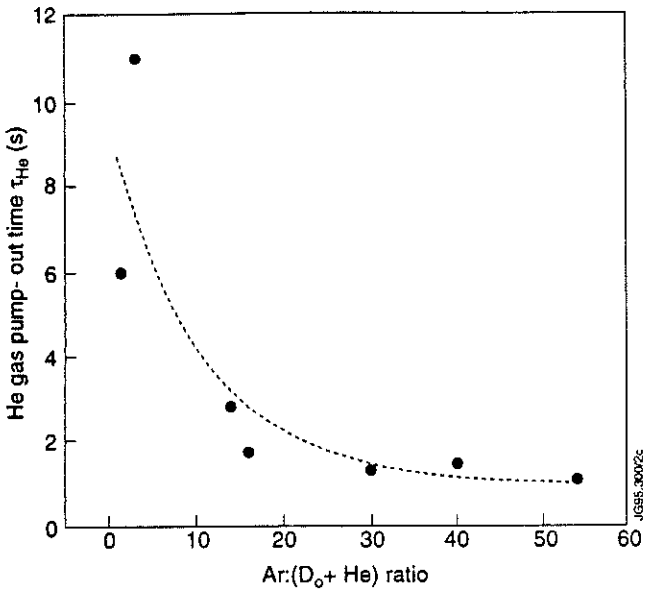

Figure 11: variation in He gas pump-out time τ_{He} as function of (D^o+He) load on the Ar layer.

- The He pumping speed S_{He} depends on the D^o load on the Ar layer (figure 11). At low D^o load, τ_{He} is about 1s, corresponding to an effective S_{He} of about $180 m^3 s^{-1}$. This speed is very near to the measured D^o pumping speed, and therefore the initial sticking coefficient for He is near to 1.
- Measurements of S_{He} as function of the He load have shown saturation effects at Ar/He ratios <100.
- S_{He} depends also on the flow rate of D^o. In particular we have evidence of "recovery" of pumping speed between pulses. This is consistent with assuming that D^o and He diffuse into the 10μm thick Ar layer in the time between discharges (typically 30min).
- Even before the He is injected ($1x10^{20}$ He atoms), the amount of Deuterium used to fuel is typically around $5x10^{22}$ D^o, corresponding to an Ar/(D^o+He) of about 20. Around this ratio and below, S_{He} starts to decrease exponentially, with loss of effective pumping.

5. SUMMARY

- The JET divertor cryopump has been routinely used during the 1994-95 campaign.
- Effective particle removal rate is obtained for all separatrix positions.
- The plasma parameters and confinement regime both affect the pressure in the divertor, and therefore the particle removal rate. The strongest pumping is observed during ELMy H modes. Depending on the nature of the ELM and fuelling, true steady state discharges or net wall depletion can be achieved.
- Broad neutral pressure profiles are measured in the sub-divertor region, consistent with the high transparency of the Mk I target.
- The gas inlet location does not strongly affect either the divertor parameters or the fuelling efficiency, for both pump on and pump off cases.
- Plasma performance is improved with active pumping. The reduction of the main chamber recycling and of the edge density are correlated to the peaking of the temperature profiles and increased fusion reactivity. In the divertor, neutral pressures, D_α and ion fluxes are typically reduced by a factor of two.
- With the pump on, the combination of fuelling and pumping allows density control during steady state ELMy H modes.
- Ar frost is very effective in pumping He, but only at low D^o and He loads. Ar contamination of the vessel and saturation of the layer have limited so far its application for He exhaust experiments.

Characterisation of Long Pulse Steady-State H-modes in the JET Pumped Divertor Configuration

D Stork, A J Bickley, D J Campbell, S Clement, S Davies, K Erents[1], M Garribba, N Hawkes[1], L D Horton, A Howman, R König, J Lingertat, A Loarte, C Maggi, K McCormick[2], R Monk[3], R Reichle, E Righi, G Saibene, M von Hellermann.

JET Joint Undertaking, Abingdon, Oxfordshire, OX14 3EA, UK.
[1] UKAEA Fusion, Culham, Abingdon, Oxfordshire, OX14 3DB, UK.
[2] Max-Planck-Institut für Plasmaphysik, EURATOM Association, 85748 Garching, Germany.
[3] Dept. of Physics, Royal Holloway College, Univ. of London, Surrey, TW20 0EX, UK.

BACKGROUND

- ELMy H-modes with ***"giant"*** (type I) ELMs have been identified as a regime of interest to Next Step devices (eg. ITER-EDA) in the route to ignition phase.
- In such H-modes, it is important to establish ***steady state*** behaviour ie. to produce discharges with;

  H-mode period $t_H >> \tau_E$, τ_p and τ_R ;

  clear control of impurities, in particular intrinsic impurities should not accumulate.
- For ignition on ITER, enhancement over L-mode (ITER89-P) of ~ 1.6 -2.0 is needed. Also a q_{95} around 3 is required for the ITER-EDA machine. Hence

  H/q_{95} ~ 0.53 - 0.65 is the region of interest.

OPERATIONAL ADVANTAGES TO THE ACHIEVEMENT OF STEADY-STATE H-MODES IN JET-PD

The present campaign on this topic in the JET Pumped Divertor (PD) machine has benefited from;

- **Engineering capability**
  - excellent power handling capabilities of the Mark I divertor CFC target;
  - ability to sweep the divertor strike zones to spread the power further;
  - the in-vessel divertor cryopump to provide non-saturable (on the timescale of a pulse) pumping for particle control.
- **Physics of the Mark I divertor configuration**
  - the Mark I divertor configuration **routinely** produces ELMy H-modes with type I ELMs. The mechanisms for this are not fully understood, but this ability over a wide range of

vessel conditions and parameters contributes to the ability to give steady-state plasmas in which impurity ingress is kept at bay.

- in particular, ELMs also give a broader average scrape-off layer width than ELM-free periods – enables further spreading of the power.

STEADY-STATE H-MODE OVERVIEW

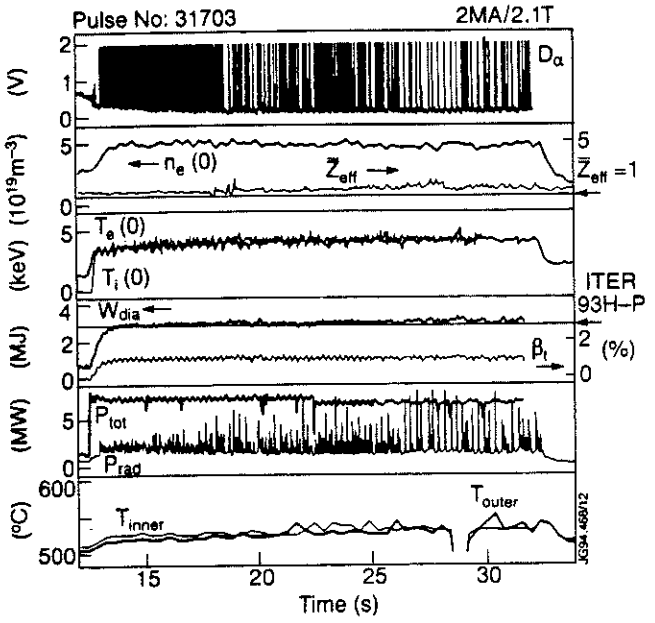

Fig 1: Time development of long pulse steady-state H-mode at 2MA/2.1T

- Figure 1 shows the longest duration ELMy H-mode achieved in the JET-PD machine. The length of the discharge is limited only by the machine engineering constraints.
- Note that this discharge (at 2MA/ 2.1T) has :
  - H-mode duration $t_H \sim 50\tau_E (\tau_E \sim 0.4s)$;
  - $t_H \sim 0.85\tau_R$ where the relevant resistive diffusion time is evaluated at mid-radius;
  - constant energy confinement time, close to the ITER93H-P scale value for ELM-free H-modes;
  - constant Z_{eff} ;
  - constant recycling conditions ;
  - constant radiated power fraction.
- Note also that the divertor tile temperature is also constant and well below design value (1500°C).

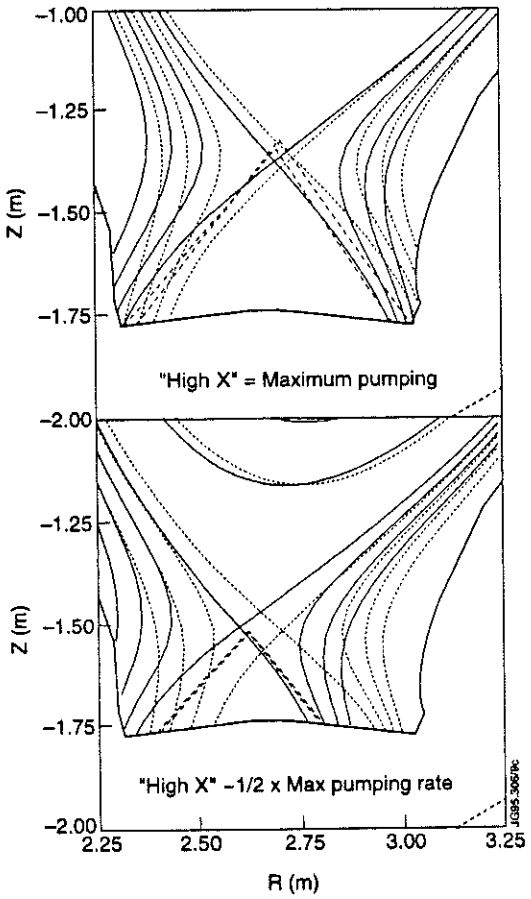

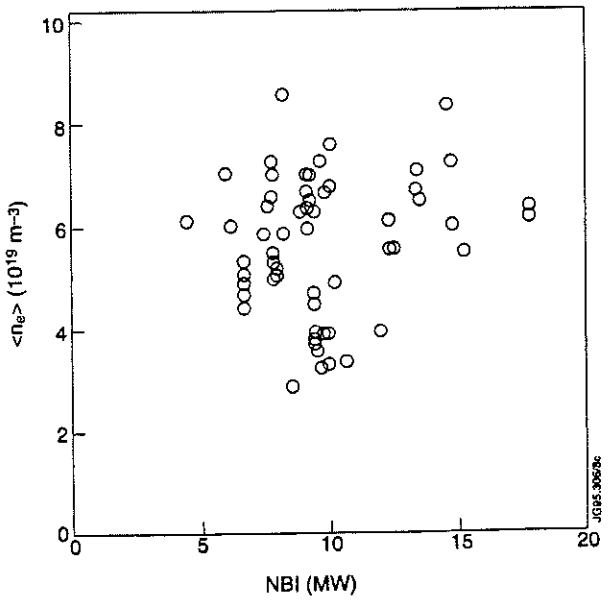

Fig 2: (a): Strike zone variation to maximise pumping effect. (Dotted/solid lines show extent of sweep within one pulse). (b): Existence diagram (density vs input power) for steady-state ELMy H-modes with $t_H > 10\ \tau_E$

The control of the density and the recycling level indicates that the pumping has not saturated, unlike the 1991-2 JET ELMy H-modes, where only wall-pumping was available.

- H-modes in steady state with $t_H \geq 20\ \tau_E$ have been obtained from 1-3MA with $2.8 \leq q_{95} \leq 4.7$.
- **The database of H-modes considered in this poster all have $t_H \geq 10\ \tau_E$.**

EXISTENCE REGION

- Ability to move strike -zone relative to entrance of cryopump (see Fig 2(a)) and to fuel heavily enables density range to be varied at different i/p powers.
  Type I ELMy steady-state H-modes have been achieved in the density range (Fig 2(b))
  $$< n_e > \sim 3.5\ 10^{19}\ m^{-3} \text{ to } 9\ 10^{19}\ m^{-3}$$
- At the high end of the density range, strong **deuterium** puffing establishes small (type III or '*grassy*') ELM behaviour (see Fig 3). Discharges such as this have an enhancement relative to L mode (ITER89P) of only ~ 1.2-1.3.

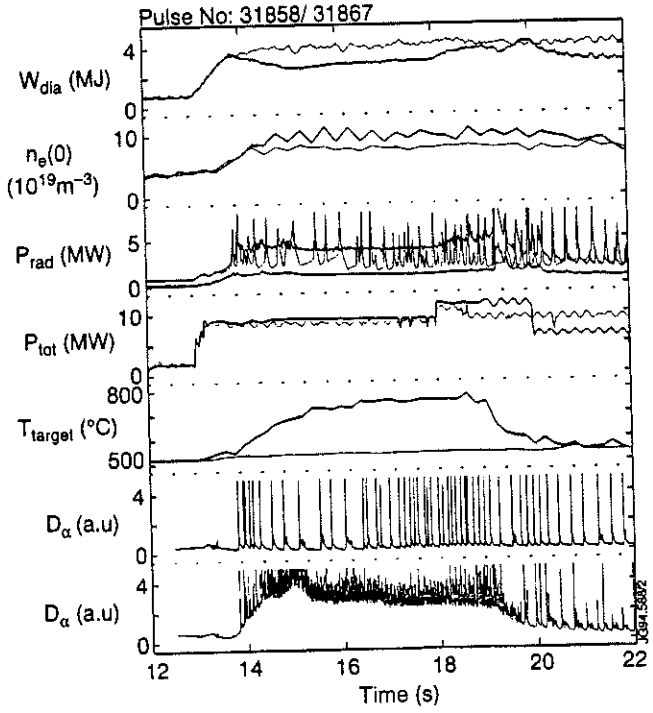

Fig 3: Strong gas puffing establishes 'grassy' ELMs at ~ 9 $10^{19} m^{-3}$

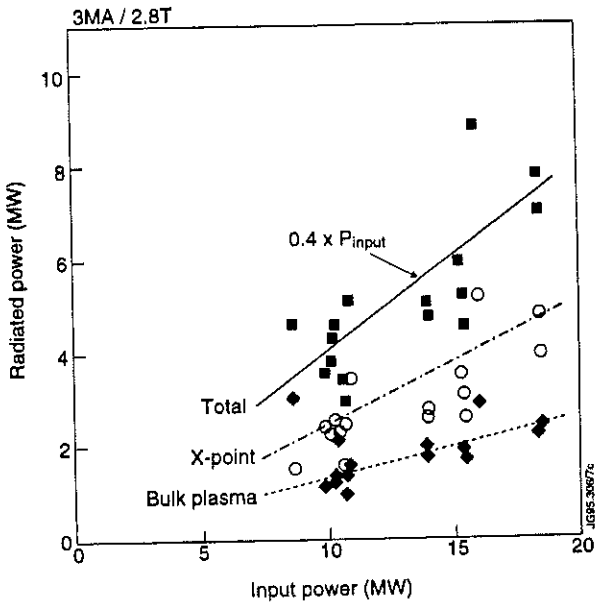

Fig 4: Radiation vs input power in steady-state ELMy H-modes (3MA/2.8T)

POWER BALANCE AND ENERGY CONFINEMENT

- Radiated power (from reconstruction of bolometer signals) is found to be split ~ 2:1 between X-point and bulk plasma in these discharges.
  Radiated power levels are typically ~ 25-40% of input power (see Fig 4). The dataset covers ELMy H-modes where the power conducted across the separatrix (P_{in}-P_{rad}(bulk)) is typically in the range ~ 1.1-1.5 × L-H transition threshold. (P_{LH} roughly goes as 0.004 $<n_e>$. B_T. S)

- **Energy Confinement enhancement** (relative to L-mode) is:
  - in the range $H_{ITER89P}$ ~ 1.6 - 2.2 ;
  - independent of density (see Fig 5(a)) ie; the density form of ITER89P seems to hold ;
  - shows a mild deterioration as the main chamber recycling (normalised to the density) increases (see Fig 5 (b)).
  - independent of q_{95}.

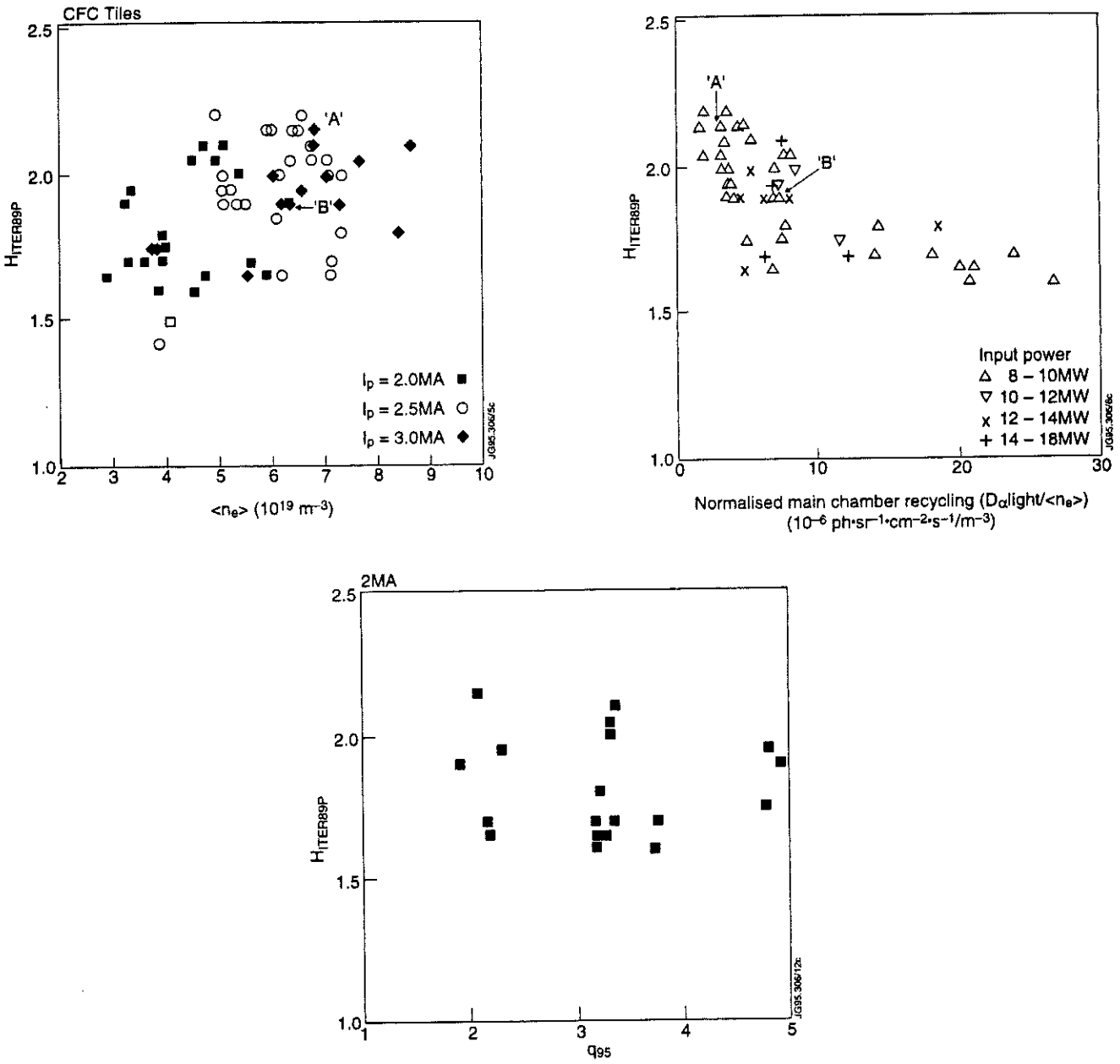

Fig.5: Confinement enhancement over L mode for steady-state H modes as a function of (a) density (diamagnetic energy used) (b): normalised main chamber recycling (c): q_{95}.

- The effects of main-chamber recycling can be seen on nominally identical discharges.

Two shots (at 'A' and 'B' in Fig 5 (a), (b)) with ~11MW input NBI power with I_p = 3MA and B_T = 2.8T show a difference of ~ 15% in the achieved stored energy and a difference of ~factor 2 in the Neutron yield.

The time traces for these shots are shown in Fig 6.

Shot 'A' (N° 31731) has around half the main chamber recycling compared to shot 'B' (N° 32743).

Profiles of the two discharges (Fig 7) show that the lower recycling leads to a 30-40% higher ion temperature in the centre, but also to a 10-15% increase in both T_e and n_e.

It may be that the main effect is that recycling is important in influencing the ELM behaviour early in shot 'B' so that the pedestal on ion and electron temperatures cannot build up (see Fig.6).

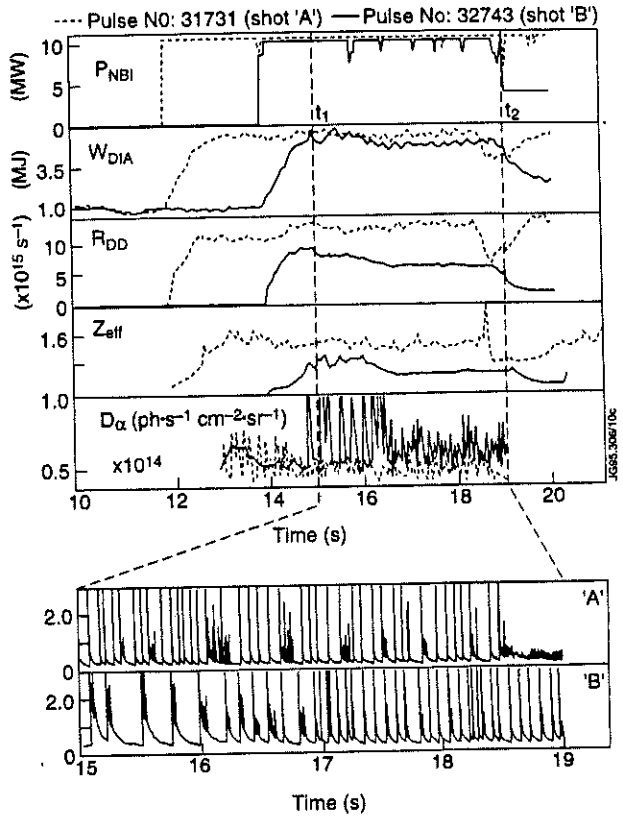

Fig 6: Confinement of two identically-powered SSHm shots at 3MA/2.8T with differing recycling behaviour

IMPURITY BEHAVIOUR

- Intrinsic impurity concentration in the Steady-state H-modes remains low and constant throughout the evolution of the discharge. ELMs are beneficial in keeping target-generated impurities from entering plasma (see behaviour of shot 'B' from 15-17s in Fig 6).
- Z_{eff} and carbon impurity profiles for a typical 3MA/ 2.8T Steady-state H-mode are shown in Figs 8(a), (b).
  Helium puffing has also been performed in these discharges and the helium density profiles become flat with no sign of accumulation.

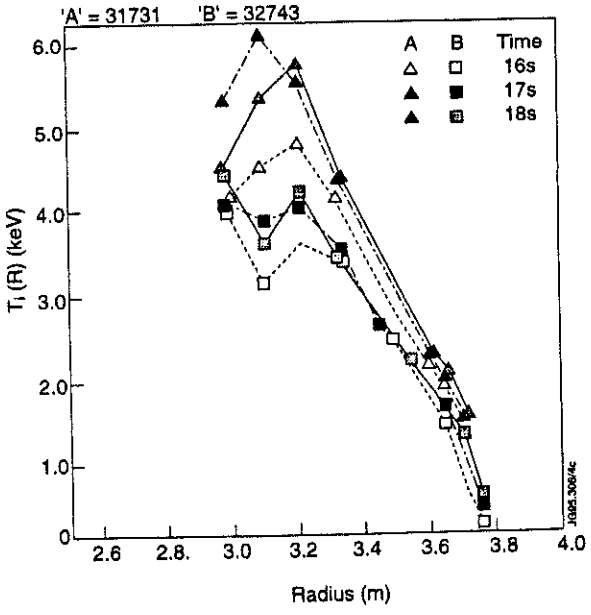

Fig 7: Ion and electron temperature and density profiles showing effects of recycling changes.

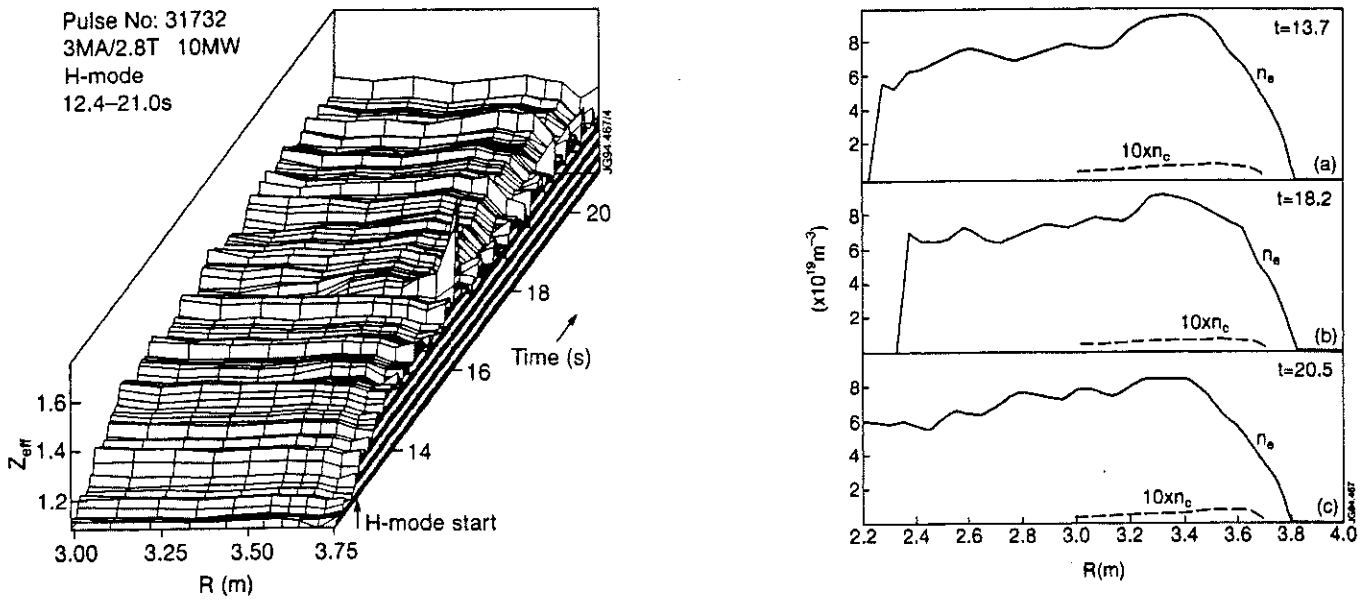

Fig.8 (a): Z_{eff} profiles as a function of time for a 3MA/2.8T 9s ELMy H mode with 10MW i/p power
(b): Carbon and electron density profiles for the same H-mode

USE OF DIFFERENT TARGET MATERIALS

- Steady-state H-modes have been generated using both the CFC and Beryllium target plates in the JET-PD configuration.

  To first order, there is very little difference between the H-modes generated on the two targets. Figure 9 shows a comparison of a CFC-target H-mode and a Beryllium target H-mode. The two plasmas exhibit very similar behaviour. Only the impurity contents show any significant difference:
  - oxygen levels are much higher on the CFC target;
  - chlorine becomes a more significant radiator in the Be case;
  - although, even with Be target the inner wall and poloidal limiters still have CFC protection, the Carbon content of the Beryllium target plasmas is minimal.

DIVERTOR AND EDGE CHARACTERISTICS

- **Although violently disturbed at the time of an ELM,** the edge recycling, impurity radiation and probe signals in Steady-state H-modes show approximately constant ' base ' levels throughout the ELMy H-mode period. Figure 10 shows normalised edge recycling, CIII and BeII signals during the two H-modes of Fig 9.

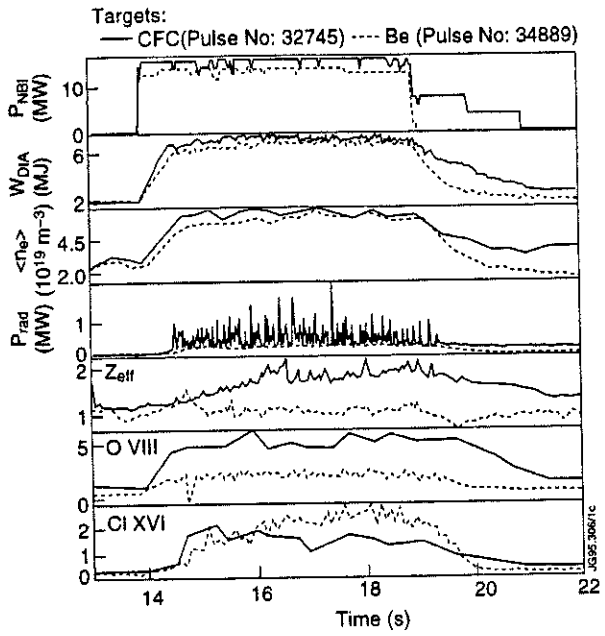

Fig 9: Comparison of SSHm development on CFC and Be targets

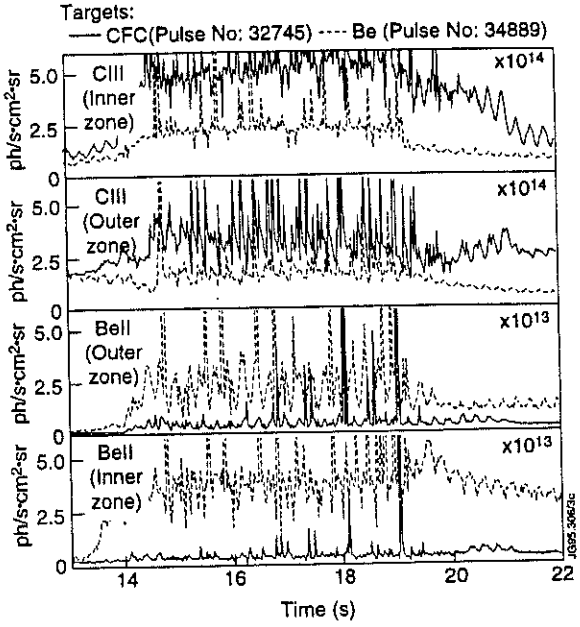

Fig 10: Time development of edge impurity conditions in the main chamber during SSHm on CFC (solid line) and Be (dashed line) targets

- **ELM frequency** increases with input power, there is a very different behaviour with density and added gas puffs (Fig 11) which will make scaling studies difficult.
- **Between ELMs,** the Scrape-off-layer (SOL) parameters measured by Langmuir probes at the target are typically as shown in Table 1 for a 2.5MA/2.4T discharge with 10MW NBI power. During ELMy periods, the SOL thicknesses can be significantly increased (up to 3-fold) as shown in Fig 12 for Ion saturation current at the Outer Strike zone.

Table 1 : Strike zone parameters between ELMs (shot 31858)

	Inner Side		Outer Side	
Parameters	**At separatrix**	**λ_{targ} (cm)**	**At separatrix**	**λ_{targ} (cm)**
j_{sat}	54.1 A.cm^{-2}	1.5	24.0 A.cm^{-2}	1.7
T_e	24 eV	1.1	49 eV	1.6
n_e	8.9 10^{19} m^{-3}	1.4	2.8 10^{19} m^{-3}	2.9
$Q_{\|\|}$	103 MW m^{-2}	1.5	94 MW m^{-2}	0.9
p_e	2.1 10^{21} eV m^{-3}	1.5	1.4 10^{21} eV m^{-3}	1.2

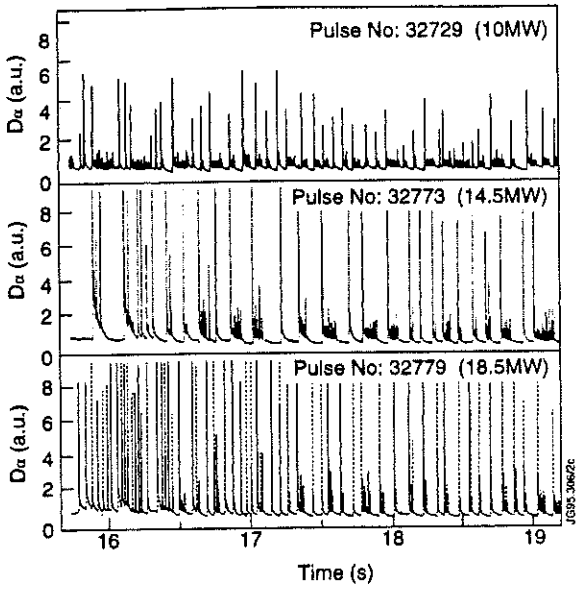

Fig 11: ELMy behaviour as power increases in 3MA/2.8T SSHm plasmas (CFC target)

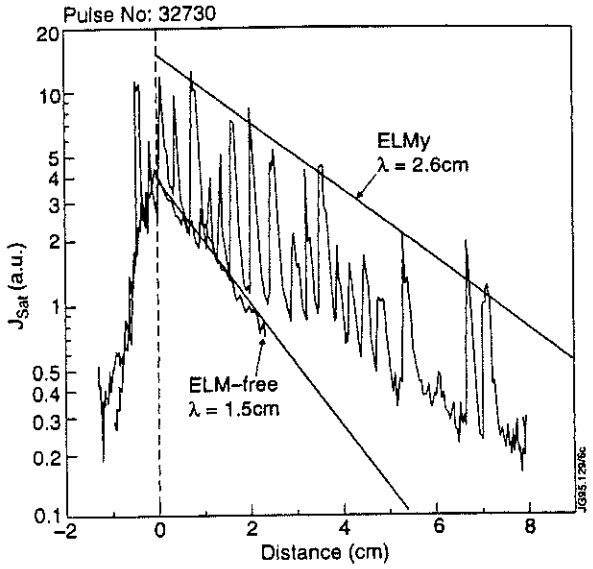

Fig 12: Ion saturation current profile at outer strike zone for ELM-free and ELMy periods in 3MA/2.8T SSHm

- **High recycling divertor conditions?**
  - similar separatrix temperatures to those at the target have been established at the mid-plane by Reciprocating probe measurements;
  - inner SZ density is >> larger than midplane density (~10^{19} m^{-3} from reflectometer), but high recycling conditions seem marginal at the outer zone between ELMs.
    However note that:
  - measured fluxes at the target (shot 31858) are typically;

    between ELMs Inner SZ $\Gamma = 8.5\ 10^{22}\ s^{-1}$ Outer SZ $\Gamma = 6.8\ 10^{22}\ s^{-1}$

    during ELMs Inner SZ $\Gamma = 1.5\ 10^{24}\ s^{-1}$ Outer SZ $\Gamma = 8.7\ 10^{23}\ s^{-1}$
  - compare this to the flux across the separatrix, in steady-state conditions;

$$\Gamma_D^{sep} \approx \dot{N}_D + N_D/\tau_p - \Gamma_{NBI}$$

with

$\dot{N}_D = 0$ $N_D \approx 6 \cdot 10^{21} m^{-3}$ $\Gamma_{NBI} \approx 10^{21}$; typically.

which shows that, for high recycling conditions **between ELMs,** $\tau_p > 2\ \tau_E$ (energy confinement time is ~ 0.5s in these discharges). This seems plausible.

CONCLUSIONS

The successful generation of Steady-state ELMy H-modes in the JET-PD (I) with duration up to 50 energy confinement times; confinement enhancement equivalent to *ELM-free* H-mode scalings under the best recycling conditions; H/q_{95} in the ITER relevant range of 0.53-0.67, and demonstrated impurity control, is an important step in the development towards ITER. The giant ELMs which accompany these discharges exist at plasma density levels up to ~$10^{20} m^{-3}$ for power conducted across the separatrix at 10-50% above the L-H transition threshold. It is likely that high recycling conditions exist in the divertor region throughout these H-mode periods.

Predictive Modelling of Energy Transport in JET Discharges

M Erba, A Cherubini, V Parail, E Springmann, A Taroni.
JET Joint Undertaking, Abingdon, Oxfordshire, OX14 3EA, UK.

1. ABSTRACT

Energy transport in the different regimes of confinement observed at JET can be studied using a Bohm-like model for L-mode electron transport [1] as a starting point:

$$\chi_e = \alpha_e \frac{c\left|\nabla(n_e T_e)\right|}{eBn_e} aq^2, \quad \chi_i = \chi_i^{neocl} + \alpha_i \chi_e \qquad (1)$$

where q is the safety factor, χ_i^{neocl} is the neoclassical ion diffusivity while α_i, α_e are numerical coefficients to be determined empirically. We have simulated several L-mode discharges where measurements of both the ion and electron temperature profiles were available, including shots with predominant electron heating; good agreement with experimental profiles is obtained for $\alpha_i = 2-3$. The same model is subsequently applied to the simulation of ohmic discharges.

To simulate ELM-free, MHD-free H-mode discharges we have used Expression (1) empirically reducing the diffusivities by a constant factor over the entire plasma volume. We remark that we did not study the Bohm versus Gyro-Bohm aspects of the scaling of heat transport in H-mode due to the restricted variation of plasma parameters in our selected discharges. At present our simulations simply show that transport has to be reduced across most of the plasma cross-section. A Gyro-Bohm-like model with a radially increasing shape [2] can be equally successful. A number of relevant JET discharges with H-factors between 2 and 4 have been successfully simulated, imposing the experimental temperature at the edge. This suggests that the underlying transport in H and VH regimes is of the same nature, while the difference in confinement is due to effects not directly related to diffusive heat transport, like the shape of the power deposition profile and the edge temperature pedestal. To simulate predictively the formation of the temperature pedestal and the time behaviour of W we assume the existence of a neoclassical transport barrier on a thin layer $\left(\sim \rho_{pi}\right)$ inside the separatrix. We have then repeated the above H-mode numerical simulation using these boundary conditions successfully reproducing the experimental trends.

2. SIMULATION OF L-MODE DISCHARGES.

In our approach we start from the observation that the results of TRANSP analysis of ordinary L-mode JET discharges indicate that $\chi_i > \chi_e$ all over the plasma column [3], so that we use eq. (1) for χ_i with $\alpha_i > 1$. We consider the following set of L-mode discharges:

DISCHARGE	$\langle n_e \rangle_{20}$	$\langle Z_{eff} \rangle$	I_p (MA)	B_t (T)
19649	0.28	2.4	3.0	3.0
19691	0.39	3.7	3.0	3.0
24693	0.33	2.1	3.1	2.8
26109	0.20	3.0	3.1	2.8
19642	0.55	3.7	3.0	3.1
16047	0.28	2.2	3.0	3.1

The simulations have been carried out in a semi-predictive way using the JETTO transport code: only heat diffusion has been modelled, while experimental density and Z_{eff} profiles have been imposed throughout the time evolution. It is found that a model with $\alpha_e = 2.0 \cdot 10^{-4}$, $\alpha_i = 3$ gives good results in all simulated cases.

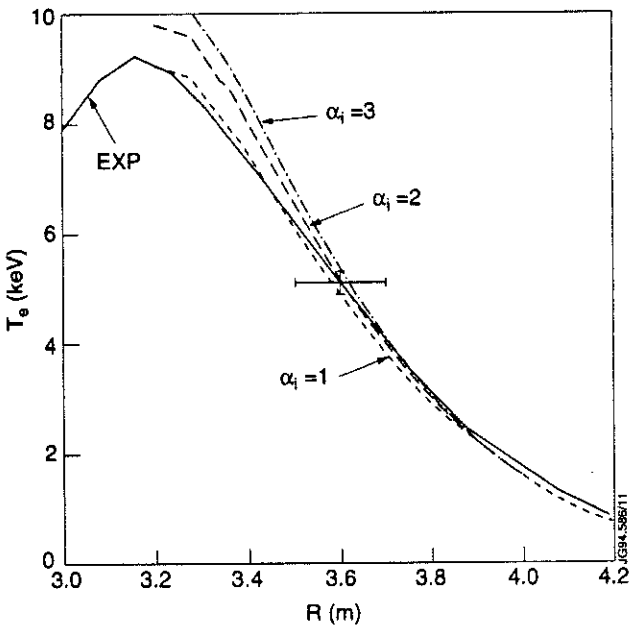

Fig.1: Experimental and simulated profiles of electron temperature in shot 16047.

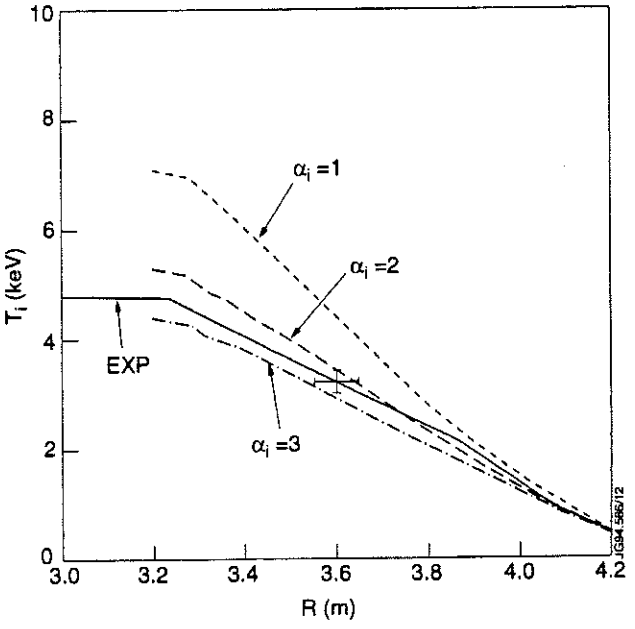

Fig.2: Experimental and simulated profiles of ion temperature in shot 16047.

In figs. 1) and 2) we show the results of the simulation of the electron and ion temperature profiles in a case with strong electron heating where it is possible to discriminate between models with different values of the parameter α_i.

3. SIMULATION OF JET OHMIC DISCHARGES

Another interesting issue is the confinement in the ohmic regime. Analysis of ohmic discharges in Asdex [4] and Toré Supra [5] has shown that when the density is too high the confinement time does not rise linearly with density as prescribed by the so-called Neo-Alcator scaling law and saturates. Recent results from ALCATOR C-MOD [6] suggest that when the density is too high the confinement time does not rise linearly with density as prescribed by the so-called Neo-Alcator scaling law and saturates, so that this regime might be described using an L-mode-like model. We choose the following set of ohmic discharges:

DISCHARGE	$\langle n_e \rangle_{20}$	$\langle Z_{eff} \rangle$	I_p (MA)	ρ_{max} (m)	B_t (T)
25255	0.10	2.5	1.0	1.4	2.8
27658	0.17	3.7	2.05	1.5	1.7
27588	0.30	3.3	3.3	1.5	2.8
20050	0.37	1.3	5.1	1.5	3.1
27897	0.28	2.3	7.0	1.6	3.3

In fig. 3 the profiles obtained with a neoalcator-like model [7], with the Bohm model and the experimental profiles are shown.

Analysis of the corresponding values of thermal energy shows that the linear scaling with density and weak scaling with current, typical of the neoalcator-like model, are not in agreement with experimental results, which are much closer to the L-mode-like scaling resulting from the Bohm model.

4. SIMULATION OF QUIESCENT H-MODE MHD-FREE DISCHARGES.

Previous analysis has shown that the evolution of plasma parameters throughout the L-H transition in JET can be reproduced only assuming that both χ_e and χ_i are changed everywhere and not only near the separatrix. It was found that good agreement is achieved if we assume that the numerical coefficient α_e is reduced by ~10 times down to $0.2 \cdot 10^{-4}$. Due to the non-linearity in the parametric dependencies of χ this results in a reduction of the numerical value of χ by a factor ~ 3. In Fig. 4 we show the radial distribution of χ_i and χ_{neocl} for typical L-mode and H-mode shots with similar plasma parameters.

It can be observed that the neoclassical ion transport becomes important in the central part of the plasma column during the H-mode phase.

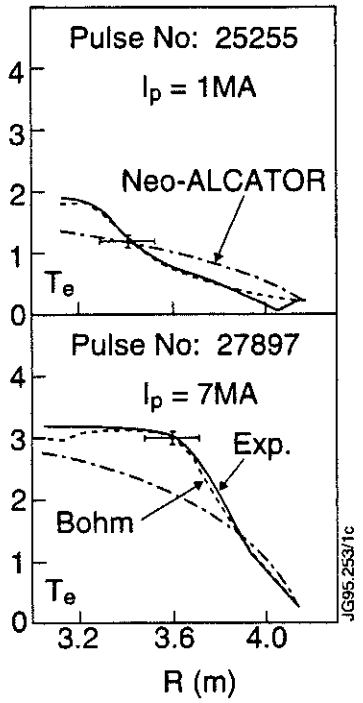

Fig.3: Experimental and simulated profiles of electron temperature with different models in a 1 MA and a 7 MA ohmic discharge.

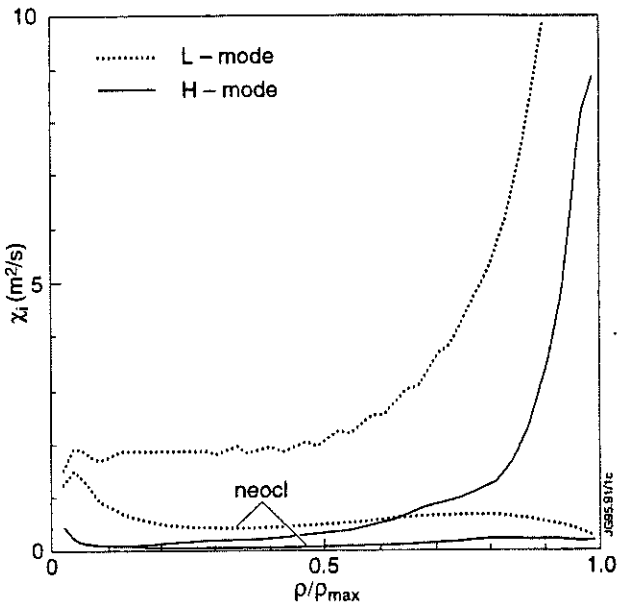

Fig.4: Ion thermal diffusivity profiles in typical H-mode and L-mode shots.

In this way we model the entire ELM-free H-mode phase for shots which have no large scale MHD activity (like roll-over). Some of the selected discharges fall into the category of VH mode with enhancement factor H>3, while others have 2<H<3.

DISCHARGE	$\langle n_e \rangle_{20}$	$\langle Z_{eff} \rangle$	I_p (MA)	B_t (T)
26087	0.19→0.30	1.6	3.2	2.8
26095	0.11→0.30	2.6	3.2	2.8
30591	0.15→0.36	2.5	2.4	2.7
30725	0.72→0.84	1.3	3.1	2.2

The temporal evolution of the measured thermal plasma energy content and that calculated with our model during the ELM-free H-mode phase for four discharges are shown in Fig. 5.

In fig. 6 experimental and simulated temperature profiles are compared at the final time of the H-mode ELM-free phase of shot 30591 $\left(I_p = 2.4MA,\ \langle n_e \rangle \approx 0.36 \cdot 10^{20} m^{-3},\ B_t = 2.7T\right)$.

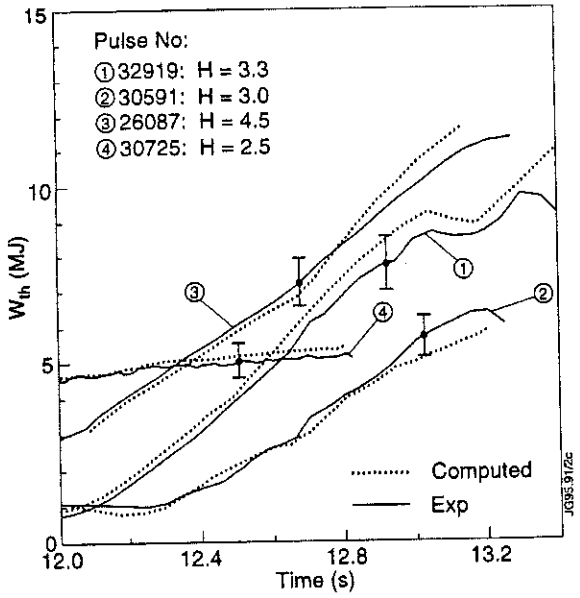

Fig.5: Experimental and simulated time evolution of thermal energy in various H-mode discharges.

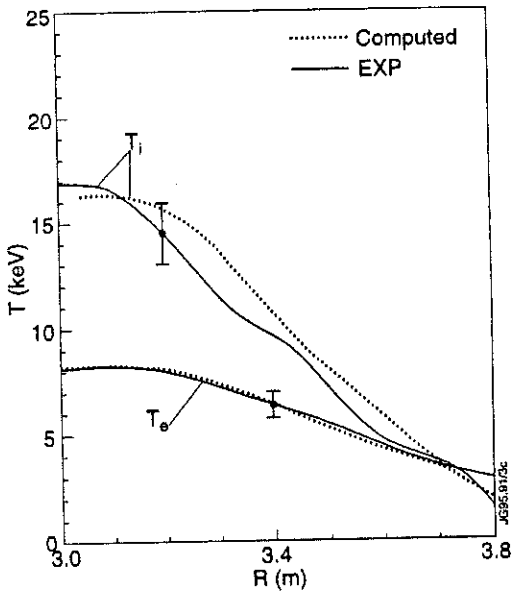

Fig.6: Experimental and simulated ion and electron temperature profiles in shot 30591.

We can simulate discharges with different values of the H-factor using the same transport model because an important role is played by effects not directly related to heat diffusion.

Numerical analysis shows that NB do not penetrate to the centre of the plasma in high density shots: Fig.7 shows ion power deposition profiles computed by TRANSP for shot 26087, with relatively low density, and shot 30725 with higher density. Another important source of the difference in plasma performance in H-mode is the energy stored in the temperature pedestal defined as:

$$W_{e-i}^{ped} = \frac{3}{2}\langle n_{e-i} \rangle T_{e-i}^{ped} V \qquad (2)$$

where <n> is the average density and V is the plasma volume. Fig.8 shows, for the shots 26087 and 30725, the temporal evolution of the total W^{ped} together with the total thermal energy as computed by TRANSP.

Two interesting features are observed in shot 26087 which are typical of the best hot-ion H-mode JET shots:

i) more than half of the plasma energy is stored in the pedestal.

ii) both the total thermal energy content W_{th} and the pedestal energy content W^{ped} continuously grow in time and do not saturate during the heating. This leads to a continuous rise in both total and thermal energy confinement time; the maximum value of the achieved confinement time is really controlled by the MHD instabilities coming about towards the end of the H-mode phase.

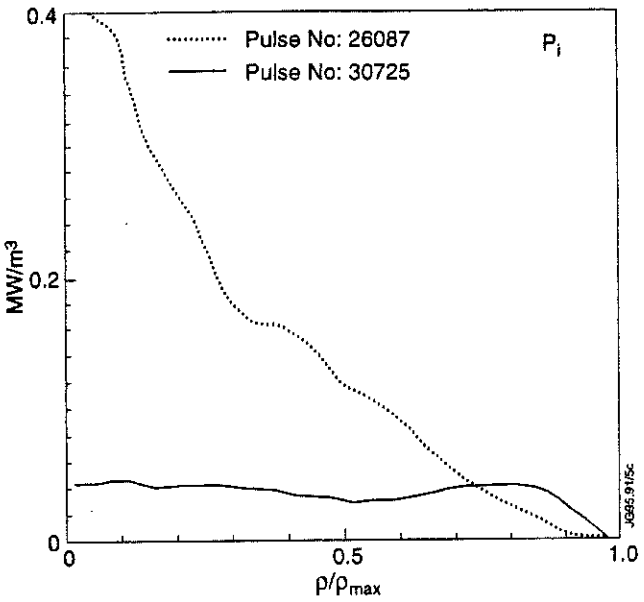

Fig.7: Auxiliary power deposition profiles in shots 26087 and 30725.

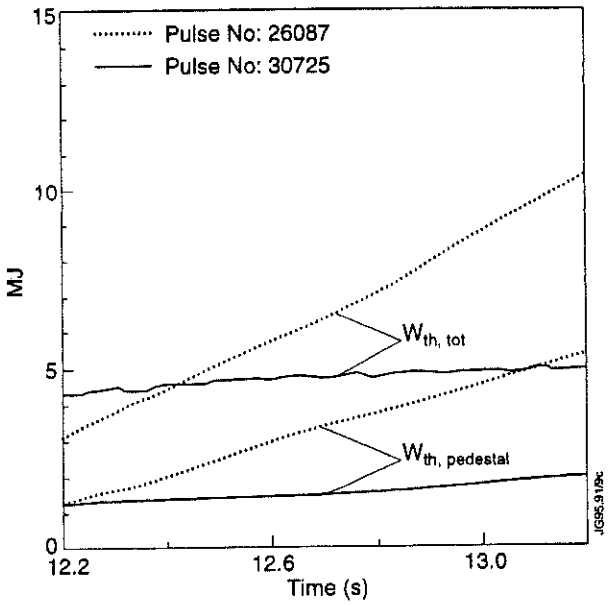

Fig.8: Time evolution of total thermal energy and pedestal energy in shots 26087 and 30725.

5. A MODEL FOR BOUNDARY CONDITIONS IN H-MODE DISCHARGES

We find that we can reproduce the experimentally observed ion and electron temperature near the separatrix only if we assume that perpendicular transport inside a transport barrier located at the plasma edge is of the order of the neoclassical one, as it results from the analysis of H-mode density and temperature profiles near the separatrix in DIII-D. Under the simple assumption that the only mechanism of ion flow through the separatrix is the direct losses of the banana ions, we obtain the following boundary conditions for ion heat flow:

$$\chi_i\, n_i\, \nabla T_i + \frac{3}{2} T_i\, D\, \nabla n_i \approx -n_i\, T_i\, \frac{\rho_{pi}}{\sqrt{\varepsilon \tau_{ii}}}\, F_T \qquad (3)$$

where ρ_{pi} is the ion poloidal Larmor radius, τ_{ii} is the ion-ion collisional frequency, ε is the inverse aspect ratio near the separatrix, F_T is a coefficient which depends on the geometry, collisionality and radial electric field and $0 \le F_T \le 1$. The boundary condition for electron heat flow is similar to eq.(3) if we assume that the remaining magnetic turbulence near the separatrix keeps the electron's particle flux at the level of the ion-neoclassical flow.

Numerical simulations of H-mode ELM-free discharges using boundary conditions (3) reproduce the experimental observations for the best hot-ion H mode shots for the evolution of the temperature pedestal and the rise of thermal energy (figs. 9 and 10). The independence of the heat flux from temperature implies a reduction in the growth of the pedestal temperature and energy when volume power losses are relevant.

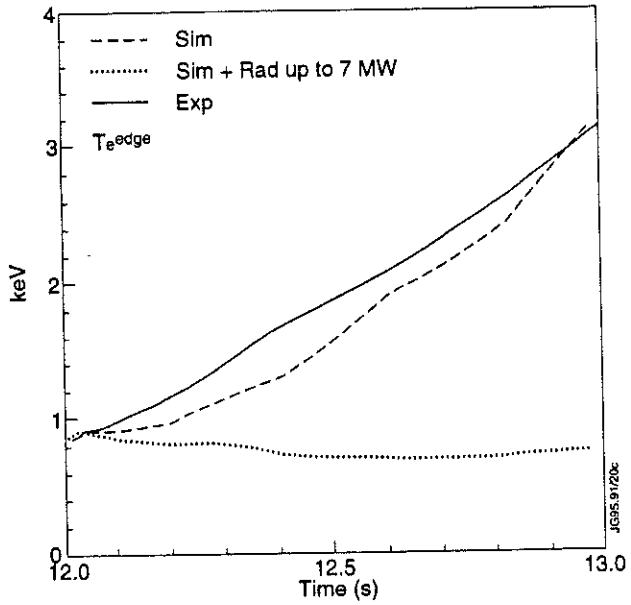

Fig.9 Time evolution of the edge electron temperature from experimental measurements (solid line) and from simulations carried out with and without the effect of 7 MW of radiated power (dotted lines).

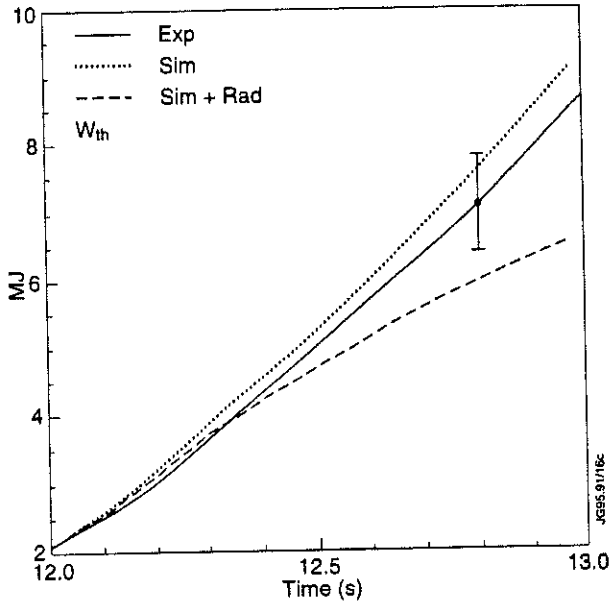

Fig.10: Time evolution of the thermal energy from experimental measurements (solid line) and from simulations carried out with and without the effect of 7 MW of radiated power (dotted lines).

An important property of boundary conditions (3) is that in the banana regime the heat flow does not depend on the temperature near the separatrix and $Q_{e-i} \propto n_i\, n_{e-i}$. This feature allows us to explain the experimentally observed fact that the global plasma energy confinement time in hot-ion VH-modes, formally defined as $\tau_E = W/(P_{tot} - dW/dt)$, grows almost linearly with time together with the total energy content W.

Indeed, in a slab-geometry plasma with uniform density n_0, uniform diffusivity χ_0, a uniform heating power deposition profile p_0 and boundary conditions:

$$\chi_0\, n_0\, \nabla T\big|_{\rho=1} = -\beta\, n_0^2\big|_{\rho=1} \tag{4}$$

the solution of the energy balance equation gives for the thermal energy confinement time:

$$\tau_{Eth} = \frac{a^2}{3\chi_0} + \frac{\left(p_0 - \beta n_0^2/a\right)\cdot t \cdot a}{\beta n_0^2} \tag{5}$$

The first term on the RHS is the contribution of the plasma core to the confinement time; the second term, which increases linearly with time, is the contribution of the temperature pedestal.

In collisional regimes the plateau expression of the ion neoclassical diffusivity must be used inside the transport barrier, leading to temperature dependent heat losses which can cause a saturation of the growth of the pedestal.

6. CONCLUSIONS

Using a Bohm-like model we have been able to simulate successfully ion and electron transport in L-mode JET discharges and electron transport in ohmic JET discharges. We have also shown that different H-factors in H-mode ELM-free, MHD-free discharges depend on effects not directly related to heat transport in the plasma core, such as power deposition profiles and the temperature pedestal at the plasma edge. A neoclassical model for the edge transport barrier in H-mode has been used to predict the edge temperature time evolution.

REFERENCES

[1] Taroni A., Erba M., Tibone F., Springmann E., Plasma Phys. Control. Fusion **36** (1994) 1629.

[2] Erba M., Springmann E., Taroni A., Tibone F., Proceedings of Workshop on Local Transport Studies in Fusion Plasmas, Varenna (1993) 39.

[3] Balet B. , Cordey J.G. , Stubberfield P.M. , Plasma Phys. Contr. Fusion **34** (1992) 3.

[4] Bessenrodt-Weberpals M. et al., Nucl. Fus. **31** (1991) 155.

[5] Garbet X. , Payan J. , Laviron C. , et al. , Nucl. Fus. **32** (1992) 2147.

[6] Porkolab M. , Bovin R. , Bombarda F. , et al. , 'Overview of recent results from Alcator C-MOD', IAEA Paper CN-60/A-1-II-2 , 15th International Conference on Plasma Physics and Controlled Nuclear Fusion Research , Seville , Spain , 1994.

[7] Merezhkin V.G. and Mukhovatov V.S., JETP Lett, **33** (1981) 446.

Kinetic Toroidicity Induced Alfvén Eigenmodes in Toroidal Shaped Plasmas

D Borba, J Candy, H Holties[1], G Huysmans, W Kerner, S Sharapov[2].
JET Joint Undertaking, Abingdon, Oxfordshire, OX14 3EA, UK.
[1] FOM Institute for Plasma Physics Rijnhuizen, Nieuwegein, The Netherlands.
[2] RRC Kurchatov Institute, Moscow, Russia.

INTRODUCTION

The physics of weakly-damped Alfvén modes has been long recognised to be of concern for the confinement of fusion alpha particles in a tokamak reactor. Within the framework of ideal magnetohydrodynamics (MHD) much attention has been given to the Toroidal Alfvén Eigenmodes (TAE), whose eigenfrequency lies in the shear-Alfvén continuum gap. As the TAE eigenfrequency does not satisfy the local Alfvén resonance condition, the TAE is more weakly damped than usual cylindrical shear Alfvén waves, and therefore it can be more easily destabilised by resonant alpha-particles. In hot plasmas, Finite Larmor Radius (FLR) effects[1] convert the TAE mode energy into Kinetic Alfvén waves increasing the outgoing wave energy flux significantly; i.e,. the overall damping of the mode via radiative damping. On the other hand for high plasma temperatures, a new branch of Kinetic Toroidal Alfvén Eigenmodes (KTAE) appears and can be driven unstable by energetic particles. Both the radiative damping and the eigenfrequencies of the KTAE spectrum are very sensitive to the plasma parameters. In particular, toroidal and shaping effects in the plasma equilibrium are important.

In this paper the KTAE spectrum is computed for toroidal plasmas with an arbitrary shape including realistic JET scenarios. The FLR kinetic effects and parallel electric field effects are included in the toroidal linear MHD spectral code CASTOR. This model allow one to compute effectively the KTAE spectrum and the radiative damping of TAE and KTAE for arbitrary plasma configurations as a function of the relevant FLR parameter. Included in this spectrum are two types of core localised modes[2], which may be particularly dangerous to plasma confinement as they are peaked near the plasma centre where the drive from fusion alphas or RF ions is strongest. We calculate the radiative damping of the lower frequency mode, and also describe the transition of the upper frequency mode into a KTAE. These results indicate a strategy for a systematic experimental[3] study of the KTAE spectrum.

MHD MODEL INCLUDING FIRST ORDER FINITE LARMOR RADIUS

- **In hot plasmas ideal MHD breaks down in the vicinity of the TAE gap surface,** satisfying

$$q(r_0) = \frac{m - \frac{1}{2}}{n}$$

where m,n are the poloidal and toroidal mode numbers, q(r) is the safety factor as a function of the minor radius r.

- Around r_0 **nonideal effects and toroidicity give**:

  I) some modification to the TAE
  II) remove the singularity of the Alfvén modes with frequencies in the shear-Alfvén continuum and give rise to a new set of discrete eigenvalues.

- The resistive MHD spectrum is symmetric below and above the toroidicity induced gap and forms a "quasi-continuum" where the natural width of each eigenvalue is larger than the distance between each eigenvalue is $\mathrm{Im}[\omega] > \delta\omega$. $\delta\omega$ is proportional to $\eta^{\frac{1}{3}}$, where η is the plasma resistivity.

- Including **first-order Larmor radius** effects and a **non zero longitudinal electric field,** a well resolved **discrete set of eigenvalues** $\mathrm{Im}[\omega] < \delta\omega$ aprears **above the gap**.

The existence and weak damping of the KTAE are caused by the combined toroidicity effects and FLR effects in the region around the TAE-gap surface. Together, these two effects prevent the KTAE energy from flowing away from the gap region (high-$k_\perp$).

- In the **outer region** away from the resonance surface both KTAE and TAE can be described by the ideal MHD equation, which reduces to a **vorticity equation**

$$L\phi = (\mathbf{b}\cdot\nabla)\nabla^2(\mathbf{b}\cdot\nabla)\phi + \nabla\cdot\left(\frac{\omega^2}{V_A^2}\nabla_\perp\right)^{\phi} = 0\,.$$

Here, ω is the eigenfrequency, v_A the Alfvén velocity, b the equilibrium magnetic field and ϕ is the TAE/KTAE perturbated potential. **First order FLR effects of core ions and finite longitudinal electric field** give the following corrections to the vorticity equation in the boundary layer around the TAE resonance region. These corrections have been calculated in detail by Rosenbluth and Rutherford[4] and lead to the **modified current moment equation:**

$$\nabla\cdot\mathbf{j} \cong -\frac{3}{4}\frac{i\omega\rho}{B^2}\rho_s^2\nabla_\perp^4\phi - \frac{i}{4\pi\omega}(\mathbf{b}\cdot\nabla)\nabla^2 E_{\parallel},\ \text{with}\ E_{\parallel} \cong -i\rho_s^2(1-i\delta)(\mathbf{b}\cdot\nabla)\nabla^2\phi.$$

- The **vorticity equation** equation takes the form:

$$(b\cdot\nabla)\nabla^2(b\cdot\nabla)\phi+\nabla\cdot\left(\frac{\omega^2}{V_A^2}\nabla_\perp\phi\right)^\phi+\frac{1}{4\pi\omega}\rho_s^2(1-i\delta)(b\cdot\nabla)\nabla_\perp^2(b\cdot\nabla)\nabla^2\phi+\frac{3}{4}\frac{\omega^2}{V_A^2}\rho_i^2\nabla_\perp^4\phi=0.$$

- The **structure of this equation is analogous** to the structure of the **resistive MHD** equation with a **general complex parameter** η defined by:

$$\eta=4\pi\omega\rho_s^2\delta(\upsilon_e)+i4\pi\omega\left(\frac{3}{4}+\frac{T_e}{T_i}\right)\rho_s^2$$

- For typical of **JET parameters**, e.g. $\mathrm{Im}[\tilde{\eta}]=4\cdot10^{-2}\ T_i[\mathrm{keV}]\ n_e^{-0.5}\left[\mathrm{cm}^{-3}\right]\ B_T^{-1}[T]$ it is convenient to express η **in normalized units**

$$\mathrm{Im}[\tilde{\eta}]=\frac{\mathrm{Im}(\eta)}{\mu_0 R_m V_A}\approx 5\cdot10^{-10}\frac{T_i[\mathrm{eV}]}{B^2[T]},$$

which gives $\mathrm{Im}[\tilde{\eta}]\approx10^{-6}$ in JET auxiliary heated discharges.

WKB APPROXIMATION

- The spectrum can be calculated within the **WKB approximation** by changing the usual resistivity into a general complex parameter η. Within this approximation Alfvén Waves are described by the second order equation,

$$\eta\nabla^2\xi+i\lambda\left(1-\frac{(k\cdot b)^2}{\rho\lambda^2}\right)\xi=0,$$

with the boundary conditions $\xi(a)=\xi(b)=0$. ρ is the density, λ the eigenvalue, ξ is the plasma displacement and $k\cdot b(r)=k_{||}$. The **fast varying solutions in the radial direction** can be described accurately by the phase integral

$$\frac{d\phi}{dr}=\sqrt{\frac{H(r)^2-\lambda^2}{i\lambda\eta}},\ \text{where}\ H(r)=\frac{k\cdot b}{\rho^2}$$

To obtain the WKB spectrum the following eigenvalue conditions for λ must be satisfied in the limit where $H(x_b)-H(x_a)<<H(x_b)$

i) no anti-Stokes line crossings:

$$\phi(x_a)-\phi(x_b)= p\,\pi,\ \ \mathrm{Im}[\phi(x_a)]<0,\ \ \mathrm{Im}[\phi(x_b)]<0,\ \ \omega=\frac{3}{2}\,\eta^{\frac{1}{3}}\,\theta^{\frac{2}{3}}\,p^{\frac{2}{3}}\,\pi^{\frac{2}{3}}+H(x_a)+\frac{\theta}{2}$$

ii) one (at x_a) and a half (at x_b), anti-Stokes line crossings

$$\phi(x_a)=-p\,\pi,\ \ \mathrm{Im}[\phi(x_b)]>0,\ \ \omega=\frac{3}{2}(-1)^{\frac{2}{3}}\,\eta^{\frac{1}{3}}\,\theta^{\frac{2}{3}}\,p^{\frac{2}{3}}\,\pi^{\frac{2}{3}}+H(x_a)$$

iii) one (at x_b), and a half (at x_a), a anti-Stokes line crossings

$\phi(x_b)=p\,\pi$, $\mathrm{Im}[\phi(x_a)]>0$ $\omega=-\frac{3}{2}(-1)^{\frac{2}{3}}\,\eta^{\frac{1}{3}}\,\theta^{\frac{2}{3}}\,p^{\frac{2}{3}}\,\pi^{\frac{2}{3}}+H(x_b)$ where x_a, x_b are the two boundaries and with $H(x_b)>H(x_a)$, $\theta=H(x_b)-H(x_a)$ and $p\in 1,2,3,....$

In the generalized case of **complex η, the spectrum is rotated, the third branch disappears, the second branch has a turning point at the Alfvén resonance and the first branch does not have a turning point** inside the plasma, thus these waves are reflected at the plasma boundary only.

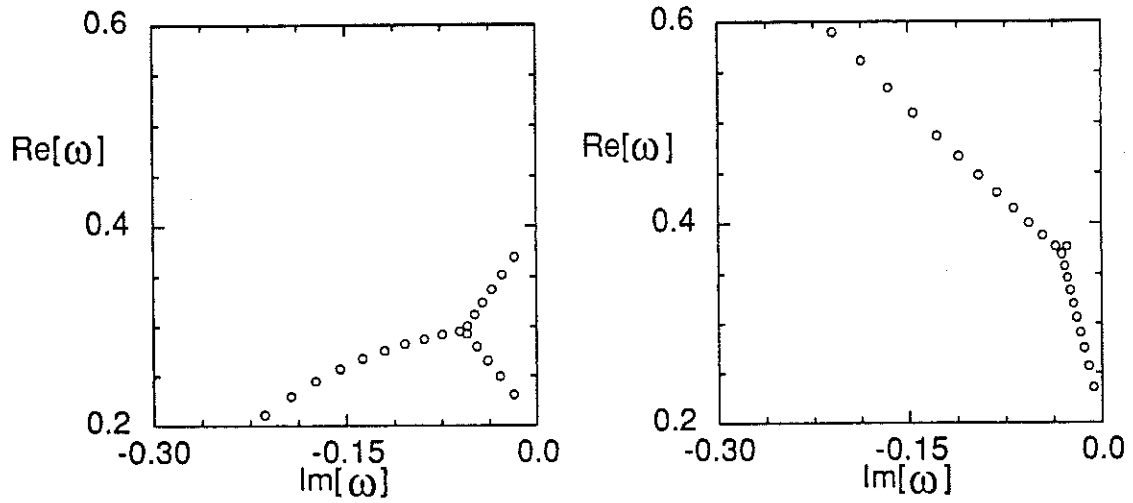

Figure 1 a) resistive Alfvén spectrum in the WKB approximation $\eta=10^{-4}$ b) Kinetic Alfvén spectrum in the WKB approximation $\eta=10^{-4}e^{i\frac{\pi}{3}}$.

MODEL GEOMETRY IN A CYLINDER (SINGLE GAP APPROXIMATION)

- Modelling of a single gap in toroidal geometry can be achived by the artificial **coupling of two Fourier harmonics in cylindrical geometry**. The **incompressible reduced MHD** equations for the **vector potential** and the **vorticity** defined by $v=\nabla U\times\hat{z}$, $B=\nabla A\times\hat{z}+B_z\hat{z}$,

$$\lambda\nabla_\perp^2 U_m+\varepsilon\lambda\nabla_\perp^2 U_{m+1}=B_0\cdot\nabla\left(\nabla_\perp^2 A_m\right)+\left(\nabla A_m\times\hat{z}\right)\cdot\nabla j_0,\qquad \lambda A_m=\varepsilon\lambda A_{m+1}=B_0\cdot\nabla\left(U_m\right)+\eta\nabla_\perp^2 A_m$$

plus the equivalent equations for the other Fourier component $m\Leftrightarrow m+1$. j_0 and B_0 are the equilibrium current and the equilibrium magnetic field.

- In **cylindrical geometry** the differential operator takes the form $\nabla_\perp^2 A = \frac{1}{r}\frac{\partial}{\partial r} r \frac{\partial A}{\partial r} - \frac{m^2}{r^2} A$. λ is the eigenvalue and ε is the artificial coupling coefficient between the two Fourier harmonics.

- This system of equations is solved numerically as a **linear eigenvalue problem** using finite cubic elements in the radial coordinate.

- Equilibrium with **constant density** and **parabolic q** profile varying from q=1 on axis to q=2 at the plasma boundary.

- Perturbation **n=1** in the z direction, the relevant poloidal Fourier harmonics **are m=1 and m=2.**

- The Alfvén wave spectrum computed for $\eta = 2.5\ 10^{-5} + 10^{-4} i$ consists of a set of discrete eigenmodes. Apart from a set of localised kinetic Alfvén waves there are **two GAE, a TAE** within the continuum gap and a spectrum of **KTAE just above the gap.**

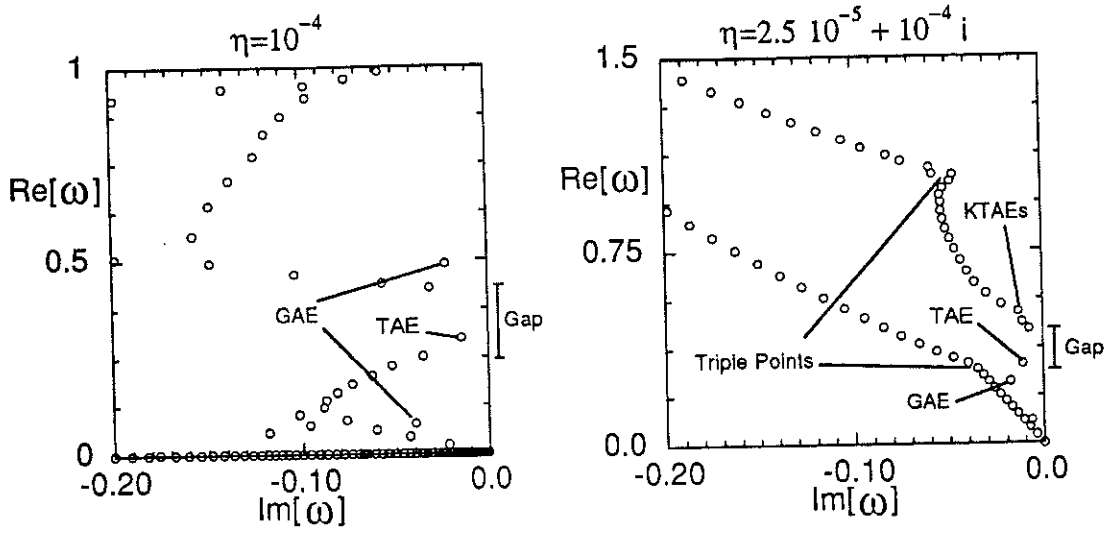

Figure 2 a) resistive Alfvén spectrum for a single gap model with parabolic q profile varying from q=1 to q=2. b) the kinetic Alfvén wave spectrum for the same equilibrium.

TOROIDAL GEOMETRY USING THE CASTOR CODE

- The CASTOR code computes **dissipative MHD spectra for arbitrary 2D axisymmetric equilibria.** (low toroidal mode numbers **n<10**).

- Small **change in the induction equation, introducing the general complex parameter**, kinetic modifications to MHD can be modelled within reasonable accuracy.
- In this fashion, a correct result is obtained for normal modes localised in the gap where $k_{\parallel} \approx \frac{1}{2qR_0}$, q is the safety factor and R_0 is the major radius.

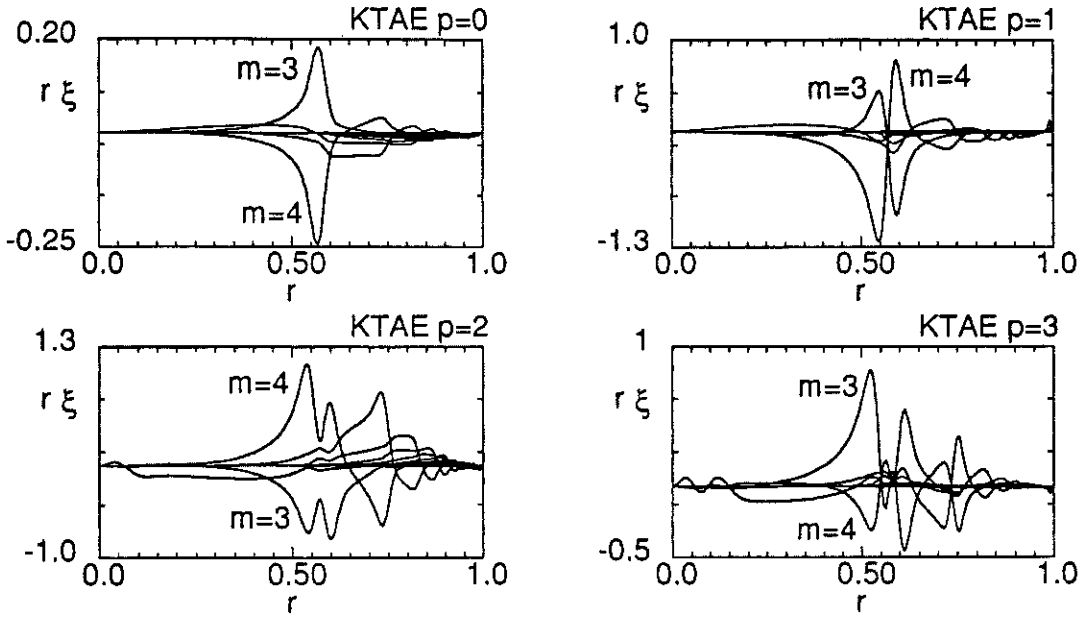

Figure 3 the radial plasma displacement of Kinetic Toroidicity Alfvén Eigenmodes (KTAE)s computed with CASTOR CODE for JET equilibrium #31638. These eigenfunctions represent modes with p=0..3, where p is the radial mode number (number of radial nodes).

MODELLING OF THE JET EQUILIBRIUM

- Applying the Castor code to a reconstructed JET equilibrium, the KTAE spectrum was computed for the shot #34188.

- In this pulse #34188 several modes were observed during **RF heating** by the Active Alfvén diagnostic in the passive mode. These mode frequencies occur around **240 KHz** and are **equally spaced** with a spacing of approximately 4 KHz.

- The **frequency of the modes is within 10% of the experimental values** and **their spacing also agrees with the experimental results** using $\mathrm{Im}[\tilde{\eta}] \approx 10^{-6}$ in the modelling.

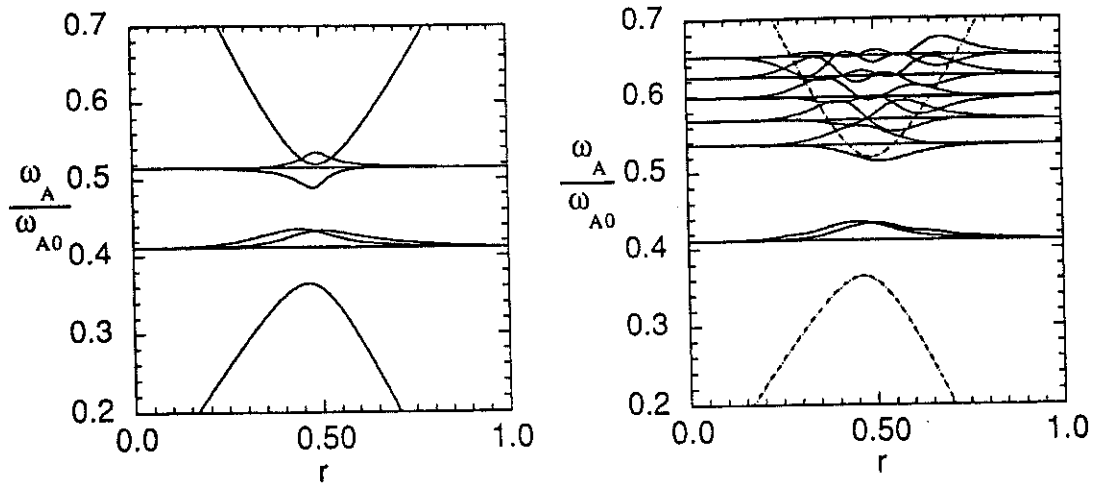

Figure 5 a) Two n=3 core localized modes that exist in a COLD plasma, in addition the continuous spectrum is displayed, b) the n=3 spectrum for an equivalent HOT plasma, the continuum spectrum (dotted line) is replaced by a discrete KTAE spectrum.

CONCLUSIONS

- **The KTAE spectrum has been computed in toroidal geometry using a reconstruction of JET equilibria**

- **In a COLD plasma one or possibly two core localized TAE modes exist**

- **In a HOT plasma the TAE mode has increased radiative damping $|\gamma_{TAE}| > 10\ |\gamma_{KTAE}|$, while a set of undamped KTAE modes appear just above the TAE gap.**

- **In a JET HOT plasma the model predicts the existence of a set of low n KTAE modes with equally spaced frequencies increasing linearly with radial mode number p and with linearly increasing radiative damping**

REFERENCES

[1] *Non-ideal Effects on toroidal Alfvén Eigenmode stability*, J.W. Connor, et al, in Controlled Fusion and Plasma Physics Vol 18 B Part II 616 (1994)

[2] *Existence of Core Localized Toroidicity-induced Alfvén Eigenmode*, G.Y. Fu, Submitted to Phys. Plasmas.

[3] *Alfvén Eigenmodes Active Excitation Experiments in JET*, A Fasoli, et al, I.A.E.A International Conference Seville, September 1994

The Distribution Function of Fusion Products at Birth

G J Sadler, P van Belle.
JET Joint Undertaking, Abingdon, Oxfordshire, OX14 3EA, UK.

ABSTRACT

It is customary to approximate well established nuclear physics cross-sections and reaction kinematics when diagnosing present day plasmas. Some adverse consequences of applying such approximations to fusion products are presented.

INTRODUCTION

- Fusion products not only carry the energy released in the fusion process but also yield information on the distribution function of the reacting particles.

- The birth energy of fusion products M_3 from the reaction:
  $M_1 + M_2 \rightarrow M_3 + M_4$ taking place in a plasma is given by:

$$\frac{\partial^2 N}{\partial\Omega_3 \cdot \partial E_3} = \iiint f_1(\vec{v}_2) \cdot f_2(\vec{v}_2) \cdot \frac{d\sigma}{d\Omega_3 \cdot dE_3 \cdot d\Omega_4 \cdot dE_4} \cdot |\vec{v}_1 - \vec{v}_2| \cdot dv_1^3 \cdot dv_2^3 \cdot dv_4^3 \qquad \text{Eq:1}$$

where $$\frac{d\sigma}{d\Omega_3 \cdot dE_3 \cdot d\Omega_4 \cdot dE_4} = \frac{d\sigma}{d\Omega_3 \cdot dE_3} \cdot \delta(E_3 - E_3^*)$$

and $$E_3^* = \tfrac{1}{2} \cdot m_3 \cdot V^2 + \frac{m_4}{m_3 + m_4} \cdot (Q + K) + \cos(\theta) \cdot V \cdot \sqrt{\frac{2 \cdot m_3 \cdot m_4}{m_3 + m_4} \cdot (Q + K)}$$

with Q = Energy release of the reaction, V = CM velocity, K = kinetic energy of reactants in the centre of mass CM, θ = angle between relative velocity and velocity of fusion product in the CM.

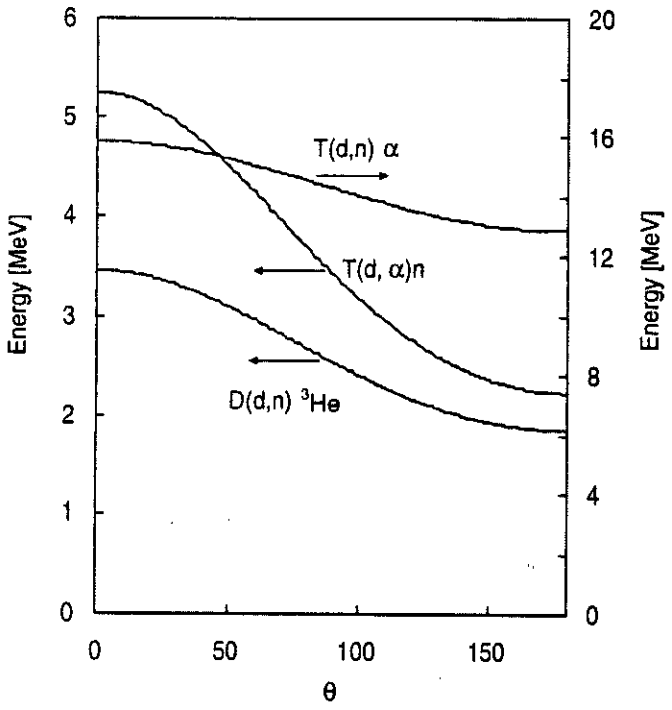

Fig.1:
Showing the variation of fusion product energy as a function of for:
a) neutrons from d->T
b) α's from d-> T
c) neutrons from d->D
for a monoenergetic d beam with
E_d = 500 keV in a cold plasma.

For neutrons from thermal D-D and D-T plasmas the dependence of the product energy on the details of the reaction kinematics is well exploited by measurements of the broadening of the neutron peak to deduce the plasma ion temperature. Conservation ofmomentum dictates a corresponding broadening for the associated charged particles. The FWHM of the α-particle distribution from a 25 keV thermal plasma will be 900 keV and 18% of the particles will have an energy in excess of 4 MeV (2% in excess of 4.5 MeV). How well will these α-particles be confined in a device designed to confine α-particles with a nominal energy of 3.5 MeV?

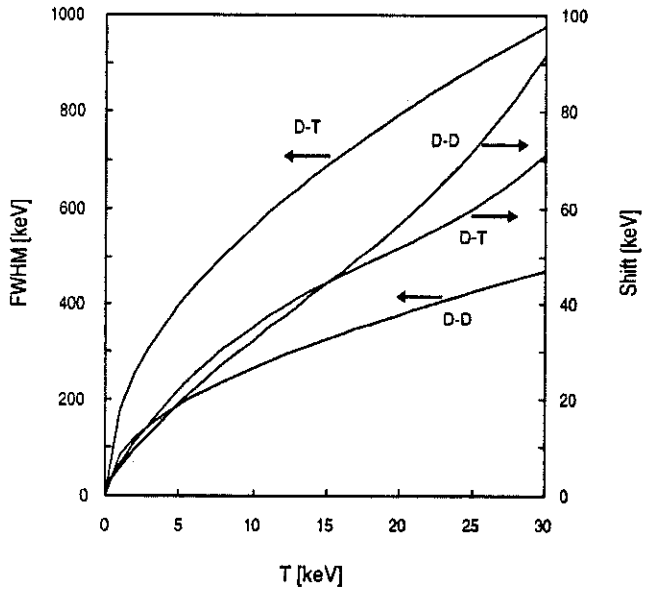

Fig.2.: The full width half maximum (FWHM) and associated energy shift for D-D and D-T neutrons as a function of temperature: $FWHM = g \cdot \sqrt{T_i}$ (ref.1) where g is weakly dependent on T_i (ref.2).
The broadening of the associated charged fusion product spectrum is identical to that of the neutron

- Most, if not all, present day simulation and interpretation codes ignore the spread in energy.

DRIVEN SYSTEMS

Doppler Shift

For driven systems the spread will be enhanced (the energy range of α-particles from 500 keV D^o beams, as proposed for ITER, will range from 2.2 to 5.3 MeV) and, moreover, anisotropy will play a role as discussed below. Results were obtained with the help of a Monte-Carlo relativistic kinematics computer code (ref. 2). The effects on the spectra are illustrated in Figs. 2 and 3. Note that the spectrum shape depends on the angle of emission.

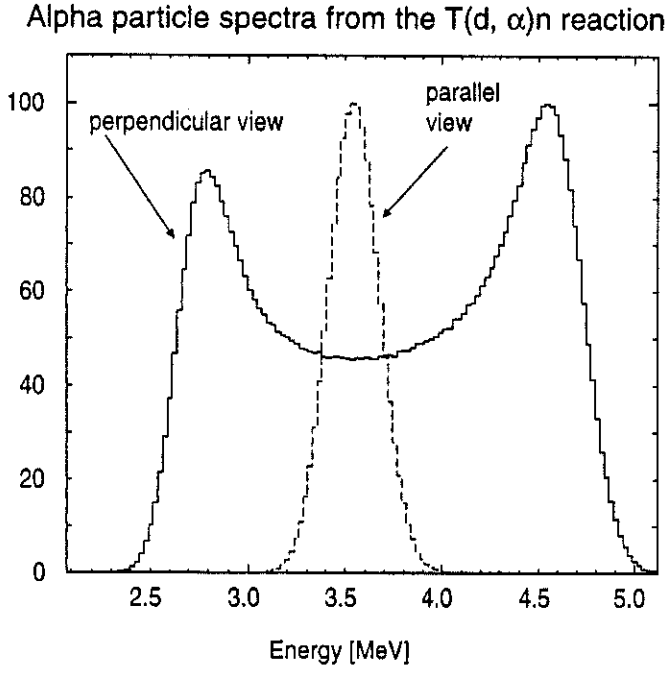

Fig.3:
Illustrating the α-particle spectrum at birth for a perpendicular (to the toroidal magnetic field, B_T) monoenergetic deuterium beam of E_d=200 keV circulating in a 5 keV plasma.(Reactivities not to scale)

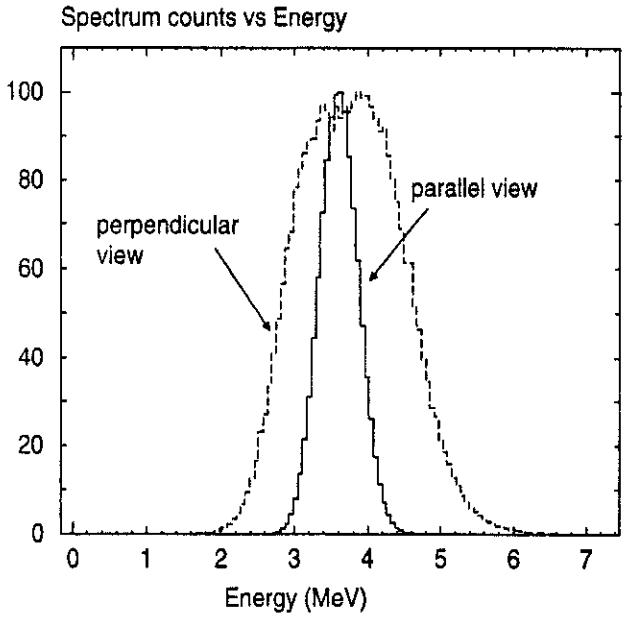

Fig.4:
Calculated α-particle birth spectra from a perpendicular RF-driven fast deuterium tail (T_{tail}= 200 keV) in a tritium background plasma (T_i=12keV). The distribution function is far from monoenergetic even if viewed parallel to B_T.

Anisotropy

Due to the relatively low mass of the neutron, neutron emission is almost isotropic in present day machines even for D-D neutrons despite the fact that there is a large deviation from isotropy in the CM cross-section of the D-D cross section above ~ 100 keV. However, this is not the case for the 1 MeV tritons released, which are often used for studying fast particle behaviour via their burn-up. The number of 140 keV D^o beam generated tritons emitted in a 30° forward cone is more than doubled (X 2.4) as compared to isotropic emission; is this part of the explanation for the extremely flat and sawtooth resistant 14 MeV neutron profiles as observed in JET?

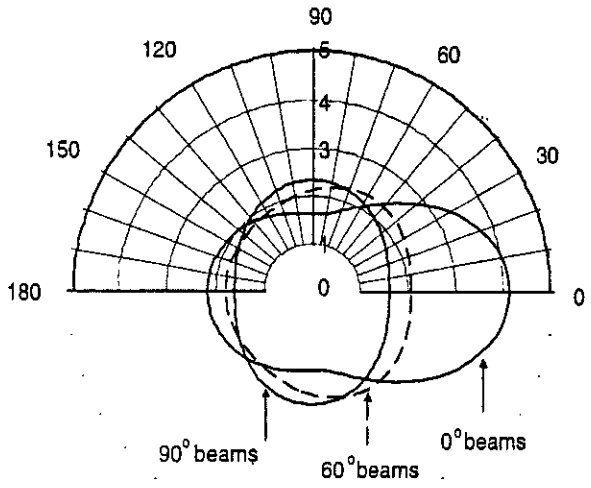

Fig.5:

$\int \frac{\partial^2 N}{\partial \Omega_3 \cdot \partial E_3} \cdot dE_3$ for tritons from 140 keV D beams injected with pitch angles of 0^0, 60^0. and 90^0 and slowing down in a 10 keV plasma (0^0 = parallel to the B_T field lines)

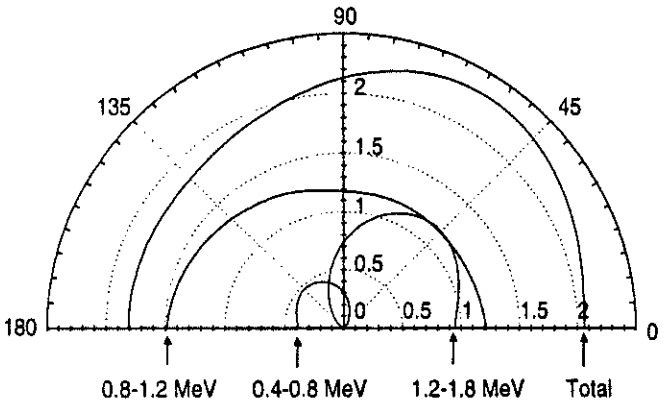

Fig.6.:

Differential cross-section for the emission of tritons in 3 energy ranges; beams with E_d=140 keV injected with 60^0 pitch angle.

D-D neutron emission from d beam heating in present day machines

The slight anisotropy in the D-D neutron emission on present day machines is normally neglected. However, if the variation in the shape of the energy spectra as a function of emission angle is taken into account and detectors with energy dependent efficiencies (as in the JET neutron profile monitor) are used, this is no longer justified.

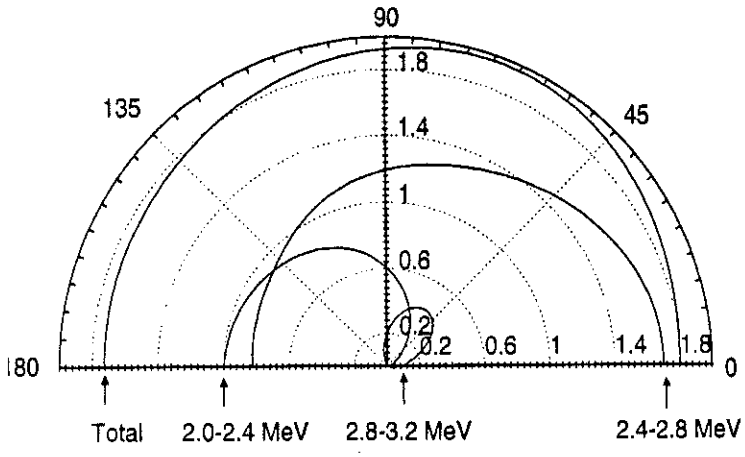

Fig.7:
Neutron emission from a 140 keV deuterium beam injected at 60^0 and slowing down in a 10 keV plasma.

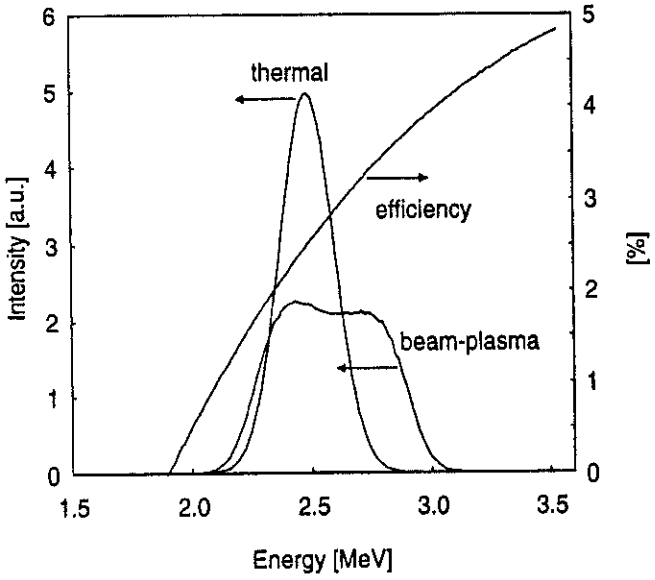

Fig.8:
Calculated neutron energy spectra for perpendicular viewing under the same conditions as in Fig.7. Also shown is the detection efficiency of the JET neutron profile monitor detector (NE213 scintillator biased at 1.9 MeV).

- At JET with 140 keV D^0 beams:

- The NE213 detectors are used as counters (in an energy window around 2.5 MeV) and their detection efficiency is determined by assuming a gaussian spectrum (as from a thermal plasma). This neglect of the variation of the detector efficiency with energy together with the shape of non-gaussian beam spectra lead to a 11 % overestimation of beam-plasma neutrons. The effect from anisotropy (< 1%) can be ignored.
- A 5% error in the NE213 bias setting or an equivalent drift in the photomultiplier gain results in a 16% overestimation.
- For beam-beam neutrons the enhancement becomes 19% and anisotropy adds 13%, leading to a total of 34%.

α-particles

Although the D-T cross section is almost isotropic in the CM frame, the number of α-particles produced in a forward cone of 30° by 140 keV D° beams is increased by 50% due to the CM-laboratory frame transformation.

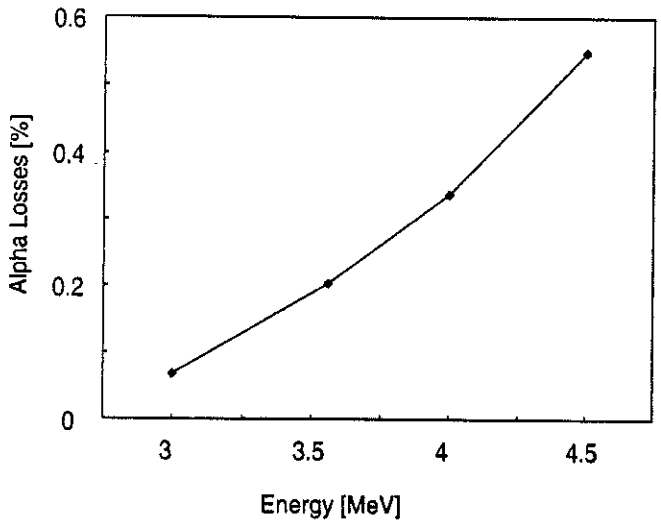

Fig.9:
Enhancement of classical α-particle losses with energy from orbit calculations for a typical JET high performance plasma equilibrium (I_p=3.8 MA and B_T=3.4 T). Isotropic birth distribution and spatial profile as from a thermal plasma.

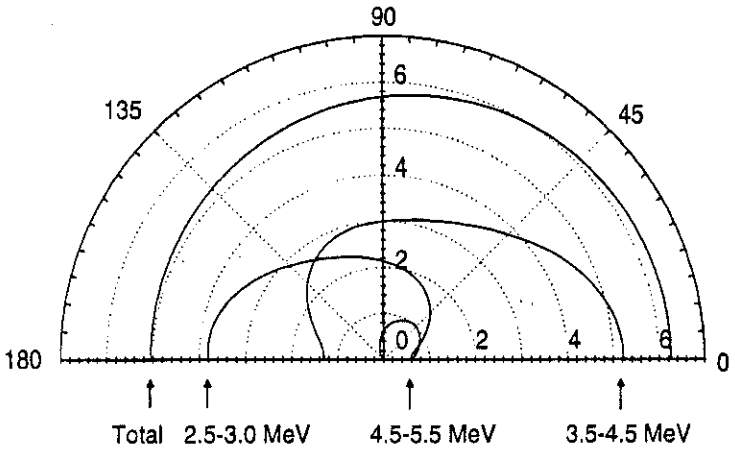

Fig.10:
α-particles generated by 500 keV d beams (as proposed for ITER) injected at ~ 60^0 and and slowing down in a 25 keV plasma.

D-D neutrons from high energy beams

Finally, at 500 keV injection energy, as proposed for ITER, even the 2.5 MeV neutron emission will become anisotropic (50% increase in a 30° forward cone) thus rendering the measurement of D-D neutron yields extremely difficult and measuring nD/nT ratios within a factor of 2 accuracy using neutron diagnostics in the presence of beams can almost certainly be excluded.

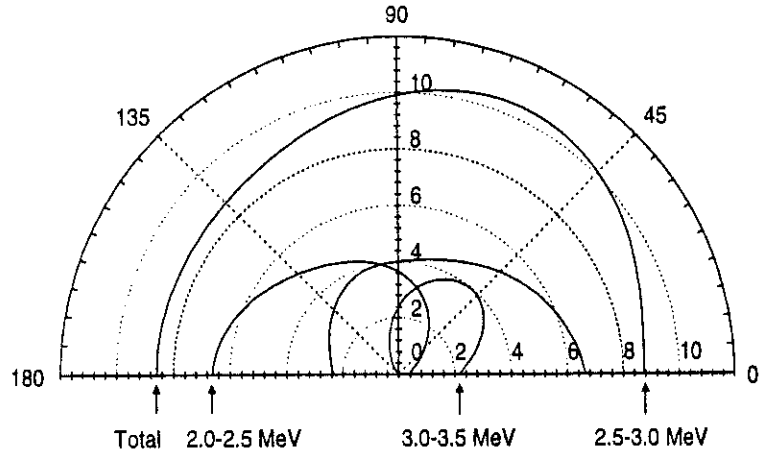

Fig.11:
D-D Neutron emission from 500 keV d beams injected at 60^0 and slowing down in a 25 keV plasma.

SUMMARY and CONCLUSIONS

- Doppler shift of fusion products is significant and should not be ignored in interpretation as well as prediction codes.

- Anisotropy of the fusion product emission in driven systems (with anisotropic drive) should not be ignored for:
  a) tritons and ^{3}He- particles from deuterium beam reactions with $E_{beam} \geq 100$ keV.
  b) α-particles from beam reactions with $E_{beam} \geq 100$ keV.
  c) neutrons from beam reactions with $E_{beam} \geq 500$ keV.

- Broadening and anisotropy needs to be incorporated into triton burn-up interpretation codes.

- Full α-particle spatial profiles at birth (including pitch angle distribution as needed for calculating α-particle densities) cannot be deduced from 2 dimensional neutron profile measurements in driven systems.

- Accurately diagnosing D-D neutrons generated from slowing down 500 keV deuterium beams in ITER-like plasmas will be extremely difficult and requires additional, non perpendicular viewing, energy sensitive neutron diagnostics.

REFERENCES:

1. Brysk H, Plasma Physics 15 (1973) 611.
2. Van Belle P, Sadler G, "The Computation of Fusion Product Spectra from High Temperature Plasmas" Basic and Advanced Fusion Plasma Diagnostic Techniques (Varenna 1986) Vol III 767 EUR 10797 EN.

Impurity Production and Erosion/Redeposition at the JET MKI Divertor

H Y Guo[1], X L Li, J P Coad, G F Matthews, P C Stangeby[2], J D Elder[2], L D Horton, A G Hwang, J Lingertat, A Loarte, R D Monk[3], M F Stamp, A Tabasso.

JET Joint Undertaking, Abingdon, Oxfordshire, OX14 3EA, UK.
[1] INRS-Energie et Matériaux, Université du Québec, Canada.
[2] University of Toronto, Institute for Aerospace Studies, Canada.
[3] Dept. of Physics, Royal Holloway College, University of London, Surrey, UK.

1. INTRODUCTION

The erosion of plasma facing materials is one of the crucial issues to be faced in the design of a fusion reactor, such as ITER. The influx of the eroded impurities and their accumulation in the plasma degrade plasma performance. The dominant erosion process under ion bombardment is physical sputtering for most materials, while chemical sputtering has also proven to be important for graphite [1]. However, the redeposition of the eroded atoms created by different erosion mechanisms and their efficiency in plasma contamination are less understood.

Colorimetry has been developed by Wienhold *et al* [2] to measure, *in situ*, and quantitatively, the erosion rate of deposited a-C:D films from their complementary colour fringes which are mainly dependant on the thickness of the co-deposits. This technique has been introduced at JET to investigate erosion/redeposition at the MKI divertor.

This poster describes:

- Colorimetric measurements of erosion rates in the JET MKI carbon divertor;
- Simulation of colorimetric results and divertor carbon profiles using DIVIMP code;
- Discussion of the relative roles of physical and chemical sputtering on the net erosion and impurity influx.

2. EROSION / REDEPOSITION AT MKI CARBON DIVERTOR

During the 1994/5 JET operations a colour viewing system has been routinely used to measure erosion/redeposition from changes in the complementary colours of redeposited films using the method of Wienhold *et al* [2].

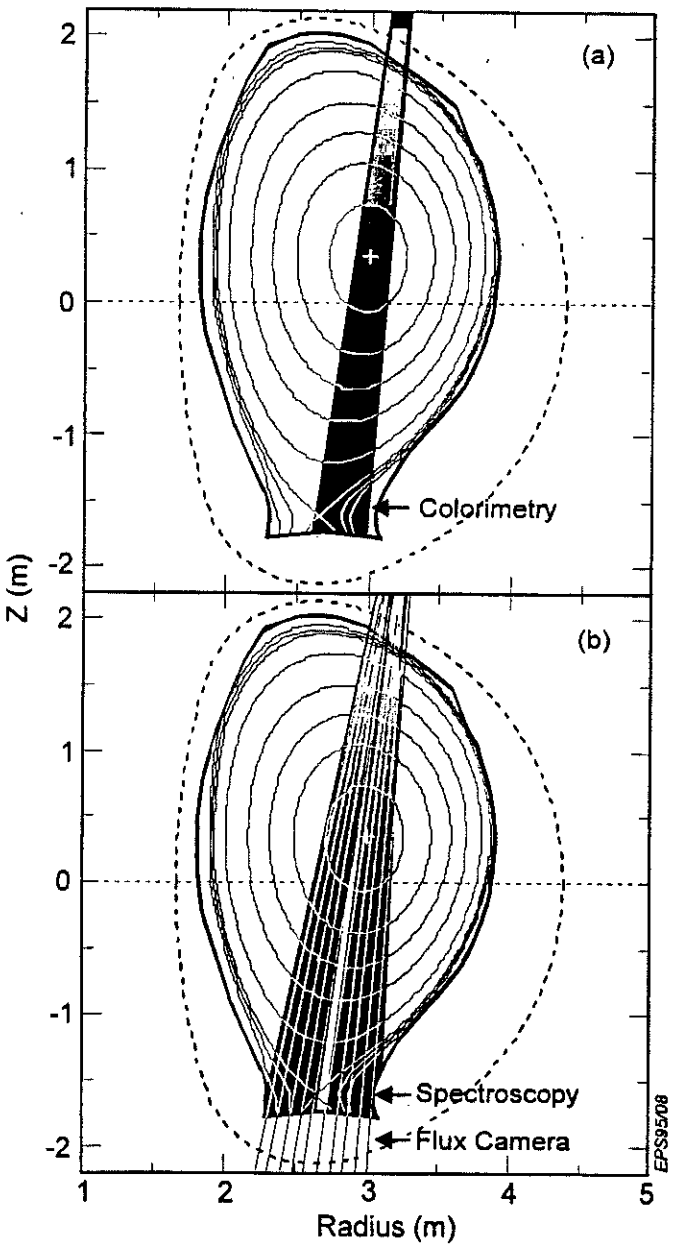

Fig.1. (a) Vertical view of Colorimetry, (b) Flux Camera view and lines of sight for visible Spectroscopy.

- A CCD video camera views outer part of the divertor floor from a port at the top of the vessel, fig.1(a).
- Illumination is provided by a halogen lamp with a dichroic reflector mounted on an adjacent port in the same poloidal plane.
- Colour images are taken automatically after each pulse and stored in the JET pulse file using a frame grabber.
- With an interactive analysis program, the colour coordinates RGB (red, green, blue) of the 24-bit colour images are converted to hue values, which are then related to the film thickness.
- Since it is difficult to follow every interference order of colour fringes, only relative thickness between successive discharges can be deduced with an error of ± 5 nm.
- The influx of eroded carbon from the target plates is detected by a flux camera and visible spectroscopy, as shown in fig1(b).

Toroidal distribution of the deposited a-C/Be:D films:

- Each divertor tile shields the edge of the adjacent one (fig.2).
- Deposition is uniform in wetted region, increasing rapidly in shadowed region (fig.3).

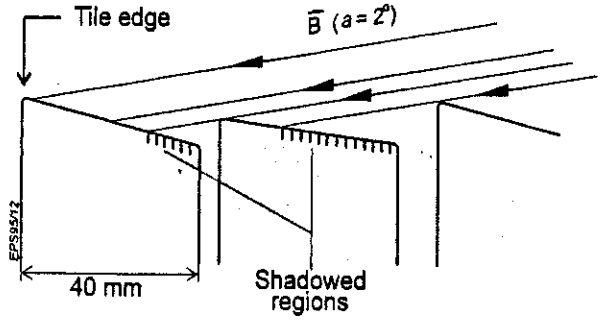

Fig.2. Schematic of toroidal cross section of divertor tiles.

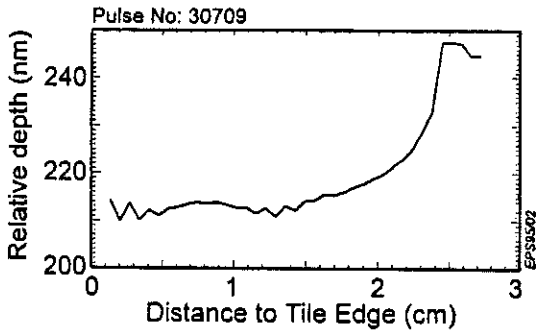

Fig.3, Toroidal distribution of the deposition

Erosion profile for a swept discharge:

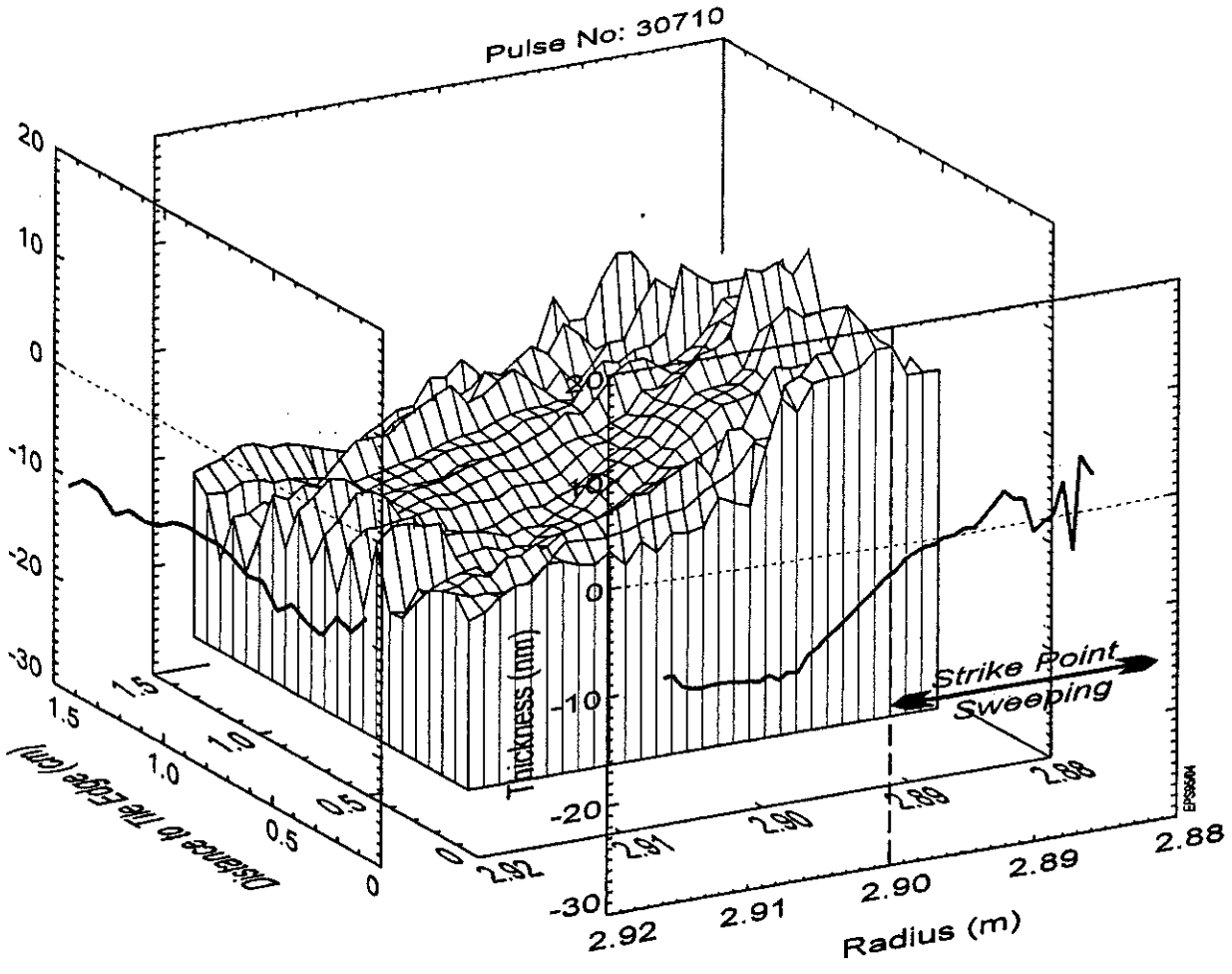

Fig.4. Erosion/Redeposition profile as a function of the radius and the toroidal distance to the tile edge for shot 30710.

Fig 4 shows the erosion/redeposition profile for shot 30710 as function of radial distance to the machine centre, and the toroidal distance to the tile edge. For this pulse, the separatrix swept over the region: R=2.8 to 2.9 m. The central plasma density is $5x10^{19}$ m^{-3}, and the input additional heating power (NBI) is 12 MW, with a duration of 3.5s. As can be seen:

- in the region swept by the plasma, there is little change on the net erosion profile,
- however, in the SOL near the turning point of the plasma sweeping the erosion is about 10 nm.

Net erosion profile for a high power, non-swept discharge: shot 34209

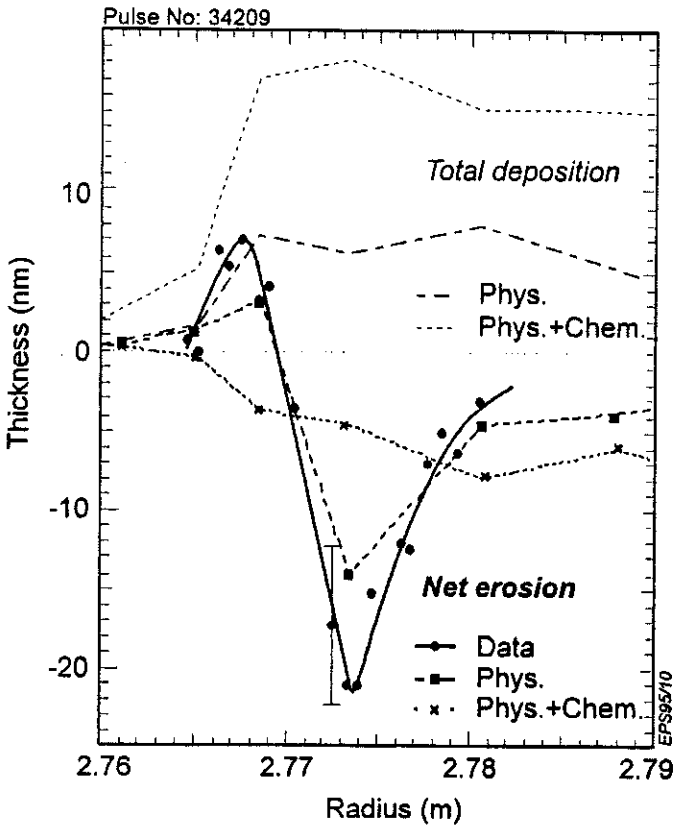

*Fig.5. Experimental and simulated **Net Erosion** profiles at the outer target plates. The calculated **Total Deposition** profiles are also shown for the different cases.*

- High heating power (hot ion H-mode),
- and the strike point is very stable (see fig.6).
- The erosion profile is very peaked and narrow (~ 1 cm).
- Net erosion at the strike point: ~ 21nm (with high power heated phase ~ 1s).
- The eroded atoms are deposited at the target in the private region.

Erosion/redeposition at the target plates is strongly dependent on strike point position, plasma duration and power deposition on the targets:

- At low power, colorimetry does not show large changes at the target.
- At medium power, ~ 10 MW, the net erosion rate is of the order of 5 nm/s.
- At high power (~20 MW), without sweeping the plasma strike points, a much higher erosion rate, ~ 20nm/s, has been observed.

3. IMPURITY PRODUCTION

To investigate the effects of different impurity production mechanisms on the erosion of target plates and impurity influx, we have simulated the measured erosion/redeposition profiles and the carbon profiles at the divertor targets, measured by Flux Camera and Visible Spectroscopy, using the DIVIMP code [3,4].

- A 2-D background plasma is generated using a one-dimensional quasi-analytic model, based on the measurements of Langmuir probes at the divertor plates to define boundary conditions, assuming $T_i = 2T_e$, $D_\perp = 1\ m^2/s$ for impurities.
- Chemical sputtering of Graphite has been newly implemented in the DIVIMP code. The chemically sputtered carbon atoms are launched at the target (600 K) with the yields calculated according to the revised formulae by Garcia-Rosales and Roth [5].

3.1 Erosion/Redeposition: shot 34209

The evolution of the plasma parameters (fig.6) and the code input (fig.7):

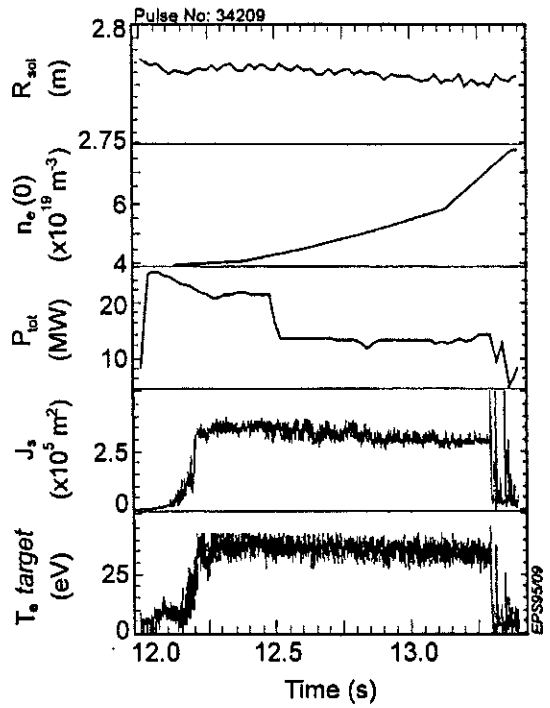

Fig.6. Evolution of plasma parameters for shot 34209.

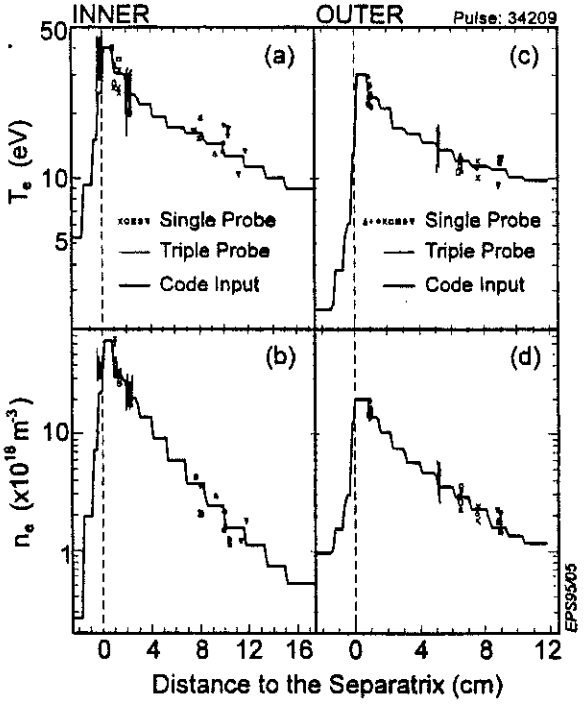

Fig.7. Langmuir probe data at target plates and the values used as input to the code.

The calculated net erosion profiles are also shown in fig.5 to compare with the data:

- The net erosion caused by physical sputtering resulted in a very peaked profile, in agreement both quantitatively and in shape with the experimental data (fig.5). The shape is not sensitive to T_i. $D_\perp$ has no effect on the net erosion near the strike point.
- With chemical sputtering, yields increase from 1.9% to 4.1%, net erosion becomes flat.
- It appears that there is, effectively, no chemical sputtering. The chemically sputtered CD_4 and fragments must redeposit promptly near their point of origin. This has also been observed by Lieder *et al*, from spectroscopic measurements at ASDEX-U [6].

3.2 CII Intensity Profiles

The CII (658 nm) intensity profiles have been recorded with an absolutely calibrated Flux Camera, which views the divertor vertically from the top of Octant 8. Fig.8 shows the CII profile for shot 34209, at 52.3s, and shot 34355, at 51.22s.

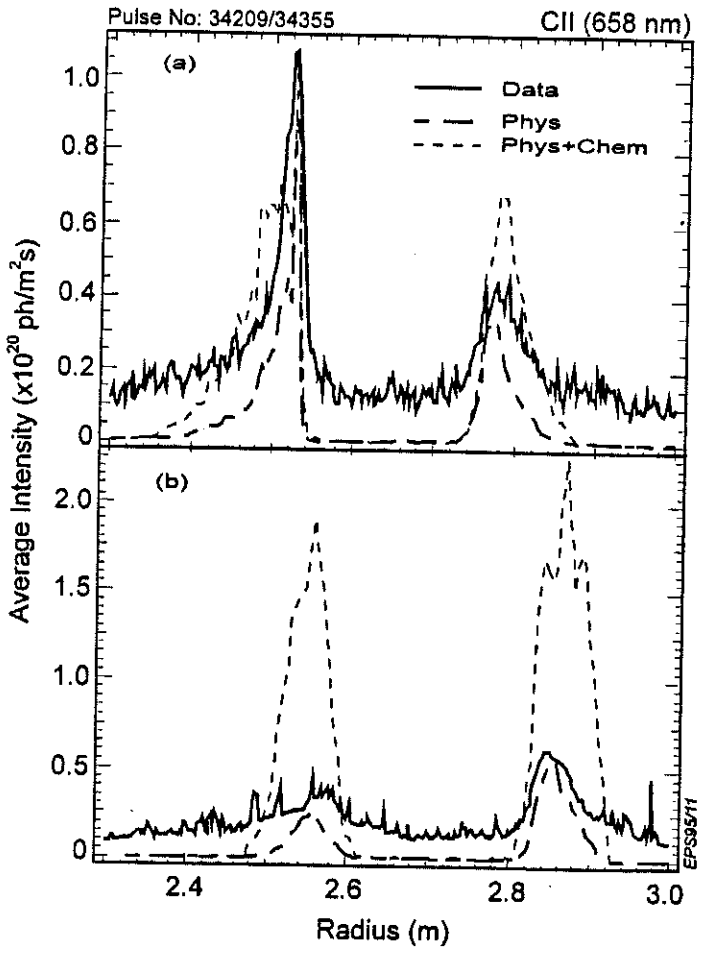

Fig.8. CII profiles for (a) shot 34209, and (b) 34355.

Shot 34209 (fig.8a):

- A larger peak at the inner strike point, smaller one at the outer.
- With only physical sputtering, the simulated CII intensities are in good agreement with the flux camera results with $T_i = 2T_e$ (peak values ↓ 25% for $T_i=T_e$).
- However, including chemical sputtering gives higher CII intensity, especially near the outer strike point, due to relatively lower temperature.

Shot 34355 - *low T_e: effect of chemical sputtering is more pronounced (fig.8b)*

- The effective yield is greatly influenced: for physical sputtering, the effective yield is Y_{eff}=0.94%, while with chemical sputtering it is 5.7%, ~ 6 times larger! Again, the CII two peaks at the targets showed little contribution due to chemical sputtering.
- It is estimated (from fig.8b) that chemically sputtered hydrocarbons would only contribute 10% of C^+.
- Shimizu *et al* have also found that only about 10% of target-produced CD_4 reaches C^+ [7], and Kallenbach *et al* estimated only 20% of the CD_4 gets to CD [8].

3.3 CIII Intensity Levels

Visible spectroscopy (KS3) has been employed to measure the integrated photon flux of CIII (465 nm) from the inner and outer divertor areas separately. The measurements and DIVIMP results for shots: 34209, 34335 and 31627 are shown in the table below:

Shot No.	Modelling Details		Outer ($x10^{18}$ ph/s/m^2/sr)	Inner ($x10^{18}$ ph/s/m^2/sr)
34209	*Exp*	*KS3 data*	*1.6*	*3.4*
(52.3s)	Phys.	$T_i = 2T_e / T_e$	3.1 / 2.3	6.4 /5.8
	Phys.+Chem.	$T_i = 2T_e / T_e$	6.6 / 8.0	10/12
34355	*Exp*	*KS3 data*	*5.0*	*2.2*
(51.2s)	Phys.	$T_i = 2T_e / T_e$	7.0 / 4.8	1.9 /0.8
	Phys.+Chem.	$T_i = 2T_e / T_e$	23 / 23	11/7.4
31627	*Exp*	*KS3 data*	*1.2*	*1.0*
(54.1s)	Phys.	$T_i = 2T_e / T_e$	2.0 / 1.1	8.6 /5.1
	Phys.+Chem.	$T_i = 2T_e / T_e$	9.7 / 7.2	27/24

- Using only physical sputtering, with $T_i = T_e$ or $T_i = 2T_e$, produces a reasonable fit to the data.
- Including chemical sputtering, the calculated CIII intensity values increase dramatically, by factors of 3 ~ 25 times higher than the experimental data.
- Thus, the rate of production of the C^{++} ions following chemical sputtering is low. This is consistent with the analysis of the C^+ data, discussed above.

4. CONCLUSIONS

- No net erosion is observed during the plasma sweeping, except in the proximity of the turning point.
- Erosion rate depends on the plasma heating power and plasma density. At medium power, ~ 10 MW, an erosion rate of order of 5 nm/s has been observed , whilst at high power, ~ 20 MW, the erosion rate at the strike point can reach ~ 20 nm/s.
- Net erosion of target plates are mainly due to physical sputtering, showing no obvious effect of chemical sputtering evidently due to the prompt and localised redeposition of CD_4 and molecular fragments.
- Spectroscopic lines of C^+ and C^{++} are quantitatively reproduced by DIVIMP with a dominant physical sputtering source, and also show little effect due to chemical sputtering, suggesting low efficiency of producing carbon ions from CD_4, ~ 10%.

5. ACKNOWLEDGEMENTS

HYG acknowledges financial support from the National Fusion Program of Canada.

6. REFERENCES

[1] J. Roth, E.Vietzke and A.A. Haasz, Supplement to Nucl. Fusion **1**, 63 (1991).

[2] P. Wienhold, F. Weschenfelder and J. Winter, to appear in J. Nucl. Mater. **220-222** (Proc. of 11th PSI Conference, Mito, Japan, 1994).

[3] P.C. Stangeby, C. Farrell, S. Hoskins and L. Wood, Nucl. Fusion **28**, 1945 (1988)

[4] P.C. Stangeby and J.D. Elder, J. Nul. Mater. **196-198**, 258(1992).

[5] C. Garcia-Rosales and J. Roth, in Proc. of 21st EPS Conference on Controlled Fusion and Plasma Physics, Vol. 18B, Part II, p. 770, Montpellier, 1994.

[6] G. Lieder, K. Behringer, A. R. Field, *et al*, in Proc. of 21st EPS Conference on Controlled Fusion and Plasma Physics, Vol. 18B, Part II, p. 722, Montpellier, 1994.

[7] K. Shimizu, N. Hosogane, T. Takizuka, et al, IAEA-CN-60/D-P-I-2, 15th IAEA Conference, Seville, Spain, 1994.

[8] A. Kallenbach, R. Neu, W. Poschenrieder, *et al*, Nucl. Fusion **34**, 1557(1994).

Physics Aspects of Coupling the ICRF A2 Antennae to JET Discharges

P U Lamalle, G Bell[1], V P Bhatnagar, M Bures, B Fechner, C Gormezano, J Jacquinot, A Kaye, M Lennholm, F Nguyen[2], E Righi, A Sibley, D F H Start, M Timms, T J Wade.

JET Joint Undertaking, Abingdon, Oxfordshire, OX14 3EA, UK.

[1] Oak Ridge National Laboratory, USA.

[2] CEA, Centre D'Etudes de Cadarache, France.

THE A2 ANTENNAE

- Designed for rf heating and current drive in the JET divertor configurations [1, 2]; operating since early 1994.
- Four arrays of four side-by-side straps. Each strap is driven by an independent amplifier (2MW, 25 to 56MHz); this allows operation with arbitrary current phasings, i.e. with various radiated power spectra (dominant parallel wavenumber $k_{//}$ adjustable between 0 and 6.4m^{-1}, Fig.3).
- Now 12-15MW routinely launched into plasma in 0ππ0 phasing, a major improvement since 1994 ([3] to [5]) due to the reliability of the new electronics. The record coupled power is 16.5MW with 0ππ0 and 10MW with progressive phasings such as (0,π/2,π,-π/2).
- Automatic matching: feedbacks on frequency (for each antenna), and on trombones and stubs (in each one of the 16 transmission lines).
- Prototype central separator installed on antenna D in March 1995 (Fig.1.b).

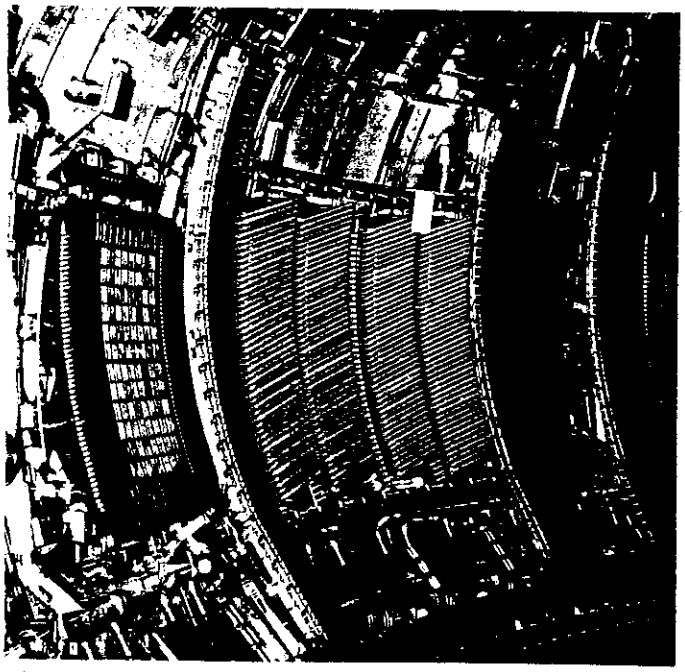

Fig.1a Original ICRH A2 antenna with its Faraday screen

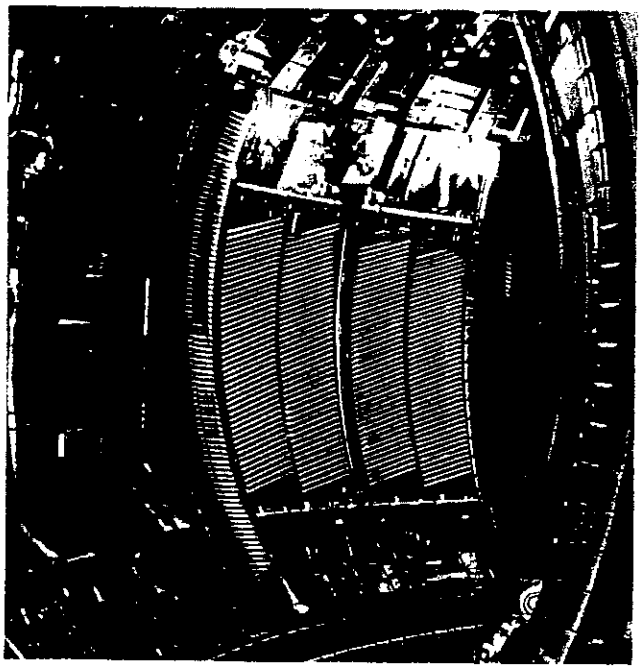

Fig.1b Antenna D after addition of the central separator

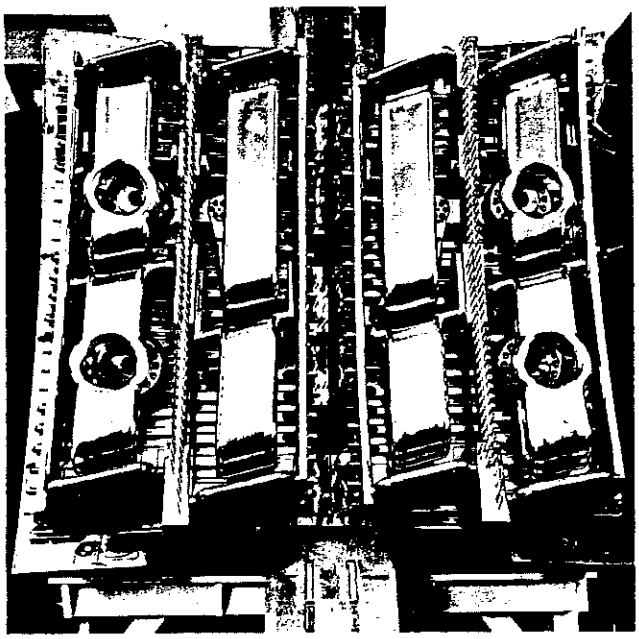

Fig.2 A2 antenna with the Faraday screen removed

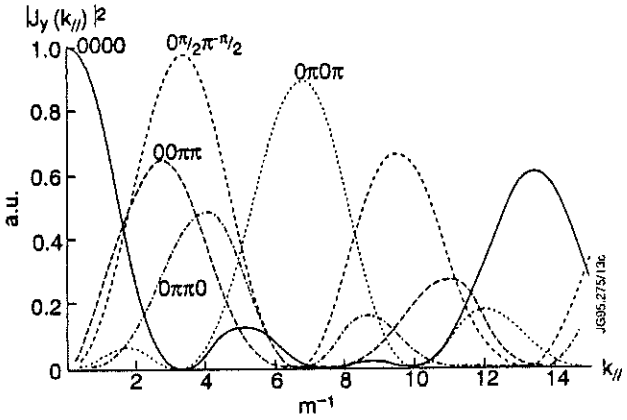

Fig.3 $k_{//}$ spectra ($|J_n|^2$) for the main phasings in use.

ANALYSIS OF COUPLING

The coupling resistance R_c is defined for each line+strap system by $P = \frac{V_{max}^2}{2\,Z_c^2} R_c$

P: generator power; V_{max}: associated maximum voltage on the main transmission line (MTL); Z_c: line characteristic impedance (30Ω). As the lines share the same admissible maximum voltage, the R_c's reflect their respective power coupling ability. In terms of the MTL reflection coefficient amplitude r and the VSWR s, $R_c = Z_c\,(1\text{-}r) / (1+r) = Z_c / s$.

- Critical dependence upon plasma conditions (boundary shape, scrape-off layer parameters, etc...)
- Important role of transmission line losses at low coupling: R_c includes a contribution $R_{loss} \approx 0.0623\ \sqrt{f_{MHz}}$ (0.3 to 0.5Ω), i.e.
  $R_c = R_{ca}+R_{loss}$, where R_{ca} corresponds to the effective strap radiation.
  ($0\pi0\pi$ phasing: ca.20% of power lost at 52MHz, up to 30% at 32MHz for typical H mode conditions)
- Below 50MHz the two inner straps of each array have a lower average R_c than the outer ones. Comprehensive measurements have been carried out on an antenna prototype loaded with absorbing foam; the analysis of these data is under way.
  Possible causes of imbalance:
  - high characteristic impedance of the 'cross-over' conductors feeding the two inner straps of each array (Fig.2)
  - intrinsic differences between the main conductors
  - enhancement of dissymmetries by the tilted Faraday shield elements

- Dependence on array phasing: R_c is lowest in dipole ($0\pi0\pi$), highest in monopole (0000) mode

  Inherent to the variable $k_{//}$ spectrum facility; see below.

Experimental determination of the antenna scattering matrix S on plasma

- 4 by 4 matrix connecting the forward (V_+) and reflected (V_-) complex voltages at the antenna input:

$$\boxed{V_- = S\,V_+} \qquad (1)$$

- S gives a synthetic description of the linear response to arbitrary excitations of the array.
- Connection with the input impedance matrix: $Z = Z_c\,(E+S)\,(E-S)^{-1}$ (E: identity matrix) (2)
- Determination in a single shot (5sec.with steady plasma required):
  - Programmed phase ramps on generator voltages ⇒ large number of independent sets of eq.(1)
  - S results from a linear least-squares fit thereto.
- Problem: voltage measurement points separated from antenna by ca.81m of transmission line and feedback-controlled matching trombones. Careful corrections ⇒ good estimates of antenna voltages.

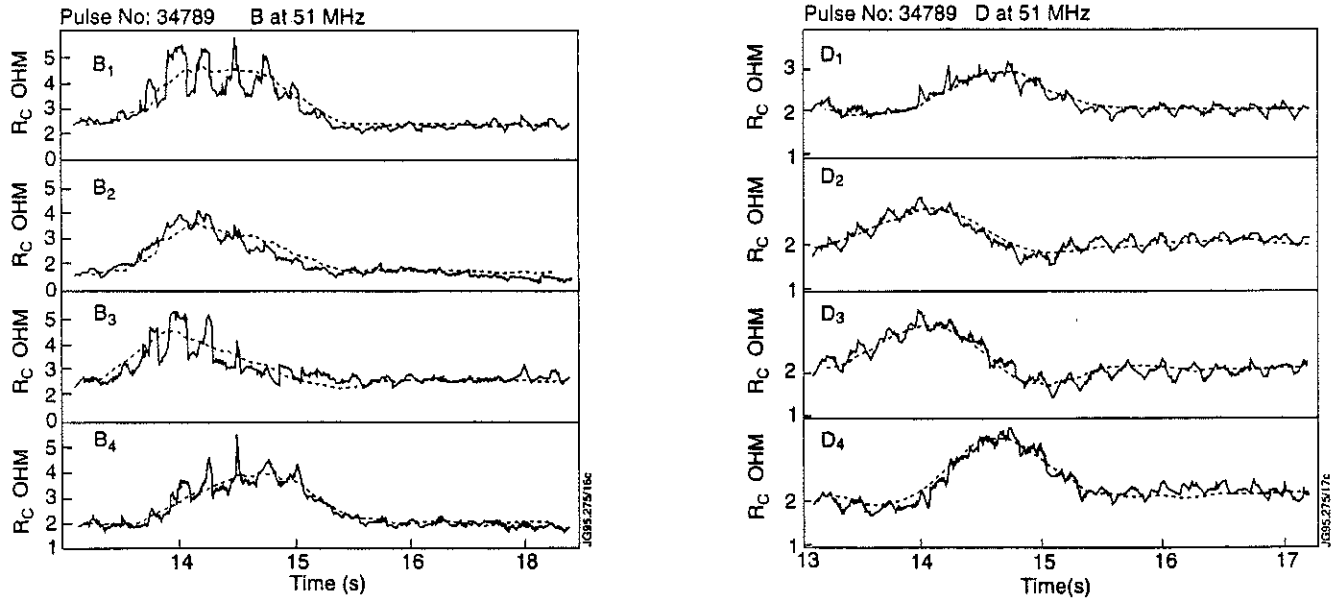

Fig.4 Evolution of the coupling resistances during phase ramps (continuous lines); estimation based on associated scattering matrices (dashed lines), showing a good fit quality.

- **Main features of the results:**
  - Large diagonal elements, $|S_{ii}| > 0.75$ ⇒ low average coupling.
  - Coupling imbalance at low frequency reflected by $|S_{11}|, |S_{44}| < |S_{22}|, |S_{33}|$.
  - * Linear regime assumption is adequate (very weak dependence of R_c on power)
  - * Models limiting interstrap coupling to first-neighbours $S_{ii\pm1}$ ⇒ fair representation of most usual phasings, but

wrong prediction of monopole (only case where wavenumbers $|k_{//}| < \omega/c$ have been excited).

* Fits using an *a priori* full matrix ⇒ correct description in all cases;
  yield interstrap coupling terms S_{ij} ($i \neq j$) all of the same order of magnitude, consistently with measurements on absorbing foam in torus.
* ⇒ The plasma spectral resistance is peaked near $k_{//}=0$. Preliminary estimation based on re Z_{1j}: Fig.5
- Moreover, sensitivity of R_c to divertor x-point sweep is strongly enhanced in 0000, $00\pi\pi$ (Fig.4, centre)

⇒ Evidence for the global edge or coaxial modes predicted by theory [6]!

• **Illustration:**

S from pulse 34789 (D at 51MHz):

$\|S_{ij}\|$				arg S_{ij} (°)			
0.831	0.062	0.049	0.053	-113	81	54	56
0.062	0.842	0.050	0.050	81	-121	58	58
0.049	0.050	0.815	0.084	54	58	-139	72
0.053	0.050	0.084	0.798	56	58	72	-110

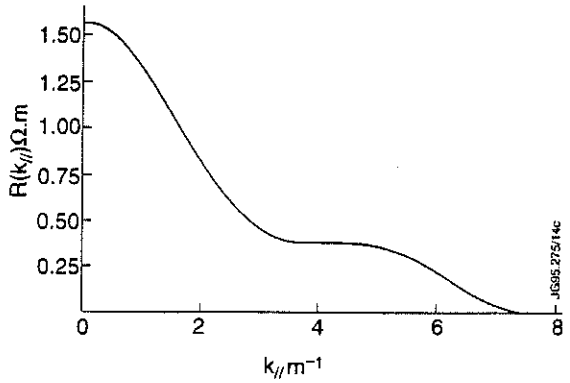

Fig.5 Preliminary (coarse) estimate of the plasma spectral resistance obtained from Z (eq.2) derived from the S on the left.

Confirms R_c's seen in neighbour fixed-phased pulses (Fig.6).

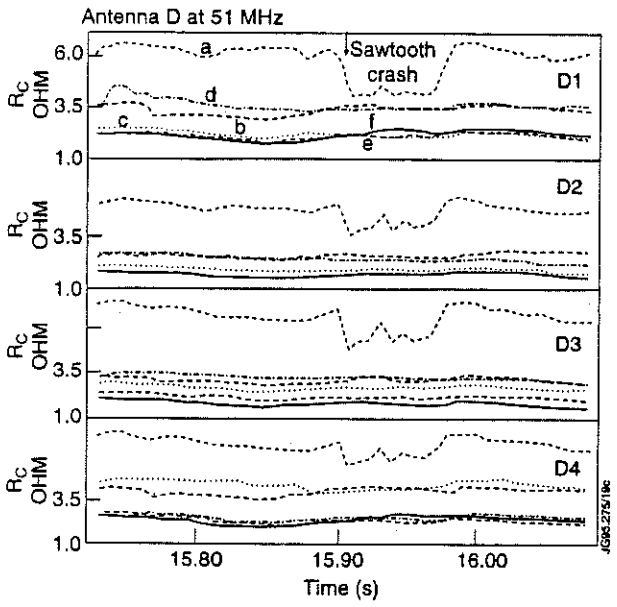

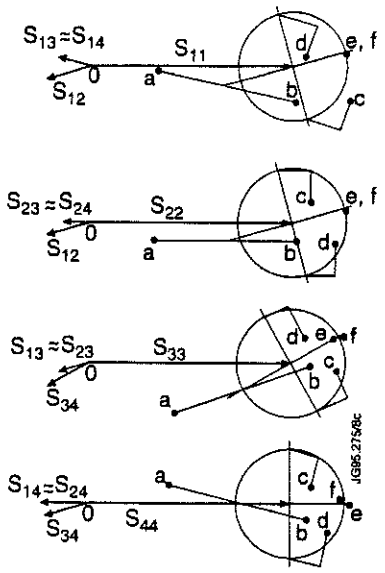

Fig.6 Coupling resistances measured for various excitations of antenna D (left). Complex reflection coefficients based on S obtained during phase ramp in pulse 34789 (right, schematic; S_{ii} is taken as phase reference for each strap), showing good agreement.

5. The relative heating efficiency, defined as the ratio between $\Delta W/\Delta P_{rf}$ at a given phasing ($k_{//}$) normalized to its dipole ($k_{//} = 6.4m^{-1}$) value.

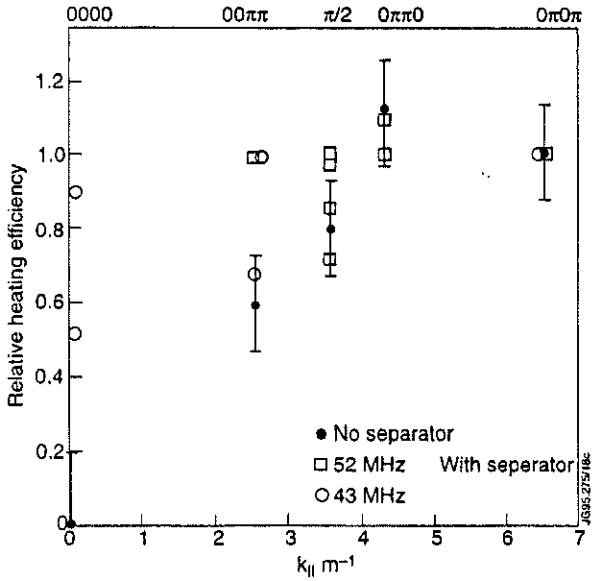

Fig.7 Heating efficiency normalized to dipole heating efficiency versus characteristic parallel wavenumber

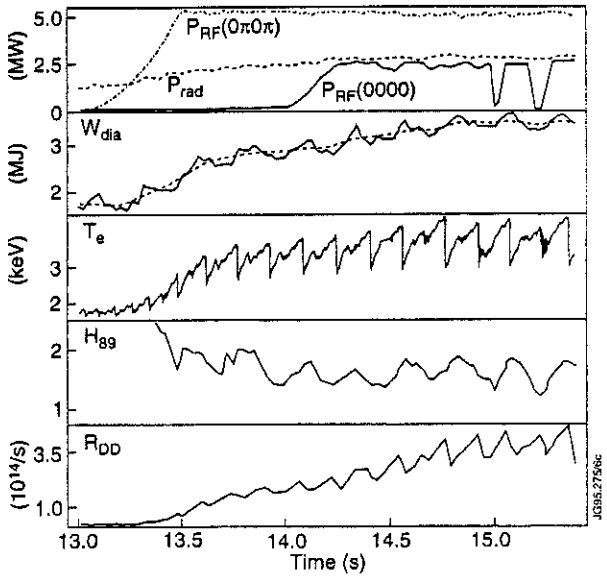

Fig.8 Improved monopole heating efficiency with separator

- Determined on the original A2 antenna using a 1Hz modulation of the rf power: low efficiency at low $k_{//}$, best in dipole phasing.
- Recently re-assessed on antenna D with separator, showing improvement of the monopole heating efficiency (Fig.8). However frequent arcs occur.

6. 'Hot' spots (for location on antenna see labels Figs.1)

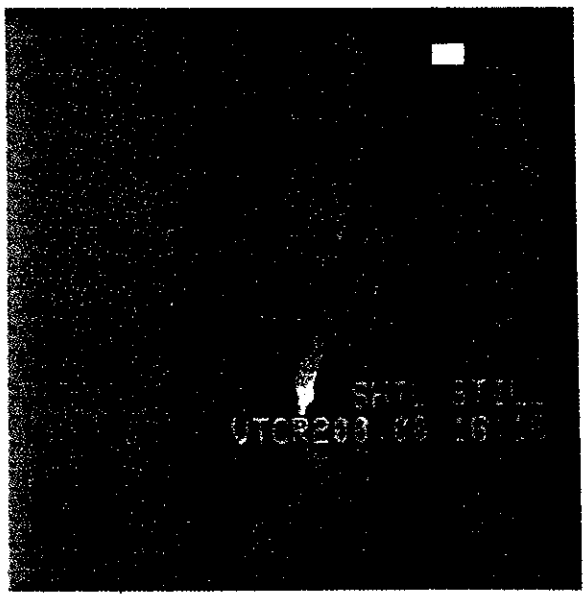

Fig.9 Typical bright spots observed during operation of antenna D

- Observed on a poloidal limiter when the adjacent antenna (D) is active, except in 0π0π and 0ππ0 phasings; also with new separator.
- Presence and intensity correlated with the antenna-plasma distance;
- Vertical position correlated with q_{95}.
- Possible link with radial currents (Fig.2)

7. Resilience to ELMs

- Giant ELMs induce rapid factor-of-4 variations in R_c ⇒ high reflection at the generators ⇒ frequent trips.
- Short-term solutions: require electronical discrimination of ELMs from arcs; then various schemes, e.g.
  - desensitize the control electronics ⇒ suppress generator tripping during the ELM (Fig.10), or
  - restore power faster after ELM-trip than after a normal trip (Fig.11) ⇒ higher average power.

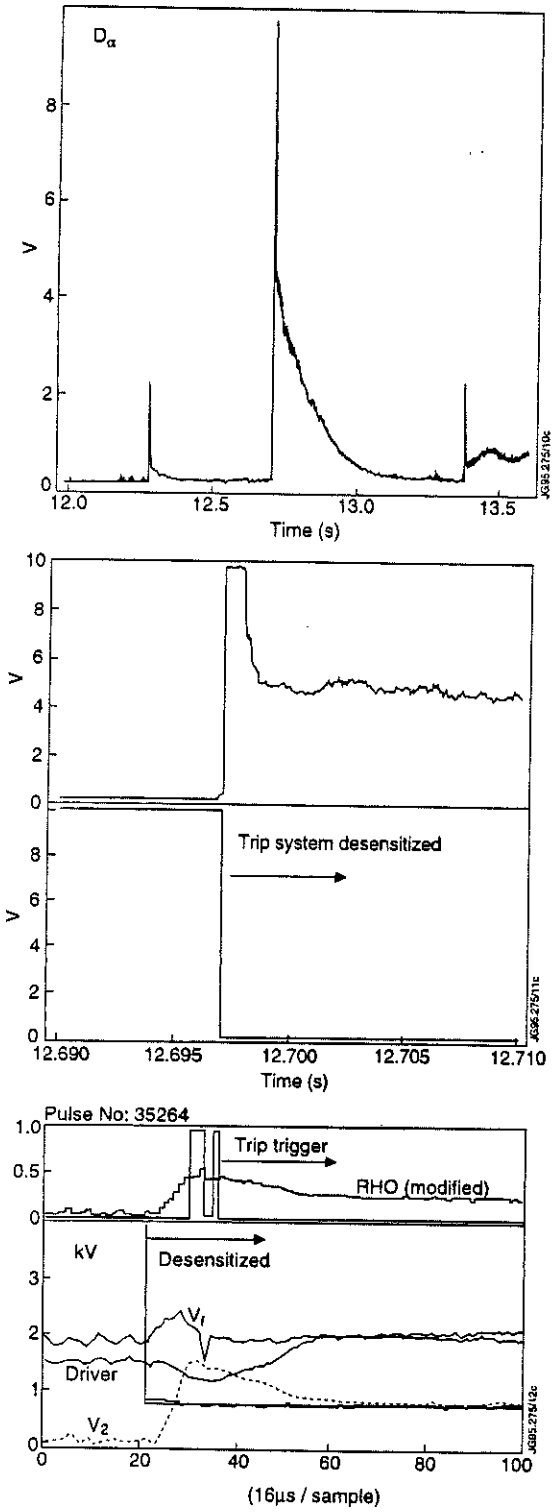

Fig.10 Fast signal acquisition showing deactivated trip signal during an ELM

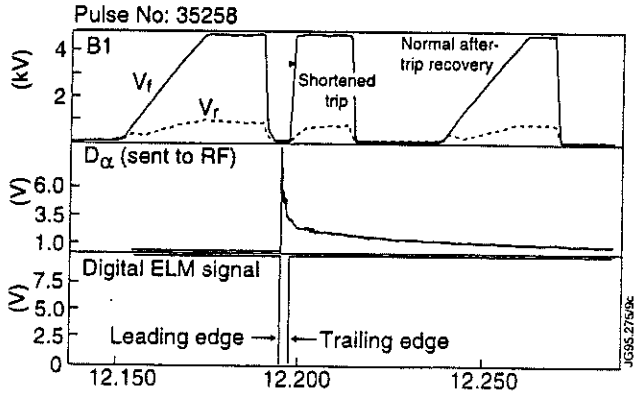

Fig.11 Prompt trip recovery after an ELM

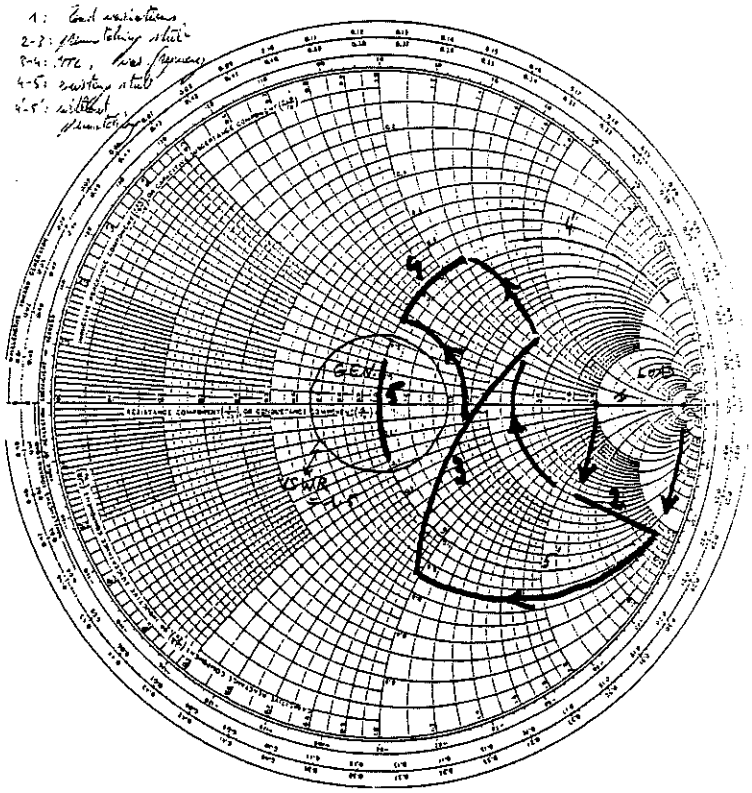

Fig.12 Optimal broadband adaptation with prematching stub and fast frequency tracking for typical ELM-induced load variations.

- Long-term rf hardware modifications for broad-band adaptation (also ITER-relevant) / favourite scenario:
  - prematching stub in each line and fast frequency variations ⇒ adaptation on ELM timescale (Fig.12).
  - additional interest: reduction of line losses.

ACHIEVEMENTS IN 1995

- The sideband problems linked with the control electronics [5] have been cured by the end of 1994 ⇒ very substantial improvement in the performance and reliability of the plant: gain of ca.50% in the routinely coupled power.

- RF-only H modes:
  - *Record power: 16.5MW in 0ππ0 (Fig.13)*
  - Sawteeth stabilization, production of giant sawteeth (2.5MA/3.5T, Figs.13, 14)
  - Also obtained at high plasma current (4.7MA/3.2T, Fig.15)
  - Low power threshold (Fig.16)

- Combined with Neutral Beam Injection heating:
  - Record auxiliary power of 32MW in a divertor plasma (15MW RF + 17MW NBI) during an ELMy H mode (Fig.17)
  - Contribution to hot-ion H modes (Fig.18, 3MA/3T)

- Improvement in heating efficiency at low $k_{//}$ after addition of a separator between the two halves of antenna D (Figs.1b, 7, 8), but power limited by arcs. Newly designed separators will be installed in all modules during the 1995 shutdown.

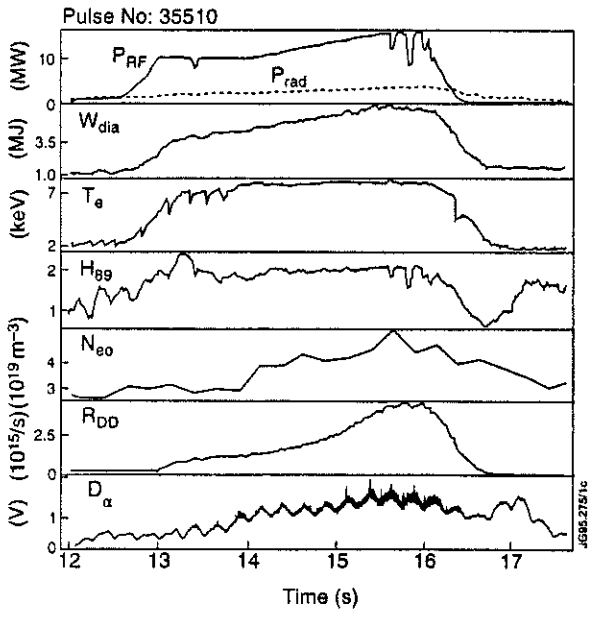

Fig.13 RF-only H mode, during which a record of 16.5MW was coupled to the plasma

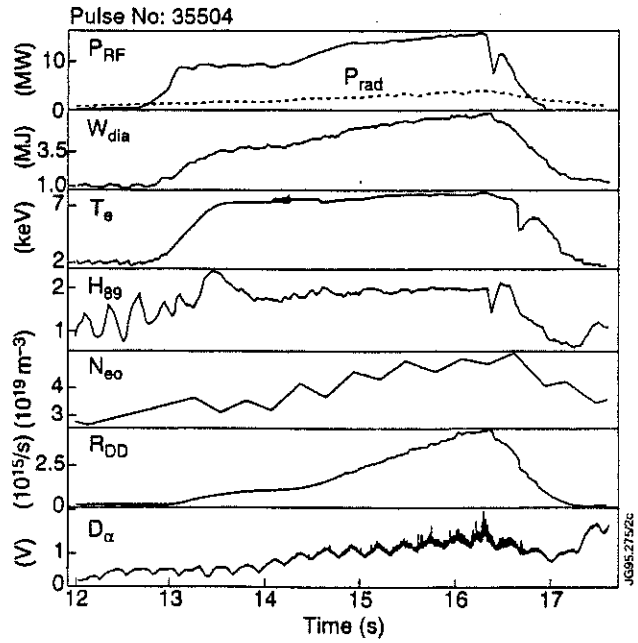

Fig.14 Giant sawtooth during high power rf heating

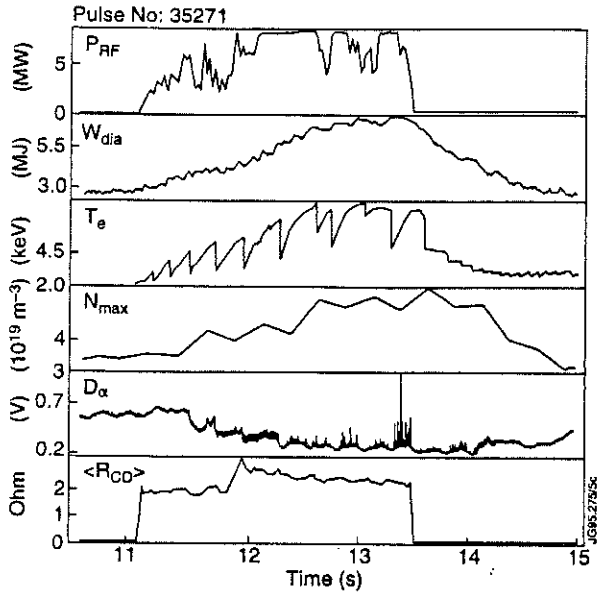

Fig.15 High current rf H mode

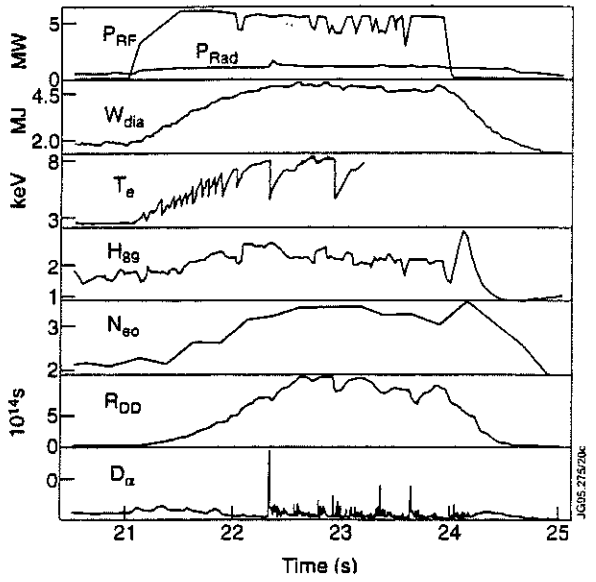

Fig.16 Low threshold rf H mode

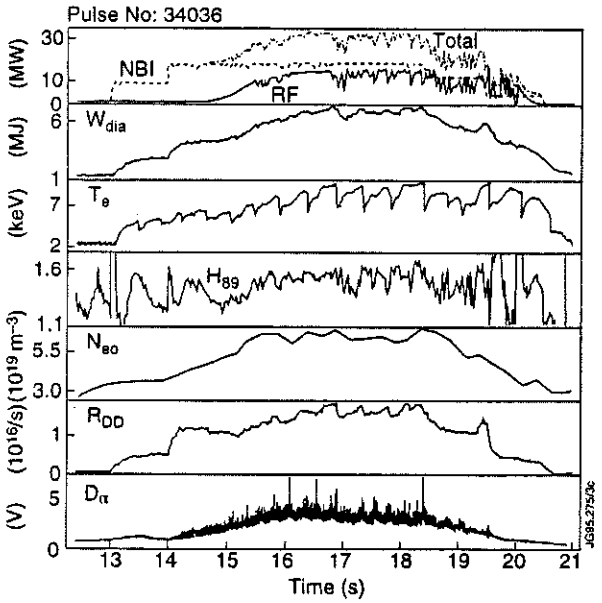

Fig.17 Record auxiliary power coupled to an ELMy H mode (32MW)

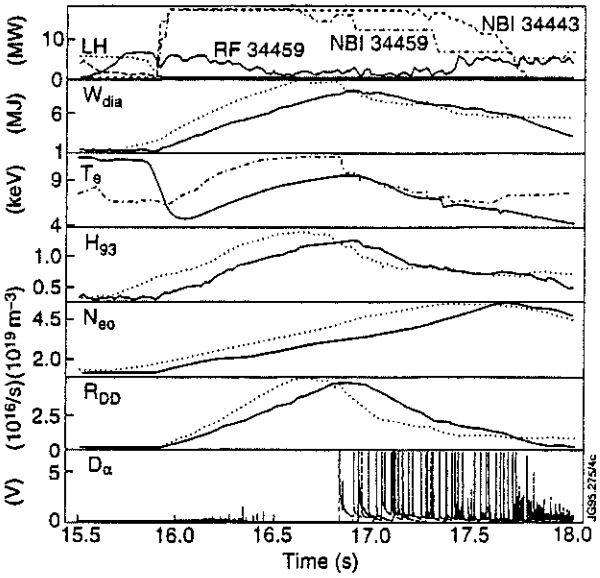

Fig.18 Contribution of ICRH to hot ion H mode

[1] A.Kaye et al., Fusion Engineering and Design 24 (1994) 1.

[2] T.J.Wade et al., Fusion Engineering and Design 24 (1994) 23.

[3] M.Bures et al., 21st E.P.S. Conference on Controlled Fusion and Plasma Physics, 1994.

[4] The JET Team (presented by F.G.Rimini), 15th I.A.E.A. Conf. on Plasma Physics and Controlled Nuclear Fusion Research, Seville, 1994.

[5] A.C.C.Sips et al., 36th Annual Meeting, A.P.S. Division of Plasma Physics, Minneapolis, 1994.

[6] A.M.Messiaen et al., 3rd Joint Varenna-Grenoble Int. Symp. on Heating in Toroidal Plasmas, 1982.

Fast Wave Current Drive Experiments in JET Divertor Plasmas

F Nguyen[1], L-G Eriksson, B Fischer, C Gormezano, E Righi, F Rimini, G Sadler, A Sips, D Start.
JET Joint Undertaking, Abingdon, Oxfordshire, OX14 3EA, UK.
[1] Permanemt address: CEA, Centre d'Etudes de Cadarache, France.

ABSTRACT:

As part of the JET experimental campaign in the pumped divertor configuration, studies of Fast Wave Heating and Current Drive scenarii have been carried out. For the experiment described in this paper, the scenario with D cyclotron 3rd harmonic layer at center and both H cyclotron 1st and 2nd harmonic layers at the edge has been chosen. Significant Fast Wave Heating has been observed and studied for varying plasma parameters (B_T, ICRF power, antenna phasing, density). The results are compared with numerical simulations of power deposition and prediction of current drive efficiency is given. This scenario has been found to provide efficient heating.

SCENARIO FAST WAVE ELECTRON HEATING AND FAST WAVE CURRENT DRIVE:

- B_T=2.2 T, f_{ICRF}=51.4 MHz, 3D(3 ^{4}He) at center.
- H and 2D (2 ^{4}He) are marginally present at the plasma edge on the high field side, 2H and 4D (4 ^{4}He) on the low field side (e.g. # 35320, I_{plasma}=1.8 MA, fig. 1).
- similar scenario has already been experimented on Tore Supra.

EXPERIMENT:

- **sensitive to layer position:**

- # 35520 ramp down of the magnetic toroidal field (fig. 2).

at 59s, n_e ↑, P_{rad} ↑, neutral H ↑ (NPA horizontal line), DD rate ↓, neutral D ↓ (NPA horizontal line):
→ 2H cyclotron layer enters in plasma on the low field side (fig. 4).

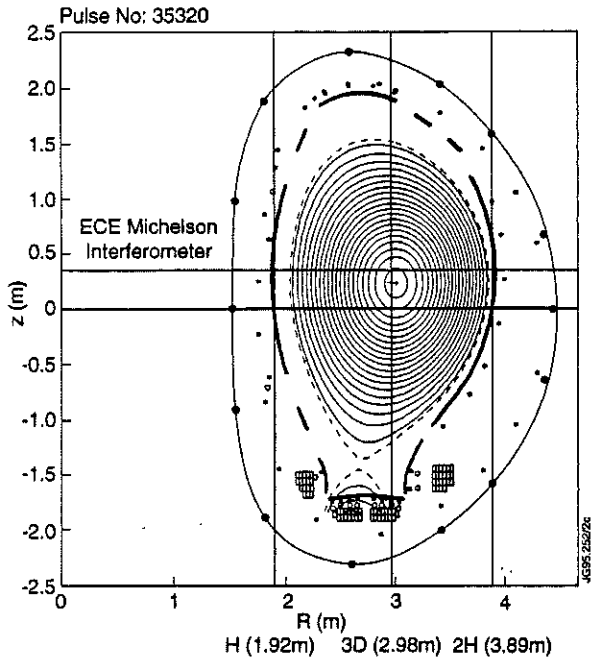

fig.1: location of the different ion cyclotron layers on a poloidal view of the plasma.

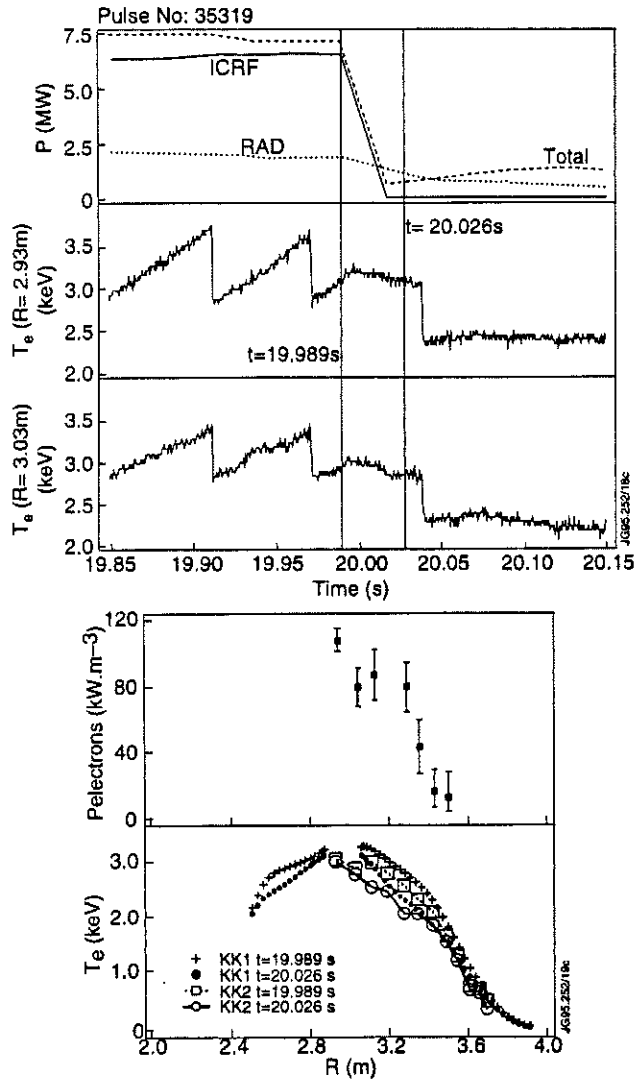

fig.3: pulse nº 35319, 0 π π 0 phasing, 51.4 MHz, 2.18 T, Deuterium, 1.8 MA, a: P_{ICRF} sharp switch off, effect on the sawteeth, ECE Grating Polychromator (z=25cm), b: direct electron heating profile deduced from the change of slope of Te, c: ECE temperature profiles in the plane z=z(axe).

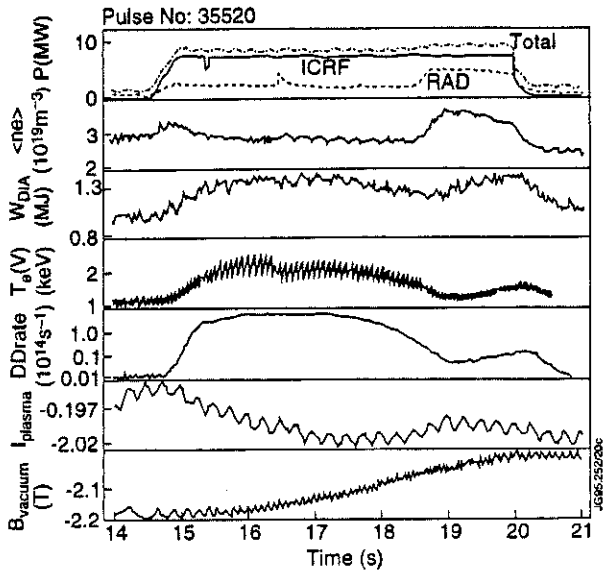

fig.2: pulse nº 35520, 0 π π 0 phasing, 51.4 MHz, 2 MA, Deuterium, ramp down of the magnetic toroidal field.

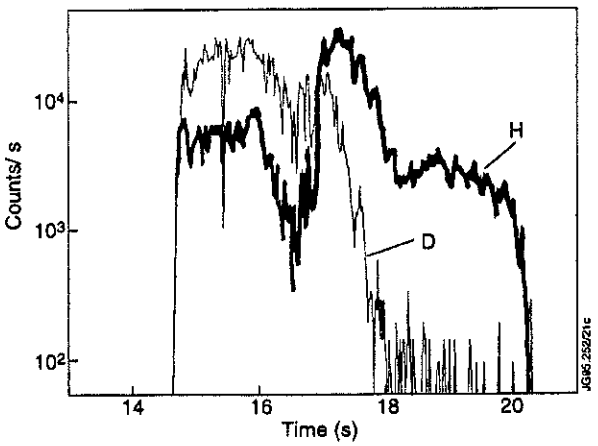

fig.4: 80 keV channel of the horizontal Neutral particle Analyser, pulse nº 35520.

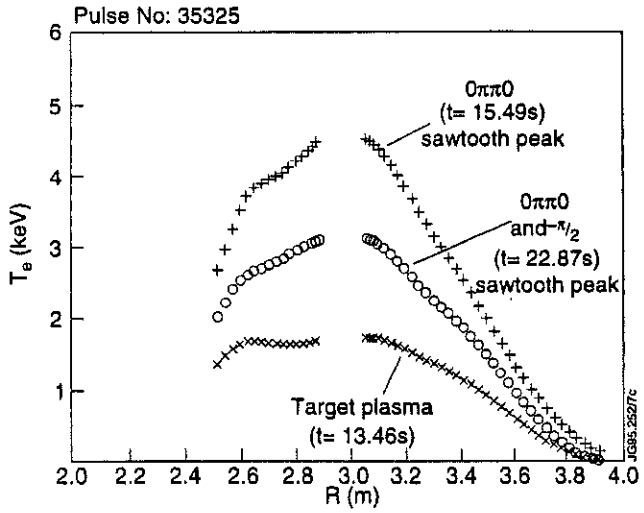

fig.5a: ECE temperature profiles of the pulse nº 35325 in the plane z=z(axe).

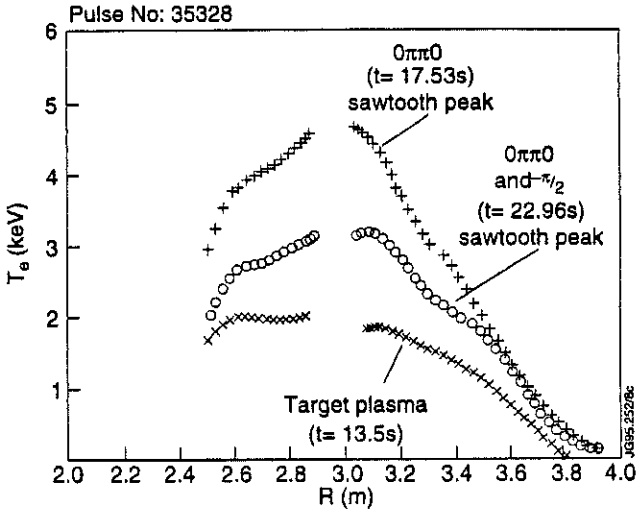

fig.5b: ECE temperature profiles of the pulse nº 35328 in the plane z=z(axe).

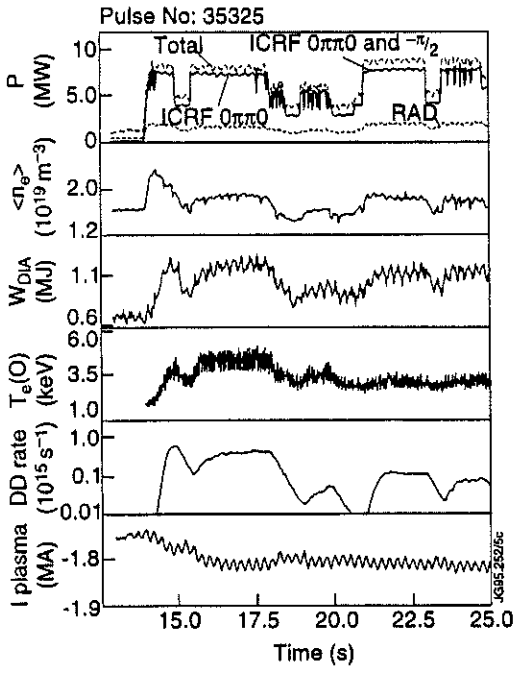

fig.5c: pulse nº 35325, 51.4 MHz, 2.18 T, Deuterium, 0 π π 0 phasing between t=14s and t=20s; between t=21s and t=30s, module D in 0 π π 0 phasing, modules A, B and C - 90 degres phasing.

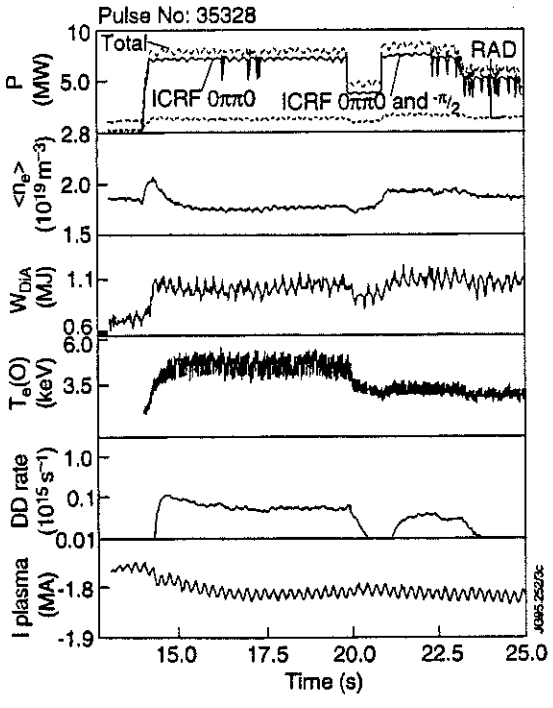

fig.5d: pulse nº 35328 (idem pulse nº 35325 but in Helium).

- **evidence of Fast Wave Electron Heating:**
- # 35319, analysis of the fast switch off of P_{ICRF} and of the sawteeth slope yields peaked deposition profiles. P_{FWEH}=0.9 MW for P_{ICRF}=6.5 MW → 14% of damping on electrons in 0 π π 0 phasing (fig. 3).
- + and - 90 degres phasing → estimated to be less than 50% of 0 π π 0 heating.
- pre-heating with LH → no visible difference.
- **similar results in ^{4}He:**
- # 35325 D plasma (fig. 5c), # 35328 second pulse in ^{4}He (→ ~50% ^{4}He, 50% D) (fig. 5d).
- the T_e profiles are identical (fig. 5a, b).
- **evidence of absorption at 3rd D cyclotron harmonic:**
- high DD rate, γ emission (3.1 MeV from ^{12}C(d, p)^{13}C with E_d>1.8 MeV)
- presence of fast D, E=1.1 MeV (vertical high energy Neutral Particle Analyser) (fig. 6, 9)
- contrasts with TS results which show dominant electron heating and no fast ions.
- **power and density scan:**
- evolution towards better perfomances with higher power and density (W_{DIA} ↑, DD rate ↑) (fig. 7) → elmy H-mode: H89~1.6, subtraction of the energy of fast particles gives 2*H93~1.6 on pulse # 35525, 0 π π 0 phasing (fig. 6) (similar results for # 35526, 0 π 0 π phasing).
- record DD rate for ICRF only: 1.8 10^{16} s^{-1} with P_{ICRF}=12.9 MW.
- W_{DIA}=3.2 MJ (with $W_{fast\ particles}$=0.6 MJ), $<n_e>$=3.9 10^{19} m^3, $T_e(0)$=5.7 keV, P_{total}=13.5 MW

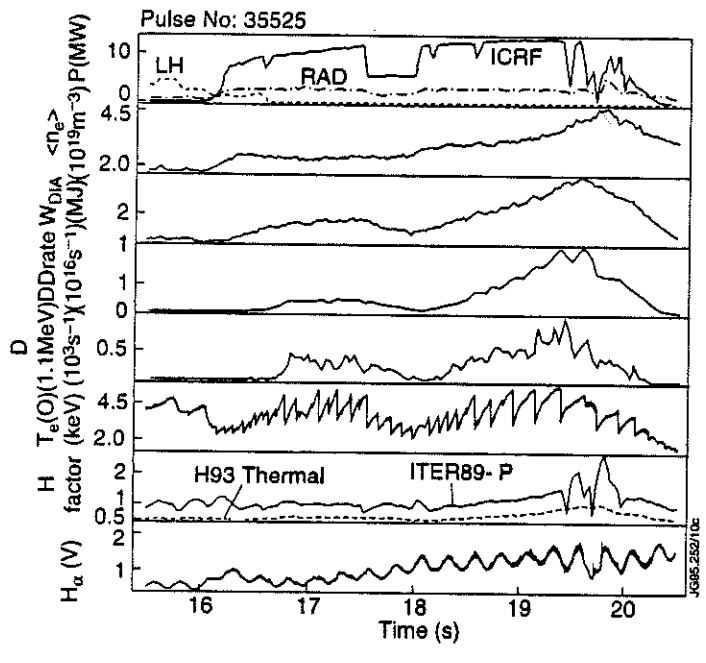

fig.6: pulse nº 35525 0 π π 0 phasing, 51.4 MHz, 2 MA, 2.18 T, Deuterium.

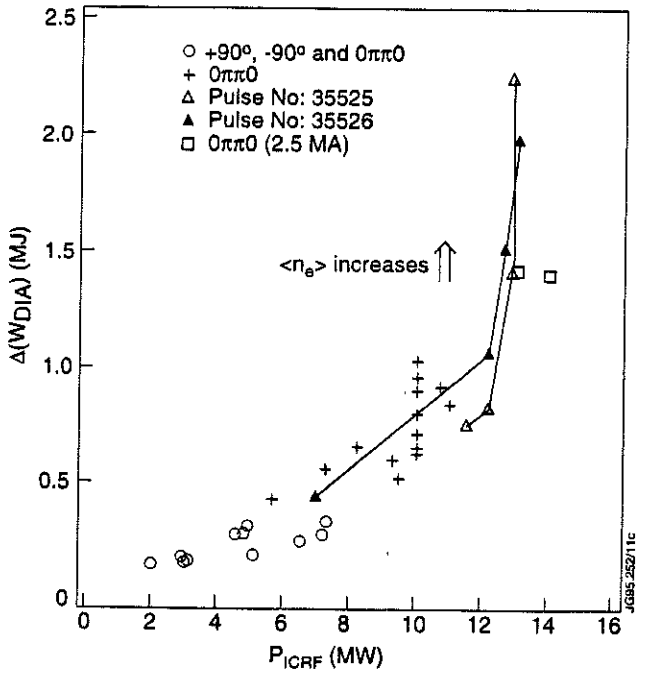

fig.7 diamagnetic energy increase in function of the ICRF power, 51.4 MHz, 2 MA, 2.18 T.

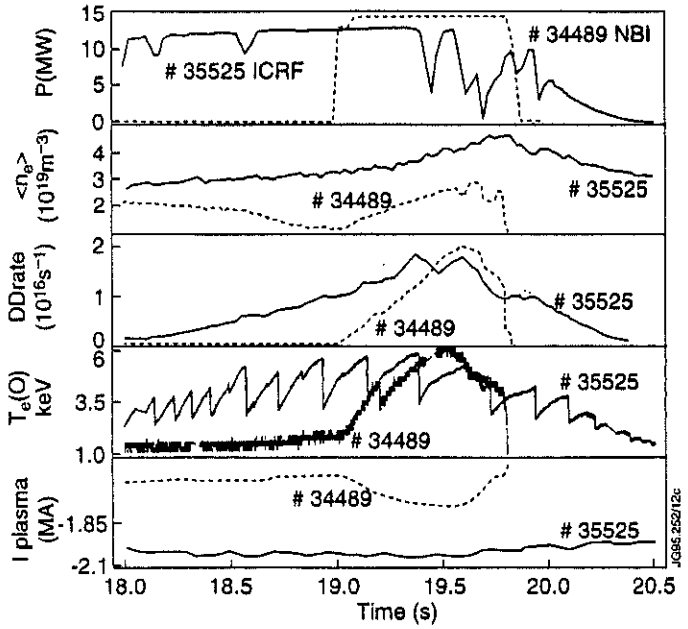

→ comparable to hot ion mode
(DD rate of 2.10^{16} s^{-1} for P_{NBI}~14.6 MW, # 34489) (fig. 8)

fig.8: comparison of performance for FW Heating scenario and hot ion H-mode

NUMERICAL SIMULATION:

- **competition between FWEH and FW3DH:**
- single pass absorption coefficient in WKB analysis

$$Im(k_\perp)=(\sqrt{\pi}/4)k_\perp\beta_e x_e.\exp(-x_e^2)G$$

where $x_e=\omega/(k_{//}v_{the})$, $G\approx(1+W_{crit}/W_{the})^2$ and $W_{crit}=W_{the}+m_e c^2\omega^2/\omega_{pi}^2$

- pulse # 35320 (fig. 9.10):
  max of $x_e.\exp(-x_e^2)$ for harmonic toroidal number N=33 ($k_{//}$=11 m^{-1} on axis)

- SINGLE code (single pass absorption) simulation (fig. 11)

- PION code simulation with cut off of D energy at 2.5 MeV → 50 % on electron 50 % on D (fig. 12) (self consistent treatment of the tail formation and the Fast Wave absorption)

- ALCYON (2D full wave code) simulation of FWCD and power deposition profile on electrons (for 1 MW coupled to electrons, - 90 degres phasing with the plasma parameters of pulse #35320) (fig. 13, 14): FWCD efficiency of 0.018 10^{20} A/W/m^2

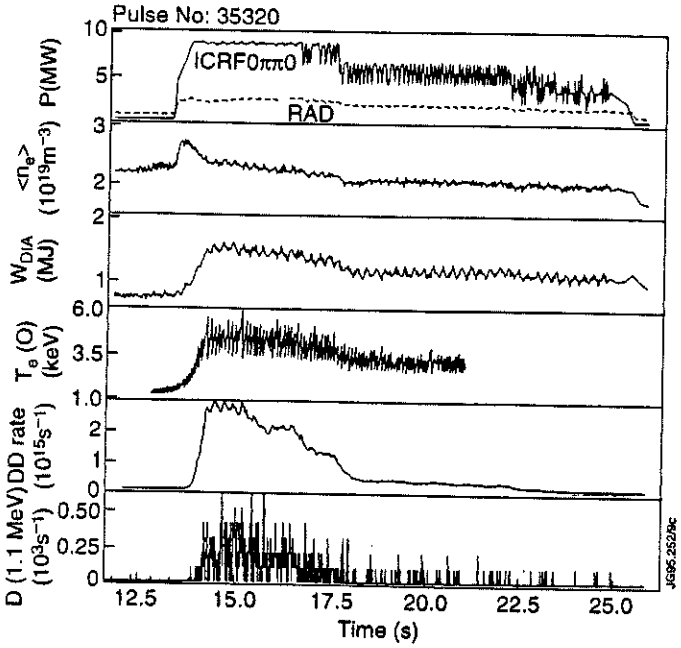

fig.9: pulse nº 35320, 0 π π 0 phasing, 51.4 MHz, 2.18 T, Deuterium.

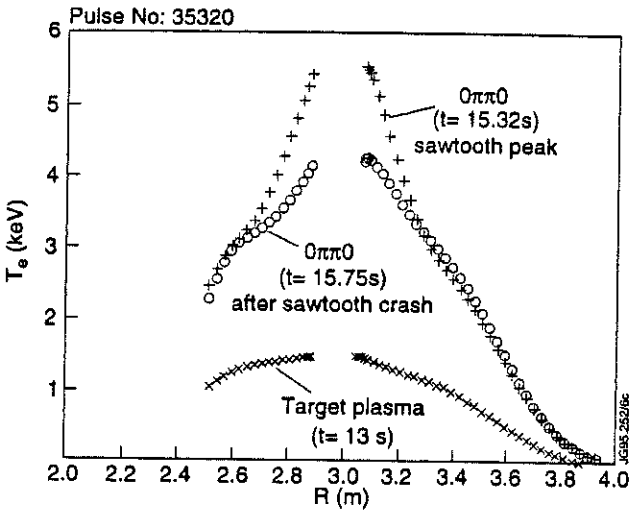

fig.10: ECE temperature profiles of the pulse nº 35320 in the plane z=z(axe).

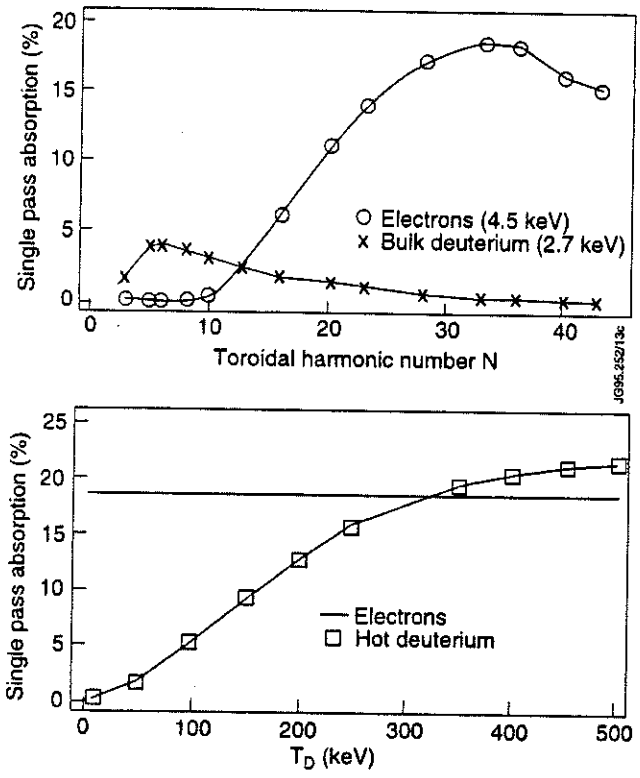

fig.11: SINGLE simulation of the pulse nº 35320 at t=16.2s, a: single pass absorption on electrons (TTMP and ELD) and on bulk Deuterium (3rd harmonic) in function of the the toroidal harmonic number N, b: single pass absorption for the toroidal harmonic number N=33 on electrons and hot Deuterium (1% of the bulk in density) in function of the hot Deuterium temperature.

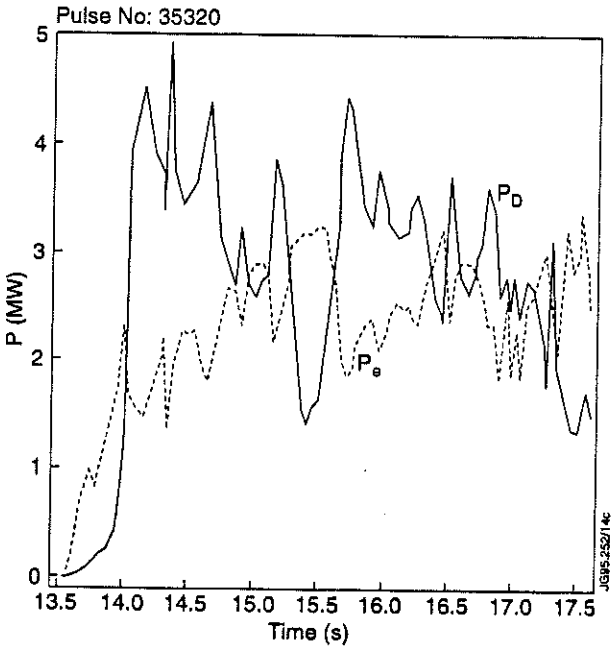

fig12 : PION simulation of the pulse nº 35320 between t=13.5 s and t=17.5 s, powers coupled directly to electrons and to Deuterium (with a limit at 2.5 MeV for D).

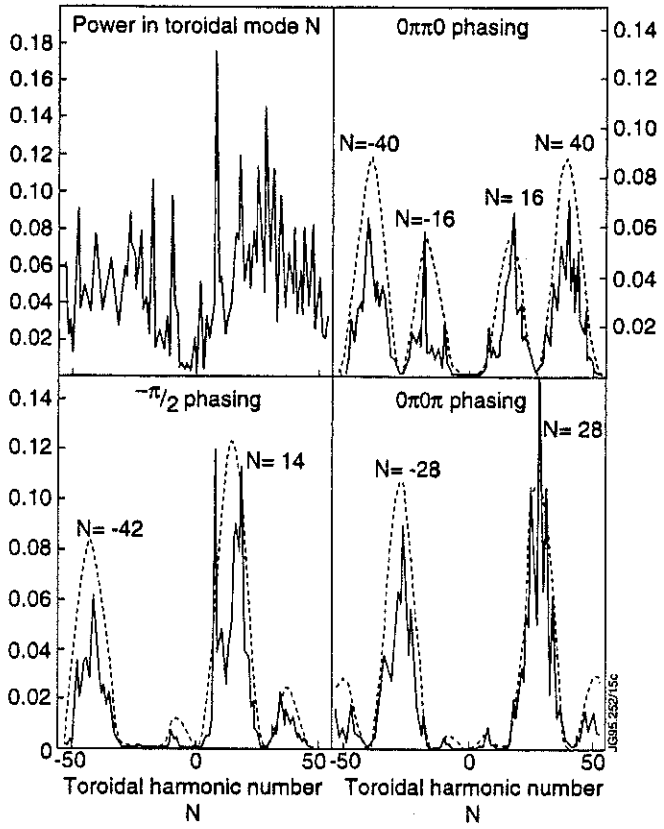

*fig. 13: ALCYON simulation of the pulse nº 35320 at t=16.2 s, dependance on the toroidal harmonic number N, a: power coupled to plasma for 1 kA in the straps, b: 0ππ0 phasing spectrum (- -) and power*spectrum*10 (-), c: - 90 degres phasing spectrum (- -) and power*spectrum*10 (-), d: 0 π 0 π phasing spectrum (- -) and power*spectrum*10 (-)*

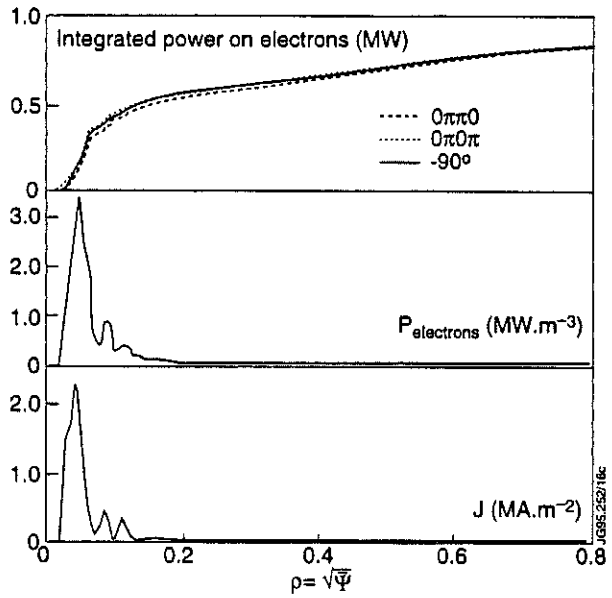

fig. 14: ALCYON simulation of the pulse nº 35320 at t=16.2 s, a: radial profile of the electrons power density for 1 MW coupled to electrons, b: radial profile of the Fast Wave Current Drive for 1 MW coupled to electrons.

CONCLUSION:

- Significant Fast Wave Direct Electron heating has been observed.
- Competing absorption by Deuterium at 3rd cyclotron harmonic is present.
- Competition with lower cyclotron harmonic (H or D) should be avoided (edge absorption).
- Fast Wave Current Drive efficiency estimated at 0.018 10^{20} A/W/m^2 for 90 degrees phasing with the plasma parameters of pulse # 35320.
- Efficient heating scenario at 2 MA, 2.2 T with no minority ion population, which can start on low T_e (1-2 keV) target plasma and might provide adequate conditions for very long pulse (60 s) operation for advanced tokamak scenario on JET.

ACKNOWLEDGEMENTS:

The work on Fast Wave Current Drive is carried out in collaboration with CEA-Cadarache. Part of the ALCYON computation has been performed at Cadarache. The authors are very grateful to Dr A. Becoulet for his active participation and to Drs J. Jacquinot, B. Saoutic and A. Gondhalekar for many fruitful discussions. We gratefully acknowlege the JET team for the accomplishment of this experiment.

High Resolution Spectroscopic Measurements of Impurity Radiation Distributions and Neutral Deuterium Profiles in the JET Scrape-off Layer

P Breger, R W T König, C F Maggi, Z A Pietrzyk[1], D D R Summers, H P Summers, M G von Hellermann.
JET Joint Undertaking, Abingdon, Oxfordshire, OX14 3EA, UK.
[1] CRPP Lausanne, Switzerland.

INTRODUCTION

A periscope has been installed to image visible radiation from the plasma scrape-off layer at the top of JET on 49 fibres with spatial resolution of about 0.45cm. The fan of viewing lines cover a vertical region of 11 degrees (Fig. 1). Passive line radiation of CIII, CVI, D I, as well as Li I beam emission were spectrally resolved on CCD cameras with integration times ranging from 50 to 500 ms. 44 of the 49 fibres are imaged on the entrance slit of an astigmatism-corrected low-resolution spectrometer (0.27m Chromex) to yield a line integrated spatial emission profile, and the remaining 5 fibres are passed to a high resolution spectrometer (1.25m SPEX) to enable spectral line profile analysis. Abel inversion of the intensity profile allows identification of emission layer positions, which are compared to the emission region of the injected thermal Li-beam, as well as the boundary position predicted by various magnetic diagnostics. The passive charge-exchange radiation of CVI (n=8-7) is used to determine the fast neutral deuterium density in the edge.

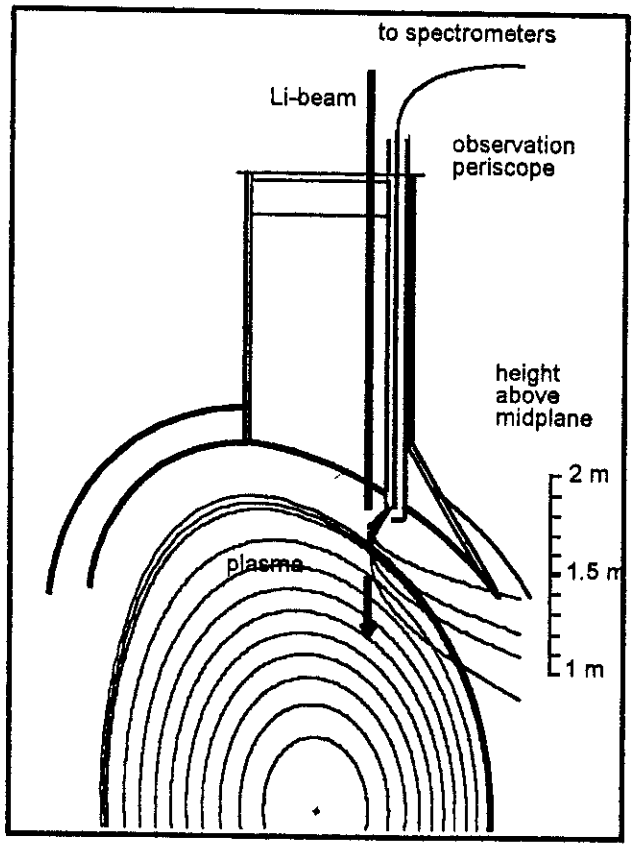

Fig. 1: Diagnostic layout and viewing line geometry.

EMISSION LAYER DETERMINATION

The observed line intensity profiles I_i are linked to local emissivity layers ε on the toroidal flux surfaces by a set of 44 coupled equations:

$$I_i = \sum_{j=1}^{25} \varepsilon_j \cdot l_{ji} \qquad (1)$$

, where i = channel no 1 to 44, l_{ji} = length in flux layer j =1 to 25 .

For the Abel inversion the flux range ψ=0.5 to 1.2 is subdivided into 25 equidistant layers in ψ-space, ψ=1.0 corresponding to the separatrix. Plasma regions inside ψ=0.5 are not traversed by the viewing lines, regions outside ψ=1.2 are assumed to be non-radiating. Visual inspection of the light intensity profiles vis-a-vis the pathlength distributions in the 25 flux layers enables the emission region in flux space to be identified qualitatively. The numerical inversion is obtained by a) a best fit solution for the 25 emissivities and b) by a fit of two gaussian emission distributions for each measurement frame. The average agreement between the measured intensity profile and the simulated profile from the 25 fitted emissivity layers is ~15%. Although the gaussian fit method is in general less accurate in simulating the measured intensity profile, it provides a parametrised form of positions and widths of emission layers.

This inversion technique relies on the accurate determination of the viewing lines in the torus at operating temperature and at vacuum conditions. A 60 keV Li-beam is injected into the plasma, and the Doppler-shifted LiI emission at 670.8nm is recorded together with a parasitic HeI line at 667.8nm and the unshifted 670.8 nm emission from thermal Li escaping into the plasma along the beam trajectory. The Doppler shift yields accurate vertical position coordinates. The toroidal alignment is measured by back-illuminating the viewing lines with a laser and recording the laser spots on the vessel wall with the in-vessel inspection system (IVIS).

The full EFIT equilibrium is used to provide a pathlength distribution along the viewing lines in flux space. Errors in the present magnetic diagnostic data can lead to uncertainties in the calculation of the top plasma boundary, and sometimes corrections of order 10cm need to be applied based on the thermal Li emission, the high energy Li-beam diagnostic and reciprocating probe diagnostic.

THE LOCATION OF THE EDGE : CIII EMISSION PROFILES

CIII profile measurements were performed on subsequent plasma shots with similar plasma boundary configuration. The pulses were from an elm-free H-mode campaign with 5MA plasma current, 3 T field with new Be-tiles in the JET divertor. For this particular plasma configuration, both EFIT equilibrium and

XLOC boundary determination repeatedly give magnetic separatrix heights at major radius R=3.252m within a range of ± 2cm during the heating phase (Fig.2). This position of the magnetic boundary and the thermal Li emission (vertical injection at R=3.252) agrees well with beam attenuation and emission models.

The CIII measured intensity profile (λ=465.0nm) for two viewing mirror positions has a max. in channels intercepting the beam trajectory at height 1.7m (Fig.3). Analysis of the path lengths in the various fluxlayers confirms that this viewing line has a maximum pathlength in the separatrix layer.

The results of the Abel-inversion for the CIII emission are shown in Fig.4 and are compared with various plasma parameters in Fig.5. The position of the CIII emission layer is at ψ=1.0, but shows some dramatic movement after 52s.

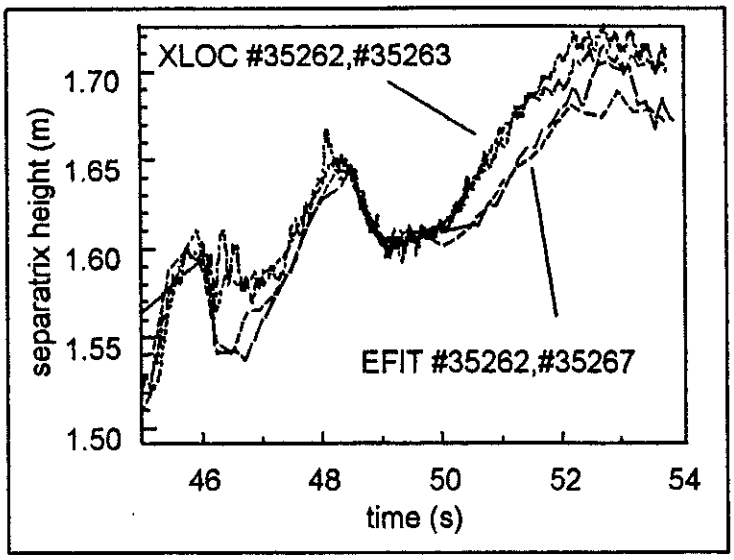

Fig. 2: Comparison of magnetic boundary positions at R=3.252 m.

Table 1: Comparison of different edge positions Zsep refers to the average magnetic separatrix, and Z(Li) to the measured position of thermal Li emission.

time [s]	Zsep [m]	Z(Li) [m]	max. dens.
51.25	1.66	1.69	3.2×10^{19}
51.75	1.68	1.71	3.6×10^{19}
52.75	1.70	1.67	5.8×10^{19}

However, this observed movement is not related to changes in the plasma edge parameters during the H-mode transition, but is an artefact of inaccuracies of the magnetic data. This is seen when correlating the magnetic data with the layer position. Although the behaviour of the emission layer position is masked by this systematic error, some additional movement can be seen, and the layer width and intensity can also be correlated with changes in the plasma edge during the heating period. During the onset of the heating phase (7 MW NBI and 2.5 MW ICRH), the H-mode is established with threshold elms. The measured width of the CIII emission shell drops to δψ=0.025, and increases with the onset of giant elms, when the total emission from the shell also increases. At the end of the ICRH heating phase, the width of the emission shell decreases by a factor of 4 and remains at δψ=0.04 until the end of the neutral beam heating phase.

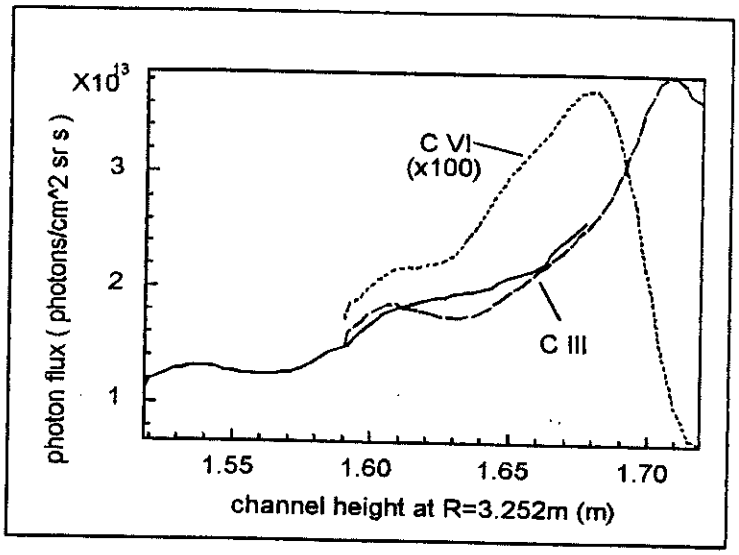

Fig. 3: Measured CIII intensity profile for two mirror positions. A CVI intensity profile is also shown.

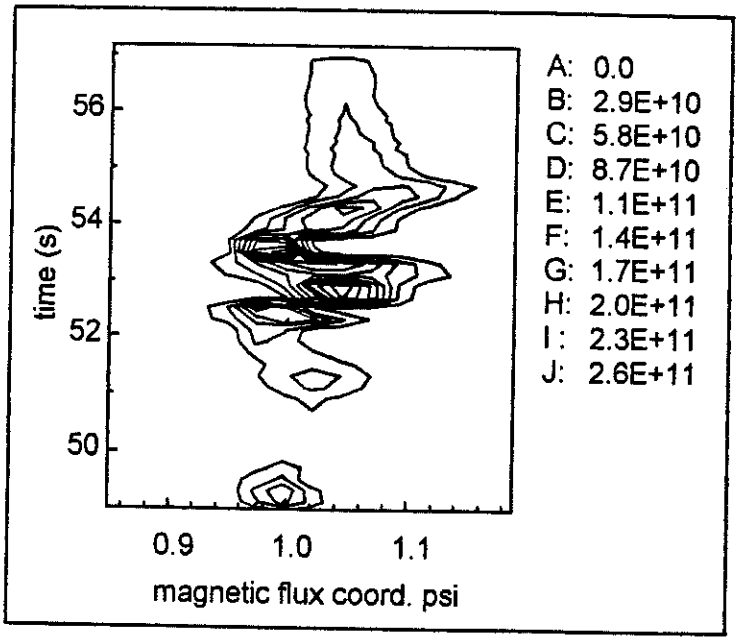

Fig. 4: Abel-inverted CIII emissivity distribution in photons/cm^3 sr s

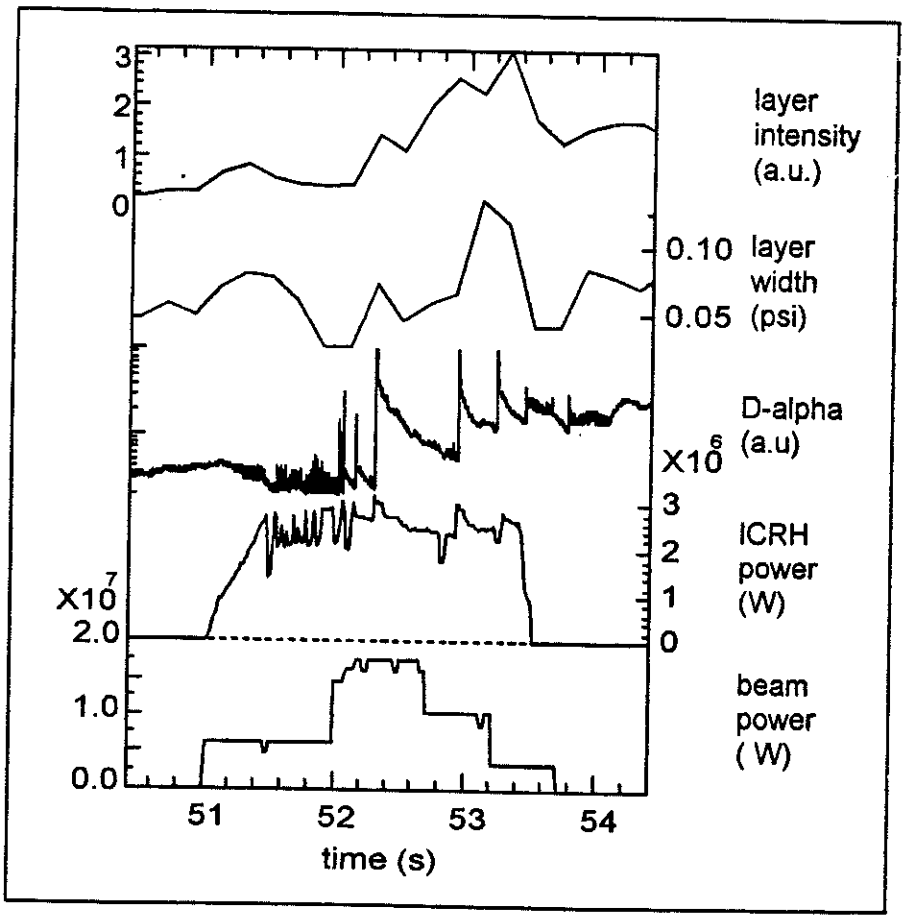

Fig.5: Time evolution of emission layer width and integrated layer intensity.

High Resolution Spectroscopic Measurements of Impurity Radiation Distributions and Neutral Deuterium Profiles in the JET Scrape-off Layer

P Breger, R W T König, C F Maggi, Z A Pietrzyk[1], D D R Summers, H P Summers, M G von Hellermann.

JET Joint Undertaking, Abingdon, Oxfordshire, OX14 3EA, UK.

[1] CRPP Lausanne, Switzerland.

INTRODUCTION

A periscope has been installed to image visible radiation from the plasma scrape-off layer at the top of JET on 49 fibres with spatial resolution of about 0.45cm. The fan of viewing lines cover a vertical region of 11 degrees (Fig. 1). Passive line radiation of CIII, CVI, D I, as well as Li I beam emission were spectrally resolved on CCD cameras with integration times ranging from 50 to 500 ms. 44 of the 49 fibres are imaged on the entrance slit of an astigmatism-corrected low-resolution spectrometer (0.27m Chromex) to yield a line integrated spatial emission profile, and the remaining 5 fibres are passed to a high resolution spectrometer (1.25m SPEX) to enable spectral line profile analysis. Abel inversion of the intensity profile allows identification of emission layer positions, which are compared to the emission region of the injected thermal Li-beam, as well as the boundary position predicted by various magnetic diagnostics. The passive charge-exchange radiation of CVI (n=8-7) is used to determine the fast neutral deuterium density in the edge.

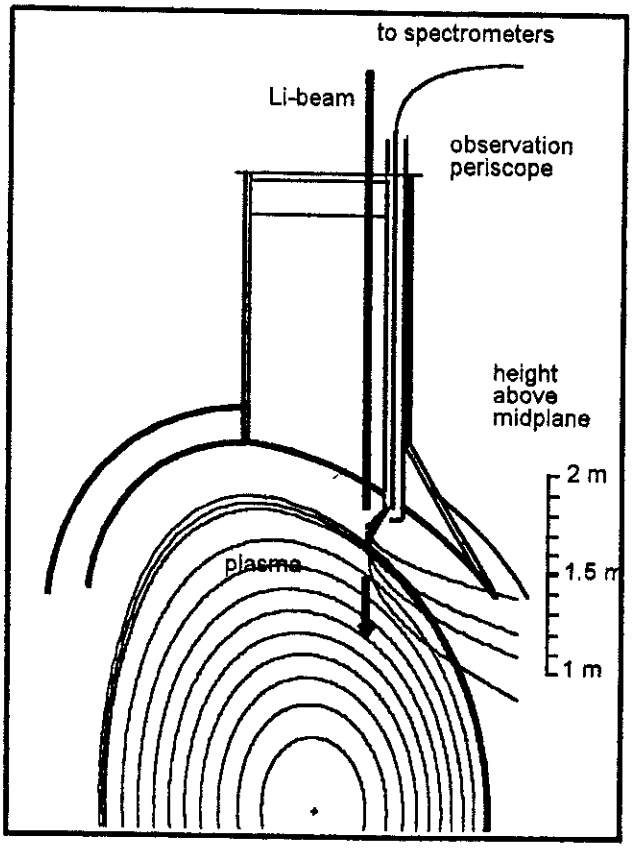

Fig. 1: Diagnostic layout and viewing line geometry.

EMISSION LAYER DETERMINATION

The observed line intensity profiles I_i are linked to local emissivity layers ε on the toroidal flux surfaces by a set of 44 coupled equations:

$$I_i = \sum_{j=1}^{25} \varepsilon_j \cdot l_{ji} \qquad (1)$$

, where i = channel no 1 to 44, l_{ji} = length in flux layer j =1 to 25 .

For the Abel inversion the flux range ψ=0.5 to 1.2 is subdivided into 25 equidistant layers in ψ-space, ψ=1.0 corresponding to the separatrix. Plasma regions inside ψ=0.5 are not traversed by the viewing lines, regions outside ψ=1.2 are assumed to be non-radiating. Visual inspection of the light intensity profiles vis-a-vis the pathlength distributions in the 25 flux layers enables the emission region in flux space to be identified qualitatively. The numerical inversion is obtained by a) a best fit solution for the 25 emissivities and b) by a fit of two gaussian emission distributions for each measurement frame. The average agreement between the measured intensity profile and the simulated profile from the 25 fitted emissivity layers is ~15%. Although the gaussian fit method is in general less accurate in simulating the measured intensity profile, it provides a parametrised form of positions and widths of emission layers.

This inversion technique relies on the accurate determination of the viewing lines in the torus at operating temperature and at vacuum conditions. A 60 keV Li-beam is injected into the plasma, and the Doppler-shifted LiI emission at 670.8nm is recorded together with a parasitic HeI line at 667.8nm and the unshifted 670.8 nm emission from thermal Li escaping into the plasma along the beam trajectory. The Doppler shift yields accurate vertical position coordinates. The toroidal alignment is measured by back-illuminating the viewing lines with a laser and recording the laser spots on the vessel wall with the in-vessel inspection system (IVIS).

The full EFIT equilibrium is used to provide a pathlength distribution along the viewing lines in flux space. Errors in the present magnetic diagnostic data can lead to uncertainties in the calculation of the top plasma boundary, and sometimes corrections of order 10cm need to be applied based on the thermal Li emission, the high energy Li-beam diagnostic and reciprocating probe diagnostic.

THE LOCATION OF THE EDGE : CIII EMISSION PROFILES

CIII profile measurements were performed on subsequent plasma shots with similar plasma boundary configuration. The pulses were from an elm-free H-mode campaign with 5MA plasma current, 3 T field with new Be-tiles in the JET divertor. For this particular plasma configuration, both EFIT equilibrium and

XLOC boundary determination repeatedly give magnetic separatrix heights at major radius R=3.252m within a range of ± 2cm during the heating phase (Fig.2). This position of the magnetic boundary and the thermal Li emission (vertical injection at R=3.252) agrees well with beam attenuation and emission models.

The CIII measured intensity profile (λ=465.0nm) for two viewing mirror positions has a max. in channels intercepting the beam trajectory at height 1.7m (Fig.3). Analysis of the path lengths in the various fluxlayers confirms that this viewing line has a maximum pathlength in the separatrix layer.

The results of the Abel-inversion for the CIII emission are shown in Fig.4 and are compared with various plasma parameters in Fig.5. The position of the CIII emission layer is at ψ=1.0, but shows some dramatic movement after 52s.

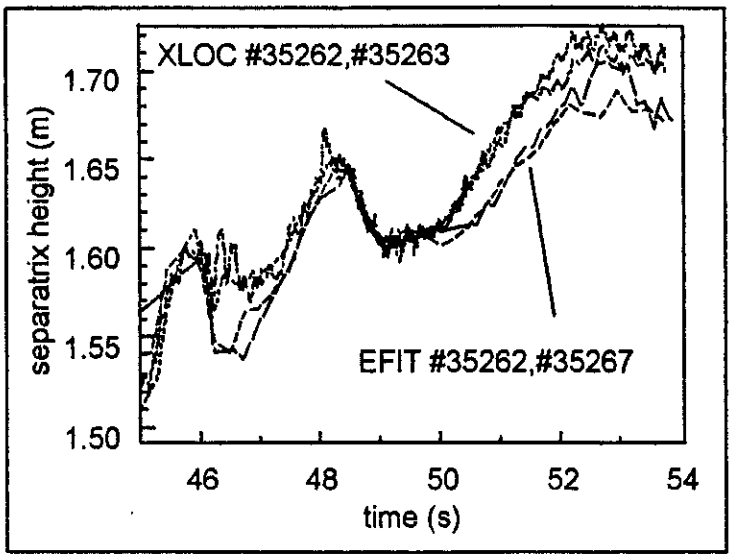

Fig. 2: Comparison of magnetic boundary positions at R=3.252 m.

Table 1: Comparison of different edge positions Zsep refers to the average magnetic separatrix, and Z(Li) to the measured position of thermal Li emission.

time [s]	Zsep [m]	Z(Li) [m]	max. dens.
51.25	1.66	1.69	3.2×10^{19}
51.75	1.68	1.71	3.6×10^{19}
52.75	1.70	1.67	5.8×10^{19}

However, this observed movement is not related to changes in the plasma edge parameters during the H-mode transition, but is an artefact of inaccuracies of the magnetic data. This is seen when correlating the magnetic data with the layer position. Although the behaviour of the emission layer position is masked by this systematic error, some additional movement can be seen, and the layer width and intensity can also be correlated with changes in the plasma edge during the heating period. During the onset of the heating phase (7 MW NBI and 2.5 MW ICRH), the H-mode is established with threshold elms. The measured width of the CIII emission shell drops to $\delta\psi$=0.025, and increases with the onset of giant elms, when the total emission from the shell also increases. At the end of the ICRH heating phase, the width of the emission shell decreases by a factor of 4 and remains at $\delta\psi$=0.04 until the end of the neutral beam heating phase.

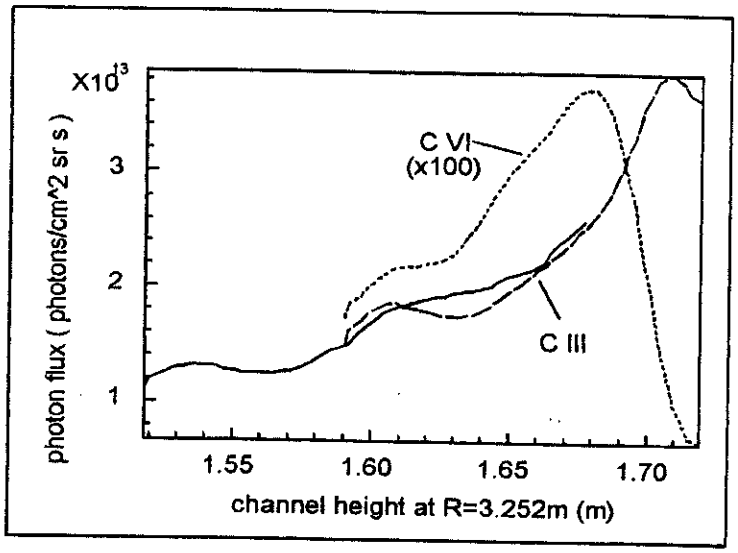

Fig. 3: Measured CIII intensity profile for two mirror positions. A CVI intensity profile is also shown.

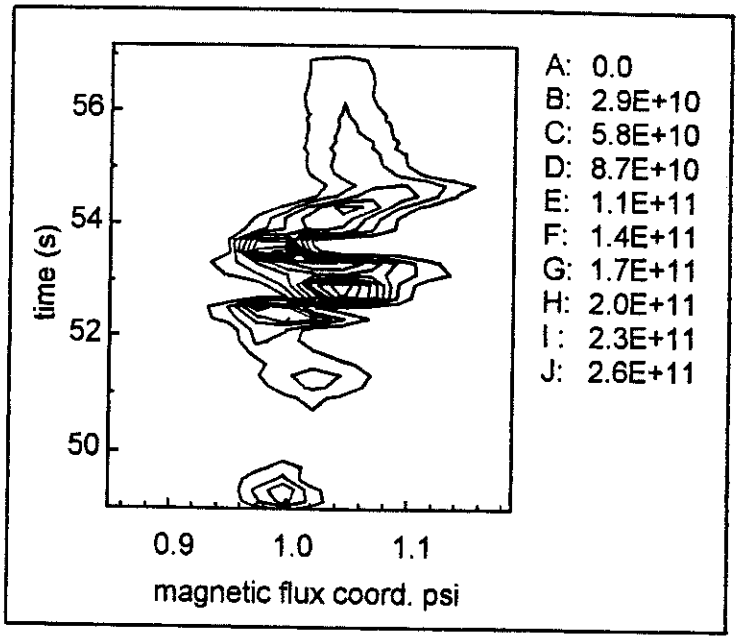

Fig. 4: Abel-inverted CIII emissivity distribution in photons/cm^3 sr s

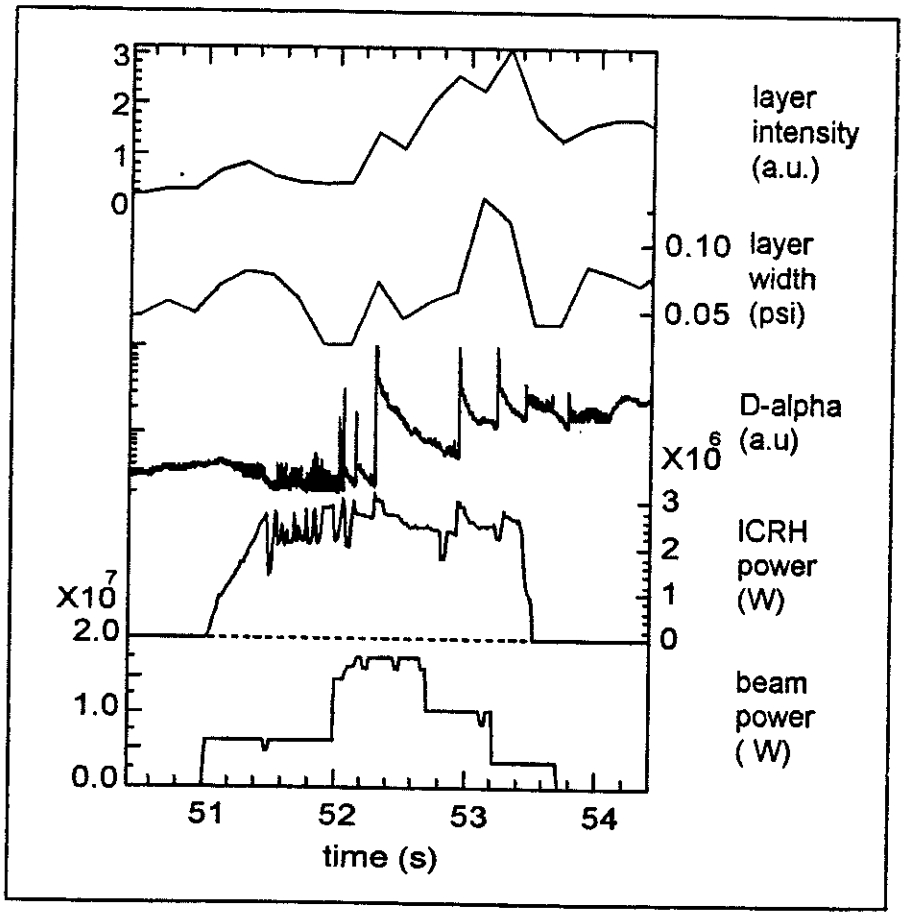

Fig.5: Time evolution of emission layer width and integrated layer intensity.

THE "LUKE-WARM" CHARGE-EXCHANGE LAYER : CVI EMISSION PROFILES

In contrast to the emission from a low-ionisation stage ion such as CIII, which is located near the plasma separatrix, the plasma induced emission from CVI (λ=529.05nm) seems to originate from two different emission layers. As a consequence, the analysis of charge-exchange (cx) spectra from heating beams has to take into account the presence of a so-called "cold" feature (T_i~480 eV), corresponding to emission induced by electron collisions in the CVI ion shell, as well as a "luke-warm" feature (T_i~4keV) corresponding to emission from CVI ions formed deeper into the plasma by cx collisions with fast deuterium atoms.

In order to investigate this model, a CVI emissivity profile was also obtained for the plasma configuration described above. Abel-inversion yields a broad CVI emission layer inside from the CIII emission layer (see also Fig.3), extending well into the confined plasma region. Resolution into two emission layers is however not possible. High resolution spectral analysis of the emitted CVI spectrum on 5 locations along the intensity profile shows for this particular plasma shot a rather low fraction of cx emission - the ratio of cx-photon flux is of the same level as that from the electron induced photon flux. This observation is in marked contrast to the typical CVI intensity profiles observed during high-performance hot-ion mode plasmas, where the passive cx feature is of order 6 times more intense than the electron induced radiation. Such an example is a hot-ion H-mode plasma with 3.8 MA plasma current at 3.3T field (#33641), similar to the recent record shot #33643 where a peak neutron rate of 4.7×10^{16} s^{-1} was attained.

Whereas agreement between the EFIT equilibrium separatrix position and the XLOC plasma boundary was very good in the earlier quoted pulses, for these hot-ion mode plasmas it is less so. The plasma would be far too low in the vessel to yield the observed intensity profiles (the outer channels would not intercept the plasma at all). For this reason, the Abel inversion was done using an EFIT equilibrium shifted upwards by ~8.5cm. The resultant Abel-inverted emissivity profiles may then be in error as far as absolute positions are concerned, but the relative spacing of layers was found to be insensitive to vertical shifts. The resultant emissivity distribution of CVI is shown in Fig. 6, the parameterised position and width of the interior layer in Figs. 7 and 8. Using the corrected pathlength distributions in the fluxlayers predicted from EFIT, the outside emissivity layer is placed at the separatrix and can be interpreted as the electron induced component. Further inwards, a more intense layer exists at ψ~0.8 which can be attributed to the charge-exchange induced feature. This ratio of the "luke-warm" to the "cold" emission layer is also obtained by spectral line shape analysis of 5 channels, which yields a passive charge-

exchange emission layer of up to 6 times more intense than the outer cold emission layer. Fig. 9 compares the ion temperature profiles for the passive charge-exchange feature for three of the

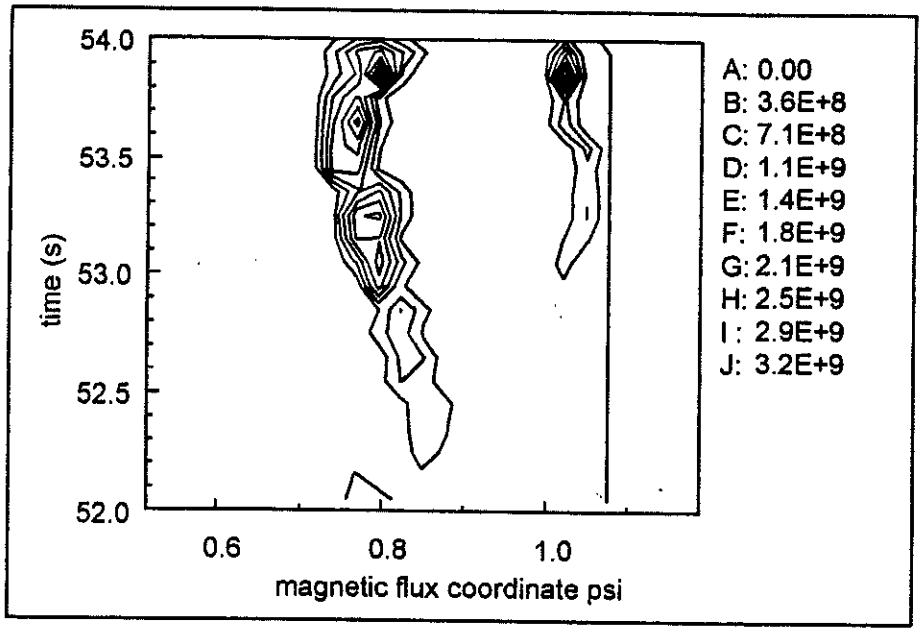

Fig.6: Emissivity distribution (photons/cm^{3}sr s)

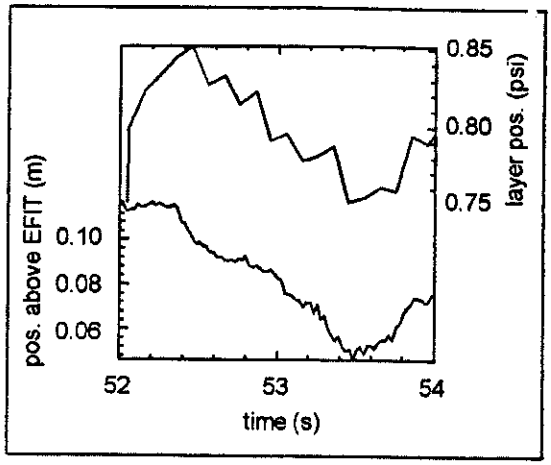

Fig.7: Time evolution of cx-emission layer position compared to offset of XLOC boundary to EFIT equilibrium

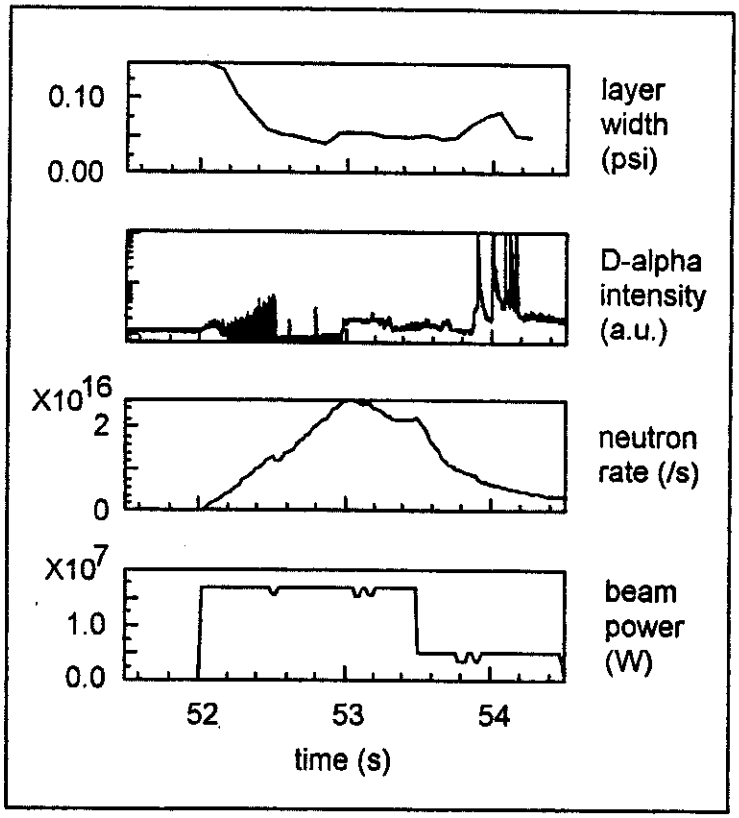

Fig 8: Time evolution of cx-emission layer width

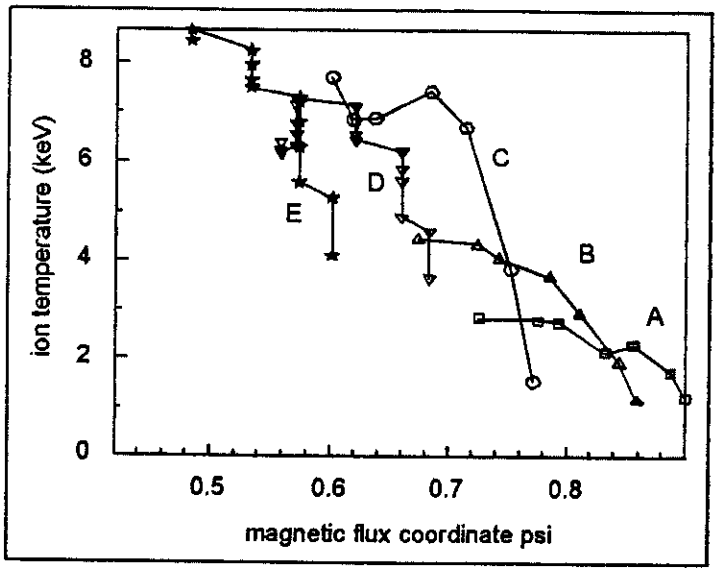

Fig. 9: Time evolution of ion temperature during heating phase after 52s. Trajectories A-C are from this edge diagnostic, D-E are from the central charge-exchange diagnostic.

channels with that of the central cx-diagnostic. The motion of the layer, however, cannot be correlated with changes in edge plasma parameters : it is seen to correlate exactly with the difference in prediction of plasma separatrix position at R=3.252m by the two magnetic calculations. The emission layer deduced from an EFIT ψ-grid moves inwards to the same extent to which the XLOC boundary moves relative to the EFIT grid. If the electron collision induced emission layer is taken to be an indicator of the plasma boundary, then good correlation with the XLOC boundary time behaviour is seen, but not with the EFIT separatrix position. This is also the case when comparing the motion of thermal Li-beam emission regions with that of the magnetic boundary. Comparing the width of the emission layer with the heating beam power and the vertical D_α-signal, a decrease during the development of the H-mode, and increase during the giant elm phase is seen (Fig. 8).

THE FAST NEUTRAL DEUTERIUM DISTRIBUTION

Fast deuterons near the plasma edge region collide with cold recycling neutral deuterium and resonant charge-exchange occurs with some of this recycling deuterium before it is ionised. The resultant fast neutrals can penetrate deeply into the confined plasma regions before re-ionising. The population fraction in the n=2 level will charge-exchange resonantly with C^{6+} to give rise to the hot CVI (n=8) radiating shell, the local emission on decay from n=8 to n=7 can be described by the following expression

$$\varepsilon_{CX}(R) = n_C^{6+}(R) \cdot n_D^{n=2}(R) \cdot Q_{eff}^{CX}(CVI, n = 8-7) \qquad (2).$$

The effective emission coefficient $Q_{eff}^{CX}(n_e, T_e, T_i)$ has been calculated for the range of electron temperatures and densities as measured by LIDAR. The ion-temperature and C^{6+} concentration profiles are measured by the heating-beam cx-diagnostics (KS5-CXRS for bulk profile, KS7-CXRS for edge profile). The fast deuterium temperature is taken to be the same as the local plasma temperature inside the confined plasma, while outside the deuterium temperature has been fixed at 5 eV. For the inner charge-exchange layer, electron excitation processes can be neglected as a source of N=8-7 radiation. From expression (2) the amount of excited n=2 population can be derived, and using a collisional radiative population model (ADAS) the total fast neutral deuterium is estimated. The results for #33641 are shown in Figs. 10 and 11 as a function of ρ=r/a.

A particular point of interest in this shot is the premature neutron rate roll-over at 53s, which is accompanied by increased levels of D_α emission. The integrated fast deuterium density rises by 25% during the roll-over at 53s, and another rise of 40% is seen during the power step-down at 53.5s.

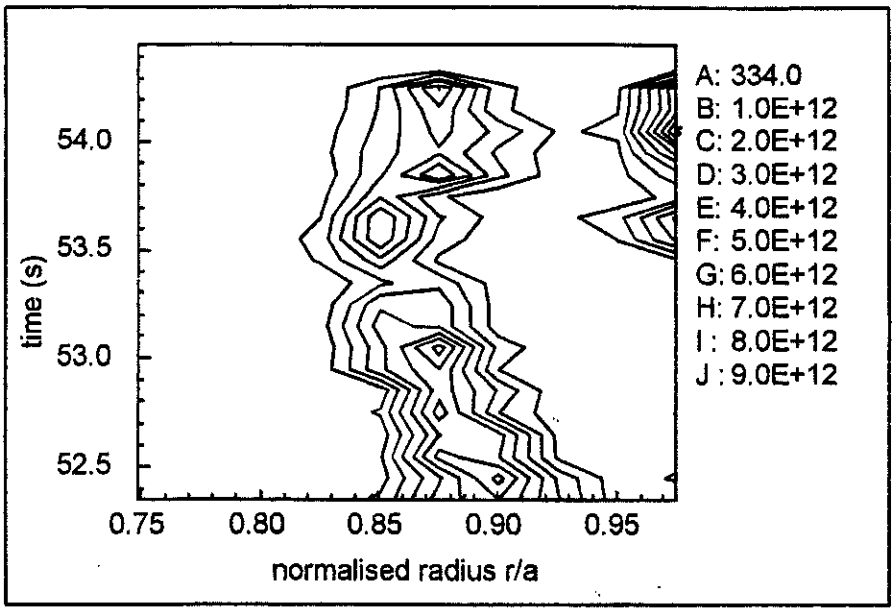

Fig. 10: Fast neutral deuterium density distribution in m^{-3}.

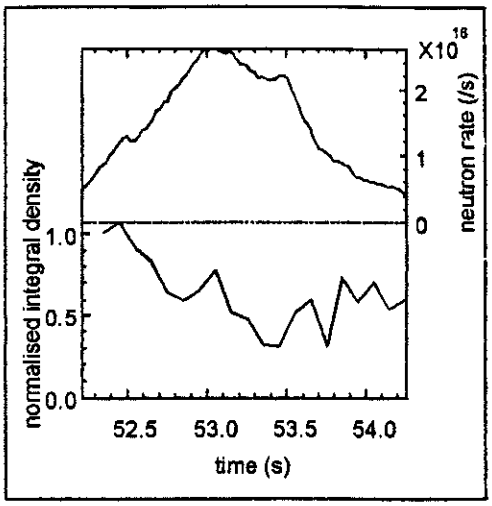

Fig. 11: Integrated deuterium density between r/a=0.8 and 0.94m compared to neutron rate

Although the neutral deuterium densities calculated at a depth of ρ=0.9 are rather small, the recycling cold deuterium which resonantly charge-exchanged with deuterons will have a much higher density, since the charge-exchange process has to compete with rapid ionisation.

CONCLUSIONS

- Passive intensity profiles may be used to identify the location of the plasma boundary, and provide an independent means to verify separatrix positions from magnetic coil measurements.
- The existence of a hot charge-exchange induced layer interior to the plasma boundary was verified, and previous crude estimates of position and width could be substantiated.
- From the cx-emission layer a hot neutral deuterium density distribution could be calculated.
- Evidence for a neutral deuterium enhancement was found during the neutron rate roll-over phase.

ACKNOWLEDGEMENTS

We should like to thank the Swiss National Science Foundation for partially funding this work.

First Observations of Collective Thomson Scattering from JET Plasmas

J A Hoekzema, H Bindslev, J Egedal, J A Fessey, C P Gatcombe, N P Hammond, T P Hughes[1], J S Machuzak[2], J W Oosterbeek, P J Roberts, A L Stevens, P E Stott.

JET Joint Undertaking, Abingdon, Oxfordshire, OX14 3EA, UK.

[1] University of Essex, Colchester, Essex, CO4 3SQ, UK.

[2] Plasma Fusion Centre, MIT, Cambridge, Mass 02139, USA.

1. INTRODUCTION

The main aim of the JET fast ion and alpha particle diagnostic is the measurement of the spatially resolved velocity distribution of the fast alpha particle population when JET enters the DT phase. It is based on collective scattering of high power 140 GHz radiation, as first proposed by Woskov *et al.* [1], with multi-channel heterodyne detection. The system and the underlying theory have been described in a number of papers (see e.g. [2], [3]). Successful experiments at similar frequencies have recently been reported on the Wendelstein W7-AS stellarator [4].

- **The first observations of collective scattering from JET plasmas, measuring the thermal ion feature, have now been made. They confirm expectations and indicate that the diagnostic will give the predicted performance for observations of alpha particles in JET.**

2. THE DIAGNOSTIC SYSTEM

- The 140 GHz gyrotron source can produce 500 kW for 0.5 s, with > 90 % in a Gaussian beam. In these experiments it delivered up to fifteen 1 to 5 ms pulses of 370 kW to the torus. The frequency was selected to allow access to the plasma at high magnetic fields (above 3 T).

- Both the injected and the received beams are steerable. They are focused to near-Gaussian waists of 30 mm radius close to the plasma centre. Their overlap is the scattering volume.

- O or X mode can be selected by adjusting the universal polarizers.

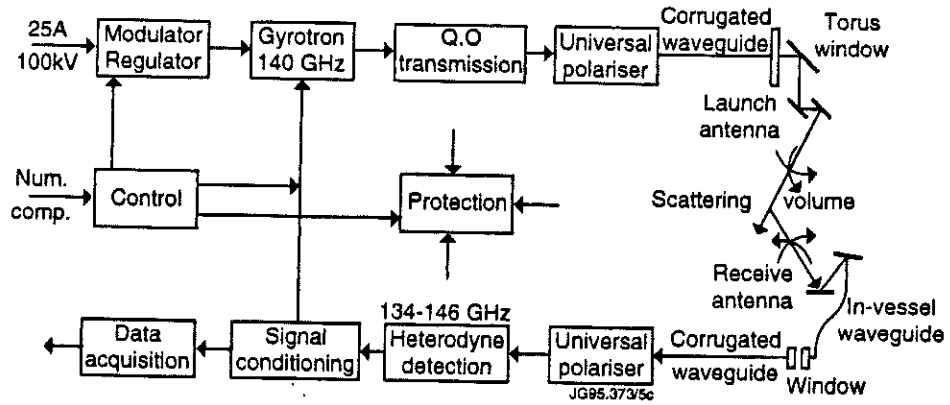

Fig. 1: Schematic overview of the KE4 diagnostic

- The gyrotron was operated at ~ 90 % of maximum power to give stable, spectrally clean operation. The measured frequency was 139.95 GHz, with only 5 MHz variation during a 1ms pulse. After filtering and polarization the power at the calorimeter was 370 kW, of which close to 100 % was transmitted to the torus via ~ 60 m of 88.9 mm ID corrugated waveguide.

- Heating rates at the water-free fused silica torus window (clear diameter 190 mm) were measured at 100° C/s during high power transmission.

- The beam profile at the torus was determined using burn paper (Fig. 2) and appeared to be closely Gaussian.

- The effective reflectivity of the torus vessel seems to be low. Even with no plasma present the high power beam caused no damage to any of the sensitive ECE and reflectometer detectors.

Fig.2: Burn pattern produced by the injected beam before the torus window. The granular structure is due to reflections from a ceramic load placed between the thermosensitive paper and the window.

3. THE RECEIVER SYSTEM

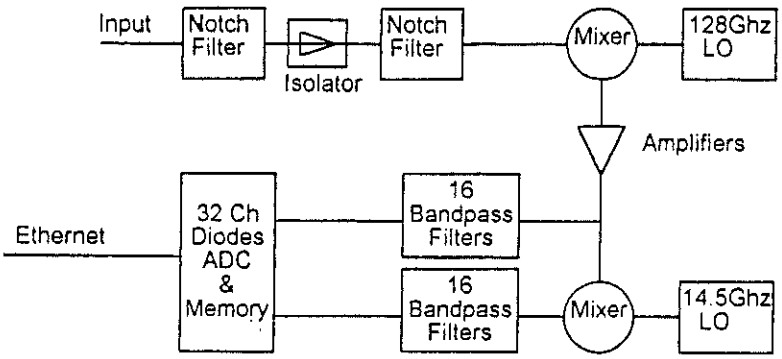

Fig.3: Schematic of the receiver

- Two notch filters in series, with at least 80 dB attenuation and a full width of 200 MHz at -3 dB, remove the stray gyrotron radiation reaching the receiver antenna, which was measured to be up to ~10 mW. Frequencies outside the notch filter are generated briefly during switch-on and switch-off of the gyrotron, leading to temporary saturation of the receiver, and causing negative spikes in the raw data.

- The total receiver bandwidth is 12 GHz, placed symmetrically about the gyrotron frequency. This is divided into 32 channels, varying in bandwidth from 20 MHz close to the gyrotron frequency, to 1.6 GHz in the upper sideband, outer channel. 21 filter channels cover the lower sideband, 10 channels the upper sideband and one monitors the stray light.

- The gyrotron will be modulated at frequencies up to ~ 10 kHz to permit discrimination between scattered radiation and the background ECE and to avoid effects of ECE modulation due to heating by the injected power. The VME-based data acquisition system can perform real-time averaging of the received signals, during modulation of the gyrotron. It is interfaced to the JET computers via ethernet.

4. RAY TRACING

- O to O mode scattering was used to minimise the effects of refraction. The two ray paths were computed for an actual plasma similar to those expected during observations.

- Fig. 4 shows ray paths in a plasma with B = 3.4 T, $n_{eo} = 3.35 \times 10^{19}$ m $^{-3}$, when intersection of the two O mode beams was required at R = 3.0 m, at a height 200 mm above the torus centre, with a scattering **k** of modulus 1520 m $^{-1}$. The angle between **B** and **k** was then calculated to be 122° and the scattering angle was 32°.

- The necessary angular settings of the upper and lower movable antenna mirrors and the corresponding O mode polarization vectors at the antennas were also found. The required settings of the two universal polarizers could then be calculated.

- The ray paths of the two X mode rays for these antenna settings are also shown in the figure.

- The refraction of the O mode rays is sufficiently small that considerable variations in the plasma density and the magnetic field did not cause serious beam misalignment.

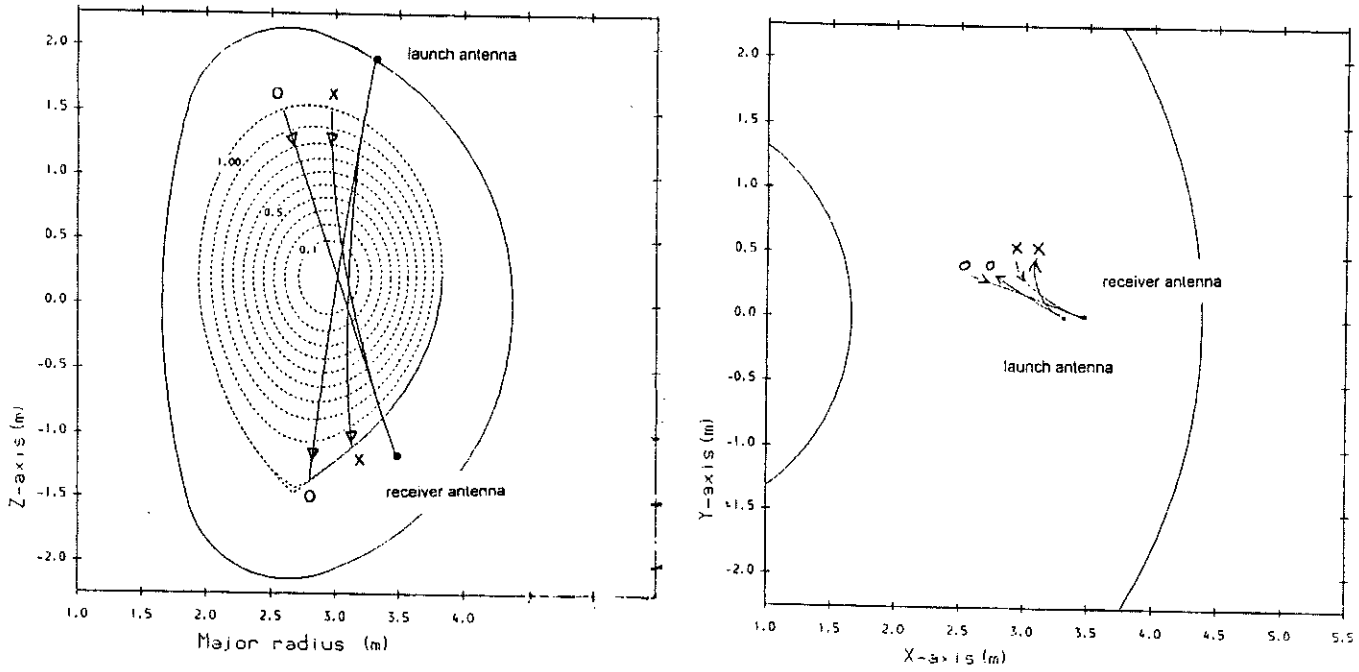

Fig.4: Ray tracing for JET shot # 34018 at t = 53 s. Antennas were set for O to O mode scattering.

5. RESULTS

- Clear scattering signals were seen from plasmas with $B_0 > 3$ T. Fig. 5[a] is a sample of the raw data.

- At lower fields (between ~2 and ~3 T) the input pulses are strongly absorbed by EC resonances, causing local heating and increased ECE around a flux surface. This, and the subsequent cooling, is seen in Fig. 5[b]. The cooling time constant of a few ms clearly identifies the heating signal. No significant local heating was seen for $B_0 > 3$ T.

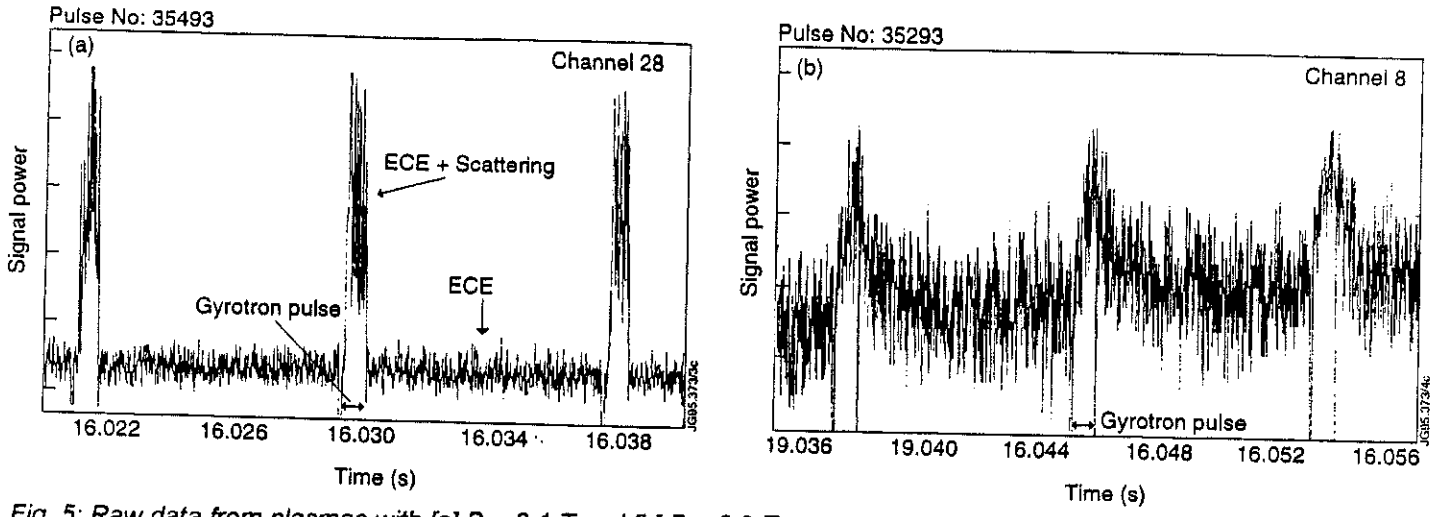

Fig. 5: Raw data from plasmas with [a] B = 3.1 T and [b] B = 2.9 T

- In the absence of plasma virtually no signals were observed except in the channel at the gyrotron frequency.

CALIBRATION

- For the present results relative calibration was obtained from detected ECE, assumed to be constant in spectral range of interest (main band: 140 GHz +- 0.5 GHz and spurious lower band 126 GHz +- 0.5 GHz). Transmission of the notch filters was measured separately and accounted for in ECE based calibration.

- System saturation varying from channel to channel was compensated for by using differences between two ECE levels near ECE levels found when scattering.

- Calibration and system nonlinearity are the most important sources of uncertainty in present spectra. In particular the channel at -100 MHz (see Fig. 6) is unreliable.

- A rough absolute calibration was obtained by comparing the detected ECE level with that measured by a calibrated ECE diagnostic. The principal uncertainty is due to different viewing directions.

SPECTRA

- Clear scattered signals were obtained for a range of shots with moderate ICRH power coupling to 2nd harmonic of the bulk deuterium. In these plasmas significant amounts of nitrogen (used for divertor studies) were present. The spectra obtained in these shots were all similar to Fig. 6.

- A few spectra with clear signals were obtained from shots with NBI. Fig. 7 shows a typical example.

- The histograms in Figs 6 and 7 represent the measured spectral intensity normalized to the intensity of the ECE at 140 GHz in each shot. The curves are the theoretical predicted spectral intensities (Bindslev [3]) based on a plausible set of plasma parameters. Magnetic field and electron density and temperature were obtained from other diagnostics while the ion parameters were fitted. The fits should be seen as illustrative rather than quantitative.

- The fit in Figure 6 assumes scattering in the wings to be due principally to a hot minority of deuterons while the sharp central peak is due to the nitrogen population.

- Both spectra appear to be shifted by 30 MHz corresponding to a toroidal drift velocity of 1.6×10^5 m/s.

- The absolute levels of the measured spectral intensity are 70 % (shot 35608) and 80 % (shot 35648) of that predicted by theory assuming perfect beam overlap and the plasma parameters used in the fit. This discrepancy is well within the uncertainties of the calibration and the scattering and plasma parameters.

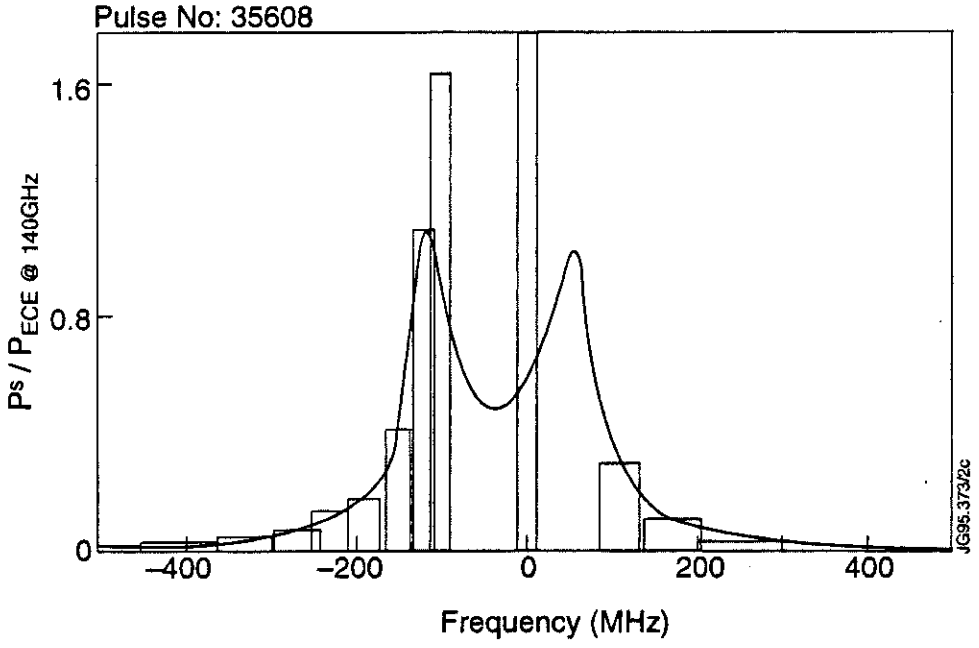

Fig. 6: Shot no. 35608 at 57.5 sec. with 5 MW ICRH. Spectral intensity of scattered light normalized to spectral intensity of ECE at 140 GHz. Histogram: experimental, curve: fitted theoretical curve. T_{ece} *@ 140GHz = 325 eV. Scattered signal integrated over 2 gyrotron pulses (1.6 ms).* ***Given:*** $B = 3.1$ *T,* $n_e = 4.1 \times 10^{19}$ m^{-3}, $T_e = 3.0$ *keV, angle* $(k_i, k_s) = 32°$, *angle(k,B) = 122°.* ***Fitted:*** $n_{D1} = 1.2 \times 10^{19}$ m^{-3}, $T_{D1} = 3$ *keV,* $n_{D2} = 0.8 \times 10^{19}$ m^{-3}, $T_{D2} = 20$ *keV,* $n_N = 0.3 \times 10^{19}$, $T_N = 3$ *keV*

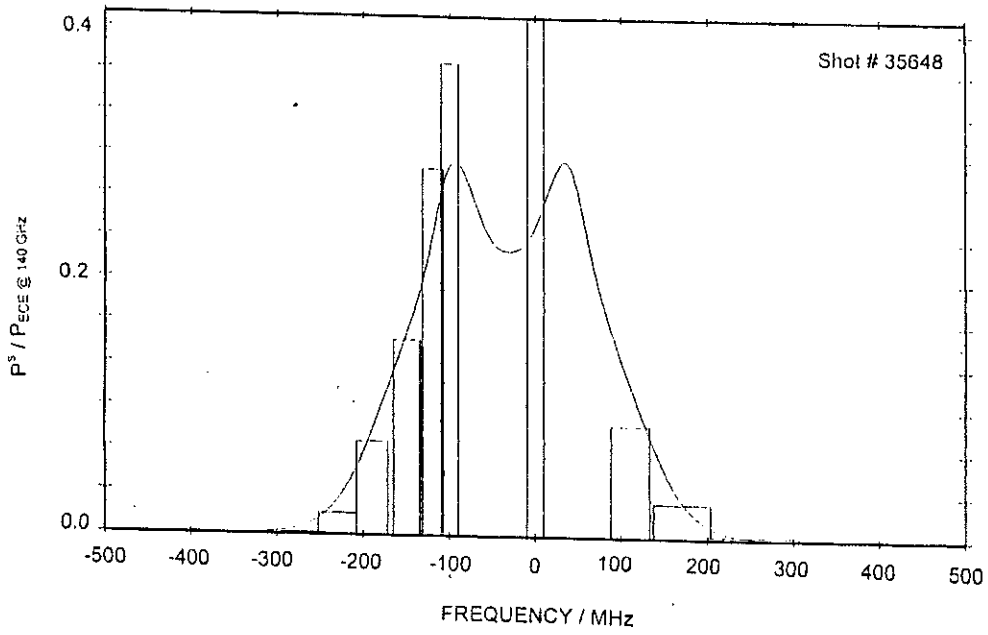

Fig. 7: Shot no. 35648 at 57.5 sec. with 10 MW NBI, 6 MW ICRH. Spectral intensity of scattered light normalized to spectral intensity of ECE at 140 GHz. Histogram: experimental, curve: fitted theoretical curve. T_{ece} *@ 140GHz = 900 eV. Scattered signal integrated over 9 gyrotron pulses (7.2 ms).* ***Given****:* $B = 3.1\ T$, $n_e = 4.7 \times 10^{19}\ m^{-3}$, $T_e = 3.2$ *keV, angle* $(k_i, k_s) = 32°$, *angle*$(k,B) = 122°$. ***Fitted****:* $n_D = 2.7 \times 10^{19}\ m^{-3}$, $T_D = 2.5$ *keV,* $n_N = 1.8 \times 10^{19}$, $T_N = 2.5$ *keV*

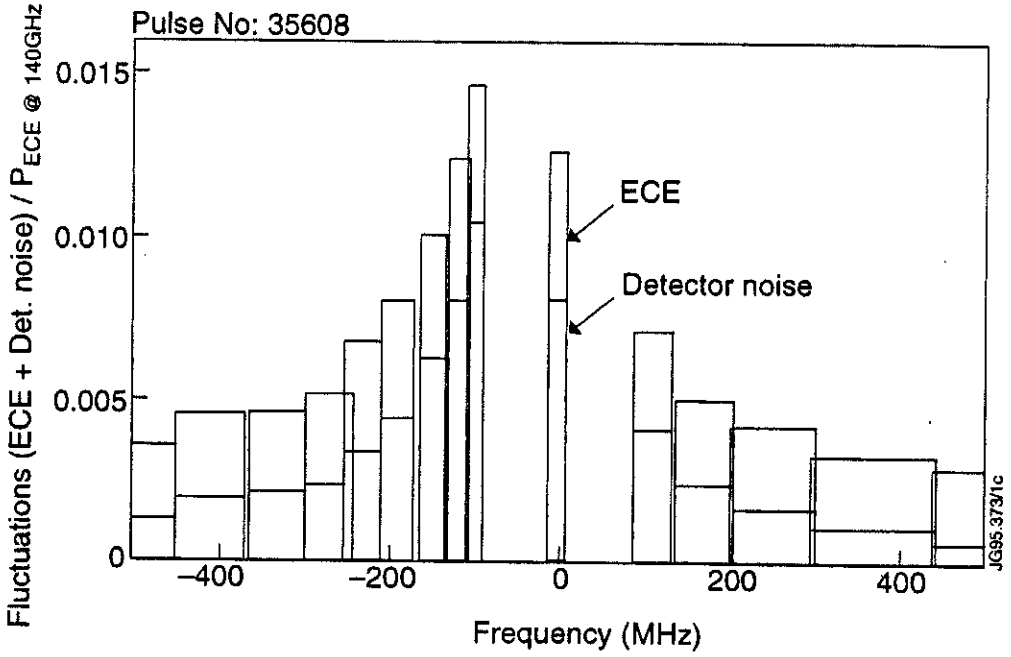

Fig.8: Shot no. 35608 at 57.5 sec. Spectral intensity of fluctuations in ECE and detector noise normalized to spectral intensity of ECE at 140 GHz. Integration time: 1.6 ms. T_{ece} *@ 140 GHz = 325 eV.*

- From Figs. 6 and 8 it can be seen that the post-detection S/N , *i.e.*
  Scattered signal / Fluctuations on integrated (signal + ECE + Detector noise)
  is in the range from 10 to 100. Similar values are found for the spectrum in Fig. 7.

CONCLUSIONS

- The diagnostic behaved as expected under the conditions of these preliminary experiments.
- The observed signal-to-noise ratios were in satisfactory agreement with theory.
- When the full pulse length of the gyrotron can be used with fast modulation, the diagnostic should be capable of giving the expected performance for observations of fast ions and alpha particles in future JET plasmas.
- The experiments provided valuable experience and identified areas for further improvement of the system and data treatment before the next JET campaign.

ACKNOWLEDGEMENTS

We are greatly indebted to many people who have contributed to the development of the diagnostic. In particular we acknowledge the unfailing support of Dr M.Keilhacker, Director of JET.
A collaborative agreement with the US Department of Energy provided equipment, valuable assistance and encouragement. The involvement of several Associations and especially the University of Stuttgart and the Institute of Applied Physics in Nizhniy Novgorod is gratefully acknowledged. Among many individuals we would especially like to thank D V Bartlett, D A Boyd, M P Comiskey, A E Costley, G G Denisov, I H Hutchinson, W Kasparek, C Laviron, A G Litvak, D Markevich, O Menicot, C Moeller, F P Orsitto, L Porte, S D Richards, S R P Smith, W B Suverkropp, M Thumm, M L Watkins and P Woskow.

REFERENCES

1. P P Woskoboinikow, D R Cohn and R J Temkin, Int. J. Infrared & Millimeter Waves **4**, 205 (1983)
2. A E Costley, J A Hoekzema, T P Hughes, P E Stott and M L Watkins, JET Report R(88) 08 (1988)
3. H Bindslev, Proc. ESGAP Meeting, Aussois (1994), to be published in J Atm. and Terr. Phys.
4. E V Suvorov et al., Proc. 9th Joint Workshop on ECE and ECRH, Borrego Springs (1994)

WEDNESDAY

Confinement of High β_{pol} Plasmas in JET

A C C Sips, C D Challis, C Gormezano, C W Gowers, G T A Huysmans, S Ishida[1], F G Rimini, B J D Tubbing, D J Ward.
JET Joint Undertaking, Abingdon, Oxfordshire, OX14 3EA, UK.
[1] JAERI, Naka Fusion Research Establishment, Ibariki-ken, 311-01 Japan.

INTRODUCTION

Experiments aimed at examining the confinement characteristics of plasmas with high values of poloidal beta (β_{pol}) have been performed over a wide range of plasma parameters in JET.

High β_{pol} plasmas have been studied in previous JET campaigns in which high β_{pol} was achieved in conditions of very high confinement ($\tau_E/\tau_{ITER89L\text{-}P} \approx 3.7$) [1,2]. In these Elm free H-mode plasmas the high β_{pol} phase collapsed after an uncontrolled rise of the plasma density. In the JET pumped divertor campaign the aim of the experiments was to achieve high β_{pol} in quasi steady state conditions to study the confinement. The results of these studies are presented in this paper.

EXPERIMENTAL BACKGROUND

ELMy H-mode plasmas form the basis of these experiments in which:

- The stored energy and density typically achieve quasi stationary conditions early in the additional heating phase (Fig.1).
- High combined heating powers are used: up to 28 MW.
- Long heating duration have been applied: up to 7 seconds.
- Toroidal fields from 1.0 to 3.4 Tesla have been used, mainly at 1 MA.
- Carbon tiles were installed in the JET divertor and the divertor cryo-pump was used.

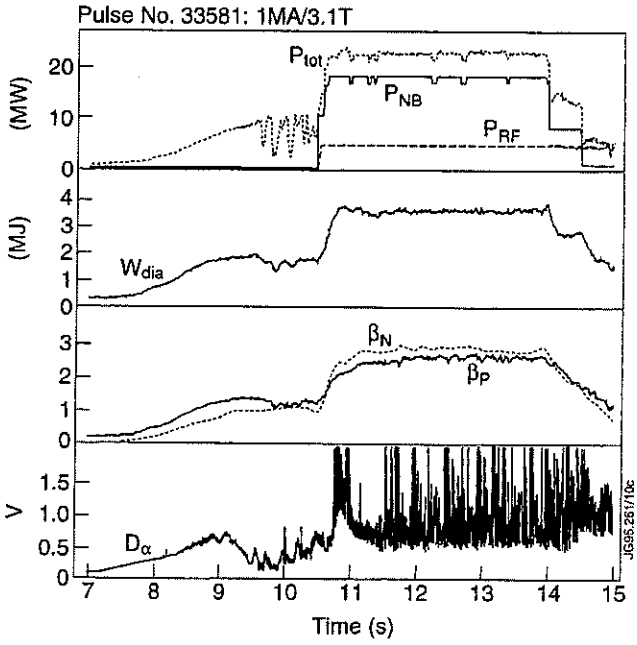

Figure 1: A high beta poloidal discharge

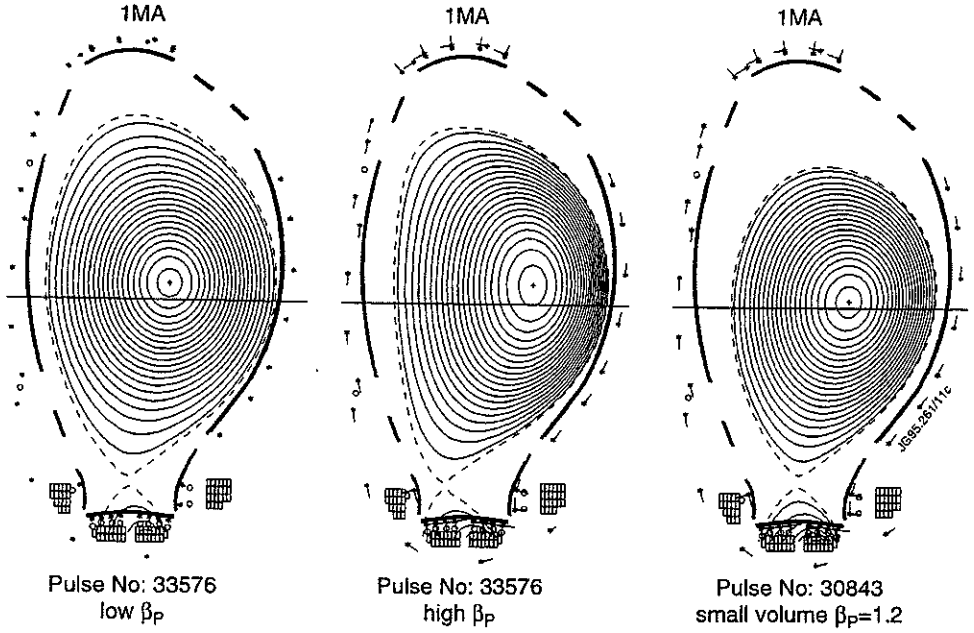

Figure 2: Plasma configurations used for high beta poloidal experiments.

CONFINEMENT

In previous JET campaigns high β_{pol} was achieved:

- Very high confinement ($\tau_E/\tau_{ITER89L-P} \approx 3.7$) Elm free H-mode plasmas at 1 MA/3.1 Tesla.
- With only 7 MW of ICRH power in double null X-point discharges.
- Only transient conditions and few discharges dedicated to high β_{pol} studies.

In the JET pumped divertor campaign the aim of the experiments was to achieve high β_{pol} in quasi steady state conditions to study the confinement. Compared with previous campaigns:

- The pumped divertor geometry offers better power handling.
- The divertor cryo-pump can be used to control the density.
- The experiments are at reduced volume and are single null X-point plasmas (Fig.2).

It was found that H-modes in the JET pumped divertor configuration are naturally ELMy, facilitating the objective of quasi steady state operation at high poloidal beta.

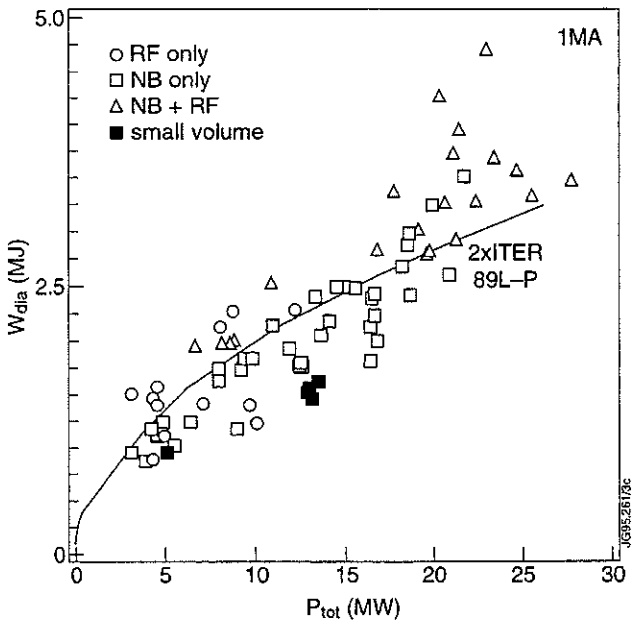

Figure 3: Stored energy vs. input power.

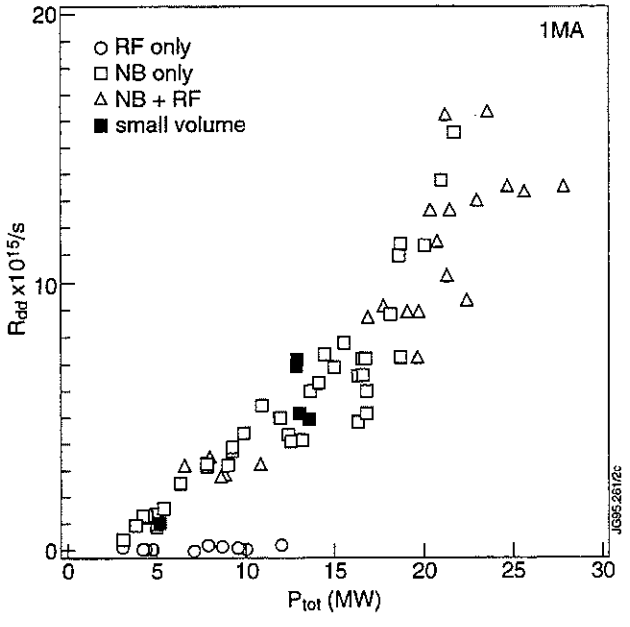

Figure 4: Reaction rate (R_{DD}) vs. input power.

In these conditions:

- The stored energy (W_{dia}) reaches typically twice the prediction of the ITER89L-P scaling expression up to the maximum additional heating power of 28 MW (Fig. 3).
- Some pulse have higher confinement and will be discussed later.
- The fusion reaction rate is proportional to the input power (Fig. 4).

- The confinement is independent of the additional heating method (NBI only, ICRF only or combined heating) (Fig. 3 and Fig. 4).
- In the high combined heated discharges a beta limit has not yet been reached [4].

From the experiments it can be concluded that:

- There is no apparent increase in confinement over H-mode scaling at high β_{pol} (Fig. 5).
- The plasma performance does not depend on the toroidal field (q_{95}, at a current of 1 MA).
- At high β_{pol} the plasma becomes naturally triangular (δ_{95}). Despite the increased triangularity the confinement in these ELMy H-mode plasmas does not improve (Fig. 6).

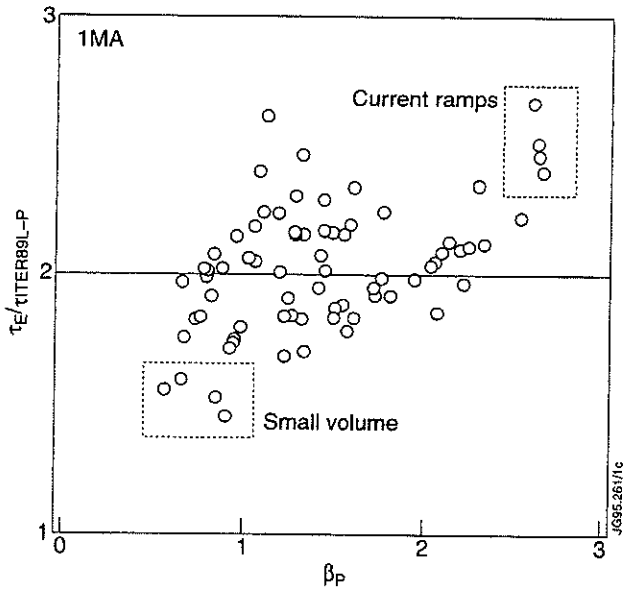

Figure 5: H-factor (ITER89L-P) vs. beta poloidal.

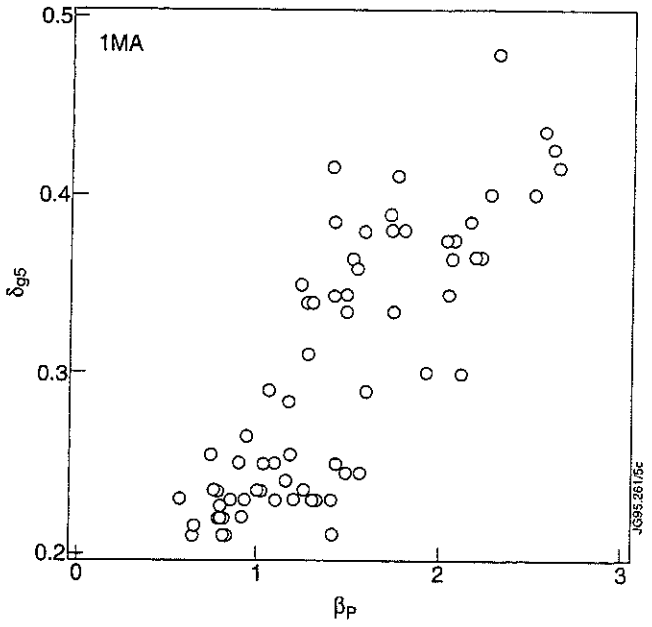

Figure 6: Triangularity (δ) vs. beta poloidal.

SMALL VOLUME PLASMAS

The data presented in the previous section also contain a variation of the aspect ratio.

- Dedicated experiments have been performed in 'small volume' plasmas in JET.
- The volume has been reduced from 85 m^3 to 55 m^3.
- The confinement in these small volume plasma is not much different from the large volume plasmas.

However, at 1 MA the confinement of the small volume plasmas is slightly below the H-mode scaling. When included in the data a possible increase in the H-factor (ITER89L-P) with plasma volume in JET is found. But, a comparison of discharges on the same day at 1.5MA shows no difference between large and small volume plasmas [3] (Fig. 7 and Fig. 8).

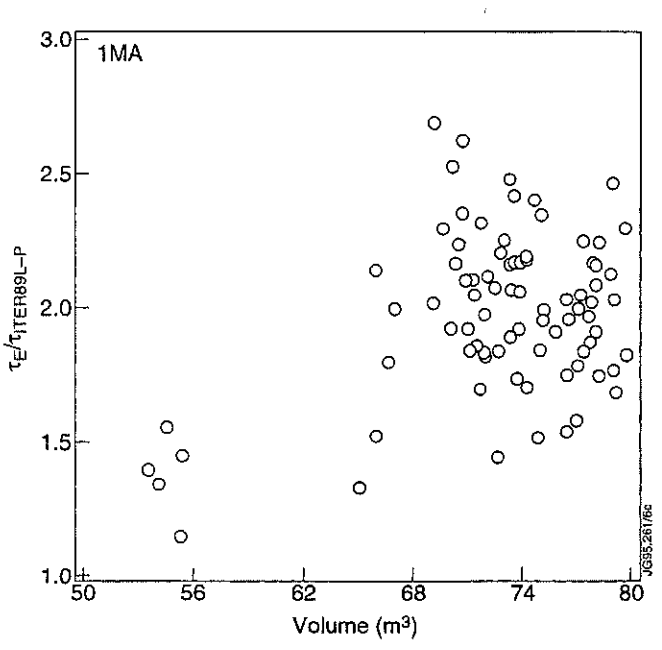

Figure 7: H-factor(ITER89L-P) and plasma volume.

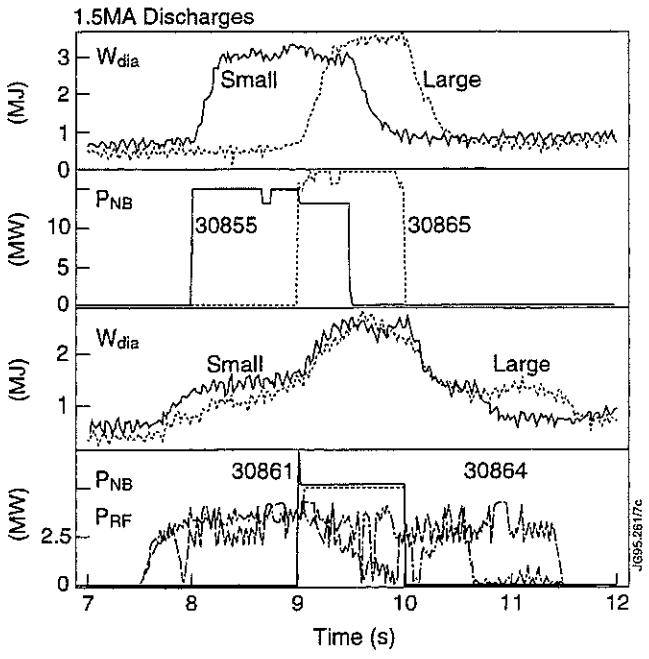

Figure 8: Small and large volume at 1.5 MA (same day).

The reduction in the H-factor compared to the rest of the 1 MA data may then be due to the fact that:

- The divertor cryo-pump was not used.
- The discharge were heavily gas fuelled to prevent neutral beam shinethrough, which could lead to a higher ELM frequency.

TRANSIENT ELEVATED CONFINEMENT

At high β_{pol} it is observed that the plasma could suddenly increase W_{dia} at constant input power:

- Correlated with oscillations on the plasma current at high β_{pol}.
- This was exploited by pre-programmed ramps of the plasma current: RAMP UP (Fig. 9)!

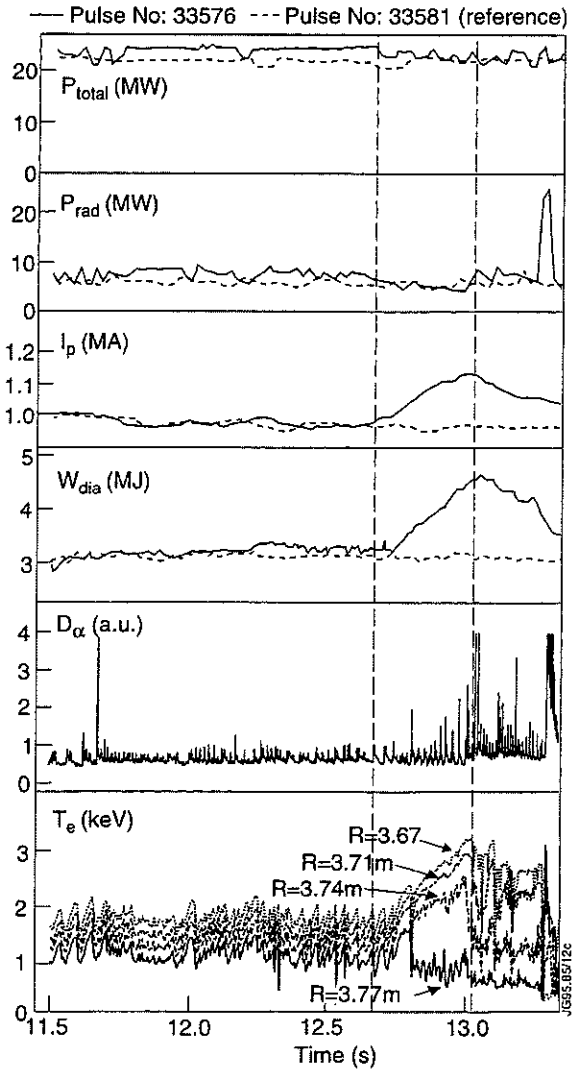

Figure 9: High beta poloidal plasma with a pre-programmed current ramp.

Speculative explanation

Assumptions:

- In the JET pumped divertor configuration the edge is limited by the first stability ballooning limit.
- Access to 2nd stable regime exists in the plasma periphery at high β_{pol}. This will allow an improved confinement regime during the heating.
- However, the ratio of j_{edge}/P_{edge} is not large enough, due to reduced edge collisionality, despite the divertor cryo-pump which helps to keep the edge density low.
- The plasma needs a modest increase in j_{edge}.

With a current ramp in high β_{pol} phase (Fig. 10):

- The link between P_{edge} and j_{edge} will be broken:
- The edge current density is increased: $j_{edge} = j_{bootstrap}(P_{edge}) + j_{ohmic}(dI/dt)$.

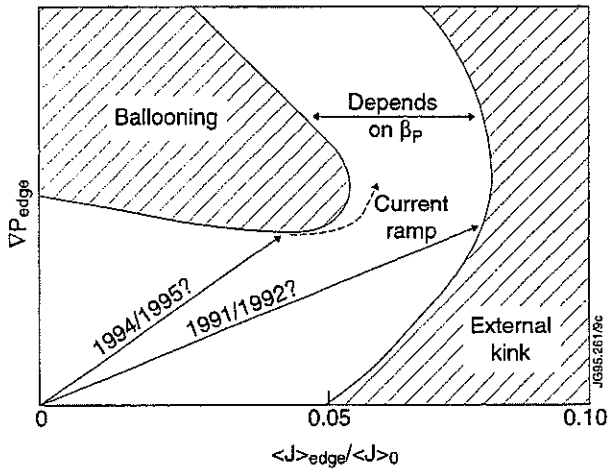

Figure 10: Stability diagram in the edge current, edge pressure gradient domain [5].

Current ramps at high β_{pol}:

- The current ramps may be used to extend the high β_{pol} regime to give improved confinement at higher currents.
- This by starting at 1MA level with full power heating and using the current ramp to 'kick' the plasma into the VH mode regime.

- After the current ramp, the improved confinement of the VH mode regime may be stable due to a larger bootstrap current at the edge generated by increased pressure gradients (but may go kink unstable).

CONCLUSIONS

1. There is no apparent increase in confinement over H-mode scaling at high β_{pol}, in quasi steady state, ELMy H-mode conditions (β_{pol} up to 2.7).
2. In this regime the confinement is also insensitive to the heating method, toroidal field, and plasma shape, although at 1 MA the small volume plasmas exhibit confinement parameters at the lower end of the spectrum.
3. Transient improved levels of confinement can be induced with plasma current ramps (up!) with the plasma already at high beta.
4. A possible explanation is that with a current ramp during the high the β_{pol} phase, the link between P_{edge} and j_{edge} is broken and the current density is increased in conditions where access to second stability exist (VH mode).
5. Current ramps could be used to achieve high β_{pol} and high fusion performance at $I_p \geq 2$ MA.

REFERENCES

[1] C.D. Challis, et al., Nucl Fusion **33** (1993) 1097.
[2] P.N. Yushmanov, et al.,Nucl Fusion **30** (1990) 1999.
[3] S. Ishida, et al., APS Conference, Minneapolis (1994).
[4] C.D. Challis, et al., this conference.
[5] G.T.A Huysmans, et al., this conference.

Sawtooth Heat Pulse Propagation in Tokamaks: Fourier Analysis and Ballistic Response

A Jacchia[1], F De Luca[2], G Gorini[2], P Mantica[1], N Deliyanakis, M Erba, L Porte.
JET Joint Undertaking, Abingdon, Oxfordshire, OX14 3EA, UK.
[1] Istituto di Fisica del Plasma, Associazione EURATOM-ENEA-CNR, 20133 Milano, Italy.
[2] Dipartimento di Fisica, Universita degli Studi di Milano, 20133 Milano, Italy.

INTRODUCTION

- The assumption that the plasma outside r_{mix} is not affected by the MHD instability is essential in order to treat the heat pulse as diffusive and to derive a meaningful value of χ_e^p ("perturbative" electron heat diffusivity).
- Fourier analysis is proposed as a tool for the recognition of non-diffusive features of heat pulse propagation in fusion plasmas.
- Fourier analysis of an example of JET sawtooth heat pulse diagnosed with the new ECE heterodyne is consistent with the results from the simulated ballistic heat pulse [1].

SIMULATION OF A BALLISTIC HEAT PULSE

The anomaly of the heat pulse propagation outside r_{mix} observed with fast (200 kHz) measurements of the electron temperature in TFTR sawtooth (ST) heat pulses [1], has been modelled in two phases: the crash phase, with a fast time scale ($\tau_{ST}\approx 100\mu s$) with $r<r_{mix}$; and the ballistic phase, occurring on a slower time scale, τ_b, with enhanced transport over $r> r_{mix}$.

In the region $r>r_{mix}$ by subtracting the steady-state power balance from the electron energy conservation equation we obtain the time evolution of the ST in terms of the perturbed quantities $\tilde{T} = T_e - T_{e0},$, and $\tilde{\chi}_e = \chi_e - \chi_{e0}$ (χ_{e0} is commonly denoted as χ_e^{PB}, the value obtained from power balance):

$$\frac{3}{2} n_{e0} \dot{\tilde{T}}_e - \nabla \cdot \left[n_{e0} \left(\chi_e \nabla \tilde{T}_e + \tilde{\chi}_e \nabla T_{e0} \right) \right] = 0 \qquad (1)$$

In order to further simplify Eq.1

- Assume ce to be a function of local macroscopic plasma parameters such as ∇Te together with small temperature perturbation (i.e., $\tilde{T}/T_{e0} << 1$).
- Heuristically model the enhancement of χ_e as: $\chi_e=\gamma(t,r)\chi_{e0}$

Eq.1 can be linearised in $\tilde{T}_e$ and $\nabla \tilde{T}_e$ yielding the equation for ST heat pulse propagation in the region $r>r_{mix}$:

$$\frac{3}{2}n_{e0}\dot{\tilde{T}}_e - \nabla\cdot\left[n_{e0}\gamma(r,t)\chi_e^p\nabla\tilde{T}_e\right] = \nabla\cdot\{[\gamma(r,t)-1]n_{e0}\chi_{e0}\nabla T_{e0}\} \qquad (2)$$

where $\chi_e^p = \chi_{e0} + \left(\partial\chi_{e0}/\partial\nabla T_e\right)\nabla T_{e0}$ is the perturbed heat diffusivity.

The simulation of Fig.1 was obtained numerically solving equation 2 with the following specifications:

a) Equilibrium Quantities:

$$n_{e0}(r) = n_0\left[1-\left(\frac{r}{a}\right)^2\right] + n_a$$

$$T_{e0}(r) = T_0\left[1-\left(\frac{r}{a}\right)^2\right]^4 \qquad (3)$$

$$\chi_{e0} = \chi_0 + (\chi_1-\chi_0)\left(\frac{r}{a}\right)^2$$

where the numerical values $n_0=3.46\cdot10^{19}$ m^{-3}, $n_a=0.12\cdot10^{19}$ m^{-3}, $T_0=7$ keV, $\chi_0=0.5$ m^2/s, $\chi_1=2$ m^2/s have been used. The plasma minor radius is a=1 m.

b) Perturbation Quantities:

$$\chi_e^p=\chi_{e0}\,\gamma(r,t) = [1+\delta\exp(-t/\tau_b - k\,r^2)] \qquad (4)$$

with $\delta=35$, $\tau_b=1$ ms and $k = 16$ m^{-2}.

The ST crash occurs at t=0. T_{e0} is flattened out to $r_{mix}=0.29$ m. Energy conserving instantaneous reconnection gives $r_{inv}=0.18$ m. As a boundary condition, $\tilde{T}_e$ is assumed to vanish at r=a=1 m.

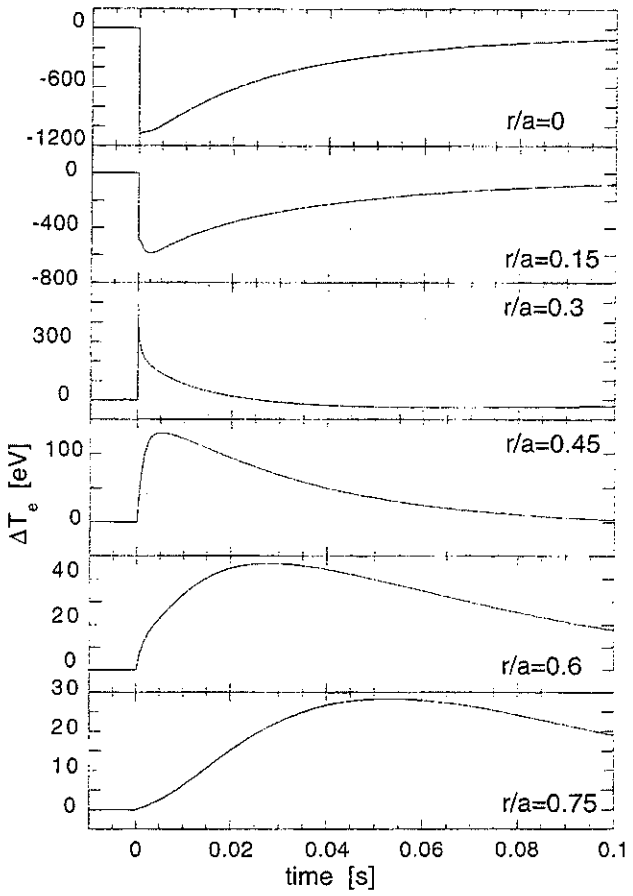

Fig.1: Simulated ballistic heat pulse shown at different radial locations of the plasma

FOURIER ANALYSIS OF A BALLISTIC HEAT PULSE

The quantities of interest to be determined with the Fourier analysis are [4]:

- the gradient of the phase (φ') and
- the logarithmic gradient (A'/A) of the Fourier transform $T\omega=Ae^{i\varphi}$ of $\tilde{T}_e$.

For a purely diffusive heat pulse in cylindrical geometry with negligible damping and not too large gradient of χ_e^p, the following relation between φ' and A'/A holds [2,3]:

$$\varphi'=(A'/A)_g \text{ where } (A'/A)g=A'/A+1/2r-1/2r_n \text{ and } r_n=-n_{e0}/n_{e0}' \tag{5}$$

Under the same conditions, the value of χ_e^p is determined from the following expression

$$\chi_g^p = \frac{3}{4}\omega\left[\varphi'(A'/A)_g\right]^{-1} \tag{6}$$

- Non-diffusive features will show up in the analysis in the form of a difference between φ' and $(A'/A)_g$.

Only if $\varphi'=(A'/A)g$ do we expect Eq.6 to provide the correct numerical value for χ_e^p. An exception would be the presence of strong damping of the pulse, in which case Eq.6 is still valid even if φ' and $(A'/A)g$ are different [3].

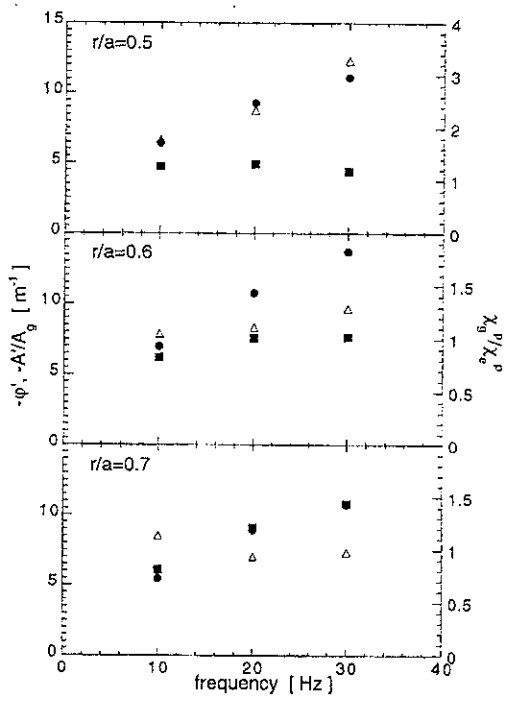

Fig.2: Fourier analysis of the ballistic simulation of Fig.1. At r=0.5m, the pulse is still strongly influenced by the ballistic effect: φ' (squares) is nearly independent of frequency and is significantly lower than (A'/A)g (circles). Application of Eq.6 to determine χ_e^p (open triangles) results in an error of a factor 2-3.

A purely diffusive behaviour of the pulse is recovered at r=0.7 m. There the agreement between φ' and (A'/A)g is very good, and the error in the determination of χ_e^p is small except for the lowest frequency $\omega/2\pi$=10 Hz, where the effect of the boundary condition starts to be significant. The heat pulse can be regarded as purely diffusive for r>2 rmix. Application of the extended time-to-peak (E-ttp) method [4] yields a χ_e^p value that is about 30% too large.

As shown in [1], simulations made under very different assumptions can result in time traces that are not too dissimilar at first sight; their Fourier spectrum, however, is significantly different. This can be understood since Fourier analysis is very sensitive to the rise phase of the pulse, which is different for a diffusive or ballistic pulse.

A PRACTICAL DEFINITION OF r_{MIX}

Fourier analysis is not always accurate enough depending on the s/n level in the data.
A possible alternative approach is to study the initial perturbation of the pulse.

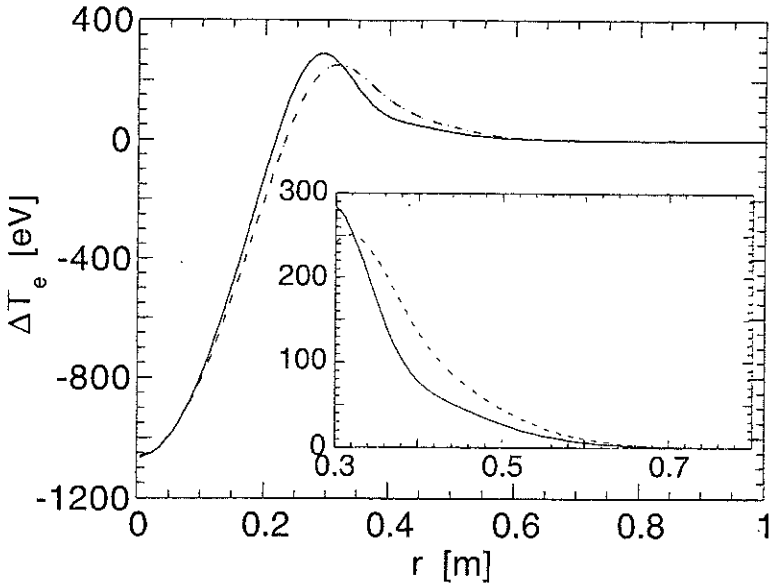

Fig.3: Temperature perturbation profile for the simulation of Fig.1 is shown at t=0.5 ms (full line) and t=1 ms (at t=0, the perturbation vanishes outside rmix).

One can see that within 1 ms of the sawtooth crash, the perturbation has extended over a region well beyond rmix as a result of the ballistic enhancement of the diffusivity. In practice the perturbation is negligibly small for r>0.6-0.7 m, both at t=0.5 ms and t=1 ms. Now r≈0.6-0.7 m is just where the heat pulse starts to be diffusive according to Fourier analysis.

On the basis of this simple observation, one can therefore justify the approach used, for instance, in previous analyses of JET sawtooth heat pulses [5]. There rmix was redefined as the radius beyond which the initial perturbation vanished, and the heat pulse analysis was carried out for r>rmix.

FOURIER ANALYSIS OF JET HEAT PULSE

It is interesting to compare the results of the simulation with a recent example of JET sawtooth heat pulse diagnosed with the new ECE heterodyne diagnostic: spatial resolution of about 3 cm, noise level 10 eV (1 kHz electrical bandwidth).

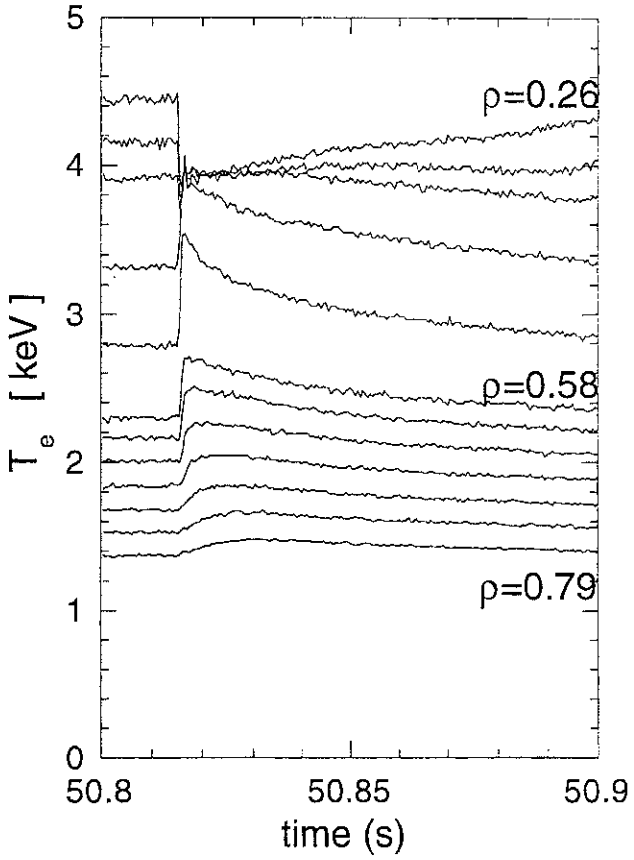

Fig.4:Time evolution of the electron temperature following a sawtooth instability in JET discharge #23425 (B=3.4 T, I_p=3.5 MA, $\langle n_e \rangle$=1.10^{19} m^{-3}, $\langle T_e \rangle$=2keV, P_{OH}=1.5 MW, P_{RF}=3.8 MW) as recorded by the ECE diagnostic at different radial locations. Sawtooth crash time at t=50.815s.

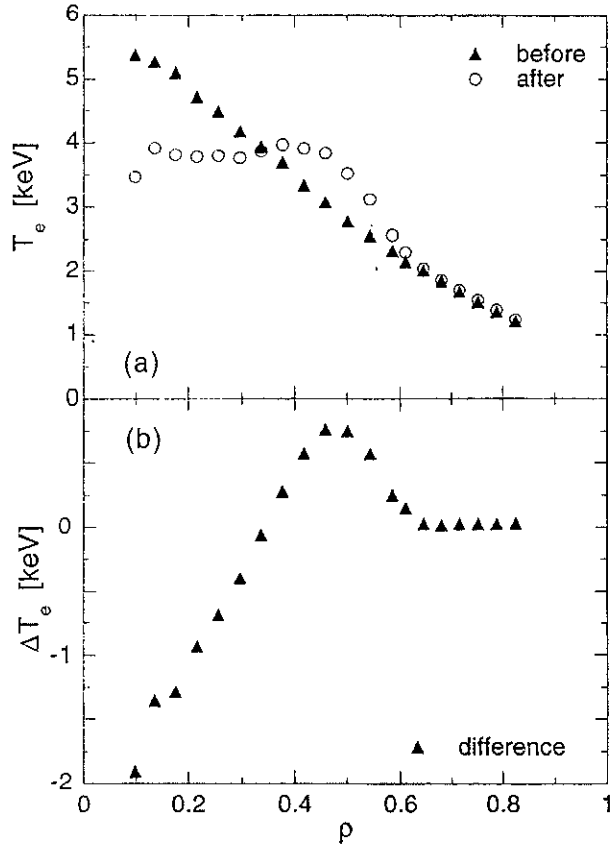

Fig.5 JET temperature profile of discharge #23425 just before the sawtooth crash and about 200-300 ms afterwards (a) as well as their difference (b). The corresponding normalised mixing radius value is ρ_{mix}≈0.7; this is more than twice the value of the inversion radius (ρ_{inv}=0.32).

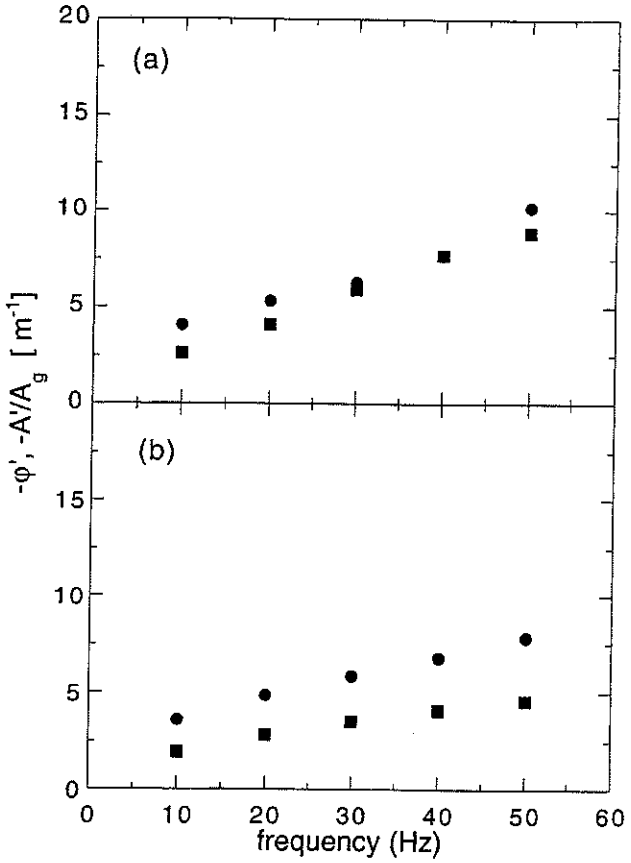

Fig.6: a Fourier analysis must be restricted to the region ρ>0.7 in order to provide a good determination of χ_e^P. The values of φ' (squares) and (A'/A)g (circles) in the region ρ>0.7 are plotted vs frequency . One can see that φ'=(A'/A)g, which confirms the diffusive behaviour of the heat pulse. The χ_e^P value determined using Eq.13 is χ_e^P=3.5 m^2/s. A similar value of χ_e^P=3.0 m^2/s is obtained with the E-ttp method.

Fig.6b Values of φ' and (A'/A)g in the region ρ>0.6 (7 channels). These values are obtained including data with ρ<ρ_{mix} in the analysis. The values of φ' are seen to be significantly smaller than in (a), while the values of (A'/A)g are almost the same.

This heat pulse has some of the features of the ballistic heat pulse shown in Fig.3. Given the time resolution of the diagnostic, however, it is not possible to decide whether the heat redistribution causing the large ρ_{mix} value occurs on a fast (τ_{ST}) time scale or on a slower (ballistic) time scale. Other sawtooth heat pulses measured with the heterodyne diagnostic have smaller ρ_{mix} and confirm the result $\chi_e^P/\chi_e^{PB}\approx$2-4 typical of JET plasmas.

CONCLUSIONS

- Application to a simulated ballistic sawtooth heat pulse has shown that Fourier analysis can identify the plasma region (far from the mixing radius) where the heat pulse is diffusive

- This region coincides with the region where a diagnostic with moderate (≈1 kHz) time resolution would find a negligible initial perturbation.

- Both Fourier and initial perturbation analysis have been used on JET ST pulses to identify the diffusive region of the pulse.

ACKNOWLEDGEMENT

Useful discussions with V.Parail, A.C.C.Sips and A.Taroni are gratefully acknowledged.

This work was performed under the JET-ENEA-CNR task agreement on perturbative transport, with financial support from JET and CNR.

REFERENCES

[1] E.D.Fredrickson et al, Phys. Rev. Lett. 65 (1990) 2869; E.D.Fredrickson et al, Nucl. Fusion 33 (1993) 1759.
[2] P.Mantica et al, Nucl. Fusion 32 (1992) 2203.
[3] A.Jacchia, et al, Phys. Fluids B 3, 3033 (1991).
[4] B.J.D.Tubbing, N.J.Lopes Cardozo, M.J.Van der Wiel, Nucl. Fusion 27, 1843 (1987).
[5] N.J.Lopes Cardozo et al, Controlled Fusion and Plasma Physics (Proc. 18th Eur Conf Berlin, 1991), Vol 15C, Part I, European Physical Society, Geneva (1991) 193. **???**

The Effect of a Sawtooth Crash on Fast Particle Behaviour

O N Jarvis, J M Adams[1], D Bond[1], M Hone, P J A Howarth[2], M J Loughlin, F B Marcus, G Sadler, P van Belle, N Watkins[1].

JET Joint Undertaking, Abingdon, Oxfordshire, OX14 3EA, UK.

[1] AEA Technology, Harwell, Oxfordshire, OX11 0RA, UK.

[2] University of Birmingham, UK.

ABSTRACT

Several experimental studies of the effect of a sawtooth crash on local nuclear reaction rates have been made on the JET tokamak, providing a general understanding of the effects of a crash on the spatial distributions of fast charged particles in ohmic, ICRF- and beam-heated discharges. This paper re-examines some high power ICRF-heated discharges and concludes that, in these discharges, only a special class of accelerated particle is significantly affected whereas the majority of the fast particles appear resilient to sawtooth crashes. The various observations are summarized.

1. INTRODUCTION

It is widely accepted that the spatial distribution of fast particles in a tokamak is significantly perturbed by the action of a sawtooth crash. Observations at JET include:

- ohmic plasmas - the total neutron emission yield displays modest, but abrupt, falls at each sawtooth crash as recognized through the electron temperature data [1].
- ICRF heating - the effect on the neutron emission is often dramatic and studies of ^{3}He-d fusion product proton emission show [2] that at least some (if not all) of the accelerated ions are expelled far from the centre of the plasma.
- neutral beam heating - strong effects of the sawteeth on neutron emissivity profiles have been observed (with both d-d and d-t plasmas) [3].
- triton burnup - the total 14 MeV neutron emission associated with burnup of the fusion product tritons released from d-d reactions is unaffected by sawteeth and their 2-D emission profile is at most marginally affected [4].
- Nuclear reaction gamma-rays - the effect of a sawtooth crash on the 2-D emission profile of gamma-rays emitted as a consequence of nuclear reactions in the plasma between highly

energetic, ICRF- accelerated, fast ions and impurity ions [5] was found to have a minor consequence on the bulk of the fast ion spatial distribution.

A re-examination of the nuclear gamma-ray data has shown that the crash does have an important effect on the orbits of a particular class of fast ions. It will be argued that all the above observations are, in fact, consistent.

2. GAMMA-RAY TOMOGRAPHY

The 19-channel neutron profile monitor (fig.1) installed on the JET tokamak has permitted tomographic inversions to be obtained of line-averaged d-d and d-t fusion neutron data and also of nuclear reaction neutron and gamma-ray data for a variety of plasma conditions [3-6].

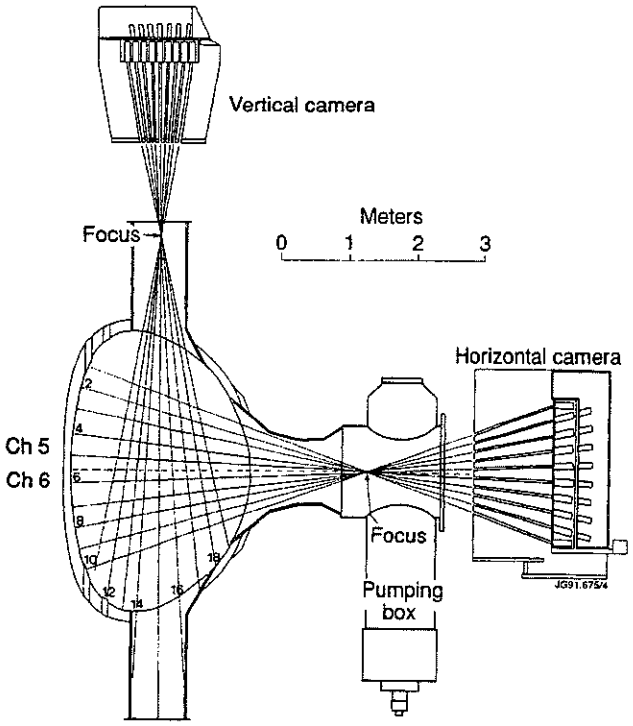

Fig.1: Schematic of the JET neutron emission profile monitor, showing the lines-of-sight for each detector channel.

The neutron and gamma-ray signals of present interest originate within the plasma as a result of interactions between ^{3}He ions accelerated during ICRF heating experiments with plasma impurities (mainly ^{12}C and ^{9}Be). The deduced 2-D profiles of the gamma-ray emission clearly indicate the presence of a localized source of emission in addition to the distributed emission from banana orbits with turning points at the resonance layer. *This localized source is attributed to a class of particle with orbits having rather small poloidal excursions, centred about 15 cm to the low-field side of the resonance layer and circulating in the direction of the current (the co-direction) with pitch-angles somewhat in excess of 90° (particles travelling parallel to the plasma current have 180° pitch-angle).* These ions represent no more than 10% of the total fast ion population but generate a very sharp off-axis peak in the 2-d emission contour plot, as presented in ref. [6].

2.1. Sawtooth Example - Gammas and Neutrons

An example of a major sawtooth crash [5] shows that particles with turning points at the resonance layer appear to be relatively unaffected while the class of particle responsible for the sharp peak in the emission profile is strongly reduced in magnitude (figs.2 and 3); presumably they are redistributed on to much larger passing or banana orbits.

This example is unique and was obtained due to a combination of special circumstances:

- ICRF power deposition suitable for accelerating minority ^{3}He ions to high energies,
- An unusually high level of impurity ^{9}Be ions in the plasma,
- A profile monitor tuned to optimize (instead of minimizing) the detection of gamma-rays.

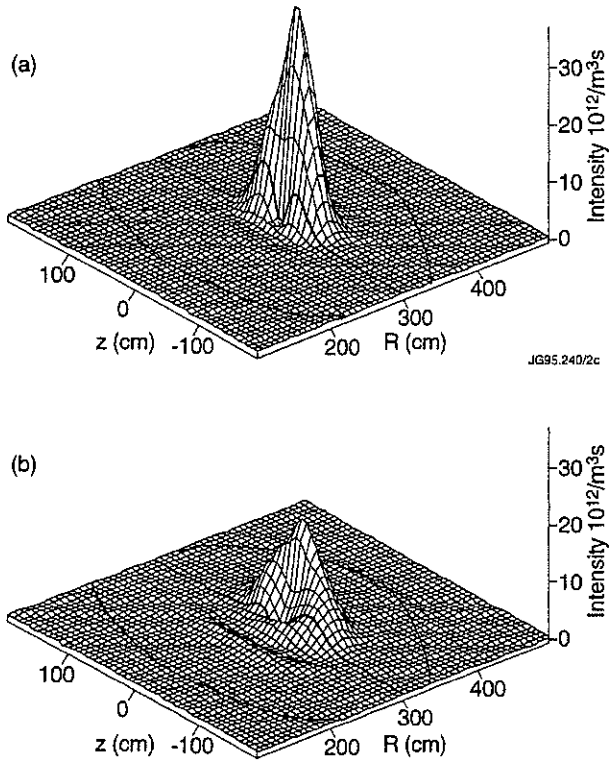

Fig.2: Tomographic reconstruction of the gamma-ray emission profiles (a) before and (b) after, the sawtooth crash at 10.17 secs in discharge 23230.

A full presentation of the experimental evidence is not possible here, where we present only the main deductions. The gamma-ray tomography shows that the global gamma-ray emission falls by less than 20% at the crash, consistent with the reduced slowing down time due to the fall in central electron temperature and implying that most of the fast ions remained confined within the plasma. The global neutron emission falls by 50% in the 50 ms following the crash, with an

exponential time constant consistent with slowing down at r/a ≈ 0.7.

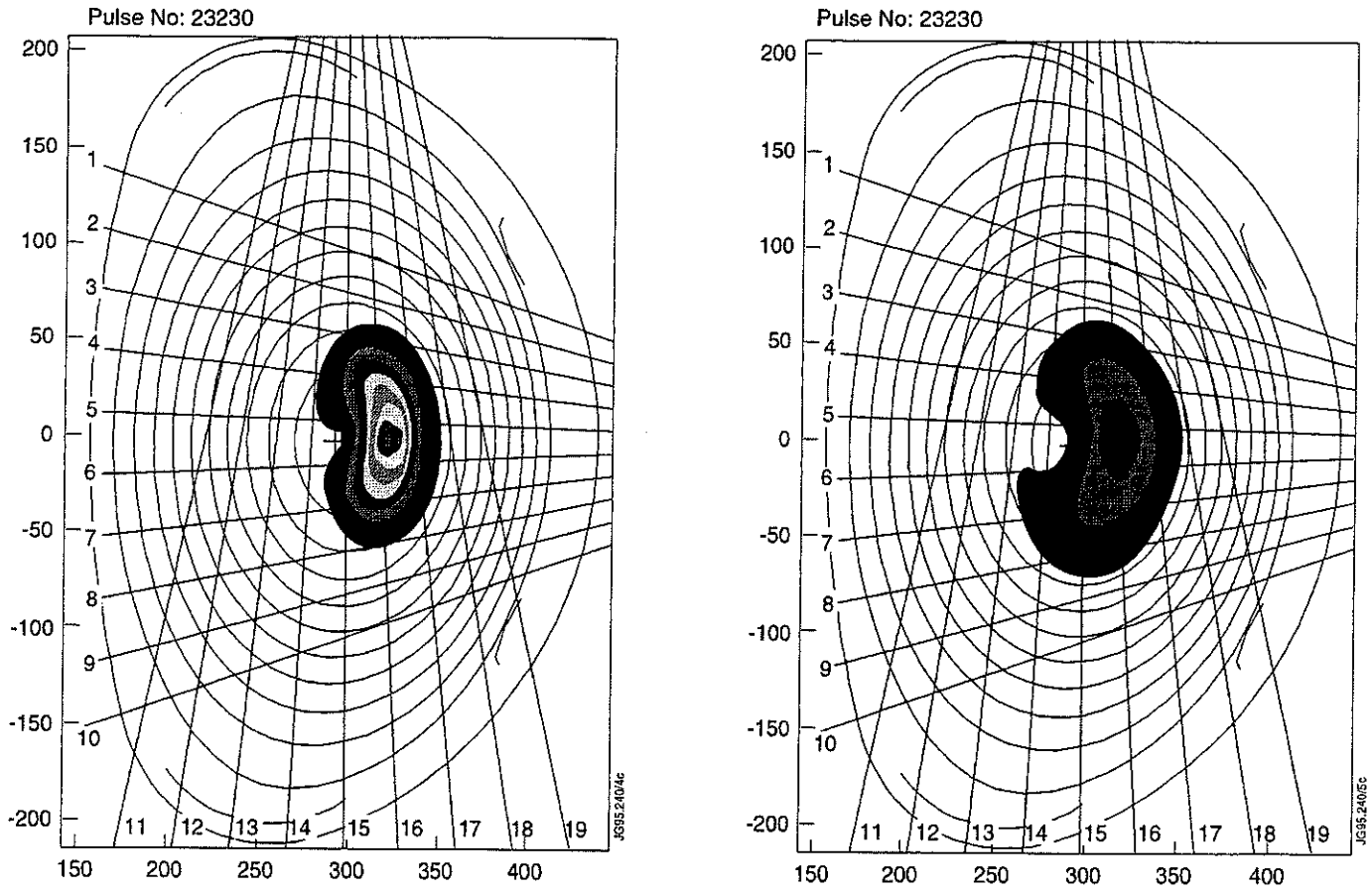

Fig.3: Contour plots of the same data presented in fig. 2 The two plots are based on a common grey scale.

This discharge also exhibited a neutron emission time dependence (fig.4) that led to a number of conflicting interpretations. For no apparent reason, the neutron emission suddenly began to increase linearly with time, while all other plasma properties apparently remained constant. The most plausible interpretation is given below.

The time traces in fact show the appearance at about 9 s of a new source of neutrons that grows in magnitude to the level of the d-d fusion emission and is not accompanied by additional gamma-ray emission from the plasma. This new source is evidently a new reaction with a high reaction threshold; $^{12}C(^{3}He, n)\,^{14}O$ is an obvious candidate as the reaction Q-value is -1.148 MeV and no gamma-radiation is expected until an excess of about 5 MeV in kinetic energy becomes available.

We associate the 50% fall in global neutron emission as being due to this reaction and also with the disappearance of the hot-spot feature (the co-passing ions). It follows that the particles responsible for the hot-spot must possess above-average energies, explained as being the result of acceleration by the RF waves by virtue of a Doppler frequency shift effect which

sustains their parallel velocities. Co-passing ions expelled from the hot-spot region leave the influence of the RF and will slow down rapidly, consistent with the observation noted above.

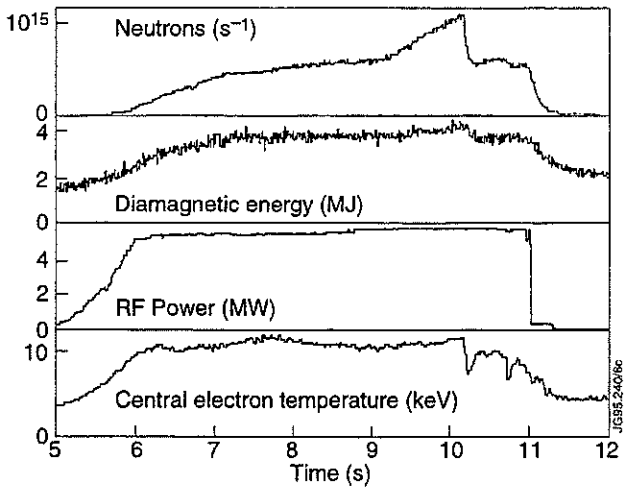

Fig.4: Time traces for discharge 23230, showing the rise in neutron emission despite the constancy of RF power and the standard plasma parameters.

2.2. Interpretation

With this background information, one may speculate as to how a sawtooth crash affects the RF-generated fast particles in the central region. It is believed that the crash is an m=1, n=1 kink instability that takes place suddenly and with a duration of order 50 s in JET. This instability affects the plasma pressure and may involve a reconnection of field lines [7]. However, on such a short time scale it is not possible for the magnetic field strength to change appreciably so that while the electrons and thermal ions, being localized to flux surfaces, should follow the motion of the field lines very readily, the MeV ions accelerated by the RF heating (the majority having D-shaped orbis with turning points in the resonance layer) are not so localized and will not follow closely any local disturbances of the flux surfaces. Indeed, to first order, their orbits should not be greatly perturbed. The main concentration of lower energy RF-accelerated ions is at the resonant surface, close to the machine mid-plane. If the thermal ions and electrons are displaced by the sawtooth crash, but not the bulk of the RF-accelerated ions, then the charge separation could cause an electrical field to be set up that possesses a scale length of the magnitude of the displacement of the disturbance. Fig.5 illustrates the situation that would then exist in the absence of relaxation of the displaced core along the field lines. In practice, such a relaxation

would be considerably more rapid than the cross-field relaxation which could take several milliseconds (hundreds of times longer than the orbital period of energetic passing particles).

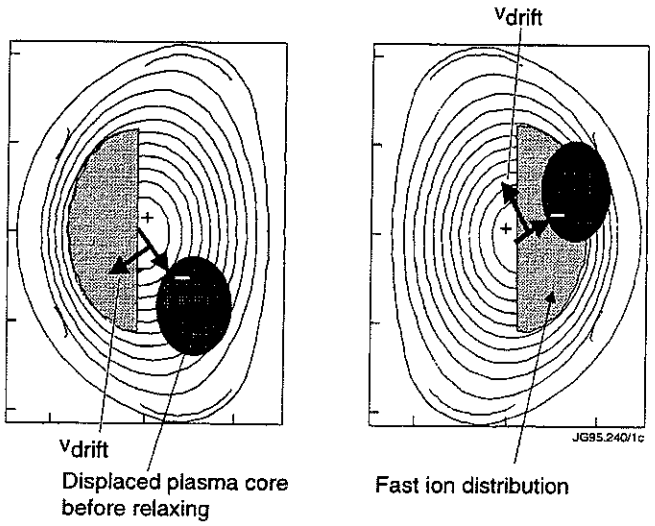

Fig.5: Illustrating the charge separation and resulting $E_{\wedge}B$ drifts suggested as a mechanism for the expulsion from the central plasma region of a selected class of fast ions by the action of a sawtooth crash.

Prior to the cross-field relaxation, the electrical field will induce a coherent **ExB** drift of the spatially localized particles in a vertical direction. (Since the time-scale of the sawtooth crash is long compared with the gyration period of the fast ions, we would expect magnetic moment conservation to apply). The co-passing particles thus have their orbits incrementally transformed into off-axis banana orbits with turning points outside the inversion radius. The trapped orbits of the bulk (less energetic part) of the RF-generated distribution possess turning points at the resonance layer and, due to their relatively slow precession, will spend little time in the region of this electrical field (the most energetic ions having orbits that lie wholly outside it) and so should not be greatly affected.

3. OHMIC, ICRF AND BEAM-HEATING; FUSION PRODUCT TRITONS.

- In the absence of ICRF-heating, there should be no persistent large-scale electrical field generation of the type suggested here. The electrons and ions will be redistributed by mechanisms such as those outlined by Kadomtsev [7] and later workers; the global neutron emission will drop because the particles within the original q=1 surface will have become dispersed within an enlarged, cooler, volume and the previously peaked temperature profile will have become flattened.

- With high power ICRF heating, we have seen that a particular class of the accelerated ions will have turning points shifted vertically to the edge of the sawtooth disturbance. These particles subsequently perform an orbital motion in outer regions of the plasma not previously accessible. This explains the very sharp (picket-fence) signals observed when recording the 16 MeV fusion product protons from ^{3}He-d reactions using an in-vessel silicon diode detector [3,8] and is compatible with the small drop in the diamagnetic energy content that indicates that the bulk of the fast ion distribution remains relatively undisturbed.

- With neutral beam (D^{o}) injection heating, the neutron sawteeth become more pronounced than with ohmic heating alone. There are three fusion reaction contributions to the neutron emission to be distinguished: beam-beam, beam-plasma and thermal.

    1. The sawtooth performance of the thermal contribution for ohmic plasmas has been discussed above. During beam heating, the central temperature variation is enhanced, resulting in larger thermal emission neutron sawteeth.
    2. The effect of the crash on the beam ions has been examined in detail [3]. A sudden redistribution of the beam ions will have negligible immediate consequences on the beam-plasma global emission; however, a significant spatial redistribution has been observed through the 2-d profile [3]. However, ref. [4] concluded that a discharge for which the beam-plasma neutron emission was wholly dominant would not display neutron sawtoothing, either globally or locally, because central flattening of a relatively broad distribution, which is the case for beam-plasma dominant discharges, would produce no observable effect on the neutron emission.
    3. Beam-beam contributions are important when the beam-ion density profiles are peaked, in which case any broadening of the profile produces an enhanced reduction in the beam-beam contribution.

Those beam ions orbiting within the central region of the plasma affected by the crash are

mostly on passing orbits (for JET). As the injected ions have relatively low energy, they will tend to follow the field lines around the flux surfaces, becoming redistributed rather less strongly than the thermal ions.

- Finally, we consider the likely response of the fusion product tritons generated by beam-heated deuterium plasmas. These tritons have energies of approximately 1 MeV and will have moderately anisotropic velocity distributions. Their birth radial profile is the same as the 2.5 MeV neutron emission profile. Their slowing down behaviour has been studied [4] through the t-d fusion neutron production (14 MeV neutrons). Only a small redistribution of the triton ion population would be expected. In practice, little is observed [4], consistent with the finding for beam ions in beam-plasma dominated discharges (the triton burnup 14-MeV neutrons have much the same profile peaking as the 2.5 MeV neutrons).

4. CONCLUSION

The study [2] of 16 MeV proton emission from ICRF-heated plasmas demonstrated dramatically that accelerated ions are expelled completely from the inner region of a plasma by the effects of a sawtooth crash, giving a misleading impression of the importance of the effect.

The work reported here indicates that the bulk of the accelerated ions barely responds to the crash and that only a special class of accelerated particle is significantly disturbed. The mechanism responsible for this effect is peculiar to ICRF-generated fast ion distributions.

In the absence of ICRF heating, highly energetic (several MeV) ions would be expected to be redistributed along with the sawtooth crash only to the extent that their orbits are closely guided by the flux surfaces, so they should experience at most a weak tendency to share the fate of the thermal ions. At lower energies (~100 keV), and in hot plasmas, little distinction between behaviour of thermal and fast ions is expected.

5. REFERENCE

1. D.J.Campbell et al, Nuclear Fusion **26** (1986) 1085.
2. G.Sadler et al, Europhysics Conference Abstracts, Vol. 10C, Part 1 (1987)105.
3. F.B.Marcus et al, Plasma Physics and Controlled Fusion **33** (1991) 277.
4. F.B.Marcus et al, Nuclear Fusion **34** (1994) 687.
5. G. Sadler et al, Proc. IAEA Technical Meeting on Alpha-particles in Fusion and Plasma Physics, Aspanas, July 1991, Vol.1, p 97.
6. P.J.A.Howarth et al, Europhysics Conference Abstracts, Vol. 18B, Part 1, p. 262.
7. B.Kadomtsev, Sov. J. Phys. **1** (1975) 389.
8. O.N.Jarvis et al., Europhysics Conference Abstracts, Vol. 18B, Part 1, p. 270.

Direct Measurement of TAE, EAE and Multiple Kinetic TAE in JET

A Fasoli[1], D Borba, N Deliyanakis, J A Dobbing, D J Campbell, C Gormezano, J Jacquinot, A Jaun[1], W Kerner, H Holties[2], P Lavanchy[1], J B Lister[1], J-M Moret[1], L Porte, S Sharapov, L Villard[1]

JET Joint Undertaking, Abingdon, Oxfordshire, OX14 3EA, UK.

[1] CRPP-EPFL, Ass. Euratom-Suisse Confederation, 21 av. des Bains, CH-1007 Lausanne.

[2] FOM Institute for Plasma Physics, Rijnhuizen, Nieuwegein, The Netherlands.

1. ABSTRACT

Results from the first experiments to drive Alfven Eigenmodes (AE) with antennas external to a tokamak plasma are presented. In ohmic plasmas, the directly measured damping rates of Toroidicity induced AE (TAE) cover a wide range, $10^{-3} \leq \gamma/\omega \leq 10^{-1}$. In plasmas heated by ion cyclotron resonance, neutral beam injection, lower hybrid waves and high plasma current ohmic heating, a new class of weakly damped AE, the Kinetic Alfvén Eigenmodes, has been identified experimentally. Preliminary results on AE excitation by ICRH beat waves are also included.

2. INTRODUCTION AND MOTIVATION

- Weakly damped AE, which exist within the shear Alfvén spectrum in toroidal devices, are important for confinement of alpha particles created by fusion reactions in D-T magnetically confined plasmas.
- Resonant wave-particle processes between AE and fast ions can both drive the modes unstable and produce modifications to the particle orbits.
- Above a certain threshold amplitude, AE can induce stochasticity in the particle trajectories and consequently anomalous phase space particle transport. By coupling to other loss mechanisms, such as magnetic ripple effects, wall damage can also be caused.
- In ignited plasmas, large amounts of energy and steep pressure gradients characterise the slowing down alphas, a significant fraction of which will be resonant, with $v \sim v_A$.
- The damping, the frequency spectra and the spatial distributions of AE are investigated by means of a new active diagnostic system.
- Goal: to assess the AE stability and to predict the effects of AE on particle orbits for cases in which the modes cannot be stabilised.

3. EXPERIMENTAL METHOD: EXTERNAL EXCITATION + SYNCHRONOUS DETECTION

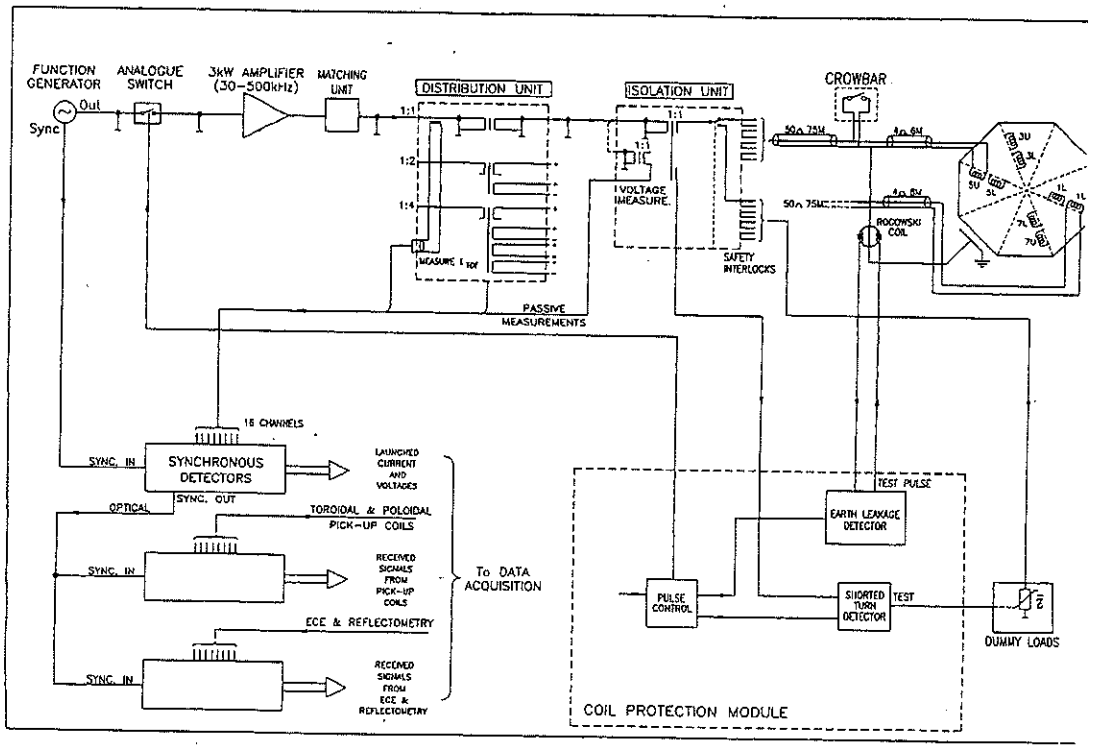

Fig.1: The saddle coil system at JET: AE exciter and detector experimental lay out $f_{exciter}$ *= 30 - 500 kHz.* $I_{saddle\ coil}$*<30 A;* $V_{saddle\ coil}$ *< 500 V (→*$\delta B/B_{core}<10^{-5}$ *)*

Synchronous detection: -**driven response** (Re, Im)

-band width in 20-500 kHz; band width out=500 Hz;
sampling rate. =1 kHz.

Diagnostic channels: -active **saddle coils V, I** (antenna impedance).

-passive saddle coils and fast magnetic coils: $\delta\mathbf{B_{pol}}$, $\delta\mathbf{B_r}$ **(→ n, m)**

-Heterodyne ECE + microwave reflectometry → **δB(r) , δn(r)**

Data analysis: diagnostic signal/driving current → transfer function H.

AE = resonance in H, with complex poles, p_k , and residues, r_k

$$H(\omega,x)=\sum_{k=1}^{N}\frac{1}{2}\left(\frac{r_k(x)}{i\omega-p_k}+\frac{r_k{}^*(x)}{i\omega-p_k{}^*}\right)+D(\omega,x)=\frac{B(\omega,x)}{A(i\omega)}$$

N = n. of resonances in the meas. range, $\omega=2\pi f_{exciter}$, x = meas. position. $p_k=i\omega_{0k}+\gamma_k$:common pole.

D accounts for direct coupling with the antenna.

Fit of data with H, with a single denominator A and separate numerators B.

Im(p) → $\mathbf{f_{obs}=\omega_{0k}/2p}$**. Real(p) (stable modes)** → $\gamma=\gamma_{damping}-\gamma_{drive}$ **Residues → Eigenfunction**

4.TAE/EAE EXCITATION AND DETECTION

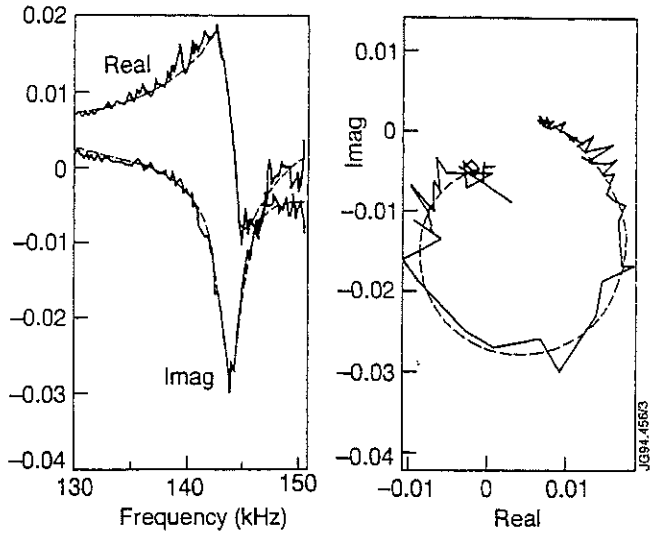

Fig. 2 TAE resonance. Real and imag. (left) and complex plane representation (right) of a magnetic probe signal, normalised to the current driven in the antenna.

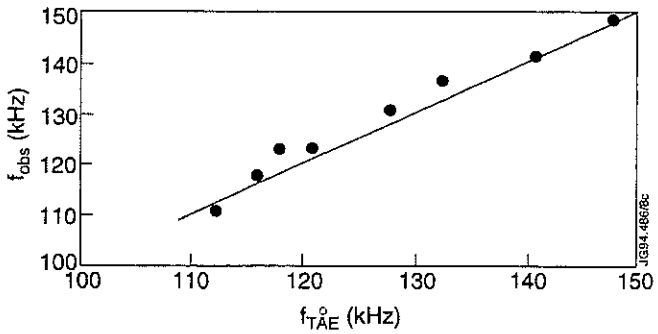

Fig. 3 AE frequency vs. B_{tor} (#31591). B_{tor} varied linearly with t from 2.2 to 3 T; density, I_p~const.. $f^0_{TAE} \equiv v_A/(4\pi qR_0)$ (q=1.5)

$\delta B_{pol,edge}/B_{tor}<10^{-7}$ for $I_{saddle\ coil}<10$ A. With numerator/denom. of order 5/2, the fit gives f_{obs}=144.2+-0.1 kHz, $\gamma/2\pi$=1400+-100 s^{-1} → Q = ω/γ ~ 125, γ/ω ~ 0.8%.

Ohmic phase of JET shot #31638. $B_{tor} \equiv 2.8$ T, $I_p \equiv 2.2$ MA, $\bar{n}_e \equiv 3x10^{19}$ m^{-3}; upper saddle coils, in phase and 180^0 apart.

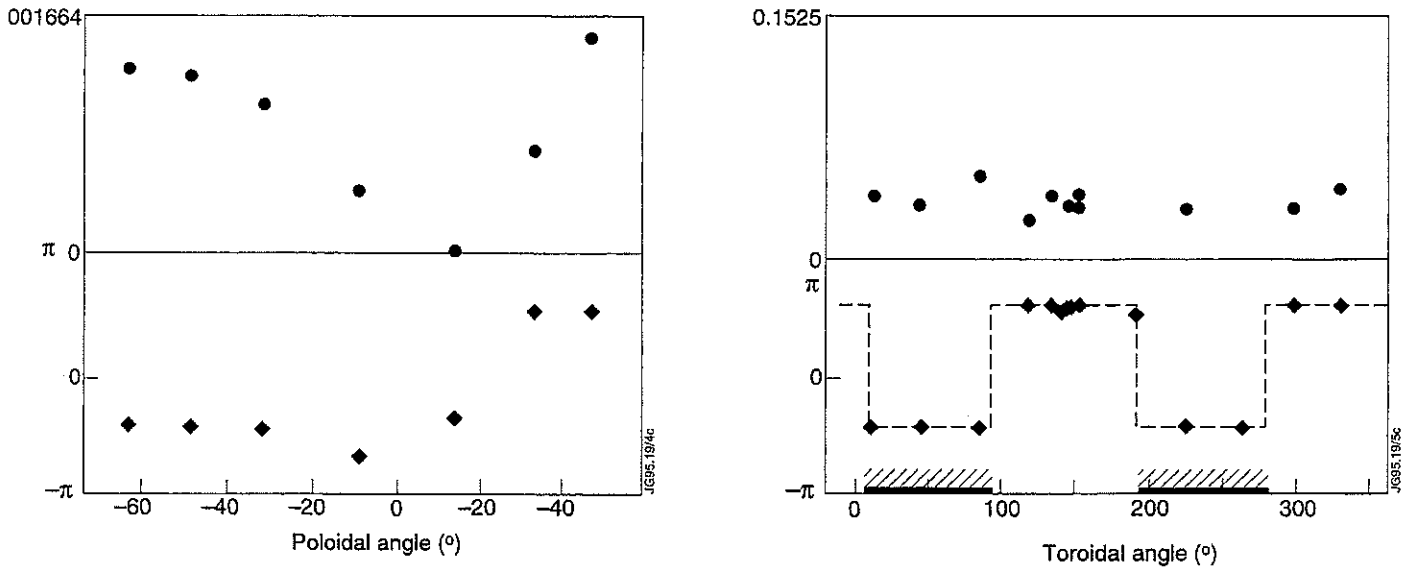

Fig. 4 TAE toroidal and poloidal structure: magn. (+), phase (x) of AE residues, lnl=2.

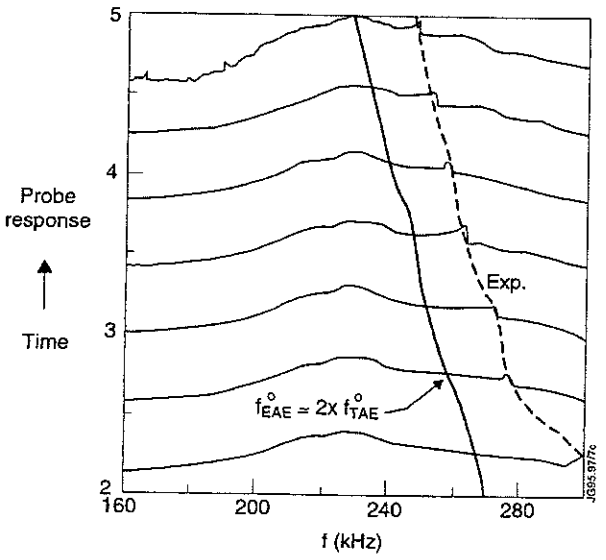

Fig. 5 Global modes with spatial distributions and damping rates similar to the TAE case were driven and detected for $f>f_{TAE}$. As in the example shown here, the mode frequencies followed $2f_{TAE}^{0}$. These modes were thereby identified as Ellipticity Induced AE (EAE).
$n_e \cong 4\text{-}8\ x10^{19}\ m^{-3}$; $B_{tor} \cong 2.85$ T, $I_p \cong 2$ MA; Inl=2.

5. DAMPING OF TAE

γ/ω was measured in ohmic plasmas, with 1 MA$<I_p<$3 MA; $1x10^{19}\ m^{-3} < \bar{n}_e < 5x10^{19}\ m^{-3}$; 1 T$<B_{tor}<$3.5 T; odd and even low-n excitation.: $\mathbf{10^{-3}} \leq \gamma/\omega \leq \mathbf{10^{-1}}$ ($\rightarrow$ extreme sensitivity to plasma equilibrium).

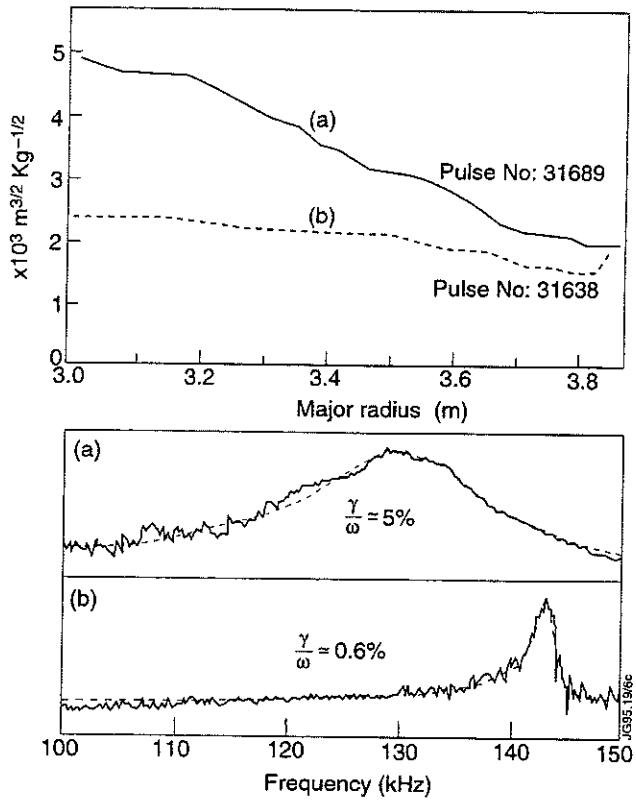

Fig. 6 Continuum damping: relationship between the profile of $g(r)=1/(q(r)\rho(r)^{1/2})$ and the TAE damping, in two similar ohmic discharges, with Inl=2; $\bar{n}_e \cong 4x10^{19}\ m^{-3}$; (a) $B_{tor} \cong 1.8$ T, $I_p \cong 2$ MA. (b) $B_{tor} \cong 2.8$ T, $I_p \cong 2.3$ MA.
Strong radial dependence of g(r), curve (a): gaps not aligned $\rightarrow$ strong damping, $\gamma/\omega \sim 5\%$.
Flatter g(r), (b): gaps aligned $\rightarrow$ less damping.

6. OBSERVATION OF MULTIPLE KINETIC ALFVÉN EIGENMODES

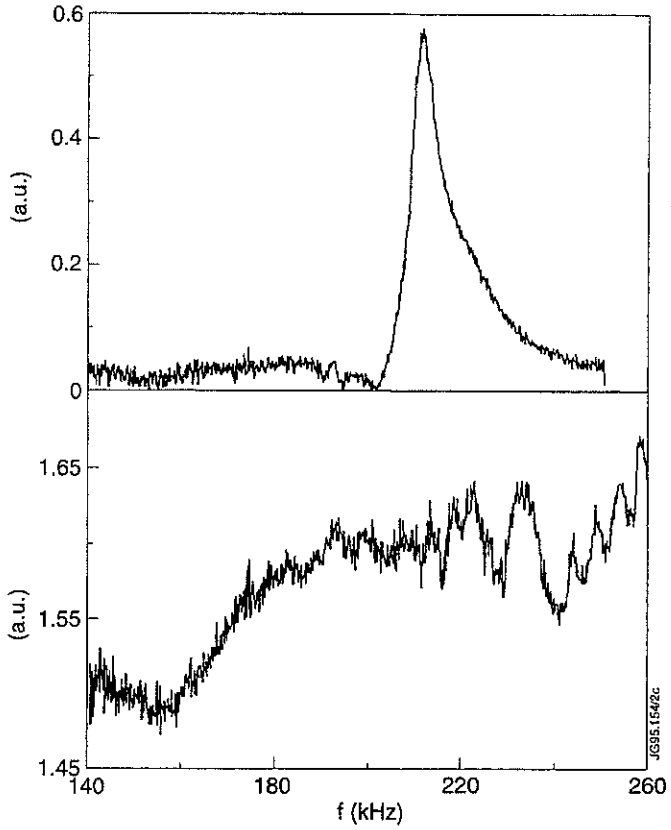

Fig. 7 B_{pol} probe signals for moderate (top) and high plasma current (bottom) in the same ohmic discharge #34073. The single TAE observed for low values of I_p is transformed into multiple peaks at higher I_p, corresponding to a hotter plasma. As these modes are externally driven with |n|=2 and the plasma rotation is negligible, they cannot correspond to Doppler shifted peaks of different n. (a): t = 3.5 s; I_p ~ 2 MA; B_{tor} ~ 2.5 T; $\bar{n}_e$ ~ 1.9 10^{19} m^{-3}; T_e ~ 2.2 keV. The single TAE has f = 210.5 kHz, γ/ω = 1.4 %; f_{TAE}^0 ~ 200 kHz. (b): t=9.5 s; I_p~4.1 MA; B_{tor}~ 2.9 T; $\bar{n}_e$ ~ 3 10^{19} m^{-3}; T_e~3.2 keV; f_{TAE}^0 ~ 180 kHz.

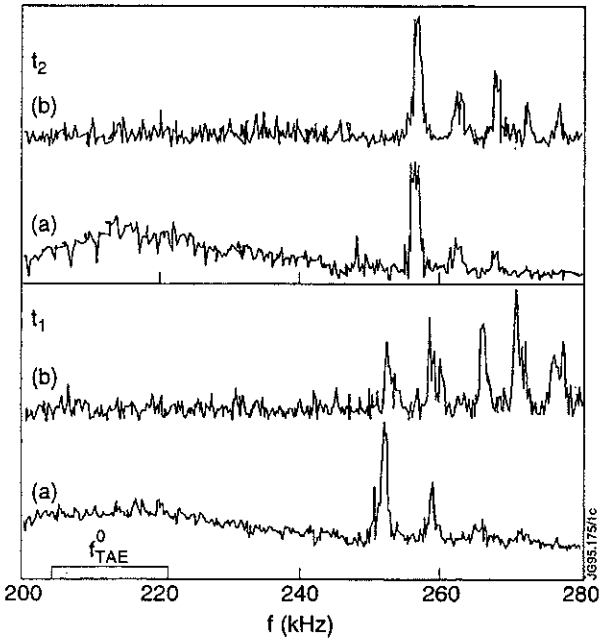

Fig. 8 Spectrum of magnetic (a) and density (b) perturbations in the AE range for LHH (2.5 MW) and ICRH (6 MW) in minority heating, raising T_e, T_i and T_e/T_i and reducing kinetic damping without significant resonant particle populations. Multiple resonances characterised by the same |n|=2 appear at $f>f_{TAE}^0$. The reflectometer frequency corresponds to r/a~0.5. These driven density perturbations in the plasma core, linked to $\delta E_{||}10$, emphasise the non-ideal MHD character of the modes.
Two successive scans, at t_1 = 19 s and t_2 = 20 s are shown. I_p ~ 3 MA; B_{tor} ~ 3.2 T; n_e ~ 2.5 10^{19} m^{-3}; T_e ~ 6.3 keV; T_i ~ 2.9 keV. $\Delta f/f$~2.5 % and $\gamma/\omega < 10^{-3}$.

Interpretation of multiple peak AE spectra:
Non-ideal MHD effects: finite Larmor radius and finite $E_{||}$.

Analytical models for hot plasmas: several weakly damped modes with regularly spaced frequencies form inside a potential well above the gap, as in a quantum harmonic oscillator. Non-ideal parameter: $\lambda = 4\ m\ s\ /(r_m\ \varepsilon^{3/2})\ \rho_i\ (3/4 + T_e/T_i)^{1/2}$, with $\varepsilon \simeq 2.5\ r_m/R$. λ is calculated at r_m, where $q(r_m)=(m+1/2)/n$. When $\lambda > \gamma/(\omega\ \varepsilon)$ a transition from a 'cold' TAE (ideal MHD) to multiple KTAE occurs.

Multiple AE spectra in the TAE/EAE frequency range, with similar peak frequency spacing, resonance width and mode numbers, have been observed with LHH only, NBI and ICRH only. Very weakly damped ($\gamma/\omega < 10^{-4}$) multiple modes were also seen, mainly on the reflectometer, during I_p ramp-down experiments, corresponding to sudden variations in l_i and presumably in magnetic shear.

The damping rates observed for the driven multiple KTAE/KEAE were in most cases significantly lower than for the 'cold' TAE: $\gamma/\omega < \mathbf{10^{-3} - 10^{-4}}$,
Wave-particle destabilisation should be easier than for TAE/EAE. Multiple peaks at $f > f_{TAE}^{0}$ have indeed been observed, for ex. with ICRH (P>6 MW) and NBI (P(140 kV)> 1.5 MW).

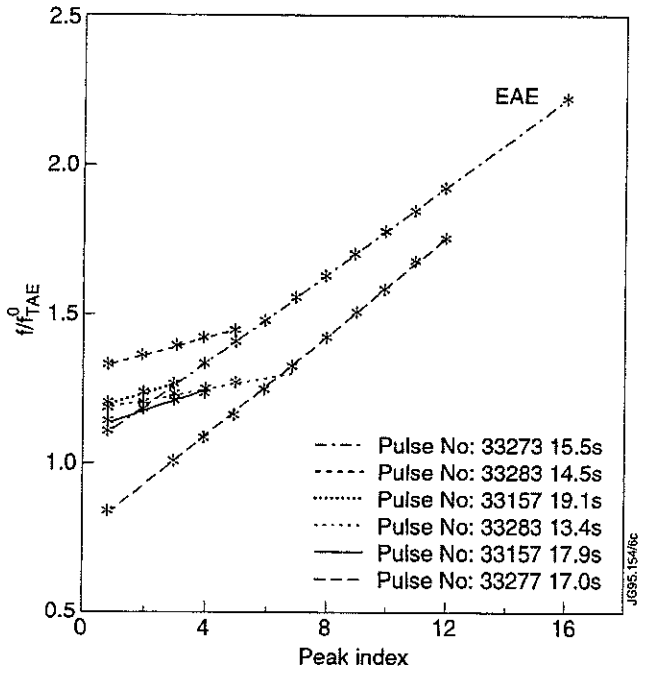

Fig. 9 Example of peak frequency distribution of the multiple kinetic AE driven by an external antenna for a number of additionally heated JET discharges. The peak spacing remained similar for consecutive sweeps when the plasma conditions were maintained approximately stationary.

7. AE EXCITATION BY ICRH BEAT WAVES

Motivation: possibly higher n and larger amplitudes —>study AE effects on particle orbits.

Wave-wave: f_1-f_2 = $\Delta f = f_{TAE}$; $\underline{k}_1$-$\underline{k}_2$ = $\underline{k}_{TAE}$ ~1/2qR (non-linearity: fluid velocity, current or pondero-motive?)

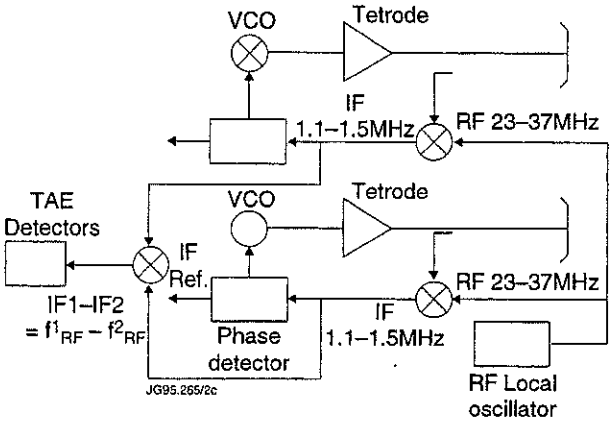

Fig.10 Passive scheme: simply measure at Δf

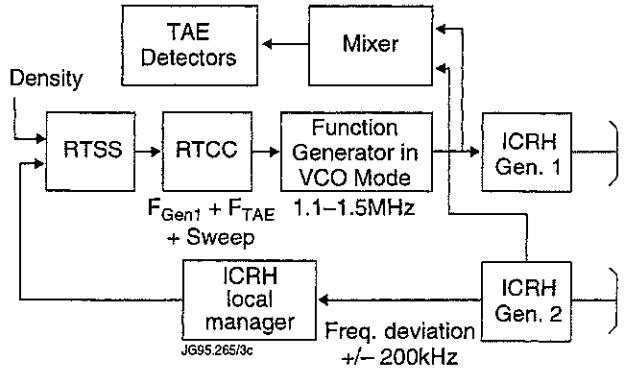

Fig. 11 Active mode: impose $\Delta f = f_{TAE}^{0}$ + sweep

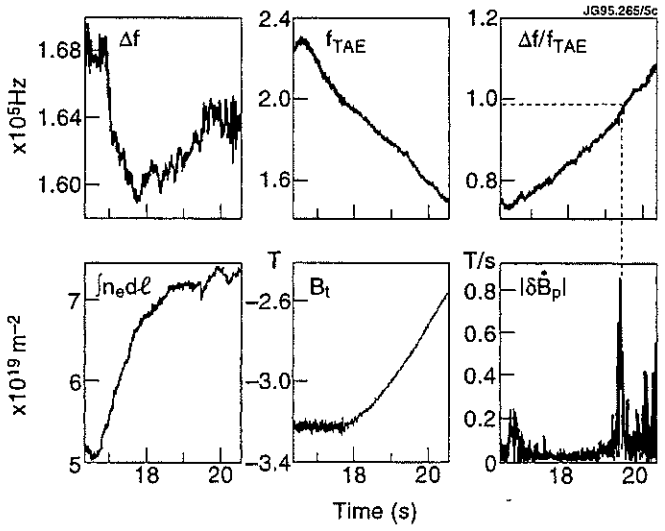

Fig.12 ICRH beat wave: passive scheme

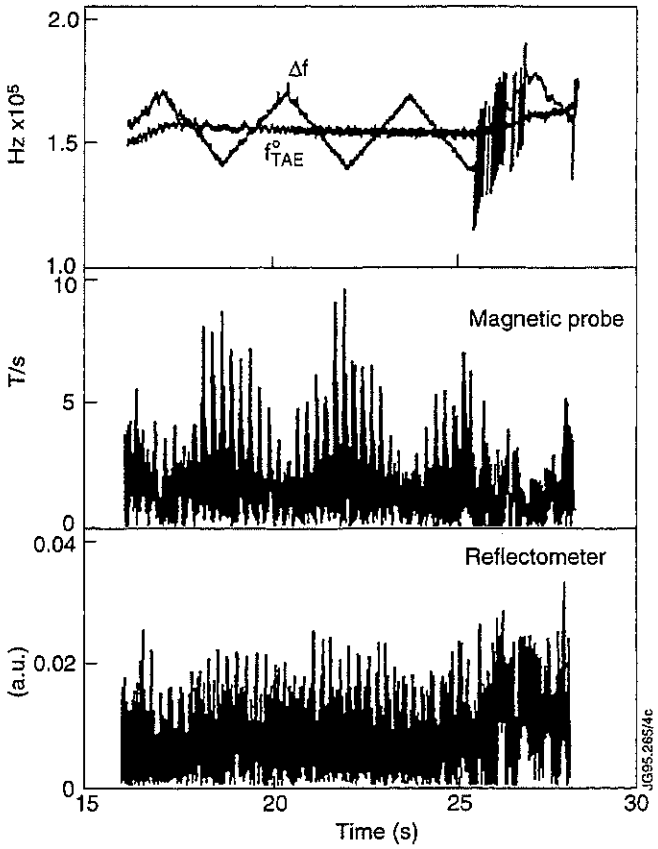

Fig.13 ICRH beat wave results: active mode

8. CONCLUSIONS

- A new active diagnostic for AE has been developed at JET. It is based on external antenna excitation and synchronous detection of the plasma response.
- Linearly stable TAE and EAE have been driven and identified by their frequency dependence on the density and the magnetic field. Driven mode structures ($|n| < 4$) have been selected and identified.
- TAE damping rates have been measured for the first time. Different absorption mechanisms and specifically continuum damping in the core and at the edge cause a large range of γ/ω in ohmic discharges, with an extreme sensitivity to the details of the plasma equilibrium.
- Under plasma conditions which correspond to the predicted departure from ideal MHD due to kinetic effects, multiple driven AE have been detected in the TAE/EAE range. Contrary to the 'cold' TAE, these modes have been observed on the reflectometer, i.e. as density oscillations in the plasma core, as well as on the magnetic probes. The observed modes belong to the general class of kinetic AE.
- AE excitation via non-linear beating of two ICRH waves has also been demonstrated experimentally.
- These studies will be continued during the JET D-T experimental phase in order to investigate the linear stability of AE as well as the effects of large amplitude AE on particle orbits in the presence of resonant alpha particles produced by fusion reactions.

The Authors would like to thank the JET Team for experimental support. This work was partly supported by the 'Fonds national suisse pour la recherche scientifique' within a JET/CRPP Task Agreement.

REFERENCES

TAE Theory: C.Z. Cheng et al., *Ann. Phys.* (New York) **161**, 21 (1985); L.Villard, G.Fu, *Nucl. Fusion* **32**, 1695 (1992).; G.T.A.Huysmans et al., *Phys. Fluids B* **5**, 1545 (1993).

AE previous observations: K.L.Wong et al., *Phys. Rev. Lett.* **66**, 1874 (1991); W.W.Heidbrink et al., *Nucl. Fusion* **31**, 1635 (1991); W.W.Heidbrink et al., *Phys. Rev. Lett.* **71**, 855 (1993).

AE Damping: R.Betti, J.P.Freidberg, *Phys. Fluids B* **4**, 1465 (1992); N.N.Gorelenkov. S.Sharapov, *Physica Scripta* **45**, 163 (1992); J.Candy, M.N.Rosenbluth, *Plasma Phys. Contr. Fusion* **35**, 957 (1993); S.Poedts et al., *Plasma Phys. Contr. Fusion* **34**, 1397 (1992).

Kinetic AE: R.R.Mett, S.M.Mahajan, *Phys. Fluids B* **4**, 2885 (1992); J.Candy, M.N.Rosenbluth, *Phys. of Plasmas* **1**, 356 (1994); H.L.Berk et al., *Phys. Fluids B* **5**, 3969 (1993); S.Sharapov et al., JET-P(94) **61**, p.105 (1994); A.Jaun, Ph.D Thesis, *CRPP/EPFL* LRP **513/95** (1995).

Radiation in JET's Mark I Divertor

R Reichle, D V Bartlett, D J Campbell, H Chen[1], J C Fuchs[2], R M Giannella, N A C Gottardi[3], N Hawkes[4], L D Horton, H J Jäckel, L Lauro-Taroni, A Maas, R Monk, M G O'Mullane[5], L Porte, R van der Linden, M von Hellermann, J Wesson.

JET Joint Undertaking, Abingdon, Oxfordshire, OX14 3EA, UK.

[1] Southwestern Institute of Physics, Chengdu, China.

[2] Max Planck Institut für Plasmaphysik, Boltzmannstr. 2, D-85748, Germany.

[3] Commission European Community, DGXVII, E2Batiment Cube, L2920, Luxembourg.

[4] UKAEA (Government Division), Fusion, Culham Laboratory, Abingdon, Oxfordshire, OX14 3DB, UK.

[5] Physics Department, University College Cork, Ireland.

INTRODUCTION

The most promising technique to avoid overheating of the target plates in large tokamaks is to increase radiative and charge exchange losses from the plasma. JET has performed many experiments with high recycling and radiative divertor operation in which this technique worked successfully. This contribution concentrates on the plasma radiation distribution as measured with JET's bolometer system [1] and evaluated with the ADMT (Anisotropic Diffusion Model Tomography) program [2] and an Abel inversion technique. Since the gain in longevity of the target is usually accompanied by a loss in core plasma performance the correlation between the two is also investigated.

EXPERIMENTAL DETAILS

The old JET Bolometer [3] has been modified (fig. 1) and a new system has been added (fig. 2).

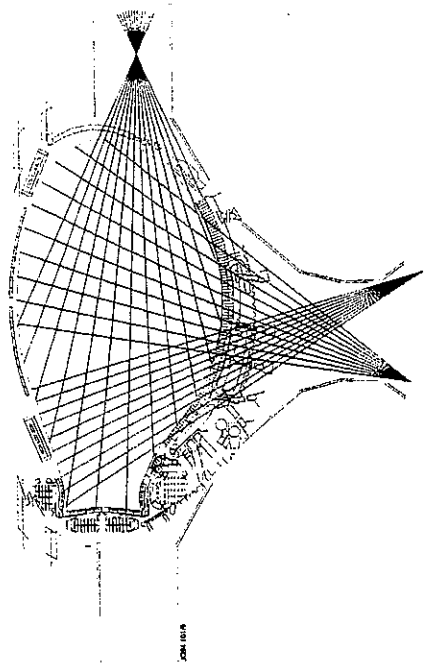

Fig.1: Lines of sight of the modified old bolometer KB1.

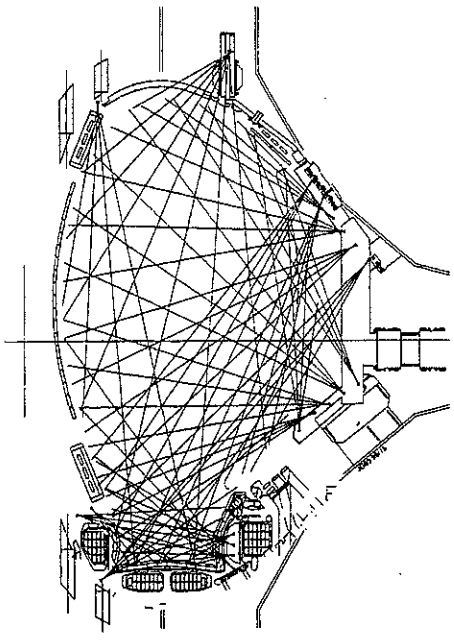

Fig.2: Lines of sight of the new bolometer KB3D and KB4 of which up to 20 have been used simultaneously.

A TYPICAL DISCHARGE EVOLUTION IN THE HIGH RADIATIVE REGIME

Discharge 34343 is a 2MA / 2T discharge with strong nitrogen seeding at 18 MW of NBI heating power. Fig. 3 gives an overview of the discharge and fig. 4 shows selected line of sight integrated radiation measurements in the divertor region.

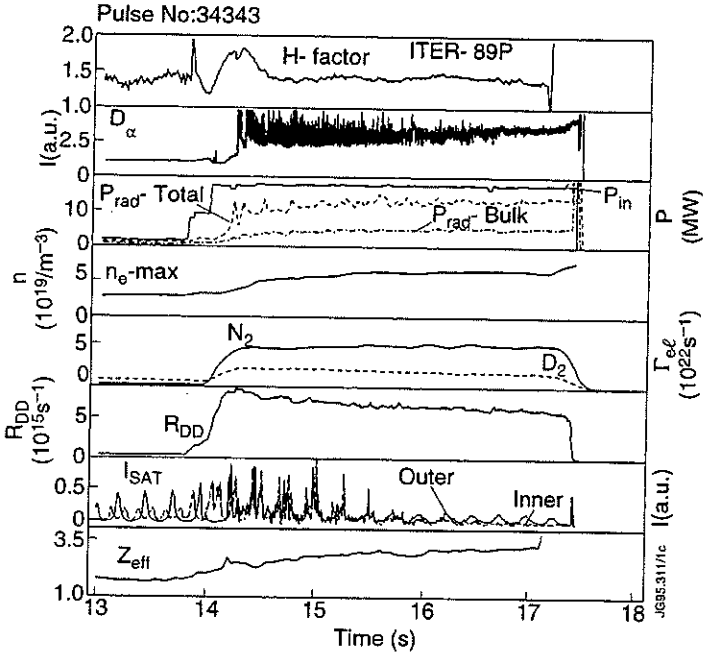

Fig.3: Example of nitrogen seeded discharge: 34343.

With the onset of the nitrogen influx the radiation rises especially in the divertor. At first the radiation maximum is well below the X-point (fig. 5). With the build up of the nitrogen the radiation maximum smoothly moves upwards and when the total radiated power has reached 70% of the input power the radiation has detached from the target and assembled around the X-point (fig. 6). JET has also cases in which a substantial up/down oscillation is superimposed to this movement [5]. The discharge can remain in the detached state for a long time and it can be terminated without disruption. However ,this example has a radiation collapse when too much radiation condensation in the X-point occurs (fig. 7,8 and 9).

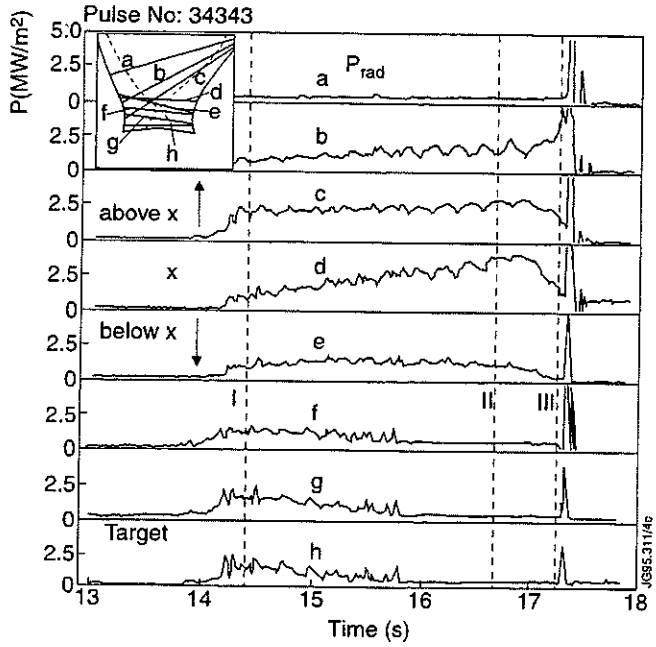

Fig.4: Line of sight integrated radiation of Nitrogen seeded discharge.

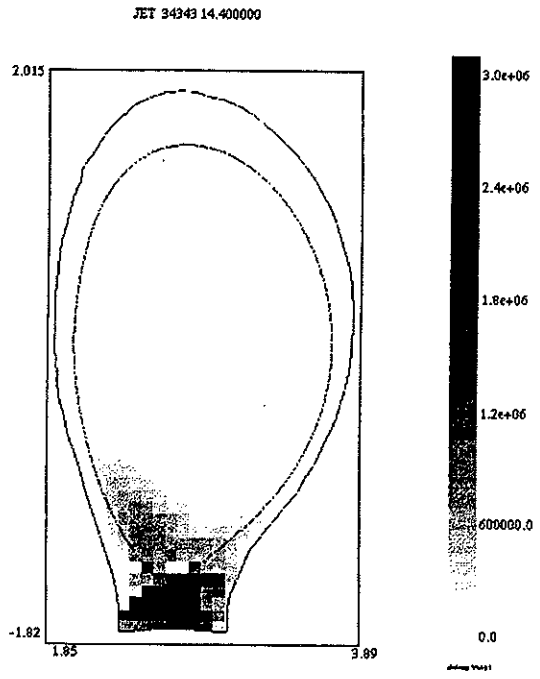

Fig.5: Radiation reconstruction at early stage - still attached.

Detachment and radiation collapse of discharge 34343

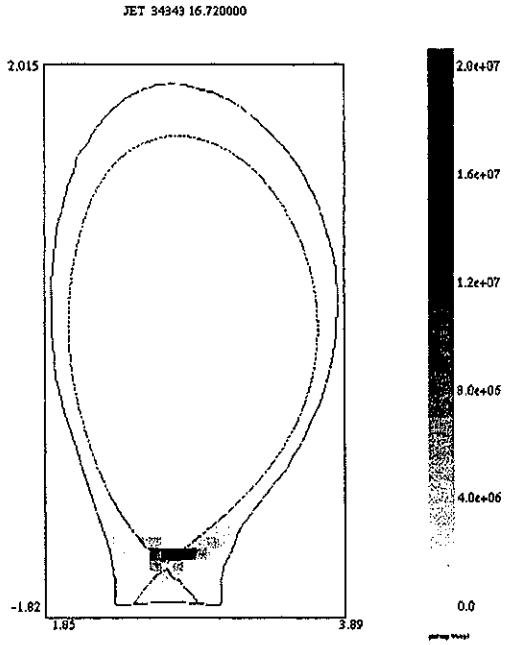

Fig.6: Detached state.

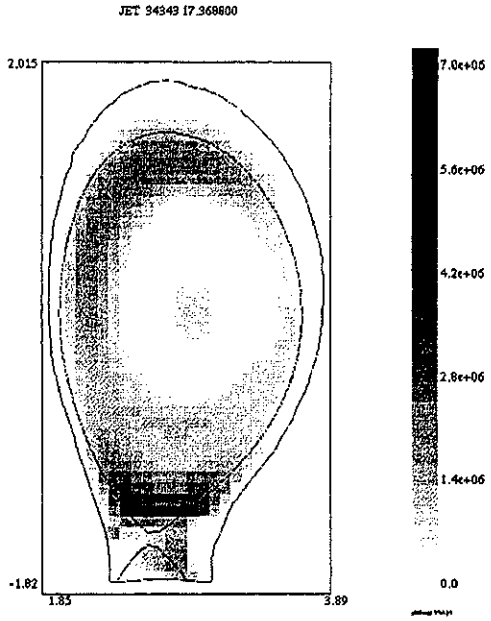

Fig.7: First stage of radiation collapse.

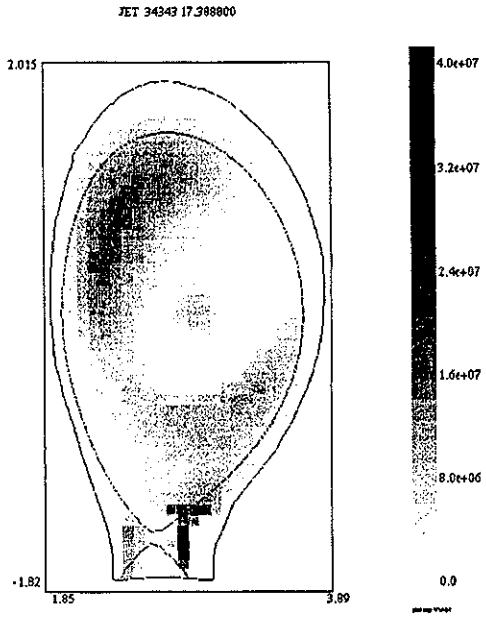

Fig.8: Main phase of the radiation collapse.

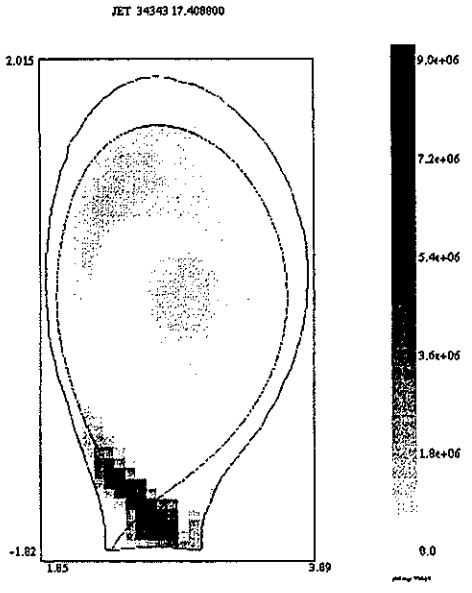

Fig.9: Final stage.

UNDERLYING PHYSICS TO THIS RADIATION BEHAVIOUR

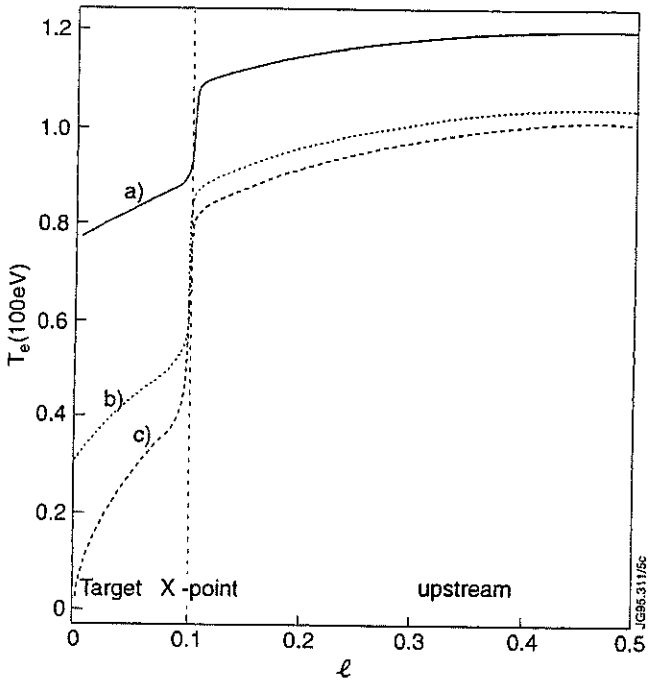

Fig.10 : Electron temperature along a flux contour close to the separatrix in the poloidal plane with its total lengthl normalised to 1.

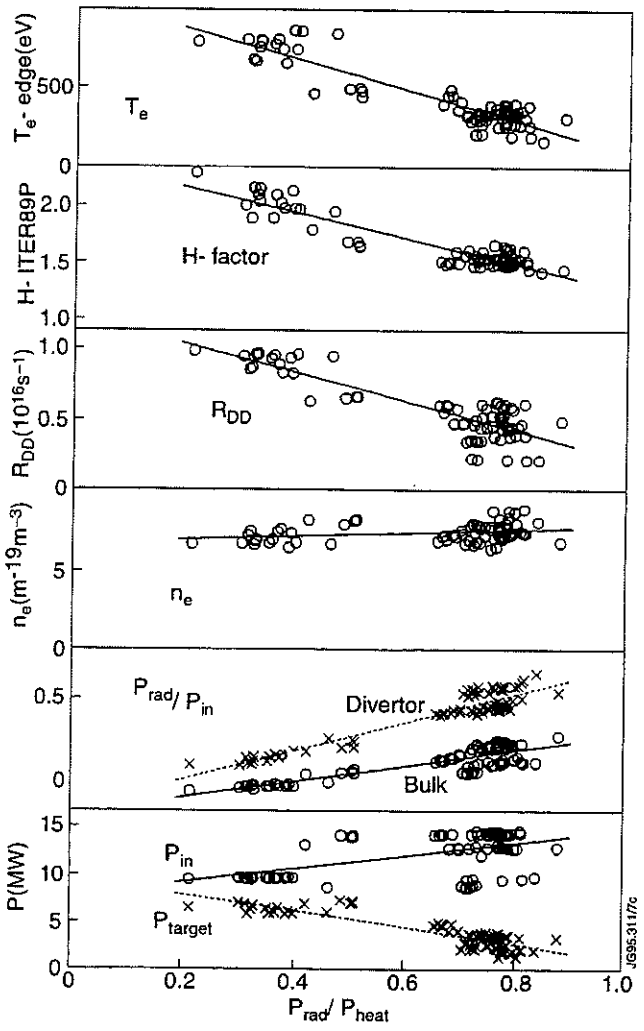

Fig.11: Statistical overview over Nitrogen seeded discharges.

Due to the shallow magnetic field line angle near the X-point, the electron temperature gradient in the poloidal plane is largest there and the X-point is a natural cold spot. Fig. 10 illustrates this behaviour for 3 different radiation levels. In coronal equilibrium the emissivity coefficients for light impurities peak between 10 eV (Carbon, Nitrogen) and 40 eV (Neon). For short residence times these values are higher (20 to 200 eV). As for Marfes, there is the tendency to bring down the temperature locally to the temperature of the maximum of the emissivity. Due to the given natural temperature gradient, this formation is stabilised at the X-point. VUV measurements of the relative intensities of the different ionisation stages corroborate this view [4]. As long as the radiation peak stays at the bottom of the steep temperature gradient this 'divertor Marfe' is stable. With a further rise of the radiative loss fraction, the radiation peak moves up further, the steep gradient disappears and the temperature along the whole plasma surface collapses.

DIFFERENCE BETWEEN IMPURITY SPECIES

1) Statistical analysis of Nitrogen seeded discharges

Nitrogen seeding was the most popular impurity seeding performed at JET due to its favourable radiation characteristics. With an increasing radiation loss fraction many of the performance parameters decrease (fig. 11): ITER-89p H-factor, edge temperature and the neutron rate. The density remains unaffected. The radiation is dominantly emitted in the divertor. The ratio of bulk to divertor radiation is 1:2. Normally H-factors (ITER-89p scaling) of 1.5 were achieved in discharges with 2-3 MA /2-3 T in the highly radiative regime (fig. 11). A 1 MA / 1.4 T discharge close to the Greenwald-limit with 65% radiative losses and an H-factor of 1.75 may be seen as an indication of possible improvements when approaching the normalised beta limit. The largest power at which the radiative divertor was operated was at 28 MW of combined NBI and RF heating.

2) Neon

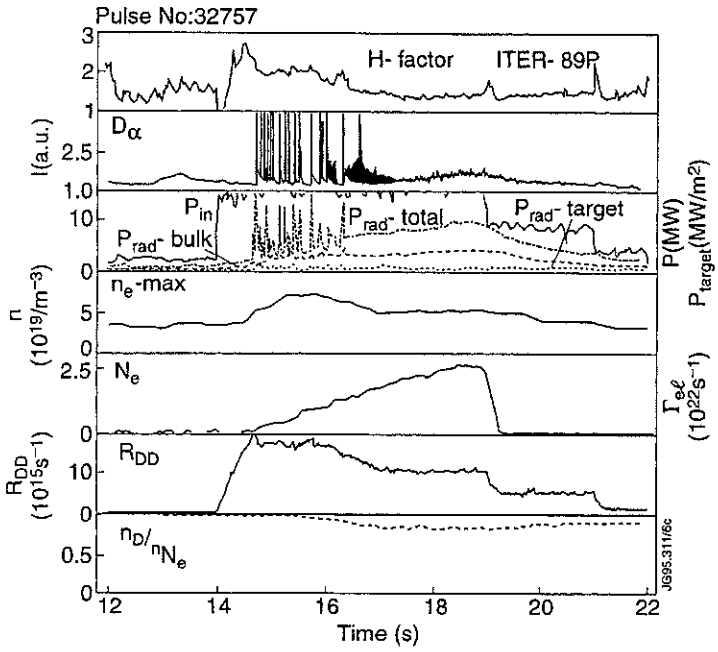

Fig.12: Example of a Neon seeded discharge: 32757.

A typical discharge with large Neon impurity content is shown in the overview in fig.12.

Halfway through the discharge **a significant loss of performance** occurs due to a confinement degradation accompanied with a loss of central density. This performance loss stopped progress to higher radiated power fractions. The fuel dilution by electrons from Neon remains small. Contrary to the Nitrogen cases, the highest radiation maximum achieved with Neon is still below the X-point (fig.13), because full detachment was not obtained. The ratio of bulk/divertor radiation is 1:1 (fig.14).

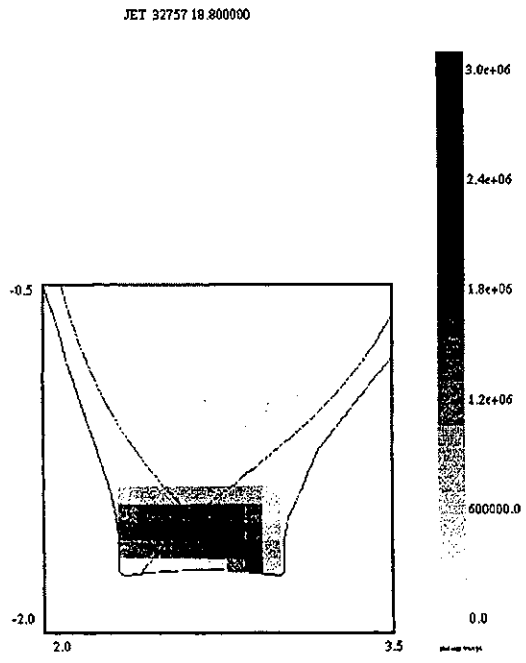

Fig.13: X-point radiation distribution with large neon content.

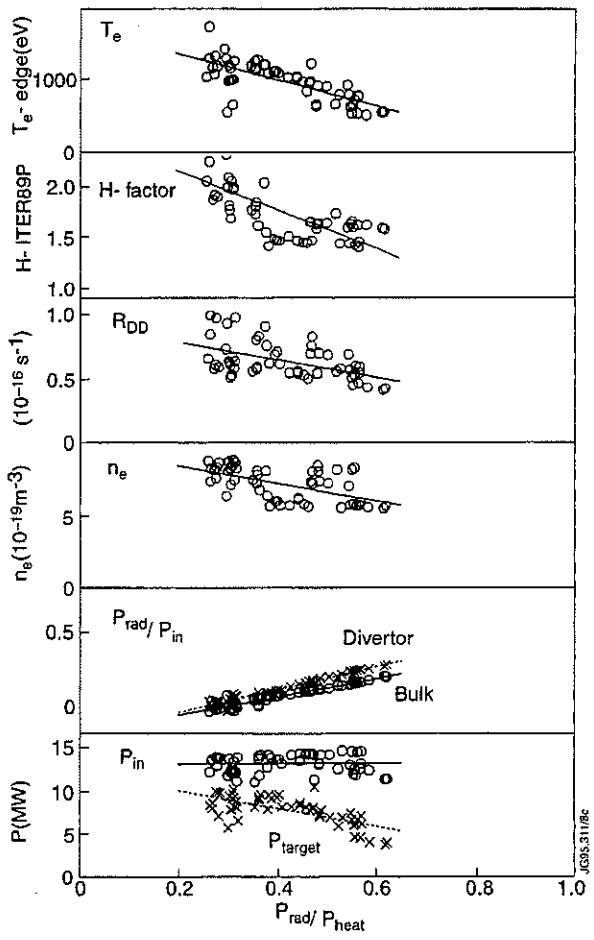

Fig.14: Statistical overview for Neon discharges.

The **edge electron temperature** of the example discharge 32757 is significantly reduced by both the confinement loss after 16.22 sec and the rising impurity radiation. The **edge ion temperature** is less affected by the increasing impurity radiation. The shape of the profile remains like in the good H-mode phase (fig. 15 and fig 16)

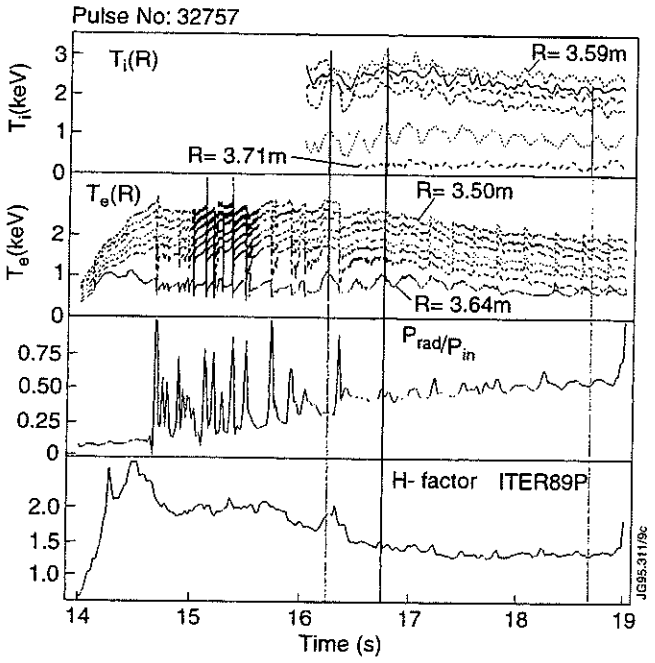

Fig.15: Temporal evolution of the edge temperature, the radiative loss fraction and the H-factor.

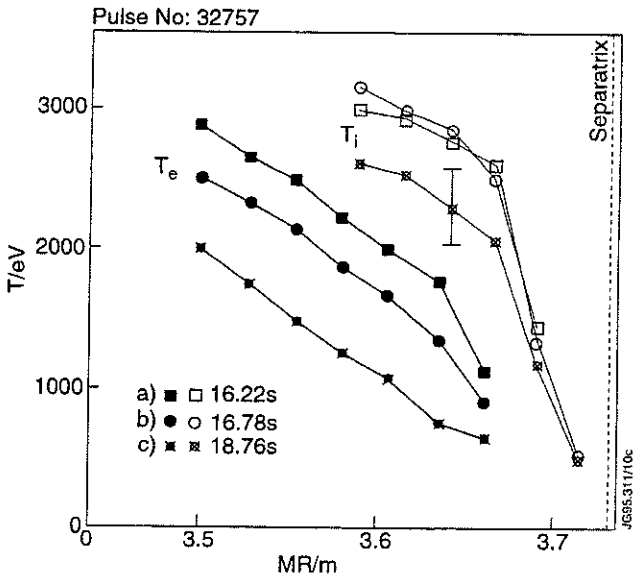

Fig.16: Edge temperature profiles.

Impurity accumulation and screening in Neon

The neon profile remains hollow (fig. 17). With top fuelling there is evidence of screening (fig. 18) [see also:[6]].

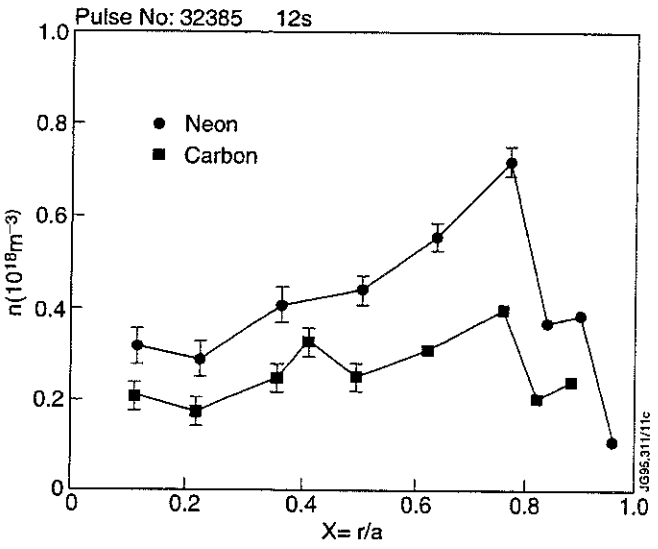

Fig.17: Charge exchange profiles of the impurity profiles.

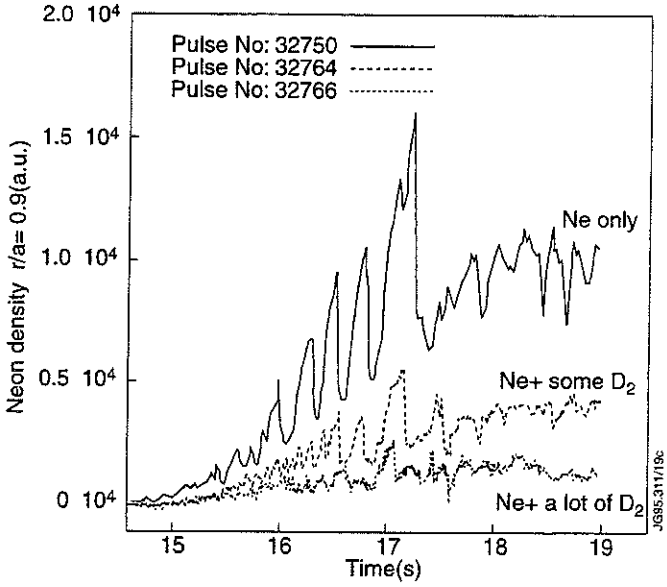

Fig.18: Charge exchange signals with different fuelling levels.

3) Intrinsic Carbon

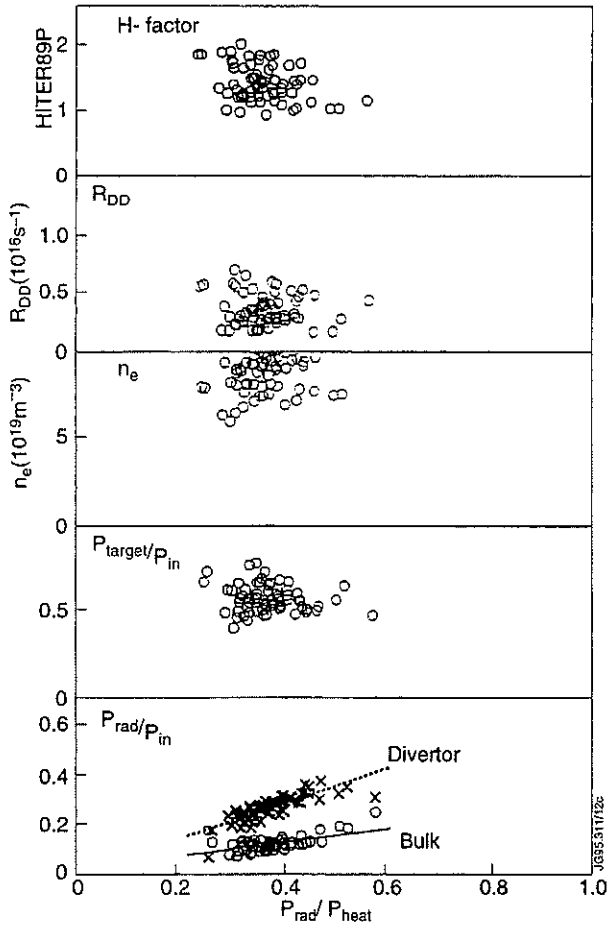

Fig.19: Statistical overview of intrinsic (mainly C) impurity radiation.

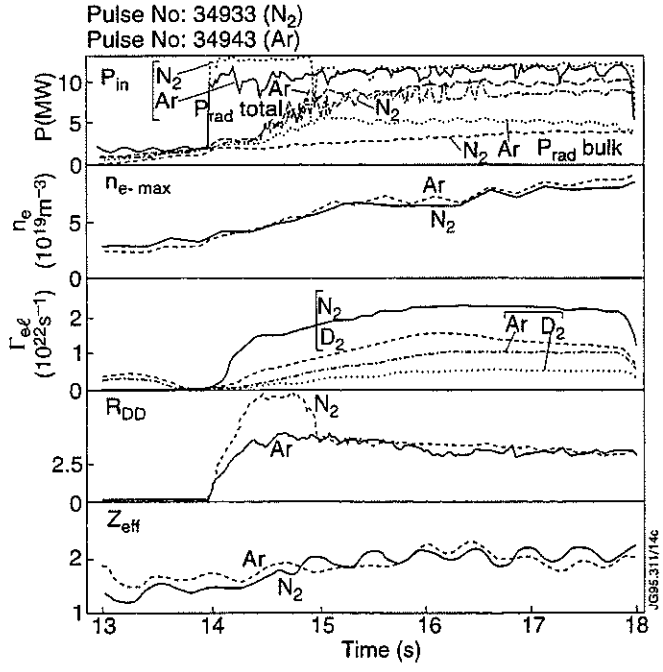

Fig.21: Argon - Nitrogen comparison.

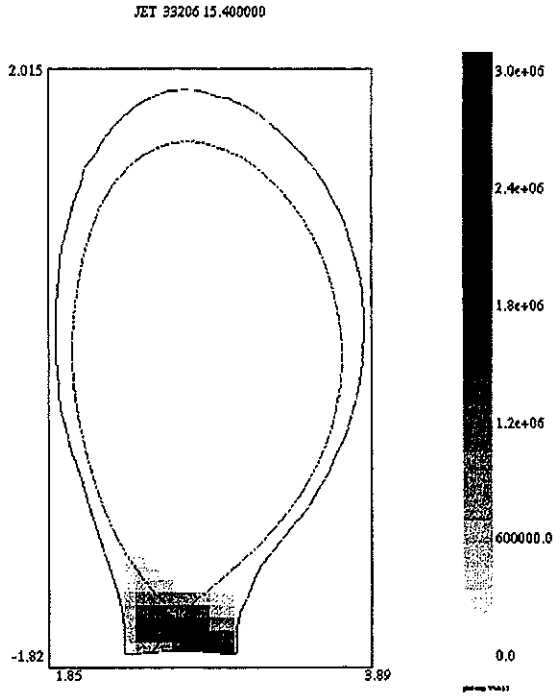

Fig.20: Radiation distribution with intrinsic carbon at high heating power.

Carbon has similar radiation properties to nitrogen (fig. 19): at high input powers the radiation stays in the divertor without detachment (fig. 20).

4) Argon

Fig. 21 shows the comparison between two very similar discharges: 34933 with Nitrogen as main impurity and 34943 with Argon as main impurity.

Argon has, like Neon, a comparatively higher fraction of bulk radiation than Nitrogen.

5) Carbon, Nitrogen, Neon, Argon comparison

Radiation from Nitrogen and Carbon impurities is more localised to the edge than from Neon. The Abel inversion of bolometer measurements (fig. 22a) and simulations performed with a time dependent predictive impurity transport code (fig. 22b) based on charge exchange measurements agree in this respect.

In the detached condition only a small proportion of the radiation comes from below the X-point. The peakedness of the X-point radiation increases from Argon over Neon to Nitrogen (fig. 23).

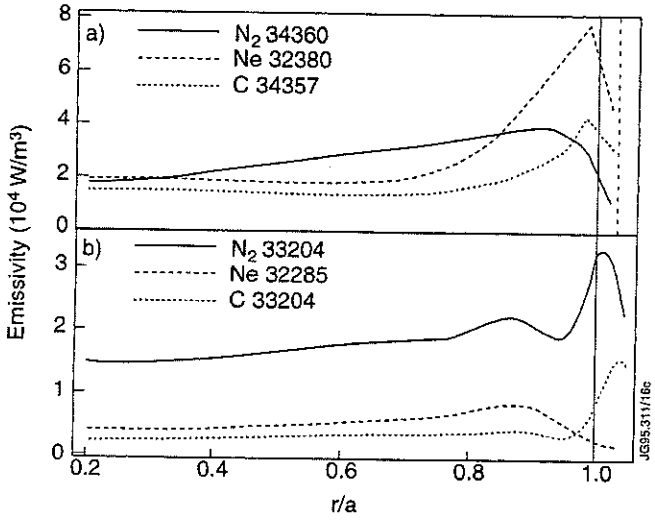

Fig.22: Nitrogen, Neon and Carbon horizontal radiation profiles: a)Abel inversion; b) Simulation with predictive code.

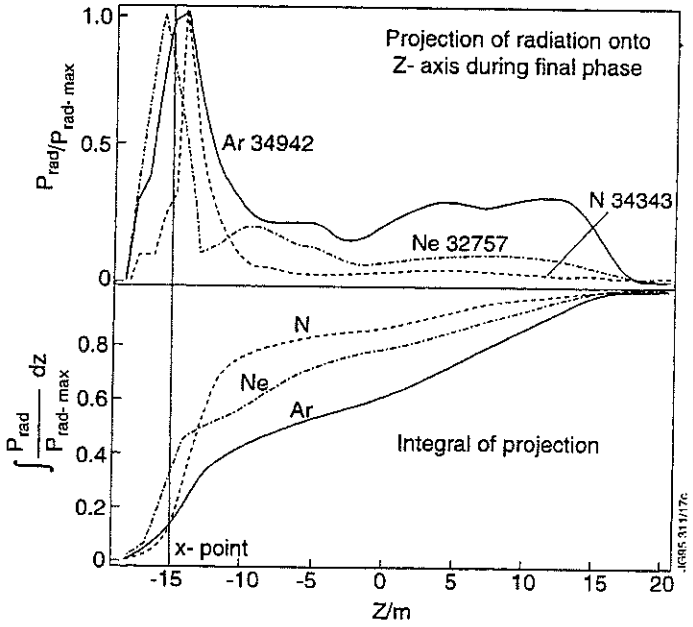

Fig.23: Projection of the radiation distribution for Nitrogen, Neon and Argon onto the vertical axis and its integration along this axis.

SUMMARY AND CONCLUSIONS

Typical evolution of divertor radiation: As the fraction of the radiated power increases, the radiation maximum moves smoothly or with oscillations from the target to the X-point. At a radiative loss fraction of 75% it forms a 'divertor marfe' which is stabilised due to the natural temperature gradient near the X-point. With a further increase in radiation the radiation maximum enters the main plasma. This yields a collapse with a strongly radiating shell. Finally the shell shrinks towards the centre of the plasma and the fraction of X-point radiation becomes more significant again.

Radiation distribution: The radiation distribution of the impurities is governed by the temperature of their maximum emissivity: Neon, like Argon, has more radiation in the bulk than Nitrogen and Carbon. The peakedness of the X-point radiation increases from Argon over Neon to Nitrogen.

Radiation below the X-point: At high fractions of radiated power only a small proportion of the total radiation can be found below the X-point.

Correlation with confinement: As detachment is approached the confinement is normally reduced to H-factors (ITER-89p) of 1.5. Operating in a high beta regime seems to yield a small improvement.

Impurity accumulation: The impurity profiles remain hollow. The dilution is small. There is some indication of impurity screening with strong Deuterium fuelling from the top.

Edge temperature: The electron temperature decreases with increasing impurity radiation and decreasing confinement. The ion temperature profile is more robust and H-mode like.

Central density: Dramatic confinement loss as seen in the Neon discharges is accompanied with a loss of the central density.

REFERENCES

[1] R. Reichle et al., 36th APS Plasma Physics, Minneapolis, Minnesota, 7-11 Nov. 1994

[2] J.C. Fuchs, K.F. Mast, A. Hermann, K. Lackner et al. , Contrib. 21st EPS, Montpellier, France, June 27 - July 1, 1994, Poster C107

[3] K.F. Mast, H. Krause, Rev. Sci. Instr. 56(5), 1985, p.969

[4] M.G. O'Mullane et al. 'Analysis of Emisssion Spectra from MARFES in JET',22nd IOP Plasma Physics Conference, 10-13 April Oxford, U.K.

[5] R.D. Monk et al., this conference

[6] P. Harbour et al., this conference

Improved Plasma Purity in the JET Pumped Divertor

M F Stamp, M von Hellermann and Members of Task Force D.
JET Joint Undertaking, Abingdon, Oxfordshire, OX14 3EA, UK.

1. INTRODUCTION

The enhancement of fusion reactivity by the control of plasma impurities is a key aspect of the JET Pumped Divertor.

It was anticipated that,

- The improved design of the Mk.1 pumped divertor, which avoids exposed edges and increases the plasma wetted area, was expected to reduce the incidence of impurity blooms during high power heating experiments.

- The improved closure (to escaping neutrals) of the pumped divertor configuration at moderate plasma density should give rise to higher divertor electron densities and lower divertor electron temperatures, leading to a reduced impurity source and cleaner plasmas.

- The establishment of a detached divertor regime would further reduce the flux of energetic particles to the target, further reducing the source of sputtered impurities.

This work compares data from old (1991/2) and recent (1994/5) plasmas to see if the plasma purity is improved in the JET Mk.1 pumped divertor.

2. IMPURITY BLOOMS

- With the old divertor, carbon blooms were generated after 10MJ had been deposited on the carbon target plates [1].

With the Pumped Divertor the strike points can be swept to spread the power load and so keep the target plate temperature low [2].

- No carbon blooms have been observed, even with 100MJ deposited on the carbon divertor tiles, fig.1.

- Beryllium blooms occur at a much lower tile temperature than carbon blooms. Blooms are avoided by tripping off the additional heating when the tiles approach melting temperature.

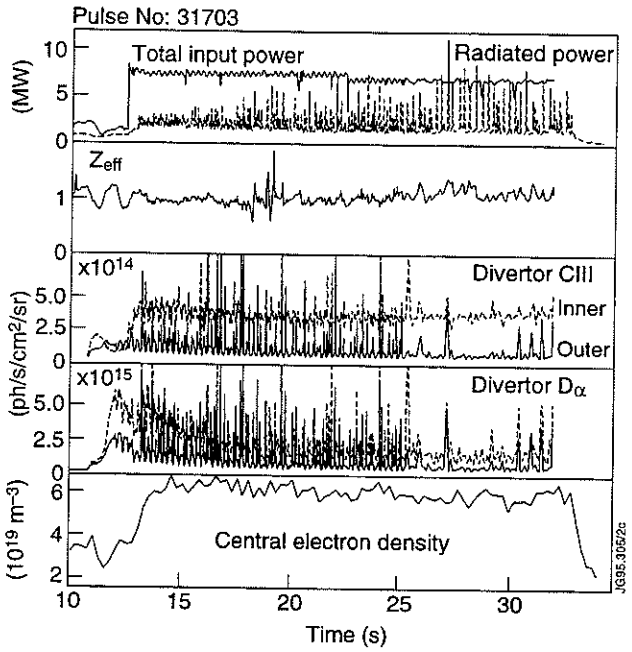

Figure.1 2MA/2.1T steady-state H-Mode with 140MJ coupled to the plasma. The strike points are swept and there is no gas feed during the NBI heating.

- 140MJ coupled to the plasma.

- 30% of input power is radiated.

- The baselines of the all the spectroscopic signals reach a steady state and show no evidence of a carbon bloom.

3. PLASMA PURITY

The line-average Z_{eff}, derived from visible bremsstrahlung measurements at 523.5nm, is used as a monitor of the plasma cleanliness. Visible spectroscopy is used to measure the fuel and impurity influxes.

Figs.2a,b show a comparison of plasma parameters, including Z_{eff}, and vertical D-alpha (as a measure of the wall recycling) for a selection of Hot-Ion H-modes using the old and new divertors.

During the Hot-Ion H-Mode, there is no significant difference between fig.2a and 2b.

- Z_{eff} is about 1.8 in both figures, though at 11-11.5 seconds the Z_{eff} is higher in the 1991 data.
- The electron densities are very similar (the faster density rise in the 1994/5 data is a result of higher NBI source).
- The vertical D-alpha signals are roughly constant during the Hot-Ion ELM-free H-mode periods, with the pumped divertor signals being a little higher.

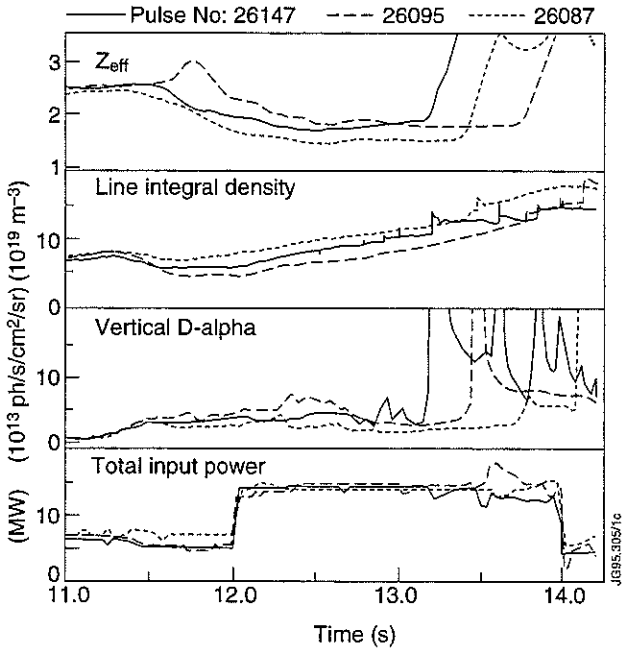

Fig.2a Plasma parameters for pulse numbers 26147, 26095, 26087; 3MA plasmas from 1991 on the old divertor carbon target.

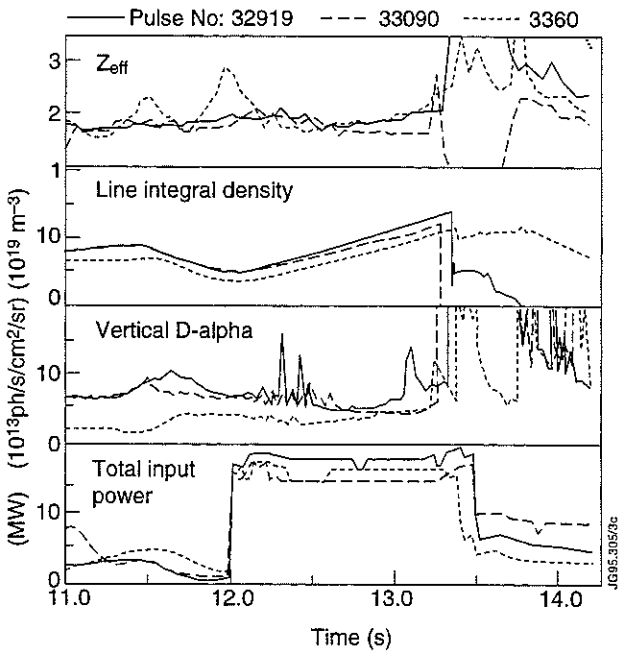

Fig.2b Plasma parameters for pulse numbers 32919, 33090, 33680; 3MA plasmas from 1994/5 on the new pumped divertor carbon target.

- The constant D-alpha signals imply that the plasma edge electron density is constant, even though the central density is rising rapidly.

Fig.3 shows the same comparison for two Steady-State H-Modes, with 7MW heating power, 27231 and 31698 (see also 31703 in Fig.1).

There is a noticable difference between the two pulses.

- Z_{eff} is about 1.3 in the pumped divertor plasma, and is much higher, about 2.0 in the old divertor comparison.

- The vertical D-alpha signal is rising in #27231, indicating that the recycling is changing, and that the plasma is not in proper steady-state.

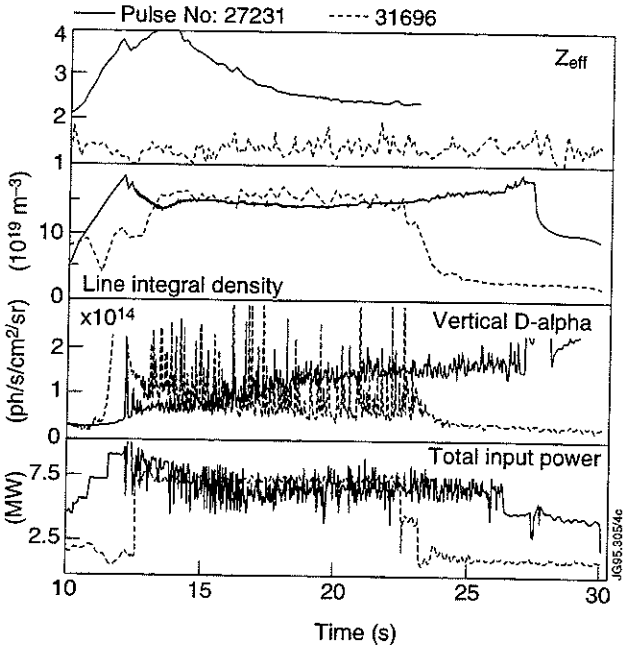

Figure 3 Comparison of two similar steady-state H-Modes. Even though the line integral density is nearly the same, Z_{eff} is much lower in the pumped divertor case.

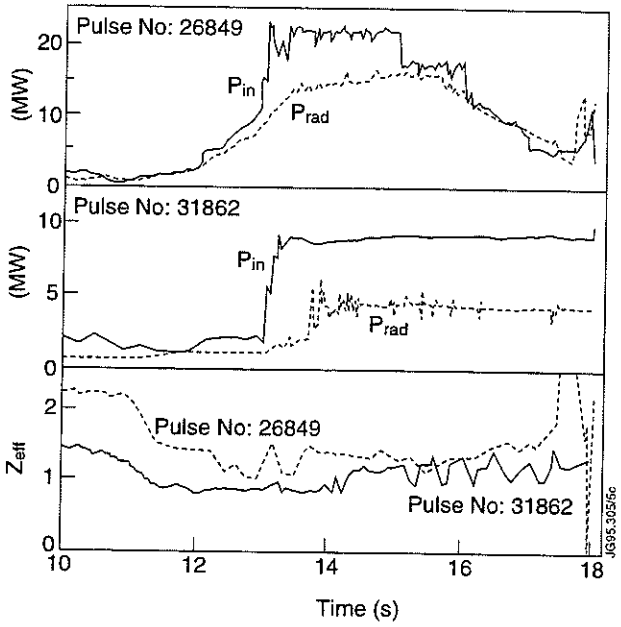

Figure 4 Comparison of deuterium fuelled radiative divertors.

- Radiative divertors were produced in 1991/2 with 22MW of input power and deuterium gas puffing [1]. These plasmas were on the beryllium divertor target and Z_{eff} fell to about 1.4 during the detached plasma phase (#26849, fig.4).

- In 1994/5, on the carbon and beryllium targets, many radiative divertor plasmas have been made. However, with just deuterium puffing, only about 50% of the input power can be radiated and Z_{eff} is about 1.2 (fig.4). Impurity seeding (Ne,N_2,Ar) is needed to raise the radiated fraction upto 85% [3].

4. IMPURITY SOURCES

Impurity source trends for ohmic discharges are shown below in figs.5a,b. The pumped divertor data (fig.5b) starts at a higher line integral density (and lower Z_{eff}), and extends up to $17x10^{19}m^{-2}$. However, beyond about $8\text{-}10x10^{19}m^{-2}$, the D-alpha photon efficiency is not calculable (the D-alpha emission varies strongly with conditions for $n_e(a) > 2x10^{19}m^{-2}$or $T_e(a) < 20eV$).

- In the old divertor, Z_{eff} decreased to close to 1 as the density increased, until at about $8x10^{19}m^{-2}$ line integral density, the outer divertor D-alpha intensity was about $2x10^{15}ph/s/cm^2/sr$, and the effective carbon sputtering yield was about 2.5%. At this density, the edge electron temperature was 20eV [4].

- The pumped divertor data (fig.5b) shows the behaviour at both the outer and inner divertor targets. The C III line intensity increases with density until it saturates at a value of 1.2 to $1.4x10^{14}ph/s/cm^2/sr$, and then decreases with increasing density. In the outer divertor this saturation occurs at an effective carbon sputtering yield of about 2%.

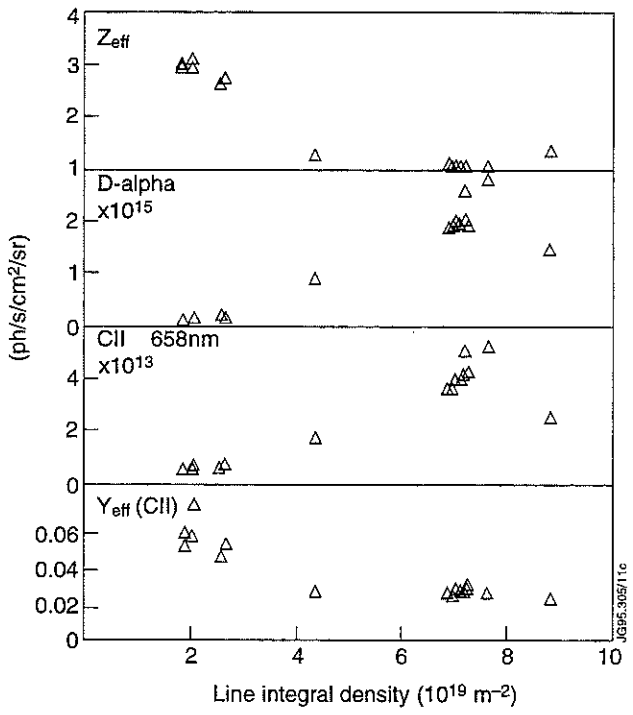

Figure 5a. Z_{eff}, C II and D-alpha intensities, and the effective sputter yield (Y_{eff}) of C II from the outer carbon target in the old JET divertor, as a function of line integral density.

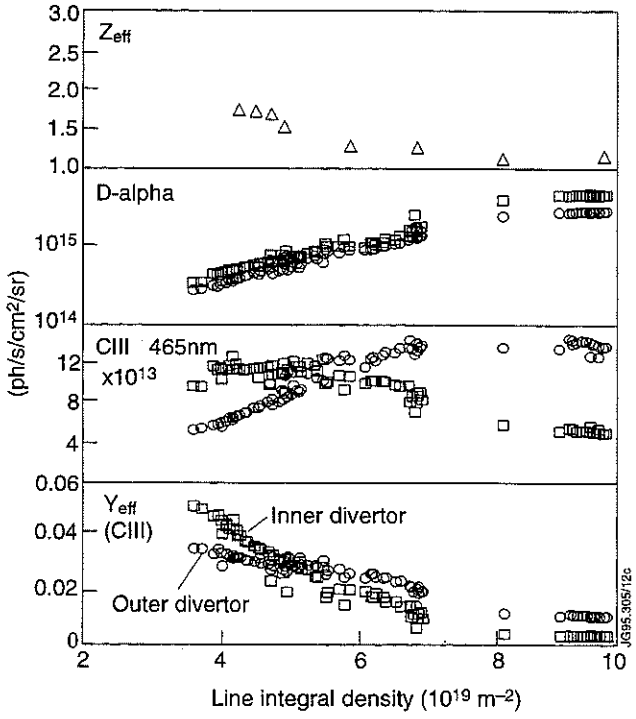

Figure 5b. Z_{eff}, C III and D-alpha intensities, and the effective sputter yield of C III from the inner and outer carbon targets in the JET pumped divertor, as a function of line integral density.

5. DISCUSSION

Why do the old and new divertors behave the same at low density (Hot-Ion H-Mode), but differently at higher density (Steady-State H-Mode)?

Typical target plasma densities for Task Force 'D'(TFD) H-Mode studies were >8x10^{19}m^{-2}, due to NBI requirements in the plasma configurations that were used. At such densities Z_{eff} is close to 1. The NBI fuelling produces an increased edge electron density at both the inner and outer target plates. The edge electron temperature rises from about 25 to 35eV in the outer divertor and actually drops to 10eV or less in the inner divertor (fig.6a). Consequently there is no or little increase in the sputtering yields, and Z_{eff} stays close to 1.

Similar H-Modes in 1991/2 had a lower edge n_e and higher edge T_e [5].

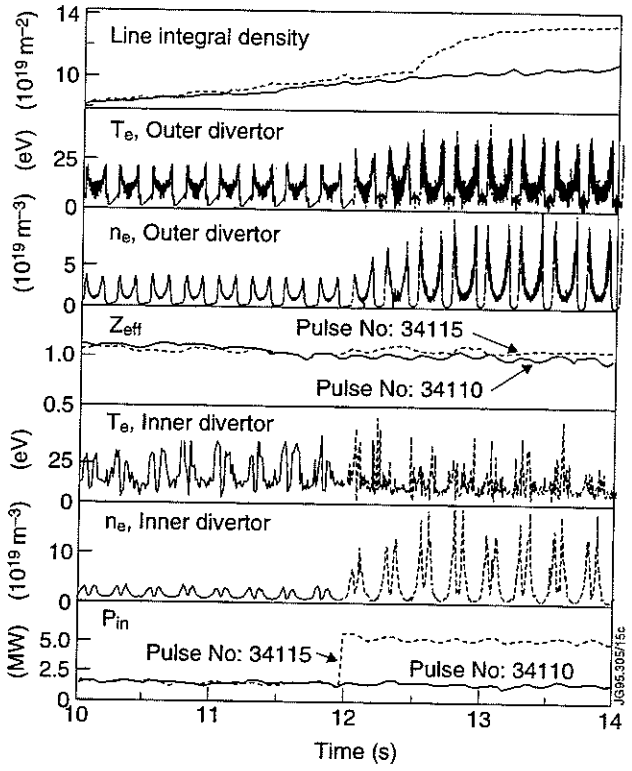

Figure.6a Evolution of the edge parameters during NBI heating. The edge electron density at the inner and outer divertor rise, but edge electron temperatures hardly change. The strike points are swept.

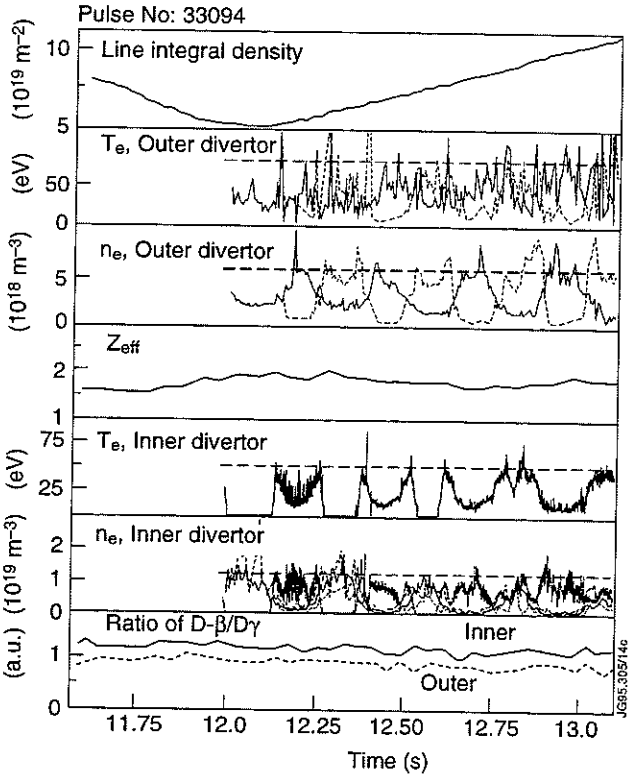

Figure.6b Evolution of the edge parameters in a Hot-Ion H-Mode. Edge electron temperature is constant, and high. The edge electron density is also constant (or even falling), and low. The strike points are swept.

The Hot-Ion H-modes of TFH have a significantly lower target plasma density and consequently a higher Z_{eff}. During the Hot-Ion H-Mode the line integral electron density increases but the edge electron density in the divertor stays constant, as shown both by the Langmuir probes and the spectroscopic ratio of D-beta/D-gamma (fig.6b). The edge electron temperatures also seem constant; 50eV at the inner divertor, and about 80eV in the outer divertor (though the outer divertor signals are very noisy).

This is the same edge behaviour as found in 1991/2.

6. NEW VISIBLE SURVEY SPECTROMETER

The new diagnostic is a novel multi-track F/2 survey spectrometer with a 1024x1024 pixel CCD camera as detector. It covers 420-730nm with a spectral linewidth of 1.0nm FWHM. Example spectra are shown in figs.7a,b. They show the presence of molecular bands from CD and BeD.

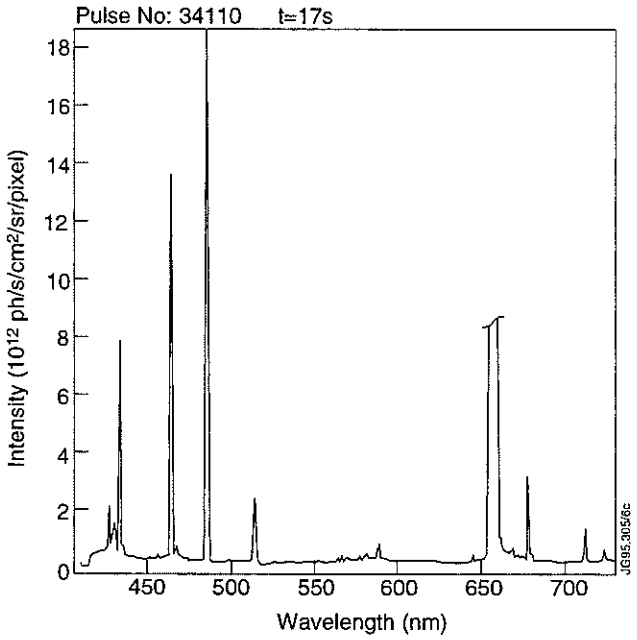

Figure 7a: Example spectrum from the inner carbon target of the JET pumped divertor.

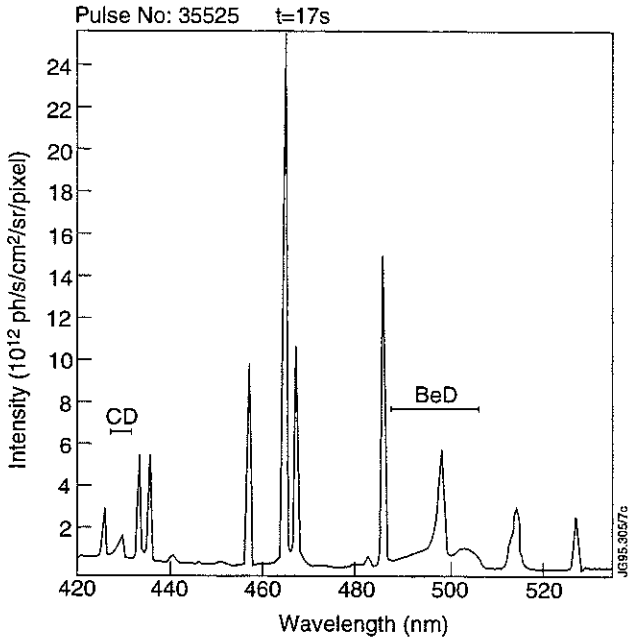

Figure 7b: Portion of the spectrum from the inner beryllium target of the JET pumped divertor.

The excellent resolution allows the intensities of many spectral lines from many different impurity ions and different charge-states to be studied. The diagnostic is very flexible, allowing the intensities of seeded impurities (e.g. He, Ne, Ar, N_2) to be easily monitored (e.g. figs.8a,b).

- Fig.8a shows the time evolution of Ne I emission for trace neon injection (note the less than 0.5MW change in radiated power). The pump-out of the injected neon can be clearly seen in this L-Mode plasma.

- Fig.8b shows the time evolution of a N II line for three consecutive plasmas, with different size nitrogen puffs. The presence of a nitrogen signal before 14s in 33182 implies the nitrogen is pumped by chemical reactions with the carbon of the divertor target. This effect is also seen on the beryllium divertor tiles.

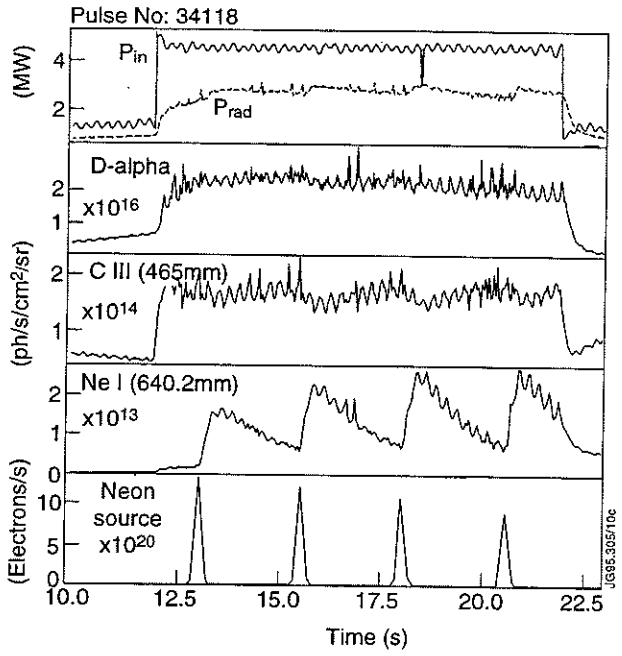

Figure 8a. Trace neon injection into an L-Mode plasma.

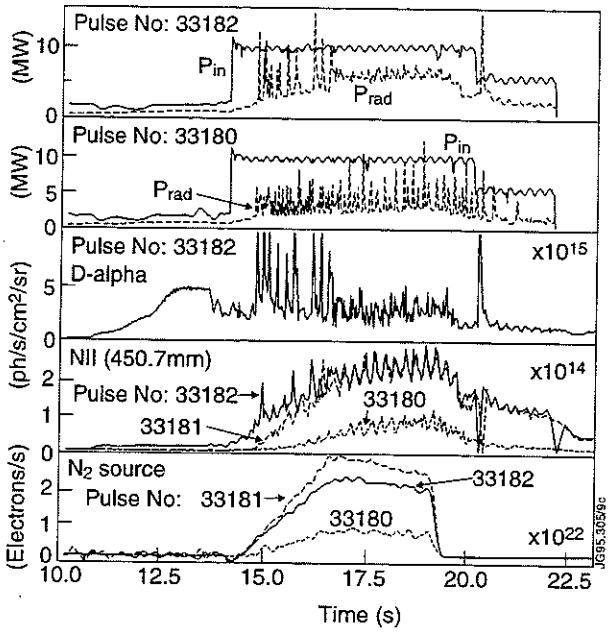

Figure 8b. Nitrogen radiative divertor plasmas (especially 33181, 33182), with different nitrogen gas feeds.

7. CONCLUSIONS

- The JET Pumped divertor produces generally cleaner plasmas than the old divertor for moderate to high density core plasmas. For the low density Hot-Ion H-Modes, the cleanliness is the same.
- The improved Z_{eff} is due to operation at a core plasma density that results in relatively low divertor electron temperatures, and relatively high divertor electron density. The low electron temperature minimises the physical sputtering source.
- Molecular emission (CD, BeD) is seen regularly from the pumped divertor target plates. The importance of chemical sputtering still needs to be assessed, but it is clearly not significantly contaminating the plasma core.
- Sweeping of the strike points and better target design has eliminated impurity blooms on the carbon targets. Blooms on the beryllium targets are avoided by tripping off the additional heating power.

8. REFERENCES

[1] C G Lowry et al., J.Nucl. Mat. 196-198 (1992) 735.
[2] D J Campbell and the JET Team, Proceedings of 15th IAEA, Seville, (1994) IAEA-CN-60/A-4-I-4.
[3] G Matthews et al., this conference.
[4] M F Stamp and P R Thomas, Proceedings of 19th EPS, Vol. 16C (1992) 819.
[5] S Clement et al, Proceedings of 35th APS, St.Louis (1993).

Impurity Ion Emission and Edge Transport during ELMy H-modes in the New JET Divertor Configuration

M G O'Mullane[1,2], H Chen[3], I H Coffey[4], M von Hellermann, L Lauro-Taroni, N J Peacock[2], A Rookes[5].
JET Joint Undertaking, Abingdon, Oxfordshire, OX14 3EA, UK.
[1] University College, Cork, Ireland.
[2] EURATOM-UKAEA Fusion Association, Culham Laboratory, Abingdon, Oxfordshire, OX14 3DB, UK.
[3] Southwestern Institute of Physics, Chengdu, China.
[4] Queens University, Belfast, Northern Ireland.
[5] Imperial College, London, UK.

INTRODUCTION

In H modes, impurities are expected to show accumulation. Experiments in DIII-D [1] have shown that the controlled removal of impurities is possible with long periods of grassy ELMs. An H-factor of 1.5 is maintained in these steady state discharges.

In contrast, giant ELMs cause periodic collapses in confinement and can expel 5–10% of plasma energy on a millisecond timescale. They have the additional deleterious effect of being a source of fresh impurity influxes following energy deposition on the target plates. Clearly it is important to understand the impurity behaviour during these giant ELMs.

This paper models the impurity transport behaviour of Neon (from gas puffing) during H mode with giant ELMs. The impurity transport following the giant ELM and during the recovery of H mode are interpreted as distinct phases.

Characterisation of Giant ELMS in JET

As a working assumption ELMs can be characterised by their D_α signal. They can either be overlapping with a high frequency (grassy or Type III) or be separated and well defined (giant or Type I). The typical giant ELM is triggered by a fast (τ~0.2ms) MHD event [2]. During this time the temperature in the outer part of the plasma falls on the same timescale with a concomitant rise in D_α.

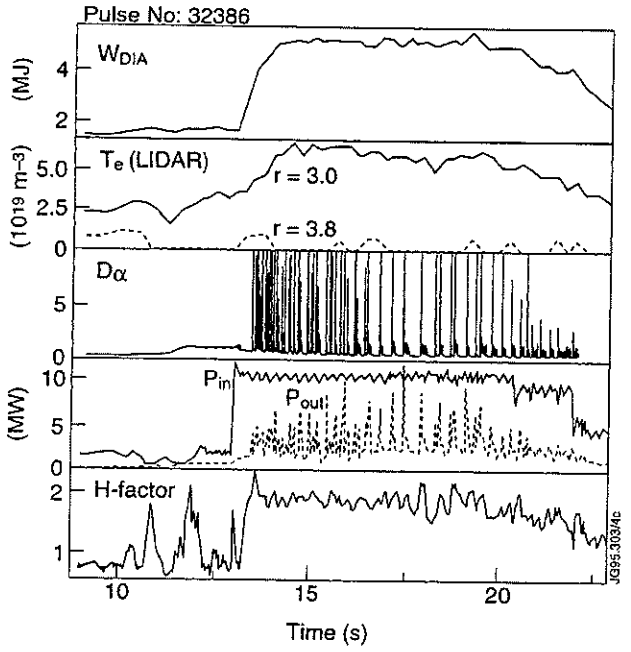

Fig.1 Plasma parameters during H-mode of #32386.

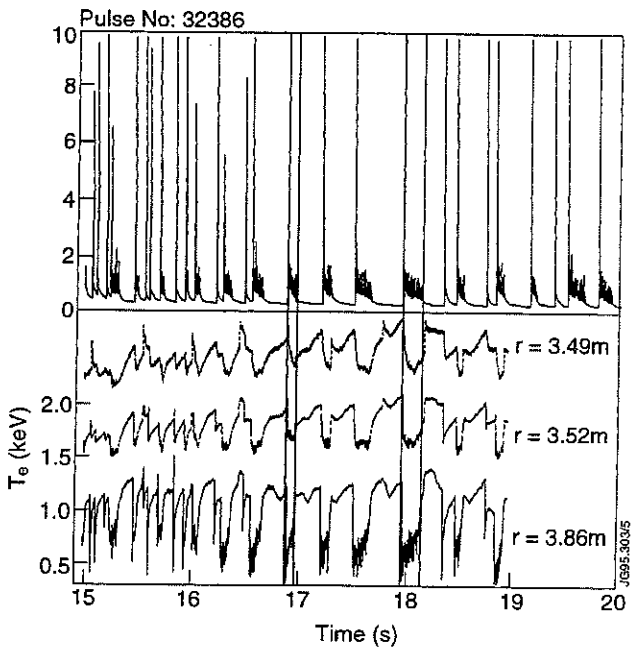

Fig. 2 Edge T_e measurements during giant ELMs.

After the ELM (Type I) crash there may be a series of smaller, higher frequency, ELMs (Type III?) before H-mode is re-established. Alternatively the recovery to H mode can be free of D_α fluctuations. High time resolution ECE temperature measurements show that during this recovery period the temperature returns to its pre-ELM value.

IMPURITY TRANSPORT SIMULATION

The SANCO 1.5-D impurity transport code has been employed in all simulations. Particle transport is described by a diffusive and convective part with the flux of each ionisation stage

$$\Gamma_i = -D(\psi,t)\nabla \cdot n_i + V(\psi,t)n_i$$

The transport functions (D,V) are heuristically chosen and the solution is iterated until there is agreement between the simulation and experiment. Then transport is consistent with experiment. The advantages of this technique are that a wide variety of plasma transport can be described in this two function formalism.

In the case of low amplitude grassy ELMs it is possible to average the transport over a number of ELM periods (i.e. when total radiation is not perturbed). In the case of giant ELMs the transport is time-dependent.

DIAGNOSTICS

The impurity transport model requires many parameters which can vary spatially and temporally. The model inputs are

- Electron temperature and density profiles
- Source function describing impurity influx

The success, and limitations, of the model depend on these inputs and experimental data used for comparison to the simulation results. Fig.3 shows the poloidal location of the diagnostics used.

Temperature and density are measured with ECE and LIDAR. Spectroscopic diagnostics, both active charge exchange and passive emission, provide the source term and comparison data for simulation evaluation.

The source function follows the peripheral NeVII ($2s^2$ – 2s2p 465.22Å) time history. The time resolution of the VUV spectrometer is 11ms which is not fast enough to follow the ELM in detail.

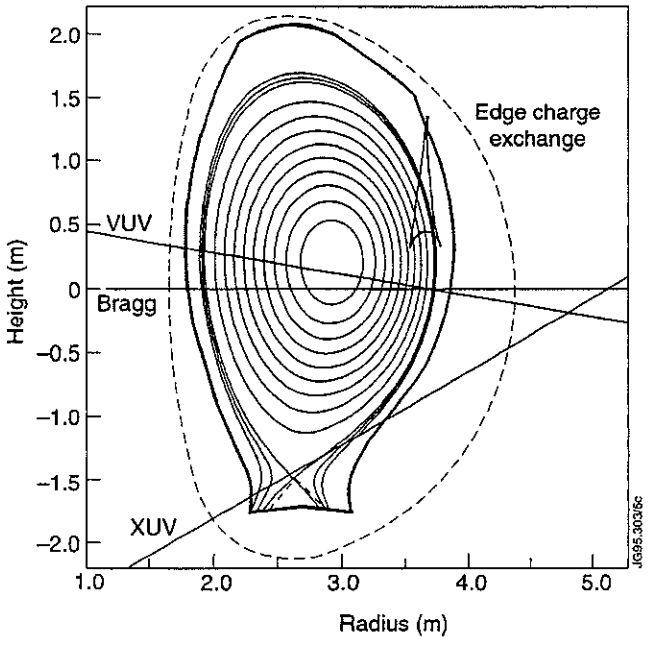

Fig.3 Lines-of-sight of diagnostics.

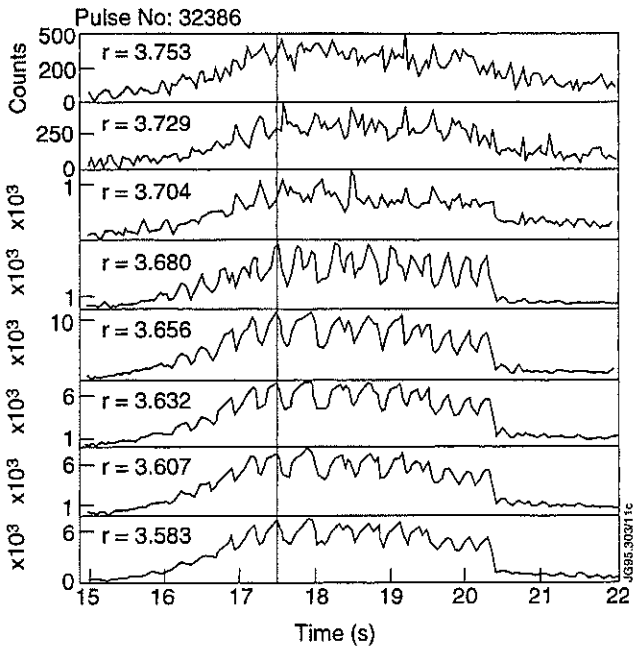

Fig. 4 Edge CX Ne^{10+} density time histories.

There is no on-axis accumulation of Neon. Charge Exchange Recombination Spectroscopy (CXRS) shows hollow profiles. This necessitates the introduction of an outward convection term [3].

The location of the transport barrier removes a free parameter from the simulations. Its location and width are set by the edge charge exchange measurements [4]. The change in density of Ne^{10+} inboard and outside of the transport barrier is shown in fig.4. The barrier is between r=3.68m and r=3.70m. The width of the barrier is ~1cm from the change in the gradient of T_i near the edge.

Fast T_e profiles are available but is not possible to make full use of these because of the limitations of the low temporal resolution spectroscopy.

MODEL OF IMPURITY TRANSPORT DURING GIANT ELMS

A phenomenological model of impurity transport is proposed within the constraints of the two function (D,V) formalism. There is an established H-mode. Following the ELM there is a period of enhanced diffusion before ELM-free conditions are restored. This will be referred to as the H→L hybrid phase. This is characterised by smaller high frequency mini-ELMs and the recovery of the edge temperature.

The transition between H-mode and the hybrid H→L phase and back to H-mode is modelled by a sharp switch (< 1ms) in the diffusion coefficient only. The transport profiles are kept constant throughout each phase.

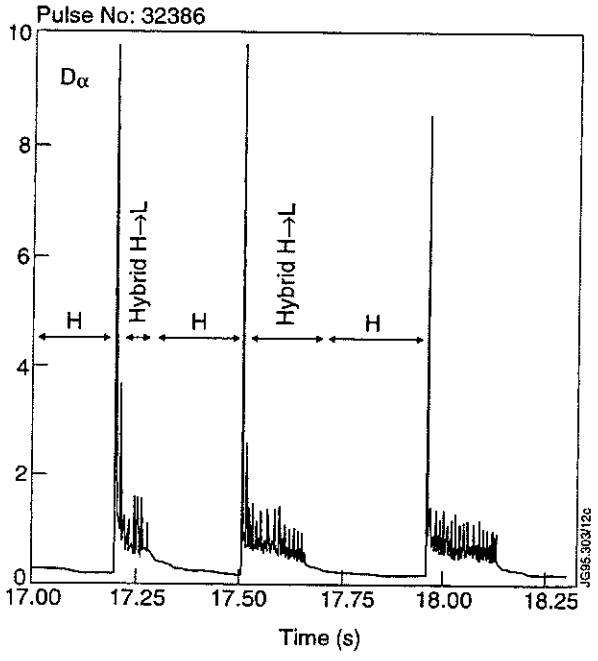

Fig.5 D_α and regions of different transport

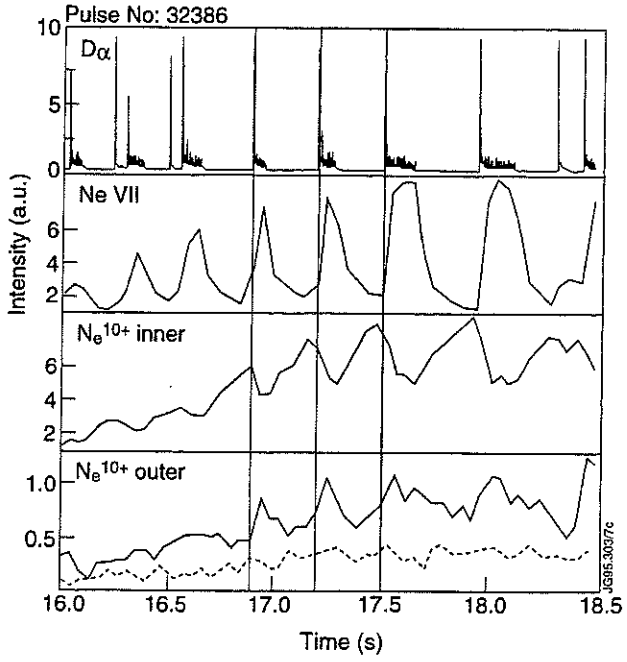

Fig. 6 Evolution of spectroscopic signals.

The edge charge exchange shows an anti-correlation in impurity density across the transport barrier.

RESULTS

The model is adjusted to match

- Total number of Neon particles from bulk charge exchange
- Profile of the Ne^{10+}
- Impurity line intensities

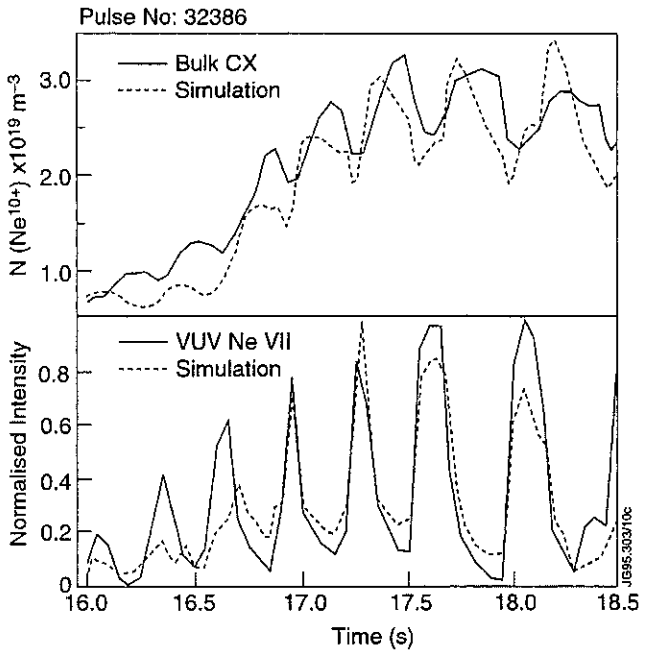

Fig.7 Comparison between simulation and spectroscopic measurements.

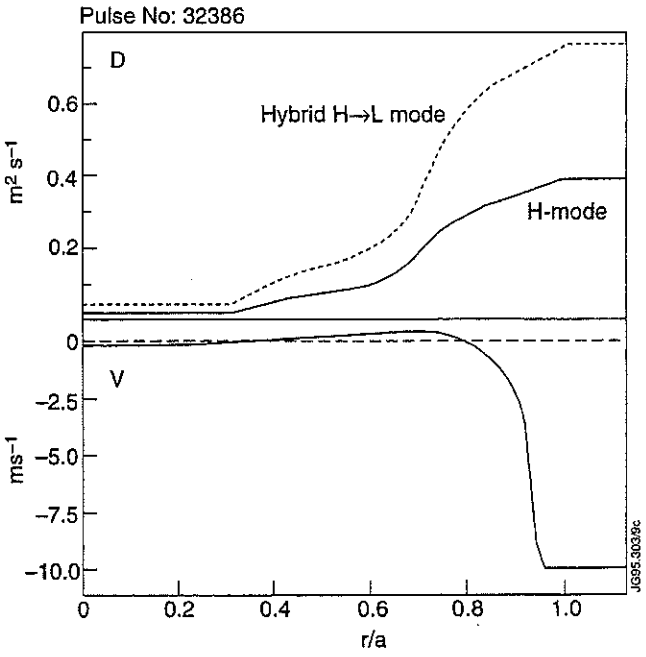

Fig. 8 Transport profiles used for simulation.

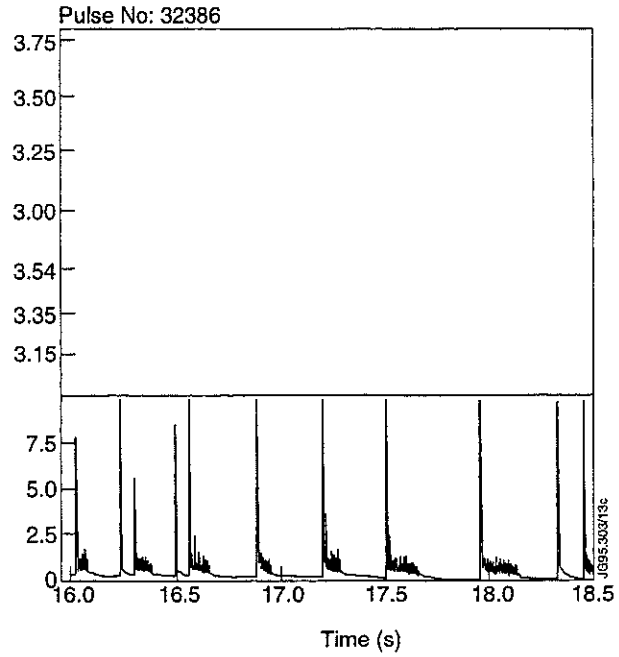

Fig. 9 Comparison between N_e^{10+} profile from CXRS and simulation.

The simulations indicate

- A sudden drop (<1ms) in diffusion following the ELM models the evolution of the Ne^{10+} profile
- The allowable value of D(r) are intermediate between H and L-mode. For the transport in fig. 10 the allowable diffusion is

  $$D_H(r)\ x2 < D_{H\rightarrow L}(r) < D_H(r)x4$$

  where the L-mode factor is typically x6–10 of H-mode value
- A transport barrier (V) is essential throughout the simulation. A 'standard' V ($=-2Dr/a^2$) during the H→L hybrid phase does not reproduce the experimental observations.
- There is a sensitivity to the size of the barrier

  $$-7\ ms^{-1} < V_{r=0.95a}(r) < -10\ ms^{-1}$$

  although the location more important.
- The source term is significant for the success of the simulation.
- There may be a ramp in D during the H-mode recovery.
- Qualitative agreement between Ne^{10+} behaviour on either side of the transport barrier.

PENETRATION OF THE ELMS

The penetration of the ELM into the plasma column can be followed from the time histories of the intrinsic impurities. NiXXV radiates at T_e ~ 500–700eV and ClXV at T_e ~ 300–400eV. These correspond to radii of r ~ 0.7a – 0.9a depending on plasma conditions. Within the time resolution of the spectrometer (~11ms) they occur simultaneously with the ELM.

The penetration depth appears to depend on the abruptness of the recovery following the ELM crash.

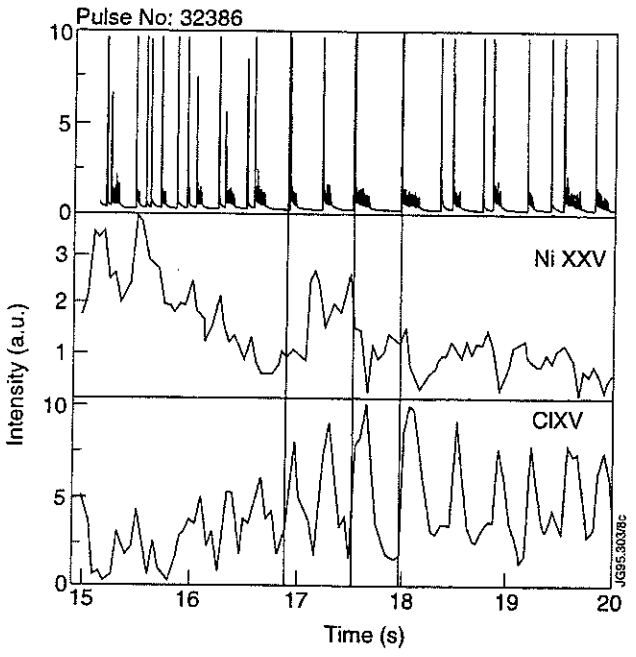

Fig.10 Time evolution of VUV lines in #32386.

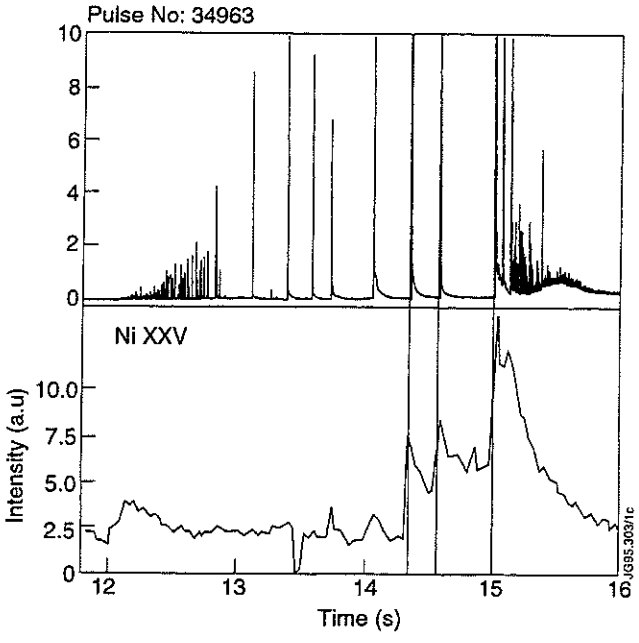

Fig.11 Time evolution of VUV lines in #34963.

CONCLUSIONS

An impurity transport model has been applied to describe the behaviour of impurities during H mode with giant ELMs. There is a period of enhanced diffusion following the ELM crash. Although it can be interpreted as a H→L transition there is *no change in the convection barrier* and the change in diffusion is intermediate between the H and L mode values.

It is necessary to improve the time resolution, to sub-ms timescales, over that of present day spectroscopic instruments in order to follow the transport barrier itself and the detailed behaviour of impurities in ELMy H modes.

REFERENCES

[1] DIII-D Team, 13th IAEA Conf. Washington, 1990, IAEA-CN-53/A-I-4
[2] V V Parail et al., 15th IAEA Conf. Seville, 1995, IAEA-CN-60/A-2-II-3
[3] L Lauro-Taroni, 21st EPS Montpellier,1994, I-120
[4] N C Hawkes, This conference

Dimensional Analysis of L-H Power Threshold Scalings

W Kerner, J G Cordey, O Pogutse[1], E Righi.
JET Joint Undertaking, Abingdon, Oxfordshire, OX14 3EA, UK.
[1] RRC Kurchatov Institute, Moscow, Russia.

INTRODUCTION

- Tokamak plasmas exhibit states of low (L) and high (H) confinement. L-mode plasmas are characterised by higher amplitude turbulent activity than H-mode plasmas.
- Following the transition the H-mode plasma develops steep temperature and density gradients near the plasma edge. Therefore, theory has also to address the question why H-mode plasmas are stable.
- A possible explanation of the L-H power threshold being due to shear flow stabilisation of the drift and interchange modes **near the separatrix**, where the magnetic field lines intersect the target plates, is examined.
- The region where the physical effects of the open field lines become important includes part of the closed field line edge plasma as well as the scrape-off-layer (SOL) plasma. This region (width x_o) is several ion gyro-radii wide (Fig. 1).
- Steep gradients in this region can drive resistive MHD and drift type instabilities, but they can also provide the strong shear flow stabilisation mainly due to the E × B drift [1,2].
- **This stabilisation of the interchange and drift modes gives the criterion for the L-H transition. The scientific method used is dimensional analysis [3,4], together with the mixing length arguments.**

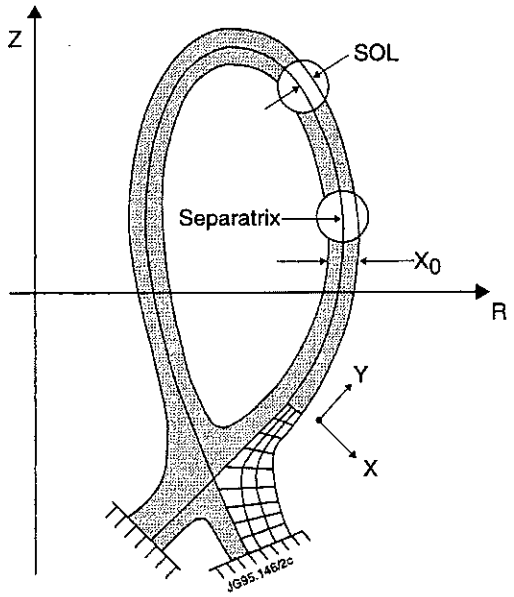

Figure 1

TURBULENT TRANSPORT COEFFICIENT $\chi_\perp$ FOR THE OPEN FIELD LINES REGION

- The linear equations for the mutual drift and interchange modes [5-7] yield the dimensional parameters of the problem.

Model;

- Ion continuity equation.

$$-i\omega\cdot n' - \frac{c}{B_0}\frac{dn_0}{dx}\frac{\partial\phi'}{\partial y} + i(\omega+\omega_*)\cdot\left(\frac{n_0 Mc^2}{eB_0^2}\right)\cdot\Delta_\perp\phi' - \frac{c}{eB_0R}\frac{\partial p_i'}{\partial y} = -\frac{\partial}{\partial s}\left(\frac{j_{\parallel i}}{e}\right)$$

where $\phi'(x,y,s) = \phi'(s)\cdot\exp\left(-i\omega\cdot t + i\vec{k}_\perp\vec{r}_\perp\right)$ is the electrostatic potential.

- Electron continuity equation:

$$-i\omega\cdot n' - \frac{c}{B_0}\frac{dn_0}{dx}\frac{\partial\phi'}{\partial y} + \frac{c}{eB_0R}\frac{\partial p_e'}{\partial y} = \frac{\partial}{\partial s}\left(\frac{j_{\parallel e}}{e}\right)$$

- We average these equations along "s" between s = 0 and s = $L_\parallel$ as in [7] and match the end values for the ion and electron currents to their values for the sheath region:

$$j_{\parallel i}\big|_{s=L_\parallel} = j_{0i}\frac{n'}{n_0}, \quad j_{\parallel e}\big|_{s=L_\parallel} = j_{0e}\left[-\frac{n'}{n_0} + \frac{e\phi'}{T_{0e}}\right].$$

- **After suitable normalisation the averaged equations can be written as:**

$$(\omega+\omega_*)\cdot(\mathbf{k}_\perp\rho_i)^2\cdot\frac{e\phi'}{T_0} + \omega_{*g}\cdot\frac{n'}{n_0} = -i\nu\cdot\left[(1-\xi)\cdot\frac{n'}{n_0} + \xi\cdot\frac{e\phi'}{T_0}\right]$$

$$\omega_*\cdot\frac{e\phi'}{T_0} - \omega\cdot\frac{n'}{n_0} + \frac{\omega_{*g}}{2}\cdot\frac{n'}{n_0} = -i\nu\cdot\left[(-\xi)\cdot\frac{n'}{n_0} + \xi\cdot\frac{e\phi'}{T_0}\right]$$

$\omega_* = -\dfrac{cT_0k_y}{eB_0n_0}\dfrac{dn_0}{dx}$ - the electron drift frequency ($T_i = T_e = T_0$);

$\rho_i^2 = \left(c^2T_0M/e^2B_0^2\right)$ - the square of the ion Larmor radius;

$\omega_{*g} = \dfrac{2cT_0k_y}{eB_0R}$ - the magnetic drift frequency;

$\nu = \dfrac{C_s}{L_\parallel}$ - characteristic frequency for the SOL plasma;

$C_s = (2T_0/M)^{1/2}$ - the ion sound velocity;

$\xi = \dfrac{j_{0\parallel e}}{j_{0\parallel i}}$ - the ratio of the equilibrium electron and ion current densities on the end plates.

- The system of equations contains the following independent parameters:

$$x_0, L_{\|}, R, \rho_i, C_s, \hat{\beta}, \xi, \text{ where}$$

$x_0 = (dp_0/p_0dx)^{-1}$: pressure gradient length; $\hat{\beta} = \left(L_{\|}^2 / Rx_0\right)\beta$ normalised beta.

- General expression for the turbulent coefficient is:

$$\chi_{\perp} = \hat{\chi}_{GB} \; f\left(\hat{\beta}, \xi, L_{\|}/R, x_0/R, \hat{\rho}\right)$$

$$\hat{\chi}_{GB} = \left(cT_0/eB_0\right)\cdot\hat{\rho} \; ; \qquad \hat{\rho} = \rho_i / x_0$$

SOL RESISTIVE INTERCHANGE AND DRIFT INSTABILITIES

- resistive interchange instability (RI)
- drift instability (DR).

growth rates

$$\gamma_{RI} = \omega_* \cdot \omega_{*g} / \nu \cdot \xi \; , \qquad \gamma_{DR} = \nu \cdot (\xi - 1) / (k_{\perp}\rho_i)^2 \; ,$$

maximum growth rates

$$(\gamma)_{RI_{max}} = C_s / (x_0 R)^{1/2} \; , \qquad (\gamma)_{DR_{max}} = C_s / \left(x_0^2 L_{\|}\right)^{1/3} \; ,$$

for the wave vector:

$$(k_{\perp}\rho_i)_{max} = \left(x_0 R / L_{\|}^2\right)^{1/4} \; , \qquad (k_{\perp}\rho_i)_{max} = \left(x_0 / L_{\|}\right)^{1/3} \; ,$$

- Thus the dimensional analysis together with the mixing length arguments give the following general expression for the turbulent transport for the mutual influence of interchange and drift instabilities;

$$\chi_{\perp} = \hat{\chi}_{GB} \cdot \mathbf{f}\left(\hat{\beta}, \xi, \mathbf{L_{\|}/R}, \hat{\rho}, \mathbf{x_0/R}\right) \approx \hat{\chi}_{GB} \cdot \mathbf{f}\left(\hat{\beta}, \mathbf{x_0/R}\right) .$$

The last expression is correct if ξ is of order unity and the weak dependence on $L_{\|}$ is omitted.

- Ansatz for the function $f\left(\hat{\beta}, x_0/R\right)$ in form of a power dependence:

$$\chi_{\perp} = \hat{\chi}_{\perp GB} \cdot \left(\hat{\beta}\right)^{\alpha} \cdot (x_0/R)^{\delta},$$

where α and δ are constants. For pure interchange $\alpha = 0$ or 1 and $\delta = 0$; for pure drift instability $\alpha = 0$ and $\delta = -1/3$.

THE CRITERION FOR STABILITY

- As a criterion for stability we apply the shear flow stabilisation condition:

$$\frac{dV_0}{dx} > \gamma_{max} ,$$

- This gives the following stability conditions $\left(V_o' \approx \frac{C_s}{x_o}\frac{\rho_i}{x_o} \right)$:

for interchange instablity

$$\hat{\rho}_{RI} > (x_0 / R)^{1/2}$$

for drift instability

$$\hat{\rho}_{Dr} > (x_0 / L_{\|})^{1/3}$$

- In order to stabilise shorter wave-length perturbations these conditions have to be more stringent:

$$\hat{\rho} > c_1 \qquad (\hat{\rho}_\theta > c_2) ,$$

where the constant C_1 is order of unity.

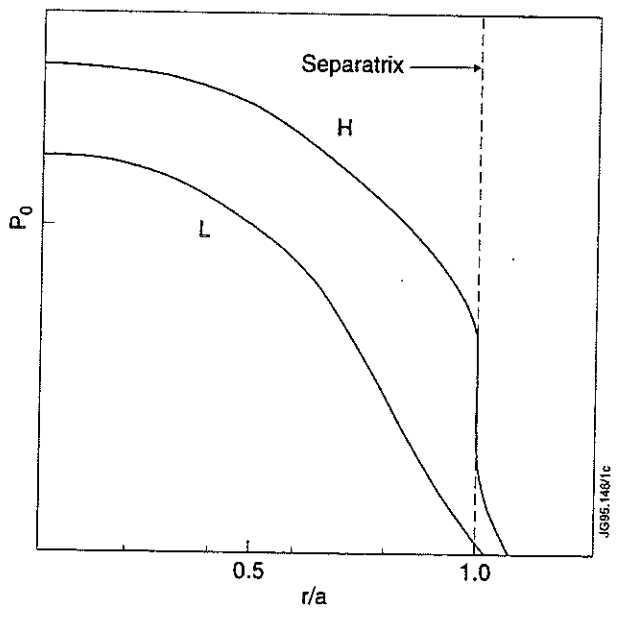

Figure 2

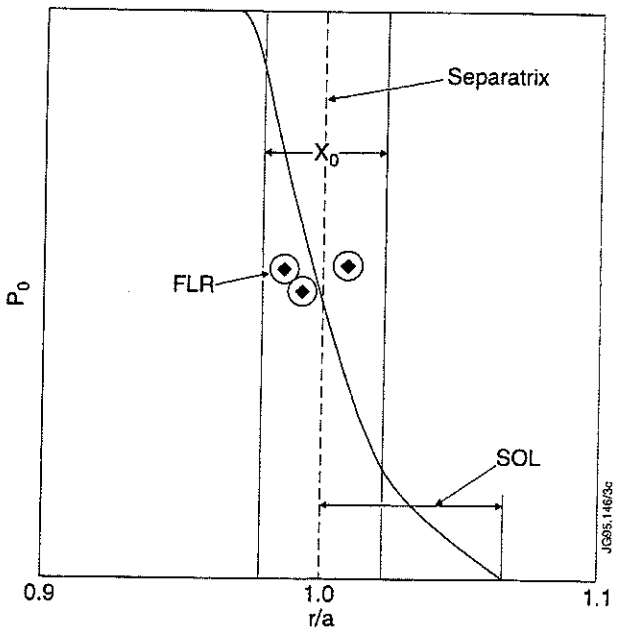

Figure 3

THE GRADIENT LENGTH X_0 AND THE SCALING FOR THE L-H THRESHOLD

- To estimate x_0 we use the energy balance equation:

$$\frac{\partial}{\partial t} T_0 = \frac{\partial}{\partial x} \chi_\perp \frac{\partial}{\partial x} T_0 - \frac{1}{\tau_\parallel} \cdot T_0$$

$\tau_\parallel$ is the characteristic time of the longitudinal losses.

- Integration yields:

$$\frac{P}{n_0 S} \approx \frac{\chi_\perp T_0}{x_0} \approx \frac{x_0 T_0}{\tau_\parallel} \quad .$$

P is the total power through the separtrix, S the tokamak plasma surface.

The longitudinal losses are described by two models, due to classical thermal conduction and due to free-streaming flow:

$$\tau_\parallel^{th} = \frac{L_\parallel^2}{\chi_\parallel} \propto \frac{L_\parallel^2 n_0}{T_0^{5/2}} \quad , \quad \tau_\parallel^{fs} = \frac{L_\parallel}{C_s} \propto \frac{L_\parallel}{T_0^{1/2}}$$

SCALINGS

- Combined drift-interchange instability

a) The collisionless limit:

$$\frac{P}{n_0 S} \propto B_0^3 \left(n_0^{-4\alpha} R^{(-5\alpha+3\delta-3)} \right)^{1/(\alpha+\delta-1)} = B_0^3 f(n_0, \alpha, \delta)$$

b) The classical parallel losses:

$$\frac{P}{n_0 S} \propto \left(\frac{B_0^{(7\alpha+7\delta-3)} \cdot R^{(-10\alpha+6\delta-6)}}{n_0^{(9\alpha+\delta+3)}} \right)^{1/(\alpha+\delta-5)}$$

for the interchange instability

a) The free-streaming case:

$$\frac{P}{n_0 S} \propto B_0^3 \frac{n_0^{\frac{4\nu}{1-\nu}}}{L_\parallel} \left(\frac{L_\parallel^2}{R}\right)^{\frac{4(1+\nu)}{1-\nu}}$$

b) The classical loss case:

$$\frac{P}{n_0 S} \propto \frac{B_0^7}{n_0 L_\parallel^2} \left(\frac{L_\parallel^{8(3+2\nu)} n_0^{8(1+\nu)}}{R^{8(1+\nu)} B_0^{32}}\right)^{1/(5-\nu)}$$

$$\frac{P}{n_0 S} \propto \frac{n_0^3}{B_0} \left(\frac{L_\parallel^2}{R}\right)^4$$ for the

single-null divertor configuration ($\nu = 1$),

$$\frac{P}{n_0 S} \propto \left(\frac{L_\parallel^2}{R}\right)^{8/5} n_0^{3/5} L_\parallel^{-2/5} B_0^{3/5}$$

the double-null configuration ($\nu = 0$).

for the drift instability

a) The free streaming case:

$$\frac{P}{n_0 S} \propto B_0^3 L_\parallel^3$$

b) The classical loss case:

$$\frac{P}{n_0 S} \propto n_0^{1/2} L_\parallel^{3/2} B_0$$

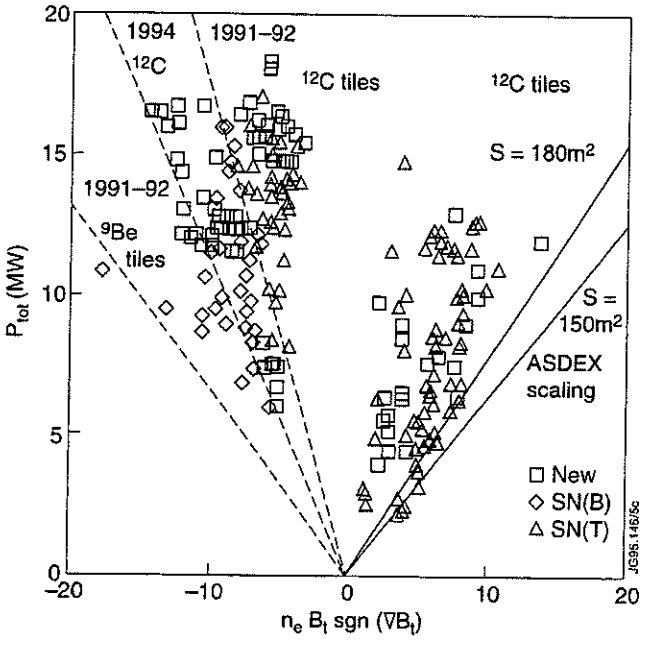

Figure.4

DISCUSSION

- Two dimensionally correct forms have been presented [8] that give a reasonable fit to the data. Both forms assume that the linear B_0 dependence is correct, and the first form takes the quadratic dependence on length scale as correct and adjusts the n_0 dependence:

$$P > 0.025 n_0^{0.75} B_0 S \qquad \textbf{(a)}$$

In the second form the n_0 dependence is assumed to be correct and the length scale is adjusted to yield a dimensionally correct result:

$$P > 0.4 n_0 B_0 R^{2.5} \qquad \textbf{(b)}$$

where P the power in MW, S the surface area in m^2, n_0 the average density in 10^{20} m^{-3}, B_0 the toroidal field in tesla.

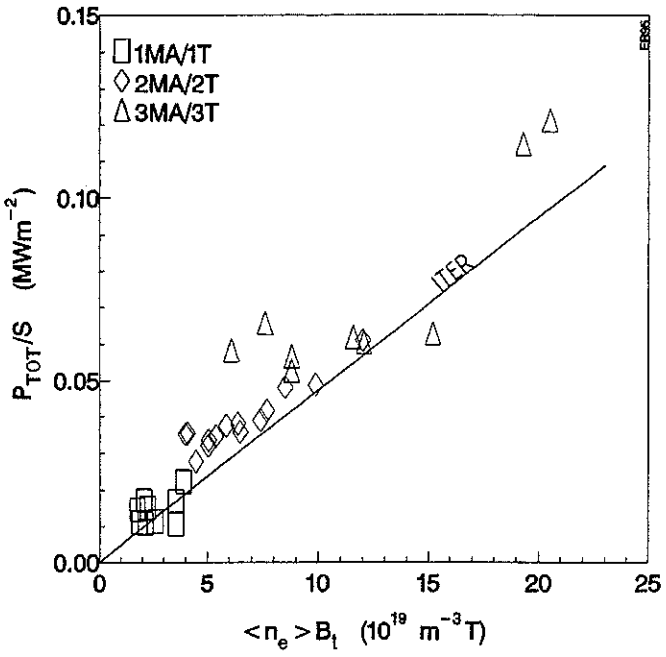

Figure.5

- In the classical parallel loss case the linear dependence on B_0 requires:

  $\mathbf{3\alpha + 3\delta = -1}$

  The density scaling (a) is reproduced by:

  $\mathbf{35\alpha + 3\delta = -17}$

  which gives $\alpha = -1/2$, $\delta = 1/6$

$$\chi_\perp = \hat{\chi}_{GB} \cdot \left(\hat{\beta}\right)^{-1/2} \cdot \left(x_0 / R\right)^{1/6} \propto \frac{T}{n_0^{1/2} B_0 x_0^{1/3}}$$

  Scaling (b) is reproducing by:

  $\mathbf{9\alpha + \delta = -3,}$

  which gives $\alpha = -1/3$ and $\delta = 0$.

$$\chi_\perp = \hat{\chi}_{GB} \cdot \left(\hat{\beta}\right)^{-1/3} \propto \frac{T^{7/6}}{n_0^{1/3} x_0^{2/3} B_0^{4/3}}$$

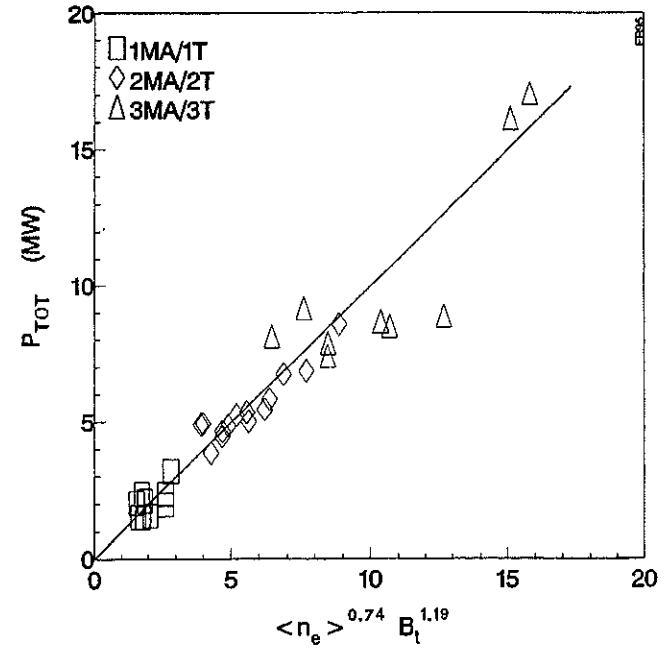

Figure.6

CONCLUSION

- The near separatrix region in tokamaks which combines the properties of closed and open field line regions provides a new length scale parameter $x_0 = (-d\ln p_0/dx)^{-1}$. This parameter is typically of the order of several Larmor radii.
- The edge gradients can drive modified drift and interchange instabilities which depend, in addition, on the conditions at the target plates. The related turbulence gives rise to perpendicular transport and regulates the width x_0. Dimensional analysis is applied to determine the scaling of the transport coefficients.
- The H-mode is set up when x_0 becomes sufficiently narrow and the shear flow stabilities these instabililities leading to the condition $\rho = \rho_i/x_0 > c_1$ where c_1 is of order unity.
- Finite beta physics $\hat{\beta} = \left(L_{\parallel}^2 / x_0 R\right) \cdot \beta \propto 0(1)$, plays an important role for electrostatic SOL turbulence.
- Classical thermal conduction provides a threshold scaling similar to the experimentally observed dimensionally correct scalings: $P \propto n_0^{0.75} B_0 S$ (or $P \propto n_0 B_0 R^{2.5}$), where n_0 is the average density, S the surface area. B_0 the toroidal magnetic field and P the heating power.
- The free-standing loss yields a cubic dependence on B_0, which could match the observed threshold scaling of high edge tempeature, low density plasmas.

REFERENCES

[1] S. Itoh and K. Itoh, Phys. Rev. Lett., 60. p.2276, 1988.

[2] K.C. Shaing and E.C. Crume Jr., Phys. Rev. Lett., 63, p.2369, 1989.

[3] B.B. Kadomtsev, Fizika Plasmy (in Russian), 1, p.531, 1975.

[4] J.W. Connor and J.B. Taylor, Nuclear Fusion, 17, p1047, 1977.

[5] V.E. Kolesnikov, A.V. Nedospasov, Sov. Phys. Dokl., 32, p.478, 1987.

[6] O. Pogutse, W. Kerner, V. Gribkov, S. Bazdenkov and M. Osipenko, Plasma Phys. Control. Fusion., 36, p.1963, 1994.

[7] H.L. Berk, D.D. Rytov, Yu. A. Tsidulko, Phys. Fluids B, 3, p.1346, 1991.

[8] H-mode Data Base Working Group, presented by F. Ryter, 21st EPS, Montpellier 1994, Vol. I p.334

The Behaviour of Divertor and Scrape-Off Layer Parameters in JET

S J Davies, S K Erents[1], H Y Guo[2], A Loarte, G F Matthews, K McCormick[3], R D Monk[4].

JET Joint Undertaking, Abingdon, Oxfordshire, OX14 3EA, UK.
[1] UKAEA Fusion, Culham, Abingdon, Oxfordshire, OX14 3DB, UK.
[2] INRS-Energie et Materiaux, Université du Quebec, Canada.
[3] Max-Planck-Institut für Plasmaphysik, EURATOM Association, 85748 Garching, Germany.
[4] Department of Physics, Royal Holloway College, University of London, Surrey, TW20 0EX, UK.

1. INTRODUCTION

Extensive studies of the behaviour of divertor and Scrape-Off Layer (SOL) parameters have been undertaken following the installation of the new JET MkI pumped divertor. Using both reciprocating and fixed Langmuir probe systems it has been possible to simultaneously measure SOL and target profiles over a wide range of plasma parameters during ohmic, L- and H-mode phases of a pulse. The data presented in this poster were obtained from a series of pulses with line-averaged densities of (1.3-6.7)x10^{19} m^{-3} at input powers up to 10MW with (1.5-3.3)T fields. Both horizontal and vertical target configurations were used with normal ($B_{\wedge}\nabla B\downarrow$) and reversed ($B_{\wedge}\nabla B\uparrow$) field.

The main topics described are :

- Comparison of SOL widths in horizontal and vertical target configurations with reversed field (see also poster by A. Loarte et al., this conference).
- Scaling of horizontal configuration SOL widths in reversed field.
- Scaling of vertical configuration SOL widths in normal field.
- Variation in target power scrape-off width, λ_P^{tgt}, with surface safety factor, q_{cyl}, for both normal and reversed field (see also poster by A. Chankin et al., this conference).
- Behaviour of target scrape-off widths as a function of X-point height and connection length.
- Calculation of radial heat diffusivity, $\chi_\perp$, using analytical model [1] and comparison with EDGE2D modelling results.
- Comparison of JET target power scrape-off widths with JT-60 scaling [2].

The SOL and target widths quoted in this poster are referenced to the midplane unless stated otherwise. Further details of the fixed and reciprocating Langmuir probe systems are given by K. Erents et al., this conference. The subject of detachment is covered in a poster by R. Monk et al., this conference.

2. COMPARISON OF SOL WIDTHS IN HORIZONTAL AND VERTICAL TARGET CONFIGURATIONS

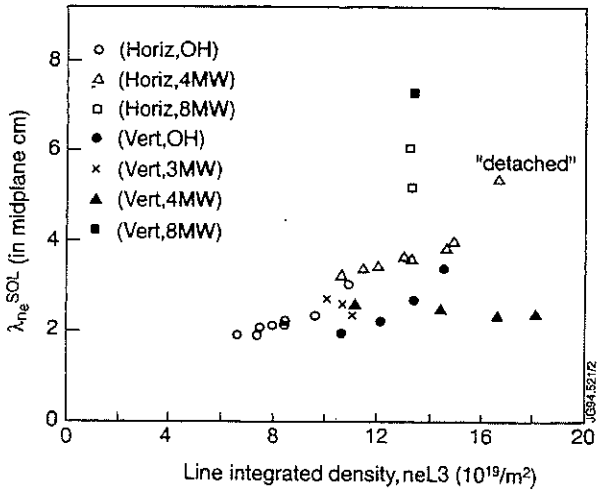

Figure 1 : Comparison between density SOL widths for horizontal and vertical target configurations.

- The vertical target SOL widths in density, λ_{ne}^{SOL}, are generally lower than for the horizontal case.
- A thinner SOL width with a vertical target configuration is consistent with modelling and is a result of different recycling patterns [3].
- λ_{ne}^{SOL} under OH conditions in the vertical target configuration does not increase as rapidly as for the horizontal target configuration.
- For moderate (<8MW) heating, λ_{ne}^{SOL} for the vertical case shows no increase with density whereas it increases rapidly for the horizontal case, leading to detachment.
- At 8MW, for the one density point available, there is no significant difference.

3. SCALING OF HORIZONTAL CONFIGURATION SOL WIDTHS IN REVERSED FIELD

- These data were obtained for B_t =(2.2-2.4)T. Regression analyses were performed on the data using total input power and line-integrated density as the regression variables.
- The best regressions are obtained by fitting to data with (i) Ohmic and input powers of <4MW and (ii) with input powers of 4-8MW.
- An example of the regression fits obtained for the upstream pressure, density, temperature and power fall-off lengths for ohmic and input powers of <4MW is shown below.
- The best fit parameters are also summarised in Table 1.

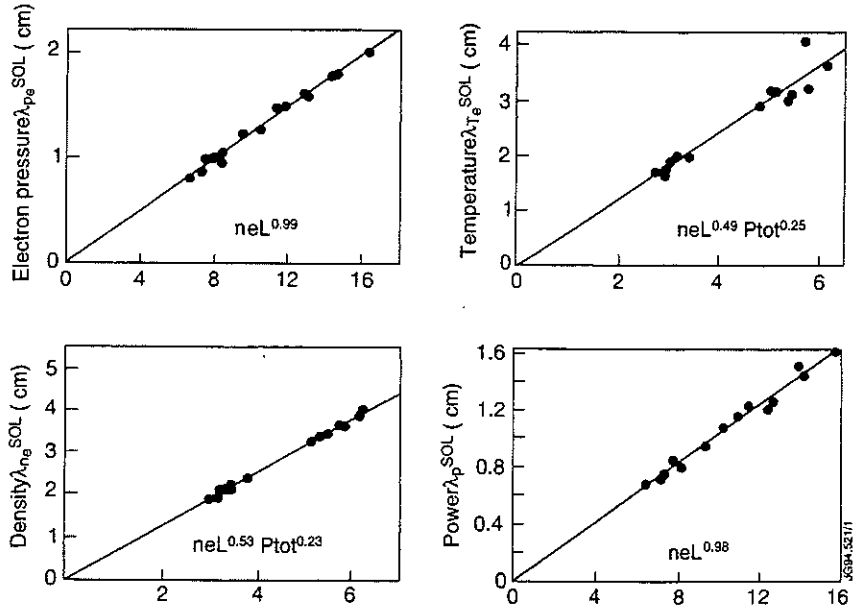

Figure 2 : Example regression fits to the SOL widths of pressure, density, temperature and power for ohmic and input powers of <4MW.

SOL width in	Const.	Line-integrated density Nel ($x10^{19}m^{-2}$)	Ptot (MW)	Fit Coeff., R	Range (cm)
Pressure	0.123	0.99±0.04	0	0.994	0.8-2.0
Jsat	0.376	0.64±0.09	0.13±0.04	0.985	1.2-2.9
Temperature	0.603	0.49±0.17	0.25±0.07	0.962	1.6-4.0
Density	0.642	0.53±0.06	0.23±0.03	0.998	1.9-4.0
Power	0.103	0.98±0.05	0	0.989	0.7-1.6

Table 1a : Fitting parameters for P_{NI} =0-4MW

Fits are of the form $\lambda_{Te}^{SOL} = 0.603\ Nel^{(0.49\pm0.17)}\ P_{tot}^{(0.25\pm0.07)}$ and R is the regression coefficient.

SOL width in	Const.	Line-integrated density Nel ($x10^{19}m^{-2}$)	Ptot (MW)	Fit Coeff., R	Range (cm)
Pressure	0.044	0.76±0.10	0.99±0.05	0.995	1.25-2.6
Jsat	0.1	0.59±0.15	0.97±0.07	0.984	1.9-3.6
Temperature	0.381	0.41±0.22	0.65±0.14	0.902	3.0-4.5
Density	0.287	0.44±0.16	0.86±0.08	0.971	3.2-5.6
Power	0.042	0.75±0.16	0.90±0.08	0.986	1.0-2.0

Table 1b : Fitting parameters for P_{NI} =4-8 MW

- Comparing the two regimes it is seen that for higher powers the density dependence is marginally reduced and the power dependence increases radically when compared to the fits for the lower powers.
- The temperature fall-off length, λ_{ne}^{SOL}, does not decrease with input power, P_{TOT}, as simple theory [1] might predict.

4. SCALING OF VERTICAL CONFIGURATION SOL WIDTHS IN NORMAL FIELD

- SOL and divertor parameters were recorded during ohmic and beam-heated phases of a series of vertical target configuration pulses in normal field.
- In parallel an investigation of the effect of fuelling position on edge parameters was also undertaken.
- The density SOL width, λ_{ne}^{SOL}, for ohmic plasmas first increases rapidly with main plasma density tending to a limit of ~4cm at higher densities.
- There is no substantial difference in λ_{ne}^{SOL} for top or divertor fuelling.

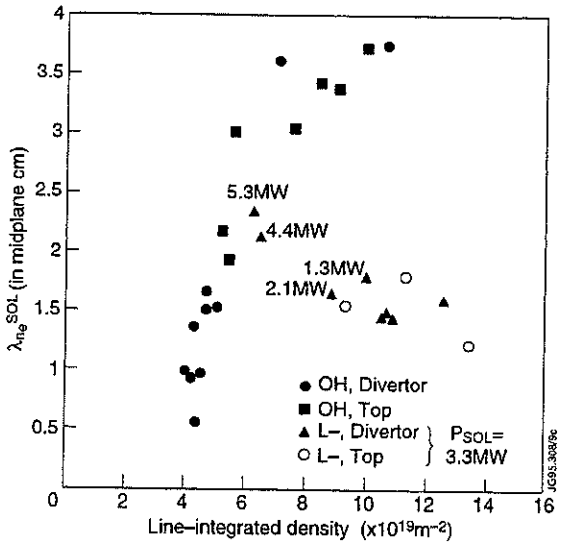

Figure 3 : λ_{ne}^{SOL} as a function of line-integrated density, fuelling location and input power.

- When beam heating is applied lower λ_{ne}^{SOL} (for the same plasma density) results as observed for the reversed field case.
- For beam-heated plasmas, λ_{ne}^{SOL} tends to ~1.5cm. Compare this to ~2.5cm for the reversed field case.

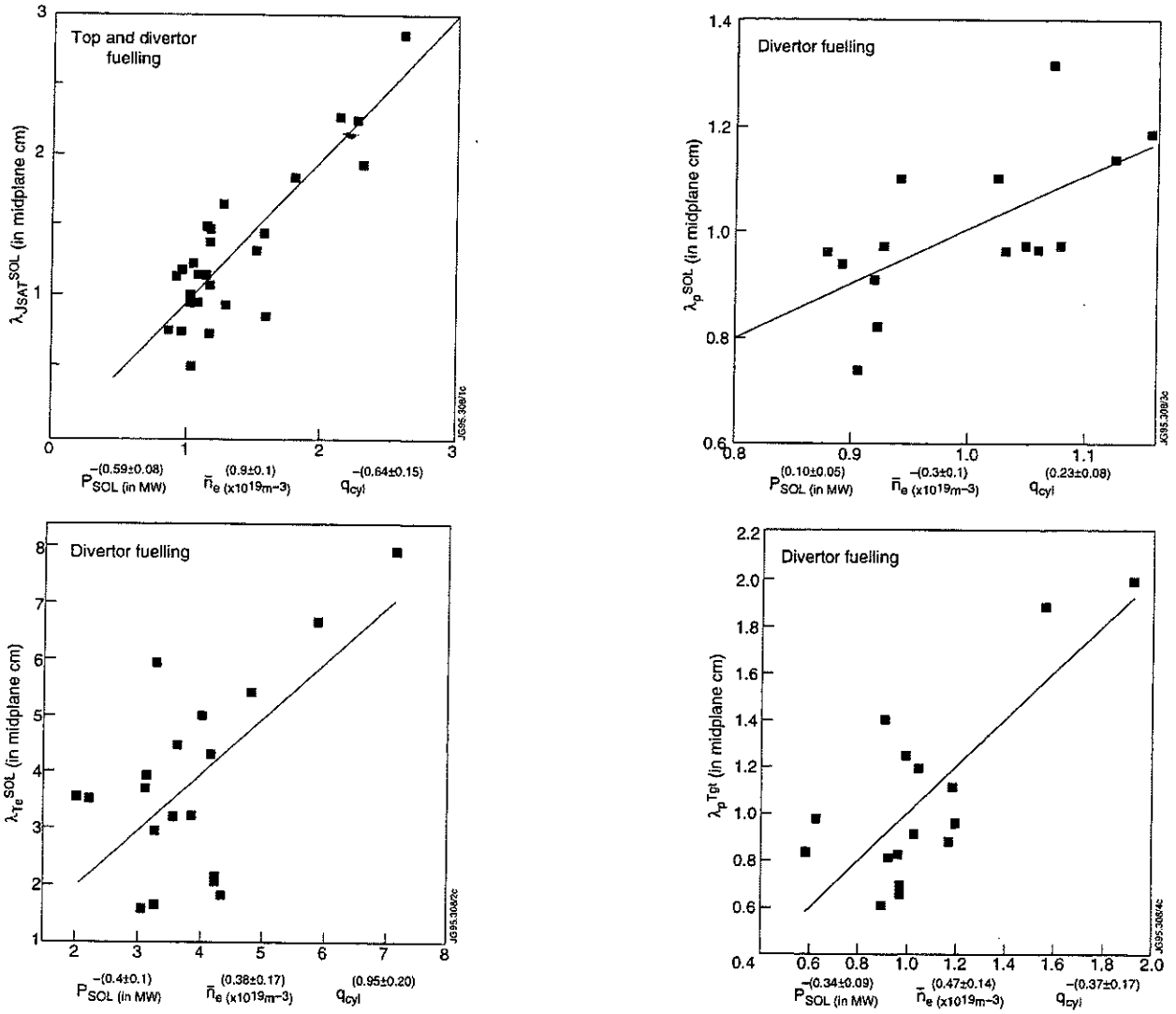

Figure 4 : Scaling of (a) λ_{Jsat}^{SOL}, (b) λ_{Te}^{SOL} (divertor fuelling), (c) λ_P^{SOL} (divertor fuelling) and (d) λ_P^{Tgt} (divertor fuelling) for vertical target configuration in normal field.

- Figure 4 illustrates the best fit regressions to the SOL widths in J_{sat}, T_e and power using as regression variables; power to the SOL, P_{sol}, line-averaged density, n_e, and the surface safety factor, q_{cyl}.
- For the latter two the regression uses only divertor fuelling SOL widths as some effect was observed on the temperature and power SOL widths as a function of fuelling position. Initial observations suggest that the temperature/power SOL widths at higher densities are lower for top fuelling by up to a factor of two. Little or no difference is observed in the target scrape-off widths.
- For comparison the target power scrape-off width (divertor fuelling) is also shown.

5. EFFECT OF q_{CYL} AND $B_\wedge\nabla B$ DRIFT DIRECTION ON TARGET POWER SCRAPE-OFF WIDTH, λ_P^{TGT}

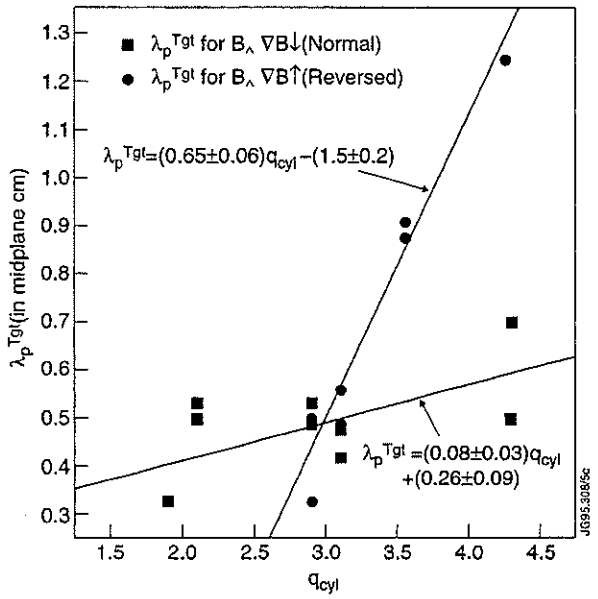

- The variation in the inner and outer strike zone target power width (derived from Langmuir probe data) as a function of q_{cyl} for both $B_\wedge\nabla B$ drift directions is shown.
- λ_P^{tgt} is larger for the reversed field case for a given q_{cyl}.

Figure 5 : Variation in λ_P^{tgt} as a function of q_{cyl} for normal ($B_\wedge\nabla B$) and reversed ($B_\wedge\nabla B\uparrow$) field.

6. BEHAVIOUR OF TARGET SCRAPE-OFF WIDTHS AS A FUNCTION OF X-POINT HEIGHT AND CONNECTION LENGTH (EQUILIBRIA DEVELOPMENT BY C. LOWRY)

- The profiles shown below are all before the 'rollover' in J_{sat} (see R. Monk et al., this conference). The ohmic profiles are at a line-averaged density of $2.4\times10^{19}m^{-3}$ whilst the L-, H-mode profiles are at a line averaged density of $4.8\times10^{19}m^{-3}$.
- See also posters by A. Loarte et al. and M. Stamp et al., this conference.

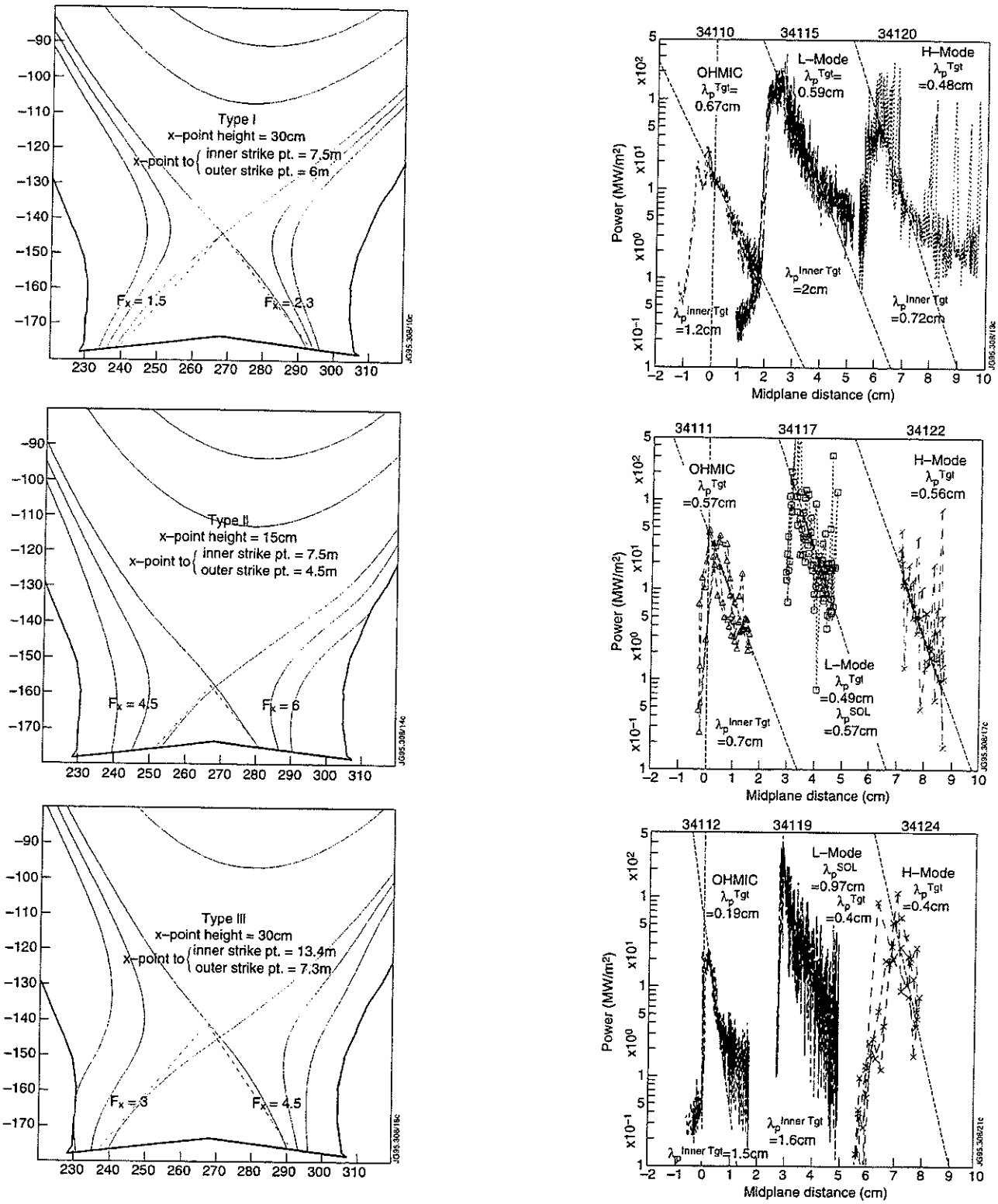

Figure 6 : X-point equilibria used to investigate effect of configuration on divertor performance. Also shown are the power profiles of the outer strike point in ohmic, L- and H-mode.

- The largest variation in target scrape-off widths mapped to the midplane is seen in the density and temperature profiles when mapped to the midplane. The comments below refer to outer strike zone profiles and the same differences where observed under OH, L- and H-mode conditions. It is the consequent flux expansion which determines the differences seen in the profiles.

- For the same X-point height but different flux expansion (2.3/4.5) the density scrape-off width at the target, λ_{ne}, was the same for example at 2.7cm (L-Mode) and the corresponding power scrape-off width at the target, λ_P, was 1.4cm/1.8cm.
- For different X-point height (30cm/15cm), λ_{ne} was 2cm (H-Mode) and the corresponding λ_P was 1.1cm/3.4cm when the flux expansion differed by a factor ~3 (2.3/6).
- For comparable (4.5/6) flux expansions λ_{ne} was 2.7cm/3.2cm (L-Mode) whilst λ_P was 1.8cm/2.9cm.

7. DETERMINATION OF RADIAL HEAT DIFFUSIVITY, $\chi_\perp$, FROM TARGET POWER SCRAPE-OFF WIDTH

- The target power fall-off length at the midplane, λ_P^{Tgt}, calculated using JET specific quantities is, from [4],

$$\lambda_P^{tgt} = \left(\frac{2e}{7}\right)^{\frac{7}{9}} (n_e \chi_\perp A_\perp)^{\frac{7}{9}} P_{tgt}^{-\frac{5}{9}} \left(\frac{7L}{8\pi R \kappa_o (B_\theta/B)_u}\right)^{\frac{2}{9}}$$

and $\chi_\perp$ has been calculated using this equation for all the pulses described in this poster.

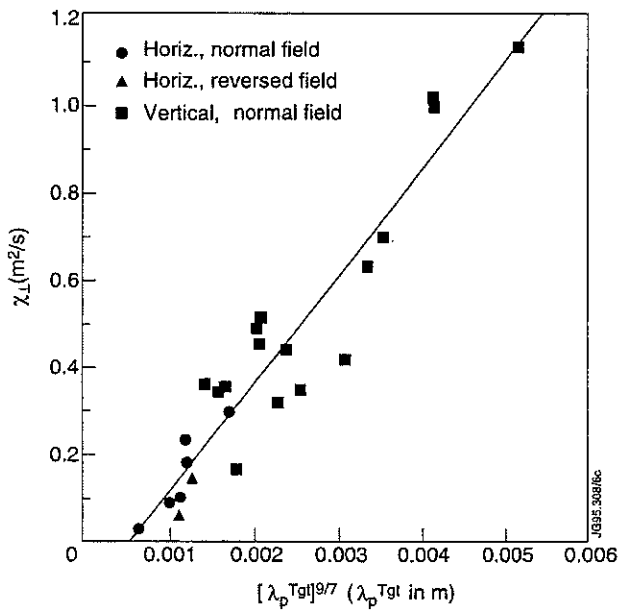

Figure 7 : $\chi_\perp$ plotted as a function of $(\lambda_p^{Tgt})^{9/7}$.

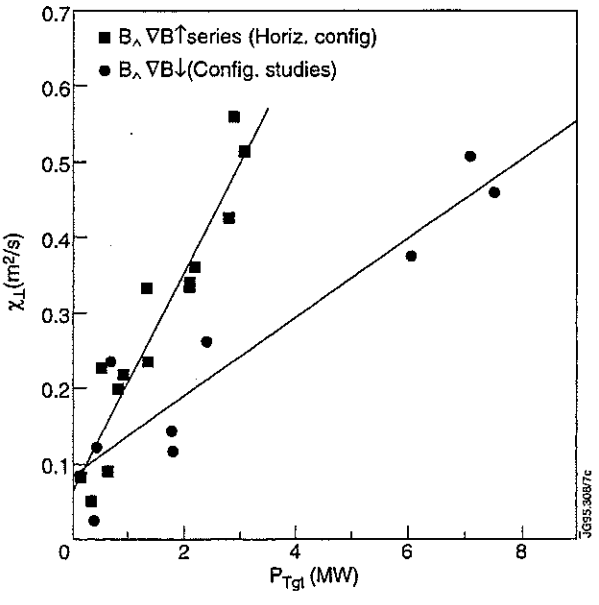

Figure 8 : $\chi_\perp$ as a function of power to target.

- EDGE2D-U/NIMBUS modelling of low density ohmic discharges with horizontal and vertical target configurations gives a $\chi_\perp$ of 1.3 m^2/s with $D_\perp$ = 0.12 m^2/s [5]. The effect of a pinch velocity on the target profiles is also considered in [5].

8. COMPARISON OF JET TARGET POWER SCRAPE-OFF WIDTHS WITH JT-60 SCALING

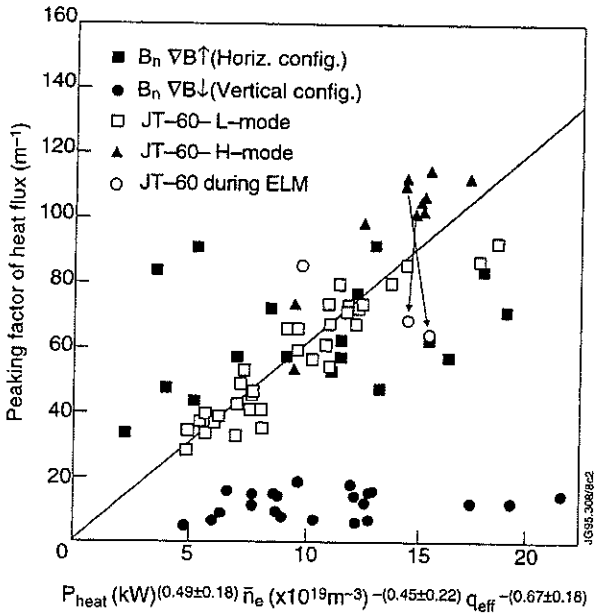

Figure 9 : 1/ λ_P at the target as a function of the JT-60 experimentally derived scaling law.

- The behaviour of λ_P at the target within the framework of the JT-60 empirical scaling law [2] is shown.
- $1/\lambda_P$ at the target from the reversed field, horizontal target and the normal field, vertical target series are plotted along with the JT-60 data.
- The horizontal target data represents the best general agreement with the JT-60 data.
- The effect of configuration is clearly shown by the vertical target data and should be increased by a factor of seven for direct comparison with the JT-60 data.
- These JET data clearly show the discrepancy with the JT-60 data. The JT-60 scaling assumes a constant $\chi_\perp$, which, as the previous section has shown, is not the case.
- The best fit scaling of $1/\lambda_P$ for the horizontal target data was P_{tgt} (kW)$^{(0.14\pm0.04)}$ n_e ($x10^{19}m^{-3}$)$^{-(0.85\pm0.22)}$ $q_{cyl}$$^{-(0.59\pm0.10)}$.

9. REFERENCES

[1] Keilhacker, M. et al., Physica Scripta, **T2/2**, 443 (1982)
[2] The JT-60 Team, presented by M. Shimada, IAEA-CN-56/a-1-3, **1**, 57 (1993)
[3] Vlases, G. et al., J. Nucl. Mat., **196-198**, 392 (1992)
[4] Stangeby, P. C., personal communication
[5] A. Loarte et al., this conference

ACKNOWLEDGEMENTS

The authors would like to acknowledge D. Campbell and Task Force D for their support of this work. They also acknowledge the expertise of C. Hogben, G. Kaveney, G. Neill, J. Vince and D. Wilson whose skill and commitment have made such measurements possible.

Edge Pressure Gradients and Velocity Shear Behaviour during H-modes and ELMs in the new JET Divertor Configuration

N Hawkes[1], A Rookes[2], D V Bartlett, D Campbell, N Deliyanakis, R Giannella, P Lomas, N Peacock[1], L Porte, R Sartori, P Thomas, G Vayakis.
JET Joint Undertaking, Abingdon, Oxfordshire, OX14 3EA, UK.
[1] Culham Laboratory, UKAEA/Euratom Association, Abingdon, Oxfordshire, OX14 3DB, UK.
[2] Imperial College of Science, Technology and Medicine, London, UK.

INTRODUCTION

Improved measurements of ion and electron pressure gradients and ion rotation velocity at the edge of H-mode plasmas in JET's new divertor phase have been studied and analysed with regard to the relationship of velocity shear profile and steep pressure gradients with enhanced confinement and edge stability.

The ECE hetrodyne radiometer has been upgraded to have the best radial resolution possible, limited by the layer width needed for the plasma to become opaque. The upgraded edge change exchange diagnostic makes simultaneous measurements of impurity ion temperature, density and flow velocity. Both diagnostics have a radial spatial resolution of 1*cm* or less under optimum conditions. Measurements of electron density on a corresponding scale are made with a multi-channel reflectometer.

H-MODE ION PROFILE EVOLUTION

The edge charge exchange diagnostic consists of two collecting lenses mounted at the top and bottom of the machine. The Doppler shift of charge exchange excited emission from a heating beam is resolved into toroidal and poloidal flow components. The intensity and broadening of the emission yields the density and temperature of the emitting species. The diagnostic collects light from eight spatial positions near the edge of the plasma.

In the new JET divertor configuration the H-mode transition is generally characterised by a rather gradual evolution of the D_α through an ELMy phase to a quiet H-mode. In such a case there is a slow development in the pressure profile. Several theories of the H-mode [1,2, for example] invoke a sheared poloidal $\mathbf{E} \wedge \mathbf{B}$ flow to account for the confinement changes. In the JET

measurements there is no evidence of such a flow in the impurity ions, implying that their diamagnetic flow speed is balanced by their $\mathbf{E} \wedge \mathbf{B}$ (or $v_{||}$) motion. The background ion diamagnetic flow would be greater than that of the impurities (for the same pressure profiles) due to their lower charge giving, in general, a different poloidal flow speed. Therefore it becomes important to study the time evolution of the radial electric field.

The chordal charge exchange measurements allow the determination of the radial electric field from the zero order force balance of the impurity ions,

$$\mathbf{E} = \frac{\nabla p}{Zen} - \mathbf{v} \wedge \mathbf{B}$$

In the slow H-transition cases, where the poloidal flow does not appear to change, the radial field evolution can be evaluated from the pressure gradients and the toroidal flows. Figure 1 shows the time development of the electric field profile in such a case. After 0.25 *s* the ELMs have ceased and the plasma remains ELM-free for the following two seconds.

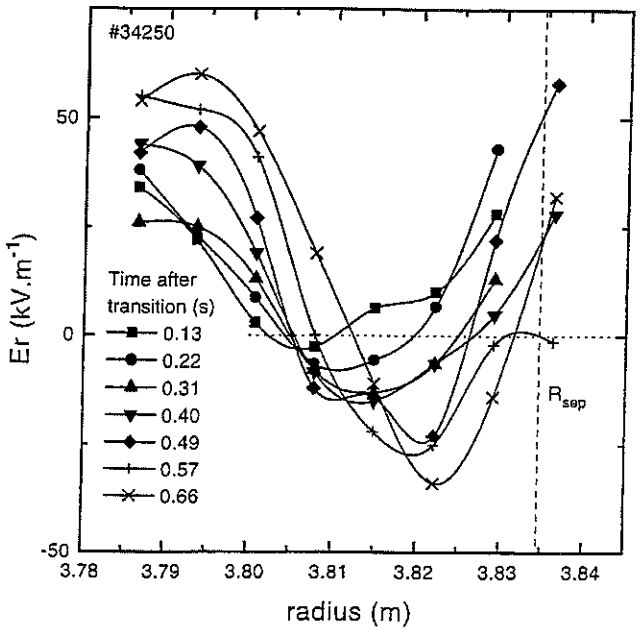

Figure 1: Time evolution of the radial electric field derived from measurements of the carbon impurity ion pressure and toroidal rotation profiles. In this instance the poloidal flow appears to be insignificant during the H-phase, although the measurements are noisy (limited by photon statistics) near the transition, and hence has been assumed to be zero throughout.

In this discharge the slow evolution of the pressure gradients lead to a slow change in E_r. The appearance of the negative electric field well is not established until after the quiet H-mode phase is entered at 0.25*s*. As the discharge evolves the boundary is moved outwards so that the position of the E_r well moves out from 3.805 to 3.825 *m* over the half second covered by the figure.

POLOIDAL VELOCITY MEASUREMENTS DURING ELMS

During strong neon gas puffing experiments a slow periodic ELM behaviour is established. Taken together with the bright emission from the neon impurity these conditions yield the most sensitive measurements of the poloidal flow. Figure 2 shows the time evolution of chords spanning the edge ion temperature gradient, together with the poloidal velocity signal of the chord located in the steep part of the temperature gradient, where the poloidal velocity has been found to be highest in the DIII-D measurements[3]. It is seen that there is no systematic change in the poloidal velocity between the ELMy and the quiescent H-phases, to within ~5 $km.s^{-1}$.

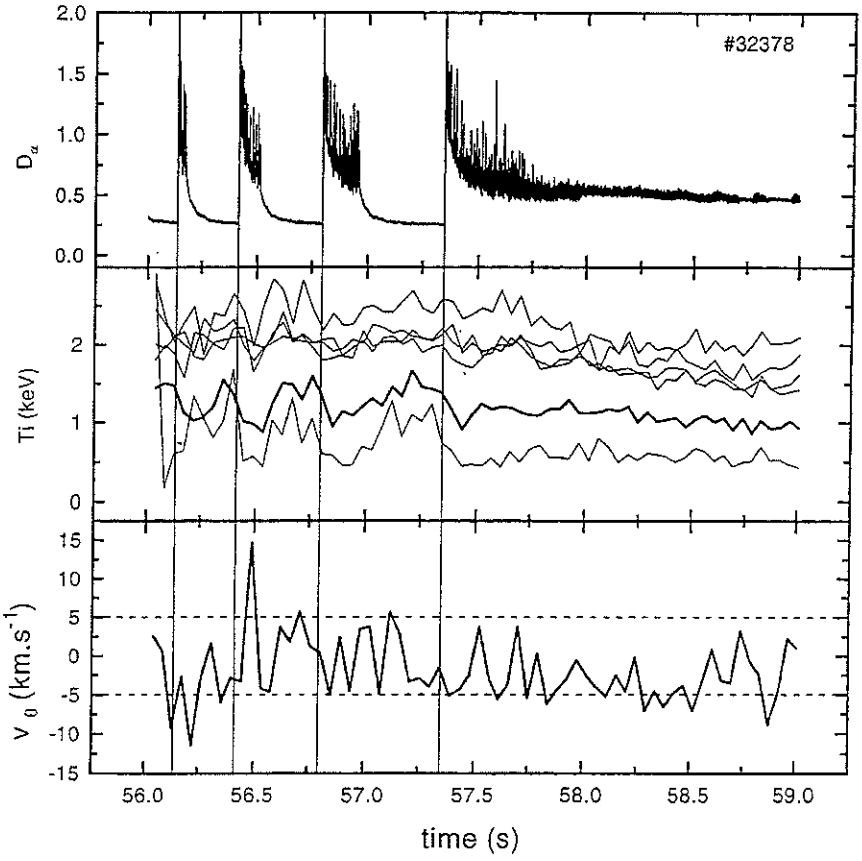

Figure 2: An example of a neon puffing experiment where the ELM behaviour becomes intermittent. The time traces show that for a chord located in the steep part of the T_i gradient there is no systematic change in the poloidal flow velocity between the ELM and quiescent H-phases.

PROFILE CHANGES DURING ELMS

During the slow ELMs the gradients of impurity density vary significantly compared to the

quiescent H-phase, whilst those of the ion temperature are almost unaffected, figure 3. The resiliance of the T_i profiles to ELMs is characteristic of most types of ELMs in JET. The profiles of poloidal flow velocity remain zero within the errors in the ELM, H and L phases.

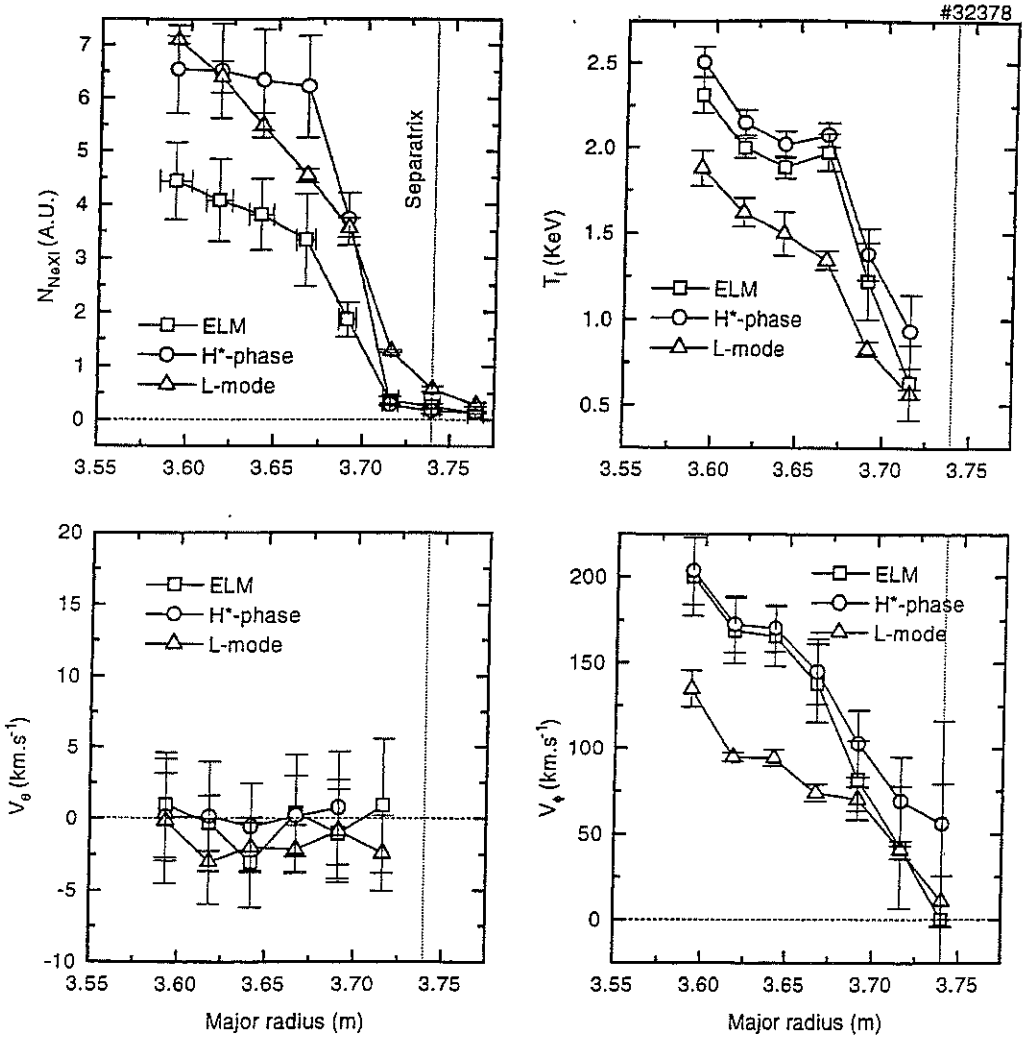

Figure 3: Profiles of neon impurity density, temperature and flow velocities during slow ELM events. Radial error bars represent the geometric space resolution of the measurement, vertical errors are ± one standard deviation of measurements over the respective time intervals.

ION TEMPERATURE GRADIENTS FROM SWEEPING

During high power discharges the X-point is swept at 4 *Hz* across the target to reduce local heat loading. This also has the effect of moving the separatrix position at the midplane where the charge exchange observations are made. When a single chord of the diagnostic intersects the steep part of the temperature profile then the sweeping takes this chord up and down the profile, modulating the temperature measurement, figure 4. The amplitude of this T_i modulation compared to the sweep amplitude provides a direct measurement of the gradient, and this is in agreement with the results from the profile measurements.

Gradients of T_i up to 66 $keV.m^{-1}$ have been recorded from adjacent chord differences, where neither chord lies in the gradient region.

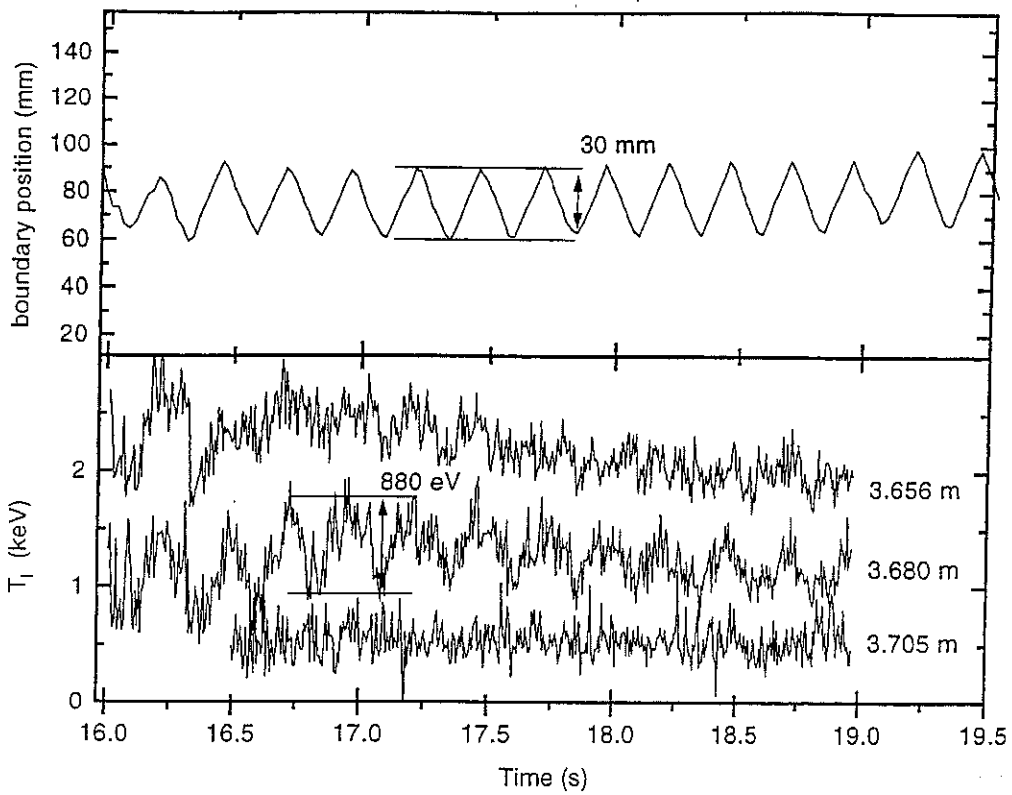

Figure 4: Variation in temperature for a chord viewing the steep part of an H-mode T_i profile when the plasma boundary is swept at 4 Hz. The amplitude of the temperature excursion directly yields a value for T_i' of 28 keV.m^{-1}, in agreement with the temperature difference between neighbouring chords.

FAST TRANSITION DATA

A fast H-mode transition was set up in order to study the changes in the profiles immediately before and after the H-transition with a magnetic geometry giving close to optimum diagnostic space resolution. Figure 5 shows the time evolution of D_α impurity density, temperature and poloidal flow during such an H-mode. At 19.25 *s* the D_α intensity falls abruptly coincident with a sawtooth crash and the transport barrier forms, as indicated by the ramp-up of the CVI density at the inner chords (R≤3.778*m*). In the 100 *ms* before the transition there is some evidence of transition ELMs, but no steepening of the impurity pressure profiles. There appears to be a small change in poloidal flow (~5 *km.s*$^{-1}$, in the ion diamagnetic direction) at the time of the transition at

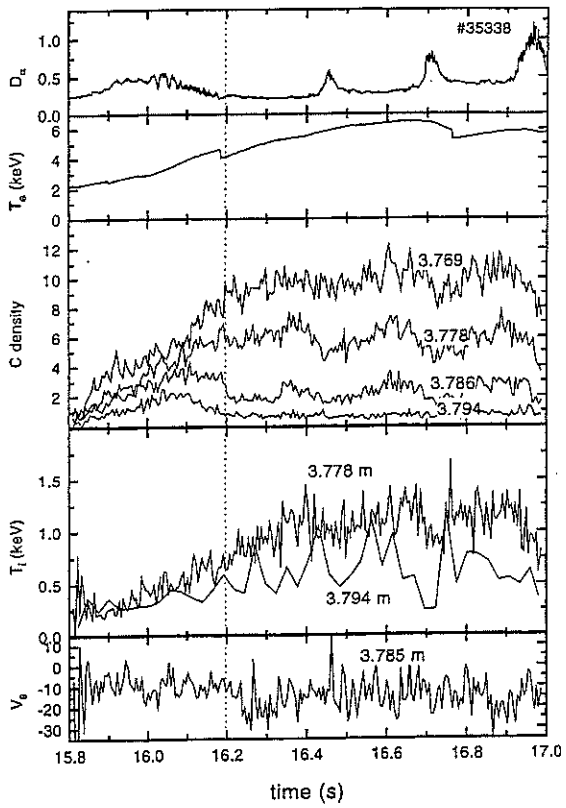

Figure 5: Time traces of impurity density, temperature and poloidal flow during a fast H-transition. Neutral beam injection is applied from 59.0 s. The poloidal flow at the outermost radial position shows a change of about 5 km.s^{-1} between the L and H-phases. Chords further inside the plasma show no systematic change at the transition, and fluctuations in the measurements are less than 5 km.s^{-1}.

3.802 *m*, at the edge of the transport barrier - inboard of this radius there is no change within the errors

Two radial profiles of electric field are shown in figure 6. The profiles have been obtained by averaging over 100 *ms* periods immediately preceeding and following the H-transition. The poloidal rotation (and errors in this measurement) dominate the total radial field, although, even 50 *ms* after the transition there is evidence of a negative field well appearing due to the p terms. However, from the time traces (figure 5) it is clear that this source of $\mathbf{E_r}$ develops linearly with time following the transition and hence is not involved in the physics of the transition itself.

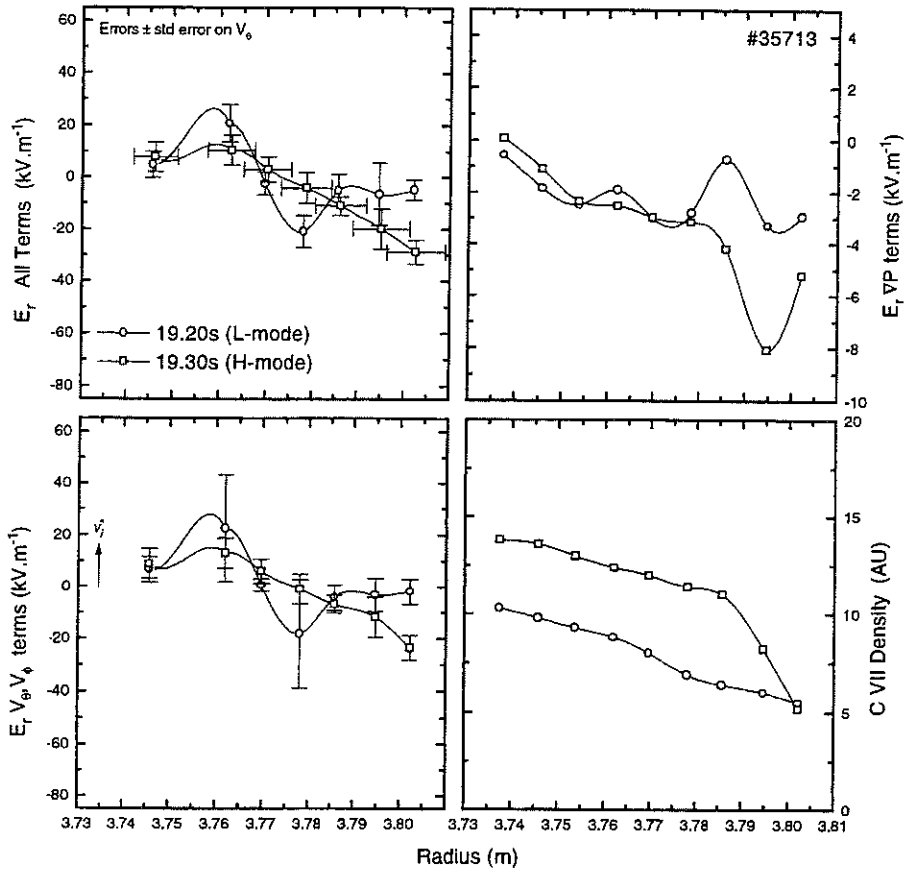

Figure 6: Profiles of the time evolution of E_r and its components obtained from the data of figure 5 at two times, 50 ms before and 50 ms after the H-transition. The vertical error bars are ± one standard error ($\sigma/\sqrt{N}$) and are taken from the v_θ measurements since these domiate the errors. The radial error bars represent the geometric resolution of the diagnostic. The separatrix position from EFIT is 3.843 m.

EDGE TEMPERATURE GRADIENTS

The profiles of figure 7 show the gradual evolution of edge plasma parameters before and during an H-mode. Steep gradients of both T_i and T_e are seen in the edge region, falling off sharply over approximately one ion poloidal gyroradius. Figure 8 shows the time behaviour of the T_i and T_e gradients. Since there is some uncertainty on the ECE radii from the calculated equilibrium fields, the maximum gradient at the edge of each profile is indicated. The two values agree quite closely, rising from ~10 *keV.m*$^{-1}$ at the start of the main heating pulse to over

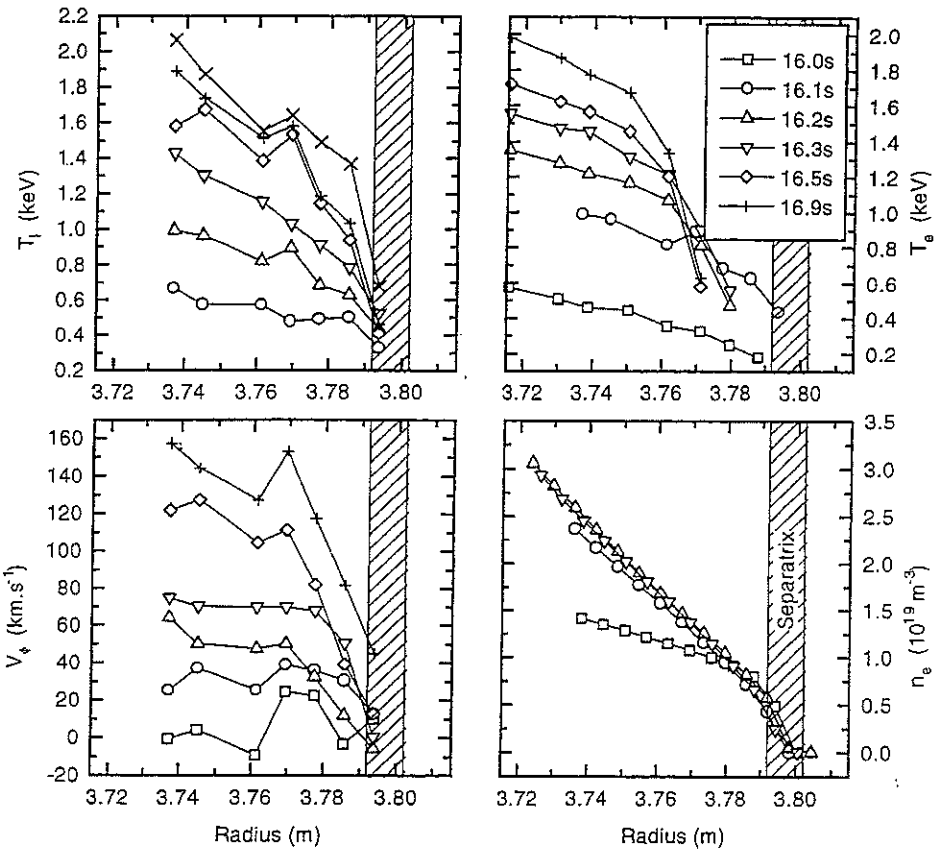

Figure 7: Profiles of ion and electron temperature and density over successive times of an H-mode.

65 $keV.m^{-1}$. The gradient is not seen to follow a local (toroidal) velocity shear, but rather the velocity evolution over a wider region, peaking when v_ϕ reaches reaches a maximum on the inner channel.

At a density of 10^{19} m^{-3} this maximum gradient gives a pressure gradient >100 $kPa.m^{-1}$. Since collisionality, $\nu*$, is low, a large parallel current density $j_{bs} \approx \varepsilon^{1/2}\nabla p/B_\theta \approx 500 kA.m^{-2}$ results from the bootstrap current. This is of the order of the central current density and so can, when fully developed, reduce local magnetic shear considerably. This must be taken into consideration when assessing, for example, ballooning and external kink stability of the edge.

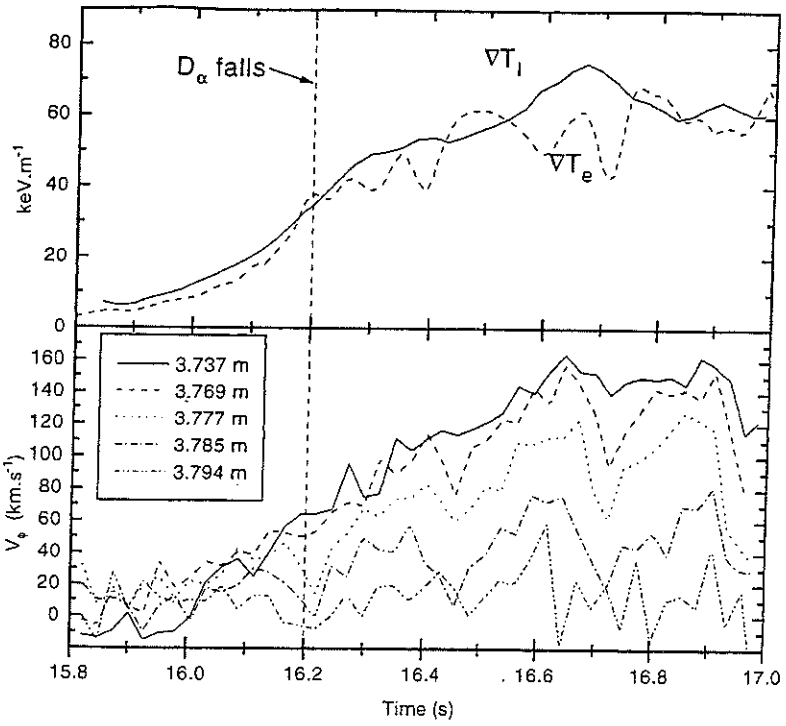

Figure 8: Time evolution of the peak ion and electron temperature gradients in an H-mode discharge.

CONCLUSIONS

An extensive dataset has been built up of edge impurity (C and Ne) poloidal rotation in the new JET. The evidence is that there is no such rotation in JET H-modes to within $|\upsilon_\theta|<5$ *km.s*$^{-1}$ within the region of the transport barrier, consistent with previous JET results[4]. Outboard of this region, the lower emission brightness results in larger errors although a slow drift in the electron diamagnetic direction is sometimes seen in the outermost channels. The $\mathbf{E}_r$ profile in JET develops a negative well at the transport barrier, relatively slowly as a consequence of confinement changes, not coincident with the H-transition.

Profiles of ion and electron temperature show strong gradients (up to 65 *keV.m*$^{-1}$). This implies the existence of a strong bootstrap current, of order of the central density, therefore considerably reducing local magnetic shear and hence affecting edge ballooning and kink stability.

In impurity puffing experiments an L-mode period following the H-mode shows that the T_i gradients are maintained. In general the T_i profile does not respond to ELMs while the density gradient undergoes a significant collapse.

REFERENCES

[1] K. C. Shaing, E. C. Crume Jr. and W. A. Houlberg, Physics of Fluids B, **2,** 6 (1990) 1492

[2] H. Biglari, P. H. Diamond and P. W. Terry, Physics of Fluids B, **2** (1990) 1

[3] P. Gohil *et al.,* Nuclear Fusion, **34**, 8 (1994), 1057

[4] N. C. Hawkes, Controlled Fusion and Plasma Physics, Proceedings of the 20th EPS, Lisboa, **17C** I (1993) 7

Edge Modes as ELM Events

O Pogutse[1], J G Cordey, W Kerner, B Schunke.
JET Joint Undertaking, Abingdon, Oxfordshire, OX14 3EA, UK.
[1] On leave from RRC Kurchatov Institute, Moscow, Russia.

1. INTRODUCTION

1. The **tokamak edge plasma** includes a part of the core plasma and a part of the scrape-off-layer about a few Larmor radii inside and outside the separatrix. These parts have quite different topology with open and closed magnetic field lines, respectively. Due to MHD activities these two areas can interact. Therefore, this edge plasma plays a critical role in the behaviour of the entire plasma.
2. With increasing edge temperature the dissipative instabilities in the edge plasma become weaker, the transport coefficients decrease and the gradients at the boundary increase. The profile of the pressure (along with temperature and density) becomes increasingly more step-like. For such steep gradients the Larmor radius stabilisation and the shear flow stabilisation take place, turbulence is suppressed and the **H-mode** is set up. Moreover, the development of a step-like pressure profile in the H-mode will lead to unstable MHD surface modes, which may explain the essential properties of the ELM phenomenon.
3. The MHD instability at first occurs near the X-point and gives rise to a precursor event. This instability throws out plasma from this region and destroys the separatrix in this point. Both these processes give a strong interaction with the end plates and the wall of the chamber.
4. Due to this interaction the region near the X-point is filled by cold dirty plasma with low conductivity. This "new" plasma acts like a new **effective low conducting limiter** for the main plasma just inside the separatrix, which becomes MHD unstable against surface modes. These surface modes have a relatively weak radial dependence which explains the macroscopic character of the ELM.
5. This model gives an estimate for the ELM repetition time and explains, in addition, the occurrence of two different time scales during a giant ELM. The initial rise ends with a fast MHD event removing a plasma layer from the periphery. The second phase is determined by the diffusive refilling of the expelled layer.

2. PERTURBED MHD EQUATIONS NEAR THE SEPARATRIX.

Coordinate System:

The magnetic field line geometry is described by the orthogonal coordinates ρ, ω, φ:

$$ds^2 = h_\rho^2 d\rho^2 + h_\omega^2 d\omega^2 + R^2 d\varphi^2 , \tag{1}$$

with $h_\rho^2 = h_\omega^2 = h^2$

$$h^2 = \frac{y_0^2}{2^{5/2}} \cdot \frac{1}{[1-\cos(\omega)+\rho^2/2]^{1/2}}; \tag{2}$$

y_0 is the distance of the current wire from the X-point. For $\rho << 1$

$$h^2 = \frac{y_0^2}{4} \cdot \frac{1}{[\omega^2+\rho^2]^{1/2}} \tag{3}$$

$$R = R(\rho,\omega) = R_0 + x(\rho,\omega), \tag{4}$$

$$x(\rho,\omega) = (+/-)y_0/\sqrt{2} \cdot [-1+\cos(\omega)+\rho+\sqrt{2}(1-\cos(\omega)+\rho^2/2)^{1/2}]^{1/2}. \tag{5}$$

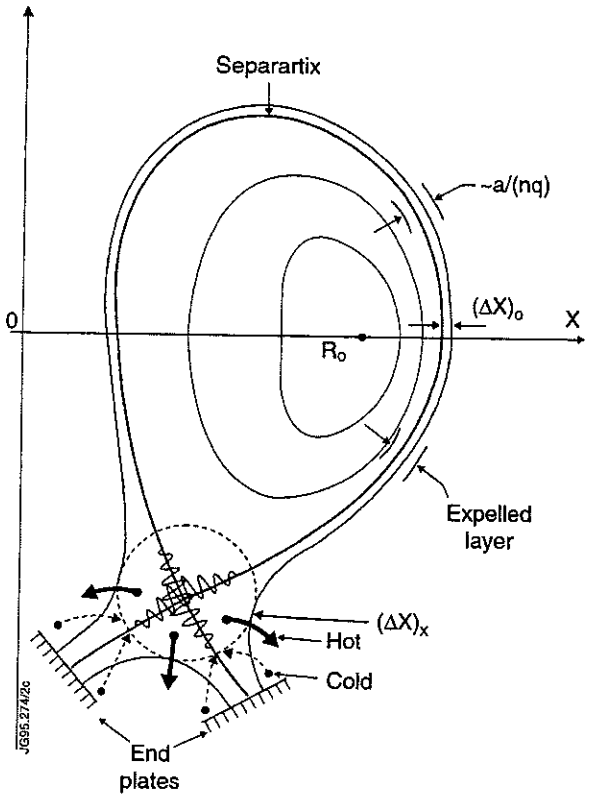

Figure.1

for $\rho << 1$.

$$x(\rho,\omega) = (+/-)\frac{y_0}{\sqrt{2}} \cdot [\rho + (\omega^2+\rho^2)^{1/2}]^{1/2}$$

(H.Niedermeyer et al 1991 Proc. 18th European Conf. on Control. Fusion and Plasma Physics (Berlin, 1991) vol 1 (Vienna: IAEA) p. 301.

W.Kerner et al., Bull. Am. Phys. Soc. 36 (1991) 2R13, p. 2310.)

MHD ballooning equation:

Eikonal representation for perturbed electrostatic potential (J.W. Connor, R.J.Hastie and B.Taylor, Proc. R. Soc. Lond. A.365, 1, 1979):

$$\phi(t,\rho,\omega,\phi) = \tilde{\phi}(\rho,\omega)\cdot\exp(-\gamma t + in\int_{\omega 0}^{\omega} q(\rho,\omega')d\omega' - in\varphi) \tag{6}$$

leads to:

$$R\left(\frac{B_\omega}{hB_0}\frac{\partial}{\partial\omega}\right)\frac{1}{R}\left(\frac{nq}{h}\right)^2(1+\zeta^2)\left(\frac{B_\omega}{hB_0}\frac{\partial}{\partial\omega}\right)\tilde{\phi} - \gamma^2 C_A^{-2}\left(\frac{nq}{h}\right)^2(1+\zeta^2)\tilde{\phi}$$
$$- \frac{4\pi}{RB_0}\left(\frac{nq}{h}\right)^2\frac{1}{h^2}\left(\frac{\partial}{\partial\rho}\frac{R}{B_0} - \zeta\frac{\partial}{\partial\omega}\frac{R}{B_0}\right)\frac{dP_0}{d\rho}\tilde{\phi} = 0 \tag{7}$$

Safety factor:
$$q = q(\rho,\omega) = \frac{B_0 h}{B_\omega R}, \tag{8}$$

shear:
$$\zeta = \zeta(\rho,\omega,\omega_0) = \left(\frac{\partial}{\partial\rho}\int_{\omega_0}^{\omega} q d\omega\right)/q \tag{9}$$

3. STABILITY ANALYSIS

Normalised ballooning equation:

$$\tilde{R}\left(\frac{\partial}{\partial\omega}\right)\frac{1}{\tilde{R}}(1+\zeta^2)\left(\frac{\partial}{\partial\omega}\right)\tilde{\phi} - \Gamma^2\tilde{h}^4(1+\zeta^2)\tilde{\phi} + \beta^*\tilde{h}^2\left(\frac{\partial}{\partial\rho}\tilde{R}^2 - \zeta\frac{\partial}{\partial\omega}\tilde{R}^2\right)\tilde{\phi} = 0, \tag{10}$$

$$\Gamma^2 = \gamma^2\frac{q(\rho,\pi)^2 R(\pi)^2}{C_A^2}, \quad \beta^* = -4\pi\frac{R(\pi)^2 q(\rho,\pi)^2}{h(\pi)^2 B_0(\pi)^2}\frac{dP_0}{d\rho} = \frac{-4\pi}{B_\omega(\rho,\pi)^2}\frac{dP_0}{d\rho}, \tag{10a}$$

$\tilde{R} = R/R(\pi)$, $\tilde{h} = h/h(\pi)$.

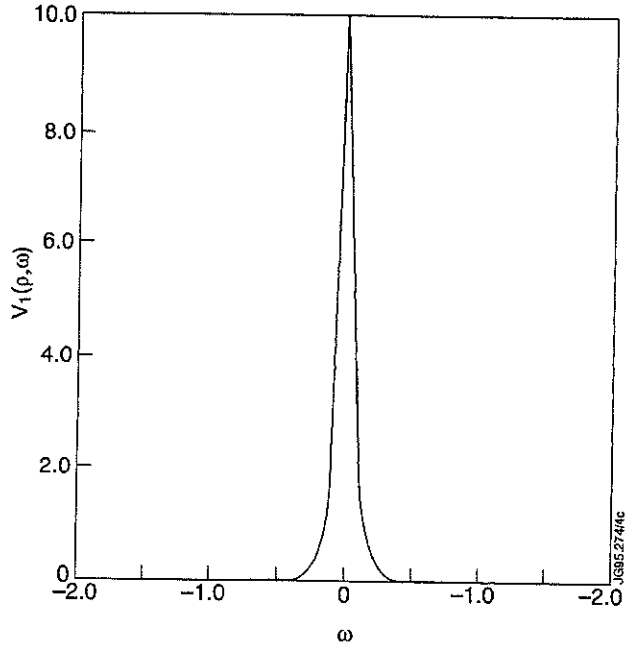

Fig. 2. Stabilising part of potential.

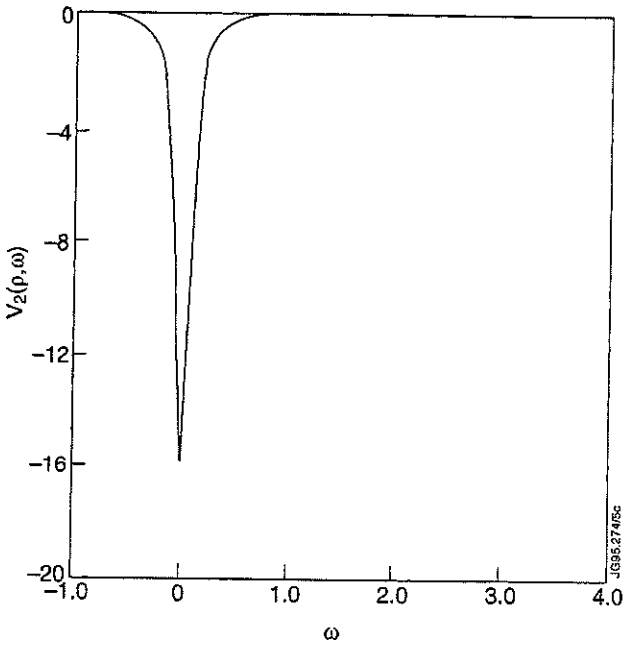

Fig. 3. Destabilising part of potential.

$\Rightarrow$ Effective potential is localised near the X-point.

Near the X-point the ballooning equation with the new variable $t = \omega/\rho$ reads:

$$\frac{\partial}{\partial t}(1+t^2)\frac{\partial}{\partial t}\tilde{\phi} - \Gamma^2\tilde{\phi} + \hat{\beta}\frac{[1+(1+t^2)^{1/2}]^{1/2}}{(1+t^2)^{1/2}}\tilde{\phi} = 0\,, \tag{11}$$

$\hat{\beta} = \frac{\sqrt{2}y_0}{R(\pi)}\rho^{1/2}\beta^* = -\sqrt{2}\cdot 4\pi\frac{R(\pi)}{y_0}\frac{q(\rho,\pi)^2}{B_0(\pi)^2}\rho^{1/2}\frac{dP_0}{d\rho}$ is the normalised beta.

Introducing the function u(t): $\tilde{\phi}(t) = \frac{1}{\sqrt{1+t^2}}u(t)$, leads to:

$$u_{tt}'' + (E - V(t))u = 0\,, \tag{12}$$

where E = 0 and the "potential" V(t) is:

$$V(t) = \left(\frac{\Gamma^2}{(1+t^2)} + \frac{1}{(1+t^2)^2} - \hat{\beta}\frac{[1+(1+t^2)^{1/2}]^{1/2}}{(1+t^2)^{3/2}}\right). \tag{13}$$

Equation (12) can be derived from the variation form:

$$W = \frac{1}{2}\int_{-\infty}^{\infty}[(u_t')^2 + V(t)\cdot u^2]dt. \tag{14}$$

Choosing the trial function $u(t) = c_1$, where c_1 is constant and varying c_1 yields the condition for the growth rate $\int_{-\infty}^{\infty} V(t)dt = 0$. The resulting threshold beta (for $\gamma = 0$), is:

$$\hat{\beta} = \frac{\sqrt{2}y_0}{R(\pi)}\rho^{1/2}\beta^*. \tag{15}$$

The condition for instability $\hat{\beta} > \hat{\beta}_{cr}$ expressed in parameters at the mid-plane is:

$$\frac{q(\pi)^2 4\pi P_0}{B_0(\pi)^2} > \frac{1}{2^{3/2}}\frac{y_0}{R(\pi)}\left(\frac{(\Delta x)_0}{y_0}\right)^{1/2} \propto \frac{b}{R_0}\left(\frac{(\Delta x)_0}{b}\right)^{1/2}. \tag{16}$$

Approximating $y_0 \sim b$ and $\frac{dP_0}{d\rho}$ as $\frac{P_0}{\Delta\rho} \sim \frac{P_0}{\rho}$, where $\rho \sim \Delta\rho \approx (\Delta x)_0 / y_0$, x_0 is the pressure gradient length on the separatrix in the mid-plane and $B_0(\pi)$ is the toroidal magnetic field of the magnetic axes.

Introducing the pressure gradient near the X-point

$$\frac{q(\pi)^2 4\pi P_0}{B_0(\pi)^2} > \frac{y_0}{R(\pi)}\left(\frac{(\Delta x)_0}{y_0}\right)^{1/2} \propto \frac{(\Delta x)_X}{R_0}, \tag{16a}$$

where $(\Delta x)_X \approx ((\Delta x)_0 y_0)^{1/2}$.

The safety factor $q(\pi) \equiv q(\rho,\pi)$ near the separatrix is related to q by the relation $q(\rho) = q(\rho,\pi)\cdot\Lambda$, where $\Lambda = 2/\pi \ln(4\pi/\rho)$, then $q_{95} \approx 3\cdot q(0.1,\pi)$.

The previous result for the slab SOL model (W. Kerner and O. Pogutse, in proceedings of 21st EPS Conference Controlled Fusion and Plasma Physics, Montpellier, France, 1994.) is:

$$\frac{q^2 4\pi P_0}{B_0^2} > \frac{(\Delta x)_0 R q^2}{L_\parallel^2} \propto \frac{(\Delta x)_0}{R}, \tag{17}$$

Here $L_\parallel$ is the connection length - the distance between the end plates along the magnetic field line, $L_\parallel \propto qR$.

4. ELM MODEL

Nonlinear evolution:

i) Interchange instability occurs near X-point.

Plasma tube of width $(\Delta x)_X \approx ((\Delta x)_0 y_0)^{1/2}$ (18)

is expelled and dumped onto the target plates in time:

$$\tau_1 \approx [(\Delta x)_X R]^{1/2} / C_s . \quad (19)$$

Related energy loss

$$\delta_X = \frac{\Delta W_X}{W} \approx \frac{\pi (\Delta x)_X^2}{\pi ab} \frac{P_{0edge}}{< P_0 >} \quad (20)$$

For $(\Delta x)_0 \sim 0.1$m, a ~ 1m, b ~ 1.5m and $P_{0edge}/P_0 \sim 10^{-1} \Rightarrow \delta_x \sim 10^{-3}$.

ii) Expelled plasma interacts with target plates, the X-point region is filled with cold dirty plasma. This plasma with low conductivity plays role of **"an effective limiter"**.

$\Rightarrow$ Plasma inside separatrix obeys unfrozen boundary conditions;

$\Rightarrow$ **Plasma inside separatrix unstable to flute type instability with growth time:**

$$\tau_2 \approx [(\Delta x)_0 R]^{1/2} / C_s ;$$

this results in a **Giant ELM**

iii) Refilling of edge region by diffusion of energy and particles from plasma core

$$\tau_3 \approx \tau_E (\Delta a / a)^2 \approx \tau_E / (nq)^2$$

(V.V.Parail et al, "The Physics of L and H-Mode confinement in JET", 15th IAEA Conf. on Plasma Phys. and Cont. Fusion Res., Seville, Spain, 1994.)

SCALING

effective radial width $\Delta a \propto a/nq_{95}$

plasma layer of width Δa peeled off nonlinearly

energy loss

$$\Delta W \approx 2\pi ab \frac{P_{0edge}}{(nq)} \tag{21}$$

$$\delta = \frac{\Delta W}{W} \approx \frac{2P_{0edge}}{(nq) < P_0 >} . \tag{22}$$

$\approx 5\%$ ($n \approx 1$, $q \approx 5$)

Time to restore the lost energy by diffusion from core

$$\frac{1}{\tau} = \frac{P}{\Delta W}, \tag{23}$$

with $W = 2ab\langle P_0 \rangle$; $\tau_E \approx W / P$

$$\tau \approx \frac{2\pi abP_{0edge}}{(nq)P} \approx \frac{1}{nq} \frac{W}{P} \frac{P_{0edge}}{< P_0 >}, \tag{24}$$

For $n \sim 1$, $q \sim 5$, $P_{0edge}/\langle P_0 \rangle \sim 0.1 \Rightarrow \tau \approx 10^2 \tau_E \sim 1$ms.

ELM frequency:

$$f = \frac{1}{\tau} \propto nq \frac{P}{W} H_p \propto \frac{PH_p}{I^3 (\Delta x)_0^{1/2}}, \tag{25}$$

I: plasma current, P: heating power, $H_p = \langle P_0 \rangle / P_{0edge} \propto P_0(0)/\langle P_0 \rangle$: peakness factor.

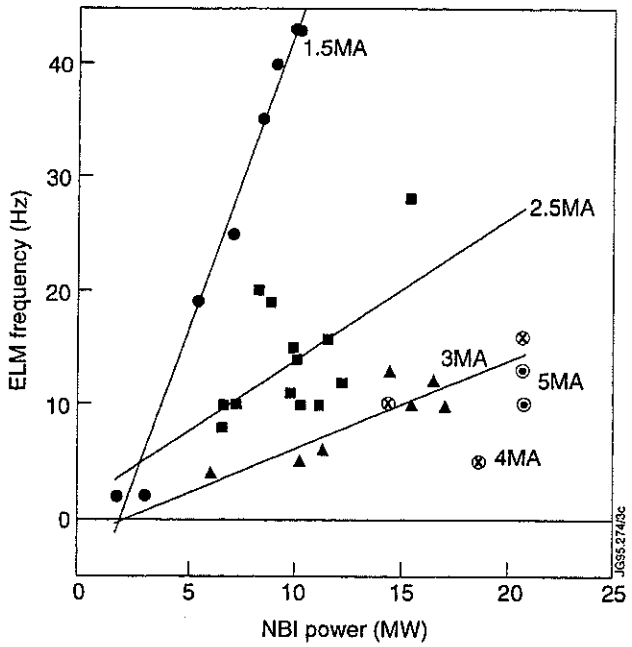

Figure.4

5. CONCLUSIONS

1. The separatrix changes qualitatively the condition for the existence of interchange MHD instabilities. With a separatrix the edge perturbations are localised mainly near the X-point.
2. The threshold beta for the perturbations which occur just outside the separatrix is given by (16). It is found that these perturbations become more easily unstable than the corresponding internal perturbations. The internal perturbations experience the stabilising effect of the magnetic well, which is absent for external perturbations.
3. These perturbations can remove only a small part of the total stored energy and destroy the magnetic separatrix near the X-point.
4. These effects lead to a filling of the X-point region by cold and dirty plasma due to the interaction with the end plates or the wall of the chamber. This cold plasma with low conductivity acts like an **effective limiter** for the plasma tube with the width of $\Delta a \approx a / (nq)$ inside the separatrix. It destabilises the interchange instability of the main plasma (Fig. 1).
5. From this scenario we can estimate the frequency of the ELMs, its dependence on the plasma current, on the heating power and on the peakness factor (25).
6. The entire process includes three stages: 1) appearance of the interchange instability near the X-point and filling of this region by dirty, cold plasma; 2) triggering of the major interchange instability due to unfreezing and 3) refilling of the empty region inside the separatrix by hot plasma from the centre on the diffusion time scale (Fig. 5).
7. There is a reasonable correlation between the above theoretical predictions and the experimental results.

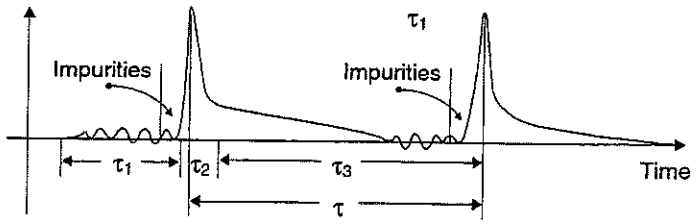

Figure.5

The Effects of ELMs on the Plasma Edge of JET

J Lingertat, B Alper, S Ali-Arshad, P E Bak[1], S Clement, P Coad, I Cortes[2], N Deliyanakis, J Ehrenberg, A Loarte, R Monk[3], L Porte, R Prentice, A Tabasso[1], and the Divertor Task Force and Topic Group.

JET Joint Undertaking, Abingdon, Oxfordshire, OX14 3EA, UK.

[1] Imperial College, Plasma Physics Department, Prince Consort Road, London, SW7 2BZ, UK.

[2] Asociacion Euratom/Ciemat, 28040 Madrid, Spain.

[3] Royal Holloway College, University of London, Surrey, TW20 0EX, Uk.

INTRODUCTION

ELMs are an unavoidable ingredient of H - mode plasmas in tokamaks. They are associated with a pulse-like release of energy and particles from the main plasma into the divertor. This may adversely affect the divertor operation or in the case of high power operation even damage the divertor target plates. On the other hand, it is well known that ELMs are beneficial in reducing the density and impurity build-up in H-mode discharges. To exploit these beneficial features of the ELMs and to avoid the detrimental ones a thorough understanding of their generation and energy release mechanism is necessary. This paper focuses on the details of the ELM - triggered energy and particle release into the divertor.

For analysis mostly giant ELMs have been used which are observed after the ELM - free phase of high performance NB-heated discharges [1].

SUMMARY OF RECENT JET RESULTS

During an ELM the release of energy and particles from the main plasma into the divertor happens in a sequence of three phases:

- Phase I the "precursor" phase with a characteristic time of $\delta t_p < 100$ µs,
- Phase II the "plasma edge determined" phase with a characteristic time $\delta t_e \sim 100$ s,
- Phase III the "confinement degradation" phase with a characteristic time $\delta t_c \sim 10 - 50$ ms.

Phase I

The precursor phase is observed at the divertor as a perturbation of the floating potential measured by the target Langmuir probes. Since the floating potential is mainly determined by the electron temperature, this phase may be regarded as the beginning of the increase of the power flux into the divertor caused by enhanced electron heat conduction. The total amount of deposited energy on the divertor target plates is below the detection limit (10^4 J).

Phase II

During the plasma edge determined phase, up to several percent of the main plasma stored energy is released into the divertor. This energy is removed from the outer region of the plasma column and assumed to be transported mainly by electron heat conduction. The maximum parallel power flux may reach values of 10^4 MW/m^2. A transient connection between the target surface and a plasma of ~ 300 - 400 eV gives the right order of magnitude for the measured power flux.

During this phase the strike points of the separatrix move rapidly (< 100 μs) inwards (inner strike point) and outwards (outer strike point). The energy deposition has its maximum at the new position of the inner strike point. This is different from the quiescent phase, where the power flux peaks at the outer strike point. The strike points move by ΔR_s ~ 20 cm. For the inner strike point ΔR_s may be so large that the main energy is released outside the divertor target onto structures of the inner wall.

Assuming the plasma column to behave like a rigid body the observed movement of the strike points translates into a movement of the main plasma upwards and inwards with Δz~10...20 cm and ΔR_p~5...10 cm.

The high power flux pulse causes a release of impurities and deuterium from the affected areas which leads to the D_α - intensity peak usually associated with an ELM, to a peak in the radiated power and to an increase of the plasma density. The amount of released material and working gas depends on the history of the surface hit by the power flux pulse. However, it is generally large because the target areas involved are regions with loosely bound deposition layers of non - stochiometric mixtures of impurities and working gas.

Finally, the impurity/deuterium release triggers a deterioration of the global plasma energy confinement.

Phase III

During the confinement degradation phase the plasma loses particles and energy due to a drop in the relevant confinement times. This drop shows in most cases the features of an H $\rightarrow$ L transition [2].

The loss of particles leads to a decrease in the total particle content of the main plasma. The time evolution of the averaged density depends on the balance between the increase due to the injected impurities and deuterium during phase II and the subsequent decrease in the particle confinement time.

The loss of energy leads to an enhanced power flux to the target plates. This energy is deposited at the initial position of the strike points with an outside /inside ratio of the power flux commonly observed during H $\rightarrow$ L transitions. The total amount of energy lost during phase III depends on the amount of confinement degradation and is usually larger than the energy loss during phase II.

After the H → L transition the plasma recovers within several 10 ms and goes again into the H mode. However, depending on the amount of injected impurities the plasma may show a reduced H factor or even after a sequence of giant ELMs remain in the L mode.

Experimental results

Fig.1 shows as an example the time evolution of the main plasma parameters during a typical discharge used in the following analysis.

The fine structure of the soft X-ray intensity perturbation caused by an ELM is shown in fig. 2. Here, the perturbation starts at the top of the plasma, moves down to the X-point and again up to the top. Note, However, that ELMs have been observed which start near the X-point region. There is no evidence of the outer midplane being the originas in [3]. The fastest time scale found in this data is ~10 μs which may be associated with the precursor time scale δt_p. The total time of the perturbation is ~100 μs. This time interval is associated with the phase II time scale δt_e.

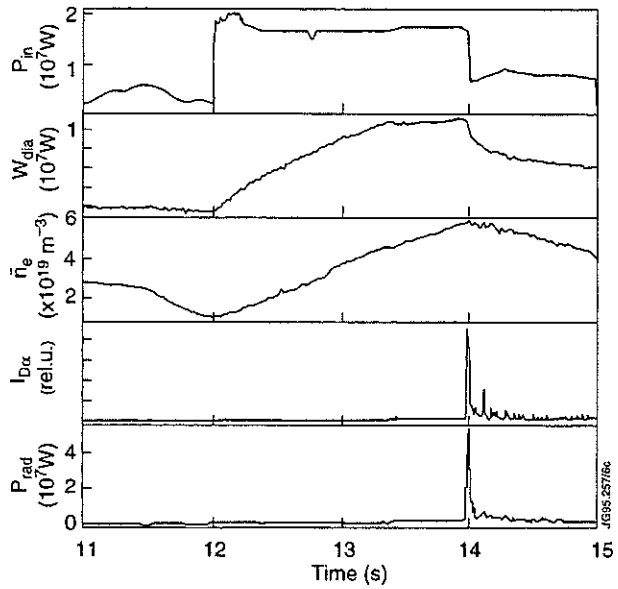

Fig. 1 Typical plasma parameters of a NB heated high performance discharge with one giant ELM, pulse 33649, B_t = 3.3 T, I_p = 3.5 MA.

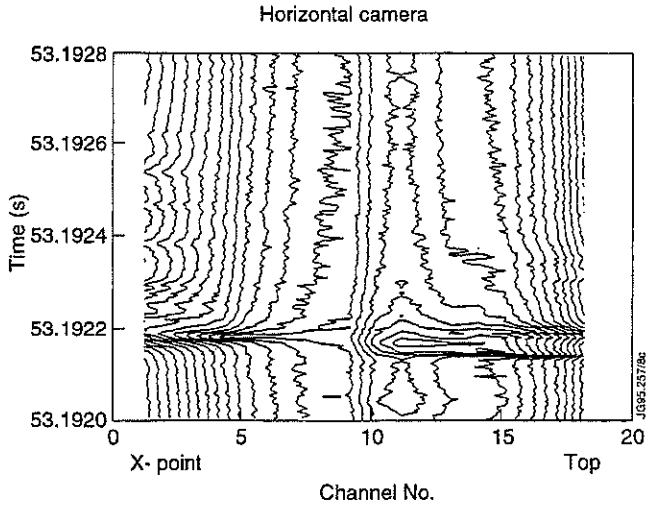

Fig. 2 Contour plot of the soft X-ray intensity as a function of time measured by a horizontal camera with 18 lines of sight, pulse 33701

Fig.3 shows the perturbation of the floating voltage during an ELM to start δt_p ~ 50 μs earlier than the density increase. This feature is not observed with every ELM and the time delay may vary between δt_p = 10 μs and 100 μs. Often the floating voltage precursor is correlated with precursors observed by the reflectometer and by magnetic probes.

A comparison between the time of arrival of the floating voltage perturbation on the outer and inner strike zones shows no time difference within 20 μs. However, there is a time difference of

0.5...1 ms between the signals obtained by a reciprocating probe inserted near the top of the plasma and the target probes [4]. This implies the X-point region to be the origin of the perturbation [4,5,6].

The floating voltage on the target plate is generally positive in the inner strike zone, negative in the outer strike zone and zero in the private flux region. This is caused by a thermoelectric current flowing from the outer to the inner strike zone [7]. During an ELM the floating voltage of probes which are located near the original strike point and inside the SOL drops to zero within the time resolution of the diagnostic t = 200 µs (fig.4). This suggests that the strike points move rapidly during an ELM thereby enlarging the private flux region. The new transient position of the strike points can be found by determining that probe in the target probe array which shows the largest and longest pulse of ion saturation current. The transient position determined in this way corresponds well with the results from the IR camera shown in figs. 5 and 6 and with profiles obtained from flux cameras which are measuring the spatial distribution of photon fluxes of the D_α line and of CII or BeII lines.

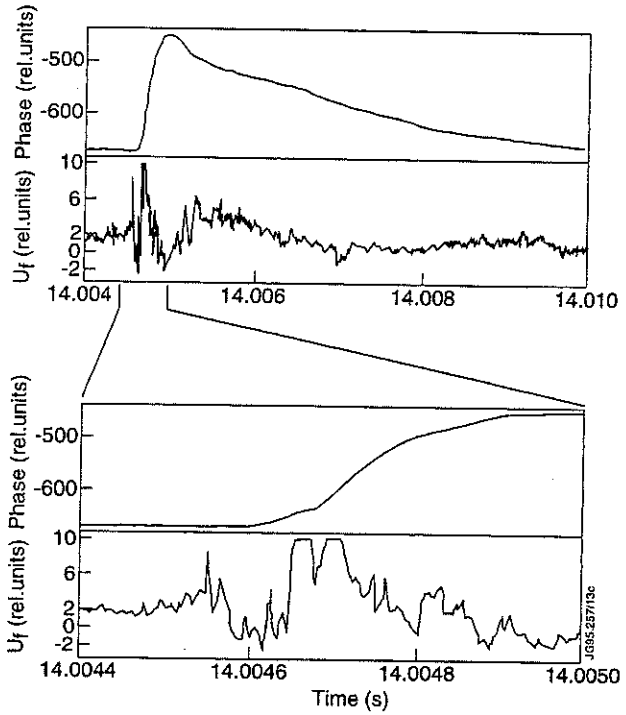

Fig. 3 Phase signal from the divertor interferometer (proportional to the line integrated density in the outer divertor leg) and floating voltage from a target Langmuir probe in the outer strike region as a function of time during an ELM, pulse 32303.

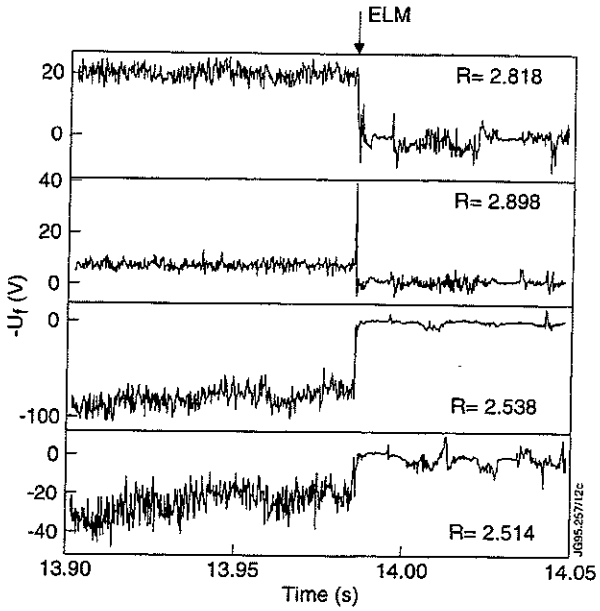

Fig. 4 The reaction of floating voltages measured by Langmuir probes located at different radii on the divertor target during an ELM, pulse 33649.

Figs. 5 and 6 show the temperature maxima at the initial strike point position to be virtually constant over the chosen time interval. That means a rather low power flux is flowing towards the strike points even during an ELM. However, additional temperature peaks appear in the scrape-off layer during the ELM. The peak in the inner SOL is much larger than the peak in the outer SOL. These additional temperature peaks disappear usually within 2 ms. The observed behaviour of the temperature can be explained by assuming a short pulse of power hitting the target plate outside the initial strike points. The length of the power pulse is estimated to be < 200 µs

from fig.4. For an estimation of the order of magnitude of the power flux this length is set exactly to δt_e = 100 μs which is taken from the total length of the soft X-ray perturbation in fig.2. The power flux pulse is assumed to be rectangular. Using simple 1-D heat conduction formulae together with the thermal data of the bulk target material an absorbed power flux of $q_{abs} \sim 2 \times 10^3$ MW/m^2 is obtained for shot 33648 which corresponds to a parallel power flux $q_{par} \sim 2 \times 10^4$ MW/m^2. Using a plasma wetted target area S ~0.5 m^2 the total absorbed power becomes $P_{abs} \sim 1 \times 10^3$ MW and the total dumped energy $\Delta W \sim 1 \times 10^5$ J. The calculated power flux may be overestimated because the effective thermal conductivity of the deposition layers may be substantial smaller than the value used for the bulk material. On the other hand the maximum temperature rise is underestimated due to spatial averaging of the thermal radiation intensity.

The observation of multiple peaked and broadened profiles on the divertor target reported previously [4] is caused by poor time resolution of the diagnostic instruments.

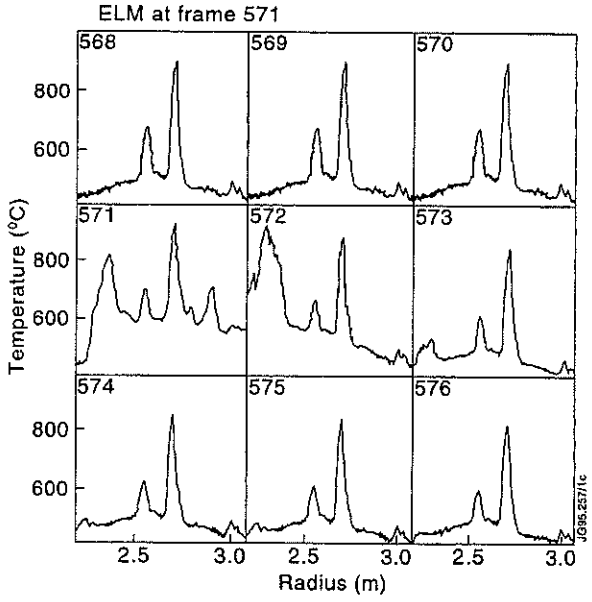

Fig.5 Evolution of the target temperature profile before, during and after an ELM, pulse 33649.

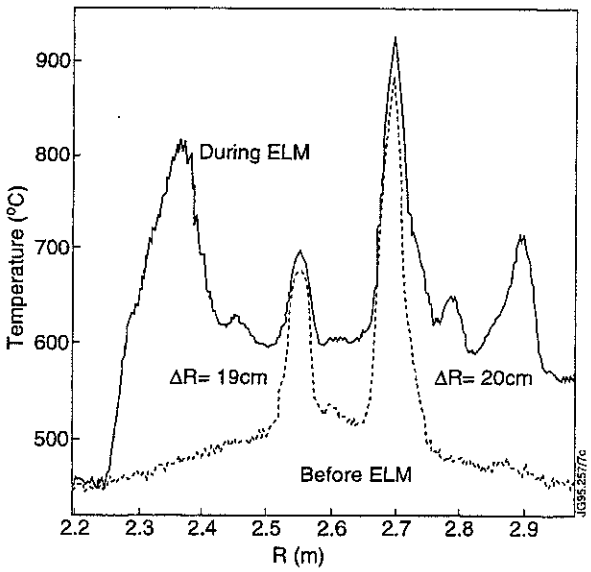

Fig.6 Comparison of the target temperature profiles before and during an ELM, pulse 33649.

The short time scale of the power flux pulse suggests the electron heat conduction plays the major part in the transport of energy [8]. A simple estimate of the necessary T_e drop to drive a power flux of 10^4 MW/m^2 using the 2-point model [9] gives T_e = 340 eV. Plasma with 340 eV is located within a few cms inside the closed flux surface region. This is approximately the position, where the ECE radiometer shows the ELM perturbation to start [10]. In this scenario the plasma instability following the precursor destroys for δt_e ~100 μs the closed flux surfaces within a few cms of the separatrix and unloads the energy and particle content to a target region deep within the inner SOL.

Assuming the plasma to behave like a rigid body during the short time period δt_e, the X-point together with the whole plasma column moves inwards and upwards during an ELM. This movement is shown schematically in fig.7 together with the profile of the floating voltage before and during an ELM. There is some additional evidence of a vertical jump of the plasma column during an ELM from the evaluation of the time behaviour of the soft X-ray centroid. However, the interpretation of these data is not free from ambiguity. Whether such a jump is responsible for vertical disruptions which seem sometimes to be correlated with the occurrence of giant ELMs remains an open issue.

Fig. 8 shows the different time behaviour of the electron temperature and ion saturation current, and of the D_α intensity during an ELM. The electron temperature always seems to increase first followed by I_{sat} and I_{D_α}. However, the observed time differences are marginal and are within the resolution of the measurement. Much more evident is the different length of the three signals. These results fit into a model where the energy deposition is started by electron heat conduction followed by a rise in the particle flux and maintained by the release and recycling of deuterium.

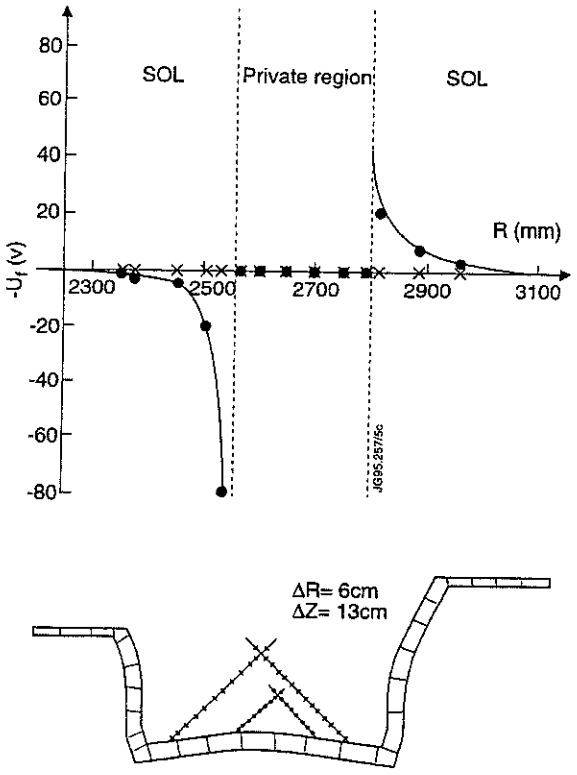

Fig.7 Reconstruction of the movement of the X-point from the measured movement of the strike points together with the floating voltage distribution on the target plate before and during an ELM, pulse 33649

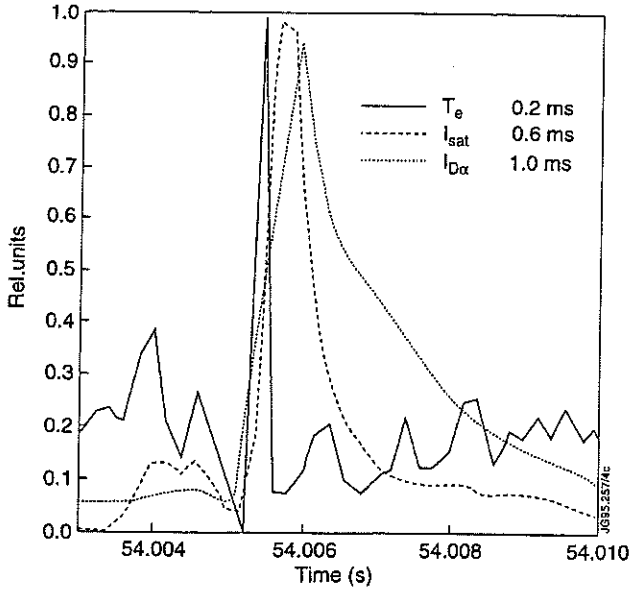

Fig.8 Time behaviour of the electron temperature T_e, the ion saturation current I_{sat} and the D_α intensity I_{D_α} during an ELM, pulse 32303, inner strike zone.

Fig.9 shows the development of the maximum temperature at the outer strike point during an ELM in a larger time scale (compared to fig.5). After the ELM the temperature increases over a time interval of 40 ms. This increase is caused by the confinement degradation or H→L transition in phase III. The absorbed power flux q_{abs} estimated from the temperature increase is q_{abs} ~24 MW/m^2 which corresponds to a total energy loss of ΔW ~0.5 MJ or 5 % of the diamagnetic energy. After this loss the target surface temperature stays constant again which corresponds to a low power flux, i. e. an H-mode behaviour.

The D_α and CII radiation intensity show in this time scale a narrow peak, the width of which is mainly determined by the time resolution of the flux cameras (5 ms), followed by a much broader peak. The first peak is assumed to be caused by deuterium and impurity release during phase II, the second one by the H→L and the following L→H transition.

The energy balance of an ELM using the experimental data can not be established. For pulse 33648 we obtain for the radiated energy W_{rad} ~1.1 MJ, for the energy dumped on the target plate in phase II ΔW_{fast} ~0.2 MJ and for the slow contribution during phase III ΔW_{slow} ~0.4 MJ. This gives a total loss of W 1.7 MJ which has to be compared with the drop in stored energy ΔW_{dia} ~1 MJ. The reason for this discrepancy is unclear.

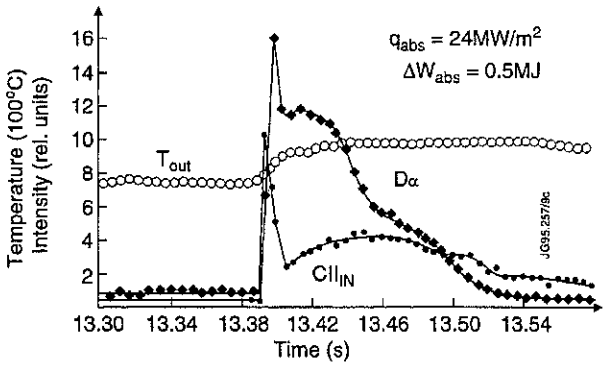

Fig.9 Time evolution of the maximum target temperature at the outer strike point T_{out}, the average of the maximum D_α intensity at the inner and outer strike point $\overline{D}_\alpha$ and the maximum of the CII radiation intensity at the inner strike point CII_{IN} during an ELM, pulse 34458.

The behaviour of the bulk plasma density during an ELM is shown in fig.10. There is an initial rise of the density in a time of 500 μs (phase II) followed by a much slower decrease (H→L transition) and eventually an increase (L→H transition).

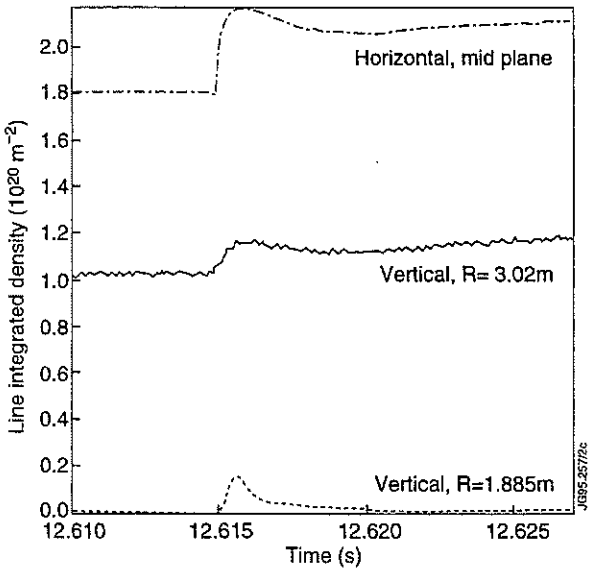

Fig.10 Time evolution of the line integrated density during an ELM obtained by different channels of the main plasma interferometer, pulse 35267.

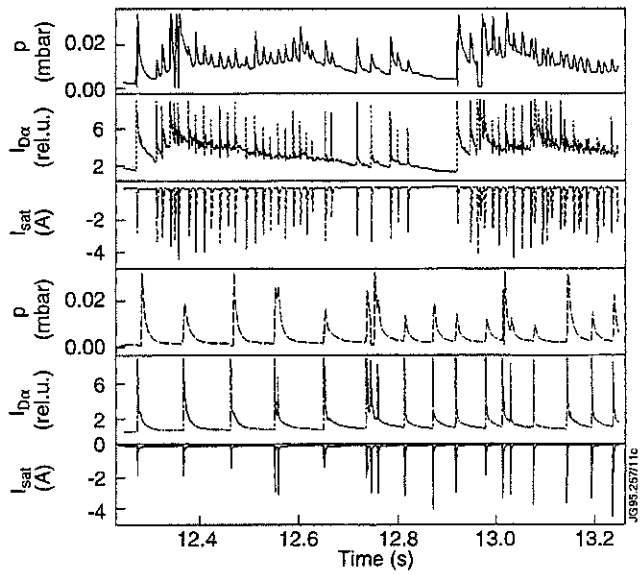

Fig.11 Time traces of the neutral gas pressure p beneath the outer target plate, the D_α intensity and the ion saturation current during two ELMy discharges with cryo pump off (pulse 32270) and cryo pump on (pulse 32285).

The behaviour of the neutral gas pressure below the divertor target plate during an ELMy H-mode is shown in fig.11 for two extreme conditions: cryo pump on and off. Each ELM is seen

as a spike in the pressure signal [11]. Additionally, there is a "pile-up" of the base line pressure in the case of cryo pump off. The D_α intensity shows the same "pile-up" behaviour, whereas the ion saturation current does not show this feature. That means the pile up is caused by neutral gas not taking part in the recycling process. Obviously, there is a strong neutral gas source at the target caused by the ELMs. This additional gas can be removed by operating the cryo pump which is located below the target in the region of the outer strike point. With the cryo pump on the ELM frequency is reduced. Presumably, the neutral influx near the X-point region influences the ELM generation mechanism.

ACKNOWLEDGEMENT

The support of Task Force H and the continuous help of P van Belle with data processing is gratefully acknowledged.

REFERENCES

1 T.T.C. Jones et al., "The Route to High Performance on JET", this conference.
2 V.V. Parail et al.,"The Physics of L and H mode confinement in JET", submitted to Nucl. Fusion.
3 D.N. Hill et al., Nucl. Fusion 28 (1988) 902.
4 J. Lingertat et al.,"The Effect of ELMs on the JET Divertor Plasma", Proceedings of the IPP/JET/Culham Workshop on H-mode and Boundary/Divertor Physics, JET 7 - 8 Nov. 1994.
5 O. Pogutse et al.,"Edge Modes as ELM Events", this conference
6 M.F.F. Nave et al., Nucl. Fusion 35 (1995) 409.
7 P.J. Harbour et al., J. Nucl. Mater. 162-164 (1989) 236.
8 H. Zohm et al., 20th EPS Conf. on Contr. Fusion and Plasmaphys., Europhysics Conference Abstracts 17C, 19.
9 K. Lackner et al., Plasma Physics and Controlled Fusion 26 (1984) 105.
10 T.C. Hender et al.,"Influence of Edge Instabilities on JET High Performance", this conference.
11 G.R. Saibene et al., "Effects of active pumping and fuelling on divertor plasma discharges in JET", this conference.

Effect of the Toroidal Field Reversal on Divertor Asymmetries

A V Chankin[1], D Campbell, S Clement, S Davies, A Loarte, G F Matthews, R Monk, R Reichle, G Saibene, M Stamp, P C Stangeby[2].
JET Joint Undertaking, Abingdon, Oxfordshire, OX14 3EA, UK.
[1] and Scientific Centre "Kurchatov Institute", INF, Moscow, Russia.
[2] University of Toronto, Institute for Aerospace Studies, Ontario, Canada.

INTRODUCTION

A series of discharges with B_T, I_p scans and both B_T directions has been performed in JET to separate the effects of the ∇B reversal from the possible dependence of asymmetry on plasma core density, confinement regime, type and repetition of ELMs.

In the normal magnetic configuration (ion ∇B drift directed towards the target) the outer strike zone usually receives higher heat flux leading. Before the installation of the MK1 divertor target, this led to the target overheating and eventually dergaration of the discharge performance due to high impurity influx (see e.g. [1]). Non-even heat flux distribution to the target aggravates power exhaust problem for ITER. In the reversed configuration (ion ∇B drift directed away from the target) the power to the target is distributed more symmetrically (see e.g. [2,3]).

The toroidal field reversal also affects the asymmetry of H_α, radiation power, n_e, T_e.
In high recycling plasmas with the ∇B reversed (see e.g. [4] and refs. therein, [5]):

- the in/out n_e ratio decreases
- the in/out T_e ratio increases,

leading to a more symmetric distribution between the strike zones, compared to much denser and cooler plasma at the inner side with high radiation and recycling in normal ∇B.

What is not clear? Are field reversal effects caused by:

- different parameters in normal/reversed ∇B plasmas (bad reproducibility of pulses)
- power redistribution between the two divertor branches as a primary source
- n_e redistribution between the sides, and if so, is it due to classical drifts? which drifts?

EXPERIMENTAL RESULTS

JET divertor plate consists of rows of individual tiles (≈35x80mm^2 size),designed to protect exposed edges (Fig.1)

IR measurements: **1D** IR array (along the major radius), photon flux averaged along toroidal direction (see [6] for details)

Temperature distribution: essentially **2D**, due to poloidal and toroidal inhomogeneities

Power calculations: **3D** program, angles between B-lines and tiles surfaces incorporated.

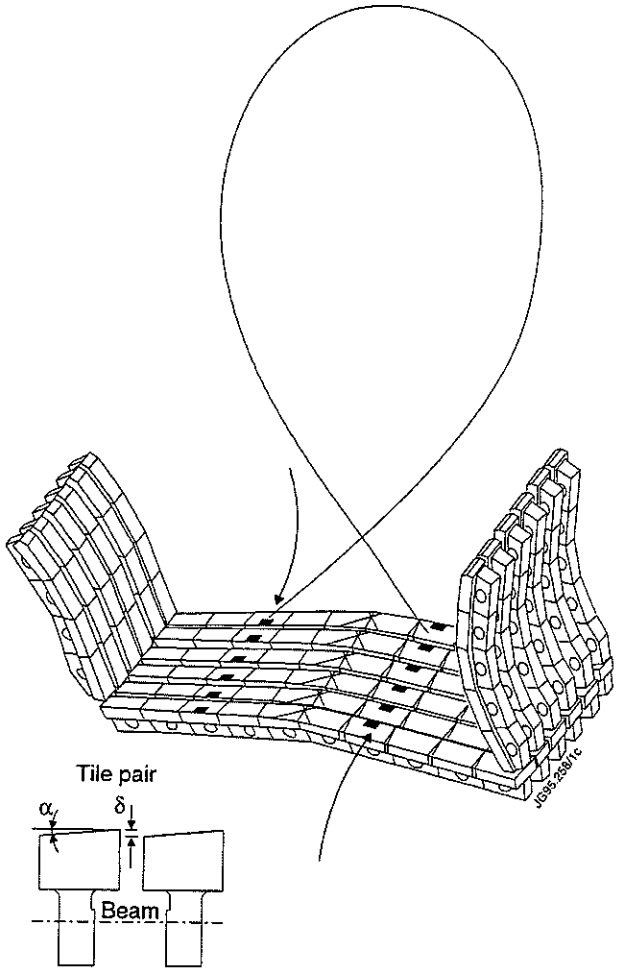

Fig.1: JET Divertor plate (three tiles' supporting beams shown)

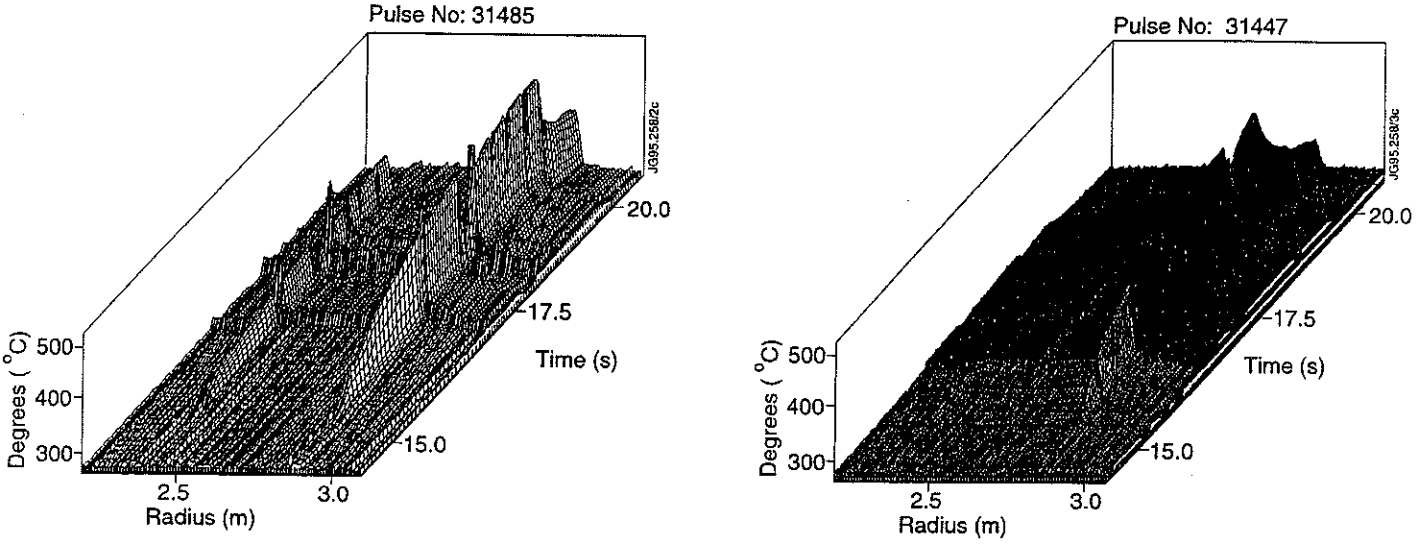

Fig.2: IR target temperature profiles for q_{95}=3.6 case: a) normal ∇B, b) reversed ∇B.

A series of L-mode discharges with medium to high density and 2.7-4.2 MW NBI input power was selected for comparison between normal and reversed SYMBOL 209 \f "Symbol"B. Both BT and Ip were reversed simultaneously.

Table 1 summarises experimental results.

q_{95}	I_p (MA)	B_t (T)	n_e (m-3/ e+19)	P_{in} (MW)	P_{rad} total (MW)	P_{target}(MW)= inner side + outer side	P_{rad}(MW/m2) , at strike zone inner side / outer side	H-alpha rad. (ph./E+15), inner side / outer side
2.3	2	1.5	18.0	3.8	2.2	Not available	0.12/0.11 = 1.1	2.3/1.4 = 1.64
	-2	-1.5	12.0	5.3	1.4	3.4 = 1.7+1.7	0.08/0.105 = 0.76	2.8/3.8 = 0.74
2.6	3	2.4	10.6	4.1	1.0	2.5 = 0*+2.5	0.08/0.042 = 1.9	1.85/1.25 = 1.48
	-3	-2.4	9.5	5.7	1.1	4.5 = 1.7+2.8	0.054/0.061 = 0.89	1.66/1.93 = 0.86
3.6	3	3.3	8.0	5.0	1.1	3.8 = 0*+3.8	0.1/0.056 = 1.79	4.2/2.3 = 1.83
	-3	-3.3	8.3	5.2	1.05	3.7 = 0.9+2.8	0.068/0.096 = 0.71	1.6/2.0 = 0.8
3.7	2	2.4	7.5	4.7	1.3	2.8 = 0*+2.8	0.112/0.007 = 1.6	8.8/3 = 2.9
	-2	-2.4	7.8	5.0	1.2	3.7 = 0.9+2.8	0.062/0.108 = 0.57	1.7/2.7 = 0.63
4.2	2	2.8	8.3	5.1	1.8	2.8 = 0.5+2.3	0.142/0.136 = 1.04	15.5/4.5 = 3.4
	-2	-2.8	8.2	4.7	1.2	2.3 = 0*+2.3	0.092/0.107 = 0.86	2.25/3.75 = 0.6
5.1	2	3.3	8.0	4.5	1.6	2.9 = 0.9+2.0	0.13/0.087 = 1.5	20/4.5 = 4.4
	-2	-3.3	7.5	4.8	1.5	3.1 = 0*+3.1	0.097/0.133 = 0.73	2.0/4.0 = 0.5

*Table 1: Comparison between normal (positive B_T and I_p) and reversed (negative B_T and I_p) field discharges. * - surface temperature from the IR camera is below the background level.*

The power balance calculations are benchmarked by comparing (P_{input}-P_{rad}) with the calculated P_{target} (0* reflects power conducted to the inner target below 0.5 MW: IR temperatures below the detection level).

- Reversed field series shows q-dependence of power distribution between the sides:

more equal power sharing at low q95 [7]

Fig.3 shows q-dependence of in/out ratios of local radiated power, P_{rad}, and H_α intensity from Table 1, and in/out ratio of peak I_{sat} values at the strike zones (from Lagmuir probes). However, since low q shots have higher density, some influence of the density dependence is not excluded.

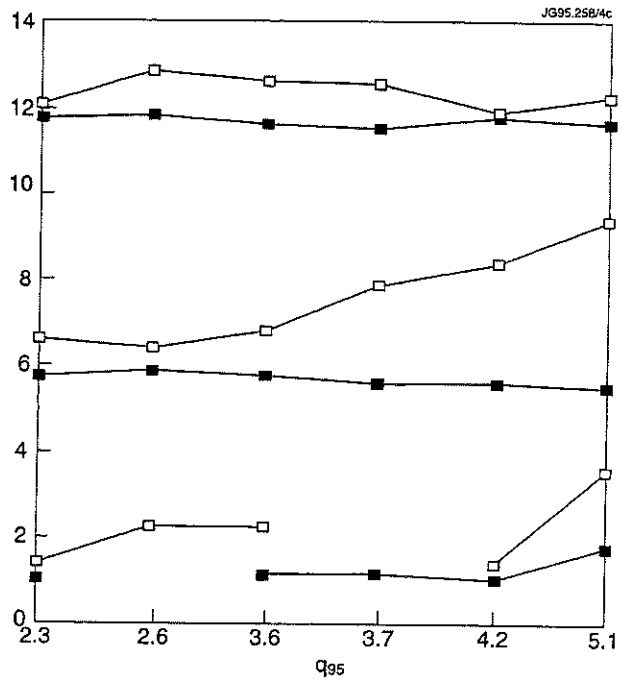

Fig.3: q-dependence of in/out asymmetries in local radiated power, H_α intensity and peak ion saturation current density

DISCUSSION

- The most persistent trend of ∇B reversal is the reversal of P_{rad}, H_α and I_{sat} asymmetries.

- T_e asymmetry: in/out ratio of T_e is generally lower in the normal field case. However, the experimental evaluation of T_e from Langmuir probes at densities of ~10^{20} m^{-3} is problematic (see [8] for details). T_e, as calculated from the probe data, is within 15-20 eV, but this value is overestimated (calculated power to the inner side is much less then that from the IR data).

- Power asymmetry: at q_{95}=4.2 and 5.1 "anomalous" behaviour was observed: more equal distribution in normal than in reversed ∇B. Highest P_{rad} and H_α were observed at the inner side in normal field, pointing to high n_e and low T_e plasma. (Bremsstrahlung contribution to the photon flux at the inner side can be significant, but it is unlikely to be a dominant effect, see below).

- For the series of discharges analysed the peak I_{sat} in normal field discharge with q_{95}=5.1 (#31591) reached 90 A/cm^2. Half of the measured total IR power to the inner side (0.45 MW) could be attributed to the surface recombination of the ion flux at the target.

A possible explanation for "anomalous" behaviour of power asymmetry at high q_{95}:

- due to a sharp drop in T_e, recombination power flux, $P_{rec} \sim 13.6eVxn\sqrt{T_e}$, becomes important compared to the sheath dominated power flux, $P_{sheath} \sim 7\, n_e T_e^{3/2}$ [7].

Provided P_e=const, $n_e^{in}T_e^{in}=n_e^{out}T_e^{out}$. Power deposition to the (cooler) inner side can be larger or smaller than that to the outer side depending on which mechanism of power deposition (recombination or sheath dominated) is the dominant one:

- Conventional picture (sheath dominated): $P_{target} \sim n_e T_e^{3/2}$.
  $P^{in}_{target} \sim P^{out}_{target} \times \sqrt{T_e}^{in}/T_e^{out}$, and power to the inner side is reduced at low T_e^{in}.

- Recombination dominated case: $P_{target} \sim n_e\sqrt{T_e}$.
  $P^{in}_{target} \sim P^{out}_{target}/\sqrt{T_e}^{in}$, and power to the inner side is increased at low T_e^{in}.

Experimental data support the following explanation for the effect of the ∇B reversal on the divertor asymmetries:

- ∇B reversal affects density/particle flux asymmetry first

- P_{target} asymmetries are affected through changes in density asymmetries

- The higher density/particle flux to the inner side in normal ∇B causes lower power deposition to the target (up to the point where recombination power becomes important)

Effect of **ExB** drifts on the particle redistribution between the sides:

Both poloidal and radial **ExB** drifts change their direction when the B_T is reversed. Fig.4 gives their directions for the normal ∇B.

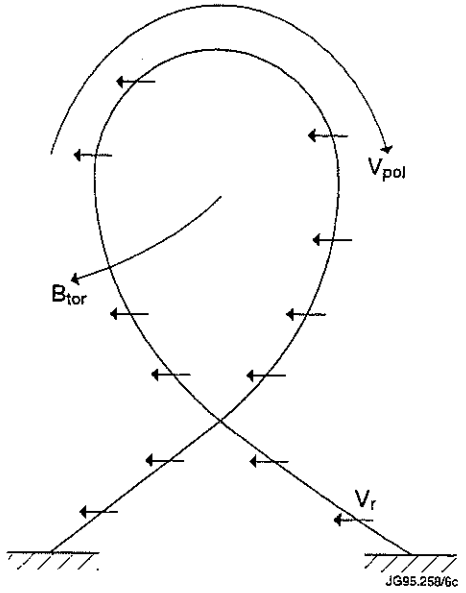

*Fig.4: Directions of radial and poloidal **E x B** drifts for the case of ion ∇B drift towards the target. These directions reverse for the reversed ∇B*

- poloidal **E** x **B** drift (analysed in [9,10]) shifts n_e in opposite direction compared to experiment
- radial **E** x **B** drift (suggested in [11]) shifts n_e in the same direction as in experiment
- in high recycling plasmas with low T_e at the target radial **E** x **B** drift dominates the poloidal one [12]

DENSITY LIMIT AND DETACHMENT

Significant difference between normal and reversed ∇B plasmas was observed approaching density limits (see [13] for details).

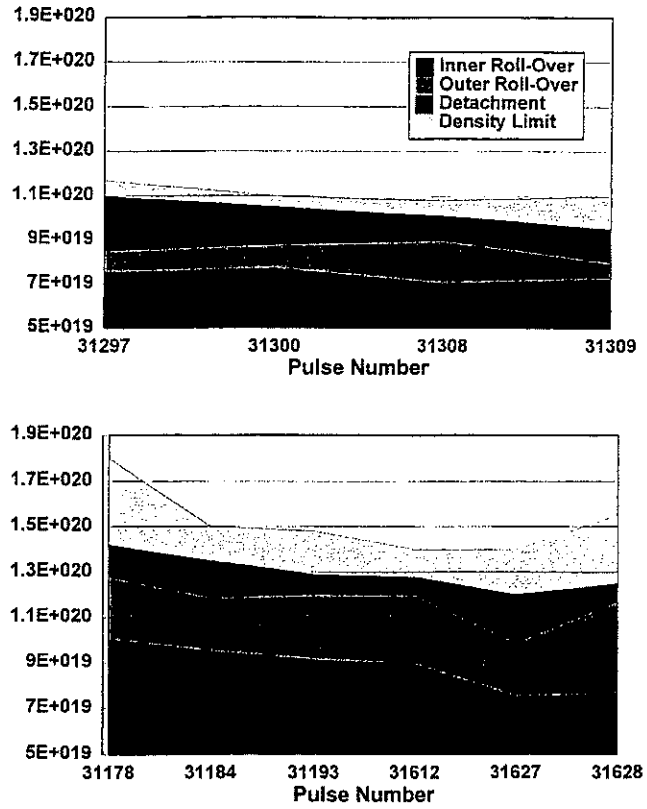

Fig5: Threshold density for "roll-over" of ion saturation current at the strike zones, detachment and disruption in Ohmic discharges: a) reversed ∇B, b) normal ∇B.

- The threshold density for "roll-over" of I_{sat} at the inner side, which indicates the beginning of the detachment, is lower for the reversed ∇B discharges. The "roll-over" at the outer side, followed by the plasma detachment, also starts at lower densities in reversed field plasmas.
- In normal ∇B discharges the operational density range is much wider with higher densities achieved (all the reversed field discharges were with B_T=2.7 T, I_p =2.7 MA, while the normal field discharges were with B_T=2.7 T, I_p =2.0 MA (all except one) and B_T=3.3 T, I_p =2.9 MA in #31612). In the reversed ∇B the density limit starts almost immediately after detachment.
- The distribution of plasma density and temperature between the strike zones is more symmetric in the reversed ∇B discharges, and the reason for the much narrower density range before the disruption in the reversed field plasmas is unclear.
- earlier disruptions in reversed ∇B plasmas are not associated with "power starvation" of the scrape-off layer compared to the normal ∇B discharges: calculated power to the target, (P_{input}-P_{rad}), is similar in both field configurations.

CONCLUSIONS

- the most persistent experimental feature of high recycling L-modes in JET is the reversal of H_α, P_{rad}, and I_{sat} asymmetries between the strike zones

- influence of the ∇B reversal on P_{target} asymmetries is more complex and is likely to be a secondary effect following density redistribution between the sides

- increase in n_e at the inner strike zone in the normal ∇B (compared to reversed ∇B case) is associated with the decrease in T_e and the decrease in P_{target} (low q_{95} data). This agrees with P_e=const and $P_{target} \sim n_e T_e^{3/2}$ (sheath dominated power flux).

- further increase in n_e / I_{sat} at the inner side and the associated drop in T_e (only indirect evidence for that is available) can lead to an increase in P_{target} (compared to the reversed ∇B) due to surface recombination of the ion flux, provided plasma stays attached to the target and the pressure is maintained.

- n_e redistribution between the sides caused by the ∇B reversal is consistent with the effect of the radial **E** x **B** drift, which is the dominant drift term in high recycling plasmas.

REFERENCES

[1] Reichle R. et al 1991 Proc. 18th Eur. Conf. on Contr. Fusion and Plasma Phys. (Berlin, 1991) vol 15C, part 3, p 105.

[2] Janeschitz G. et al 1993 Proc. 20th Eur. Conf. on Controlled Fusion and Plasma Phys. (Lisboa, 1993) vol 17C, part 2, p 559.

[3] Reichle R., Summers D.D.R., Stamp M.F., J. Nucl. Mater. 176&177, 375 (1990).

[4] Chankin A.V., Clement S., Erents S.K. et al., Plasma Phys. Control. Fusion 36 (1994) 1853.

[5] Asakura N., Itami K., Hosogane N. et al, J. Nucl. Mater, 220-222 (1995) 395.

[6] Clement S. et al., this conference.

[7] Campbell D.J. and the JET team, in 15th Int. Conf. on Plasma Phys. and Contr. Fusion Research, Seville, Spain, Spain (1994).

[8] Guenther K., this conference.

[9] Tendler M. and Rozhansky V., Comments Plasma Phys. Controlled Fusion 13 (1990) 191. [10] Cohen R.H., Ryutov D., Comments Plasma Phys. Controlled Fusion 35 (1993) 1271.

[11] Staebler G.M., Nuclear Fusion 31 (1991) 729.

[12] Stangeby P.C., Chankin A.V., JET-P(95)07, submitted to Nuclear Fusion.

[13] Monk R. et al, this conference.

Divertor Plasma Detachment in JET

R D Monk[1], D J Campbell, S Clement, S J Davies, J Ehrenberg, S K Erents[2], H Y Guo[3], L D Horton, A Loarte, C G Lowry, J Lingertat, G F Matthews, A Tabasso[4], R Reichle, G Saibene, G C Vlases.

JET Joint Undertaking, Abingdon, Oxfordshire, OX14 3EA, UK.

[1] Department of Physics, Royal Holloway University of London, Surrey, TW20 0EX, UK.

[2] UKAEA Fusion, Culham, Abingdon, Oxfordshire, OX14 3DB, UK.

[3] INRS-Energie et Materiaux, Université du Quebec, Canada.

[4] Imperial College of Science, Technology and Medicine, London, SW7 2BZ, UK.

1. INTRODUCTION

The divertor configuration has been successfully employed in many present day tokamaks to reduce impurity contamination of the plasma core. Given the large power exhaust expected from a reactor plasma (such as ITER) and reasonable estimates for the width of the scrape-off layer, it is clear that the divertor target will not survive without some additional means to dissipate a significant fraction of the power. By creating a cold and dense plasma in the divertor it is possible to access a "detached" regime [1] whereby atomic physics loss mechanisms, such as charge exchange and hydrogenic radiation provide significant reductions in the particle, momentum and energy fluxes to the target plates. Detached divertor plasmas are now considered the primary solution to the problem of engineering the ITER divertor. Consequently, experiments have been carried out in the JET tokamak using the new pumped divertor configuration to investigate plasma detachment under a wide range of conditions. This paper outlines the results from experiments where only the intrinsic impurities (e.g. carbon and beryllium) are present., while impurity seeding experiments are described by Matthews et al. and Reichle et al., this conference.

2. DIAGNOSTIC SYSTEMS

- An array of single and triple Langmuir probes mounted in the divertor target.
- Reciprocating Langmuir probes that measure profiles of the main SOL.
- Spatially resolved and fast integrated D_α and C-II (or Be-II) in the divertor.

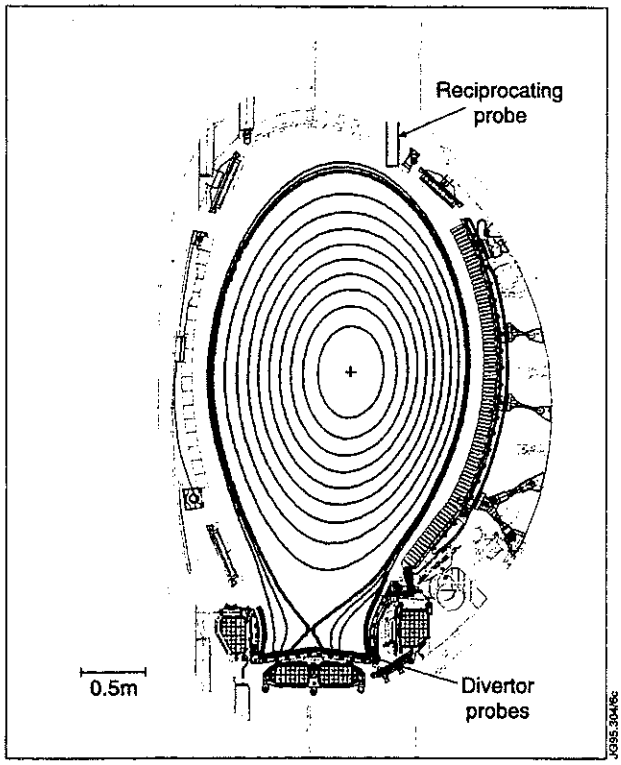

Figure 1 : Cross-section of the JET pumped divertor configuration with an example of a reconstructed plasma equilibrium used for divertor physics.

- Infra-red thermography of the divertor surface.
- Bolometer array.
- Divertor neutral pressure gauges.

3. DETACHMENT REGIMES

3.1 Ohmic Plasmas

As the plasma density $\langle \bar{n}_e \rangle$ is increased by gas puffing the following features are generally observed (figure 2) :-

- The ion flow (I_{sat}) to the divertor target, D_α photon flux and neutral pressure increase more than linearly with $\langle \bar{n}_e \rangle$ - "high recycling".
- Approaching $\langle \bar{n}_e \rangle \approx 3 \times 10^{19}$ the I_{sat} reaches a peak value and begins to "roll-over".

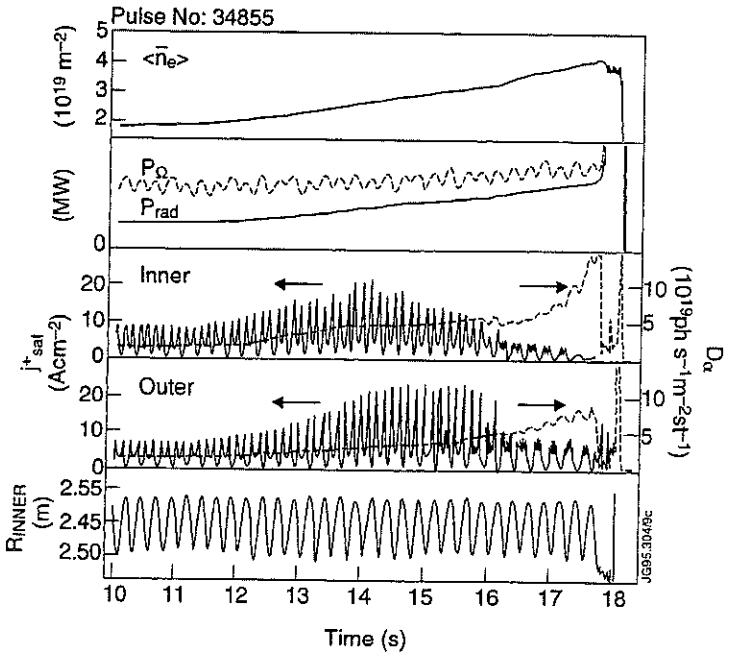

Figure 2 : Characteristics of divertor detachment during an ohmic discharge.

- While D_α and neutral pressure continues to increase, the I_{sat} falls to low values - "detachment".
- Finally, if the main plasma density is further increased a "MARFE" escapes from the divertor with a characteristic drop in the D_α signal and usually ends in a density limit disruption.
- Detachment begins near the separatrix at the inner strike zone and moves outwards into the SOL while the outer strike zone starts to detach at a slightly higher density.

Since the strike points are swept across the target plates at 4Hz to reduce the power loading, it is possible to construct high resolution radial profiles from the triple Langmuir probes (see figure 3).

- During the high recycling phase, the electron temperature at the divertor plates falls and the associated reduction in sputtered impurities is reflected by the level of Be-II emission.
- The D_α intensity increases across the whole profile and a large peak in I_{sat} is seen to emerge from a broader exponential profile on the outer divertor plate.
- Langmuir probe characteristics under these high density conditions tend to exhibit low electron to ion saturation current ratios (in some cases <1) which is reflected in an overestimation of T_e and

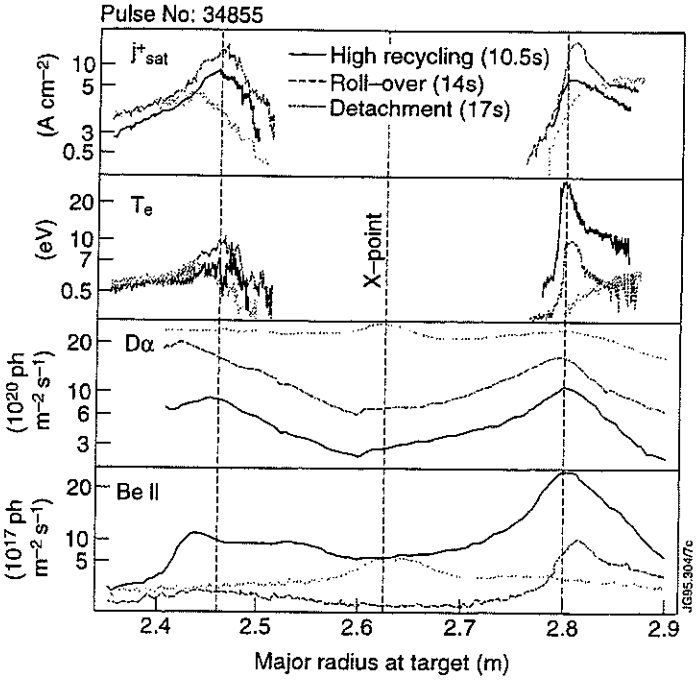

Figure 3 : Spatial profiles of ion saturation current (I_{sat}), electron temperature (T_e), D_α and Be-II photon fluxes across the divertor target.

subsequently of the calculated power flux. (A new approach to the interpretation of probe characteristics under these conditions is described in the poster by Gunther, this conference).

- As the plasma detaches, the I_{sat} near the separatrix drops by an order of magnitude and the T_e falls to approximately 2eV at the inner plate and 3eV on the outer. The D_α profile broadens and has a peak value in the vicinity of the x-point rather than the strike points.
- Complete detachment is usually only observed at the inner strike zone while the outer is partially detached.
- Throughout this period, the maximum in radiated power determined from the bolometer array is seen to migrate from the strike zones to the x-point region (see figure 7 for the L-mode example).
- Close to the density limit the peak in radiated power appears to be located inside the separatrix just above the x-point.
- The bremsstrahlung radiation seen by the infrared camera indicates a region of very high density (>$10^{20}m^{-3}$) in the vicinity of the x-point.
- Detachment is observed to be a gradual process rather than a bifurcation and typically develops over a timescale of seconds.

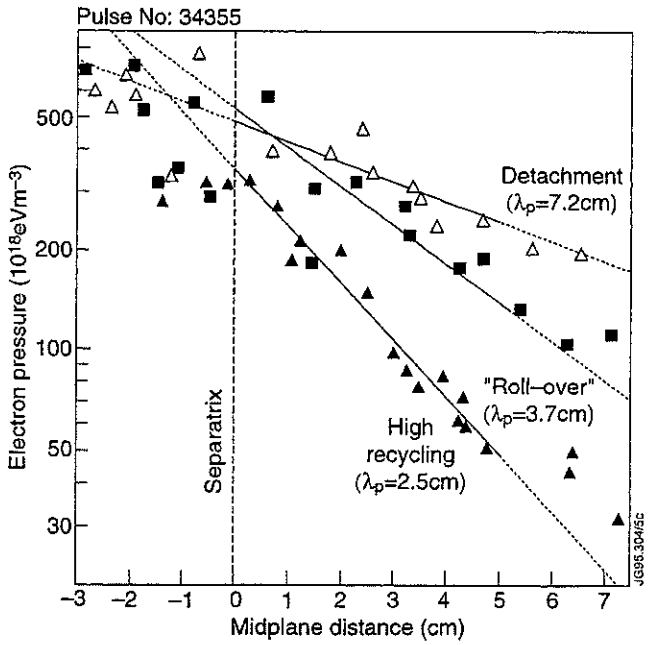

Figure 4 : Scrape-off layer profiles measured by the reciprocating probe indicating the broadening of the pressure profile on the approach to detachment.

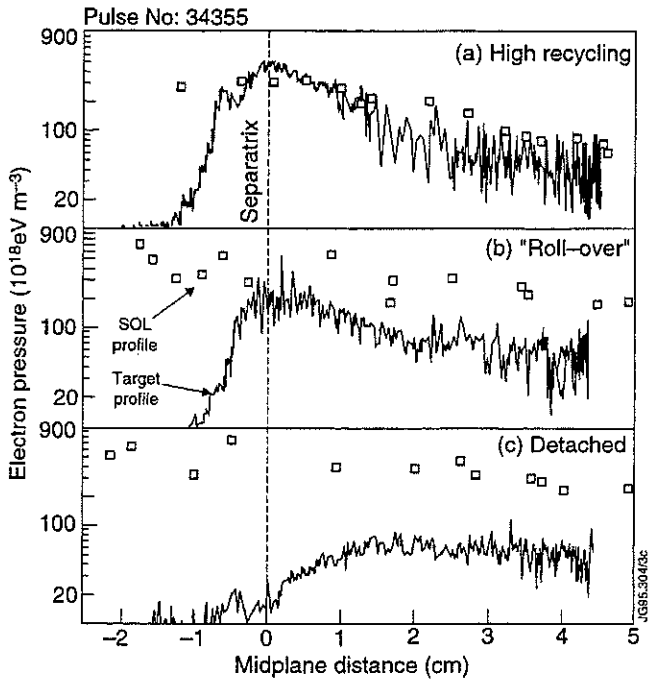

Figure 5 : Comparison of scrape-off layer and divertor pressure profiles from an outer target triple probe showing the drop in electron pressure as the plasma detaches.

3.2 L-Mode Plasmas

- Similar general trends are observed for the L-mode plasmas as for the ohmic cases.
- Steady-state detached discharges of >5s have been produced on carbon and beryllium divertor targets with 3-4MW of neutral beam heating.
- Feedback control of the D_2 injection using the divertor probe I_{sat} has been used to operate with stable detached plasmas close to the density limit [2].

- Profiles of the scrape-off layer measured by the reciprocating probe show that the upstream pressure at the separatrix remains constant but the fall-off lengths broaden by almost a factor of three in moving to detachment (figure 4).
- Divertor probe measurements indicate that during the "high recycling" phase there is approximate electron pressure balance at the separatrix between target and the upstream scrape-off layer.
- During the detached phase there is an order of magnitude drop in the separatrix electron pressure measured at the target compared to the upstream SOL (figure 5).
- Throughout the discharge the peak surface temperature of the divertor target stays below the detection threshold of 380°C for the infra-red thermography system.

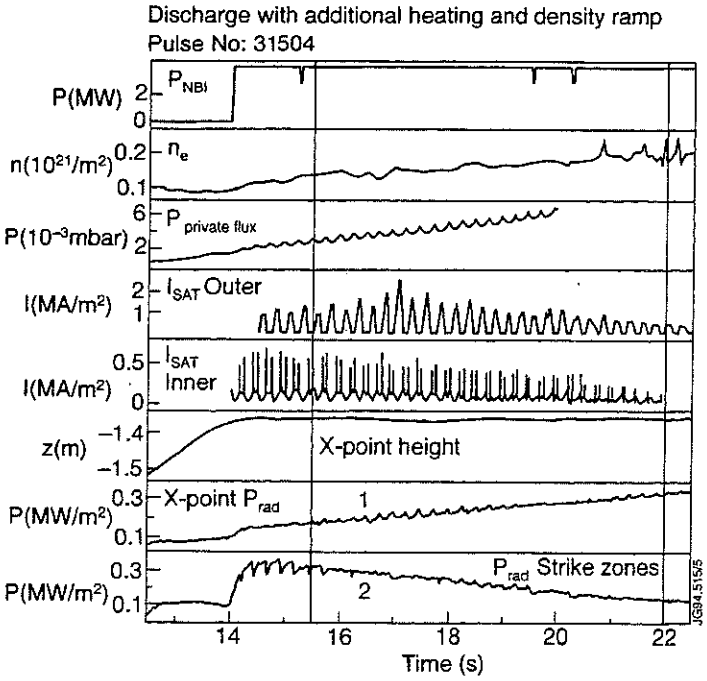

Figure 6 : Overview of plasma parameters for an L-mode density ramp discharge from which the distribution of radiated power is shown below.

- Density limits are observed to occur when the radiated power fraction exceeds approximately 70% (carbon target) or 85% (beryllium target) with the formation of a MARFE.
- I_{sat} measurements from probes mounted in the side panels of the divertor target show that there is no evidence for enhanced cross-field losses of ions during detachment.

The role of geometrical effects and the influence on the characteristics of detachment is discussed by Loarte et al., this conference.

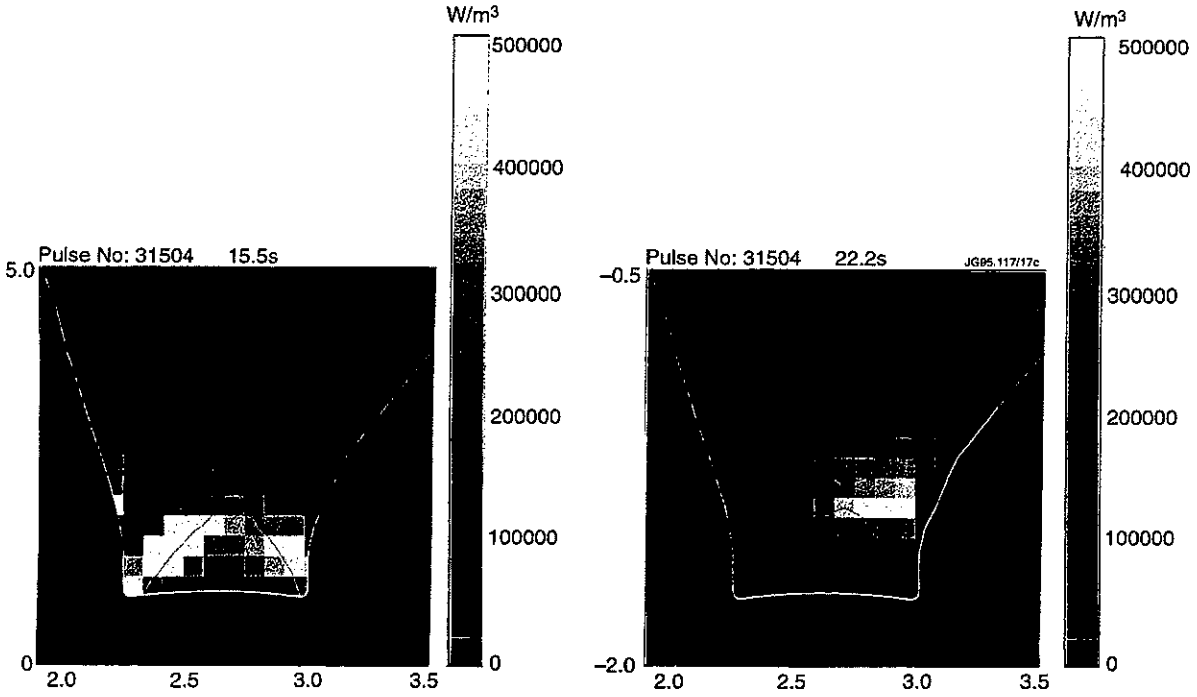

Figure 7 : Tomographic reconstruction of the Radiated Power during (a) the attached phase at 15.5s and later (b) during detachment at 22s.

3.3 H-Mode Plasmas

- With D_2 gas injection into ELMy H-modes it is observed that the ELM frequency increases and the energy confinement time is degraded (figure 8).
- At radiated power fractions of approximately $P_{rad}/P_{in} \approx 50\%$ there is a transition back to the L-mode which effectively determines the H-mode density limit.
- At the highest densities compatible with H-mode operation, the I_{sat} between ELMs is reduced.
- However, it is highlighted by Clement et al., this conference, that the net effect of increasing the density is to *increase* the peak temperature measured by IR thermography. This is due to the degraded energy confinement and reduced spreading of the power load due to the high frequency "grassy" ELMs.
- Since the power and particle fluxes are dominated by the ELMs, this has motivated investigations into impurity seeded plasmas in an attempt to obtain acceptable core plasma confinement times and low power fluxes to the divertor target (see Matthews et al. and Reichle et al., this conference).

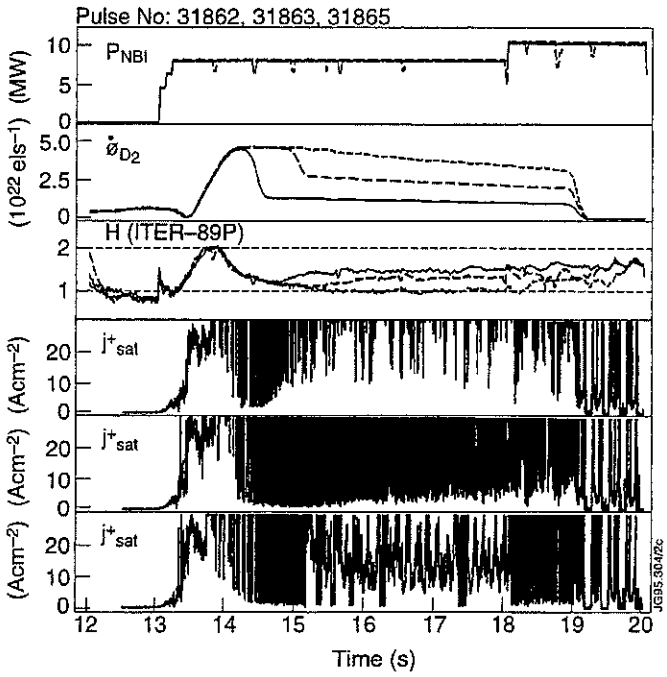

Figure 8 : The effect of D_2 injection into ELMy H-modes on the ITER89-P energy confinement scaling and I_{sat} divertor probe measurements.

4. THE EFFECT OF THE ION B DRIFT DIRECTION

- On JET and other tokamaks it has been observed that directing the ion B drift direction away from the divertor target can result in more symmetric power deposition at the inner and outer strike zones, see Chankin [this conference].
- In terms of divertor detachment, the behaviour with the ion B drift away from the target is similar to the normal configuration with the I_{sat} roll-over occurring at similar main plasma density (figure 9).

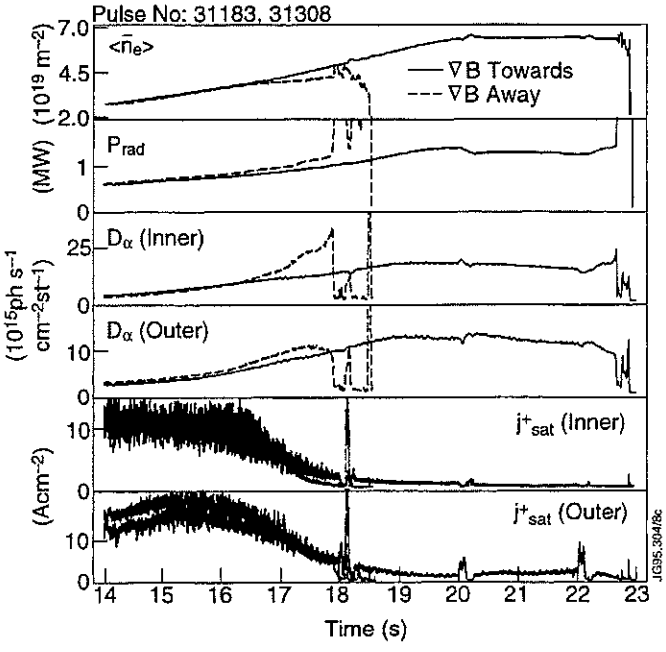

Figure 9 : Comparison of ohmic density ramp discharges in normal and reverse B_T directions (Note that the D_2 fuelling rate is identical in both cases).

- However, in ohmic discharges it the density limit and consequently the operating window for detachment, is reduced by approximately 30% compared to the normal field case.

5. THE COMPARISON OF CARBON AND BERYLLIUM DIVERTOR TARGETS.

- The general behaviour during the approach to detachment and the density limit is similar during high density operation with carbon and beryllium divertor targets (figure 10).
- With the beryllium target it has been possible to sustain L-mode detached plasmas with up to 85% radiated power fraction compared with 70% for the equivalent carbon case.
- However, for the beryllium discharges studied it appears that the additional radiation is due mainly to the core plasma region rather than the divertor.
- Preliminary results from the beryllium campaign suggest that carbon remains the dominant source of impurity radiation in the divertor region. This may be due to the carbon first wall protection and limiters.

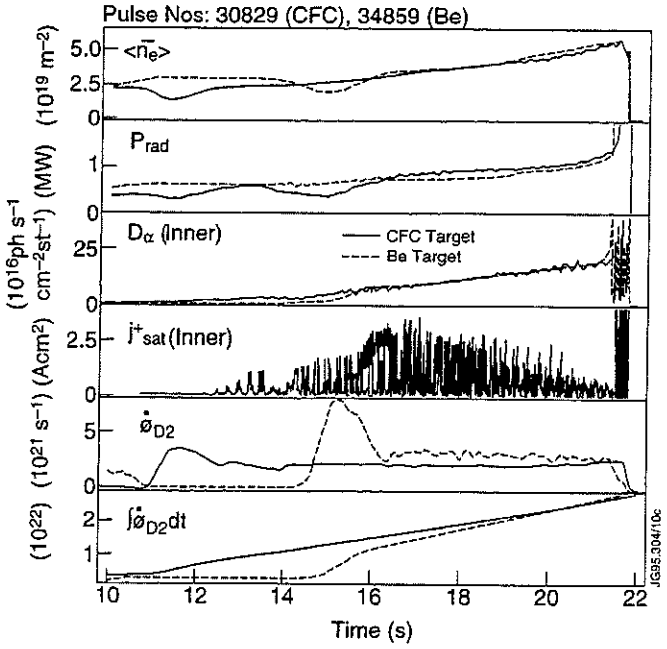

Figure 10 : Density limit discharges in carbon and beryllium with similar integrated gas input (cryopump off)

6. THE "DETACHMENT WINDOW"

- As an operational definition we take the detachment window to be the headroom (in terms of main plasma density) between the "roll-over" of the ion flow to the plates and the density limit.
- In general, it is observed that the "roll-over" and density limit scale weakly as a function of the input power (figure 11).
- Increased flux expansion appears to allow access to detachment at lower main plasma densities although the density limit also scales accordingly.
- Wall clearance and plasma purity are of course critical in achieving a favourable split between divertor and bulk radiation (typically 2:1 for most equilibria used for divertor physics studies) and consequently maintaining a high density limit.
- As highlighted by Saibene [this conference], the cryopump can also locally influence the degree of detachment,

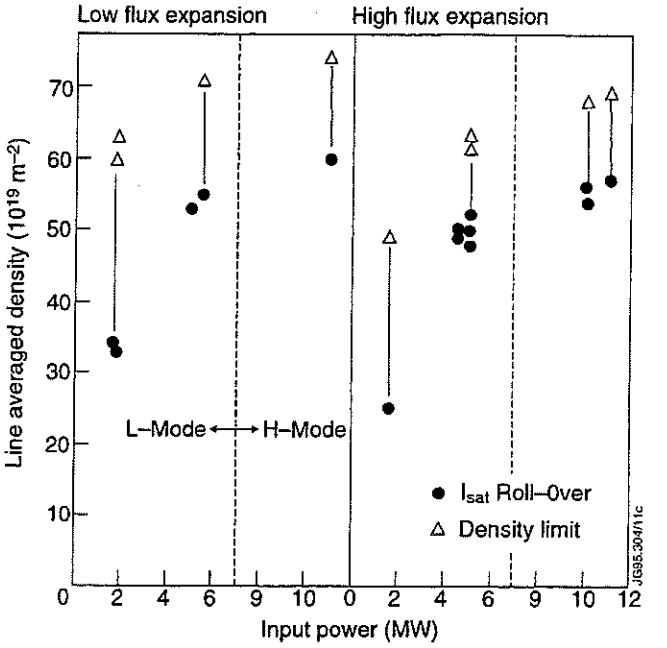

Figure 11 : Scaling of the detachment window (between the "roll-over" in I_{sat} and the density limit) with input power and main plasma density for discharges with high and low flux expansion (Note: The H-mode density limits are non-disruptive)

presumably through the reduction of neutral gas pressure, without significantly changing the main plasma density.

7. DIVERTOR OSCILLATIONS ON THE APPROACH TO DETACHMENT

During L-mode high density discharges, periods of unstable behaviour in the divertor and edge plasma parameters are commonly observed (figure 12). These are characterised by the following observations :-

1. Dramatic drop in I_{sat}, neutral pressure, D_α, C-II/Be-II photon fluxes and radiated power at the strike zones.
2. Increase in the edge plasma density with larger D_α, C-II/Be-II emission and radiated power in the vicinity of the x-point region.
3. After typically 10ms there is a large increase in I_{sat} that resembles an ELM, with associated strong C-II/Be-II and bolometer signals at the strike zones.
4. The divertor plasma re-attaches to the target and the parameters return to the equilibrium conditions for approximately 50-100ms and then the cycle repeats.

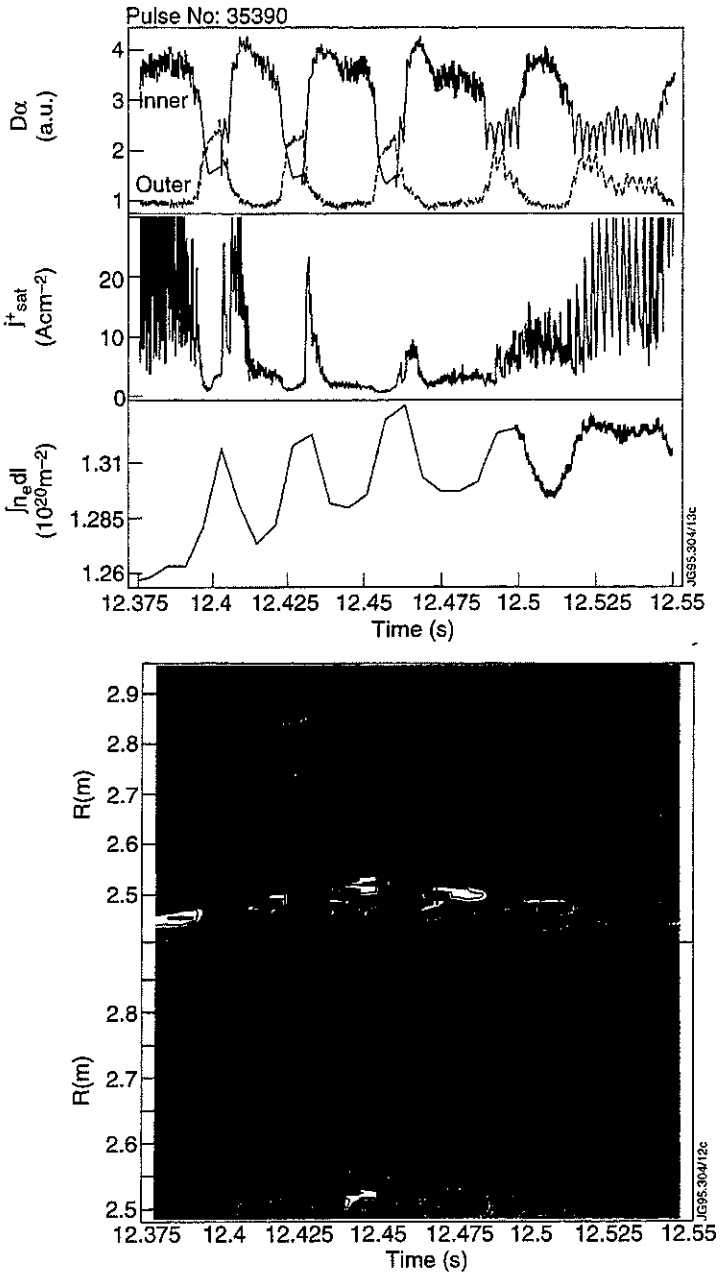

Figure 12 : Experimental evidence for unstable divertor and edge plasma parameters during high density L-mode discharges.

- The oscillations are observed to occur over a reproducible range of input power and density and are most evident in the approach to the "roll-over" when the I_{sat} is high and T_e is in the region of ≤10eV.
- The frequency of the oscillations increases with the level of power flowing into the scrape-off layer. They cease during the detached phase when the radiation approaches 60-70% of the input power.
- Such periodic detachment may be driven by the requirement to maintain the principal impurity source, i.e. the interaction of the divertor plasma with the target.

- The increase in the edge density with the detachment is probably associated with the ionisation of the neutral particles inside the separatrix which were previously confined to the divertor region.
- However, further work is required to determine the role of the edge plasma in these phenomena and examine the impurity and radiation distribution in more detail.

8. CONCLUSIONS

- Steady-state detached plasmas with 70-80% radiated power can be achieved with D_2 injection for ohmic and L-mode plasmas.
- During detachment the parallel pressure is observed to fall by over an order of magnitude in moving from the scrape-off layer to the divertor target where electron temperatures of 3-5eV are measured.
- During high density H-modes the ion flow to the divertor can be reduced in-between ELMs although the confinement is degraded and reverts to L-mode at around 50% fractional radiated power.
- Operating with the ion ∇B drift direction away from the divertor target lowers the density limit without lowering the density at which detachment begins. Consequently, the operating window for stable detached plasmas is much narrower than for the normal field case.
- Similar detachment and density limit behaviour is observed with carbon and beryllium although higher radiated power fractions (85% compared with 70%) can be sustained with the beryllium target.
- During high density L-mode plasmas a form of periodic detachment is frequently observed which is correlated with changes in the divertor and edge plasma parameters. The phenomena decrease in frequency as the fraction of radiated power increases.

ACKNOWLEDGEMENTS

RDM acknowledges financial support from the Engineering and Physical Sciences Research Council and the JET Joint Undertaking.

REFERENCES

[1] G.F. Matthews, Journal of Nuclear Materials **220-222** (1995) 104

[2] The JET Team (Presented by D.J. Campbell), IAEA-CN-60/A-4-I-4, 15th International Conference on Plasma Physics and Controlled Fusion Research, Seville, Spain (1994).